Edited by B C Gilbert, M J Davies and D M Murphy

Electron Paramagnetic Resonance

Volume 21

Volume 21

A Specialist Periodical Report

Electron Paramagnetic Resonance

Volume 21

A review of the literature published between 2006 and 2007

Editors
B. C. Gilbert, *University of York, UK*
M. J. Davies, *Heart Research Institute, Sydney, Australia*
D. M. Murphy, *Cardiff University, Cardiff, UK*

Authors
D. Becker, *Oakland University, Michigan, US*
D. Beckert, *University of Leipzig, Leipzig, Germany*
A. B. Boeer, *The University of Manchester, Manchester, UK*
D. R. Bolton, *University of St Andrews, St Andrews, UK*
M. Chiesa, *University of Torino, Torino, Italy*
D. Collison, *The University of Manchester, Manchester, UK*
P. A. S. Cruickshank, *University of St Andrews, St Andrews, UK*
G. R. Eaton, *University of Denver, Colorado, US*
S. S. Eaton, *University of Denver, Colorado, US*
D. Goldfarb, *Weizmann Institute of Science, Rehovot, Israel*
S. K. Jackson, *University of the West of England, Bristol, UK*
P. E. James, *Cardiff University, Cardiff, UK*
E. J. L. McInnes, *The University of Manchester, Manchester, UK*
D. A. Robertson, *University of St Andrews, St Andrews, UK*
S. Ruthstein, *Weizmann Institute of Science, Rehovot, Israel*
M. D. Sevilla, *Oakland University, Michigan, US*
G. M. Smith, *University of St Andrews, St Andrews, UK*
S. Van Doorslaer, *University of Antwerp, Wilrijk-Antwerp, Belgium*

If you buy this title on standing order, you will be given FREE access to the chapters online. Please contact sales@rsc.org with proof of purchase to arrange access to be set up.

Thank you

Preface

Bruce Gilbert, Damien Murphy and Michael Davies

Volume 21 of the EPR Specialist Periodical Report series is again intended to illustrate the widespread and potentially powerful advances in the development and application of EPR spectroscopy and related ENDOR, pulse, and imaging techniques to contemporary science. We have again aimed to reflect the wide-ranging and special applications of EPR in chemistry, as well as in interdisciplinary fields including physics, material science, biology and medicine; and to provide articles of potential interest both to specialists in particular fields and to potential EPR users who wish to learn more about the scope of the technique.

Authors with specialist expertise have been invited to write authoritative, selective, and critical reviews which, whilst concentrating on major developments up to the end of 2007, also provide accounts which are set in context and give overviews suitable for potential EPR users, as well as experts currently working in the relevant fields. Emphasis, as before, is on the sophisticated information relating to structure, dynamics and interactions in paramagnetic systems.

We set out to balance different types of article in this volume, not least to provide a general overview of the range of applicability of EPR, with emphasis on some areas where progress is particularly rapid or potentially important. For example, in some cases we have continued our coverage of developments in relatively well-established fields in which detailed updates are appropriate: for example, in describing recent advances in the use of EPR in the study of metalloproteins, radiation damage to DNA and related species, and short-lived organic radicals via time-resolved techniques, as well as exchange-coupled oligomers and paramagnetic species on solid surfaces.

The scope for applications of EPR spectroscopy in other rapidly-developing fields, most notably of biological relevance, is reflected in the articles on biomedical applications of the technique and on the use of EPR for measurement of interspin distances. We have also added two distinct articles to the more regular features for this volume—a particularly timely review of progress with the development of high-field pulsed EPR instrumentation, and a survey of the use of the EPR 'toolbox' for exploring the formation and properties of ordered template mesoporous materials.

Again, we hope that EPR users, and potential users, will find these articles of value: and that readers will be encouraged in their research and interests. We would be delighted to receive feedback and suggestions for future topics.

Finally, we express our gratitude—to all out authors for sharing their expertise and for their promptness in providing their articles, and to the skills and support of the RSC staff. And, from two of us (BG, DM) our special thanks to our colleague Michael Davies, who steps down from the team this year, for his invaluable work and advice over many years as author and co-editor of the EPR series.

CONTENTS
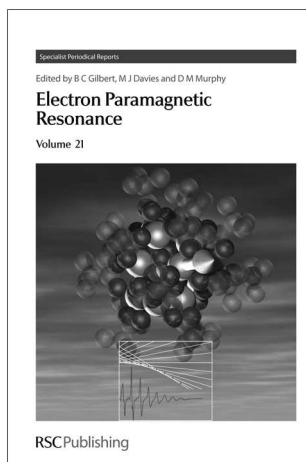
Cover

The cover depicts a single crystal EPR study of a dodeca-metallic Cr(III) cluster with an S = 6 ground state.

Specialist Periodical Reports

Edited by B C Gilbert, M J Davies and D M Murphy

Electron Paramagnetic Resonance

Volume 21

RSCPublishing

Biomedical applications of EPR spectroscopy

Simon K. Jackson and Philip E. James

EPR studies of radiation damage to DNA and related molecules   33

David Becker and Michael D. Sevilla

Measurement of interspin distances by EPR   59

Gareth R. Eaton and Sandra S. Eaton

Time-resolved electron paramagnetic resonance studies of transient organic radicals   76

Dieter Beckert

EPR of paramagnetic centres on solid surfaces   105

Damien M. Murphy and Mario Chiesa

EPR of exchange coupled oligomers 131

Angelika B. Boer, David Collison and Eric J. L. McInnes

Continuous wave and pulsed EPR analyses of metalloproteins 162

Sabine Van Doorslaer

An EPR tool box for exploring the formation and properties of ordered template mesoporous materials 184

Sharon Ruthstein and Daniella Goldfarb

High-field pulse EPR instrumentation 216

Graham M. Smith, Paul A. S. Cruickshank, David R. Bolton and Duncan A. Robertson

Biomedical applications of EPR spectroscopy

Simon K. Jackson*[a] and Philip E. James[b]

1. Introduction

EPR spectroscopy can provide useful and even unique information pertinent to the study of oxidative stress and consequent disease settings. The parameters that can be measured include (a) oxygen-centred radicals (by spin trapping); (b) carbon-centred radicals (by spin trapping and sometimes by direct observation); (c) sulphur-centred radicals (by spin trapping and sometimes by direct observation); (d) nitric oxide (by spin trapping); (e) molecular oxygen (using oxygen sensitive paramagnetic materials); (f) redox state (using metabolism of nitroxides); (g) thiol groups (using special nitroxides); (h) pH (using specific nitroxides); (i) perfusion (using wash out of paramagnetic tracers) and (j) redox active metal ions (chromium, manganese). For an excellent review the reader is referred to ref. 1. In this chapter we highlight recent biomedical applications of EPR spectroscopy. This field is vast and growing; we concentrate here on the use of EPR spectroscopy in studying reactive oxygen and nitrogen species, damage to biomacromolecules and the major disease settings associated with such damage. We also review the application of particular techniques that have evolved primarily for the biomedical field.

2. Reactive oxygen species

Perhaps one of the more influential developments during recent times has been the synthesis and characterization of better DEPMPO-type spin traps for the detection of hydroxyl and superoxide radicals. 5-(2,2-dimethyl-1,3-propoxy cyclophosphoryl)-5-methyl-1-pyrroline N-oxide (CYPMPO)[2] is a cyclic nitrone that is colourless, crystalline and freely soluble in water. In practical terms it is useful to know that this is stable as the solid or in aqueous solution and does not develop an EPR signal for at least 1 month under ambient conditions. It has readily assignable EPR spectra for both hydroxyl and superoxide adducts with no conversion from the latter to the former (as tested *in vitro* in UV-illuminated H_2O_2 solution and hypoxanthine/xanthine oxidase model systems).

Mito-DEMPO,[3] a new DEPMPO analogue bearing a triphenylphosphonium group, was synthesized *via* a novel NH_2-reactive DEPMPO. The half life of the superoxide adduct generated in intact mitochondria was >40 min. This exhibits an eight-line EPR spectrum with partial asymmetry. The mito-DEPMPO adduct formed from glutathionyl centered radicals (DEPMPO-SG) is 3-times more persistent than that of the parent DEPMPO adduct. Thus the EPR parameters of mito-DEPMPO adducts are distinctly different and highly characteristic in the case of superoxide, hydroxyl, glutathionyl and carbon-based radicals,[4] and in many cases mito-DEPMPO nitrone and its analogues are more effective than most nitrone spin traps. It has long been recognized that redox status is critical to health and is offset in disease, and EPR techniques have contributed significantly to this understanding. There is a plethora of examples where the antioxidant capacity of compounds, cells, and tissues has been tested. Tempol (4-hydroxy-2,2,6,6-tetramethyl-1-piperidinyloxy) has long been known

[a] *Centre for Research in Biomedicine, Faculty of Health and Life Sciences, University of the West of England, Frenchay Campus, Coldharbour Lane, Bristol, UK, BS16 1QY. E-mail: simon.jackson@uwe.ac.uk; Fax: 0117 3282904; Tel: 0117 3283514*
[b] *Department of Cardiology, School of Medicine, Cardiff University, Heath Park, Cardiff, UK, CF14 4XN. E-mail: JamesPP@cf.ac.uk; Fax: 029 2074 3690; Tel: 029 2074 3512*

to protect experimental animals from the injury associated with oxidative and inflammatory conditions. In the latter case, a parallel decrease in tissue protein nitration levels has been observed. Protein nitration represents a shift in nitric oxide actions from physiological to pathophysiological, and potentially damaging pathways involving oxidants derived from this species such as nitrogen dioxide and peroxynitrite. In infectious diseases, protein tyrosine nitration of tissues and cells has been taken as evidence for the involvement of nitric oxide-derived oxidants in microbicidal mechanisms. To examine whether tempol inhibits the microbicidal action of macrophages, its effects on *Leishmania amazonensis* infection *in vitro* (RAW 264.7 murine macrophages) and *in vivo* (C57Bl/6 mice) was tested.[5] The results indicated that tempol exacerbated *L. amazonensis* infection by a dual mechanism involving downregulation of iNOS expression and scavenging of nitric oxide-derived oxidants. Thus, the development of therapeutic strategies based on nitroxides should take into account the potential risk of altering host resistance to parasite infection. This work also highlights the synchrony between oxidative and nitrosative stress, and how EPR techniques can (with appropriate understanding) yield important insights; further examples are summarized in relevant sections below. Antioxidant capacity was also tested in studies using flow-injection EPR to investigate hydroxyl radical scavenging activity of Gd(III) containing MRI contrast media[6] and more recently of C60 and newly synthesized fulleropyrrolidine derivatives encapsulated into liposomes.[7]

3. Reactive nitrogen species

One of the major advantages of EPR is the specific detection of radical species. Nowhere is this better observed than in the case of nitric oxide (NO) rather than its oxidative metabolites. Thus there is considerable overlap with the cardiovascular field (below). In most cases, the spin trap will react with NO only, although great care must be taken when undertaking such experiments to ensure that the NO metabolites themselves do not generate NO in the system that can then be spin trapped. In particular nitrite is a concern, where it is critical that pH and oxygenation are maintained. An excellent example of where this has been utilized to maximum benefit is in the understanding that NO production from nitrite occurs primarily in tissues, and not in blood, and primarily by the reductase activity of tissue xanthine oxidase and aldehyde oxidase.[8] In addition, this study also highlights the use of ^{15}N isotope trapping to specifically identify the source of the nitrogen in NO (the isotope gives rise to a characteristic and readily identifiable spin trapped adduct).

The options in terms of NO spin traps include nitronyl nitroxides and their derivatives (cPTIO, tPTIO) that can be used to report on NO in general or, as in the former case, from intracellular locations. These compounds have been used ubiquitously in cardiovascular research to confirm that NO is directly involved (in other words, used as an inhibitor of NO activity), although in most cases EPR is not utilized to analyze the product. Other traps include DETC and MGD ferrous complexes (the latter being more water soluble) that essentially chelate NO. Cryogenic EPR is also useful for examining NO, with the "trapping agent" being an endogenous molecule such as haem or haemoglobin. Controversy has been generated in the cardiovascular field as a result of a considerable body of data that suggests that deoxyhaemoglobin reduces nitrite to NO with this eliciting hypoxic vasodilatation of blood vessels.[9] Certainly *ex vivo* chemistry shows this is possible, but more recent work (alluded to above) probably negates the importance of such a mechanism *in vivo*. The power of using continuous-wave and pulsed electron paramagnetic resonance methods for structural analysis of ferric forms and nitric oxide-ligated ferrous forms of globins has also been tested.[10] Interaction of NO with soluble guanylate cyclase (sGC), its primary effective receptor in vascular smooth muscle, to form ferrous nitrosyl complexes has also been studied.[11] *In vivo* investigation of NO generation from nitric oxide synthase (NOS) was also undertaken in mature rat brain after injury,[12] and oxygen-induced radical

intermediates were identified in the nNOS oxygenase domain that are regulated by L-arginine, tetrahydrobiopterin, and thiols.[13]

EPR continues to play a prominent role in understanding the radical mechanisms involved in tissue ischemia (I, the lack of oxygen to a given tissue area) and reperfusion (R, where supply is resumed). It has been recognized for some time that radicals produced during the latter phase are damaging and cause tissue injury, yet relatively little progress has been made in terms of prophylaxis. The redox status in hepatic I/R injury has been monitored *in vivo* in mice,[14] and the formation and roles of plasma S-nitrosothiols in liver I/R identified.[15] NO has also been monitored in rats following kidney transplantation[16] and following I/R injury in kidney.[17] Early work identified free radical formation during myocardial I/R,[18] whereas the nitric oxide donor SNAP was shown to increase radical formation and degrade left ventricular function after myocardial I/R.[19] Finally, evidence for nitrite derived formation of NO and subsequent signaling in post ischemic heart tissue was obtained for the first time by cryogenic EPR analysis,[20] and confirmation that endothelium-derived NO regulates post-ischemic myocardial oxygenation by modulating mitochondrial electron transport.[21]

4. Consequences of free radical reactions with biomolecules

Free radical damage to biomolecules is a consequence of oxidative stress and may result in tissue damage or loss of function that produce the symptoms of disease. The detection and elucidation of processes leading to such damage to biomolecues is therefore important in understanding disease pathology. Studies investigating free radical damage to some individual biomolecues is reviewed below, with the role of these processes in disease reviewed in later sections.

4.1 Damage to lipids

Lipid peroxidation remains an important index of oxidative stress and numerous studies have used this process as a measure of free radical production and tissue damage in biological systems. Lipid peroxidation has also been widely used to assess antioxidant deficiency or to evaluate new antioxidant compounds. Radical damage to lipids and membranes is often detected by non-radical lipid peroxidation products, produced as secondary events from the initiating oxidative stress. EPR spectroscopy allows the detection of radical intermediates generated during the radical chain reactions of lipid peroxidation and thereby can provide information on the possible origins of the process. Spin-trapping has been the method of choice to detect free radical intermediates during lipid peroxidation.

The antioxidant properties of many novel compounds on lipid peroxidation have been evaluated by EPR spectroscopy. Thus, the antioxidant activities of trans-resveratrol (trans-3,5,4′-trihydroxystilbene) and trans-piceid (trans-5,4′-dihydroxystilbene-3-O-beta-*d*-glucopyranoside), its more widespread glycosilate derivative, have been compared by measuring their inhibitory action on peroxidation of linoleic acid (LA) and their radical scavenging ability towards different free radicals (such as DPPH) and radical initiators.[22] Studies using spin labelled phosphatidylcholine liposomes demonstrated that the susceptible hydroxyl groups of these compounds are located in the lipid region of the bilayer close to the double bonds of polyunsatured fatty acids, making these stilbenes particularly suitable for the prevention and control of lipid peroxidation in membranes.

Novel metalloporphyrins bearing 2,6-di-tert-butylphenol pendants as antioxidant substituents, and a long chain hydrocarbon palmitoyl group have been synthesized.[23] The oxidation of the compounds by PbO_2 lead to the formation of the corresponding 2,6-di-tert-butylphenoxyl radicals as detected by EPR. The activity of the porphyrins against lipid peroxidation was examined using *in vitro* lipid peroxidation induced by tert-butylhydroperoxide in respiring rat liver

mitochondria, *in vitro* lipid peroxidation in liver homogenates of Wistar strain rats, and a model process of peroxidation of (Z)-octadec-9-enic (oleic) acid as a structural fragment of lipids.

EPR spin-trapping and spin-labelling techniques have been applied to investigate the antioxidative capacities of fullerene C60 and newly synthesized fulleropyrrolidine derivates (N-methyl (2-quinolyl) fulleropyrrolidine 60, Q-C 60 and N-methyl (2-indolyl) fulleropyrrolidine 60, I-C60) encapsulated in phospholipid multilamellar liposomes. The capacity for removal of OH and O_2^- and for the prevention of lipid peroxidation were found to be the most relevant biological antioxidative parameters.[24] Spin-labelling was also used to examine a new potential antioxidant compound, spin-labelled lutein (SL-lut).[25] The approximate location of nitroxide free radical groups of SL-lut incorporated into phosphatidylcholine liposomes was determined from their EPR spectra. Lipid peroxidation was measured by thiobarbituric acid reactive species (TBARS) compared with unlabelled lutein and SL-lut was found to be the most powerful antioxidant, significantly reducing lipid peroxidation.

Antioxidant supplements are being promoted for their potential health benefits and some of these have been investigated. An interesting study on the effect of *Ginkgo biloba* (Gb) supplementation *in vivo* on lipid peroxidation of microsomal membranes has been performed.[26] Administration of up to 100 mg/kg/day Gb to rats did not significantly affect the activity of microsomal enzymes, the rate of generation of superoxide anion, or the iron reduction rate by rat liver microsomes. However, lipid peroxidation, assessed by the generation of lipid radicals measured by EPR spectroscopy using POBN as the spin trap was modulated. This suggests that Gb extracts at these concentrations are able to limit lipid peroxidation and scavenge lipid radicals *in vivo* and protect membranes from oxidative damage.

Oxidative damage to membranes and lipids continues to be assessed by EPR spectroscopy. Using EPR and sensitive spin trapping detection with 5-(diethoxyphos-phoryl)-5-methyl-1-pyrroline-N-oxide (DEPMPO), Culcasi and co-workers[27] compared the respective roles of cigarette smoke- and gas phase cigarette smoke- derived free radicals on smoke-induced cytotoxicity and lipid peroxidation of filtered and unfiltered, machine-smoked experimental and reference cigarettes with a wide range of tar particulate matter yields. In buffer bubbled with cigarette smoke the DEPMPO/superoxide spin adduct was the major detected nitroxide. Unexpectedly a protective effect of tar particulate matter on murine 3T3 fibroblasts was observed in early (< 3 h) free radical-, gas phase cigarette smoke-induced cell death, and carbon filtering decreased free radical formation, toxicity and lipid peroxidation in three cell lines (including human epithelial lung cells) challenged with gas phase cigarette smoke. These results highlight an acute, free radical-dependent, harmful mechanism specific to gas phase cigarette smoke, whose physical or chemical control may be of great interest with regard to reducing the toxicity of smoke. An interesting study challenges the putative role of iron and hydroxyl radicals in the oxidative stress-mediated cytotoxicity of the anti-cancer drugs doxorubicin and bleomycin.[28] Using different iron chelators and measuring the formation of hydroxyl radicals by *in vitro* EPR, and quantifying oxidative stress and cellular damage as TBARS formation, glutathione (GSH) consumption and lactic dehydrogenase (LDH) leakage, it was found that all chelators inhibited $\cdot OH$ radical formation induced by H_2O_2/Fe^{2+}. However, the chelators that decreased doxorubicin and bleomycin-induced oxidative stress and cellular damage were not able to protect against H_2O_2/Fe^{2+}, suggesting that the ability to chelate iron as such is not the sole determinant of a compound protecting against doxorubicin or bleomycin-induced cytotoxicity. This finding may have implications for the development of new compounds designed to protect against this toxicity.

In a study on lead toxicity, the EPR signal of ascorbyl radical in caput epididymis, cauda epididymis, testis and liver of lead acetate-treated rats revealed a significant decrease by 53%, 45%, 40% and 69% versus control tissues, respectively.[29] In the

group exposed to lead, the concentrations of lipid peroxide in homogenates of the reproductive system organs was significantly elevated versus control groups. It was assumed that the decreased EPR signal intensity was caused by decreased tissue concentrations of L-ascorbic acid. This may result from consumption of ascorbic acid by high levels of reactive oxygen species (ROS) in tissues of animals chronically exposed to lead.

The free radical reducing activity and membrane fluidity were examined by EPR spectroscopy in selenium deficient rats.[30] Selenium deficiency caused the induction of liver microsomal cytochrome P-450 activity, and the reduction rate of nitroxyl radicals present at shallow depths in the membrane was increased. Although selenium-deficiency caused induction of liver cytochrome P-450 and chronic increases of H_2O_2, this did not result in oxidative liver damage. An increased level of glutathione in selenium-deficient liver was also evident, likely due to an absence of GSH-Px activity. Thus, using the EPR spin label method, this article shows that selenium deficiency causes complicated redox changes in the liver, notably, alterations in the levels of cytochrome P-450 and GSH-Px systems.

4.2 Damage to DNA

Oxidative damage to DNA and production of DNA radicals continues to be researched with EPR methodology. In addition to studying the mechanisms of DNA damage and identifying sites involved in potential pathological processes, attention has also been focussed on deliberate DNA damage in therapeutic settings.

Chronic inhalation of high concentrations of respirable quartz particles has been implicated in various lung diseases including lung fibrosis and cancer and generation of reactive oxygen species (ROS) and oxidative stress is considered a major mechanism of quartz toxicity. Curcumin, has been considered as a 'nutraceutical' because of its strong anti-inflammatory, antitumour and antioxidant properties. This has been tested in a recent study by Li and co-workers[31] who used EPR and spin-trapping with DMPO to demonstrate that curcumin reduces hydrogen peroxide-dependent hydroxyl-radical formation by quartz. Although curcumin was also found to reduce inflammatory responses in rat lung epithelial cells, it failed to protect these cells from oxidative DNA damage induced by quartz. Indeed, curcumin was found to be a strong inducer of oxidative DNA damage itself and also enhanced the mRNA expression of the oxidative stress response gene heme oxygenase-1. These observations indicate that caution should be excercised with the potential use of curcumin in the prevention or treatment of lung diseases associated with quartz exposure.

Mechanisms of direct radiation damage in DNA were examined to provide a model for the dose-response curves of the more prevalent end products and to provide a means of measuring their chemical yields.[32] Dose-response curves were measured for the formation of direct-type DNA products in X-irradiated d(GCACGCGTGC)(2) prepared as dry films and as crystalline powders. The yield of trappable radicals was measured at 4 K by EPR of films X-irradiated at 4 K. This analytical approach, combined with the mechanistic model, may prove important in predicting risk due to exposure to low doses and low dose rates of ionizing radiation. A similar study investigated the mechanisms of DNA strand breakage by direct ionization of variably hydrated plasmid DNA.[33]

Autoxidation of S(IV) in the presence of 2′-deoxyguanosine or DNA produced 8-oxo-7,8-dihydro-2′-deoxyguanosine and DNA strand breaks, respectively.[34] Oxidation of 2′-deoxyguanosine and DNA damage were attributed to oxysulfur radicals formed as intermediates in S(IV) autoxidation catalyzed by transition metal ions. SO_3^- and OH radicals were detected by EPR-spin trapping experiments with DMPO (5,5-dimethyl-1-pyrroline-N-oxide).

It has been proposed that oxidative DNA damage may be an important component of copper toxicity. This theory was tested in an elegant experiment by using *Escherichia coli* with knocked out copper export genes, copA, cueO, and

cusCFBA.[35] It was found that the copper-loaded mutants were actually less sensitive to killing by H_2O_2 than cells grown without copper supplementation. EPR spin trapping showed that the copper-dependent H_2O_2 resistance was not caused by inhibition of the Fenton reaction, as copper-supplemented cells exhibited substantial hydroxyl radical formation. However, copper EPR spectroscopy suggested that the majority of H_2O_2-oxidizable copper is located in the periplasm; therefore, most of the copper-mediated hydroxyl radical formation occurs in this compartment and away from the DNA. It is clear that copper does not catalyze significant oxidative DNA damage *in vivo*, suggesting that copper toxicity must occur by a different mechanism.

The anticancer drug camptothecin (CPT), which inhibits topoisomerase I (Topo I) by forming a ternary DNA-CPT-Topo I complex, also produces significant DNA damage to cancer cells when UVA-irradiated in the absence of Topo I. A recent study, identified free radicals generated in these processes.[36] The loss in EPR signal intensity of the Cu(II)-CPT complex upon irradiation was accompanied by the appearance of a new EPR signal at *g* approximately 2.0022. Spin trapping experiments with nitrosodurene revealed that continuous irradiation of CPT in DMSO solutions produced the hydroxyl radical and superoxide radical. These experiments indicate that CPT is a promising photosensitizer and that radicals and singlet oxygen generated upon illumination of this compound play a central role in DNA cleavage and the induction of apoptosis in cancer cells.

In another study on photodynamic therapy, the photochemical and phototoxic activity of berberine on murine fibroblast NIH-3T3 and Ehrlich ascites carcinoma cells was monitored by EPR.[37] The EPR spectra detected upon photoexcitation of aerated solutions of berberine have provided good evidence for the efficient activation of molecular oxygen with the generation of superoxide anion radical and singlet oxygen. The DNA damage generated by a combination of berberine with UVA irradiation induced a significant blockage of EAC cells in the S and G(2)/M phases and the stopping/decrease of cell proliferation after 24 h.

4.3 Damage to proteins

Davies and co-workers continue their investigations into protein oxidation and cardiovascular impacts. Zinc has been postulated to displace iron from critical sites and thereby protect against damage leading to atherosclerotic lesions. In an interesting study,[38] they quantified metal ion and protein oxidation levels in human carotid and abdominal artery specimens containing early-to-advanced lesions, to determine whether zinc concentrations correlate inversely with iron levels and protein oxidation. They found that accumulation of zinc in human atherosclerotic lesions correlated with calcium levels but did not protect against protein oxidation.

Studies into modification of myosin by oxidative stress and activated haem proteins have also been carried out.[39] Oxidative changes to myosin have been correlated with altered meat properties, in human physiology and disease (*e.g.* cardiomyopathy, chronic heart failure) although the mechanisms of these reactions are incompletely understood. The transient species generated on myosin as a result of the reaction with activated haem proteins were investigated by EPR spectroscopy and amino-acid consumption; the generation of thiyl and tyrosyl radicals in this process was consistent with the observed consumption of cysteine and tyrosine residues. The authors suggest that these changes are consistent with the altered function and properties of myosin in muscle tissue exposed to oxidative stress arising from disease or from food processing.

The formation of a nitric-oxide induced dinitrosyl-iron complex bound to intracellular proteins was investigated to understand how the complex is formed, the identity of the proteins involved, and the physiological role of this process.[40] EPR spectroscopy and enzyme activity measurements were used with hepatocytes to identify the complex as a dinitrosyl-diglutathionyl-iron complex (DNDGIC) which bound to Alpha class

glutathione S-transferases (GSTs) with high affinity ($K_d = 10^{-10}$ M). This complex was seen to form spontaneously through NO-mediated extraction of iron from ferritin and transferrin, in a reaction that required only glutathione. This suggests that glutathione transferases sequester toxic dinitrosyl-iron complexes in cells as a physiological protective mechanism operating in conditions of excessive levels of NO.

Tissue damage from inflammation is largely due to the production of oxidative mediators by activated leukocytes. Peroxidases, such as EPO (eosinophil peroxidase) and MPO (myeloperoxidase) are highly basic haem enzymes that can catalyse the production of HOBr (hypobromous acid). They are released extracellularly by activated leukocytes and can bind to polyanionic glycosaminoglycan components of the extracellular matrix. A recent study has shown that one-electron reduction of the N-bromo derivatives generates radicals detected by EPR spin trapping.[41] The species detected are consistent with metal ion-dependent polymer fragmentation and modification being initiated by the formation of nitrogen-centred radicals. This suggests that HOBr induces the degradation of extracellular matrix glycosaminoglycans and proteins that may contribute to tissue damage associated with inflammatory diseases such as asthma.

The effect of peroxynitrite/peroxynitrous acid ($ONOO^-$/ONOOH), generated at sites of inflammation, on extracellular matrix has also been studied.[42] EPR spin trapping experiments provided evidence for the formation of carbon-centered radicals on glycosaminoglycans and related monosaccharides. The similarity of the EPR spectra obtained to those obtained with authentic $\cdot$OH led the authors to suggest that $ONOO^-$/ONOOH-mediated damage involved the generation of $\cdot$OH. These data suggest that extracellular matrix fragmentation at sites of inflammation may be due, in part, to the formation and reactions of ONOOH.

A novel multifunctional role of plasma ascorbate in removing key precursors of oxidative damage has been described.[43] Ascorbate was found to effectively reduce plasma methaemoglobin, ferryl haemoglobin and globin radicals. The ascorbyl free radicals formed are efficiently re-reduced by the erythrocyte membrane-bound reductase. In addition to being relevant to the toxicity of haemoglobin-based oxygen carriers, these findings have implications for situations where haem proteins exist outside the protective cell environment, *e.g.* haemolytic anaemias and subarachnoid haemorrhage. A review of EPR spin-trapping of protein radicals to investigate biological oxidative mechanisms highlights the effectiveness of simple experiments in providing insights into the biological activity of oxidants and signalling mechanisms.[44]

5. Free radicals and disease

5.1 Cancer

The role of free radicals in the pathogenesis of cancer and in the mechanisms of chemotherapeutic agents continues to provide a plethora of articles which have utilised EPR spectroscopy to examine radical-mediated effects.

5.1.1 Chemotherapy, radiotherapy and photodynamic therapy. EPR spectroscopy has been used to evaluate new potential anti-cancer therapies and to explore mechanisms of accepted therapeutic agents. Development of drug resistance is an important reason for the failure of cancer therapies. EPR was used to measure the effects of NO generation and changes in redox state induced by a novel compound, NCX-4040, a nitric oxide-releasing aspirin, in sensitizing drug-resistant human ovarian xenograft tumors to cisplatin by depletion of cellular thiols.[45] Nitric oxide associated effects were also studied in redox-active cobalt complexes on tumor tissue.[46] Photodynamic therapy continues to be studied due to its potential in cancer treatment. Photodynamic therapy employs the combination of nontoxic photosensitizers and harmless visible light to generate reactive oxygen species and kill cells.

A water-soluble nitrosyl complex with large two-photon absorption was used to generate NO induced by one- or two-photon irradiation.[47] NO release was detected by EPR spectroscopy with a Fe(II)-N-(dithiocarbamoyl)-N-methyl-d-glucamine (Fe-MGD) complex, upon one- or two-photon light irradiation. The light-dependent cytotoxicity against cancer cells of the water-soluble nitrosyl complex shows that two-photon-functionalized nitrosyl complexes can be effective NO donors for light-activated treatment. In a study to evaluate fullerene-containing composites as potential agents for photodynamic therapy, reactive oxygen species were induced in thymocytes, ascitic cells from Erlich's tumour and L1210 leukemia cells by visible light.[48] In a different approach, functionalized fullerenes were used to mediate photodynamic killing of cancer cells *via* Type I and Type II photochemical mechanisms.[49]

Tumour oxygenation can predict cancer therapy response and malignant phenotype and thus there is considerable interest in tumour oximetry. The group of Swartz continues to investigate EPR oximetry with applications in many fields of biomedicine and tumour oximetry in particular. A recent review by this group[50] on repetitive tissue pO_2 measurements by EPR oximetry summarizes the current status and future potential for experimental and clinical studies. EPR imaging is a novel technique for providing quantitative high-resolution images of tumour and tissue oxygenation. Elas and co-workers have shown that EPR oxygen images correlate spatially and quantitatively with oxygen measurements using an Oxylite oxygen probe.[51] Measurement of oxygenation has important consequences for radiation therapy. A study of efaproxiral, an allosteric modifier of haemoglobin that facilitates oxygen release from hemoglobin, used EPR oximetry to measure the resultant increase in tumour pO_2.[52] This was correlated with growth inhibition of RIF-1 tumours in mice that received X-radiation (4 Gy) plus oxygen breathing compared to radiation plus oxygen plus efaproxiral daily for 5 days. EPR oximetry was used to investigate the mechanism of reoxygenation after antiangiogenic therapy using SU5416 and its importance for guiding combined antitumour therapy.[53] It has been reported that insulin significantly enhances tumour oxygenation and increases radiation-induced tumour regrowth delay in experimental models. This effect was measured by EPR in a trial of the preclinical safety and anti-tumour efficacy of insulin combined with irradiation.[54] The same laboratory have used EPR oximetry to determine tumour oxygenation after thalidomide administration as a potentiation of cyclophosphamide chemotherapy.[55] Several other studies have assessed the utility of EPR oximetry to measure tumour oxygen,[56] tumour monitoring,[57] and response to treatment.[58]

In other studies on enhancing cancer therapy mechanisms, Mn-superoxide dismutase overexpression was found to enhance G2 accumulation and radio-resistance in human oral squamous carcinoma cells.[59] The reductive activation of the anti-tumour drug RH1 to its semiquinone free radical by NADPH cytochrome P450 reductase and by HCT116 human colon cancer cells was investigated.[60]

5.1.2 Pathogenesis and mechanisms. EPR has been used to characterise protein, lipid, and DNA radicals in UVA-induced skin damage and its modulation by melanin,[61] while an EPR technique has been described to study intramelanocyte radical generation, that may allow a sunscreen protection factor to be determined.[62] The role of dietary components as potential carcinogens continues to be debated and researched. The potential for serum albumin as a novel test for cancer diagnosis and monitoring has been investigated by several groups.[63] A novel study investigated the accumulation of low molecular mass biomarkers related to cancer on human serum albumin. Using an albumin-specific spin probe, the serum samples of 98 patients with a variety of cancer types, and 86 cancer-free individuals, were analysed by EPR spectroscopy.[64] Resultant EPR spectra showed significant differences between these

groups that were most apparent in the intensities and widths of the spectral lines corresponding to the different types of albumin binding sites.

EPR spin-trapping has been used to study apigenin, a dietary flavone with anti cancer properties.[65] The prooxidant effect of apigenin was suggested to oxidize a variety of thiols through the formation of phenoxyl radicals that play a role in the abortive apoptotic pathway switching to necrotic cell death. The potential cancer protective effects of the Mediterranean diet were investigated by measuring free radical scavenging capacity and antiproliferative activity among different genotypes of autumn olive.[66] Extracts of all autumn olive genotypes inhibited proliferation of the human cancer cells tested. The early stages of estrogen-dependent carcinogenesis have been studied by evaluating the dynamics of oxidative damage to cellular macromolecules such as proteins, lipids and DNA.[67]

The accumulation of PBN trapped adducts and the decay of the spin probe methoxycarbonyl-PROXYL was used as evidence for free radical generation in liver after administration of the carcinogen diethylnitrosamine.[68] A report on the detection of NO generation *in vivo* without the requirement to stimulate the immune system demonstrated the utility of non-invasive spin trapping of NO in tumours of non-treated, living animals.[69]

5.2 Infectious disease

A serious form of anthrax, caused by *Bacillus anthracis*, can be induced by inhalation of endospore forms of the bacillus. Spores of *B. anthracis* enter the lungs and are phagocytosed by host alveolar macrophages. However, how the spores then migrate to other sites remains unclear. A study describes the spin labelling of *B. anthracis* endospores and their subsequent phagocytosis by RAW 264.7 macrophages providing a potential tool for EPR imaging of the spread of spores in animals.[70] Sepsis remains a clinical emergency which carries a high morbidity and mortality. A role for NO in the pathogenesis of sepsis is widely accepted, although its precise mechanisms of action in affecting respiration remain to be determined. A study by Dungel and co-workers[71] aimed at clarifying whether low level illumination at specific wavelengths recovers mitochondrial respiration inhibited by NO and glycerol-trinitrate (GTN), a clinically-used NO mimetic. They found that inhibition of mitochondrial respiration by GTN is not sensitive to visible light, which suggests an inhibition mechanism that does not involve NO. Brain pO_2 of animals with septic shock have been described.[72] A decline in pO_2 levels from severe hypotension during sepsis was detected, and generation of NO in brain tissues was confirmed by spin trapping. This study highlights the applicability of EPR spectroscopy to monitor pO_2 and NO production simultaneously and repeatedly at the same site *in vivo*. Another report suggests that anemia in neonatal sepsis is associated with free radical production and oxidative stress.[73] The immune responses to infection included the production of oxidants and free radicals in cellular compartments. It has been reported that high HOCl production can inactivate catalase, with consequences for tissue damage and cell signalling. The mechanism of this inactivation was recently described with experiments that trapped catalase radicals in discrete cellular compartments.[74] Emerging connections between copper and prion diseases have been reviewed.[75]

5.3 Alzheimers disease

Mounting evidence suggests that dysregulation of redox-active biometals such as Cu and Fe, can lead to oxidative stress, which plays a key role in the neuropathology of Alzheimer's disease (AD). It has been demonstrated with EPR spectroscopy, that copper markedly potentiates the neurotoxicity exhibited by beta-amyloid (Aβ peptide) *via* the formation of Cu(II)-Aβ1-40 complexes.[76] The role of copper in AD has been investigated in further studies where EPR was used to show the

presence of Cu(II) appears to induce fibril-fibril association,[77] and the formation of toxic Aβ-Cu(II) complexes.[78] Free radical attack on the amyloidogenic proteins beta-amyloid and alpha-synuclein (implicated in AD and Parkinson's disease, respectively) were studied with the spin trap 3,5-dibromo-4-nitrosobenzenesulfonate.[79] The results support the hypothesis that oxidative damage to beta-amyloid and related proteins in the brain in AD could be due, at least in part, to the self-generation of ROS. Spin-probe and spin-label techniques were used to study the interactions of the Aβ 1-28 peptide involved in Alzheimer's disease and the PrP 106-126 peptide suspected to be preferentially involved in spongiform encephalo-pathies with three different types of dendrimers.[80] A recent review highlights the applications of EPR to studies of neurological disease.[81]

5.4 Diabetes

Much of the pathology associated with diabetes, including micro- and macro-vascular complications has been linked to reactive oxygen and reactive nitrogen species (ROS/RNS) mechanisms. The application of EPR techniques to the study of diabetes and diabetes-related syndromes is varied and wide reaching encompassing *in vitro*, cell, and *in vivo* studies. Hyperglycemia-induced ROS toxicity to endothelial cells has been shown to be dependent on paracrine mediators rather than to direct effect of elevated glucose on cells. Using spin trapping techniques it was shown that radicals were generated in response to cytokines and other stimuli, but not in response to 25 mM glucose.[82] EPR techniques should be considered complimentary to others that often provide different and important information. An excellent example is in the work on human islet amyloid polypeptide (hIAPP) misfolding[83] thought to play an important role in the pathogenesis of Type II diabetes mellitus. It has recently been shown that membranes can catalyze the misfolding of hIAPP *via* an α-helical intermediate of unknown structure. This study used site-directed spin labeling and EPR spectroscopy to generate a three-dimensional structural model of this membrane-bound form. The combination of molecular and fluorescence techniques has provided a better understanding of the mechanism of membrane-mediated misfolding.

The microhemocirculation plays a major role in the development of micro- and macroangiopathy during diabetes. Changes in free-radicals and deformability of erythrocytes were monitored using the filtration-photometric and EPR methods in white rats during alloxan-induced diabetes at different stages.[84] Erythrocyte deformability was sharply reduced and the blood vessel walls were damaged by the initiation of lipid peroxidation and inhibition of the antioxidant system.

Control of plasma glucose level has been achieved *in vitro* and *in vivo* by the administration of vanadium and zinc in the form of inorganic salts. However, these elements are poorly absorbed and require high doses which have been associated with undesirable side effects. Many researchers have therefore focused on metal complexes prepared from $VOSO_4$ or $ZnSO_4$ and low-molecular-mass bidentate ligands.[85] Seven kinds of 1-hydroxy-4,6-disubstituted and 1-hydroxy-4,5,6-trisubstituted-2(1H)-pyrimidinones were synthesized by reaction of N-benzyloxyurea and beta-diketones and subsequent removal of the protecting group. Six kinds of 1-hydroxy-4-(substituted)amino-2(1H)-pyrimidinones were synthesized by the substitution reaction of 1-benzyloxy-4-(1′,2′,4′-triazol-1′-yl)-2(1H)-pyrimidinone with various alkyl amines or amino acids. Treatment with $VOSO_4$ and $ZnSO_4$ or $Zn(OAc)_2$ afforded vanadyl(IV) and zinc(II) complexes which were characterized by means of ^1H NMR, IR, EPR, and UV-Vis spectroscopies, and combustion analysis. The *in vitro* insulin-mimetic activity of these complexes was evaluated from 50% inhibitory concentrations (IC_{50}) on free fatty acid (FFA) release from isolated rat adipocytes treated with epinephrine. It was found that the balance of hydrophilicity and hydrophobicity is important for higher insulin-mimetic activity. The *in vivo* insulin-mimetic activity was evaluated with streptozotocin

(STZ)-induced diabetic rats. Blood glucose levels were lowered from hyperglycemic to normal levels after the treatment with bis(1,2-dihydro-4,6-dimethyl-2-oxo-1-pyrimidinolato)oxovanadium(IV) by daily intraperitoneal injections.

Endothelial dysfunction (ED) is a common occurrence in Type 2 diabetes (T2DM), as evidenced by a diminution of flow-mediated arterial dilatation and, by implication, further ED in T2DM in response to post-prandial lipaemia (PPL) at 4 h. This is possibly mediated by oxidative stress/alteration of the nitric oxide (NO) pathway. T2DM subjects tend to exhibit both exaggerated and prolonged PPL. The relationship of PPL to the duration of ED in T2DM subjects and oxidative stress with or without added antioxidant (vitamin C) was studied in 20 subjects with T2DM with moderate glycaemic control (mean HbA1c 8.4%).[86] Endothelial function (EF), lipid profiles, and venous free radicals were measured in the fasting, peak lipaemic phase (4 h) and postprandially to 8 h. The study was repeated in a double-blinded manner with placebo, vitamin C (1 g) therapy for 2 days prior to re-testing and with the fat meal. Oxidative stress was assessed by lipid-derived free radicals in plasma, *ex vivo* by EPR and by markers of lipid peroxidation (TBARS). Patient endothelial function was assessed by flow-mediated vasodilatation (FMD) of the brachial artery. The study showed PPL is associated with prolonged endothelial dysfunction for at least 8 h after a fatty meal. Vitamin C treatment improved endothelial dysfunction at all time points and attenuates PPL-induced oxidative stress. This highlights the importance of low-fat meals in T2DM and suggests a role for vitamin C therapy to improve endothelial function after meal ingestion.

5.5 Cardiovascular disease

Both superoxide and NO are essential to the maintenance of normal blood flow and vessel tone and function. This holds true for blood vessels, the cells in blood (including platelets and macrophage family) and extends to the heart itself. It follows that disturbance to these interlinked systems results in oxidative and nitrosative stresses, with antioxidant enzyme systems being overwhelmed in the process. One question which drives continuous active research in this broad field is whether ROS/RNS are intrinsic to the disease process or simply a consequence and by-product of it. By making complementary measures of free radical production and antioxidant activity versus expression some significant progress has been made. In the human failing myocardium, for example, DEPMPO has been used to demonstrate increase superoxide production. A decrease in MnSOD activity despite increased mRNA expression could reflect decreased translation or processing, or a post-translational modification of MnSOD, but the two-fold increase in superoxide is consistent with the hypothesis that increased oxidative stress results in increased transcription of antioxidant enzymes.[87]

From a biological perspective the term "*in vivo* EPR" is used loosely to reflect a study that reports "from" a whole body system. From a methodological perspective, there is a vast difference between true "*in vivo*" spin trapping and other EPR techniques and what is more correctly termed "*ex vivo*" measurements. This does not infer that less important information is acquired by either one of these, simply the model must be taken into account when drawing conclusions from the data obtained. This is important when considering the heart and human studies where true *in vivo* studes are often impractical. Despite this, EPR studies have yielded valuable new insights. Cardiogenic shock is the leading cause of death among patients hospitalized with acute myocardial infarction (MI). Understanding the mechanisms for acute pump failure is therefore important. To examine in an acute MI dog model whether mitochondrial bio-energetic function within non-ischemic wall regions are associated with pump failure, measurements of hemodynamic status, mitochondrial function, free radical production and mitochondrial uncoupling protein 3 (UCP3) expression were determined over a 24 h period.[88] Hemodynamic measurements revealed a $>50\%$ reduction in cardiac output at

24 h post infarction when compared to baseline. Biopsy samples were obtained from the posterior non-ischemic wall during acute infarction. ADP/O ratios for isolated mitochondria from non-ischemic myocardium at 6 h and 24 h were decreased when compared to the ADP/O ratios within the same samples with and without palmitic acid (PA). GTP inhibition of (PA)-stimulated state 4 respiration in isolated mitochondria from the non-ischemic wall increased by 7% and 33% at 6 h and 24 h post-infarction respectively when compared to sham and pre-infarction samples. This would suggest that the mitochondria are uncoupled and this is supported by an associated increase in UCP3 expression observed on western blots from these same biopsy samples. Blood samples from the coronary sinus measured by EPR confirmed an increase in reactive oxygen species (ROS) over baseline at 6 h and 24 h post-infarction.

Assessment of cardiovascular drug mechanism and efficacy has also featured EPR techniques as a key tool. For example benidipine, a long-lasting calcium (Ca) channel blocker, may exert its protective effect against vascular disorders by increasing nitric oxide (NO) production. To investigate whether orally administered benidipine might influence membrane function in patients with essential hypertension, membrane fluidity of erythrocytes was measured using EPR and spin-labeling.[89] In the preliminary study using erythrocytes obtained from healthy volunteers, results indicated that benidipine increased the membrane fluidity and improved the microviscosity of erythrocytes. In addition, it was demonstrated that the effect of benidipine on membrane fluidity of erythrocytes was significantly potentiated by the NO-substrate, L-arginine. In a separate study, orally administered benidipine for 4 weeks significantly increased the membrane fluidity of erythrocytes with a concomitant increase in plasma NO metabolite levels in hypertensive subjects. The results of this study demonstrated that benidipine might increase the membrane fluidity and improve the microviscosity of erythrocytes both *in vitro* and *in vivo*, to some extent, *via* an NO-dependent mechanism.

To design and evaluate hirudin (HIR) derivatives with low bleeding risk, the factor (F) XIa, FXa, and thrombin recognition peptides (EPR, GVYAR, and LGPR, respectively) were linked to the N-terminus of HIR.[90] The intact derivatives have no anticoagulant activity because of the extension of the N-terminus of HIR. After cleavage by the corresponding coagulation factor that occurs on the activation of the coagulation system and in the presence of the thrombus, its activity is released. This limited the anticoagulant activity of these derivatives to the vicinity of the thrombus, and as a result, systemic bleeding complications were avoided. The definite antithrombotic effect and low bleeding parameters of these derivatives were investigated in rat carotid artery and inferior vena cava thrombosis models. In both models, the three derivatives showed significant antithrombotic effects, indicating that anticoagulant activity could be successfully released *in vivo*. Moreover, the bleeding parameters of these derivatives were lower than that of HIR as indicated by the values of activated partial thromboplastin time (APTT) and thrombin time (TT). To further assess the safety of these derivatives, bleeding time was measured in a mouse tail-cut model. Although the derivatives had obvious effects on bleeding at a dose of 6 mg/kg, the effect of these derivatives on bleeding was significantly weaker than that of HIR at a dose of 1.5 mg/kg. Thus, the benefit-to-risk profiles of the derivatives were superior to that of HIR.

Heart manipulation and displacement are common manoeuvers during beating heart surgery to expose coronary arteries for revascularization. Effects of heart displacement on free radical generation have not been previously described. Seven adult male dogs were anesthetized, a left lateral thoracotomy performed to expose the heart, and the coronary sinus cannulated for ROS sampling during different manipulation protocols:[91] (1) heart in normal position; (2) 90 degree manual heart displacement; (3) trendelenburg position while the heart displaced 90 degrees; and (4) return heart to normal resting anatomical position plus the operating table returned to horizontal. Heart displacement followed by anatomical re-positioning

significantly increased the ROS signal as measured by EPR (50-fold compared with control values; $p < 0.01$).

Exercise is associated with an increase in oxygen flux through the mitochondrial electron transport chain, and it that recently been demonstrated using EPR spin trapping techniques to increase the production of ROS in skeletal muscle.[92,93] To examine whether exercise also causes free radical production in the heart, ROS production was measured in seven chronically instrumented dogs during rest and treadmill exercise (6.4 km/h at 10 degrees grade; and heart rate, 204 +/− 3 beats/min) using EPR with the spin trap alpha-phenyl-tert-butylnitrone (PBN) (0.14 mol/l) in blood collected from the aorta and coronary sinus (CS).[94] To improve signal detection, the free radical adducts were deoxygenated over a nitrogen stream for 15 min and extracted with toluene. The hyperfine splitting constants of the radicals were alpha(N) 1.37 mT and alpha(H) 0.1 mT are consistent with the trapping of an alkoxyl or carbon-centered radical. Resting aortic and CS PBN adduct concentrations were 6.7 and 6.3×10^8 arbitrary units (P = not significant). Both aortic and CS adduct concentrations increased during exercise, but there was no significant difference between the aortic and CS concentrations. Thus, in contrast to skeletal muscle, submaximal treadmill exercise did not result in detectable free radical production by the heart.

EPR systems leading to our further understanding of the normal myocardium and heart function are expanded on below, where site directed *in vivo* spectroscopy and imaging methods have been useful.

5.6 Miscellaneous conditions

EPR spectrometry was used to investigate the effect of haemodialysis and oxidative stress on alterations in erythrocyte structure and cellular susceptibility in patients with chronic renal failure.[95] Intrinsic reactive oxygen species (ROS) in a rat model of human minimal-change nephropathy were detected directly using an *in vivo* EPR method with 1-acetoxy-3-carbamoyl-2,2,5,5-tetramethylpyrrolidine (ACP) in real time.[96] Further studies on kidney disease have evaluated a role for free radicals in radiation nephropathy[97] and the induction of complex redox alterations in mesangial cells induced by indoxyl sulfate.[98] Studies have examined the protective effects of echinacoside on carbon tetrachloride-induced hepatotoxicity,[99] and erythrocytes with T-state-stabilized hemoglobin as a therapeutic tool for postischemic liver dysfunction.[100] Crohn's disease and ulcerative colitis, known as inflammatory bowel disease, are fairly common chronic inflammatory conditions of the gastrointestinal tract. A recent review explores whether oxidative stress is a cause of inflammatory bowel disease or an epiphenomenon.[101]

6. Selected biomedical EPR techniques

6.1 *In vivo* EPR oximetry

In part because of the importance of oxygen in biology and pathophysiology but also because of the contribution oximetry makes in return to the field, EPR oximetry (both spectroscopy and imaging) is perhaps one of the most important and expanding applications of EPR techniques. In terms of oximetric probe development and use several key studies stand out. These include the synthesis and characterization of a perchlorotriphenylmethyl (trityl) triester radical as a potential sensor for superoxide radicals and molecular oxygen in biological systems,[102] the reactivity of molecular oxygen with ethoxycarbonyl derivatives of tetrathiatriarylmethyl radicals as reporters of molecular O_2,[103] the assessment of EPR oximetry as a quantitative method to measure cellular respiration,[104] through to new oximetric probes that are highly sensitive, biocompatible, and useful for imaging of oxygen concentration in tissues.[105]

For purposes of this chapter we consider oximetry measured by *in vivo* EPR spectroscopy and *in vivo* EPR imaging separately, although it is important to realise that both approaches yield specific and important information. In terms of spectroscopy the studies encompass a very broad spectrum that could be included in the sections above. An estimation of mean and median pO_2 values from a composite EPR spectrum has been made,[106] whereas multi-site EPR oximetry (with additional applied field gradients to separate EPR signals arising from specific tissue locations) has also been utilized to great effect.[107] A similar technique has been used by the same group to study the effect of oxygen therapy on brain damage during transient focal cerebral ischemia in the rat.[108] Oximetry has also been applied to stem cell research, where molecular oxygen levels were monitored *in vivo* following stimulation of peri-implant vascularization with bone marrow-derived progenitor cells[109] and *in vivo* measurement of oxygenation at the site of stem cell therapy in a murine model of myocardial infarction.[110] The current status and future potential for EPR spectroscopic oximetry in experimental and clinical studies has been reviewed.[50]

Significant advances have been made in the field of monitoring tumour oxygenation *in vivo*. These are wide ranging and include dynamic monitoring of localized tumour oxygenation changes using RF pulsed EPR in conscious mice,[111] the effects of radiation on murine tumours,[112–114] a comparative evaluation of EPR versus Oxylite oximetry,[52] and monitoring oxygenation during growth of a transplanted tumour.[115] The application of EPR oximetry to imaging is complex, but strategies for improved temporal and spectral resolution have been developed using time-domain EPR[56] and continuous wave EPR at 300 MHz using radiofrequency power saturation effects.[116]

6.2   *In vivo* EPR imaging

There have been significant developments in instrumentation, in methodologies and their application to true *in vivo* imaging. There is also considerable overlap with oximetry (above). We focus here on work based on particular pathologies (rather than process or method development) and developments in nitroxide MRI contrast imaging are excluded, although this is an exciting area of development.

Anthrax is caused by the gram-negative bacterium, *Bacillus anthracis*. Infection by this microbe results from delivery of the endospore form of the bacillus through direct contact, either topical or inhalation. With regard to the latter route of administration, it is proposed that endospores of *B. anthracis* enter the lungs and are phagocytized by host alveolar macrophages. Thereafter, it is unclear as to how endospores travel to distal loci and what tissues are the targets. By spin labelling endospores through two different approaches with aminoxyls, it was possible to monitor by EPR the endospores phagocytized by the infected macrophage, thus develop a potential tool for EPR imaging in animals.[70]

Paramagnetic probes have been developed with imaging in mind. Examples include the synthesis and characterization of ester-derivatized tetrathiatriarylmethyl radicals as intracellular oxygen probes,[117] studies on the reactivity of superoxide anion radical with a perchlorotriphenylmethyl (trityl) radical,[118] and synthesis and spin-trapping properties of a new spirolactonyl nitrone.[119]

Slice selective images have been obtained *in vivo* in a number of studies. It is noteworthy that time required for imaging is a limiting factor—not least in order to acquire sufficient resolution, but in order for the image to be informative in the disease model or pathology. Slice-selective images of free radicals in mice using modulated field gradient EPR imaging has been achieved,[120] and proof-of-concept experiments successfully conducted on imaging melanin in melanomas.[121]

Studies combining EPR imaging with MRI also feature prominently, excellent examples include molecular imaging of ROS by a EPR-MRI dual-imaging system,[122] brain redox imaging using a blood-brain barrier-permeable nitroxide MRI

contrast agent,[123] and studies using flow-injection EPR to investigate hydroxyl radical scavenging activity of Gd(III) containing MRI contrast media.[124]

References

1   N. Khan and H. Swartz, *Mol. Cell. Biochem.*, 2002, **234**, 341.
2   M. Kamibayashi, S. Oowada, H. Kameda, T. Okada, O. Inanami, S. Ohta, T. Ozawa, K. Makino and Y. Kotake, *Free Radic. Res.*, 2006, **40**, 1166.
3   M. Hardy, F. Chalier, O. Quari, J. P. Finet, A. Rockenbauer, B. Kalyanaraman and P. Tordo, *Chem. Commun.*, 2007, **10**, 1083.
4   M. Hardy, A. Rockenbauer, J. Vasquez-Vivar, C. Felix, M. Lopez, S. Srinivasan, N. Avadhani, P. Tordo and B. Kalyanaraman, *Chem. Res. Toxicol.*, **20**, 1053.
5   E. Linares, S. Giorgio and O. Augusto, *Free Radic. Biol. Med.*, 2008, **44**, 1668.
6   Y. Mori, R. Watanabe, S. Sakamoto, N. Endo, S. Nakano, K. Kanaori, H. Takashima, M. Ohkawa and K. Tajima, *J. Med.*, 2004, **35**, 49.
7   M. Lens, L. Medenica and U. Citernesi, *Biotechnol. Appl. Biochem.*, 2008, [Epub ahead of print].
8   H. Li, H. Cui, T. K. Kundu, W. Alzawahra and J. L. Zweier, *J. Biol. Chem.*, 2008, [Epub ahead of print].
9   N. Sibmooh, B. Piknova, F. Rizzatti and A. N. Schechter, *Biochemistry*, 2008, **47**, 2989.
10 S. Van Doorslaer and F. Desmet, *Methods Enzymol.*, 2008, **437**, 287.
11 E. R. Derbyshire, A. Gunn, M. Ibrahim, T. G. Spiro, R. D. Britt and M. A. Marletta, *Biochemistry*, 2008, **47**, 3892.
12 M. Ziaja, J. Pyka, A. Machowska, A. Maslanka and P. M. Plonka, *J. Neurotrauma*, 2007, **24**, 1845.
13 V. Berka, L. H. Wang and A. L. Tsai, *Biochemistry*, 2008, **47**, 405.
14 H. P. Kobayashi, T. Watanabe, S. Oowada, A. Hirayama, S. Nagase, M. Kamibayashi and T. Otsubo, *Surg. Res.*, 2008, **147**, 41.
15 G. K. Glantzounis, S. A. Rocks, H. Sheth, I. Knight, H. J. Salacinski, B. R. Davidson, P. G. Winyard and A. M. Seifalian, *Free Radic. Biol. Med.*, 2007, **42**, 882.
16 T. Xu, X. Chen, X. F. Wang, X. B. Huang, X. K. Qu, H. Y. Ye, X. D. Zhang, S. K. Hou and J. C. Zhu, *Chin. Med. J. (Engl.)*, 2004, **117**, 1552.
17 M. Okamoto, K. Tsuchiya, Y. Kanematsu, Y. Izawa, M. Yoshizumi, S. Kagawa and T. Tamaki, *Am. J. Physiol. Renal Physiol.*, 2005, **288**, F182.
18 E. Tiravanti, A. Samouilov and J. L. Zweier, *J. Biol. Chem.*, 2004, **279**, 11065.
19 Y. Zhang, L. R. Davies, S. M. Martin, W. J. Coddington, F. J. Miller, Jr, G. R. Buettner and R. E. Kerber, *Resuscitation*, 2003, **59**, 345.
20 C. Vergely, V. Maupoil, G. Clermont, A. Bril and L. Rochette, *Arch. Biochem. Biophys.*, 2003, **420**, 209.
21 X. Zhao, G. He, Y. R. Chen, R. P. Pandian, P. Kuppusamy and J. L. Zweier, *Circulation*, 2005, **111**, 2966.
22 S. Fabris, F. Momo, G. Ravagnan and R. Stevanato, *Biophys. Chem.*, 2008, epublication.
23 E. R. Milaeva, O. A. Gerasimova, Z. Jingwei, D. B. Shpakovsky, S. A. Syrbu, A. S. Semeykin, O. I. Koifman, E. G. Kireeva, E. F. Shevtsova, S. O. Bachurin and N. S. Zefirov, *J. Inorg. Biochem.*, 2008, **102**, 1348.
24 M. Lens, L. Medenica and U. Citernesi, *Biotechnol. Appl. Biochem.*, 2008, epublication.
25 K. A. Broniowska, I. Kirilyuk and A. Wisniewska, *Free Radic. Res.*, 2007, **41**, 1053.
26 A. D. Boveris, M. Galleano and S. Puntarulo, *Phytother. Res.*, 2007, **21**, 735.
27 M. Culcasi, A. Muller, A. Mercier, J. L. Clément, O. Payet, A. Rockenbauer, V. Marchand and S. Pietri, *Chem. Biol. Interact.*, 2006, **164**, 215.
28 H. Kaiserová, G. J. den Hartog, T. Simůnek, L. Schröterová, E. Kvasnicková and A. Bast, *Br. J. Pharmacol.*, 2006, **149**, 920.
29 M. Marchlewicz, B. Wiszniewska, B. Gonet, I. Baranowska-Bosiacka, K. Safranow, A. Kolasa, W. Głabowski, R. Kurzawa, K. Jakubowska and M. E. Rać, *Biometals*, 2007, **20**, 13.
30 K. Matsumoto, A. Suzuki, H. Washimi, A. Hisamatsu, A. Okajo, I. Ui and K. Endo, *J. Nutr. Biochem.*, 2006, **17**, 677.
31 H. Li, D. van Berlo, T. Shi, G. Speit, A. M. Knaapen, P. J. Borm, C. Albrecht and R. P. Schins, *Toxicol. Appl. Pharmacol.*, 2008, **227**, 115.
32 S. G. Swarts, D. C. Gilbert, K. K. Sharma, Y. Razskazovskiy, S. Purkayastha, K. A. Naumenko and W. A. Bernhard, *Radiat. Res.*, 2007, **168**, 367.
33 S. Purkayastha, J. R. Milligan and W. A. Bernhard, *J. Phys. Chem. B*, 2006, **110**, 26286.
34 R. G. Moreno, M. V. Alipázaga, O. F. Gomes, E. Linares, M. H. Medeiros and N. Coichev, *J. Inorg. Biochem.*, 2007, **101**, 866.

35 L. Macomber, C. Rensing and J. A. Imlay, *J. Bacteriol.*, 2007, **189**, 1616.
36 V. Brezová, D. Dvoranová, V. Zúbor, M. Breza, M. Mazúr and M. Valko, *Mol. Biotechnol.*, 2007, **37**, 48.
37 S. Jantová, S. Letasiová, V. Brezová, L. Cipák and J. Lábaj, *J. Photochem. Photobiol. B*, 2006, **85**, 163.
38 N. Stadler, N. Stanley, S. Heeneman, V. Vacata, M. J. Daemen, P. G. Bannon, J. Waltenberger and M. J. Davies, *Arterioscler. Thromb. Vasc. Biol.*, 2008, **28**, 1024.
39 M. N. Lund, C. Luxford, L. H. Skibsted and M. J. Davies, *Biochem. J.*, 2008, **410**, 565.
40 J. Z. Pedersen, F. De Maria, P. Turella, G. Federici, M. Mattei, R. Fabrini, K. F. Dawood, M. Massimi, A. M. Caccuri and G. Ricci, *J. Biol. Chem.*, 2007, **282**, 6364.
41 M. D. Rees, T. N. McNiven and M. J. Davies, *Biochem. J.*, 2007, **401**, 587.
42 E. C. Kennett and M. J. Davies, *Free Radic. Biol. Med.*, 2007, **42**, 1278.
43 J. Dunne, A. Caron, P. Menu, A. I. Alayash, P. W. Buehler, M. T. Wilson, R. Silaghi-Dumitrescu, B. Faivre and C. E. Cooper, *Biochem. J.*, 2006, **399**, 513.
44 O. Augusto and S. Muntz Vaz, *Amino Acids*, 2007, **32**, 535.
45 A. Bratasz, K. Selvendiran, T. Wasowicz, A. Bobko, V. V. Khramtsov, L. J. Ignarro and P. Kuppusamy, *J. Transl. Med.*, 2008, **26**, 9.
46 I. I. Ganusevich, A. P. Burlaka, E. P. Sidorik, I. Y. Levitin, A. L. Sigan and S. P. Osinsky, *Exp. Oncol.*, 2007, **29**, 203.
47 Q. Zheng, A. Bonoiu, T. Y. Ohulchanskyy, G. S. He and P. N. Prasad, *Mol. Pharm.*, 2008, epublication ahead of print.
48 S. V. Prylutska, A. P. Burlaka, O. P. Matyshevska, A. A. Golub, G. P. Potebnya, Y. I. Prylutskyy, U. Ritter and P. Scharff, *Exp. Oncol.*, 2006, **28**, 160.
49 P. Mroz, A. Pawlak, M. Satti, H. Lee, T. Wharton, H. Gali, T. Sarna and M. R. Hamblin, *Free Radic. Biol. Med.*, 2007, **43**, 711.
50 N. Khan, B. B. Williams, H. Hou, H. Li and H. M. Swartz, *Antioxid. Redox Signal.*, 2007, **9**, 1169.
51 M. Elas, K. H. Ahn, A. Parasca, E. D. Barth, C. Lee, C. Haney and H. J. Halpern, *Clin. Cancer Res.*, 2006, **12**, 4209.
52 H. Hou, N. Khan, O. Y. Grinberg, H. Yu, S. A. Grinberg, S. Lu, E. Demidenko, R. P. Steffen and H. M. Swartz, *Radiat. Res.*, 2007, **168**, 218.
53 R. Ansiaux, C. Baudelet, B. F. Jordan, N. Crokart, P. Martinive, J. DeWever, V. Grégoire, O. Feron and B. Gallez, *Cancer Res.*, 2006, **66**, 9698.
54 B. F. Jordan, N. Beghein, N. Crokart, C. Baudelet, V. Grégoire and B. Gallez, *Radiother. Oncol.*, 2006, **81**, 112.
55 J. Segers, V. D. Fazio, R. Ansiaux, P. Martinive, O. Feron, P. Wallemacq and B. Gallez, *Cancer Lett.*, 2006, **244**, 129.
56 D. S. Vikram, A. Bratasz, R. Ahmad and P. Kuppusamy, *Radiat. Res.*, 2007, **168**, 308.
57 K. Ichikawa, E. Sakabe, K. Kuninobu, T. Yamori, T. Tsuruo, T. Yao, M. Tsuneyoshi and H. Utsumi, *Antioxid. Redox Signal.*, 2007, **9**, 1699.
58 A. Bratasz, R. P. Pandian, Y. Deng, S. Petryakov, J. C. Grecula, N. Gupta and P. Kuppusamy, *Magn. Reson. Med.*, 2007, **57**, 950.
59 A. L. Kalen, E. H. Sarsour, S. Venkataraman and P. C. Goswami, *Antioxid. Redox Signal.*, 2006, **8**, 1273.
60 B. B. Hasinoff and A. Begleiter, *Free Radic. Res.*, 2006, **40**, 974.
61 R. Haywood, F. Rogge and M. Lee, *Free Radic. Biol. Med.*, 2008, **44**, 990.
62 L. P. Lund and G. S. Timmins, *Pharmacol. Ther.*, 2007, **114**, 198.
63 S. C. Kazmierczak, A. Gurachevsky, G. Matthes and V. Muravsky, *Clin. Chem.*, 2006, **52**, 2129.
64 A. Gurachevsky, E. Muravskaya, T. Gurachevskaya, L. Smirnova and V. Muravsky, *Cancer Invest.*, 2007, **25**, 378.
65 N. Miyoshi, K. Naniwa, T. Yamada, T. Osawa and Y. Nakamura, *Arch. Biochem. Biophys.*, 2007, **466**, 274.
66 S. Y. Wang, L. Bowman and M. Ding, *Planta Med.*, 2007, **73**, 468.
67 J. Kobiela, T. Stefaniak, J. Krajewski, B. Kalinska-Blach, D. Zurawa-Janicka, A. Lachinski, D. Gackowski, R. Olinski, J. Nowak, N. Knap, B. Lipinska, Z. Sledzinski and M. Wozniak, *Acta Biochim. Pol.*, 2007, **54**, 289.
68 K. Yamada, I. Yamamiya and H. Utsumi, *Free Radic. Biol. Med.*, 2006, **40**, 2040.
69 K. Pustelny, J. Bielanska, P. M. Plonka, G. M. Rosen and M. Elas, *Nitric Oxide*, 2007, **16**, 202.
70 P. Tsai, G. L. Cao, T. J. Merkel and G. M. Rosen, *Free Radic. Res.*, 2008, **42**, 49.
71 P. Dungel, R. Mittermayr, S. Haindl, A. Osipov, C. Wagner, H. Redl and A. V. Kozlov, *Arch. Biochem. Biophys.*, 2008, **471**, 109.
72 H. Fujii, K. Itoh, R. P. Pandian, M. Sakata, P. Kuppusamy and H. Hirata, *Magn. Reson. Med. Sci.*, 2007, **6**, 83.

73 N. Sanodze, N. Uberi, E. Uberi and B. Kulumbegov, *Georgian Med. News*, 2006, **140**, 65.

74 M. G. Bonini, A. G. Siraki, B. S. Atanassov and R. P. Mason, *Free Radic. Biol. Med.*, 2007, **42**, 530.

75 G. L. Millhauser, *Annu. Rev. Phys. Chem.*, 2007, **58**, 299.

76 X. L. Dai, Y. X. Sun and Z. F. Jiang, *Acta Biochim. Biophys. Sin.*, 2006, **38**, 765.

77 J. W. Karr and V. A. Szalai, *Biochemistry*, 2008, **47**, 5006.

78 D. P. Smith, D. G. Smith, C. C. Curtain, J. F. Boas, J. R. Pilbrow, G. D. Ciccotosto, T. L. Lau, D. J. Tew, K. Perez, J. D. Wade, A. I. Bush, S. C. Drew, F. Separovic, C. L. Masters, R. Cappai and K. J. Barnham, *J. Biol. Chem.*, 2006, **281**, 15145.

79 B. J. Tabner, S. Turnbull, J. E. King, F. E. Benson, O. M. El-Agnaf and D. Allsop, *Free Radic. Res.*, 2006, **40**, 731.

80 B. Klajnert, M. Cangiotti, S. Calici, J. P. Majoral, A. M. Caminade, J. Cladera, M. Bryszewska and M. F. Ottaviani, *Macromol. Biosci.*, 2007, **7**, 1065.

81 J. F. Boas, S. C. Drew and C. C. Curtain, *Eur. Biophys. J.*, 2008, **37**, 281.

82 J. V. Busik, S. Mohr and M. B. Grant, *Diabetes*, 2008, [epub ahead of print].

83 M. Apostolidou, S. A. Jayasinghe and R. Langhen, *J. Biol. Chem.*, 2008, [epub ahead of print].

84 V. A. Kipiani, M. N. Katsade, D. G. Delibashvili, M. S. Namoradze and N. V. Kipiani, *Georgian Med. News*, 2006, **130**, 97.

85 M. Yamaguchi, K. Wakasugi, R. Saito, Y. Adachi, Y. Yoshikawa, H. Sakurai and A. Katoh, *J. Inorg. Biochem.*, 2006, **100**, 260.

86 R. A. Anderson, L. M. Evans, G. R. Ellis, N. Khan, K. Morris, S. K. Jackson, A. Rees, M. J. Lewis and M. P. Frenneaux, *Diabet. Med.*, 2006, **23**, 258.

87 F. Sam, D. L. Kerstetter, D. R. Pimental, S. Mulukutia, A. Tabaee, M. R. Bristow, W. S. Colucci and D. B. Sawyer, *J. Card. Fail.*, 2005, **11**, 473.

88 Z. A. Almsherqi, C. S. McLachlan, M. B. Slocinska, F. E. Sluse, R. Navet, I. Kocherginsky, S. L. Liu, P. Mossop and Y. Deng, *Cell Res.*, 2006, **16**, 297.

89 K. Tsuda, *Heart Vessels*, 2008, **23**, 134.

90 C. Zhang, A. Yu, B. Yuan, C. Dong, H. Yu, L. Wang and C. Wu, *Thromb. Haemost.*, 2008, **99**, 324.

91 Z. A. Almsherqi, C. S. McLachlan, I. Kostetski, C. S. Lai, C. C. Chiu, S. L. Liu, S. K. Tay and Y. Deng, *Circ. J.*, 2006, **70**, 1226.

92 G. W. Davison, T. Ashton, B. Davies and D. M. Bailey, *Free Radic. Res.*, 2008, **42**, 379.

93 D. M. Bailey, L. Lawrenson, J. McEneny, I. S. Young, P. E. James, S. K. Jackson, R. R. Henry, O. Matieu-Costello, J. M. McCord and R. S. Richardson, *Free Radic. Res.*, 2007, **41**, 182.

94 J. H. Travese, Y. E. Nesmelov, M. Crampton, P. Lindstrom, D. D. Thomas and R. J. Bache, *Am. J. Physiol. Heart Circ. Physiol.*, 2006, **290**, H2453.

95 J. Brzeszczynska, M. Luciak and K. Gwozdzinski, *Free Radic. Res.*, 2008, **42**, 40.

96 A. Ueda, A. Hirayama, S. Nagase, M. Inoue, T. Oteki, M. Aoyama and H. Yokoyama, *Free Radic. Res.*, 2007, **41**, 823.

97 B. Balabanli, N. Türközkan, M. Akmansu and M. Polat, *Mol. Cell. Biochem.*, 2006, **293**, 183.

98 A. K. Gelasco and J. R. Raymond, *Am. J. Physiol. Renal Physiol.*, 2006, **290**, F1551.

99 Y. Wu, L. Li, T. Wen and Y. Q. Li, *Toxicology*, 2007, **232**, 50.

100 K. Suganuma, K. Tsukada, M. Kashiba, A. Tsuneshige, T. Furukawa, T. Kubota, N. Goda, M. Kitajima, T. Yonetani and M. Suematsu, *Antioxid. Redox Signal.*, 2006, **8**, 1847.

101 A. Rezaie, R. D. Parker and M. Abdollahi, *Dig. Dis. Sci.*, 2007, **52**, 2015.

102 V. Dang, J. Wang, S. Feng, C. Buron, F. A. Villamena, P. G. Wang and P. Kuppusamy, *Bioorg. Med. Chem. Lett.*, 2007, **17**, 4062.

103 S. Xia, F. A. Villamena, C. M. Hadad, P. Kuppusamy, Y. Li, H. Zhu and J. L. Zweier, *J. Org. Chem.*, 2006, **71**, 7268.

104 T. Presley, P. Kuppusamy, J. L. Zweier and G. Ilangovan, *Biophys. J.*, 2006, **91**, 4623.

105 A. Bratasz, A. C. Kulkarni and P. Kuppusamy, *Biophys. J.*, 2007, **92**, 2918.

106 R. Ahmad, D. S. Vikram, L. C. Potter and P. Kuppusamy, *J. Magn. Reson.*, 2008, [epub ahead of print].

107 B. B. Williams, H. Hou, O. Y. Grinberg, E. Demidenko and H. M. Swartz, *Antioxid. Redox Signal.*, 2007, **9**, 1691.

108 H. Hou, O. Grinberg, B. Williams, S. Grinberg, H. Yu, D. L. Alvarenga, H. Wallach, J. Buckey and H. M. Swartz, *Physiol. Meas.*, 2007, **28**, 963.

109 O. I. Butt, R. Carruth, V. K. Kutala, P. Kuppusamy and N. I. Moldovan, *Tissue Eng.*, 2007, **13**, 2053.

110 M. Khan, V. K. Kutala, S. Wisel, S. M. Chacko, M. L. Kuppusamy, P. Kwiatkowski and P. Kuppusamy, *Adv. Exp. Med. Biol.*, 2008, **614**, 45.

111 S. Matsumoto, M. G. Espey, H. Utsumi, N. Devasahayam, K. Matsumoto, A. Matsumoto, H. Hirata, D. A. Wink, P. Kuppusamy, S. Subramanian, J. B. Mitchell and M. C. Krishna, *Magn. Reson. Med.*, 2008, **59**, 619.

112 H. Fujii, K. Sakata, Y. Katsumata, R. Sato, M. Kinouchi, M. Someya, S. Masunaga, M. Hareyama, H. M. Swartz and H. Hirata, *Radiother. Oncol.*, 2008, **86**, 354.

113 B. F. Jordan, N. Christian, N. Crokart, V. Grégoire, O. Feron and B. Gallez, *Radiat. Res.*, 2007, **168**, 428.

114 A. Bratasz, R. P. Pandian, G. Ilangovan and P. Kuppusamy, *Adv. Exp. Med. Biol.*, 2006, **578**, 375.

115 N. Devasahayam, S. Subramanian, R. Murugesan, F. Hyodo, K. Matsumoto, J. B. Mitchell and M. C. Krishna, *Magn. Reson. Med.*, 2007, **57**, 776.

116 Y. Hama, K. Matsumoto, R. Murugesan, S. Subramanian, N. Devasahayam, J. W. Koscielniak, F. Hyodo, J. A. Cook, J. B. Mitchell and M. C. Krishna, *Antioxid. Redox Signal.*, 2007, **9**, 1709.

117 Y. Liu, F. A. Villamena, J. Sun, Y. Xu, I. Dhimitruka and J. L. Zweier, *J. Org. Chem.*, 2008, **73**, 1490.

118 V. K. Kutala, F. A. Villamena, G. Ilangovan, D. Maspoch, N. Roques, J. Veciana, C. Rovira and P. Kuppusamy, *J. Phys. Chem B*, 2008, **112**, 158.

119 Y. Han, B. Tuccio, R. Lauricella, A. Rockenbauer, J. L. Zweier and F. A. Villamena, *J. Org. Chem.*, 2008, **73**, 2533.

120 H. Sato-Akaba, H. Abe, H. Fujii and H. Hirata, *Magn. Reson. Med.*, 2008, **59**, 885.

121 E. Vanea, N. Charlier, J. Dewever, M. Dinguizli, O. Feron, J. F. Baurain and B. Gallez, *NMR Biomed.*, 2008, **21**, 296.

122 H. Fujii, *Nippon Hoshasen Gijutsu Gakkai Zasshi*, 2007, **63**, 1172.

123 F. Hyodo, K. H. Chuang, A. G. Goloshevsky, A. Sulima, G. L. Griffiths, J. B. Mitchell, A. P. Koretsky and M. C. Krishna, *J. Cereb. Blood Flow Metab.*, 2008, [epub ahead of print].

124 Y. Mori, R. Watanabe, S. Sakamoto, N. Endo, S. Nakano, K. Kanaori, H. Takashima, M. Ohkawa and K. Tajima, *J. Med.*, 2004, **35**, 49.

EPR studies of radiation damage to DNA and related molecules

David Becker and Michael D. Sevilla*

1. Introduction

1.1 Scope of this report

This Report, which covers the years 2004 through 2007, is an update of three previous Reports in this series which concern Electron Paramagnetic Resonance (EPR) studies of radiation damage to DNA, and related model compounds, covering the years 1991–1993, 1994–1997, 1998–2003, respectively.[1–3] The nature of charge transfer in DNA has received increasing attention and two recent reviews were published regarding this topic.[4,5] A review regarding the chemical pathways and reactions resulting from DNA damage also appeared in the time period covered by this report.[6] The role of low energy electrons (LEE) in the radiation damage of DNA continues to be a topic of interest. A comprehensive review of the effect of LEE in the solid state includes a discussion of their effects on plasmid DNA and smaller model compounds.[7] The number of theoretical calculations regarding the interpretation of EPR experimental data and the chemical pathways that lead to DNA radiation radical damage have dramatically risen in the past four years; a complete volume of "Advances in Quantum Chemistry" is devoted to this field and treats topics from the deposition of energy to clinical applications.[8]

1.2 Recent trends in DNA radiation chemistry

Recent single crystal and model compound research in amorphous systems has focused not only on the identification of radicals, but also on probing the factors that determine, and the mechanisms of, radical formation and stabilisation. This includes the details of how the local environment affects radical formation and stabilisation, especially the stabilisation due to proton transfer, the role of low energy electrons (LEE), the role of charge transfer, and the role that the protonation state of the one-electron loss radicals of both guanine and adenine plays in radical formation and stabilisation. There is still some disagreement in the literature regarding protonation states in model compounds, and much effort has been devoted to clarify this topic. Much work has also been done on exploring the details of formation of sugar moiety radicals from excited states, especially with regard to how pH, the presence of phosphate groups, and oligomer length determines which specific sugar radicals are formed.

With regard to DNA itself, there is now a wide consensus that the major base radicals stabilised in irradiated DNA at low temperatures are the guanine cation radical and the one-electron gain radicals of thymine and cytosine.[3,6,9,10] Because base radicals are not responsible for induction of significant amounts of strand breaks,[5] the search for radicals on the deoxyribose moiety, which are the likely precursors to strand breaks, has become very prominent in recent work. In the previous report in this series, the formation of sugar moiety radicals from excited state base radicals was reported.[3] In the intervening years, this phenomenon has been thoroughly explored in a large variety of model systems and in DNA. For the first time, track structure and radical clustering have been determined in Ar-ion beam irradiated DNA using PELDOR techniques.

Department of Chemistry, Oakland University, Rochester MI, USA.
E-mail: sevilla@Oakland.edu; Fax: 248-370-2321; Tel: 248-370-2328

As a result of the tremendous improvement in computational power and methodologies, *ab initio* calculations have become very useful in calculating radical properties pertinent to EPR spectroscopy, such as hyperfine coupling constants, spin densities, and *g*-values. An important aspect of these has been the ability to include solvation effects, since these greatly affect radical stabilisation. Molecular properties that effect radical formation such as ionization potentials and electron affinity are a continuing topic of interest.[8,10]

In summary, the last four years have seen substantial advances in both experimental design and theoretical calculations regarding radiation effects in DNA. Environmental effects, excited state phenomena, charge transfer processes, the role of LEE and the nature of radical clusters have been explored, and are summarized in this report.

1.3 Symbols used

The same abbreviations that were used in our previous reports,[1–3] have also been employed here for continuity. Radicals are symbolized in the text by giving the location and the type of chemical damage. For example, the radical formed as a result of reversible protonation at the N3 site of the cytosine radical anion would be C(N3)H$^{\bullet}$. Only the isotropic component of hydrogen hyperfine couplings are shown on structures, even if the coupling is a highly anisotropic α-proton coupling. The principle values for nitrogen hyperfine couplings are given in the narrative rather than on structures. All hyperfine coupling constants are given in millitesla (1 mT = 10 G). Unless otherwise stated, the conversion factor from megahertz (MHz) to millitesla (mT) is A(mT) = [A(MHz)/28.03]. The spin densities shown are, at times, an average of those calculated from isotropic couplings and, separately, from dipolar interactions; they are meant to be indicative only and the original work should be consulted for details. We have used Roman numerals for numbering the structures of the undamaged compounds, whereas, for radicals Arabic numerals have been employed. The parent (undamaged) structures of the compounds reported on in this section of the report are shown in Table 1.

2. DNA constituents

2.1 Single crystal studies

2.1.1 Purines. *Hypoxanthine hydrochloride monohydrate*. In a study of X-irradiated hypoxanthine hydrochloride monohydrate (ı) single crystals, three radical species (Table 2, 1–3) were found using room temperature irradiation, or irradiation at 10 K followed by warming to room temperature.[11] In this crystal, the hypoxanthine is protonated at N7. ENDOR-induced EPR (EIE) investigation of a crystal irradiated at 10 K and warmed to room temperature gave line components from radicals 1–3 (shown as the fully protonated molecules.) Selective deuteration to give three forms of the molecule (Table 1) allowed the authors to assign hyperfine coupling constants with a high degree of confidence. One of the radicals characterized is the biologically relevant C8 hydroxyl adduct, radical 3.[12]

Radical 1 gave four ENDOR lines in the fully protonated crystal and only one line for the molecule deuterated at the nitrogen atoms. The hyperfine coupling constants shown without asterisks were determined from these ENDOR spectra. The large beta proton couplings at C8 were evaluated from EPR spectra observed after storage of crystals at room temperature for "extended" periods. Nitrogen hyperfine couplings of (1.52, 0, 0) mT (N7) and (0.678, 0, 0) mT (N9) were estimated from the EPR spectral simulations. The spin densities shown were determined from the experimental hyperfine coupling constants. Spin densities were also calculated (Gaussian 03, B3LYP functionals, 6-311G(2df,p) after opitimization) and are shown in Table 3. The calculated spin densities at C2, N7 and N9 agree quite well with three

Table 1 Undamaged compounds considered in section 2
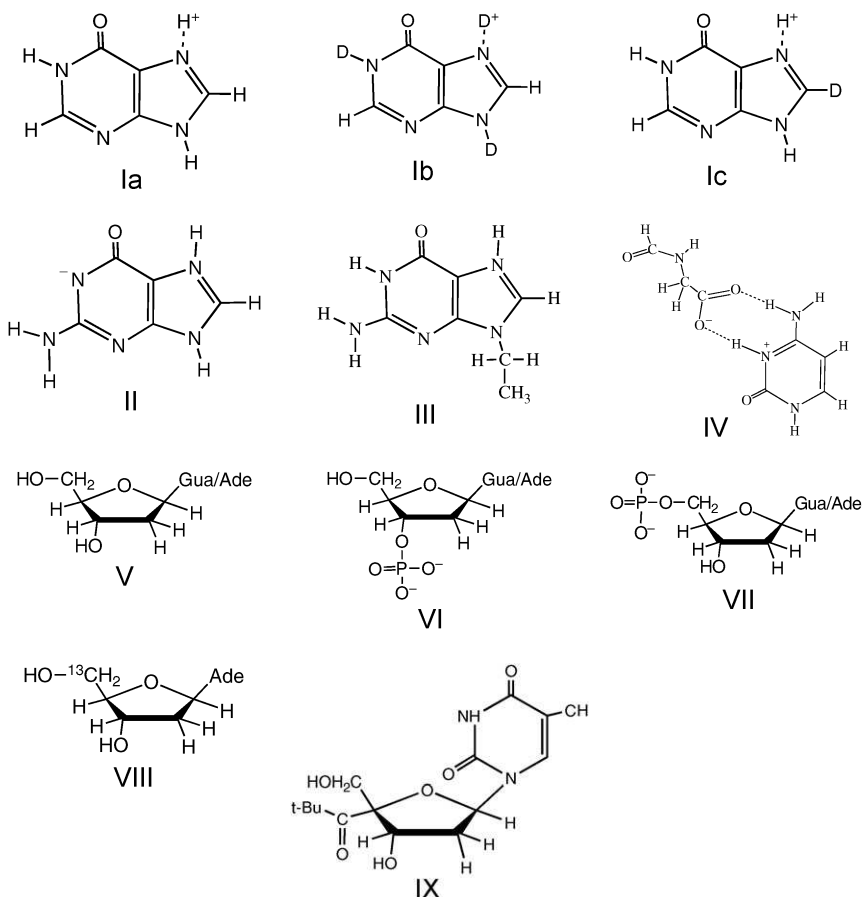
experimentally determined spin densities at these positions. This radical was the only radical that remained after 2 months storage at room temperature.

Radical 2, the C2 H-addition radical, gave two ENDOR lines which disappeared after two months storage at room temperature. Although the line from C8(H) could be analyzed, a full angular ENDOR analysis could not performed for the second line. It was concluded that it originated with the easily exchangeable proton at N1. EPR simulations resulted in the C2(H) beta proton hyperfine couplings shown and nitrogen couplings of (0.21, 0, 0) mT for N1 and (2.11, 0, 0) mT for N3.

Radical 3, the C8(OH)$^\bullet$ addition species is important in DNA radiation processes. In guanine, the C8(OH)$^\bullet$ addition radical can produce the biologically significant (diamagnetic) 8-oxo-G lesion by a simple one electron oxidation.[13,14] In hypoxanthine, 3 gave four ENDOR lines, including one which was absent in C8 deuterated crystals and two which were from exchangeable protons. Nitrogen couplings of (0.368, 0, 0) mT for N7 and (0.264, 0, 0) mT for N9 were determined by simulating EPR spectra. Calculations on an optimized structure for this radical resulted in hyperfine coupling constants that were in excellent agreement with the experimental values. For example, calculated isotropic couplings of 0.34 mT for C2(H), 1.72 mT for C8(H), 0.770 mT for N7(H) and 0.30 mT for N9(H) were obtained. The original work should be consulted for details.

Table 2 Radicals considered in section 2

Table 2 (*continued*)

22   23   24
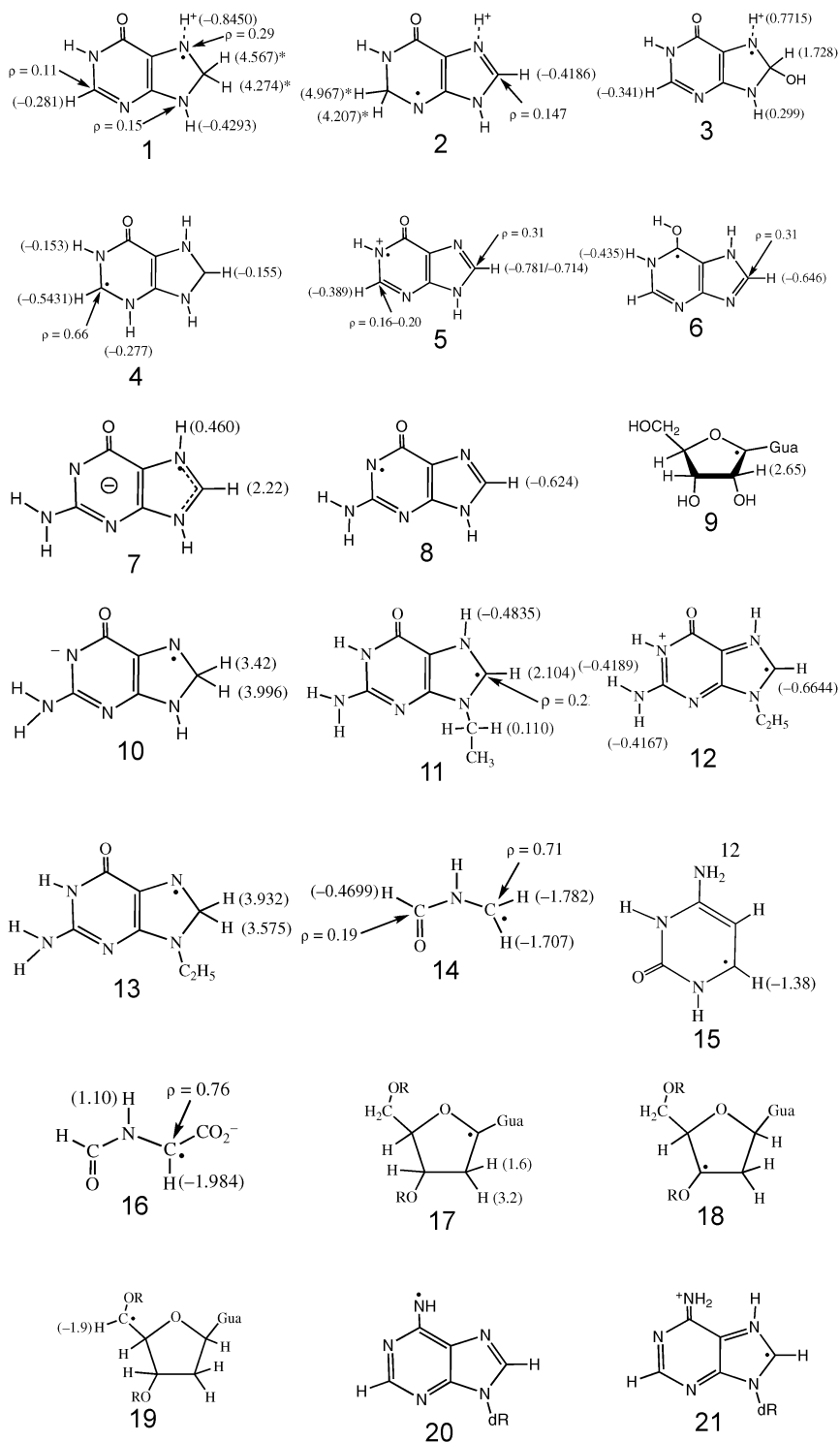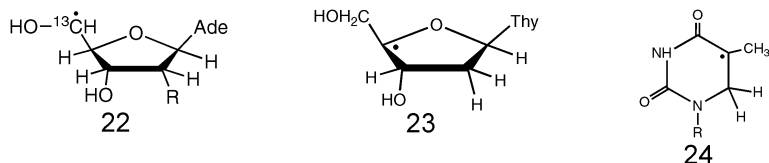
Table 3 Calculated spin densities for hypoxanthine radicals

Radical	N1	C2	N3	C4	C5	C6	O6	N7	C8	N9
1	−0.02	0.08	−0.03	0.06	0.25	−0.02	0.19	0.31	−0.03	0.15
3	−0.02	0.09	−0.02	0.08	0.27	−0.02	0.21	0.28	−0.01	0.12

Since no products from ˙OH were observed, the C8(OH)˙ adduct in hypoxanthine is presumed to form by water addition followed by deprotonation, as suggested earlier for guanine in DNA.[13,14] Because the location of the water in this mono-hydrate crystal is known, some mechanistic details of the formation of 3 could be derived. In this crystal, the single water is located 3.28 Å above the imidazole ring of the purine, very near C8 (Scheme 1). In guanine · HCl · 2H$_2$O, a water is similarly located and the C8(OH) adduct is also found, [15] although in this system the adduct forms at low temperature after irradiation. On the other hand, in hypoxanthine,[11] warming is required to form the ˙OH adduct. However, in the monohydrates guanine · HCl · H$_2$O and guanine · HBr · H$_2$O, the water is coplanar with the purine and no ˙OH adduct is formed[16,17] even though the guanine cation radical is detected. The authors, thus, conclude that the position of the water above C8 is the optimum position for addition to the purine.
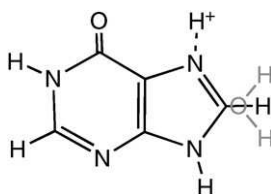
Scheme 1

Hypoxanthine hydrochloride monohydrate was used again in a single crystal study to investigate the manner in which proton transfer affects the stability of primary radicals.[18] Of primary concern is understanding the manner in which the environment, including the presence of proton donor and/or acceptor sites, affects radical stabilities. Whereas the previous paper[11] (*vide supra*) focused on room temperature products in this system, this paper was concerned with the effects at low temperature. Crystals were X-irradiated (50–100 kGy) at 10 K and EPR and ENDOR studies were also performed at 10 K. In this crystal, hypoxanthine is protonated at N7 (Structure I). Normal crystals, crystals which were deuterated at exchangeable positions only, *i.e.* nitrogen, or at C8 only, or at both were used to help identify the radicals formed. Extensive DFT calculations were performed in order to assist in radical identification. This paper presents the computational results for a very large number of protonation states for the hypoxanthine radicals observed. Based on EPR simulations for non-deuterated crystals, the three radicals 4, 5 and 6 (described below) form in the proportions 52.3%, 36.5% and 11.3%, respectively.[18]

Radical 4 is thought to be the N3 protonated one-electron addition radical. It gave four proton hyperfine interactions both in ENDOR and EIE spectra. Eigenvector directions and/or the hyperfine coupling tensors indicated that all four couplings are α-like. The isotropic component of the C2(H) coupling is smaller than that expected relative to the dipolar component. In addition, ρ(C2) calculated from the McConnell relation using the isotropic hyperfine coupling is very different from that calculated from the Gordy-Bernhard relation using anistropic hyperfine couplings, indicating the C2 radical site is non-planar.[19] Calculations and experimental data suggest that C2 is bent *ca.* 20° out of the plane of the ring. The spin density calculated from the anisotropic couplings, ρ(C2) = 0.66, is the favoured value. EPR simulations required an N1 coupling of (0.550, −0.14, −0.14) mT and N3 coupling of (0.453, −0.12, −0.12) mT in order to match experimental spectra. For simulations, all nitrogen couplings were assumed to be axial.

A second radical found is the deprotonated one-electron loss radical 5. Two hyperfine couplings were observed from 5, both with α-like character. EPR simulations required an N1 coupling of (0.217, −0.0442, −0.0442) mT and N3 coupling of (0.3747, −0.0888, −0.0888) mT in order to match experimental spectra. The spin densities shown were calculated from the McConnell and Gordy-Bernhard relations. Both radical sites were planar or near planar. A likely second conformer of 5 with a different hyperfine coupling for C8(H) was observed in crystals in which the nitrogen positions had been deuterated, but not in normal crystals, nor in crystals with only the C8 position deuterated. This raises the possibility that deuterium isotope effects are involved in its formation.

Radical 6 is likely formed by one-electron reduction accompanied by gain of a proton at the oxygen and loss of a proton from N9. The site at C8 appears to be planar. The hydrogen at oxygen is located in or close to the plane of the purine ring, thus, no hyperfine coupling is observed for it. EPR simulations required an N1 coupling of (0.4357, −0.218, −218) mT, an N3 coupling of (0.231, −0.116, −0.116) mT and N7 coupling of (0.3775, −0.189, −0.189) mT in order to match experimental spectra. As in previous radicals, all nitrogen couplings were assumed to be axial. The ENDOR lines for 6 were observed only in non-deuterated crystals, even though crystals with a C8(H) and deuterons at the nitrogens should show a C8(H) resonance and crystals with C8(D) but hydrogens at nitrogen sites should show a N1(H) resonance. This is attributed to a deuterium isotope effect in radical formation (*vide infra*).

Two additional α-proton hyperfine couplings were observed in hypoxanthine hydrochloride monohydrate, one with a_{iso} = −0.996 mT and a second with a_{iso} = −0.703 mT. The first appeared to be due to a C2(H) coupling on a conformer of 4 that is more planar at C2 than is 4; the second could not be reliably assigned.

Deuterium isotope effects. In deuterated crystals at 10 K, a higher yield of a minor conformer of 4 (with a relatively planar C2) site is formed than in normal nondeuterated crystals. It is speculated that in deuterated crystals, the bending at C2 required to form 1 is hindered by the presence of deuterons at exchangeable positions and the minor conformer is formed instead.

Sodium guanosine dihydrate. In a study of sodium guanosine dihydrate (II) single crystals at high pH (>12), three radicals were found at 10 K after X-irradiation at 10 K.[20] After warming to room temperature, a fourth radical is produced. Table 4 summarises the radicals detected. Even though these results are for the nucleoside rather than the deoxyribonucleoside, the base radicals formed are likely pertinent to DNA nucleobase radical formation.

Radical 7 is the N7 protonated guanine radical anion. The C8(H) hyperfine couplings and hyperfine principal axes eigenvectors in this radical have unusual properties that can be explained by assuming the radical is pyramidal around C8. For the alpha like C8(H) coupling, the isotropic component of the hyperfine coupling, a_{iso} is positive rather than negative as is normally found for α-hydrogen couplings at a planar site. A positive a_{iso} is known to occur for circumstances in

Table 4 Radicals found in guanosine dihydrate at pH > 12

Radical	Percentage at 10 K	Couplings	Remarks
7	60%	Two H, two N	N7 H-adduct of electron-loss radical, distorted geometry
8	27%	One H, one N	Primary electron-loss radical
9	13%	One H	C1′•
10	—		C8(H) Adduct at 298 K

which the radical site is substantially nonplanar.[19] In fact, for a sodium guanosine dihydrate model, DFT calculations [B3LYP/6–311G(2df,p)//6–31(d,p)] indicate the C8–H bond is out of the N7–C8–N9 plane by 45.05°. These same calculations result in principal value system eigenvectors for the C8(H) coupling which are very close to the experimentally determined ones. In similar fashion, a_{iso} for N7(H) is thought to be positive with the N7–H bond 31.5° out of the N7–C8–N9 plane. However, it is noted that interactions between N7(H) hydrogen and the neighboring ribose C2′O group from which the hydrogen likely transferred might result in a negative a_{iso} and pyramidal N7 site and still be consistent with the experimental results. Fitting of simulated EPR spectra to the experimental spectra result in nitrogen hyperfine couplings of (1.71, 0.724, 0.724) mT for N7 and (0.831, 0.0053, 0.0053) mT for N9. For each these nitrogen atoms, the largest coupling is associated with an eigenvector perpendicular to the purine ring plane, as expected. The authors note that the formation of this radical at 10 K indicates that the activation energy for proton transfer from an adjacent C2′O(H) to N7 in the radical must be very low.

A second radical found in sodium guanosine dihydrate is the primary electron loss radical 8. Based on the observation of its single ENDOR line, the radical is present at 10 K, begins to decay at 40 K with no successor radical observed, and is still present at 200 K. Because N1 is deprotonated above pH 9, radical 8 has zero charge. A single experimental nitrogen hyperfine coupling of (1.50, 0.039, 0.039) mT was assigned to N3 using EPR simulations to determine the coupling itself and DFT calculations to determine which nitrogen gave rise to it; with this assignment, the full breadth of the EPR spectrum was accounted for, thus N2 is presumed to have no observable hyperfine interactions. A recent investigation, at low temperature, of radical 8 in 2′-deoxyguanosine in a LiCl glass reports $a_{iso} = -0.707$ mT for the α-proton hyperfine coupling for C8(H), and couplings of (1.20, 0, 0) mT for N3 and (0.80, 0, 0) mT for N2 (*vide infra*).[21] There is quite good agreement between the C8(H) and N3 couplings in the two systems considering the very different environments.

A third radical found in X-irradiated sodium guanosine dihydrate single crystals is 9, the C1′• sugar radical. Only one ENDOR line is observed for this radical and it shows very little anisotropy, indicating the coupling involved is a β-coupling. The ENDOR induced EPR spectrum indicated no other couplings were present in this radical. The authors considered the possibility that C2′• radical may be responsible for the single hyperfine coupling observed and the expected couplings from the protons at C3′ and C2′O reduced to near zero by the conformation of the radical. The authors note that for this to occur, however, improbably large changes in the conformation of the ribose group from its original geometry in the single crystal would be required. The possibility that C3′• or C4′• might be responsible for the single ENDOR line observed was not mentioned. After storing the crystals overnight at room temperature, the EPR spectrum was dominated by the well known C8 hydrogen addition radical 10.

9-Ethylguanine. In an effort to further understand radical formation in guanine, a single crystal EPR and ENDOR study of 9-ethylguanine (III) was carried out with irradiation at 10 K and at room temperature.[22] Deuteration at the easily exchangeable positions and at C-8 was used to help characterise the various radicals observed.

Extensive DFT calculations were performed to support the radical assignments. The recent observation of dissociative electron attachment processes in DNA and related model systems from low energy electrons[23,24] focused new attention on anionic radical states of guanine, a principal topic of this work. The authors properly note that the condensed state will stabilise valence bound anions relative to dipole bound states.

Immediately after irradiation at 10 K, a radical thought to be the N7 protonated anion (11) was observed. The EPR spectra of the radical indicated a π-radical which had coupling to one or more of the nitrogen atoms in the purine ring. The ENDOR line associated with the C8(H) coupling was found in crystals with a hydrogen at C8, but not in crystals that were deuterated at C8. The directional characteristics of the coupling, and the fact that the spin density at C8 calculated using the McConnell relation ($\rho = 0.74$) is different from that calculated using the Gordy-Bernhard relation ($\rho = 0.53$) indicates that the C8 site is non-planar. Theoretical calculations indicated an ''extremely'' bent structure with the C8–H bond bent out of the radical plane and the N7–H bond less severely out of plane. It is well known that out of plane bending at a radical site can cause the normally negative isotropic component of an α-coupling from a hydrogen atom become positive and large.[19] Hence, the relatively large positive isotropic coupling for C8(H) was thought to occur because of the unusual non-planar structure around C8. The authors note that the coupling assigned to the hydrogen atom on the ethyl group displayed typical β-coupling features and was from a nonexchangeable site. These features permitted a straight-forward assignment. Using EPR spectra, hyperfine couplings of (1.39, 0.428. 0.428) mT were observed for N7 and (0.678, 0.121, 0.121) mT were observed for N9. As expected, the eigenvectors connected with the larger components of the nitrogen hyperfine couplings were normal to the radical plane. The authors offer a hypothesis that 11 is formed through a two step process, electron capture followed by a barrier free or low activation energy protonation. This radical disappears at 125 K with no apparent successor radical.

Radical 12 is the irradiation formed primary one-electron oxidation product, the guanine cation radical, $G^{\bullet+}$. ENDOR lines from 12 were observed immediately after irradiation at 10 K. The coupling to C8(H) was typical for an α-proton and the eigenvectors obtained consistent with the assignment. Since both the McConnell relation and Gordy-Bernhard relation gave the same spin density at C8, it was concluded that the C8 site was planar. The ENDOR lines from the two hydrogen atoms at N2 were not observed in crystals in which exchangeable positions were deuterated. The isotropic component of each of these couplings was approximately equal to the dipolar value, a feature that the authors note is typical of an N(H) α-coupling. Using EPR, N3 hyperfine couplings of (0.967, 0.043, 0.043) mT and N2 couplings of (0.410, 0.061, 0.061) mT were determined, with the larger component of each normal to the radical plane. The authors note that existence of $G^{\bullet+}$ indicates the barrier to deprotonation from this radical is too high for the reaction to occur at 10 K.

When crystals of 9-ethylguanine irradiated at 10 K were warmed to room temperature, no EPR signal was detectable. However, room temperature irradiation gave an EPR signal dominated by radical 13, the C8 H-addition radical. This behavior indicates that the thermal energy needed to mount the activation energy barrier for formation of the radical must be present at the time of irradiation.

Two other radicals were observed in 9-ethylgaunine, one formed by 10 K irradiation with a coupling to an ethyl group hydrogen atom and one formed by room temperature irradiation with two EPR visible line components of *ca.* 2.6 mT separation. These two radicals could not be identified.

2.2.2 Pyrimidines. A search of a variety of electronic data bases revealed no papers on the EPR of radiation damaged DNA related pyrimidine single crystals in the time period covered by this review.

2.2.3 Mixed crystal systems. In an effort to explore the nature of electron transfer in DNA, a single crystal study of a N-formylglycine-cytosine complex (IV) was undertaken.[25] A body of earlier work had indicated that net electron transfer from nucleoproteins to DNA occurs in a variety of DNA/nucleoprotein complexes.[26–28] This electron transfer would be radioprotective were the transferred electrons to recombine with electron-loss sites, which are known to be an important source of strand breaks. However, it is also true that these electrons may form electron gain damage sites, potentially leading to clustered damage.

Single crystals of the complex were X-irradiated at 10 K and at 273 K and studied at temperatures between 10 K and 293 K. EPR, ENDOR and EIE were performed using X-band (EPR) and K-band instruments (EPR, ENDOR, EIE). Extensive DFT calculations were used to explicate and confirm assignments.

Radical 14 is observed immediately after irradiation at 10 K. All three observed couplings, including the observed eigenvectors, were characteristic of α-proton couplings. In order to simulate an EPR spectrum that matched the experimental spectrum for 14, a very small nitrogen coupling (0.20 mT) has to be included; this coupling was not very anisotropic. Radical 14 is the familiar amino acid decarboxylation product that arises from one-electron oxidation. Theoretical calculations suggested that the decarboxylation process was barrier free and could, therefore, plausibly occur at 10 K. The spectrum from 14 disappeared slowly as the crystal is warmed above 150 K.

An analysis of a single coupling observed using ENDOR indicated it was from the one electron reduced cytosine species (15). In this single crystal, cytosine is protonated at N3 from the N-formylglycine, thus the one-electron reduced radical is neutral. A second α-proton coupling with isotropic value −1.21 mT and eigenvectors identical to those in 15 was also observed. The possibility exists that the radical responsible for this is a different conformation of 15, but not enough information was available to "plausibly" identify the radical. As with 14, the signal from 15 and its possible conformer disappeared slowly with warming above 150 K.

Irradiation of an N-formylglycine-cytosine single crystal (H_2O) at 275 K and EPR analysis indicated the presence of three radicals, one on the amino acid and two on the cytosine. The higher temperature irradiated samples did not give observable ENDOR signals.

A strong central feature in the EPR spectrum was attributed to radical 16, the well known glycine backbone radical. The coupling for the hydrogen atom on the central backbone carbon is typical for an α-proton coupling. The hydrogen coupling at the N(H) is fairly isotropic, as expected for a β-proton coupling. Theoretical calculations and experimental data indicated that in this radical there is an approximate 38° rotation of the N–H bond around the C–N bond, reducing the N–H dihedral angle from the expected 171° for the pristine radical to 128° for the observed species. The EPR spectra also indicated a fairly isotropic nitrogen coupling $a_N \leq 0.36$ mT. This radical is thought to form as a result of hydrogen abstraction by radical 14.

The two other radicals observed from 275 K irradiation were the cytosine C6 hydrogen addition radical and the C5 hydrogen addition radical. Because they have been well characterized in the past, they were not extensively investigated. For room temperature irradiation, the relative amounts of radicals present were 16 (40%), C5 addition (5–8%), C6 addition (5–8%), unidentified singlet with line width *ca.* 1.4 mT (50%).

The fact that no oxidation products were observed at cytosine suggests that hole transfer from the (protonated) cytosine to the (deprotonated) N-formylglycine occurred at 10 K. DFT calculations (apparently on the gas phase species) indicated that the ionization potential of the N-formylglycine species is less than that of cytosine; this provides a driving force for hole transfer from cytosine to N-formylglycine. Calculations also indicated that the electron affinity of the cytosine species was positive and that of the N-formylglycine species negative. This provides a driving force for electron capture by the cytosine after irradiation. In summary, the

electron-loss product and electron-gain product are separated at low temperature immediately after irradiation, indicating that hole transfer has occurred. The nature of the secondary radicals formed on annealing suggests that no further hole or electron transfer occurs as samples are annealed. It should be noted that the possibility exists that some number of the radiation-ejected electrons may actually attach to the N-formylglycine, but then rapidly tunnel to the cytosine at 10 K.

2.3 Amorphous systems

2.3.1 Excited state phenomena in DNA model systems. The period covered by this review saw a significant advance in the understanding of the role that excited state radicals may play in giving rise to strand break precursors from the irradiation of DNA. The impetus for these investigations was the experimental finding that high LET radiation (O and Ar ion beams) of DNA resulted in higher yields of neutral sugar radicals than did low LET (γ) radiation. A possible explanation for this result was that excited state processes in the ion-beam high energy-density core produced relatively high yields of sugar radicals.[29]

Guanine model compounds. In an investigation to explicate excited state radical mechanisms, guanine deoxyribonucleosides and -tides (V, VI, VII) were studied at low temperatures.[30] In the experiment, a sample of the compound to be studied and the electron scavenger potassium persulfate ($K_2S_4O_8$) are γ-irradiated in an aqueous LiCl glass at 77 K. Gamma irradiation results in $Cl_2^{\bullet-}$, and $SO_4^{\bullet-}$, both oxidizing agents. On careful annealing, $SO_4^{\bullet-}$ reacts to form additional $Cl_2^{\bullet-}$ and the aggregate $Cl_2^{\bullet-}$ oxidizes the guanine moiety of the nucleoside/tide to form relatively pure guanine radical cation, $G^{\bullet+}$ (Fig. 1A–D).

At the natural pH of the LiCl (*ca.* 5), the guanine cation radical is *ca.* 50% deprotonated from N1.[21] Hence, visible/UV illumination (at 143 K or 77 K) results in the formation of relatively large amounts of sugar radicals from $G^{\bullet+}$ (Fig. 2A–C).
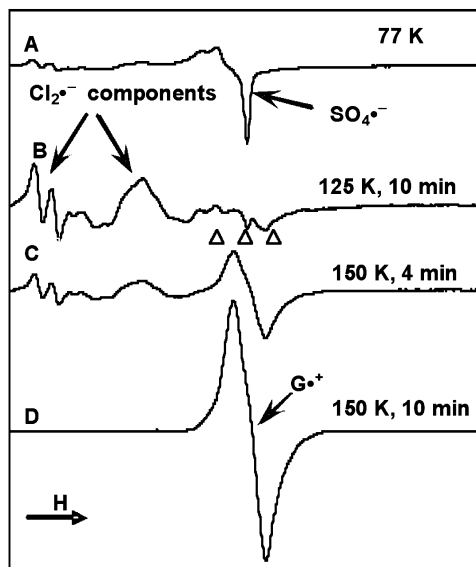
Fig. 1 (A) EPR spectrum from γ-irradiated (2.5 kGy) 5′-D,D-2′-dG in the presence of $K_2S_2O_8$ in a 7 *M* N_2-saturated LiCl/D_2O glass. $SO_4^{\bullet-}$ and $Cl_2^{\bullet-}$ formed by the irradiation. (B) After annealing to 125 K for *ca.* 10 min. (C) After further annealing at 150 K for 4 min. (D) After annealing for another 6 min (*i.e.*, total 10 min) at 150 K. Only the spectrum of $G^{\bullet+}$ is observed at this point. Reprinted with permission from ref. 30, *Nucleic Acid Research*, Copyright (2005), Oxford University Press.
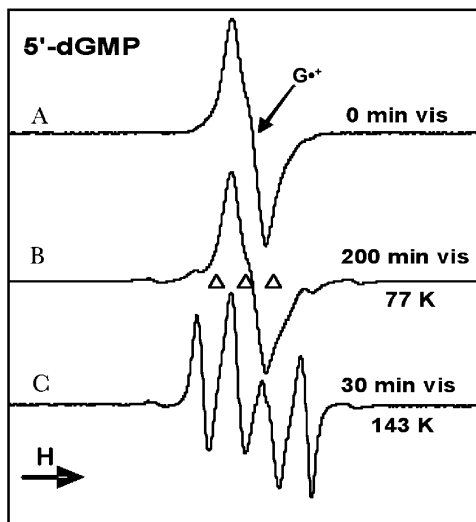
Fig. 2 (A) $G^{\bullet +}$ in 5′-dGMP. (B) Photo-excitation at 77 K with produces C3′$^{\bullet}$ and C1′$^{\bullet}$. (C) Photo-excitation of a new sample of $G^{\bullet +}$ at 143 K results in 95% conversion to primarily C1′$^{\bullet}$. All spectra were recorded at 77 K. Reprinted with permission from ref. 30, *Nucleic Acid Research*, Copyright (2005), Oxford University Press.

Analysis of the EPR spectra obtained has been used to determine the identity and amount of each sugar radical produced. In order to determine correct benchmark spectra for the various sugar radicals and other radicals found in the composite spectra obtained, extensive studies were carried out using selectively deuterated deoxyguanosine at C3′ and C5′. Table 5 summarizes the conversion efficiency and cohort of radicals found for the compounds investigated. As can be seen, the presence of a phosphate group at C3′ or C5′ deactivates sugar radical formation at that site. This is consistent with theoretical calculations of the energies of the radicals formed.[31,32] It should also be noted that the wavelength of light used for illumination had no effect on sugar radical formation in the 310 nm–700 nm range. At pH $\geq$ 9, sugar radical formation did not occur. The structures of C1′$^{\bullet}$, C3′$^{\bullet}$ and C5′$^{\bullet}$ are shown in Table 5 as radicals 17, 18 and 19, respectively.

Table 6 shows the hyperfine coupling constants found for the sugar radicals in the deoxyguanine model compounds investigated. The couplings were derived from the benchmark spectra used to deconvolute the composite spectra found after UV/ visible light illumination. Because of this, the actual hydrogen responsible for a specific coupling is not always known. The *g*-value reported is an apparent *g*-value, determined from the centre of the experimental spectrum.

Table 5 Sugar radicals in photolysed $G^{\bullet +}$

Compound	Illumination temperature (K)	Percent $G^{\bullet +}$ convertedto sugar radicals	C1′$^{\bullet}$	C3′$^{\bullet}$	C5′
2′–dG	143	90	10%	35%	55%
	77	30	10%	40%	50%
5′-dGMP	143	95	95%	5%	—
	77	30	15%	30%	5%
3′-dGMP	143	85	40%	—	60%
	77	15	40%	—	60%

Table 6 EPR parameters for sugar radicals in photolysed G$^{\bullet+}$

Radical	Hyperfine coupling constants (mT)	g-value
C1′$^{\bullet}$		
2′-dGuo, 5′-D,D-2′-dG, 5′-dGMP	1.6 (1βH), 3.2 (1βH)	2.0029
3′-dGMP	1.55 (1βH), 3.5 (1βH)	2.0029
DNA (77 K illumination)	1.5 (1βH), 3.7 (1βH)	2.0029
C5′$^{\bullet}$		
2′-dG, 5′-D,D-2′-dG, 3′-dGMP	*ca.* 1.9 (1αH)	2.0025
C3′$^{\bullet}$		
2′-dG, 5′-D,D-2′-dG	*ca.* 2.1 (1βH), 2.5 (1βH), 4.2 (1βH)	2.0032
5′-dGMP	*ca.* 2.0 (1βH), 3.0 (1βH), 4.1 (1βH)	2.0032
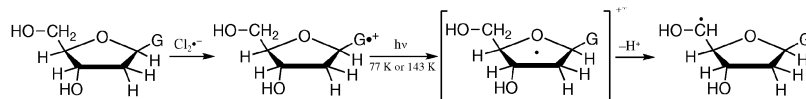
Scheme 2 Reprinted with permission from ref. 30, *Nucleic Acid Research*, Copyright (2005), Oxford University Press.

DFT calculations were performed in order to understand a possible mechanism through which UV/visible illumination of a radical with spin density entirely on the guanine base could result in stable radicals located on the deoxyribose sugar. It was concluded that the illumination of G$^{\bullet+}$ resulted in a core-excited state with significant positive charge and spin density on the sugar moiety. Fast deprotonaton from the sugar would then follow and result in formation of a relatively stable neutral sugar radical (Scheme 2, using C5′$^{\bullet}$ as an example).

As previously indicated, pH was found to have a great effect on sugar radical formation in these systems. The native pH of aqueous (D$_2$O) 7.5 *M* LiCl is *ca.* 5, thus about half the radicals in one-electron oxidized guanine are in the deprotonated form, G(–H)$^{\bullet}$ and about half are in the G$^{\bullet+}$ form. The deprotonated form does not give sugar radicals when photolyzed.

In summary, it was concluded that excited state base radicals in these systems do form neutral sugar radicals and that the high yields of neutral radicals in ion beam irradiated DNA might well originate with excited state core processes.[30]

Adenine model compounds. In continuing work regarding the role of excited state radicals in DNA radiation damage, Adhikary *et al.* explored the formation of deoxyribose radicals in 2′-deoxyadenosine and its derivatives.[33] In this work, dAdo, 3′-dAMP and 5′-dAMP (V, VI, VII) were investigated in 7 *M* LiCl aqueous glasses. Using techniques similar to those just discussed for dGuo and its derivatives, C3′$^{\bullet}$ and C5′$^{\bullet}$ radicals were efficiently generated from the one electron oxidized adenine base in these model systems. In this case, nearly pure one-electron oxidized adenine radical was formed using Cl$_2^{\bullet-}$ as the oxidant. Because the pK_a of A$^{\bullet+}$ is *ca.* 1 and A$^{\bullet+}$ is proposed to be deprotonated in adenine crystalline systems even at 4K,[6,34],[12] at the natural pH of 7 M LiCl (*ca.* 5), this one-electron loss radical was assumed to be deprotonated at the exocyclic nitrogen to form A(–H)$^{\bullet}$.[19] However, recent work in our laboratory indicates that the adenine cation is actually stabilised at 150 K in LiCl glasses. Therefore we correct this assignment of A(–H)$^{\bullet}$ [20] to A$^{\bullet+}$.[21] UV/visible illumination of the electron loss adenine radical at 143 K resulted in the radicals shown in Table 7.

The hyperfine couplings and g-values found for the benchmark sugar radical spectra were similar to, but not identical to, those found for the same radicals in deoxyguanine radicals (*vide supra*). The g-value reported is an apparent g-value, determined from the centre of the experimental spectrum (Table 8).

Table 7 Sugar radicals in photolysed one electron oxidized adenine

Compound	Percent conversion to sugar radicals	C1'•	C3'•	C5'
2'-dAdo (pH *ca.* 5)	100	5%	15%	80%
(pH 12)	80	—	100%	—
5'-dAMP	100	—	50%	50%
3'-dAMP	100	5%	—	95%

Table 8 EPR parameters for sugar radicals from photolysed one electron oxidised adenine

| Compound	Hyperfine coupling constants (mT)	g-value
C1'•		
2'-dAdo, 3'-dAMP	1.55 (1βH), 3.5 (1βH)	2.0029
C3'•		
2'-dAdo, 5'-dGMP	2.1 (1βH), 28 (1βH), 50.5 (1βH)	2.0032
2'-dAdo (pH 12)	1.86 (1βH), 28 (1βH), 38 (1βH)	2.0032
C5'•		
2'-dAdo, 3'-dAMP, 5'-dAMP	*ca.* 2.1 (1αH)	2.0032

As observed with guanine model compounds, the presence of a phosphate group at C3' or C5' deactivated radical formation at that site, relative to the presence of an OH. In addition sugar radical formation was not sensitive to the wavelength of light used for illumination in the 310 nm to 700 nm range.

This work unambiguously identified the C5'• radical by use of ^{13}C labeled dAdo, [5'-^{13}C]–dAdo. A principal goal of this work was to ascertain whether the prominent doublet observed in many sugar radical spectra (*e.g.*, Fig. 3B and C) was due to C5'• or C4'•. Theoretical calculations (DFT, B3LYP functional, 6-31G(d) basis set, full optimization) indicated that the ^{13}C hyperfine couplings at C5' in C5'• should differ significantly from that at C5' in C4'• (Scheme 3).
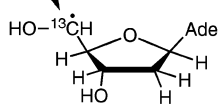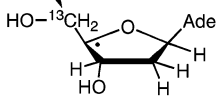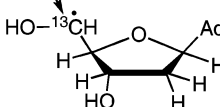
Fig. 3 shows the EPR spectra representing the conversion of one electron oxidized adenine in [5'-^{12}C]–dAdo to sugar radicals and computer isolation of the presumed C5'• spectrum. Fig. 4 shows the same conversion of one electron oxidized adenine to sugar radicals in [5'-^{13}C]–dAdo and computer isolation of the presumed C5'• spectrum. A computer simulation of the C5'• spectrum, using ^{13}C5' hyperfine couplings of (2.8, 2.8, 8.4) mT and a single −2.1 mT α-proton coupling is also shown. The agreement between spectra 4C and 4D shows that C5' is the site of the large ^{13}C coupling and verifies the formation of C5'• rather than C4'•.

DFT calculations indicated that sugar radical formation in the adenine model compounds proceeded through an inner core excited state in which significant positive charge and spin density are located on the sugar moiety carbon atoms, as found previously with guanine model compounds (*vide supra*). Fast deprotonation from the sugar carbon atoms in the excited state results in formation of relatively stable neutral sugar radicals. One interesting aspect is that this work also reports what was thought to be the first β-^{13}C coupling in the literature. While the C3' is produced only to about 20% at pH 5, at higher pH (*ca.* 12) C3'• is the only radical formed and a clearly resolved 1.6 mT β-^{13}C coupling from the ^{13}C labeled 5'-site is detected.[33]

2.3.2 Protonation states of G•+. The differences observed in sugar radical formation from excited state one-electron-oxidized guanine radicals at different pH prompted further investigation into the nature of the deprotonation for G•+ in LiCl glasses.[21] Aqueous (D$_2$O) solutions of dGuo (2'-dG) were investigated using EPR and UV/visible spectroscopy in the pH range 3 to 12. In this work, the three prototropic forms of one-electron-oxidized guanine in dGuo, G•+ (pH 3–5), G(–H)•
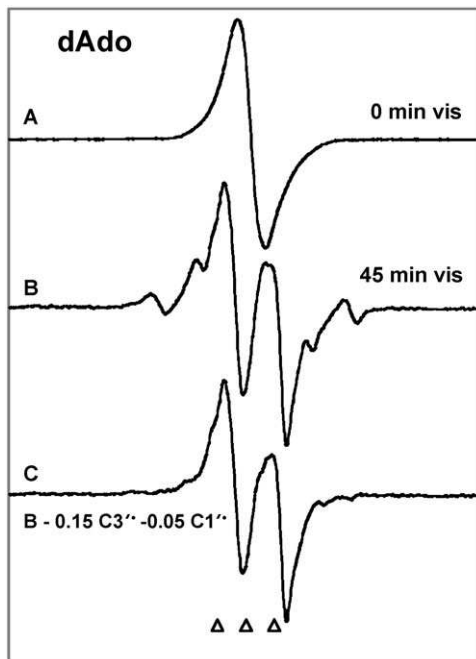
Fig. 3 (A) EPR spectrum of one electron oxidized adenine formed by oxidation of dAdo in 7 *M* LiCl glass/D$_2$O with Cl$_2$$^{\bullet-}$. (B) After illumination with visible light for 45 min at 143 K, C5′′$^{\bullet}$, C3′$^{\bullet}$ and C1′$^{\bullet}$ are present. (C) C5′′$^{\bullet}$, found after subtraction of C1′$^{\bullet}$ and C3′$^{\bullet}$ spectra from 2B. Reprinted with permission from ref. 33, *Nucleic Acids Research*, Copyright (2006), Oxford University Press.

Scheme 3 Reprinted with permission from ref. 33, *Nucleic Acid Research*, Copyright (2006), Oxford University Press.

(pH 7–9) and G(–2H) (pH > 11) were distinguished from each other and characterized. Also, the sites of deprotonations of the guanine cation radical were determined using suitable isotopically (^{15}N, D) substituted deoxyguanosines. The underlying prototropic equilibria for one-electron-oxidized guanine are shown in Scheme 4.

For EPR analysis, dG was oxidized at different pHs in 7 *M* LiCl and the EPR spectrum obtained compared with simulated spectra. Nitrogen hyperfine couplings in the plane of the purine ring were too small to be observed in amorphous samples and assumed to be 0 mT. In samples using D$_2$O, exchangeable hydrogen atoms do not show observable hyperfine coupling.

By deuterating the C8 position of the guanine ring, the nitrogen atom hyperfine couplings at different states of the prototropic equilibria of the guanine cation
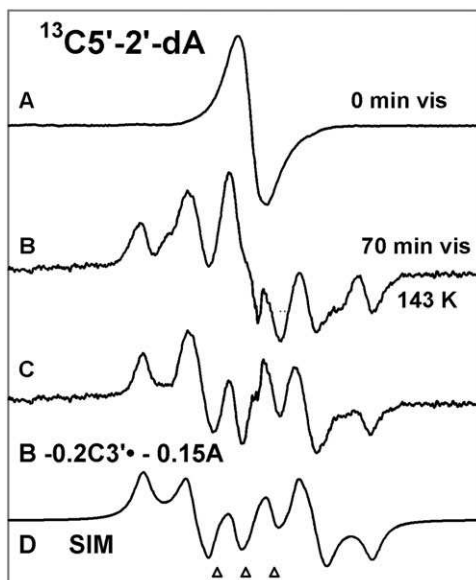
Fig. 4 (A) EPR Spectrum from one electron oxidized adenine in [5′-13C]-dAdo in 7 *M* LiCl glass/D$_2$O. (B) After illumination for 70 min with visible light at 143 K, C5′′ and C3′′ are present; both radicals possess substantial ^{13}C couplings.[33] (C) After subtraction of simulated C3′′ spectrum (20%) and of A (15%) (Fig. 1A) from B. This spectrum is assigned to C5′′. (D) Simulation of spectrum in C showing a large ^{13}C coupling.[33] All spectra were recorded at 77 K. Reprinted with permission from ref. 33, *Nucleic Acids Research*, Copyright (2006), Oxford University Press.

**Table 9** Experimental hyperfine couplings in one-electron-oxidised guanine in dGuo[a]

Radical	^{14}N3 (mT) A_{xx}, A_{yy}, A_{zz}	^{14}N2 (mT) A_{xx}, A_{yy}, A_{zz}	C8(H) A_{xx}, A_{yy}, A_{zz}	g_{xx}, g_{yy}, g_{zz}
G$^{\bullet +}$	0, 0, 1.30	0, 0, 0.65	−1.05, −0.35, −0.75	2.0045
				2.0045
				2.0021
G(–H)	0, 0, 1.20	0, 0, 0.80	−1.05, −0.35, −0.72	2.0041
				2.0041
				2.0021
G(–2H)	0, 0, 1.32	0, 0, 1.62	−0.75, −0.25, −0.55	2.0041
				2.0041
				2.0021

[a] Nitrogen hyperfine couplings in the ring plane were too small to be observed in amorphous samples and are set at 0 mT for spectral simulations. N1 couplings are not evident in the spectra.

radical could be observed. ^{15}N isotropic substitutions at N1, N2 and N3 in the guanine ring were used to verify these couplings. With knowledge of these couplings, it was possible to simulate EPR spectra that allowed determination of the C8(H) hyperfine couplings in different protonation states of guanine (Table 9). The simulated spectra using these hyperfine couplings fit the experimental spectra well.

Ab initio DFT calculations using 7–10 water molecules around the guanine moiety in the various one electron oxidized guanine radicals shown in Scheme 4 confirmed the assignment of the experimentally observed couplings to nitrogen atoms. Both the
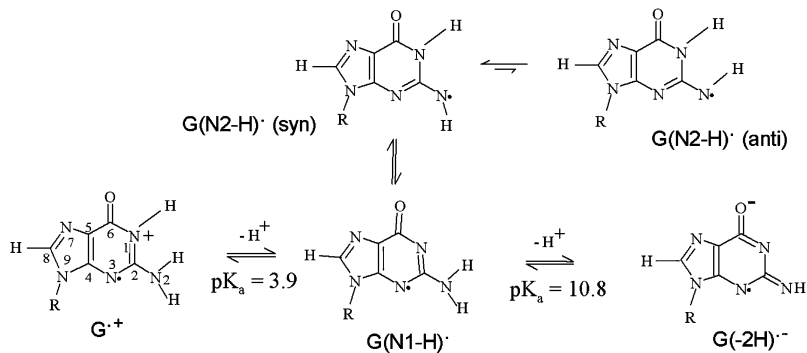
Scheme 4

experimental and theoretical efforts confirm that the site of deprotonation in $G^{\bullet+}$ is at N1 in aqueous solution. Theoretical calculations suggest that in a low dielectric medium, deprotonation is from the exocyclic nitrogen, but in an aqueous environment it occurs from N1 instead. This paper reports EPR spectra and associated hyperfine couplings and *g*-values for various forms of one-electron-oxidized G in dGuo and should be consulted for further details.

2.3.3 Electron transfer. Electron transfer in a DNA model compound was investigated using 4′-pivaloyl substituted thymidine (IX) to specifically generate the C4′′ radical (23) and follow its fate, even though C4′′ itself is not observed.[35] The goal of the work was to investigate electron transfer in a system in which both the donor and acceptor species could be spectroscopically monitored, and, also, in which the specific donor and acceptor sites were known. In the experiment, a solution of IX (H_2O, D_2O, acetonitrile) was photolyzed at 77 K and EPR spectra recorded (77 K and 4 K) after photolysis. Computer analysis of the resulting spectra permitted characterisation of the radicals formed.

Three radicals were observed using EPR at 77 K after photolysis of IX, to wit, the tertiary butyl radical $(CH_3)_3C^\bullet$, the thymyl C6 addition radical (24), and an unknown radical, characterized by a broad central triplet, which might be a rearranged sugar radical originating with C4′′. It is notable that C4′′ itself was not observed, even at 4 K.[36] On the basis of the detection of these radicals, the reaction sequence in Scheme 5 was proposed.

The principal conversion of interest is that from 23 to 24, in which net hydrogen atom transfer from 23 to the thymine moiety has occurred. It is proposed that the transfer may be accomplished through proton-coupled electron transfer, in which ET from C4′′ to thymine is followed rapidly by proton transfer from C4′′. The well-known doublet from $T^{\bullet-}$ is not observed in this experiment, leading to the conclusion that the proton transfer is fast.
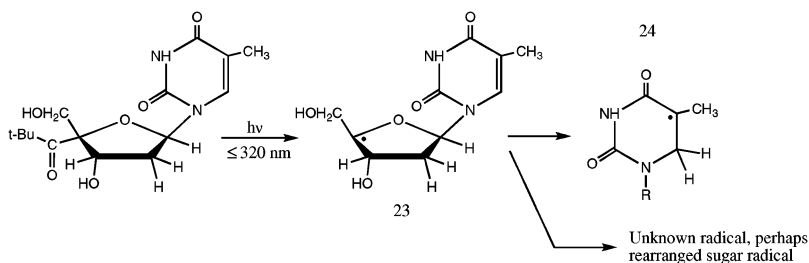
Scheme 5

A number of controls and observations confirmed that confounding effects were not occurring in the experiment: (1) it was shown the tertiary butyl radical did not react with thymidine, (2) with D_2O as solvent, protonation with hydrogen occurred, suggesting protonation did not originate with solvent, (3) with the conditions used, photolysis does not cause radical formation in thymidine, (4) intermolecular ET does not occur, and (5) the unknown (possibly sugar) radical is not the precursor to the thymyl radical.

It is noted that C4′• in DNA suffers a different fate from that in thymidine. When phosphate groups are present, C4′• undergoes β-elimination to give a cation which can then oxidize guanine. In thymidine, reduction of the thymine base is observed.[35] Finally, the authors note that even though proton-coupled ET is proposed for the observed reaction, it could also occur through hydrogen atom transfer. The fact that no effect of D_2O as solvent was found may suggest that this latter mechanism may dominate.

3. DNA

3.1 Track structure in DNA irradiated with heavy ions

Recently Bowman *et al.* performed a pioneering study of the spatial distribution of trapped radicals produced in heavy-ion-irradiated solid hydrated DNA at 77 K using pulsed electron paramagnetic double resonance (PELDOR or DEER) techniques.[37] Salmon testes DNA hydrated to 12 water molecules per nucleotide was irradiated with ^{40}Ar ions of energy 100 MeV/nucleon with LET (linear energy transfer) ranging from 300 to 400 keV/μm at 77 K. These samples were kept in liquid nitrogen and PELDOR experiments were performed on the trapped radicals. The EPR spectra detected were attributed to DNA base electron loss/gain radicals as well as neutral carbon-centred radicals that predominantly arise from sugar damage. PELDOR measurements used a refocused echo detection sequence that is very sensitive to the dipolar interactions between trapped radicals (Fig. 5). Thus, measurements of radical to radical distances of 10 nm or higher are possible. These workers found a radical concentration of *ca*. 1.4×10^{18} spins/cm³ in the tracks and a track "core" radius of 6 to 7 nm which are in good agreement with the corresponding values obtained using Monte Carlo track structure calculations.[38,39] The cross section of the tracks suggests a lineal radical density of 2.6 radicals/nm. This linear density corresponds to an LET of 270 keV/μm in reasonable agreement with the calculated experimental range of values (300–400 keV/μm) using the TRIM program.[37] The authors state that these are the first direct measurements of track radical density and spatial extent in irradiated DNA. Such measurements are critical to understanding the details of radiation damage to DNA *via* high and low LET radiation.[37]
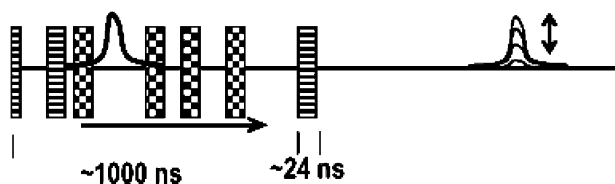
Fig. 5 The PELDOR pulse sequence for measurement of weak interactions between free radicals. The striped blocks represent microwave pulses of the same (observation) frequency that generate a two-pulse primary echo at time $2t$ and a refocused echo at time $2t + 2t'$. The checkered blocks represent possible locations of a microwave pulse at a second (pump) frequency that is swept between the second and third observation pulses. Reprinted with permission from ref. 37, *Radiation Research*, Copyright (2005) Radiation Research Society.

3.2 Studies of DNA-iron complexes

3.2.1 Neutral radical formation in gamma irradiated DNA. Shukla *et al.* reported a study in which the electron scavenger ferricyanide, Fe(III), and hole scavenger ferrocyanide, Fe(II) were employed to scavenge electrons and holes in γ-irradiated DNA.[40] The authors credit Weiland and Huettermann for pioneering the use of Fe(III) with DNA as an electron scavenger.[41] The results show that 1 scavenger per 20 base pairs is sufficient to nearly completely remove trapped electrons or holes from DNA. When both scavengers are employed, a spectrum composed of predominantly neutral sugar radicals is found.[40] The spectrum of the sugar radicals is reported to be an overlap of the spectra of a number of radicals on the sugar phosphate backbone including the C1′•, C3′•, C5′• formed by deprotonation of sugar cation radicals as well as radicals resulting from electron induced cleavage of the phosphate-sugar link (C3′•$_{dephos}$ and C5′•$_{dephos}$, Table 10). Since C3′•$_{dephos}$ and C5′•$_{dephos}$ can only form from a single strand break, their finding is considered significant. When both Fe(III) as well as Fe(II) were used as scavengers, the neutral radicals are less readily scavenged as they are apparently less redox active than the holes and excess electrons.[40] As shown in Fig. 6, the yield of trapped radicals in irradiated DNA is 38% G•$^+$, 48% DNA•$^-$ (38% C(N3)H• and 10% T•$^-$) and 12% neutral radicals. The neutral radicals are predominantly on the sugar phosphate

Table 10 Radicals considered in section 3
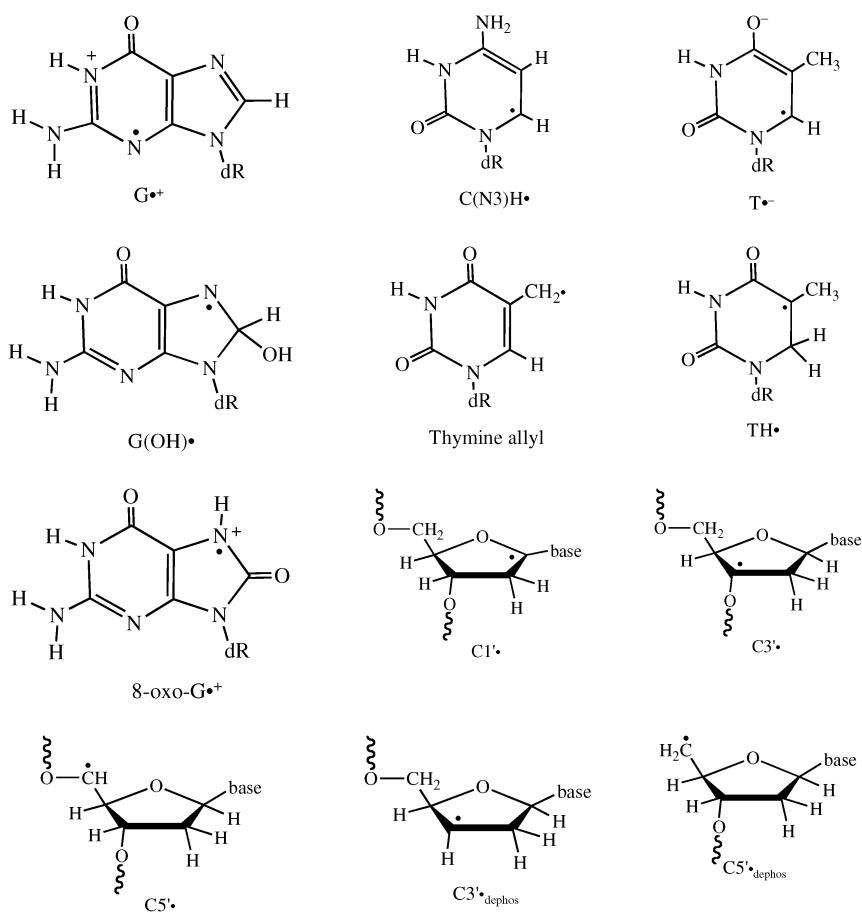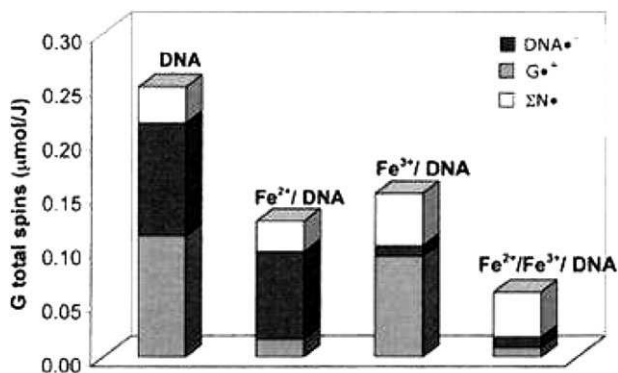
Fig. 6 The relative yields of DNA anion radicals (thymine and cytosine) guanine cation radical, $G^{\bullet+}$ and sugar radicals, $N^{\bullet}$ for DNA and DNA with scavengers for holes, Fe(II), electrons, Fe(III), and both holes and electron, Fe(II)/Fe(III), Fe(II) and Fe(III) represent ferro- and ferricyanide, respectively. Reprinted with permission from ref. 40, *Radiation Research*, Copyright (2005), Radiation Research Society.

backbone.[40] It is interesting to note that compared to DNA alone, the trapped sugar radicals in DNA increased in the presence of Fe(III) and only slightly decreased in the presence of Fe(II) (Fig. 6). This suggests that the transient sugar cation radical precursor and its deprotonation product, the sugar radical, may be protected from recombination with electrons by electron scavenging by Fe(III). Conversely, Fe(II) does not repair these species effectively.

3.2.2 Iron binding to DNA. A study of the influence of Fe(III) and Fe(II) binding to DNA on radical formation and strand breaks is reported by Ambroz *et al.*[42] The major findings are that Fe(III) binds to the DNA bases and distorts the DNA conformation. It is found that at levels of one Fe(III) per 60 bps, Fe(III) is able to capture 70% of radiation-induced electrons and completely thwart production of $TH^{\bullet}$. This is in contrast to Fe(II) which binds to the phosphate groups and has little effect on geometry. In an earlier work by this group, the influence of dithiothreitol (DTT) on DNA radiolysis at low temperatures was investigated *via* EPR.[43] It was found that DTT was able to repair about 30% of the oxidative DNA radicals (guanine cation radical and thymine allyl radical). However, no effect on the reductive DNA radicals was observed. Interestingly, increasing the concentration of DTT from 10 mM to 1 M in these systems resulted in no further repair of the DNA radicals. This suggests a phase separation on sample freezing.

3.3 Formation of 8-oxo-G in irradiated DNA by multiple one-electron oxidations

Recent work has elucidated the mechanism of formation of 8-oxo-$G^{\bullet+}$ in gamma-irradiated DNA.[13,14] In order for this radical to form in irradiated DNA from guanine, multiple one-electron oxidative steps must occur at a single guanine site in DNA. The authors report that the mechanism begins with nucleophilic addition of a water molecule at the C8 position in $G^{\bullet+}$ to form $^{\bullet}GOH$ (8-hydroxyguanine radical) on annealing from 77 K to 240 K. A second hole transfer to $^{\bullet}GOH$ is found to result in 8-oxo-G *via* one-electron oxidation and a third hole transfer oxidizes 8-oxo-G to 8-oxo-$G^{\bullet+}$ (Scheme 6).[13]

To confirm this mechanism, careful annealing studies were performed on DNA samples with ^{17}O–isotopically enriched water and an identical (*i.e.*, matched) set of ^{16}O water samples. The authors report that ^{17}O substitution broadened the $^{\bullet}GOH$ spectrum (*via* large ^{17}O couplings) so that the subtraction of EPR spectra of $H_2{}^{17}O$ samples from the corresponding matched sample containing $H_2{}^{16}O$ at each
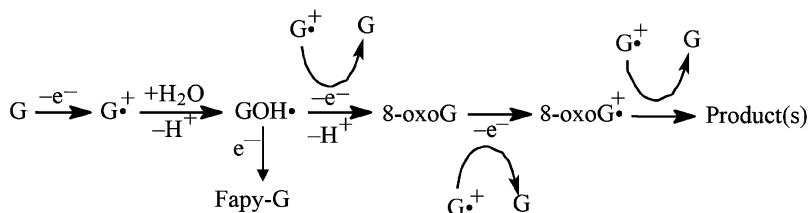
Scheme 6 Reprinted with permission from ref. 13, *Nucleic Acids Research*, Copyright (2004), Oxford University Press.

temperature selectively exposed the EPR spectra of the water addition radicals such as $^{\bullet}G^{16}OH$. In addition, the EPR spectrum of ^{17}O-labeled 8-oxo-$G^{\bullet +}$ was also significantly broadened so that the spectrum ^{16}O-labeled 8-oxo-$G^{\bullet +}$ was again easily isolated *via* subtraction. In this work, the authors established the formation of $^{\bullet}GOH$ and 8-oxo-$G^{\bullet +}$ in DNA as well as strong evidence for their sequential production (Scheme 7).
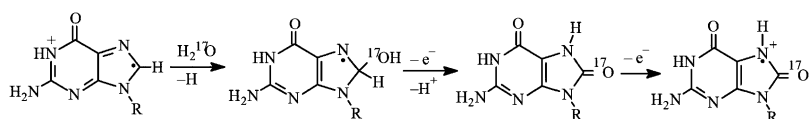
Scheme 7 Reprinted with permission from ref. 13, *Nucleic Acids Research*, Copyright (2004), Oxford University Press.

This technique highlighted the application of ^{17}O–isotopically enriched water for the detection of a radical formed *via* water addition at a selective site. The authors also suggest the multiple hole transfer to a single site may have a radioprotective effect by channeling oxidative damage to a repairable site.[13] This demonstrates that formation of 8-oxo-G in DNA readily occurs at temperatures as low as 250 K. From this, it is clear that the activation barriers for these multiple one-electron oxidative processes (Schemes 6 and 7) are small, and the corresponding one-electron oxidations will be fast at biologically relevant temperatures.

3.4 Electron transfer *versus* differential fading of radicals

Recently a work examining electron transfer *versus* differential radical decay in DNA systems was reported by Pal and Huettermann.[44] Free radical formation in X-ray-irradiated DNA and DNA mixed with the electron traps mitoxantrone and ribo-flavin were monitored in frozen aqueous glasses (7 M LiBr/D$_2$O) at 77 K by EPR spectroscopy. Free radical spins on DNA and the traps were investigated with time, in part to test the results earlier reported by Messer *et al.*[45] who reported electron transfer from DNA to mitoxantrone. Pal and Huettermann report that the observed relative change in contributions of DNA and of intercalator radical components to the experimental spectra with time could be ascribed to differential fading of component radicals rather than electron transfer within DNA.[44] The post-irradiation radical fading mechanism is attributed to recombination with matrix holes. In this system, the hole spectra are very broad and are thus nearly EPR mute.[44] This paper thus challenged the previous work of Messer *et al.*[45] and several subsequent publications.[3,4,46–49] This report brought a reply from Sevilla that showed plots of the original data described but not presented visually by Messer *et al.*[45] in their original work.[50] The plots confirmed that no rapid initial decay with time was found for DNA intercalated with mitroxantrone (MX) at two ratios of MX to DNA base pairs, 1/23 and 1/46; Pal and Huettermann's[44] work does not explain the results of Messer *et al.*[50] The results of the two groups are, therefore, very different for very

similar systems. Sevilla points to several differences in procedures and potential pitfalls that could account for this difference.[50]

3.5 Role of excited states in DNA damage—experimental and theoretical results

As was pointed out in section 2.3.1, a series of recent works have focused on sugar radical formation from the excited states of DNA base cation radicals.[5,30,31,51–54] A hypothesis was proposed that a multiple hit effect, such as excitation of a DNA base cation radical, could lead to the sugar radical formation.[3,5,29,51] To test this hypothesis, photo-excitation of the one-electron oxidized guanine, $G^{\bullet+}$ in a number of systems was investigated. These included γ-irradiated DNA[30,51] as well as guanine deoxynucleosides and deoxynucleotides,[30,51] and DNA-oligomers[52,53] in aqueous (D_2O) glassy systems. For DNA, $G^{\bullet+}$ was formed by γ-irradiation and visible light was employed to excite the cation radical.[30,51] It was found that for high molecular mass salmon sperm DNA, exposure of $G^{\bullet+}$ to near UV-visible wavelengths (from 310 to 480 nm) produced the $C1'^{\bullet}$ sugar radical with *ca.* 50% yield, but beyond 500 nm no effect was observed.[30] In the model systems (nucleosides and tides), the photo-excitation of $G^{\bullet+}$ at visible wavelengths of 540 nm and above produced sugar radicals in abundant yields (80 to 90%).[30]

Adhikary *et al.* have also presented evidence that photoexcitation of $G^{\bullet+}$ in TpdG, dGpdG and in a series of DNA-oligonucleotides (TGT, TGGT, TGGGT, TTGTT, TTGGTT, TTGGTTGGTT, AGA, and AGGGA) in frozen glassy aqueous solutions at low temperatures leads to photoinduced hole transfer to the sugar phosphate backbone and results in high yields of deoxyribose radicals.[52,53] They found that $G^{\bullet+}$, on photoexcitation at 143 K, leads to the formation of predominantly $C5'^{\bullet}$ and $C1'^{\bullet}$ with small amounts of $C3'^{\bullet}$. Photoconversion yields of $G^{\bullet+}$ to sugar radicals in oligonucleotides decreased as the overall chain length of the DNA-oligonucleotides increased.[53] Moreover, within the cohort of sugar radicals formed, a relative increase in the formation of $C1'^{\bullet}$ with length of the DNA-oligonucleotide was found along with decreases in $C3'^{\bullet}$ and $C5'^{\bullet}$.[53] This is consistent with the finding that, for high molecular mass dsDNA (salmon testes) in frozen aqueous solutions, substantial (*ca.* 50%) photo-conversion of $G^{\bullet+}$ to only $C1'^{\bullet}$ was found.[30] No significant temperature dependence for the conversion of $G^{\bullet+}$ to $C1'^{\bullet}$ was found over the temperature range 77–180 K for these DNA samples.[53] Visible light (wavelength > 540 nm) was observed to be about as effective as light with wavelengths under 540 nm for photoconversion of $G^{\bullet+}$ to sugar radicals for short DNA-oligonucleotides.[53] But, the longer wavelengths gradually lost effectiveness with increasing chain length of the DNA-oligonucleotides.[53] This wavelength dependence is attributed to base-to-base hole transfer for wavelengths > 540 nm. However, base-to-sugar hole transfer, leading to the formation of neutral sugar radicals, is suggested to dominate under 540 nm.[53] Theoretical TD-DFT studies[52] for $TpdG^{\bullet+}$, and for other one-electron oxidized dinucleoside phosphates (TpdG, dGpdG, dApdA, dApdT, TpdA, and dGpdT)[54] show that the lower energy (*i.e.,* longer wavelength) transitions in all these systems involve base-to-base $\pi-\pi^*$ hole transfers. Thus, theoretical calculations for dinucleoside phosphates provide support for the hypothesis that the excitation process induces base-to-base hole transfer at long wavelengths and low excitation energies in stacked DNA base systems, whereas shorter wavelengths induce base-to-sugar hole transfer[5,30,52,54] (Fig. 7).

3.6 Photoinduced radical formation in DNA

Several works have been published by Barton and coworkers on photo-induced radical formation in DNA using EPR.[55,56] An early work reported a guanine radical spectrum at room temperature during photolysis of polydGdC with $[Ru(phen)_2(dppz)]^{+2}$ and a $[Co(NH_3)_5Cl]^{+2}$ quencher.[55] The spectrum reported is an asymmetric singlet of 8 G line-width with a *g*-value of 2.0048. This spectrum was
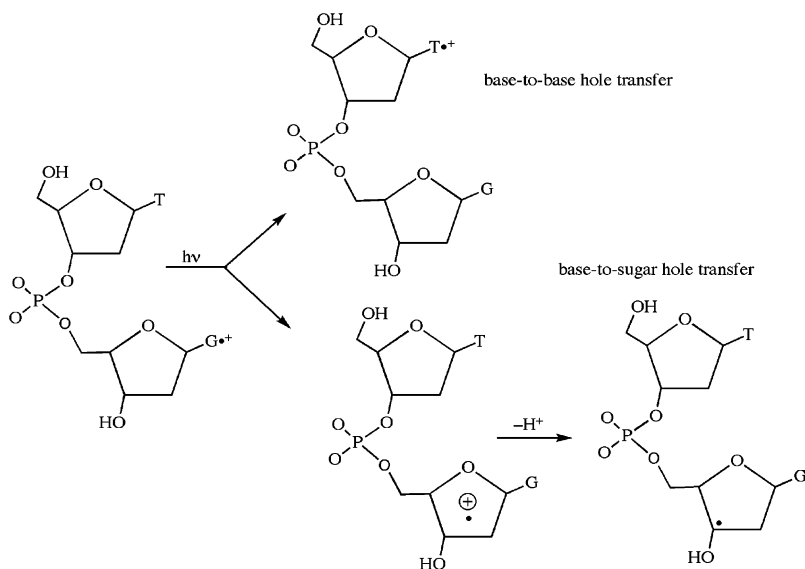
Fig. 7 Schematic diagram showing the results of theoretical calculations regarding the effect of light on TpdG$^{\bullet+}$. The calculations predict that long wavelengths ($>$ 540 nm) induced base-to-base hole transfer while shorter wavelengths (310–500 nm) induce transfer of the hole from base to the sugar moiety which, by deprotonation, produces a neutral sugar radical. Reprinted with permission from ref. 52, *Radiation Research*, Copyright (2006), Radiation Research Society.

assigned to the deprotonated guanine radical (G(–H)$^{\bullet}$). However, these EPR characteristics do not appear to be those of G(–H)$^{\bullet}$[21] and other recent work has clearly identified a radical with identical EPR characteristics in irradiated DNA at elevated temperatures as the 8-oxoguanine radical (8-oxo-G$^{\bullet+}$).[13,14] This species was identified by ^{17}O labeling studies and thus there is high confidence in its assignment (section 3.3). The production of 8-oxo-G$^{\bullet+}$ is actually expected in systems in which DNA is undergoing oxidative processes since G$^{\bullet+}$ undergoes a rapid nucleophilic addition reaction with water to form $^{\bullet}$GOH and this species is easily further oxidized to 8-oxo-G.[13] Since 8-oxo-G has a much lower redox potential than G, 8-oxo-G is a locus for further one-electron oxidation resulting in 8-oxo-G$^{\bullet+}$.[13] In the works of Barton group,[55,56] spin trapping was employed to trap the oxidized guanine radicals formed in DNA systems *via* photolysis. The spin trapped radicals were reported to be those from G(–H)$^{\bullet}$. Since the spin trapping is likely to act earlier in the reaction processes, the precursor radical (G(–H)$^{\bullet}$) is likely to be trapped as reported rather than those (*i.e.*, G(8OH)$^{\bullet}$ and 8-oxo-G$^{\bullet+}$) formed by subsequent one-electron oxidation (see Schemes 6 and 7). However, as evident from Scheme 7 and the above discussion, the reaction of a spin trap with G(–H)$^{\bullet}$ is a competitive kinetics process, and hence further work would be needed to prove this point unequivocally.

Two other EPR works by the Barton group have investigated DNA mediated charge transfer (CT) to a bound enzyme containing iron sulfur clusters.[57,58] The CT leads to oxidation of the bound base excision repair enzyme MutY by oxidization of its [4Fe–4S]$^{2+}$ component to [4Fe–4S]$^{3+}$.[57] Clear EPR spectra of the oxidized iron sulfur clusters on DNA were detected, with these observations confirmed *via* electrochemical oxidation.[58]

3.7 DNA yields and strand breaks

3.7.1 The role of hydration in DNA radical yields. The role of hydration in the distribution of free radicals trapped in directly ionized plasmid DNA was

investigated by Bernhard and coworkers.[59] Solid-state films of pUC18 (2686 bp) plasmids were hydrated in the range of Γ = 2.5 to 22.5 waters per nucleotide. Free radical yields at 4 K ranged from 0.28 µmol/J at the lowest hydration (Γ = 2.5) to 0.63 µmol/J at the highest (Γ = 22.5).[59] The authors described a semi-empirical model of damage based on these values which suggests that two-thirds of the holes formed on the inner solvation shell (first 10 waters of hydration) transfer to the sugar-phosphate backbone.[59] Of the holes directly formed on the sugar phosphate backbone, about one-third deprotonate to form neutral sugar-phosphate radical species, while the remaining two-thirds are suggested to transfer to the bases. The authors used these values to predict that the distribution of holes formed in fully hydrated DNA at 4 K will be 78% on the bases and 22% on the sugar-phosphate.[59] Including the reductive pathway (anion radicals on thymine and cytosine), the distribution of all trapped radicals is predicted to be 89% on the bases and 11% on the sugar-phosphate backbone.[59] These results are in good agreement with previous results found at 77 K by Shukla *et al.*[40] who reported 12% sugar phosphate backbone radicals, 88% on the bases.

3.7.2 The connection between radical yield and strand breaks. The Bernhard group has also been investigating the connection between the yield of free radicals found at low temperature in DNA model systems, such as crystalline double stranded DNA-oligomers and plasmid films, with subsequent strand breaks.[59–63] This work is based on the ability to distinguish the sugar radicals, which for the most part result in strand breaks, from base radicals, which do not form strand breaks.[60] In their initial EPR work,[30] the authors show, that sugar radicals in X-irradiated crystalline DNA oligomers at 4 K can be distinguished from the DNA-base anion and cation radicals by their different dose saturation behavior. The authors report the G values for radical production and the k values for destruction by fits of data to the eqn $[C = (G/k)[1 - e^{-kD}]]$ assuming sugar and base radicals acted independently so that a G-value and, also a k value are found for each. The G values for production of base and sugar radicals suggest that 80–90% of initial radicals are on the bases and the remainder on the sugar phosphate backbone in agreement with the work of Shukla *et al.*[40] The k values for radiation induced destruction of base radicals were 28 to 81 times larger than those for destruction of sugar radicals. This destruction occurs by radiation induced hole and electron reactions with existing radicals. The lower reactivity of the neutral sugar radicals toward radiation destruction is a striking and significant result. In subsequent works by these authors,[61–64] the analyses for sugar radicals at low temperatures are compared with products formed after annealing to room temperatures. The yields of sugar radicals were reported in an initial study to be less than the number of strand breaks found in plasmids at 22.5 mol water/nucleotide.[61,62] A subsequent study compared the yields of sugar radicals and free base release in crystalline of d(CGCGCG)$_2$ or films of d(CGCGCG)$_2$ at low hydrations (2.5 to 7.5 waters/nucleotide).[64] Free base release is generally accepted as a good estimate of single strand breaks.[64] The authors again reported a shortfall of trapped sugar radicals as compared to the base release (or, strand breaks). To account for this shortfall, the authors suggest a double oxidation event bypasses the free trapping radical step and results in a diamagnetic product. Oxidation of a sugar radical by a nearby base cation radical is suggested as the mechanism of this proposed double oxidation event.[60–64] Additional work involving single strand break (SSB) measurements on plasmids as a function of hydration by this group provide some new evidence for this mechanism.[62] It was observed that, at the lowest hydrations (*ca.* $\Gamma \leq 10$), the yield of strand breaks (observed at room temperature) exceeded the yield of *trapped* sugar radicals (at 4 K) in the same samples for X-ray-irradiated pUC18 plasmid DNA films.[62] Low trapping efficiency of ion radicals at low hydrations may account for this phenomenon as it would likely lead to the increased double oxidations on sugars and consequently free radicals yields that did not match DNA-SSB.

3.7.3 Correlation of radical yields with specific DNA damage at base and sugar groups.

In a recent work by Swarts et al.[65] an HPLC, GC/MS investigation of base damage and sugar damage products on the oligo d(GCACGCGTGC)$_2$ in films and crystalline powders were performed. This study presents the yields of base release, strand break products containing both 3'- and 5'-terminal phosphates, various base damage products, and compares these with yields of free radicals measured by EPR spectroscopy in the same sample at 4 K. The work presents many interesting findings, including the fact that base/sugar damage products are found to be in a 3/1 ratio and that there is a rough balance between electron loss and electron gain products. This paper should be consulted for details.

3.8 Electron induced cleavage of thymine dimers

Giese and coworkers report a study of electron induced cleavage of thymine dimers in oligos and model systems.[66] They present results which suggest that electron transfer barriers in oligomers are approximately equal to the barrier to electron-induced thymine dimer cleavage. The EPR spectrum of a model compound was found to produce, on photolysis, a protonated thymine anion analog with large β-proton hyperfine couplings as found in previous work for the 5,6 dihydrothymin-5yl radical.[35]

Acknowledgements

References

1   M. D. Sevilla and D. Becker, in 'Electron Paramagnetic Resonance, Specialist Periodical Reports', ed. B. C. Gilbert, The Royal Society of Chemistry, Cambridge, UK, 1994, vol. 14, pp. 130–165.
2   D. Becker and M. D. Sevilla, in 'Electron Paramagnetic Resonance, Specialist Periodical Reports', ed. B. C. Gilbert, The Royal Society of Chemistry, Cambridge, UK, 1998, vol. 16, pp. 79–115.
3   M. D. Sevilla and D. Becker, in 'Electron Paramagnetic Resonance, Specialist Periodical Reports', ed. B. C. Gilbert, The Royal Society of Chemistry, Cambridge UK, 2004, vol. 19, pp. 243–278.
4   Z. Cai and M. D. Sevilla, in 'Long Range Transfer in DNA II', ed. G. B. Shuster, Springer-Verlag, Berlin, Heidelberg, New York, Topics in Current Chemistry, 2004, vol. 237, pp. 103–128.
5   D. Becker, A. Adhikary and M. D. Sevilla, in 'Charge Migration in DNA: Physics, Chemistry and Biology Perspectives', ed. T. Chakraborty, Springer-Verlag, Berlin, Heidelberg, 2007, pp. 139–175.
6   W. A. Bernhard and D. M. Close, in 'Charged Particle and Photon Interactions with Matter Chemical, Physicochemical and Biological Consequences with Applications', eds. A. Mozumdar and Y. Hatano, Marcel Dekkar, Inc., New York, Basel, 2004, pp. 431–470.
7   A. D. Bass and Leon Sanche, in 'Charged Particle and Photon Interactions with Matter Chemical, Physicochemical and Biological Consequences with Applications', eds. A. Mozumdar and Y. Hatano, Marcel Dekkar, Inc., New York, Basel, 2004, pp. 207–257.
8   Advances in Quantum Chemistry 52, Theoretical Treatment of the Interaction of Radiation with Biological Systems, eds. J. R. Sabin and E. Brandas, Elsevier, 2007.
9   D. Becker and M. D. Sevilla, Adv. Radiat. Biol., 1993, 17, 120–180.
10 Y. Shao et al., Phys. Chem. Chem. Phys., 2006, 8, 3172–3191.
11 S. Tokdemir and W. H. Nelson, Radiat. Res., 2005, 163, 663–672.
12 S. Steenken, Chem. Rev., 1989, 89, 503–520.
13 L. I. Shukla, A. Adhikary, R. Padzro, D. Becker and M. D. Sevilla, Nucleic Acids Res., 2004, 32, 6565–6574.
14 L. I. Shukla, A. Adhikary, R. Padzro, D. Becker and M. D. Sevilla, Nucleic Acids Res., 2007, 35, 2460–2461.

15 W. H. Nelson, E. O. Hole, E. Sagstuen and D. M. Close, *Int. J. Radiat. Biol.*, 1988, **54**, 963–986.
16 D. M. Close, E. Sagstuen and W. H. Nelson, *Radiat. Res.*, 1988, **116**, 379–392.
17 E. O. Hole, E. Sagstuen, W. H. Nelson and D. M. Close, *Radiat. Res.*, 1991, **125**, 119–128.
18 S. Tokdemir and W. H. Nelson, *J. Phys. Chem. A*, 2005, **109**, 8732–8744.
19 P. Erling and W. H. Nelson, *J. Phys. Chem. A*, 2004, **108**, 7591–7595.
20 N. Jayatilaka and W. H. Nelson, *J. Phys. Chem. B*, 2007, **111**, 800–810.
21 A. Adhikary, A. Kumar, D. Becker and M. D. Sevilla, *J. Phys. Chem. B*, 2006, **110**, 24171–24180.
22 N. Jayatilaka and W. H. Nelson, *J. Phys. Chem. B*, 2007, **111**, 7887–7896.
23 Y. Zheng, P. Cloutier, D. Hunting, L. Sanche and J. R. Wagner, *J. Am. Chem. Soc.*, 2005, **127**, 16592–16598.
24 P. Swiderek, *Angew. Chem. Int. Ed.*, 2006, **45**, 4056–4059.
25 E. Sagstuen, D. M. Close, R. Vagane, E. O. Hole and W. H. Nelson, *J. Phys. Chem. A*, 2006, **110**, 8653–8662.
26 S. C. Lillicrap and E. M. Fielden, *Int. J. Radiat. Biol.*, 1972, **21**, 137–144.
27 M. Olast and A. J. Bertinchamps, *Int. J. Radiat. Biol.*, 1973, **24**, 589–594.
28 P. M. Cullis, G. D. D. Jones, M. C. R. Symons and J. S. Lea, *Nature*, 1987, **330**, 773–774.
29 D. Becker, A. Bryant-Friedrich, C. Trzasko and M. D. Seviila, *Radiat. Res.*, **160**, 174–185.
30 A. Adhikary, A. Y. S. Malkhasian, S. Collins, J. Koppen, D. Becker and M. D. Sevilla, *Nucleic Acids Res.*, 2005, **33**, 5553–5564.
31 A.-O. Colson and M. D. Sevilla, *Int. J. Radiat. Biol.*, 1995, **67**, 627–645.
32 A.-O. Colson and M. D. Sevilla, *J. Phys. Chem.*, 1995, **99**, 3867–3874.
33 A. Adhikary, D. Becker, S. Collins, J. Koppen and M. D. Sevilla, *Nucleic Acids Res.*, 2006, **34**, 1501–1511.
34 L. Kar and W. A. Bernhard, *Radiat. Res.*, 1983, **93**, 232–253.
35 O. Schiemann, E. Feresin, T. Carl and B. Giese, *ChemPhysChem*, 2004, **5**, 270–274.
36 Y. Razskazovskiy, M. G. Debije and W. A. Bernhard, *Radiat. Res.*, 2003, **159**, 663–669.
37 M. K. Bowman, D. Becker, M. D. Sevilla and J. D. Zimbrick, *Radiat. Res.*, 2005, **163**, 447–454.
38 A. Chatterjee and W. R. Holley, *Adv. Radiat. Biol.*, 1993, **17**, 181–226.
39 J. L. Magee and A. Chatterjee, in 'Radiation Chemistry: Principles and Applications', ed. Farhataziz, Micheal and A. J. Rogers, VCH Publishers, Inc., New York, 1987, pp. 173–199.
40 L. I. Shukla, R. Padzro, D. Becker and M. D. Sevilla, *Radiat. Res.*, 2005, **163**, 591–602.
41 B. Weiland and J. Huettermann, *Int. J. Radiat. Biol.*, 1998, **74**, 341–358.
42 H. B. Ambroz, T. J. Kemp, A. Rodger and G. Przybytniak, *Radiat. Phys. Chem.*, 2004, **71**, 1023–1030.
43 H. B. Ambroz, T. J. Kemp, A. Rodger and G. Przybytniak, *Radiat. Phys. Chem.*, 2002, **64**, 107–113.
44 C. Pal and J. Hüttermann, *J. Phys. Chem. B*, 2006, **110**, 14976–14987.
45 A. Messer, K. Carpenter, K. Forzley, J. Buchanan, S. Yang, Y. Razskazovskii, Z. Cai and M. D. Sevilla, *J. Phys. Chem. B*, 2000, **104**, 1128–1136.
46 Z. Cai, Z. Gu and M. D. Sevilla, *J. Phys. Chem. B*, 2000, **104**, 10406–10411.
47 Z. Cai, Z. Gu and M. D. Sevilla, *J. Phys. Chem. B*, 2001, **105**, 6031–6041.
48 Z. Cai, X. Li and M. D. Sevilla, *J. Phys. Chem. B*, 2002, **106**, 2755–2762.
49 Z. Cai and M. D. Sevilla, *J. Phys. Chem. B*, 2000, **104**, 6942–6949.
50 M. D. Sevilla, *J. Phys. Chem. B*, 2006, **110**, 25122–25123.
51 L. I. Shukla, R. Pazdro, J. Huang, C. DeVreugd, D. Becker and M. D. Sevilla, *Radiat. Res.*, 2004, **161**, 582–590.
52 A. Adhikary, A. Kumar and M. D. Sevilla, *Radiat. Res.*, 2006, **165**, 479–484.
53 A. Adhikary, S. Collins, D. Khanduri and M. D. Sevilla, *J. Phys. Chem. B*, 2007, **111**, 7415–7421.
54 A. Kumar and M. D. Sevilla, *J. Phys. Chem. B*, 2006, **110**, 24181–24188.
55 O. Schiemann, N. J. Turro and J. K. Barton, *J. Phys. Chem. B*, 2000, **104**, 7214–7220.
56 F. Shao, B. Elias, W. Lu and J. K. Barton, *Inorg. Chem.*, 2007, **46**, 10187–10199.
57 E. Yavin, A. K. Boal, E. D. A. Stamp, E. M. Boon, A. L. Livingston, V. L. O'Shea, S. S. David and J. K. Barton, *Proc. Natl. Acad. Sci. USA*, 2005, **102**, 3546–3551.
58 A. K. Boal, E. Yavin, O. A. Lukianova, V. L. O'Shea, S. S. David and J. K. Barton, *Biochemistry*, 2005, **44**, 8397–8407.
59 S. Purkayastha, J. R. Milligan and W. A. Bernhard, *Radiat. Res.*, 2006, **166**, 1–8.
60 S. Purkayastha and W. A. Bernhard, *J. Phys. Chem. B*, 2004, **108**, 18377–18382.
61 S. Purkayastha, J. R. Milligan and W. A. Bernhard, *J. Phys. Chem. B*, 2005, **109**, 16967–16973.
62 S. Purkayastha, J. R. Milligan and W. A. Bernhard, *J. Phys. Chem. B*, 2006, **110**, 26286–26291.

63   S. Purkayastha, J. R. Milligan and W. A. Bernhard, *Radiat. Res.*, 2007, **168**, 357–366.
64   K. K. Sharma, S. Purkayastha and W. A. Bernhard, *Radiat. Res.*, 2007, **167**, 501–507.
65   S. G. Swarts, D. C. Gilbert, K. K. Sharma, Y. Razskazovskiy, S. Purkayastha, K. A. Naumenko and W. A. Bernhard, *Radiat. Res.*, 2007, **168**, 367–381.
66   B. Giese, B. Carl, T. Carl, T. Carell, C. Behrens, U. Hennecke, O. Schiemann and E. Feresin, *Angew. Chem. Int. Ed.*, 2004, **43**, 1848–1851.

Measurement of interspin distances by EPR

Gareth R. Eaton*[a] and Sandra S. Eaton*[b]

The determination of electron–electron interspin distances by continuous wave (CW) and pulsed EPR is reviewed for the period from late 2003 to early 2008. Papers that provide new methodology are highlighted. The wide range of applications is summarized in tables.

1. Introduction to distance determination

The measurement of distances between pairs of unpaired electron spins in biomolecules and in polymers has become one of the most important applications of pulsed EPR. By "distances" we implicitly mean "long" distances, so we exclude cases in which paramagnetic centers are separated by only a few atoms, as in many transition metal complexes and diradicals. There are many exciting advances in polyradicals and metal clusters,[1] but they are beyond the scope of this review. Each quantitative EPR determination of distances between spins involves measurement of an aspect of CW or pulsed EPR that exhibits the dipolar interaction. These include spin–spin splitting in the CW EPR line, dipolar modulations in electron spin echo (ESE), and changes in spin-lattice (T_1) and spin–spin (T_2) relaxation times, monitored indirectly by CW power saturation or directly by saturation recovery or ESE. In addition, there are qualitative measures of relative distances *via* the effect of exchange interactions on splittings and relaxation times. Sometimes exchange interactions can be larger over a longer distance if the orbital overlaps are more favorable, so larger exchange interaction does not always mean shorter distance. Theory is not yet well-enough developed to convert exchange interactions into quantitative determination of distances. However, if the intervening pathways are believed to be similar, reasonable relative distance estimates can be based on interactions even where exchange is believed to make a significant contribution.

An important question is how many distance constraints are needed to define a structure. Sparse spin labeling EPR data has been used together with the *de novo* structure prediction algorithm Rosetta and compared with the known crystal structures of T4-lysozyme and αA-crystallin. Distance constraints for amino acids far apart in sequence but spatially close were the most valuable for structure determination.[3]

Although single-crystal X-ray diffraction has been assumed to be the "gold standard" for structure determination, increasingly, EPR and especially EPR distance determination, reveals cases in which the structure found in the crystal does not match that determined in solution or in the membrane. For example, it has been shown that materials that are often used to crystallize proteins affect the structure determined by EPR.[4] The DEER measurements on arrestin spin labeled in 18 locations revealed only one case in which the experimentally determined interspin distances were close to the predictions based on the tetramer structure determined by X-ray crystallography,[5] and data for the other sites were clearly incompatible with the crystal structure.

[a] *Department of Chemistry and Biochemistry, University of Denver, Denver, Colorado, USA. E-mail: geaton@du.edsu; Fax: 303-871-2254; Tel: 303-871-2980*
[b] *Department of Chemistry and Biochemistry, University of Denver, Denver, Colorado, USA. E-mail: seaton@du.edu;; Fax: 303-871-2254; Tel: 303-871-3102*

2. Related reviews

This review covers material since our previous review in this series.[6] Other reviews of distance determination by EPR include many of the chapters in Biological Magnetic Resonance (volumes 19, 23 and 24),[2,7,8] and articles by Dzuba on pulsed EPR methods.[9–11] Attention is called to reviews of a wide range of distance measurements by Lakshmi and Brudvig,[12] Prisner,[13] Steinhoff,[14] Bennati and Prisner,[15] Schiemann and Prisner.[16] A recent review of site-directed spin labeling highlights distance determinations.[17] Many distance measurements in photosystem II were reviewed by Kawamori[18,19] and applications to the reaction center of Rhodobacter sphaeroides were reviewed by Lubitz, Möbius and coworkers.[20] Jeschke has published several introductions to DEER and/or reviews of the field, which will be valuable for those seeking to learn about potential applications to their field of interest.[21–28] Applications to ribonucleotide reductase were reviewed by Lendzian.[29] DEER at 180 GHz has also been reviewed.[30]

3. CW

Some CW power saturation measurements that reflect interaction of spins yield only qualitative measures of the distances between the spins, because the CW power saturation depends on products of T_1, T_2 and spectral diffusion times. Although current effort is largely focused on refining development of quantitative distance determinations, qualitative relative distance estimates can be extremely important. Detailed line shape analysis, especially at high enough magnetic field/frequency to resolve g_x, g_y and g_z transitions (e.g., 95 GHz for nitroxyls) showed that di-spin-labeled peptides did not assume conformations corresponding to any of the common helical structures in proteins.[31] Spin–spin contributions to CW line shape reveal changes in conformation upon binding of ATP to the multidrug transporter MsbA.[32] Spin–spin interactions causing line broadening, including unusual single-line spectra indicative of multi-radical interactions, have been observed in fibrils of amyloid proteins, providing a powerful tool for the study of these important structures,[33–35] and similarly in vementin, an intermediate filament, of which over a 100 spin labeled variants have been studied.[36]

Dipolar broadening of CW spectra and statistical analysis were used to describe the distribution of spin labels on the surface of a gold nanoparticle.[37] For different loadings of spin labels, average distances between spins ranged from 14.6 to 42 Å. Another study of spin labels on gold nanoparticles combined CW and DEER measurements.[38]

Dipolar broadening of CW lineshapes of dual spin labeled RNA was used to measure distances in the range of 10–21 Å.[39] This paper demonstrated that SDSL and EPR are useful for distance measurements in RNA complexes. Detailed analysis of the CW spectra of double-labeled arrestin revealed two populations centered around 11 and 17 Å for the I16R1/A381R1 variant.[40] These interactions became too weak to observe in the presence of phosphorhodopsin.

The distance between spin labels in double mutant talin rod was determined by fitting calculated spectra to the experimental spectra.[41] For example, a mean distance of 14.9 Å and a 4 Å distance distribution fit in one mutant, and when vinculin Vd1 domain was added, the distance increased to 17.2 Å.

EPR spectra of double-spin-labeled T4-lysozyme exhibited broadening due to dipolar spin–spin interactions, which disappeared when the T4-lysozyme was bound to α-crystallin, revealing that binding increased distances between the labeled sites.[42]

Distances in dinuclear metal complexes can be measured in CW EPR. For example, the X-band and Q-band spectra of a dinuclear copper(II) complex with adeninate ligand bridging the two Cu(II) ions exhibited half-field transitions. The X-ray crystal structure shows that the Cu–Cu distance is 3.247 Å. Using this distance, and the parameters that fit the CW EPR spectrum, the exchange interaction is about twice the dipolar interaction.[43] Larger zero-field splitting parameters

were observed in X- and Q-band spectra of a dinuclear Cu(II) complex of N-substituted thiazole sulfonamides.[44]

Dipolar coupling of two Mn(II) ions, replacing Mg(II) in a Diels-Alderase ribozyme, showed that the sites were *ca.* 6 Å apart.[45]

The half-field transition intensity for species involving a Co(II) ion in cob(II)alamin and a free radical was consistent with the 5′-carbon of the anhydroadenosyl radical 3.5 and 4.1 Å from Co(II).[46]

4. Accessibility to paramagnetic relaxation reagents

The Hubbell laboratory makes extensive use of site-directed spin labeling (SDSL) together with relaxation effects from collisions of O_2 and NiEDDA with the nitroxyl spin labels to map out structures and conformational changes of proteins. Since NiEDDA is water-soluble, and O_2 is more soluble in membranes, these two reagents provide complementary information. Accessibility of these two reagents to the spin label reveals the location of the spin label relative to the membrane and hence the location of segments of the protein in the membrane. Such interactions have been monitored *via* broadening of the CW EPR signal, but more recently, long pulse saturation recovery has provided a more accurate measure and has extended the range of measurements to smaller effects on nitroxyl relaxation times.[47] Some of the systems studied recently in the Hubbell laboratory are included in Table 1. NiEDDA and O_2 accessibility of apo-MsbA defines the location and orientation of transmembrane helices and maps the regions of aqueous solvation.[32] Absolute Heisenberg

Table 1 Relaxation of radicals due to O_2 or paramagnetic metals

Spin system	Spin–spin distance (Å)	Notes and keywords	Ref.
Cu-nitroxide in alanine-based peptides	17–20 temperature-dependent	Inversion recovery at 305 K	59
Dy(III)—spin label on DNA	*ca.* 19	CW power saturation	60
$[Fe_4S_4]^+$ to FAD semiquinone in ETF-QO	18	Inversion recovery	61 and 62
Heat shock protein Hsp16.5	Many pairwise distances short enough to broaden CW spectra	CW lineshape and accessibility to O_2 and NiEDDA^b by power saturation	63 and 64
NH_2Y_{730} to diferric center	Distant, no interaction	CW power saturation	65
Synaptotagmin SDSL with NiEDDA^b and O_2	Range of *ca.* 20 Å relative to membrane surface		66 and 67
Tryptophan radical to heme in versatile peroxidase + H_2O_2	*ca.* 10	CW power saturation	68
T4 lysozyme	Accessibility of sites 128 to 135 along the helix	Saturation recovery	47
Vitamin B transporter SDSL and NiAA^c and O_2	Dual spin labels in the ton box; bimodal 12 and 18 Å	Structure inferred from accessibility	69
$Y_D^{\bullet}$—Mn cluster	*ca.* 30	Inversion recovery	70–72

^{a} SDSL denotes that nitroxyl radicals were introduced by site-directed spin labeling. ^{b} NiEDDA is the Ni(II) complex of ethylenediamine-N,N′-diacetic acid, which is commonly used for relaxation enhancement of nitroxyl radicals. ^{c} NiAA is bis(acetylacetonato) Ni(II).

exchange rates between nitroxyl spin labels and NiEDDA or O_2 were calculated, converting the qualitative measures of accessibility into quantitative measures.[48]

Accessibility of Ni(II) in the aqueous phase to semiquinone in the cytochrome bc_1 complex was monitored by CW power saturation to determine how deeply the semiquinone was buried in the protein.[49] Interactions of radicals with paramagnetic DyHEDTA (HEDTA: N-hydroxyethylenediaminetriacetate) in frozen solution were modeled and tested for Dy(III) with hemeNO relaxation.[50] The fluid solution and frozen solution methods are very different, both experimentally and computationally.

In addition to nitroxyl–nitroxyl interactions between sites in dimerized ApoA-I, Lagerstedt *et al.*, used accessibility to O_2 and chromium(III) oxalate (CrOX) to define helical regions.[51] In the lipid-bound state, the N-terminal region of ApoA-I adopts an elongated helix on the surface of a high density lipoprotein particle. The crystal structure does not reflect the substantial conformational dynamics of ApoA-I in solution.

5. Relaxation of free radicals due to nearby paramagnetic metals

Dipolar interaction between Co(II) and a nitroxyl spin label was observable in CW spectra up to *ca.* 25 Å, and was used to monitor changes in the distance between sites in a metallo-beta-lactamase due to conformational changes during the catalytic reaction. Rapid freeze-quench EPR was combined with site-directed spin labeling (SDSL) and computer simulation of spectra to make these measurements.[52] This is a nice example of the effect of the metal relaxation time on the dipolar splitting. The dipolar splitting can be observed only at temperatures at which the Co(II) EPR spectrum can be observed.

Using 140 GHz EPR to obtain better dispersion of g-anisotropy of the radicals, it was observed that isotropic exchange interaction with the di-iron cofactor caused a decrease in the T_1 of the tyrosyl radical of ribonucleotide reductase (RNR) from yeast.[53] The spin–spin interaction is stronger in yeast than in E. coli or mouse RNR.

Hung *et al.*, provided a detailed analysis of the dipolar interaction model of the effect of a nearby heme ($r > 10$ Å) on the relaxation of the [3Fe 4S] cluster in succinate–ubiquinone reductase.[54]

A non-heme di-iron center in the hydroxylase component of soluble methane monooxygenase relaxes a nitroxyl spin label at Cys89. The distance, estimated as 15 ± 4 Å, provided evidence for a specific model of binding of the components.[55]

One has to be careful in pulse measurements of T_1 to check for effects of spectral diffusion, as illustrated in the case of radicals in photosystem II measured by saturation recovery at 130 GHz.[56] In this study, high-spin (S = 2) Fe(II) reduced the T_1 of $Tyr_D{}^{\cdot}$ more than Car^+, and this more than Chl^+, showing that the distances increased in the order listed. With this information, possible β-carotene binding sites in PS II were proposed.

A detailed protocol for measuring distances between a radical and a metal ion by saturation recovery was published by Hirsh and Brudvig.[57]

This method is not restricted to interactions of organic radicals with metals. Interaction of Cu in cytochrome c oxidase with the more rapidly relaxing heme in cytochrome c was measured by changes in the 9.7 and 180 GHz electron spin echo decay of the Cu(II) in the 5 to 30 K temperature range.[58] High orientation selection was provided at 180 GHz. Additional examples are gathered in Table 1 above.

6. DEER (PELDOR)

One of the primary quantitative pulsed EPR methods is known by the acronym DEER (double electron–electron resonance) also called PELDOR (pulsed electron electron double resonance). It is rumored that some laboratories seek to buy "a DEER machine," not an EPR spectrometer! Fortunately, Gunnar Jeschke has developed, and shares *via* his web site, a MatLab analysis package called

Table 2 Interspin distances measured by DEER

Spin system	Spin–spin distance (Å)	Notes and keywords	Ref.
Di-nitroxides			
2 Di-nitroxyl radicals	19.4 ± 0.02	Liquid crystal orientation increased parallel features	82
2 Long rigid dinitroxyls	50, 74.9	Comparing constant time and variable time DEER and deuteration	74
Di-, tri-, and tetra-nitroxyl radicals	34, 33,33, 25 and 34, 20, 34, and 39	Rigid polyradicals	89
di-nitroxyl	37.5	95 GHz; analysis of conformational distributions	103
Tri-nitroxyl	*ca.* 25–42		
Peptides			
Alamethicin, spin labeled	30 and 58 for pairs of labeled peptides	in $CHCl_3$: toluene	104 and 105
``	Broad distribution centered at 23 Å	Large multilamellar vesicles	105
``	30 Å (30%) and 70 Å (70%)	Aggregate of two tetramers	106
Peptide trichogin GA IV, spin labeled	28 in α helix32 in 3_{10} helix	Aggregation depends on toluene/ methanol ratio	107
,,	12.5 in α helix17.5 in elongated 3_{10} helix	No aggregates in membranes	108 and 109
,,	Range of 15 to 40, 25 between antiparallel dimers	Dimers form in membranes at higher concentration	110
Zervamicin, doubly spin labeled	33	Solvent dependent	106
DNA, RNA			
DNA duplex	8 distances, 20 to 40 Å	Each strand was spin labeled	111
5 DNA, spin-labeled	28 ± 3 to 48 ± 3		112
3 RNA duplexes, spin-labeled	$19.3 \pm 1.033.0 \pm 2.040.9 \pm 2.0$		113
6 RNA, spin-labeled	From 19.3 ± 1.2 to 38.7 ± 1.3		114
Proteins			
Arrestin	< 18 to *ca.* 60	Spin labeled at 18 locations	5
ATP-binding cassette transporter, Msba	Distance changes of 10 to 33 Å	Domain reconfiguration upon ATP hydrolysis	115
BtuB SDSL	3 sets of distance distributions for each of 3 pairs, 20 to 37 Å	Dual spin label	96
BtuB and FecA	25 to 36	Note the effect of osmolytes	4
Cardiac troponin C	26.0 monomer 27.2 fibers	SDSL	116
Cyt b_{559}^{+}-Q_A	40 ± 1		117
	42 ± 1, 43 ± 1	17.4 GHz	118

Table 2 (*continued*)

Spin system	Spin–spin distance (Å)	Notes and keywords	Ref.
Flavin semiquinone in monoamine oxidase			
2 flavin radicals in augmenter of liver regeneration	26.1 ± 0.8		119
F_0F_1-ATP synthase, tether domain	29 Å in each mutant		120
hemoglobin with 3 different spin labels	25.3, 26, 28.8	Labeled at β-93	121
HIV-1 protease SDSL dual spin label	26–48	Interflap distances	122
Iso-1-cytochrome c folding, doubly spin labeled	19.6 (folded), 27.8 and 36.6 (partially unfolded)	17.3 GHz	91
Lactose permease	24 to 55	Interhelical distance changes induced by sugar binding	123
Light-harvesting chlorophyll a/b protein	6 distances from 28 to 55 Å	At least 2 conformational states	124
NhaA Na^+/H^+ antiporter of E coli	44	NhaA exists as a dimmer	125
NhaA Na^+/H^+ antiporter of E coli	9 pairs 18.9 to 48.4 Å		126
$P_{865}^{\bullet+}Q_A^{\bullet-}$	28.9	95 GHz	127
Pargyline inhibitor in monoamine oxidase, spin labeled	47 ± 1 to 62 ± 1 for various cases	17.4 GHz	118
2 tyrosyl radicals in R2 homodimer subunit of RNR[a]	33.5 ± 0.4		76
''	33	180 GHz	30
''	33	180 GHz; determined relative orientation	85
Tyrosyl biradical in RNR	32.5	9, 35 GHz, could not measure orientation	128
Tyrosyl biradical in RNR	32.5	180 GHz, radicals are oriented in almost antiparallel fashion	87
RNR $Y_{122}^\bullet$ to $DOPA^\bullet$ at residue 356	30.6 ± 0.5		102
RNR $Y_{122}^\bullet$ to $NH_2Y^\bullet$	38.1 ± 1.2		102
$Y^\bullet–N^\bullet$ in RNR	48	DEER at X-band and DQC at 17.4 GHz	129
$N^\bullet–N^\bullet$	33		
$Y_D^\bullet$-QA-$Chlz^+$	$Q_A–Chl_z^+$ 34	Triangulation of 3-spin system	130
	$Q_A–Y_z$ 34		
$Y_D^{\bullet+}$-$Chlz^+$	29.5	3-Pulse DEER	131
$Y_Z^\bullet$-Q_A^-	34.5	Spin polarized ESEEM	
^3Chl-Q_A^-	25.9		
Semiquinone to spin label in photosynthetic reaction center	30.5		132
α-Synuclein, interhelix distances	30 to 45	DEER and DQC at 17.4 GHz	133

Table 2 (*continued*)

Spin system	Spin–spin distance (Å)	Notes and keywords	Ref.
T4 lysozyme	45.223.6 and 29 (bimodal)	Compared DEER and DQC at 17.3 GHz	91
Ubiquitin	35.5 DEER35.8 DQC	SDSL; DEER and DQC at X-band	134
Von Willebrand factor A domains	61.5	Trimer; in deuterated glycerol and D_2O	135
Miscellanous			
Au nanoparticles, spin labeled	14, part increased to 30–50 after hydrolysis and heating	May be too short for reliable DEER measurement; CW line broadening also was used	38
Fremy's salt associated with ionic polymer	24 and 4729 and 45	Two polymers were measured. Distances are between radicals associated with the ionic polymers.	136
5 Poly(para-phenylene-ethynylene)s, flexibility	5 lengths, up to *ca.* 75 Å	In deuterated o-terphenyl	137
Poly(ethylene glycol) nano-objects, spin labeled	12 Å, not 35 Å	DEER excluded 35 Å and CW broadening revealed 12 Å	138
Stabilizer-derived nitroxyls in ABS polymer and biradical	17 and 19.5 for diradical, and local concentrations	Combined EPR imaging and DEER	139
Synthetic layered silicate with spin-labeled surfactants	15 to 200	Measured pair correlation function	140

[a] RNR is ribonucleotide reductase.

DeerAnalysis for interpretation of DEER spectra http://dg3.chemie.uni-konstanz.de/~agje/G1.htm (accessed 06/08/08). These data analysis procedures have been discussed elsewhere.[73,169]

Table 2 lists many recent papers that applied the DEER method. For those unfamiliar with this method, a synopsis is presented here. Almost all applications involve two nitroxyl spin labels, so we will refer to the nitroxyl EPR spectra, but the principles embedded in this specific example are general and can be applied to other paramagnetic species.

For nitroxyl radicals at long distances, measuring the oscillation frequency yields the distance between the spins *via* the relation:

$$\omega_{dd}(\theta, r) = \frac{2\pi g_1 g_2}{g_e^2}(3\cos^2\theta - 1)\frac{52.04}{r^3}$$

where θ is the angle between the interspin vector and the external magnetic field, r is the distance in nanometers and ω_{dd} is the dipolar oscillation frequency. The approximation in this equation is that the nitroxyl radicals have random orientations relative to one another. If they do not, it is potentially possible to obtain the relative orientations as well as the distances.

An electron spin echo (ESE) measurement is set up on the nitroxyl radical at low enough temperature that the nitroxyl is immobilized. A 3-pulse spin echo is created. Then, a microwave pulse at a second frequency is used to excite spins that resonate at another magnetic field (hence a different microwave frequency). The second frequency is applied between the 2nd and 3rd pulses at the first frequency, and it is stepped in

time such that it starts prior to the ESE that is created by the first 2 pulses, passes through the time of the echo, and ends after the echo but before the 3rd pulse. If there is no interaction between spins, then the pulse at the second microwave frequency has no effect on the echo created by the pulses at the first microwave frequency. Since the experiment is performed with fixed times between the 3 pulses at the first microwave frequency, the echo amplitude recorded as a function of time will be a constant—just a straight line in the digitized signal. However, if the spins have a dipolar interaction, the recorded echo will oscillate in amplitude at a frequency that is characteristic of the dipolar interaction. This is the DEER signal. The Fourier transform of this signal is the dipolar spectrum. The depth of the modulation depends on the fraction of spins that interact, so usually the frequency at which the echo is observed is chosen to correspond to resonance on the low field side of the maximum in the field-swept, echo-detected EPR spectrum, and the second frequency is chosen to be at the maximum in the spectrum, so that a maximum fraction of the pairs are excited. In practice, the frequencies are about 70 MHz apart, so even with an overcoupled, low-Q resonator, the two frequencies have to be carefully located within the resonator bandwidth to optimize S/N. Since nitroxyl T_m values are of the order of 2 μs in frozen solutions containing proton spins, the echo signal becomes very weak beyond a couple of μs. One records a small difference in echo amplitudes, so the S/N is inherently low. A careful tradeoff of increased echo amplitude at lower temperature, and longer T_1 at lower temperature has resulted in choosing roughly 50 K as an optimum temperature for the measurement. Jeschke[74] described ways to enhance sensitivity in DEER measurements, including use of a variable-time analog of the usual DEER experiment, which yielded improved S/N, and the use of deuterated solvents to increase T_m and hence increase the time during which dipolar evolution could be observed. There is a dynamic phase shift in the DEER signal[75] that results in changes in the position and shape of the detected echo. Essentially, this is the well-known off resonance effect on magnetic resonance transitions. A method of calibrating the pump pulse position and amplitude was outlined.[75]

Intermolecular interactions inherently have a distribution of distances, and contribute a "background" decay to the echo amplitude, which is superimposed on the dipolar oscillation. This effect is minimized by having a low concentration of spin pairs to minimize inter-molecular interactions. The concentration dependence of the DEER signal has been demonstrated.[76]

One of the very powerful aspects of the DEER method is that a distribution of intra-molecular distances results in a sum of dipolar interaction frequencies, with the mathematically expected destructive interference effect on the oscillation pattern. Consequently, analysis of the DEER patterns yields not just a distance, but also the distribution of distances. It is to be emphasized that one obtains a distribution, not just an uncertainty. Full analysis of the results yields a most probable distance, and distribution of distances, that reveals the stereochemistry of the species containing the pair of spins, and the experimental uncertainty in each of these. Modeling of distributions has permitted identification of structures of aggregates of spin labeled peptides in a variety of environments, as illustrated in several papers by Milov and coworkers cited in Table 2.

This introduction to DEER was expressed in terms of two microwave frequencies, but equivalently, one could use two magnetic fields. Because of the resonator Q effect, operating at the resonant frequency of the EPR resonator and using two different magnetic fields could have an advantage, if the magnetic field steps could be accomplished fast enough. Fast magnetic field steps for pulsed ELDOR have been accomplished by several laboratories.[77–81] Magnetic field step was combined with the use of two microwave frequencies to measure distances between spins in two di-nitroxyls.[82]

Routinely, the difference between the two microwave frequencies is set to about 70 MHz for measuring the distance between two nitroxyl radicals. Astashkin et al., described a 26.5 to 40 GHz pulsed spectrometer in which the separation between the two frequencies can be several hundred MHz because the resonator has a Q of 300 to 500.[83]

6.1 Determination of relative orientations of radicals in DEER

In the usual DEER measurement, one selects pump and observe frequencies for the best signal-to-noise ratio, and assumes that the dipolar interaction angle is randomly distributed. However, the frozen solution nitroxyl spectrum inherently contains orientation information due to the g and hyperfine anisotropy. The more rigid the spin label and the more rigidly it is incorporated into the protein, the greater the opportunity for obtaining orientation as well as distance information. In some cases, the biological molecules could also be preferentially oriented in the magnetic field, thus selecting a particular range of θ. The problem, or the opportunity, is greater the higher the microwave frequency. The orientation-selection can be explored with two methods, both of which have been used in the cited reports: the frequency separation can be kept constant as the magnetic field is stepped, or the probe frequency separation can be stepped while the pump frequency is held at the center of the spectrum.

Several groups are extracting orientation information from DEER spectra. Margraf *et al.*, stepped the frequency offsets between the two DEER frequencies to explore the orientation selection, and found that they could better simulate their DEER data with a particular non-random geometric model.[84] Higher frequency EPR provides enhanced capability for orientation dependence, as was shown by Bennati using 180 GHz.[85] Gajula *et al.*, considered a quinone and a nitroxyl radical, whose g values are such that the quinone and the central portion of the nitroxyl are pumped, and the $g_z m_I = \pm 1$ components of the nitroxyl are observed.[86] They found a small effect (< 1 Å) on the estimated distance by assuming a particular orientation of the nitroxyl relative to the vector between the nitroxyl and the semiquinone. The distance between two tyrosyl radicals in bacterial photosynthetic reaction center was measured at 95 GHz and changes in orientation of one of them upon light illumination was determined to be beyond the uncertainty in the measurements.[20] The anisotropy dispersed by 180 GHz EPR permitted the demonstration that the two tyrosyl radicals in mouse R2 RNR are oriented almost exactly antiparallel to one another.[85,87] Similarly, ribonucleotide reductase was measured at 180 GHz, in order to obtain the mutual radical orientation under conditions where the spectrum is dominated by g anisotropy. Different field positions for DEER (with constant frequency separation) are different orientations of the magnetic field relative to the g-tensor principal axis.[85,87] The larger anisotropy of Cu(II) EPR spectra relative to nitroxyl radicals provided greater opportunity to test orientation selection. DEER measurements were made at several magnetic field locations in the spectrum of the Cu–Cu dimer. Simulations indicated that orientation dependence would be more important than was observed, possibly due to flexibility of the peptide linking the two Cu ions.[88]

6.2 More than two spins

Two papers have explored very different cases beyond the spin-pair model on which most DEER applications have focused. Bode *et al.*, measured rigid di-, tri-, and tetra-radicals, and showed that the multiple intramolecular interspin distances could be observed in the distance distributions.[89] Ruthstein *et al.*, tested the DEER method on monomeric spin probes in micelles, and showed that the decays due to the spin–spin interactions could be fit with models of the micelles.[90]

6.3 Uncertainty in distributions

The longer the distance measured by DEER, the greater the uncertainty in the distribution of distances. Fortunately, for most purposes, the distribution becomes less important the greater the distance. Jeschke and coworkers judged that if one can observe about three periods of the dipolar oscillation, a good estimate of the distance distribution can be determined.[73,74] At 75 Å, an observation window of 20 µs

achievable in a fully deuterated rigid matrix corresponded to about three periods and resulted in a full width at half height of the distribution of *ca.* 8 Å. Another example they report is that if the dipolar oscillation can be observed for 2.5 μs, distance distributions can be reliably estimated at distances up to 40 Å, and rough estimates of distances can be estimated up to about 50 Å. These results from the literature emphasize the importance of increasing T_m so that the dipolar oscillation can be observed for longer times.

Bowman *et al.*, point out that "there are many, quite different distributions of radicals that could produce the same experimental dipolar spectrum."[39] Two methods for approximating the distance distributions when the width of the distribution is more than a few percent of the mean were presented. One method used a coordinate transformation and the other used a least-squares approach with Tikhonov regularization. Details of maximum entropy and Tikhonov regularization for determining pair distribution functions have been discussed.[91,92]

6.4 Metal–metal distances by DEER

Most applications of pulsed methods of distance determination have been to pairs of nitroxyl radicals or other organic radials such as semiquinones. In principle, the methods could be used for any pair of spins, but the broader the EPR spectra, the smaller the fraction of spins that can be involved in forming the dipolar modulation. Thus, there are major signal-to-noise limitations to applying DEER to, for example, Cu(II)–Cu(II) interactions, but Huber and coworkers succeeded in measuring a Cu–Cu distance of 26 Å.[93] A Cu–Cu distance measured by Yang *et al.*,[88] was mentioned in section 6.1. Similarly, Kay *et al.*, used DEER to measure the distances between the copper binding sites in dicupric transferrin (41.6 ± 0.6 Å) and lactoferrin (42.4 ± 0.6 Å).[94] Raitsimring *et al.*, measured a Gd(III)–Gd(III) distance of 20 to 20.5 Å, using DEER at 29.6, 33.78. and 94.9 GHz.[95]

6.5 Limitations of the DEER method

The primary factors that limit the longest distances one can measure are (a) signal-to-noise (S/N) and (b) the phase memory time, T_m, of the nitroxyl spin echo. If the intra-molecular distance is large, the overall spin concentration has to be low to avoid dominance of inter-molecular spin–spin interactions.[96] Hence, the limit occurs when the spin concentration is too low to achieve good S/N. The longer the spin–spin distance, the lower the frequency of the oscillation due to the dipolar coupling, and hence the longer the time during which the echo has to be recorded to be able to well define the frequency of the oscillation.

Most of the distances measured by pulsed EPR are large enough, relative to the sizes of the paramagnetic species, that the point dipole approximation is valid. However a distance of 18.4 Å measured by DEER between a [3Fe-4S]$^+$ center and a [NiFe] center was 3 Å shorter than the known distance between the centers of the clusters. It was concluded that the Fe closest to the [NiFe] center had the largest contribution to the observed distance.[97,98]

Distance measurements in the borderline region, between the applicability of CW and DEER measurements (16–19 Å), have been examined by Banham *et al.*[99] Corrections are needed for DEER measurements below about 20 Å. Milov and coworkers showed that for short distances between spins (less than *ca.* 20 Å) it is necessary to take account of the finite duration of microwave pulses, because the dipolar width becomes comparable to the spectrum width of the pulse.[100]

6.6 Examples of applications of DEER

Examples of distance measurements by DEER (PELDOR) are gathered in Table 2. All measurements were at X-band frequency and between two nitroxyl radicals, unless noted otherwise.

A detailed protocol for spin labeling oligonucleotides and measuring distances between two nitroxyl radicals by DEER was published.[101]

The measurement, by DEER, of the distance between RNR Y_{122} and the DOPA radical introduced at site 356 was the "first structural information for this residue, which is invisible in all crystal structures solved to date."[102]

7. Other spin echo methods

It has been known since 1969 that electron–electron dipolar interactions can be observed in standard 2-pulse ESEEM measurements.[141] Kulik *et al.*, showed that for a biradical with interspin distance 19.6 ± 0.2 Å, a peak in the Fourier transform of the 2-pulse ESEEM corresponded to the PELDOR result.[9,142] If 3-pulse echo detection is used for spin A, and the time between the second and third pulses is long enough that the neighboring spin B has time to undergo an odd number of spin flips, the echo intensity will be modulated with a frequency dependent on the Pake pattern. This is called relaxation-induced dipolar modulation enhancement, RIDME, and was demonstrated on the same diradical. Distances observed in photochemical reactions are summarised in Table 3.

7.1 DQC and DEER

Although most of the recent activity has applied the DEER method, the other methods described in ref. 2, ranging from half-field transitions to double quantum coherence (DQC), continue to have important applications. Coherent pulse methods have the advantage of improved S/N because a larger portion of the EPR spectrum can be excited, in contrast to the DEER method, which excites different portions of the spectrum with pulses at each of the two frequencies. Borbat and Freed have written an introduction to the DQC method,[143] and another chapter compares DQC and DEER.[144]

Freed and coworkers have published several recent papers using DQC. Eight doubly labeled T4 lysozyme mutants, prepared by Mchaourab, exhibited distances from 20 to 47 Å. Six-pulse DQC measurements were made at X-band and at 17.3 GHz.[145] Six-pulse DQC at 17.4 GHz with $B_1 \approx 28$ G, showed that spin-labeled gramicidin A formed dimers with interspin distance of 30.9 ± 0.5 Å.[146] A new method, double-quantum filtered refocused electron spin echo (DQFR-ESE), was developed to further suppress nuclear spin diffusion shortening of the nitroxyl spin echo decay, thus providing increased acquisition time (about 10 μs) that allows determination of longer distances.[147] Doubly-labeled double-stranded RNA, with an estimated 70 ± 5 Å (by molecular modeling) between spins, was used. Deuterated solvent was used to increase T_m. The measured distance was 72 ± 4 Å. An analogous measurement with DQC was possible up to 55 Å. Saxena and coworkers demonstrated that by exploiting the so-called observer blind spots, which are functions of the ESEEM frequencies, the ESEEM modulation in DQC can be suppressed.[148] Using a $\tau = 34$ ns slice, ESEEM was suppressed for DQC of a diradical with spin–spin distance of 28 Å. It is important to note that this demonstration was performed on a standard Bruker E580 X-band spectrometer with a 3 mm split ring resonator. DQC studies of dual spin-labeled peptoid oligomers found many distances between 12.2 and 21.5 Å with variances ranging from 3.3 to 6.5 Å.[149]

DQC and DEER measurements of distance have been compared for nitroxyl spin labels,[91,92,133,134] but additional studies are needed to give guidance to potential users. One might anticipate that DQC will be the method of choice for radicals that exhibit narrower lines than do nitroxyls, such as semiquinone and tyrosyl radicals.

Even for Cu–Cu distances, measurements have been made both by DQC[150] and by DEER.[88]

Table 3 Radical pairs occurring in photochemical reactions

Spin system	Spin–spin distance (Å)	Notes and keywords	Ref.
Flexible biradicals		Solvent viscosity effect on motional regime	159
Covalently linked radical ion pairs	17 to 20.5		160
Radical pairs in synthetic hairpin DNA			161
Photoinduced ion pairs	22	In blends of polythiophene and fullerene derivatives	162
Phenothiazine-C_{60} linked systems		Magnetic field effects	163
Triradical donor–chromophore–acceptor-TEMPO			164
Double spin labeled DNA duplexes	Multiple distances, 28 to 68 Å	In deuterated ethylene glycol and D_2O	165
$^3PQ_A^-$	Same as in $P^+Q_A^-$		166
$^3PQ_A^-$		Out-of-phase FID detection	154
$P_{700}^+ A_1^-$		Out-of-phase echo and FID detection	167
$P_{700}^+ A_1^-$ wild type and two mutants	25.01 ± 0.02	Out-of-phase ESEEM	168
	24.27 ± 0.02		
	25.43 ± 0.01		

7.2 Out-of-phase echo detection

Spin polarization in light-induced radical pairs, monitored with out-of-phase spin echo detection, has been used extensively to study short-lived intermediates in photosystem I.[151] By using oriented single crystals, both the distance and the orientation of the dipolar coupling axes relative to the crystallographic axes were determined. The modulation frequency of the out-of-phase echo gives the distance between the unpaired spins. The method has been calibrated for a case in which the distance was known from the crystal structure. Many of the distances measured are of the order of 25 Å. A vector model of the echo formation has been described.[151] As an example of the utility of this method, a distance of 25.3 ± 0.3 Å was found between $P700^+$ and A_1^- in a photosystem I mutant, which was the same as in wild-type, showing that the absence of an F_x cluster does not affect the distance between these sites.[152] This method was reviewed by Bittl and Weber.[153] Multiple distances between about 25 and 35 Å were measured by DEER and spin polarized ESEEM in photosystem II to map out the locations of chlorophylls.[131] A conformation transition was detected in a protein of the photosynthetic reaction center between 13 and 20 K. The distance monitored was about 29 Å.[154] Additional motion was observed above about 200 K.[155]

Use of quantum beat oscillations to explore the structure of radical pair intermediates was reviewed,[156] and applied to the secondary radical pair $P_{700}^+ A_1^-$.[157]

EPR methods for study of transient radicals and radical pairs occurring in photochemical reactions were reviewed by Savitsky and Möbius, with an emphasis on high-field EPR.[158]

8. Biological studies at room temperature

Since EPR studies are specific for the electron spins, there are opportunities eventually (limited by S/N) to study biological structure and function under physiological conditions. Since the distance measurements are based on dipolar interactions, the tumbling rate must be less than the dipolar interaction. The first steps in this direction have involved isolated proteins, membranes, *etc.*, usually spin labeled, studied near room temperature. Especially powerful have been dual-spin-labeled systems in which the interactions between the spin labels change under some controlled parameter.

9. Sample preparation limitations

As stated in the introduction, there is a tradeoff between intermolecular and intramolecular contributions to spin–spin interaction, and hence a sample concentration and S/N limitation on distance measurements. To measure the longest distances, pulse methods have to be used, and those that depend on measurement of T_1 are limited by potential problems not usually mentioned in the literature: solvent and O_2. Even seemingly small differences in solution composition, such as ratio of buffer to cryoprotectant, can affect T_1. Removal of O_2 affects relaxation not only in fluid solution at room temperature. "Degassing" (*i.e.*, removal of O_2) by freeze-pump-thaw methods is fairly routine for samples in 4 mm tubes, but this aspect of sample preparation becomes increasingly difficult as sample diameter decreases in order to use high frequency EPR or to use small diameter resonators to achieve higher B_1 pulses at X-band. If the sample cannot be thawed without modifying it, alternative methods of ensuring reproducible sample environment need to be employed. Interpretation of T_1 values requires diligence concerning these potential confounding variables.

As shown in some of the cited papers, the DEER observation window can be usefully lengthened by increasing T_m when it is possible to deuterate the environment of the radical.

Acknowledgements

References

1 M. Baumgarten, in *'High spin molecular molecules directed toward molecular magnets'*, eds. A. Lund and M. Shiotani, Dordrecht, 2003.
2 *'Distance Measurements in Biological Systems by EPR'*, eds. L. J. Berliner, G. R. Eaton, and S. S. Eaton, *Biol. Magn. Reson.*, New York, 2000, vol. 19.
3 N. Alexander, M. Bortolus, A. Al-Mestarihi, H. Mchaourab and J. Meiler, *Structure*, 2008, **16**, 181.
4 M. Kim, Q. Xu and D. S. Cafiso, *Biochemistry*, 2008, **47**, 670.
5 S. M. Hanson, N. van Eps, D. J. Francis, C. Altenbach, S. A. Vishnivetsky, V. Y. Arshavsky, C. S. Klug, W. L. Hubbell and V. V. Gurevich, *EMBO J.*, 2007, **26**, 1726.
6 S. S. Eaton and G. R. Eaton, *Specialist Periodical Report on Electron Spin Resonance*, 2005, **19**, 318.
7 *'Biomedical EPR—Part A: Free Radicals, Metals, Medicine, and Physiology'*, eds. S. S. Eaton, G. R. Eaton and L. J. Berliner, *Biol. Magn. Reson.*, New York, 2005, vol. 23.
8 *'Biomedical EPR-Part B Methodology Instrumentation and Dynamics'*, eds. S. S. Eaton, G. R. Eaton and L. J. Berliner, *Biol. Magn. Reson.*, New York, 2005, vol. 24.
9 L. V. Kulik and S. A. Dzyuba, *J. Struct. Chem.*, 2004, **45**, 298.
10 S. A. Dzuba, *Russian Chem. Rev.*, 2005, **74**, 619.
11 S. A. Dzuba, *Russian Chem. Rev.*, 2007, **76**, 699.
12 K. V. Lakshmi and G. W. Brudvig, *Current Opinion in Structural Biology*, 2001, **11**, 523.
13 T. Prisner, M. Rohrer and F. MacMillan, *Ann. Rev. Phys. Chem.*, 2001, **52**, 279.
14 H.-J. Steinhoff, *Biol. Chem.*, 2004, **385**, 913.

15 M. Bennati and T. Prisner, *Reports on Progress in Physics*, 2005, **68**, 411.
16 O. Schiemann and T. Prisner, *Quart. Rev. Biophys.*, 2007, **40**, 1.
17 G. E. Fanucci and D. S. Cafiso, *Curr. Opin. Struct. Biol.*, 2006, **16**, 644.
18 A. Kawamori, *Appl. Magn. Reson.*, 2007, **31**, 205.
19 A. Kawamori, in *'Electron transfer and structure of plant photosystem II'*, eds. A. Lund and M. Shiotani, Dordrecht, 2003.
20 A. Schnegg, A. A. Dubinskii, M. R. Fuchs, Y. A. Grishin, E. P. Kirilina, W. Lubitz, M. Plato, A. Savitsky and K. Möbius, *Appl. Magn. Reson.*, 2007, **31**, 59.
21 G. Jeschke, *ChemPhysChem.*, 2002, **3**, 927.
22 G. Jeschke, *Curr. Opin. Solid State Mat. Sci.*, 2003, **7**, 181.
23 G. Jeschke, *Biochim. Biophys. Acta*, 2005, **1707**, 91.
24 D. Hinderberger and G. Jeschke, in *'Site-specific characterization of structure and dynamics of complex materials by EPR spin probes'*, ed. G. A. Webb, 2006.
25 G. Jeschke, in *'Double resonance ESR methods'*, ed. S. Schlick, Hoboken, NY, 2006.
26 G. Jeschke and H. W. Spiess, *Lect. Notes Phys.*, 2006, **684**, 21.
27 G. Jeschke and Y. Polyhach, *Physical Chemistry Chemical Physics*, 2007, **9**, 1895.
28 S. Schlick, in *'Advanced ESR Methods in Polymer Research'*, Hoboken, NJ, 2006.
29 F. Lendzian, *Biochim. Biophys. Acta*, 2005, **1707**, 67.
30 V. P. Denysenkov, T. Prisner, J. Stubbe and M. Bennati, *Appl. Magn. Reson.*, 2005, **29**, 375.
31 C. Elsaesser, B. Monien, W. Haehnel and R. Bittl, *Magn. Reson. Chem.*, 2005, **43**, 526.
32 J. Dong, G. Yang and H. S. Mchaourab, *Science*, 2005, **308**, 1023.
33 N. J. Cobb, F. D. Sonnichsen, H. S. Mchaourab and W. K. Surewicz, *Proc. Nat. Acad. Sci. US*, 2007, **104**, 18946.
34 M. Chen, M. Margittai, J. Chen and R. Langen, *J. Biol. Chem.*, 2007, **282**, 24970.
35 M. Margittai and R. Langen, *Proc. Nat. Acad. Sci. US*, 2004, **101**, 10278.
36 M. S. Budamagunta, J. F. Hess, P. G. Fitzgerald and J. C. Voss, *Cell Biochem. Biophys.*, 2007, **48**, 45.
37 P. Ionita, A. Caragheorgheopol, B. C. Gilbert and V. Chechik, *J. Phys. Chem. B*, 2005, **109**, 3734.
38 P. Ionita, A. Volkov, G. Jeschke and V. Chechik, *Anal. Chem.*, 2008, **80**, 95.
39 M. K. Bowman, A. G. Maryasov, N. Kim and V. J. DeRose, *Appl. Magn. Reson.*, 2004, **26**, 23.
40 S. M. Hanson, D. J. Francis, S. A. Vishnivetsky, E. A. Kolobova, W. L. Hubbell, C. S. Klug and V. V. Gurevich, *Proc. Nat. Acad. Sci. US*, 2006, **103**, 4900.
41 A. R. Gingras, K.-P. Vogel, H.-J. Steinhoff, W. H. Ziegler, B. Patel, J. Emsley, D. R. Critchley, G. C. K. Roberts and I. L. Barsukov, *Biochemistry*, 2006, **45**, 1805.
42 D. P. Claxton, P. Zou and H. S. Mchaourab, *J. Mol. Biol.*, 2008, **375**, 1026.
43 J. L. Garcia-Gimenez, G. Alzuet, M. Gonzalez-Alvarez, A. Castineiras, M. Liu-Gonzales and J. Gorras, *Inorg. Chem.*, 2007, **46**, 7178.
44 R. Cejudo, G. Alzuet, M. Gonzalez-Alvarez, J. L. Garcia-Gimenez, J. Borras and M. Liu-Gonzales, *J. Inorg. Biochem.*, 2006, **100**, 70.
45 N. Kisseleva, S. Kraut, A. Jaschke and O. Schiemann, *HFSP Journal*, 2007, **1**, 127.
46 S. O. Mansoorabadi, O. T. Magnusson, R. R. Poyner, P. A. Frey and G. A. Reed, *Biochemistry*, 2006, **45**, 14362.
47 J. Pyka, J. Ilnicki, C. Altenbach, W. L. Hubbell and W. Froncisz, *Biophys. J.*, 2005, **89**, 2059.
48 C. Altenbach, W. Froncisz, R. Hemker, H. Mchaourab and W. L. Hubbell, *Biophys. J.*, 2005, **89**, 2103.
49 J. L. Cape, M. K. Bowman and D. M. Kramer, *Proc. Nat. Acad. Sci. US*, 2007, **104**, 7887.
50 R. MacArthur and G. W. Brudvig, *J. Phys. Chem. B*, 2004, **108**, 9390.
51 J. O. Lagerstedt, M. S. Budamagunta, M. N. Oda and J. C. Voss, *J. Biol. Chem.*, 2007, **282**, 9143.
52 N. Sharma, Z. Hu, M. W. Crowder and B. Bennett, *J. Am. Chem. Soc.*, 2008, **130**, 10.1021/ja0774562.
53 G. Bar, M. Bennati, H.-H. T. Nguyen, J. Ge, J. Stubbe and R. G. Griffin, *J. Am. Chem. Soc.*, 2001, **123**, 3569.
54 S.-C. Hung, C. V. Grant, J. M. Peloquin, A. R. Waldeck, R. D. Britt and S. I. Chan, *J. Phys. Chem. A*, 2000, **104**, 4402.
55 R. MacArthur, M. H. Sazinsky, H. Kuhne, D. A. Whittington, S. J. Lippard and G. W. Brudvig, *J. Am. Chem. Soc.*, 2002, **124**, 13392.
56 K. V. Lakshmi, O. G. Poluektov, M. J. Reifler, A. M. Wagner and M. C. Thurnauer, *J. Am. Chem. Soc.*, 2003, **125**, 5005.
57 D. J. Hirsch and G. W. Brudvig, *Nature Protocols*, 2007, **2**, 1770.

58 S. Lyubenova, M. K. Siddiqui, M. J. M. P. DeVries, B. Ludwig and T. F. Prisner, *J. Phys. Chem. B*, 2007, **111**, 3839.

59 S. Jun, J. S. Becker, M. Yonkunas, R. Coalson and S. Saxena, *Biochemistry*, 2006, **45**, 11666.

60 X. J. Chen, J. Schramm, C. Tuohy, H. Skiff, K. Hummel, A. R. Szklarski, N. Vacira, B. A. Wolf and D. J. Hirsch, *Biophysical Chemistry*, 2007, **129**, 148.

61 A. J. Fielding, R. J. Usselman, N. Watmough, M. Simkovic, F. E. Frerman, G. R. Eaton and S. S. Eaton, *J. Magn. Reson.*, 2008, **190**, 222.

62 R. J. Usselman, A. J. Fielding, F. E. Frerman, G. R. Eaton and S. S. Eaton, *Biochemistry*, 2008, **47**, 92.

63 H. A. Koteiche, S. Chiu, R. L. Majdoch, P. L. Stewart and H. S. Mchaourab, *Structure*, 2005, **13**, 1165.

64 J. Shi, H. A. Koteiche, H. S. Mchaourab and P. L. Stewart, *J. Biol. Chem.*, 2006, **281**, 40420.

65 M. R. Seyedsayamdost, J. Xie, C. T. Y. Chan, P. G. Schultz and J. Stubbe, *J. Am. Chem. Soc.*, 2007, **129**, 15060.

66 A. A. Frazier, C. R. Roller, J. J. Havelka, A. Hinderliter and D. S. Cafiso, *Biochemistry*, 2003, **42**, 96.

67 E. Rufener, A. A. Frazier, C. M. Wieser, A. Hinderliter and D. S. Cafiso, *Biochemistry*, 2005, **44**, 18.

68 R. Pogni, M. C. Baratto, S. Giansanti, C. Teutloff, J. Verdin, B. Valderrama, F. Lendzian, W. Lubitz, R. Vazquez-Duhalt and R. Basosi, *Biochemistry*, 2005, **44**, 4267.

69 G. E. Fanucci, K. A. Coggshall, N. Cadieux, M. Kim, R. J. Kadner and D. S. Cafiso, *Biochemistry*, 2003, **42**, 1391.

70 F. Mamedov, P. J. Smith, S. Styring and R. J. Pace, *Phys. Chem. Chem. Phys.*, 2004, **6**, 4890.

71 K. G. Havelius, J.-H. Su, Y. Feyziyev, F. Mamedov and S. Styring, *Biochemistry*, 2006, **45**, 9279.

72 F. M. Ho, S. F. Morvaridi, F. Mamedov and S. Styring, *Biochim. Biophys. Acta*, 2007, **1767**, 5.

73 G. Jeschke, V. Chechik, P. Ionita, A. Godt, H. Zimmermann, J. Banham, C. R. Timmel, D. Hilger and H. Jung, *Appl. Magn. Reson.*, 2006, **30**, 473.

74 G. Jeschke, A. Bender, H. Paulsen, H. Zimmermann and A. Godt, *J. Magn. Reson.*, 2004, **169**, 1.

75 M. K. Bowman and A. G. Maryasov, *J. Magn. Reson.*, 2007, **185**, 270.

76 M. Bennati, A. Weber, J. Antonic, D. L. Perlstein, J. Robblee and J. Stubbe, *J. Am. Chem. Soc.*, 2003, **125**, 14988.

77 S. K. Rengan, V. R. Bhagat, V. S. S. Sastry and B. Venkataraman, *J. Magn. Reson.*, 1979, **33**, 227.

78 J. P. Hornak and J. H. Freed, *Chem. Phys. Lett.*, 1983, **101**, 115.

79 J. W. Saalmueller, H. W. Long, G. G. Maresch and H. W. Spiess, *J. Magn. Reson. A*, 1995, **117**, 193.

80 M. Willer, J. Granwehr, J. Forrer and A. Schweiger, *J. Magn. Reson.*, 1998, **133**, 46.

81 A. A. Dubinskii, Y. A. Grishin, A. Savitsky and K. Möbius, *Appl. Magn. Reson.*, 2002, **22**, 369.

82 L. V. Kulik, Y. A. Grishin, S. A. Dzuba, I. A. Grigoryev, S. V. Klyatskaya, S. F. Vasilevsky and Y. D. Tsvetkov, *J. Magn. Reson.*, 2002, **157**, 61.

83 A. V. Astashkin, J. H. Enemark and A. Raitsimring, *Conc. Magn. Reson. B (Magn. Reson. Engin.)*, 2006, **29B**, 125.

84 D. Margraf, D. E. Bode, A. Marko, O. Schiemann and T. Prisner, *Mol. Phys.*, 2007, **105**, 2153.

85 V. P. Denysenkov, T. Prisner, J. Stubbe and M. Bennati, *Proc. Nat. Acad. Sci. US*, 2006, **103**, 13386.

86 P. Gajula, S. Milikisyants, H.-J. Steinhoff and M. Huber, *Appl. Magn. Reson.*, 2007, **31**, 99.

87 V. P. Denysenkov, D. Biglino, W. Lubitz, T. Prisner and M. Bennati, *Angew. Chem.*, 2008, **47**, 1224.

88 Z. Yang, J. Becker and S. Saxena, *J. Magn. Reson.*, 2007, **188**, 337.

89 B. E. Bode, D. Margraf, J. Plackmeyer, G. Durner, T. Prisner and O. Schiemann, *J. Am. Chem. Soc.*, 2007, **129**, 6736.

90 S. Ruthstein, A. Potapov, A. Raitsimring and D. Goldfarb, *J. Phys. Chem. B*, 2005, **109**, 22843.

91 Y.-W. Chiang, P. P. Borbat and J. H. Freed, *J. Magn. Reson.*, 2005, **172**, 279.

92 Y.-W. Chiang, P. P. Borbat and J. H. Freed, *J. Magn. Reson.*, 2005, **177**, 184.

93   I. M. C. van Amsterdam, M. Ubbink, G. W. Canters and M. Huber, *Angew. Chem. Int. Ed.*, 2003, **42**, 62.
94   C. W. M. Kay, H. E. Mkami, R. Cammack and R. W. Evans, *J. Am. Chem. Soc.*, 2007, **129**, 4868.
95   A. Raitsimring, C. Gunanathan, A. Potapov, I. Efremenko, J. M. L. Martin, D. Milstein and D. Goldfarb, *J. Am. Chem. Soc.*, 2007, **129**, 14138.
96   Q. Xu, J. F. Ellena, M. Kim and D. S. Cafiso, *Biochemistry*, 2006, **45**, 10847.
97   C. Elsaesser, M. Brecht and R. Bittl, *J. Am. Chem. Soc.*, 2002, **124**, 12606.
98   C. Elsaesser, M. Brecht and R. Bittl, *Biochem. Soc. Trans.*, 2005, **33**, 15.
99   J. E. Banham, C. M. Baker, S. Ceola, I. J. Day, G. H. Grant, E. J. J. Groenen, C. T. Rodgers, G. Jeschke and C. R. Timmel, *J. Magn. Reson.*, 2008, **193**, 10.1016/j.jmr.2007.11.023.
100 A. D. Milov, B. D. Naumov and Y. D. Tsvetkov, *Appl. Magn. Reson.*, 2004, **26**, 587.
101 O. Schiemann, N. Piton, J. Plackmeyer, B. E. Bode, T. F. Prisner and J. W. Engels, *Nature Protocols*, 2007, **2**, 904.
102 M. R. Seyedsayamdost, C. T. Y. Chan, V. Mugnaini, J. Stubbe and M. Bennati, *J. Am. Chem. Soc.*, 2007, **129**, 15748.
103 Y. Polyhach, A. Godt, C. Bauer and G. Jeschke, *J. Magn. Reson.*, 2007, **185**, 118.
104 A. D. Milov, R. I. Samoilova, Y. D. Tsvetkov, C. Peggion, F. Formaggio, C. Toniolo and J. Raap, *Dokl. Phys. Chem.*, 2006, **406**, 21.
105 A. D. Milov, R. I. Samoilova, Y. D. Tsvetkov, F. Formaggio, C. Toniolo and J. Raap, *J. Am. Chem. Soc.*, 2007, **129**, 9260.
106 A. D. Milov, M. I. Samoilova, Y. D. Tsvetkov, M. Jost, C. Peggion, F. Formaggio, M. Crimsa, C. Toniolo, J.-W. Handgraaf and J. Raap, *Chemistry & Biodiversity*, 2007, **4**, 1275.
107 A. D. Milov, Y. D. Tsvetkov, F. Formaggio, C. Toniolo and J. Raap, *Phys. Chem. Chem. Phys.*, 2004, **6**, 3596.
108 A. D. Milov, D. A. Erilov, E. S. Salnikov, Y. D. Tsvetkov, F. Formaggio, C. Toniolo and J. Raap, *Phys. Chem. Chem. Phys.*, 2005, **7**, 1794.
109 A. D. Milov, R. I. Samoilova, Y. D. Tsvetkov, F. Formaggio, C. Toniolo and J. Raap, *Appl. Magn. Reson.*, 2005, **29**, 703.
110 E. S. Salnikov, D. A. Erilov, A. D. Milov, Y. D. Tsvetkov, C. Peggion, F. Formaggio, C. Toniolo, J. Raap and S. A. Dzuba, *Biophysical J.*, 2006, **91**, 1532.
111 Q. Cai, A. K. Kusnetzow, W. L. Hubbell, I. S. Haworth, G. P. C. Gacho, N. V. Eps, K. Hideg, E. J. Chambers and P. Z. Qin, *Nuclei Acids Research*, 2006, **34**, 4722.
112 G. Sicoli, G. Mathis, O. Delalande, Y. Boulard, D. Gasparutto and S. Gambarelli, *Angew. Chem. Int. Ed.*, 2008, **47**, 735.
113 N. Piton, O. Schiemann, Y. Mu, G. Stock, T. Prisner and J. W. Engels, *Nucleosides, Nucleotides and Nucleic Acids*, 2005, **24**, 771.
114 N. Piton, Y. Mu, G. Stock, T. F. Prisner, O. Schiemann and J. W. Engels, *Nuclei Acids Research*, 2007, **35**, 3128.
115 P. P. Borbat, K. Surendhran, M. Bortolus, P. Zou, J. H. Freed and H. S. Mchaourab, *PLoS Biology*, 2007, **5**, 2211.
116 M. Nakamura, S. Ueki, H. Hara and T. Arata, *J. Mol. Biol.*, 2005, **348**, 127.
117 S. Kuroiwa, M. Tonaka, A. Kawamori and K. Akabori, *Biochim. Biophys. Acta*, 2000, **1460**, 330.
118 A. K. Upadhyay, P. P. Borbat, J. Wang, J. H. Freed and D. E. Edmondson, *Biochemistry*, 2008, **47**, 1554.
119 C. W. M. Kay, C. Elsasser, R. Bittl, S. R. Farrell and C. Thorpe, *J. Am. Chem. Soc.*, 2006, **128**, 76.
120 S. Steigmuller, M. Borsch, P. Graber and M. Huber, *Biochim. Biophys. Acta*, 2005, **1708**, 143.
121 J. Banham, G. Jeschke and C. R. Timmel, *Mol. Phys.*, 2007, **105**, 2041.
122 L. Galiano, M. Bonora and G. E. Fanucci, *J. Am. Chem. Soc.*, 2007, **129**, 11004.
123 I. Smirnova, V. Kasho, J.-Y. Choe, C. Altenbach, W. L. Hubbell and R. H. Kaback, *Proc. Nat. Acad. Sci. US*, 2007, **104**, 16504.
124 G. Jeschke, A. Bender, T. Schweikardt, G. Panek, H. Decker and H. Paulsen, *J. Biol. Chem.*, 2005, **280**, 18623.
125 D. Hilger, H. Jung, E. Padan, C. Wegener, K.-P. Vogel, H.-J. Steinhoff and G. Jeschke, *Biophysical J.*, 2005, **89**, 1328.
126 D. Hilger, Y. Polyhach, H. Jung and G. Jeschke, *Biophys. J.*, 2007, **93**, 3675.
127 A. Savitsky, A. A. Dubinskii, M. Flores, W. Lubitz and K. Möbius, *J. Phys. Chem. B*, 2007, **111**, 6245.
128 D. Biglino, P. P. Schmidt, E. J. Reijerse and W. Lubitz, *Phys. Chem. Chem. Phys.*, 2006, **8**, 58.

129 M. Bennati, J. H. Robblee, V. Mugnaini, J. Stubbe, J. H. Freed and P. P. Borbat, *J. Am. Chem. Soc.*, 2005, **127**, 15014.
130 A. Kawamori, N. Katsuta and H. Hara, *Appl. Magn. Reson.*, 2003, **23**, 557.
131 A. Kawamori, T.-A. Ono, A. Ishii, S. Nakazawa, H. Hara, T. Tomo, J. Minagawa, R. Bittl and S. A. Dzuba, *Photosynth. Research*, 2005, **84**, 187.
132 I. V. Borovykh, S. Ceola, P. Gajula, P. Gast, H.-J. Steinhoff and M. Huber, *J. Magn. Reson.*, 2006, **180**, 178.
133 P. P. Borbat, T. F. Ramlall, J. H. Freed and D. Eliezer, *J. Am. Chem. Soc.*, 2006, **128**, 10004.
134 H. Hara, T. Tenno and M. Shirakawa, *J. Magn. Res.*, 2007, **184**, 78.
135 J. E. Banham, C. R. Timmel, R. J. M. Abbott, S. M. Lea and G. Jeschke, *Angew. Chem. Int.Ed.*, 2006, **45**, 1058.
136 D. Hinderberger, O. Schmelz, M. Rehahn and G. Jeschke, *Angew. Chem. Int. Ed.*, 2004, **43**, 4616.
137 A. Godt, M. Schulte, H. Zimmermann and G. Jeschke, *Angew. Chem. Int. Ed.*, 2006, **45**, 7560.
138 G. W. M. Vandermeulen, D. Hinderberger, H. Xu, S. S. Sheiko, G. Jeschke and H.-A. Klok, *ChemPhysChem*, 2004, **5**, 488.
139 G. Jeschke and S. Schlick, *Phys. Chem. Chem. Phys.*, 2006, **8**, 4095.
140 Q. Mao, S. Schleidt, H. Zimmermann and G. Jeschke, *Phys. Chem. Chem. Phys.*, 2008, **10**, 1156.
141 V. F. Yudanov, A. K. Salikhov, G. M. Zhidomirov and Y. D. Tsvetkov, *Theoret. Expt. Chem.*, 1969, **5**, 451.
142 L. V. Kulik, S. A. Dzuba, I. A. Grigoryev and Y. D. Tsvetkov, *Chem. Phys. Lett.*, 2001, **343**, 315.
143 P. P. Borbat and J. H. Freed, *Biol. Magn. Reson.*, 2000, **19**, 383.
144 P. P. Borbat and J. H. Freed, *Meth. Enzymol.*, 2007, **423**, 52.
145 P. P. Borbat, H. S. Mchaourab and J. H. Freed, *J. Amer. Chem. Soc.*, 2002, **124**, 5304.
146 B. G. Dzikovski, P. P. Borbat and J. H. Freed, *Biophysical J.*, 2004, **87**, 3504.
147 P. P. Borbat, J. H. Davis, S. E. Butcher and J. H. Freed, *J. Am. Chem. Soc.*, 2004, **126**, 7746.
148 M. Bonora, J. Becker and S. Saxena, *J. Magn. Reson.*, 2004, **170**, 278.
149 A. T. Fafarman, P. P. Borbat, J. H. Freed and K. Kirshenbaum, *Chem. Commun.*, 2007, 377.
150 J. S. Becker and S. Saxena, *Chem. Phys. Lett.*, 2005, **414**, 248.
151 R. Bittl and S. G. Zech, *Biochim. Biophys. Acta*, 2001, **1507**, 194.
152 G. Shen, M. L. Antonkine, A. v. d. Est, I. R. Vassiliev, K. Brettel, R. Bittl, S. G. Zech, J. Zhao, D. Stehlik, D. A. Bryant and J. H. Golbeck, *J. Biol. Chem.*, 2002, **277**, 20355.
153 R. Bittl and S. Weber, *Biochim. Biophys. Acta*, 2005, **1707**, 117.
154 L. V. Kulik, I. V. Borovykh, P. Gast and S. A. Dzuba, *J. Magn. Reson.*, 2003, **162**, 423.
155 I. V. Borovykh, P. Gast and S. A. Dzuba, *J. Phys. Chem. B*, 2005, **109**, 7535.
156 G. Link, O. Poluektov, M. C. Thurnauer and G. Kothe, *RIKEN Review*, 2002, **44**, 109.
157 G. Link, O. G. Poluektov, L. M. Utschig, J. Lalevee, T. Yago, J.-U. Weidner, M. C. Thurnauer and G. Kothe, *Magn. Reson. Chem.*, 2005, **43**, S103.
158 A. Savitsky and K. Möbius, *Helv. Chim. Acta*, 2006, **89**, 2544.
159 M. D. E. Forbes, K. E. Dukes, N. I. Avdievich, E. J. Harbron and J. M. DeSimone, *J. Phys. Chem. A*, 2006, **110**, 1767.
160 S. Shaakov, T. Galili, E. Stavitski, H. Levanon, A. Lukas and M. R. Wasielewski, *J. Am. Chem. Soc.*, 2003, **2003**, 6563.
161 S. Nakajima, K. Akiyama, K. Kawai, T. Takada, T. Ikoma, T. Majima and S. Tero-Kubota, *ChemPhysChem*, 2007, **8**, 507.
162 L. Franco, M. Ruzzi and C. Corvaja, *J. Phys. Chem. B*, 2005, **109**, 13431.
163 S. Moribe, H. Yonemura and S. Yamada, *Chemical Physics*, 2007, **334**, 242.
164 Q. Mi, E. T. Chernick, D. W. McCamant, E. A. Weiss, M. A. Ratner and M. R. Wasielewski, *J. Phys. Chem. A*, 2006, **110**, 7323.
165 R. Ward, D. J. Keeble, H. El-Mkami and D. G. Norman, *ChemBioChem*, 2007, **8**, 1957.
166 I. V. Borovykh, L. V. Kulik, S. A. Dzuba and A. J. Hoff, *J. Phys. Chem. B*, 2002, **106**, 12066.
167 S. A. Dzuba, A. Kawamori, N. Katsuta, H. Hara, H. Mino and S. Itoh, *Chem. Phys. Lett.*, 2002, **362**, 307.
168 S. Santabarbara, I. Kuprov, W. V. Fairclough, S. Purton, P. J. Hore, P. Heathcote and M. C. W. Evans, *Biochemistry*, 2005, **44**, 2119.
169 G. Jeschke, G. Panek, A. Godt, A. Bender and H. Paulsen, *Appl. Magn. Reson.*, 2004, **26**, 233.

Time-resolved electron paramagnetic resonance studies of transient organic radicals

Dieter Beckert

1. Introduction

This report presents an overview of time-resolved electron paramagnetic resonance studies on transient organic radical ions and free radicals published between 2002 and 2007. The literature about time-resolved electron paramagnetic resonance studies until 2001 was presented in the Volume 18 of this series.[1] Previous volumes of this series have considered several reviews with different aspects of time-resolved EPR (TR EPR).[2–9]

In TR EPR experiments of transient radicals structural and kinetic aspects are of interest. In the structural analysis of transient radicals, the well-known rules of hyperfine interactions are applicable, whereas in the kinetic analysis the superposition of the chemical kinetics and the different processes of spin chemistry (chemically induced electron spin polarization phenomena (CIDEP))[10–12] has to be considered. Often, the separation of the contributions of different spin polarization mechanisms is a difficult task, but this separation gives unique information about the primary processes in radical generation and the subsequent reaction pathways.

In the time period between 2002 and 2007 several reviews dealing with applications of TR EPR to different problems in radical chemistry were published. The "Spin-chemical approach to photochemistry: reaction control by spin quantum operation" has been reviewed by Murai.[13,14] Besides TR EPR this review discusses some methods related to TR EPR, like reaction yield-detected magnetic resonance (RYDMR), fluorescence-detected magnetic resonance (FDMR), transient absorption-detected magnetic resonance (ADMR) and photoconductivity detected magnetic resonance (PCDMR), respectively. The application of TR EPR to study short-lived excited triplet states is considered by Hirota and Yamauchi,[15] where most of the experimental results are obtained in the solid phase at low temperatures. More recent developments in multifrequency TR EPR and their applications in studying photoinduced electron transfer and photochemical reactions in liquids, frozen solutions and proteins have been reviewed by Savitsky and Möbius.[16] Still the most frequent application of TR EPR is to studying the mechanisms of photosynthesis. The latest results are presented and discussed by Lubitz,[17–19] Bittl and Weber,[20] Kothe et al.,[21,22] and Kandrashkin.[23] The application of time-resolved electron spin echo (ESE) spectroscopy to study biomembranes has been reviewed by Bartucci et al.[24] The review discusses two applications of the ESE technique in biomembrane research, firstly, the study of librational lipid chain motions in low-temperature phases in bilayer membranes, and secondly, the study of the transmembrane profiles of water penetration in phospholipid bilayers. Both types of measurements use ESE spectroscopy of nitroxide spin-labelled probes, but in different ways.

Since the first TR EPR experiments in 1968 by Atkins et al.[25] and Smaller et al.,[26] this experimental technique has developed into a powerful tool for studying transient paramagnetic species in the nanosecond and microsecond time range. Modern pulsed EPR instrumentation[27–33] has resulted in improved sensitivity and time resolution, and measurements similar to pulsed nuclear magnetic resonance can be performed.

This contribution provides a general survey of the more recent TR EPR papers on organic radicals, and especially the Fourier transform EPR studies conducted in the authors' laboratory in the past few years.

2. Photochemical applications

Basic research in the field of molecular photophysics and photochemistry has been continued over the last few years. In order to achieve a deeper understanding of the photophysical and photochemical processes time-resolved EPR techniques are used in many research groups. The fields of applications are important in such diverse areas as photosynthesis in bacteria and plants, chemical synthesis, photodegradation of pollutants, solar energy conversion and storage, and molecular-scale optoelectronic devices. Thanks to the availability of high-power UV pulse lasers with nanosecond pulse length, such as solid-state lasers and excimer lasers, the photoexcitation of the systems of interest in TR EPR spectroscopy can be easily achieved. The most commonly used wavelengths of excitation are in the range of 248–355 nm, and energy per pulse up to 30 mJ is sufficient to obtain a good signal-to-noise ratio in TR EPR studies.

The photochemical generation of transient radical ions and/or radicals is dominated by the processes of photoionization, photo-induced electron/hydrogen transfer (photoreduction/photooxidation), and homolytic bond scission. Photoexcitation populates higher vibrational singlet states which decay by internal conversion to the vibration ground state of S_1, fluorescence to the ground state S_0, homolytic bond scission or intersystem crossing (isc) to the lowest triplet state T_1. Photoionization and photo-induced electron/hydrogen transfer are mostly observed from the triplet state T_1 due to its long lifetime. Here the paramagnetic transients are produced in radical-ion pairs or pairs of neutral free radicals. This reaction pathway *via* triplet states generates non-equilibrium populations of the doublet spin states by the CIDEP triplet mechanism (TM) and by the CIDEP radical pair mechanism (RPM), respectively. Therefore, the time profiles of transient radicals not only reflect the chemical kinetics of radical formation and decay, but are strongly affected by CIDEP effects. CIDEP mechanisms will be not discussed in this review (see for instance refs. 2, 12 and 34), however, the typical reaction scheme of radical generation with spin polarization mechanisms is shown in Fig. 1.

This scheme indicates the additional information about the precursor of primary radical-ion pair and the interaction in the spin-correlated radical pair that can be derived from the CIDEP spectra of transient radicals.
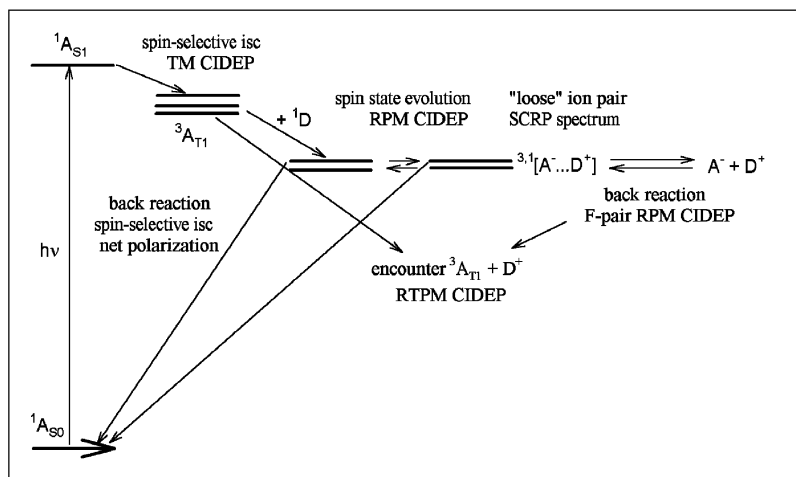

Fig. 1 Photoexcitation and radical-pair generation by triplet-sensitized electron transfer with the spin-polarization mechanisms acting in this scheme.

2.1 Photoionization

The photoionization of phenols and phenolates was discussed in the previous review in detail.[1] The interest on the photophysics and photochemistry of phenols is related to their application as antioxidants in organic materials and polymers, as well as due to their importance as constituents of many biological systems, and also because OH-bond dissociation of the aromatic amino acid tyrosine may play an important role in protein photodegradation.

By FT EPR experiments the wavelength dependence of the photochemistry of phenols was studied by van Willigen $et\ al.$[35] The photoexcitation of phenol, p-cresol and tyrosine with 266 nm and 193 nm laser light (see Fig. 2 and 3) generates hydrated electrons e_{aq}^-, hydrogen atoms $H^\bullet$ and phenoxyl radicals $PhO^\bullet$. The FT EPR spectra in Fig. 2 and 3 show different yields and CIDEP polarization patterns of all three radicals in dependence on pH values, which is the result of different precursor excitation states S_1 and S_2 by the two excitation wavelengths. The detailed analysis of the polarization patterns and the scavenging effects of e_{aq}^- by N_2O with the 266 nm excitation lead to the overall reaction scheme

$$^1PhOH^* \to [PhO^\bullet \cdots e_{aq}^-] + H^+ \to PhO^\bullet + e_{aq}^- + H^+$$

$$e_{aq}^- + H^+ \to H^\bullet$$
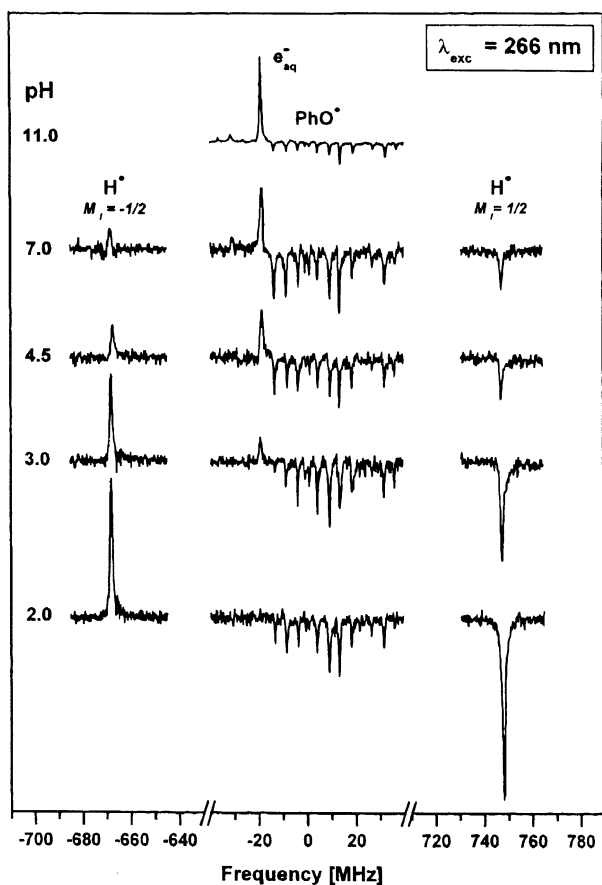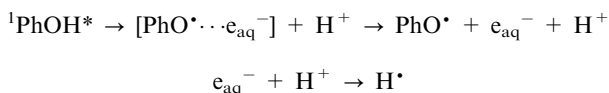
Fig. 2 FT EPR spectra observed upon photoexcitation of 10^{-3} M phenol in aqueous solution at different pH. Excitation wavelength: 266 nm with 20 mJ. Delay time between laser and microwave pulse: 80 ns. Reproduced with permission of ref. 35.
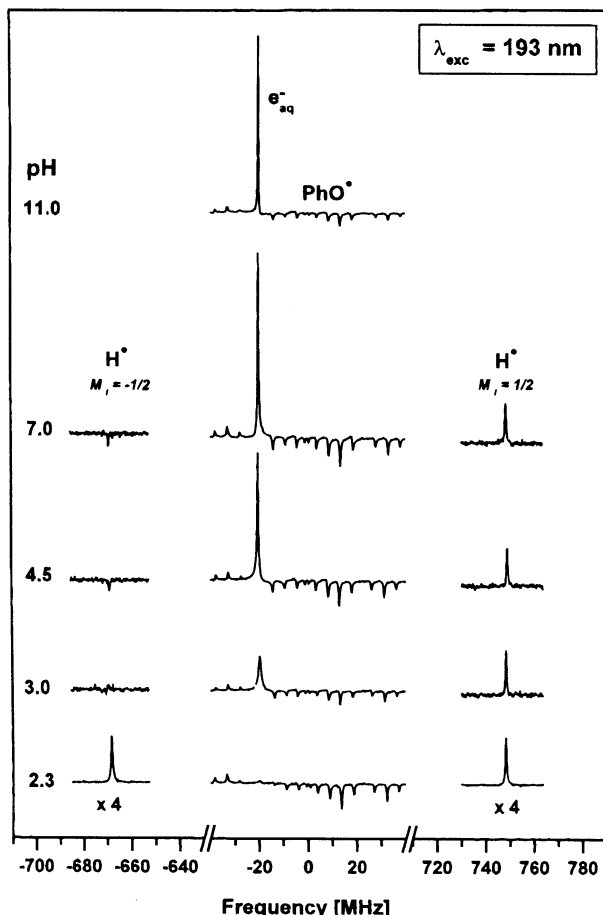
Fig. 3 FT EPR spectra observed upon photoexcitation of 10^{-3} M phenol in aqueous solution at different pH. Excitation wavelength: 193 nm with 20 mJ. Delay time between laser and microwave pulse: 80 ns. The H-atom signal intensities are expanded by a factor of 4. Reproduced with permission of ref. 35.

The FT EPR results provide no evidence of in-cage charge neutralization such as

$$[PhO^{\bullet} \cdots e_{aq}^{-}] + H^{+} \rightarrow [PhO^{\bullet} \cdots H^{\bullet}] \rightarrow PhO^{\bullet} + H^{\bullet}$$

or

$$[PhOH^{+} \cdots e_{aq}^{-}] \rightarrow [PhO^{\bullet} \cdots H^{\bullet}] \rightarrow PhO^{\bullet} + H^{\bullet}$$
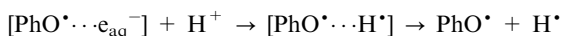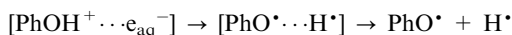
In the microsecond time range the FT EPR spectra show additional line groups which can be attributed to the cyclohexadienyl radical. The quantum yield of the H-atom formation is significantly smaller with 266 nm than for S_2 excitation with 193 nm. This indicates that intersystem crossing (ISC) to the excited triplet state can be an important S_1 decay channel. From this fact the authors conclude, that triplet-state formation accounts for generation of a cyclohexadienyl-type radical in a bimolecular hydrogen abstraction reaction involving ground-state phenol and triplet-state phenol (Scheme 1, reproduced with permission of ref. 35).
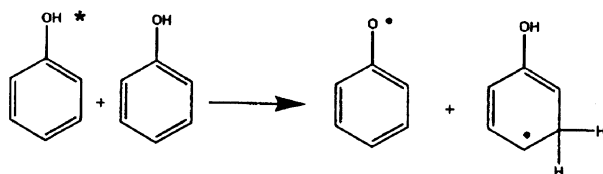
Scheme 1 Reproduced with permission of ref. 35.

This reaction has also been found for p-cresol and sesamol. The hydrogen transfer from the ground-state phenol has been confirmed by experiments in D_2O. The excitation by a 193 nm laser pulse opens a second reaction channel for H-atom formation, giving rise to an E/A signal with small net A component, which is not affected by N_2O addition showing that it is independent of the photoionization step. This signal contribution is attributed to direct photoinduced O–H bond homolysis via the S_2 excited state,

$$^1PhOH^*(S_2) \rightarrow [PhO^\bullet \cdots H^\bullet] \rightarrow PhO^\bullet + H^\bullet$$
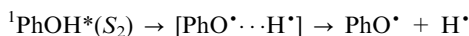
Biodegradable materials such as lignins are a topic of current interest. The phenoxyl radical formation mechanism from the UV photolysis of lignins in organic solvents has been investigated by steady-state and TR EPR.[36] The experimental results indicate that the phenoxyl radicals are generated from the o-methoxy phenol moiety in the main chain of the polymer through dissociative photoionization by a biphotonic process from the excited triplet state.

2.2 Photoreduction of sensitizers

2.2.1 Benzophenone. The photophysics and photochemistry of benzophenone are widely studied as it can be used as a model compound of aromatic ketones. Earlier results about the spectroscopic properties of the transient radicals and their reactivities are discussed in several reviews.[37,38]

The CIDEP spectra of benzophenone (BP) in alcoholic solutions with different benzophenone concentrations were studied at different laser wavelength by Jones and Woodward.[39] At high benzophenone concentrations (up to 100 mM) the emissive polarization of the benzophenone anion radical is strongly enhanced at excitation with 266 nm laser light in comparison to the excitation with 355 nm. From the discussion of different reaction pathways the authors conclude that the additional polarization is generated by an electron transfer reaction between two triplet states:

$$^3BP + {}^3BP \rightarrow BP^{\bullet+} + BP^{\bullet-}$$
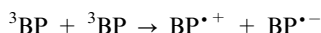
The alternative reaction pathway via hydrogen abstraction has been excluded by considering the polarization results in different alcohols (methanol to cyclohexanol) which indicate a higher electron transfer rate (that means also a higher TM polarization) at higher dielectric constant.

A comparative TR EPR study on benzophenone, and o-, m-, and p-hydroxybenzophenones in 2-propanol investigates the reaction-controlled TM and the lifetime-controlled TM.[40] Whereas in benzophenone systems the reaction-controlled TM is dominant, the spin polarization is attributed to lifetime-controlled TM in hydroxybenzophenones. Participation of the hydroxyl group of hydroxybenzophenone in forming a hydrogen bond with the solvent cage of 2-propanol is proposed to play a major role in the dynamics of the geminate radical pair.

2.2.2 Quinones. Quinones are often used as sensitizers in photochemical reactions, and much more interesting is their important role in biochemical reactions.[19]

Because of the high electron affinity of the excited-state quinones electron transfer reaction are very fast and the quantum yield of their photoreduction is often nearly one. But, the EPR spectra of the quinone radicals are often complex because of the different protonation states and the self-exchange of the radical anions with ground state molecules.[41]

The complex continuous wave (cw) TR EPR spectra of p-benzosemiquinone in water-2-propanol solutions have been studied at different pH by Jäger et al.[42,43] Neutral and anionic semiquinones are observed at different pH's with a protonation–deprotonation equilibrium. The complex spectra with magnetization transfer are described by means of a kinetic matrix incorporated into the Bloch equations. Numerical calculations considering all hyperfine components (resulting in a 162 × 162 matrix) have been compared with the experimental cw TR EPR spectra. Analysis of the three-dimensional EPR signal obtained at three different pH values and in a deuterated solvent mixture confirmed the dependence of the chemical exchange rates on the pH of the solution. At pH 2.0, exchange was interpreted to proceed via intermolecular proton transfer between neutral semiquinones, at pH 5.4, neutral and anionic radicals are interconnected via a protonation–deprotonation process, and at pH 8.3, the spectrum shows a uniform signal of the semiquinone anion radical with E/A polarization pattern.

Xu Xinsheng et al.[44] studied the CIDEP spectra in the p-benzoquinone/formamide system in acid, basic and micellar environments. The signals observed have been assigned to the p-benzoquinone anion radical $BQ^{\bullet-}$, the neutral p-benzosemiquinone radical $BQH^{\bullet}$, and the formamide radical $HCON^{\bullet}H$. The proposed reaction mechanism in formamide solution is a hydrogen abstraction by p-benzoquinone from formamide as the primary step, following a deprotonation generating the p-benzoquinone anion radical. This interpretation is supported by experiments at different pH's. With Triton X-100 added to the BQ/formamide/H_2O system a strong p-benzoquinone anion radical $BQ^{\bullet-}$ spectrum was detected, and only a very weak formamide radical signal was observed. These results are explained by a primary hydrogen abstraction from TX-100 micelles polyethylene glycol shell, and a following fast deprotonation caused by the high pH in the glycol shell.

The spin dynamics of the duroquinone anion radical $DQ^{\bullet-}$ generated by photo-induced electron transfer from triplet eosin Y (EY^{2-}) and erythrosine B (EB^{2-}) to duroquinone was studied by using optical transient absorption and pulsed FT EPR spectroscopy by Tachikawa et al.[45,46] In these papers the kinetics, radical yield and intrinsic enhancement factors of electron spin polarization for the EY^{2-}/DQ system and the EB^{2-}/DQ system were investigated to verify the heavy atom effect[12,47] on the properties of the triplet exciplex intermediate. The observation of the unusual net-A polarization suggests the generation of a triplet exciplex as the reaction intermediate, because the spin–orbit coupling (SOC) interaction due to heavy atoms is a short range interaction.[47,48] Scheme 2 (reproduced with permission of ref. 45) shows the net electron spin polarization mechanism from the spin-polarized and
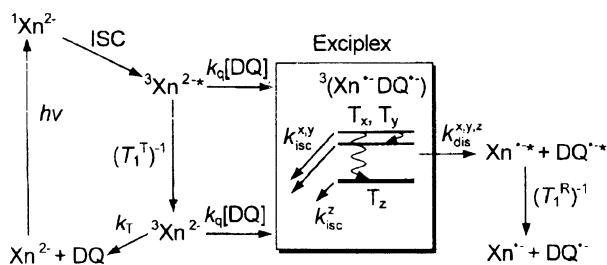
Scheme 2 Reproduced with permission of ref. 45.

spin-equilibrated triplet precursor *via* the triplet exciplex in the presented photo-sensitized reaction.

The photoinduced electron transfer occurs dominantly from the p-TM polarized triplet states of xanthene dyes ($^3Xn^{2-}$) because of the fast ISC. By measurements of the intrinsic enhancement factor in different alcohols (methanol to 1-butanol) and in the temperature range from 259 K to 298 K the dependence on the viscosity of the solvent has been determined, and compared with analytical expression derived by Serebrennikov *et al.*[49] From this comparison the ZFS parameters of the triplet exciplex were determined. The results presented clarify that the heavy atoms significantly affect the D value of the triplet exciplex as well as the sublevel selective ISC rates.

Net absorptive CIDEP spectra observed in the photoinduced hydrogen abstraction reaction of chromone (CR) and chromone-2-carboxylic acid (CRCA) from 2-propanol with addition of HCl were investigated with FT-EPR by Ohara *et al.*[50] The FT-EPR spectra of CR and CRCA in pure 2-propanol show E/A polarization for CR and E*/A polarization for CRCA due to the S_0T radical pair mechanism with a small contribution of triplet mechanism for CRCA. By addition of HCl to the solution the FT-EPR spectra change to E/A*. This increase of the net absorptive polarization with the increase of HCl concentration is explained by a change of the primary step of CR and CRCA triplet deactivation. Whereas in pure 2-propanol a direct hydrogen abstraction reaction by CR and CRCA from 2-propanol deactivates the triplet, in solutions containing HCl the chloride anion is the electron-donating species to generate CR and CRCA anion radicals. This process is much faster than the direct hydrogen abstraction reaction, and the 2-hydroxy-2-propyl radicals are generated by hydrogen abstraction from 2-propanol by chloride radical Cl$^{\bullet}$.

2.2.3 Photoreduction of aromatic nitro compounds. The photoreduction of aromatic nitro compounds by alcohols is a well-known reaction, but the primary reaction step is still discussed controversial. Using laser photolysis TR EPR experiments of nitrobenzene, 5-nitrouracil, *p*-nitroacetophenone, and *o*-propylnitrobenzene in ethylene glycol the primary radical species were characterized as *N*-hydroxy-arylnitroxide radical (ArNO$^{\bullet}$OH), whereas for 2-nitroresorcinol the radical anion ArNO$^{\bullet}$O$^-$ was detected.[51] These observations indicate that hydrogen abstraction and electron transfer are competing in the photoreduction mechanism of aromatic nitro compounds.

2.3 Photooxidation

2.3.1 Amino acids. The damage of amino acids, peptides, and proteins caused by oxidative processes attracts the attention of scientists in many research branches as those substances are of vital concern for every living organism. Especially, modifications of biological molecules induced by various reactive oxidative species are of significance.[52] Recent investigations of the simplest model systems as aliphatic amino acids in aqueous solutions have revealed that the mechanisms of such processes are more complicated then anticipated earlier.[53–57] At this point TR EPR studies can be very helpful to get more detailed information about the structure of intermediate species and their reactivity.

Using TR EPR and transient optical spectroscopy, the photooxidation of glycine, α-alanine, α-aminoisobutyric acid, and model compounds β-alanine, methylamine and sodium acetate, by excited triplets of anthraquinone-2,6-sulfonate dianion (2,6-AQDS^{2-}) has been studied in aqueous solutions in the pH range 5–13.[58] The 2,6-AQDS triplet is a strong one-electron oxidizing agent and is therefore efficiently quenched by many electron donors. Furthermore, the 2,6-AQDS triplet is strongly

spin-polarized by the triplet mechanism as shown in the following reaction scheme:

$$A_{S0} \xrightarrow{h\nu} A_{S1} \xrightarrow{ISC} A_T^* \xrightarrow{+D} \{A^{\bullet -*} \cdots D^{\bullet +*}\}$$
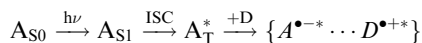
Here with * spin-polarized species are denoted. The primary radical ion pair $\{A^{\bullet -}* \ldots D^{\bullet +}*\}$ additionally generates radical pair polarization with E/A pattern, which is mainly detected in the successor radicals of $D^{\bullet +}*$. Considering the amino acids as electron donors there are two sites for electron transfer from amino acids to the 2,6-AQDS triplet, the amino group $-NH_2$ and/or $-COO^-$, depending on the pH with different protonation state. As an example, the FT-EPR spectra with β-alanine at pH 6.9 and pH 13 are shown in Fig. 4 and 5.

The assignment of the spectra to the radicals $^+NH_3-CH_2-C^{\bullet}H_2$ (pH 6.9) and $^{\bullet}NH-(CH_2)_2-COO^-$ (pH 13) is confirmed by a simulation procedure,[59] where $^+NH_3-CH_2-C^{\bullet}H_2$ is a successor radical, generated by decarboxylation of the primary radical $^+NH_3-CH_2-CH_2-COO^{\bullet}$. The reaction scheme of the different generation mechanisms is depicted in Scheme 3 (reproduced with permission of ref. 58).

The same FT EPR experiments were carried out with glycine, α-alanine, α-aminoisobutyric acid and different amines. Some of the results for the radical structures (*hfs* constants) are presented in Table 1 (reproduced with permission of ref. 58).

With quantitative analysis of the TR EPR time profiles of the radicals observed, and under consideration of the relaxation of spin polarization and the chemical kinetics, the polarization factor and relaxation times T_1 of the radicals have been determined. The quenching rate constants of the 2,6-AQDS triplet by the different donors have been independently measured by transient optical spectroscopy. These results allow the authors to formulate a complete reaction scheme, like in Scheme 3, for all amino acids and amines used in this study.[58,59]

The photooxidation of glycine esters by photoinduced electron transfer to 2,6-AQDS triplet in aqueous solution was investigated by FT EPR.[60] By substitution of the carboxylic group by an ester group the decarboxylation reaction of intermediate radicals can be suppressed, and other reaction channels can be opened. In the pH range 9 to 10, aminyl radicals $^{\bullet}NH-CH_2-CO_2R$, glycyl radical $NH_2-^{\bullet}CH-CO_2R$ and the radical $^{\bullet}CH_2-CO_2R$ have been detected. Fig. 6 shows a low field part of the
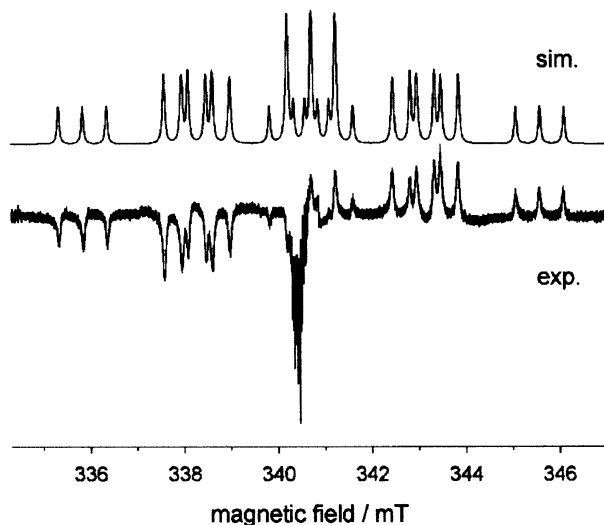
Fig. 4 Experimental and simulated FT EPR spectra of the radical $NH_2-CH_2-^{\bullet}CH_2$ (pH 6.9). Reproduced with permission of ref. 58.
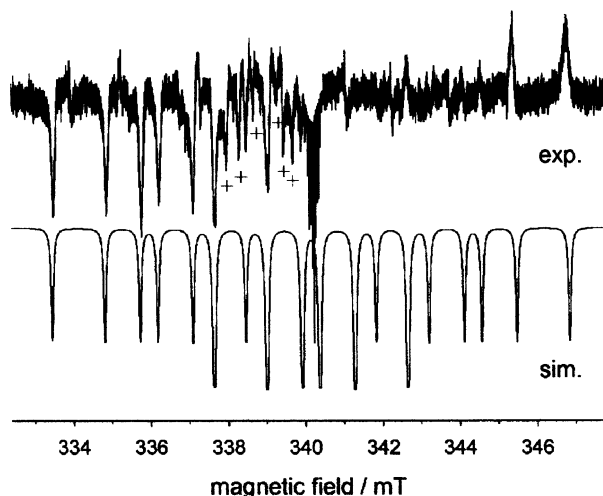
Fig. 5 Experimental and simulated FT EPR spectra of the radical $^\bullet NH–(CH_2)_2–CO2^-$ (pH 13). Reproduced with permission of ref. 58.
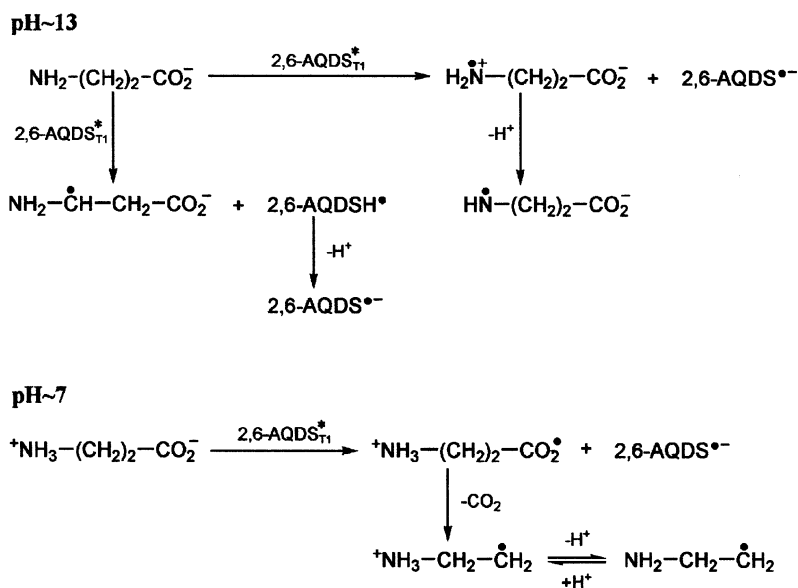
Scheme 3 Reproduced with permission of ref. 58.

FT EPR spectrum where glycyl radicals can be observed as a superposition of two very similar radical structures. These two subspectra are assigned to the (Z)- and (E)-isomeric structures of the glycyl radical $NH_2–^\bullet CH–CO_2CH_3$.

Similar results are obtained for glycine ethyl ester. The simulation of the well resolved FT EPR spectra measured in H_2O and D_2O allows the assignment of the *hfs* coupling constants to all coupling nuclei. The assignment was supported by quantum chemical calculations by DFT methods. The radical $^\bullet CH_2–CO_2R$, as a minor product in these experiments, is generated by a deamination reaction caused

Table 1 Hyperfine coupling constants A (in mT) and g-factors for the radicals derived from amino acids. In parenthesis the number of equivalent protons is shown. Reproduced with permission of ref. 58

Donor	Radical	$A(N)$/mT	$A(H\text{–}N)$/mT	$A(H\text{–}C)$/mT	$A(CH_3)$	g value
Gly⁻	$NH_2\text{–}{}^\bullet CH_2$	0.500	0.448 (2)	1.518 (2)	—	2.00289
	$NH_2\text{–}{}^\bullet CH\text{–}CO_2{}^-$	0.610	0.339; 0.290	1.369	—	2.00347
Ala⁻	$NH_2\text{–}{}^\bullet C(CH_3)H$	0.325	0.645 (2)	1.466	2.105 (3)	2.00300
	$NH_2\text{–}{}^\bullet C(CH_3)\text{–}CO_2{}^-$	0.507	0.193; <0.02	—	1.386 (3)	2.00334
Ala±	${}^+NH_3\text{–}{}^\bullet C(CH_3)H$	0.33	1.75 (3)	2.27	2.67 (3)	2.00251
	${}^+ND_3\text{–}{}^\bullet C(CH_3)H$	0.329	0.265 (3)	2.27	2.68 (3)	2.00273
α-MeAla⁻	$NH_2\text{–}{}^\bullet C(CH_3)_2$	0.130	0.599 (2)	—	1.879 (6)	2.00295
α-MeAla±	${}^+NH_3\text{–}{}^\bullet C(CH_3)_2$	0.286	1.59 (3)	—	2.43 (6)	2.00271
β-Ala⁻	${}^\bullet NH\text{–}(CH_2)_2\text{–}CO_2{}^-$	1.367	2.28	4.17 (1β) 4.22 (1β)	—	2.0044
β-Ala±	${}^+NH_3/NH_2\text{–}CH_2\text{–}{}^\bullet CH_2$	0.514	n.d.	2.249 (2α) 2.625 (2β)	—	2.00263

α-MeAla = α-Aminoisobutyric acid; n.d. = not determined.
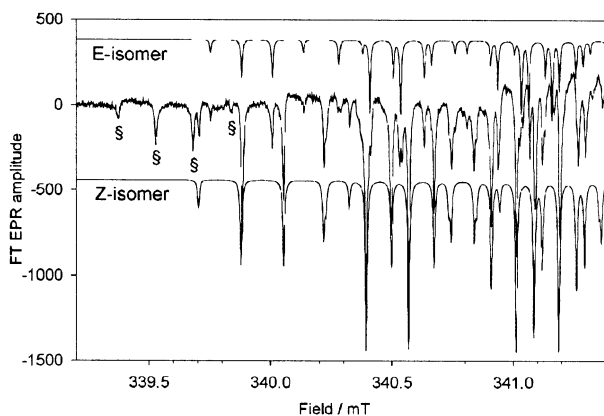
Fig. 6 Low field part of the FT EPR spectra of the glycyl radicals $NH_2\text{–}{}^\bullet CH\text{–}CO_2CH_3$ in H_2O in comparison with the simulated spectra for (Z) and (E) isomers. The lines indicated by § belong to the radical ${}^\bullet CH_2\text{–}CO_2CH_3$. Reproduced with permission of ref. 60.

by hydrated electrons which are produced by a two photon ionization of 2,6-AQDS.[61]

The L-methionine radical cation and its N-acetyl derivative have been studied in aqueous solution by TR EPR in X- and Q-band by Forbes et al.[62] The oxidation of methionine was intensively investigated by pulse radiolysis experiments with transient optical spectroscopy by the groups of Naito,[63] Asmus,[64] and Bobrowski.[65,66] These optical experiments provide evidence for dimeric structures containing S–S three electron bonds as well as neighbouring group effects with heteroatoms such as nitrogen and oxygen. Such neighbouring group effects led these researchers to postulate six- and five-membered ring intermediates with S–O and S–N three-electron bonds. In the paper by Forbes et al.,[62] these radical structures were for the first time detected by cw TR EPR techniques in which the primary radical cation was produced by photooxidation with anthraquinone sulfonate sodium salt (AQS) triplets. At low pH (below 9) the structure has been assigned to a dimer radical cation (5b in Scheme 4) due to the well resolved –CH₂– and –CH₃ groups adjacent to

Scheme 4 Reproduced with permission of ref. 62.
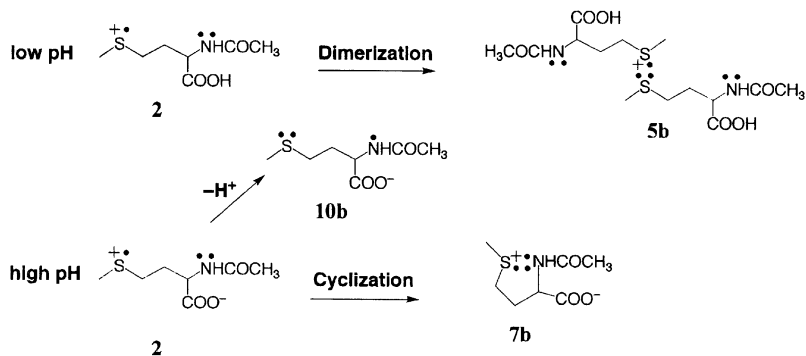
the S-S three electron centre of *N*-acetyl methionine. At high pH (higher pH 11) a five-membered ring structure was identified by resolution of the *hfs* coupling with all *hfs*-active nuclei in the ring. Remarkable in these results is the very small coupling constant of the nitrogen nucleus in the three-electron bond of the ring. The structure of the radicals detected is presented in Scheme 4 (reproduced with permission of ref. 62).

Furthermore, the comparison of the CIDEP behaviour (superposition of TM and RPM polarization with different contributions at the different magnetic field values) in the X- and the Q-band confirms the mechanism of photooxidation by anthra-quinone sulfonate triplets.

The direct observation of peroxyl radicals has been reported by Forbes *et al.*[67,68] By UV photolysis of hydrogen peroxide in oxygenated aqueous solutions of *N*-acetyl glycine, serine, and diglycine the peroxyl radicals were detected by TR EPR spectroscopy. The peroxyl radicals are characterized by a single line with *g*-factor 2.01300, and show CIDEP effects with polarization strength from the originally created substrate radicals (compare Fig. 7). These experiments provide a new field for the study of an important class of reactive intermediates in the oxidation chemistry of peptides and proteins under physiological conditions.

The selenocysteinyl radical has been generated by laser flash photolysis (266 nm, 355 nm) of dimethyl bis(*N-tert*-butoxycarbonyl)-L-selenocysteine and of [(9-fluorenylideneamino-oxocarbonyl]methyl(*N-tert*-butoxycarbonyl)-L-selenocysteine
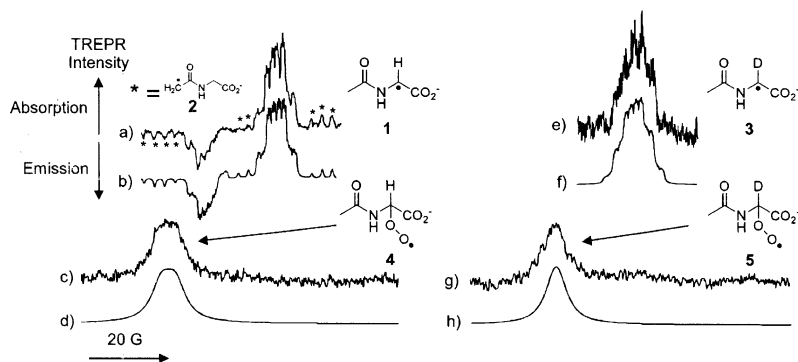
Fig. 7 TR EPR spectra taken upon 248 nm laser irradiation (1 μs delay) of aqueous solution (pH 5.5) of 0.8 M H_2O_2 and 0.4 M *N*-acetyl glycine in (a) deoxygenated and (c) oxygenated solutions with respective simulations (b) and (d) and of 0.1 M *N*-acetyl glycine-d$_2$-solution in (e) deoxygenated and (g) oxygenated solutions with respective simulations (f) and (h). Reproduced with permission of ref. 67.

(9-FMBSeC) in acetonitrile and characterized by time-resolved UV/Vis, Fourier transform infrared spectroscopy and TR EPR.[69,70] Laser photolysis of 9-FMBSeC with TR EPR detection showed a 1:1:1 triplet which evolves during the laser pulse and reaches maximum intensity after 220 ns. The spectrum is assigned to the 9-fluoreno-neiminyl radical. The results of TR EPR reveal that after laser irradiation with 355 nm 9-FMBSeC is cleaved into carbon dioxide, the selenocysteinyl radical and the 9-fluorenoneiminyl radical.

2.3.2 Diglycine. In extension to the studies with amino acids TR EPR experiments upon photooxidation of glycylglycine induced by triplet-sensitized electron transfer to 2,6-AQDS in aqueous solution at pH 6–10 has been carried out.[71] The main aim of this study was to examine the role of the peptide functional group, –CONH–, as a possible additional site for an oxidative attack. Transfer of an electron from gly–gly in anionic form could thereby occur from all three functional groups (NH_2–, –CONH–, and COO^-). Oxidative attack at the amino group leads to the formation of N-centered aminyl radicals which have been identified by their FT EPR spectrum. Parallel to this process a formation of the decarboxylated radical $^+NH_3/NH_2$–CH_2–$CONH$–$^\bullet CH_2$ occur. Their formation mechanism can be associated with the electron transfer from the one or from both other functional groups to the 2,6-AQDS triplet. The resulting
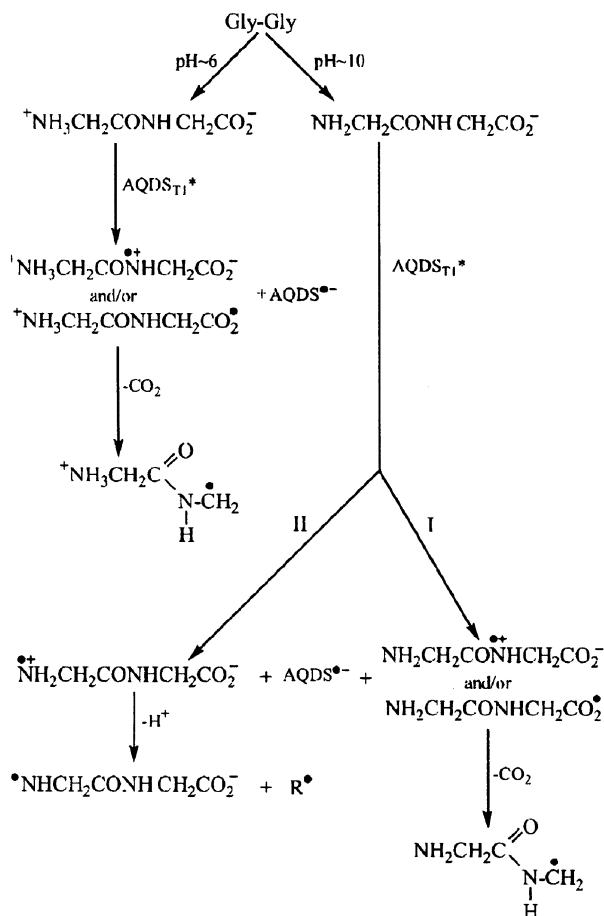
Scheme 5 Reproduced with permission of ref. 71.

primary radical species could not be experimentally observed because of the very fast CO_2 elimination and transformation into $^+NH_3/NH_2$–CH_2–$CONH$–$^•CH_2$ radicals. The later were the only products observed upon photooxidation of gly–gly in its zwitterionic form. Radicals produced by the oxidation of the peptide functional group were not observed. The reaction mechanisms proposed from the FT EPR experiments in the acid and basic pH range are shown in Scheme 5 (reproduced with permission of ref. 71).

A direct hydrogen abstraction from the –CH_2– group in the photooxidation of cyclic dipeptides glycine, alanine, and sarcosine anhydrides initiated by $SO_4^{•-}$ or 2,6-AQDS triplet in oxygen free aqueous solutions has been observed.[72] Using transient optical spectroscopy the per $^\alpha$C-H bond second order rate constants have been determined to be about two times higher for the reaction with $SO_4^{•-}$ than with 2,6-AQDS triplet for all three anhydrides. By TR EPR piperazine-2,5-dione-3-yl type radicals are detected for all three anhydrides as the first observed transient. Therefore, a direct hydrogen atom abstraction from the anhydride $^\alpha$C–H position is proposed as the most likely reaction mechanism. The number of lines observed in the FT EPR spectra of cyclic peptide radicals reveals a high delocalization of the unpaired electron within the radicals. The polarization patterns of the FT EPR spectra are discussed in detail in the paper.[72]

The photooxidation of diglycine in confined media has been studied by Forbes *et al.*[73,74] The main results of these papers are related to the relaxation of longitudinal magnetization in spin-correlated radical pair. Three types of longitudinal relaxation are observed, the relaxation in spin-correlated radical pairs, the relaxation in uncorrelated pairs, and the ordinary longitudinal relaxation in non-interacting radicals.

2.3.3 Biological applications. TR EPR spectroscopy has been used to study melanin free radicals in human retinal pigment epithelium cells and tyrosine-derived synthetic melanin.[75,76] The TR EPR spectra allow detailed insights into *in vivo* light-induced melanin free radical photochemistry and the mechanism of photoprotection in human retinal pigment epithelium cells.

Proteins and enzymes catalyse chemical reactions at their active regions in biological systems. Considerable interests have been directed to biological functions of protein dynamics and protein-surface interactions. Using cw TR EPR the photoinduced proton-coupled electron transfer has been observed between 2,6-AQDS and the amino acid residue of tryptophan in human serum albumin.[77] CIDEP spectra show that the photoinduced electron transfer takes place from the specific tryptophan residue to the excited triplet state of 2,6-AQDS.

The photoinduced homolytic bond cleavage of the Co–C bond in methyl- and 5′-adenosyl-cobalamine (B_{12} coenzyme) and methyl(4-*t*-butyl-pyridyl)cobalamine has been studied by FT TR EPR.[78] The CIDEP spectra of the methyl radicals observed are accounted for the Co–CH_3 bond cleavage *via* a singlet excited state of the cobalamines.

2.4 Homolytic bond scission

2.4.1 Azo compounds. Azo compounds such as 2,2′-azobisisobutyronitrile (AIBN) are widely used as polymerization initiators.[79,80] Upon UV excitation AIBN decomposes into a nitrogen molecule and a geminate pair of two 2-cyano-2-propyl radicals[81,82]

$$\text{AIBN} \xrightarrow{h\nu} N_2 + 2(CH_3)_2C^•CN$$
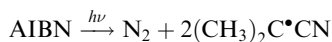
The cleavage occurs from an excited singlet state and therefore, a considerable fraction of the geminate (G-) pairs decays rapidly by radical termination to form 'in-cage' recombination and disproportionation products. Those species that escape the geminate cage diffuse apart and form F-pairs after random free-diffusive

encounters. The radicals in the G- and F-pairs develop radical pair polarization (RPM). The ratio of both polarizations, P_F/P_G has been found[81] to have a sensitive dependence on essentially only the initial spatial separation of the two radicals in the spin-correlated pairs. The ratio P_F/P_G determined experimentally by photolysis of AIBN in liquid solutions of different viscosity reflects a certain viscosity dependence on the initial separation of the two 2-cyanoprop-2-yl radicals in the geminate pair. The paper[82] compares the experimental results of P_F/P_G with a primary caging model for nonpolar (azocumene) and polar 2-cyanoprop-2-yl radicals in dependence on viscosity.

The triplet-sensitized photo-decomposition of azocumene into nitrogen and cumyl radicals has been investigated by TR EPR and optical spectroscopy.[83] The cumyl radicals observed carry an initial spin polarization and are formed with a yield which depends on both the solvent viscosity and the strength of the external magnetic field. This phenomenon is interpreted in terms of a depopulation-type triplet mechanism, *i.e.* competition between decay into radicals and fast triplet sub-level intersystem crossing[33,84] back to the azocumene ground state. The energetically lower zero field triplet substate is depopulated by ISC about seven times faster than the upper one and about two orders of magnitude faster than depopulation by cleavage occurs.[83]

2.4.2 Phosphine oxide. Phosphinoyl radicals have been investigated in benzene solution of three acylphosphine oxide photoinitiators, diphenyl-2,4,6-trimethyl-benzoyl phosphine oxide, bis(2,6-dimethoxybenzoyl)-(2,4,4-trimethylpentyl) phosphine oxide, and bis(2,4,6-trimethylbenzoyl) phenylphosphine oxide by TR EPR at four different microwave frequencies.[85] The CIDEP pattern shows strong spin polarization generated by the triplet mechanism as well as by ST_0 and ST_{-1} radical pair mechanism. The polarization patterns change in dependence on the microwave frequency and were analyzed by TR EPR at both low and high microwave frequencies, covering S-(2.8 GHz), X-(9.7 GHz), Q-(34.8 GHz), and W-(95 GHz) bands. The TM polarization dependence on microwave frequency was determined in absolute units and explained quantitatively by a numerical solution of the stochastic Liouville equation (SLE) following the Pedersen and Freed approach.[10,86] The agreement between experimental results and the SLE solution gives quantitative proof for the correctness of the theoretical model for the TM polarization.

2.4.3 ω-Bond dissociation of aromatic ketones. Photodissociation of the carbon–sulfur bond in *p*-mercaptomethylbenzophenone (MMBP) in acetonitrile has been investigated by means of steady-state photolysis, TR EPR and laser photolysis techniques.[87] MMBP undergoes photodecomposition to yield *p*-methylbenzophenone in acetonitrile at room temperature. The initial intermediate due to photodecomposition of MMBP is revealed to be the *p*-benzoylbenzyl radical from transient optical absorption and from CIDEP measurements. The net emissive CIDEP spectrum of the *p*-benzoylbenzyl radical due to the triplet mechanism clearly suggests that the free radicals obtained in the transient optical absorption upon laser photolysis of MMBP are generated in the triplet state of MMBP. In additional papers[88–90] the photoinduced ω-bond dissociation of *p*-halomethylbenzophenones and *p*-benzoylbenzyl phenyl sulfite has been studied by laser photolysis with transient optical spectroscopy, TR EPR, and theoretical DFT calculations.

2.4.4 Photocleavage. The reaction and spin dynamics of the photocleavage reaction of 2-chloro-2'-acetylnaphthalene[91] and bromoacetylnaphthalene[92] have been studied by time-resolved FT EPR and transient optical spectroscopy. The advantage of such systems is that the compounds generate organic radicals easily by unimolecular photoreactions, because the energy of the excited state is large enough for dissociation of the C–X (X = Cl, Br) bond. Therefore, both singlet and triplet precursors can be expected from photocleavage reactions. The analysis of the
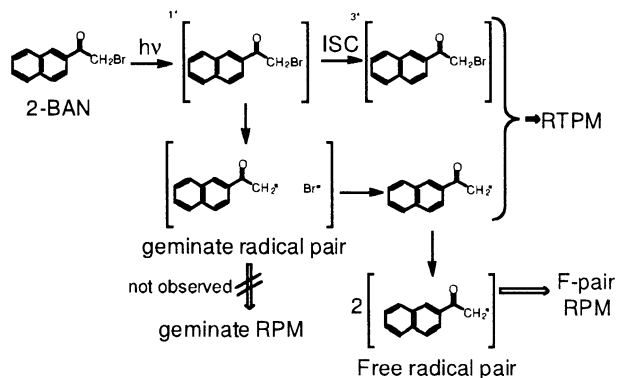
Scheme 6 Reproduced with permission of ref. 92.

intensity behaviour of the three *hfs* lines of the naphthoyl–methyl radical indicates no polarization from the geminate singlet radical pair, because of the large SOC of the Cl or Br atoms, but a strong net emissive contribution from the radical triplet pair mechanism. The reaction scheme proposed is presented in Scheme 6 (reproduced with permission of ref. 92). The primary photocleavage reaction occurs from the singlet precursor in competition with the ISC to the triplet state. The lifetime of the triplet state was estimated to be 1.5 μs.

2.5 Addition reactions to double bonds

2.5.1 Radical addition to alkenes. The addition of carbon-centred radicals and phosphinoyl radicals to alkenes and other unsaturated compounds is one of the main reaction steps in generating polymeric compounds, and in organic synthesis reactions. The investigation of this important chemical reaction type by EPR spectroscopy started long ago, and has been extensively reviewed[93–95] (see also the review[1] in a previous contribution of this series).

The addition of diphenyl phosphinoyl radical and 2-hydroxy-2-propyl radical to bifunctional alkene and vinyl acrylate has been investigated by both TR EPR, steady-state (SS) EPR, and laser flash photolysis.[96] The structures of the adduct radicals detected are shown in Scheme 7 (reproduced with permission of ref. 96, see also Scheme 9). The radicals are generated efficiently and under controlled conditions by photolytic α-cleavage of the used photoinitiators. The strong spin polarization of the primary photoinitiator radical assures spin-polarized adduct radicals which can be detected by cw TR EPR with a high signal-to-noise ratio. The *hfs* coupling constants have been determined with high precision by cw TR EPR, and the comparison with the results of SS EPR shows a good agreement.

In the cw TR EPR spectrum of the acrylate adduct **6b** some of the lines are broadened by an internal dynamic process. This behaviour is a feature of a dynamic two-site exchange process which can be described by a two-site jump model.[97] In the adduct radical, **6b**, the phosphorus moiety interacts with the carbonyl bond of the acrylate when these two groups find themselves in proximity of each other. This proximity results in a steric interaction which leads to two preferred possible geometric configurations or two sites of phosphinoyl *vs.* acrylate group which are presented in the following Newman projections of the two conformations A and B (Scheme 8, reproduced with permission of ref. 96). The absolute rate constants for radical addition to alkenes have been directly measured by laser flash photolysis with optical detection. The rate constants obtained are in the order of 10^7 M^{-1} s^{-1} in good agreement with previous results.[98]

A novel approach for measuring absolute rate constant of radical addition reactions by pulsed FT EPR has been introduced by Weber and Turro.[99] By
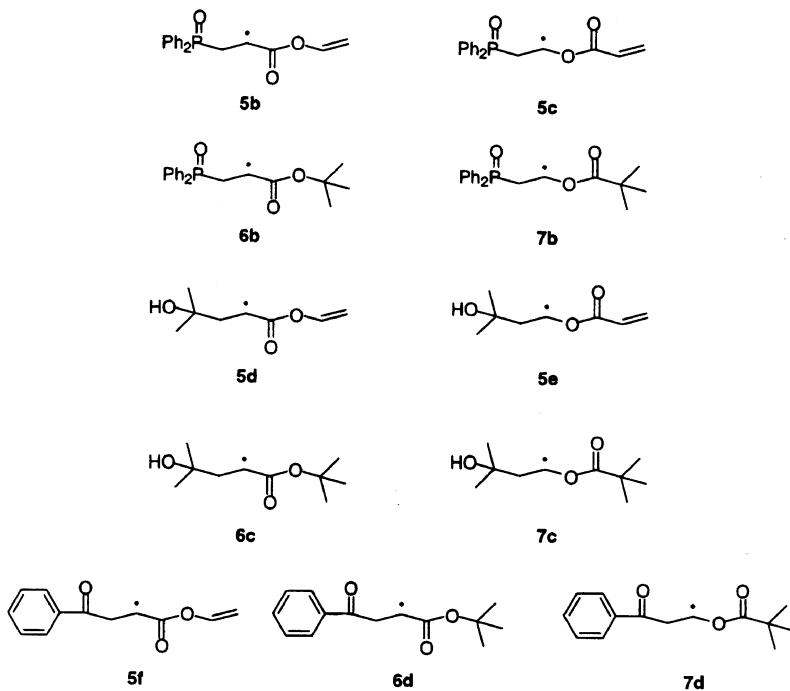
Scheme 7 Reproduced with permission of ref. 96.

measurements of the phase memory times T_M using electron spin–echo experiments the rate constants of radical addition reactions of phosphinoyl and 2-hydroxy-2-propyl radicals to several alkenes can be extracted from the linear relationship between the reciprocal of the T_M values and the alkene concentration. This novel approach to determine rate constants is an extension of the line width analysis method introduced by Gatlik et al.[98] where the linear relationship between $1/T_2^*$ and the quencher concentration, is given by

$$1/T_2^* = 1/T_{20}^* + k_{add} [A].$$

T_{20}^* is the quencher-independent relaxation time, k_{add} is the rate constant of addition reaction and [A] is the quencher concentration. The TR ESE technique has several advantages compared to cw TR EPR, such as higher precision, lower influence by instrumental artefacts, and the use of lower scavenger concentrations. The new method allows the determination of absolute rate constants over several orders of magnitude up to the diffusion-controlled region (10^9 M^{-1} s^{-1}). To demonstrate the performance of the TR ESE method several reaction systems as shown in Scheme 9 (reproduced with permission of ref. 99) have been used.

The results obtained with phosphinoyl and 2-hydroxy-2-propyl radicals and the different alkenes shown in Scheme 9 are in good agreement with earlier data.[98] These results demonstrate that the new ESE method to determine rate constants compete with the transient optical spectroscopic method.

Using cw TR EPR in X- and W-band the addition reaction of benzoyl radicals to butyl acrylate in toluene solutions has been investigated by Gescheidt et al.,[100,101] where acylphosphinoxide and different α-aminoketones were used as photoinitiators. By line width analysis of the single line EPR spectrum of the benzoyl radical with a Gaussian function a linear relationship for butyl acrylate concentrations <1.25 M was found, and the addition rates were determined from the slope of this linear relationship. This linear relationship is broken at acrylate concentration

5b, 5c, 6b, 7b   A   B
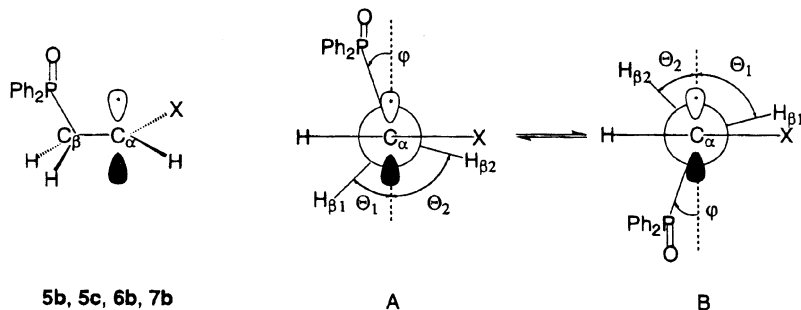
Scheme 8   Reproduced with permission of ref. 96.
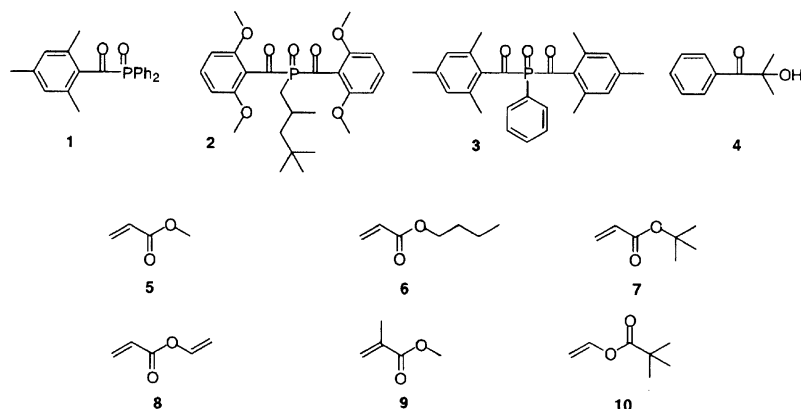
Scheme 9   Reproduced with permission of ref. 99.

>1.25 M which is caused by a strong increase of the viscosity of solutions with high acrylate concentrations. The rate constants of acrylate concentration with different benzoyl radicals used differ slightly, and are discussed by structure-reactivity considerations supported by quantum chemical calculations of the activation barriers. The rate constant of acrylate addition reaction at high concentrations (>1.25 M) is reduced by ~1 order of magnitude in comparison to lower concentrations.

2.5.2   Polymerization kinetics. The application of EPR spectroscopy to polymer research has a long tradition[102] and is reviewed in a previous contribution in this series.[1] The history of application of EPR spectroscopy in research of polymerization processes has been recently reviewed.[103] The steady-state EPR spectra of the propagating radicals from vinyl monomers, methacrylates, styrene, butadiene and dienes, respectively, are discussed. TR EPR measurements of the benzoyl radical and the phosphinoyl radical are also presented including the initiation rate constants for different monomers.

The photoinitiation of polymerization of isobornyl acrylate has been studied by magnetic field effects and TR EPR.[104] A small magnetic field effect on the conversion of monomers was found for vinylacetate, *n*-butylacrylate and methyl methacrylate. Time-resolved EPR spectra are presented for the phosphinoyl radical, the benzoyl radical, and the monomer radical of isobornyl radical where the isobornyl radical spectrum shows a spin polarization transfer from the phosphinoyl radical.
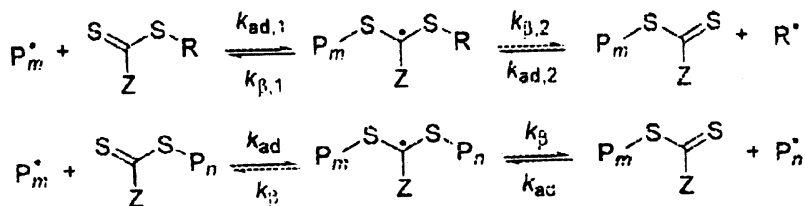
Scheme 10 Reproduced with permission of ref. 109.

The development of more effective photoresists is of great commercial interest. α-aminoalkylphenones are the most recent type of α-cleavage photoinitiators commercially available, which are being widely applied to photoinduced radical polymerization such as photoresists. Introduction of the thiol group drastically improve photosensitivity in alkaline developable resist formulation composed of a prepolymer and a multifunctional acrylate monomer. Steady-state EPR measurements, spin trapping experiments, and TR EPR with laser photolysis with different α-aminoalkylphenones have been reported.[105] The TR EPR spectra of different α-aminoalkylphenones are assigned to benzoyl radicals, and their time profiles are influenced by different thiol substituents depending on available hydrogen atoms from the thiol moiety. The mechanisms of hydrogen abstraction and radical chain transfer reaction are discussed in detail.

Reversible addition fragmentation chain transfer (RAFT) polymerization[106] has developed into a important method for generating polymeric materials with controlled molecular weights and complex molecular architectures. RAFT polymerization proceeds *via* a degenerative chain transfer mechanism in which the two following equilibria are superimposed on a conventional radical polymerization scheme (Scheme 10, reproduced with permission of ref. 109).

Steady-state TR EPR in the millisecond to second range with a single laser pulse excitation has been used to measure the kinetic parameters k_{ad}, k_β, and k_{term} for the BMPT-mediated polymerization of butyl acrylate and dodecyl methacrylate. (BMPT = S-S'-bis(methyl-2-propionate)-trithiocarbonate).[107–110]

2.5.3 Photodegradation of polymers. Another point of interest in polymer research is the photodegradation in the area of lithographic photoresists. The development of more robust coatings and their controlled degradation both rely on a detailed understanding of the degradation mechanism. Using TR EPR main chain radicals from acrylic polymers have been studied in the group of Forbes.[111–113] By laser photolysis (248 nm) of liquid solutions of acrylic polymers at ~100 °C and in a flowing sample system the main chain radicals were generated, and detected in the μs time scale. The radicals are produced by laser photolysis excitation of the carbonyl group *via* the triplet state, and subsequent loss of the side chain functionality by Norrish I α-cleavage. In the investigation are included poly(methyl methacrylate), poly(ethyl acrylate), poly(ethyl methacrylate), poly(methyl d₃-methacrylate), poly(fluorooctyl methacrylate), and poly(ethyl cyanoacrylate). In all polymers studied the main chain radicals and oxo-acyl radicals were detected, and at the temperatures used fast-motion spectra with conformationally averaged hyperfine interactions were observed. The influence of tacticity of the polymer chain, of solvent used, and of the side-group structure on the chain stiffness is discussed in detail. Additional TR EPR experiments on small molecule model compounds and gel permeation chromatography results of the photolyzed polymers support the conclusion that the primary photodegradation mechanism proposed is general for acrylic polymers.

TR EPR has been used to investigate the effect of pH-dependent poly(methacrylic acid) clustering on the radical pair generated from photolysis of a poly(methacrylic acid) acid sample randomly labelled with an α-hydroxy-ketone photoinitiator.[114]

The TR EPR spectra for the ketyl radical show a dramatic change in spin polarization, from a predominantly triplet mechanism at low pH (below 6) to predominantly radical pair mechanism at high pH (above 7). The change in spin polarization mechanism as a function of pH agrees well with poly(methacrylic acid) cluster opening as studied by other methods.

2.6 CIDEP studies

2.6.1 CIDEP theory. The theoretical description of the spin polarization effects like CIDNP and CIDEP, respectively, has been well established.[10,11,84] The investigation of the interactions in radical ion pairs and pairs of neutral radicals which are important in the generation of spin-polarized transients started with the discovery of the CIDNP and CIDEP effects.[115–120] Many excellent reviews of the theory of CIDNP and CIDEP effects have been published in the past.[10–12,34,84] Therefore, only a few recent publications dealing with new developments in the CIDEP theory and in the field of radical pair interactions are summarized here.

The Green's function calculation[121–125] for multistate Schrödinger-type equation has been applied to study theoretically magnetic field effects in radical pair recombination in the presence of an interaction potential.[126] Analytical formulas for CIDEP amplitudes are derived with the use of the sudden perturbation approximation, properly treating the effect of the spin exchange interaction, and two approaches, the cage and interpolation ones, which allow for an accurate description of diffusive motion of radicals in the potential. The accuracy of these two approaches and specific features of CIDEP generation in the presence of the interaction potential are discussed in detail.

The triplet radical quenching is a very important spin selective process in liquids that is influenced by the magnetic field. Shushin[127] has developed a fast and slow approximation for the description of the kinetics of triplet radical quenching and the kinetics of generation electron spin polarization.

The dynamics of photochemical reactions showing CIDEP effects are described by a set of kinetic equations that include all relevant parameters, including reaction of the excited precursor as both a singlet and a triplet and spin exchange during radical encounter (see Scheme 11, reproduced with permission of ref. 128). These kinetic equations are solved by analytical expressions, and used to analyse the CIDEP spectra obtained in the photolysis of the acetone/2-propanol system. By systematic least-squares fitting procedure of the experimental results from Levstein *et al.*[129] and Ohara *et al.*[130] all parameters of the kinetic model were determined with an excellent agreement between the experimental time profiles of the FT EPR spectra and the simulated signal intensities.

In a recent review[131] the various mechanisms for magnetic field effects (MFE) and CIDEP due to the d-type triplet mechanism are summarized. CIDEP and MFE's due to the d-type TM can be observed only if the $T_1 \rightarrow S_0$ intersystem crossing can compete with both radical escape and spin relaxation between the triplet sublevels, such as $T_1 \rightarrow S_0$ ISC with rates above $10^9 \ s^{-1}$ are satisfied only in rare cases. On the

$$P \xrightarrow{h\nu} {}^1P* \begin{cases} +S \xrightarrow{{}^1k} {}^1\overline{R^\bullet_M \ R^\bullet_{M'}} \rightarrow R^\bullet_M ... R^\bullet_{M'} \\ \xrightarrow{k_{isc}} {}^3P* + S \xrightarrow{{}^3k} {}^3\overline{R^\bullet_M \ R^\bullet_{M'}} \rightarrow R^\bullet_M ... R^\bullet_{M'} \end{cases}$$

$$R^\bullet_{\beta/\alpha,M} + R^\bullet_{\alpha/\beta,M'} \xrightarrow{k_{ex}} R^\bullet_{\alpha/\beta,M} + R^\bullet_{\beta/\alpha,M'} \text{ (spin exchange)}$$

$$R^\bullet_{\beta/\alpha,M} + R^\bullet_{\alpha/\beta,M'} \xrightarrow{k_c} \begin{cases} products \\ F\overline{R^\bullet_M \ R^\bullet_{M'}} \rightarrow R^\bullet_M ... R^\bullet_{M'} \end{cases}$$
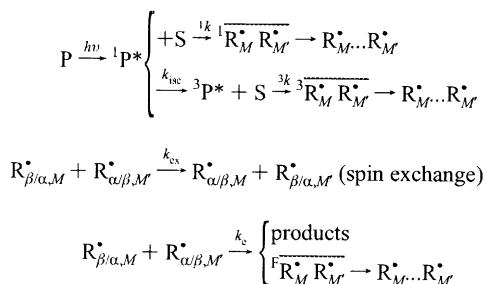
Scheme 11 Reproduced with permission of ref. 128.

other hand, Pauls's group and that of the authors have recently found CIDEP and MFE's due to d-type TM for intramolecular reaction from photo-excited triplet states of azoalkanes[83,132] and triarylphosphines,[85] respectively, irrespective of solvent polarity. These studies have extended the research field of the d-type TM from the very limited reactions through triplet exciplexes to more general intra-molecular ones of triplet molecules.
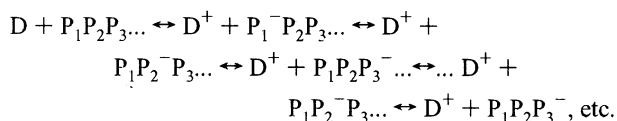
A quantitative theoretical treatment that combines the time-integrated solution of the stochastic Liouville equations for precursor triplet and triplet exciplex (p-type TM) with kinetic rate equation of the bimolecular quenching process (d-type TM) has been developed by Katsuki et al.[133] The equations derived allow the extraction of the two polarization enhancement factors, V_d for the pure d-type and V_{pd} for the combined p- and d-type triplet mechanism from the concentration dependence of the time dependent CIDEP signals. The theoretical equations are applied to the analysis of cw TR EPR and FT EPR results of semireduced thionine radicals produced by reacting thionine triplets with aniline and halogenated anilines.

A theoretical calculation of the exchange interaction, J, for radical–triplet encounter pairs has been carried out by considering exchange integral and intermolecular charge transfer interaction.[134] According to the calculated J value and the diffusion theory for CIDEP magnitude, experimental polarization values were theoretically reproduced as a function of ΔG. The results presented confirm the previous reported charge transfer model[135] explaining the complex nature of the sign of J values in radical–triplet pairs. The theoretical expressions were applied to the experimental CIDEP results of different galvinoxyl–triplet systems in benzene solutions.

Since the discovery of carbon nanotubes in 1991 these new materials have been attracting much attention for commercial application with exceptional electronic and mechanical properties, as well as for scientific interest as one-dimensional nanoreactors with well-defined geometry. Using this peculiar feature two papers[136,137] have been published dealing with the theoretical calculation of transient CIDEP spectra of spin-correlated radical pairs in nanotubes. The simulation of CIDEP spectra of transient radical pairs in nanotubes were carried out by numerical solution of the stochastic Liouville equation for the density matrix of the radical pair. The Hamiltonian used in the calculation includes the Zeeman energy of both radicals, the exchange interaction, and the secular part of dipolar interaction of radical pair, respectively. The CIDEP spectra were calculated for oriented nanotubes with the angle θ between the magnetic field B_0 and the axis of nanotube as parameter, and for poly-oriented nanotubes. The dependence of the spectra on the strength of the exchange interaction, the dipolar coupling, and the one-dimensional diffusion coefficient is discussed.

The density vector method developed for CIDEP calculations[138,139] has been applied to study theoretically the electron spin polarization in simple molecular wires.[140] In photoconductive polymers a photoinduced radical ion pair $D^+P_n^-$ can be generated by UV irradiation, and a one-dimensional electron transfer along the polymer chain can be started, like in the following Scheme 12 (reproduced with permission of ref. 140).

Regarding the spin polarization in this system the magnetic environment of radical ion pair is changing with the forward and backward electron hopping process. Appling the density matrix vector theory the CIDEP spectra were calculated

$$D + P_1P_2P_3... \leftrightarrow D^+ + P_1^-P_2P_3... \leftrightarrow D^+ +$$
$$P_1P_2^-P_3... \leftrightarrow D^+ + P_1P_2P_3^-...\leftrightarrow... D^+ +$$
$$P_1P_2^-P_3... \leftrightarrow D^+ + P_1P_2P_3^-, \text{ etc.}$$

Scheme 12 Reproduced with permission of ref. 140.

for a different numbers of electron transfer steps. The results show an interesting change between net polarized and anti-phase polarized spectra in successive electron transfer steps.

Spin catalysis with spin triads[141] is an interesting method to study radical pair interactions. Net and multiplet CIDEP of the observer/catalyst spin generated in recombination of radical-biradical pairs have been theoretical investigated by Ivanov.[142] Analytical expressions for the observer spin CIDEP in high magnetic field and for the multiplet polarization in zero magnetic field were obtained. The results show that the observer spin methodology can be useful for probing magnetic interactions in short-lived spin triads.

The unambiguous determination of the parameter involved in TR EPR time profiles is often a difficult task. The TR EPR time profiles contain all information about chemical kinetics, spin polarization of the system, and relaxation times. This problem has been theoretically treated for transient EPR spectra with unresolved hyperfine structure by Makarov *et al.*[143] The method proposed is based on considering the magnetic field integral of the magnetization, instead of single lines of overlapping EPR transitions. For a radical system involving chemical kinetics, CIDEP, and spin relaxation, an analytical solution is found for the evolution of the integral magnetization in the Laplace domain. The formulae presented are suitable observables, which characterize the chemical kinetics, CIDEP, and electron spin relaxation of radical systems.

Magnetization transfer by chemical exchange, electron transfer, and secondary radical generation is a general phenomenon in radical reactions. An algorithm for the calculation of TR EPR time profiles by means of incorporation of a kinetic matrix into the Bloch equations has been proposed.[43] The utilized approach takes into account the complete set of hyperfine states of all involved species. Solutions for the linear differential equations are calculated numerically. The TR EPR spectra of *p*-benzoquinone are analysed in terms of magnetization transfer, and an excellent agreement between the experimental data and the computations is achieved.

2.6.2 CIDEP experiments on various systems.

Although the fundamental experimental and theoretical principles of the CIDEP effects are fully understood,[2,84,120] some detailed problems are still under investigation. Some of the newest papers concerning these problems are reviewed here shortly. Most of these papers deal with the question of how to obtain more detailed insights into the interactions in geminate radical pairs.

The dynamic behaviour of transient free radicals generated by laser photolysis (351 nm) of 2,2-dimethoxy-2-phenylacetophenone in ethylene glycol solutions have been studied by TR EPR at room temperature.[144] The formation and decay of the two spin-polarized radicals, 7,7-dimethoxy-benzyl and benzoyl radical, have been observed. The TR EPR spectra of both radicals exhibit strong CIDEP effects produced by TM and, to a much smaller extent, RPM ST_0 mechanism. The time dependencies of the TR EPR spectra at resonance and near resonance positions of close nearby nuclear spin states were described using Bloch equations with spin polarization, relaxation and the kinetics of first and second order reactions. The complete reaction scheme has been proposed.

CIDEP spectra of transient radicals generated by laser photolysis (248 nm) in solutions of melamine (2,4,6-triamino-s-triazine) in ethylene glycol have been studied by TR EPR.[145] The radicals $HO^\bullet CHCH_2OH$ and $^\bullet CH_2OH$ generated from ethylene glycol and an unresolved spectrum attributed to the melamine radical were observed. The electron spin polarization results from radical pair mechanism and additionally from a small part of triplet mechanism. In order to establish the possible structure of the melamine radical quantum chemical DFT calculations have been included.

The energy transfer from aromatic photo-excited triplet states to different azo compounds in liquid solutions has been investigated by Caffrey *et al.*[146] The CIDEP

spectra of the radicals generated deliver precise information about the spin physics and the mechanism of energy transfer. As sensitizers, benzophenone and naphthalene derivatives were used in the solvents methanol and benzene. The results are discussed in terms of Dexter and Förster mechanisms for energy transfer, the properties of the excited states, and the diffusive properties in the used solvents.

Inverted A/E CIDEP is observed for random encounters of radical pairs such as the phenoxyl radical together with either e_{aq}^- or the radical anion of benzoate.[147] Steady-state and TR EPR experiments were carried out to study the nature of F-pair CIDEP for a number of different radical pairs consisting of a phenoxyl radical together with radical anions of para-substituted benzoates, like 4-methyl-, 4-methoxy-, and 4-carboxy-benzoate. These pairs show inverted A/E polarization, where the phenoxyl radical and 4-formyl-benzoate system shows normal E/A polarization. The experimental results are discussed in terms of the electron transfer reaction within the radical pairs using the approach presented by Kobori et al.[135,148] The inverted CIDEP is clearly assigned to the change in the energy ordering of the radical pairs states so that the triplet states are lower.

Carbon-centred radicals which are generated by hydrogen abstraction or electron transfer show mostly a non-symmetric RPM CIDEP, so-called E/A* pattern. This effect was observed in the early days of TR EPR.[149–151] Recently this problem is again under discussion.[68,72,152] The most likely interpretation proposed in these papers is a superposition of a symmetrical polarized E/A spectrum with an absorptive spectrum of the same radical in thermal equilibrium.

The electron spin relaxation times of three acyl radicals (benzoyl, 2,4,6-trimethyl-benzoyl, and hexahydro-benzoyl) have been measured by TR EPR.[153] The relaxation is induced by a spin-rotation coupling arising from two different types of radical movements: overall rotation of the whole radical and hindered internal rotation of the CO group.

2.6.3 Spin-correlated radical pairs.

TR EPR spectra and the decay kinetics of spin-correlated radical pairs (SCRP) polarization in an acyl–benzyl biradical (generated by laser photolysis with 308 nm of 1-phenyl-cyclotetradecanone) have been measured over a wide temperature range (180–274 K).[154,155] The major mechanism of intersystem crossing in this biradical is the spin rotation induced relaxation of the acyl moiety, which is associated with the rotation of the carbonyl group about neighbouring C–C bond axis.

Three flexible biradicals of varying chain length and structure have been investigated in liquid and supercritical carbon dioxide solutions by TR EPR,[156] and are compared with results in conventional solvents. For C_{16} acyl–alkyl biradical, an average spin exchange interaction J_{avg} between the radical centres was obtained by spectral simulation using a simple model for spin-correlated radical pairs. A large solvent effect on J_{avg} was observed, varying by almost one order of magnitude from spectra obtained under supercritical conditions ($J_{avg} = -120$ MHz) to heavy mineral oil ($J_{avg} = -11$ MHz). These results are discussed in terms of solvent properties such as dielectric constant, viscosity, and specific interactions.

The reorganization energies for the intermolecular charge recombination processes have been determined for the electron donor-acceptor systems involving quinones and methoxy aromatic molecules by TR EPR and cyclic voltammetry measurements in polar solvents.[157] The RPM CIDEP indicates that the sign of the spin exchange interaction J is inverted from positive to negative with increasing temperature. These results are interpreted by the charge transfer interaction mechanism, which is supported by theoretical considerations. Further experimental results to the charge transfer mechanism under different conditions are reported.[158–161]

The dynamics of spin-correlated radical pairs in non-ionic surfactant solutions has been studied by Forbes et al.[162] Perdeuterated benzophenone in poly(ethylene

glycol) based surfactants (Brij-35, Triton X-100, and Cremiphor EL) was photolysed at 308 nm. The spectra show that hydrogen abstraction is taking place in the poly(ethylene glycol) outer shell of Brij 35 and Triton X-100 rather than in the alkyl chain core. Strong spin-correlated radical pair polarization is observed at temperatures above 40 °C. Using known micellar dimensions, the diffusion coefficient of the radicals in the micelle interior and their escape rates can be estimated.

The photoredox chemistry of the surfactant dioctyl sulfosuccinate ester (AOT) has been investigated using the photo-excited triplet state of anthraquinone-2,6-sulfonate[163] and of anthraquinone-1,5-sulfonate.[164] In the AOT reverse micelles with 1,5-AQDS as photooxidant the polarization pattern varies from E*/A spectra of the SCRP to the antiphase structure of SCRP in the early period after the laser pulse depending on the molar ratio between water and AOT. A consecutive reaction mechanism is proposed for the generation of the SCRP within the water pool where with decreasing water content an increase in the magnitude of the exchange interaction was observed. White *et al.*[163] detected with 2,6-AQDS as photooxidant several different radicals resulting from two independent oxidation pathways (electron transfer and hydrogen abstraction).

A TR EPR study on the photolysis of benzaldehyde in homogeneous solvent, micelles and microemulsions has been published by Mu *et al.*[165] The homogeneous solvent used was ethylene glycol, and the surfactants were sodium dodecyl benzene sulfonate, and octyl phenol polyoxyethylene ether (TX 100), respectively. The different parts of TM and RPM polarization are explained by the different microstructure of media.

Charged radical pairs formed by the photooxidation of glycyl–glycine by water soluble anthraquinone derivates in the water pool of AOT reverse micelles are spin polarized by three different CIDEP mechanisms, TM, RPM, and SCRPM.[74] The different polarization contributions from the three mechanisms in dependence on the delay time and water pool size are assigned to differences in the rates of internal and ordinary longitudinal relaxation in radical pairs.

The CIDEP polarization pattern in low field (1–2 GHz) of micellized SCRP's with one large *hfs* coupling constants (phosphonyl radical) are reported by Bagryanskaya *et al.*[166,167] The major difference to the spectra in high field consists in the absence of the anti-phase structure of SCRP polarization. The experimental results are in close agreement with theoretical predictions.

2.6.4   CIDEP in radical–triplet pairs. The investigation of the spin polarization behaviour of radical–triplet pairs allows to obtain information on the J-value of the spin exchange interaction.[168–170] The theory of the CIDEP effects in these doublet–quartet spin states has been reviewed recently.[171] Kawai *et al.*[172] has used this method to study various systems with the DPPH radical and organic triplet molecules. For most of the excited states (*e.g.* pyrene, naphthalene, 9-fluorenone, benzophenone) the DPPH spectrum is observed in emission, which indicates a value $J < 0$, but the DPPH-coronene system shows an absorptive DPPH spectrum ($J > 0$). The energy level schemes and the ΔG relation of the systems studied are discussed in detail. The same experiments with galvinoxyl radical–triplet chrysene result in net emissive galvinoxyl spectra in polar solvents, and net absorptive spectra in non-polar solvents.[173] These CIDEP results indicate that galvinoxyl–triplet chrysene pairs show ferromagnetic and antiferromagnetic coupling in non-polar and polar solvents, respectively. Similar results were obtained with the galvinoxyl radical–triplet naphthalene system, and the galvinoxyl radical–triplet biphenyl system.[174,175]

The quenching mechanism of molecular excited states by stable radicals like TEMPO (2,2,6,6-tetramethylpiperidine-1-oxyl) with coronene[176] and singlet molecular oxygen $O_2(^1\Delta_g)$[177] has been studied by TR EPR, thermal lensing, transient optical spectroscopy, and fluorescence measurements. The unusually large CIDEP effects in the $O_2(^1\Delta_g)$-TEMPO system are assigned to the quenching mechanism of

$O_2(^1\Delta_g)$ by TEMPO, and it is proposed that the quenching takes place through the enhanced ISC accompanied by strong electron exchange interaction between an oxygen molecule and a TEMPO radical. In the coronene-TEMPO system in benzene both absorptive and emissive CIDEP were observed which are created by RTPM and quenching of the singlet (S_1) and triplet (T_1) state of coronene. From the results it is concluded that the S_1–T_1 enhanced intersystem crossing occurs through both charge transfer and exchange mechanisms while T_1 quenching occurs only through exchange mechanism.

The quenching rate of singlet oxygen $O_2(^1\Delta_g)$ by TEMPO derivates and the polarization transfer efficiency of TEMPO, 4-oxo-TEMPO, and 4-hydroxy-TEMPO by singlet oxygen have been studied by Martinez et al.[178] by TR EPR. The relative spin polarization efficiencies decrease in the order 4-hydroxy-TEMPO > TEMPO > 4-oxo-TEMPO, whereas an opposite trend was observed for the total quenching rate constant of singlet oxygen by nitroxides in the order 4-hydroxy-TEMPO < TEMPO < 4-oxo-TEMPO.

3. Pulse radiolysis EPR

Pulse radiolysis is an alternative method to generate transient reactive excited states, free radicals, and radical ions, respectively. In most of pulse radiolysis experiments the time-resolved optical UV/Vis spectroscopy is used for detection of transient species, but also some of equipments have been constructed with the coupling of TR EPR.[26,179–181] The advantage of pulse radiolysis over pulse photolysis is the possibility to generate more different radical structures, but the experimental difficulties with pulse radiolysis TR EPR are much higher than with laser photolysis TR EPR. Therefore, in the recent years, only a few papers using this technique have been supported.

The oxidation of organic molecules by the $^\bullet$OH radical is a usual method in pulse radiolysis experiments. Using this technique cw TR EPR experiments have been carried out to investigate the oxidation of amino acid α-aminoisobutyric acid (α-methylalanine) by $^\bullet$OH radicals.[182] When N_2O saturated aqueous solutions of α-methylalanine in the basic region (pH > 11) were pulse irradiated the TR EPR spectrum (time window 1 to 4.2 µs) consists of the superposition of three radicals, $HN^\bullet$–$C(CH_3)_2$–CO_2^-, H_2N–$^\bullet C(CH_3)_2$, and H_2N–$C(CH_3)(^\bullet CH_2)$–CO_2^-. The assignment of the different line groups in the spectrum was supported by DFT quantum chemical calculations of hfs coupling constants of the three radicals. The spectra of all three radicals are spin-polarized by RPM, which is attributed to randomly F-pair encounters. The TR EPR experiments were replenished by spin trapping measurements under in-situ radiolysis conditions with nitromethane $CH_2{=}NO_2^-$ as a spin trap. The spin trapping experiment results in the EPR detection of the radical ^-O_2C–CH_2–$NO_2^{\bullet-}$, which is generated from the reaction $^\bullet CO_2^-$ with nitromethane. The direct TR EPR observation of the first order decay of the aminyl radical, $HN^\bullet$–$C(CH_3)_2$–CO_2^-, and the observation of $^\bullet CO_2^-$ spin adducts with $CH_2{=}NO_2^-$ indicate that β scission is prominent in chemistry of this aminyl radical, and are in agreement with the results of optical pulse radiolysis of Bonifacic et al.[183]

One of the classic reaction pathways available to free radicals in organic systems consists in bimolecular homolytic substitution. In pulse radiolysis cw TR EPR experiments of α-(methylthio)acetamide an unexpectedly large quantity of acetamide radicals was detected. Using a recently developed method to determine the radical yields via TR EPR,[184] in different scavenging experiments, the conclusion was drawn that the acetamide radical is generated by a bimolecular homolytic substitution (S_H2) of the acetamide radical fragment, in α-(methylthio)acetamide, by hydrogen atoms (and not by hydroxyl radicals).

Radiolytically generated hydrogen atoms in water-saturated Vycor glass have been generated at different temperatures (−94 °C to +29 °C), and their CIDEP

spectra have been studied by TR EPR.[185] The measurements were carried out with field-swept FID technique. It was found experimentally that the kinetics of the RPM polarized hydrogen atoms, and the relative intensities of the emissive and absorptive polarizations in the water-saturated Vycor glass vary widely with the temperature. The kinetic curves can be described by a bi-exponential function with the rate constants k_{rise} and k_{decay}, and the intensities of the two lines are different. The emissive low-field line is always more intense than the high-field absorptively polarized line. This additional emissive polarization of the low-field line is attributed to a contribution of the ST_{-1}-RPM mechanism, whereas the multiplet E/A polarization is generated due to ST_0-RPM. To understand this RPM CIDEP effects the hydrogen atom needs another partner. In the paper different possible paramagnetic partners are discussed. These are OH radicals, defects on or near the surface of the pores, and triplet excitons, such as ^{3}exciton + SiOH → SiO$^\bullet$ + $^\bullet$H as a geminate pair. To simulate the kinetics of the two spin-polarized lines by the stochastic Liouville equation it was assumed that the radical pair partner to the H atom has negligible *hfs* coupling and an isotropic *g*-factor. With the assumption that the Heisenberg spin-spin exchange interaction is the only inter-radical interaction in such pairs the experimental results are quantitatively simulated. The diffuse motion of the H atom in the Vycor glass cavity is assumed to be anisotropic in cylinders of finite length with a diameter of 0.4 µm, and the spin interaction within the pair is described by two states called "contact" and "separate". The simulation reveals an excellent agreement with the experimental kinetic curves. These results demonstrate the usefulness of TR EPR experiments to study physical-chemical properties of nanoscale media.

4. Concluding remarks

The TR EPR in the nanosecond and microsecond time scale has been established as a powerful experimental technique in studying transient paramagnetic species. The development of time-resolved cw/FT EPR equipments in a wide field/frequency range from the S- to the W-band expands the possibilities of investigations of the dynamics in radical interactions in more details. Besides the studies of chemical kinetics, the spin polarization effects (CIDEP) provide unique experimental and theoretical evidence of radical precursors and dynamic processes in radical pairs. In the last years the fields of application of time-resolved EPR to various problems in physics, chemistry and biochemistry have been considerably increased. Besides the traditional application in organic radical chemistry, the TR EPR has been introduced in such topical fields as photoinduced energy conversion, photosynthesis and nanosciences. The author is convinced that further fields for application of time-resolved electron paramagnetic resonance in modern science will be developed in the future.

References

1   D. Beckert, *Electron Paramagnetic Resonance*, eds. B. C. Gilbert, M. J. Davies and D. M. Murphy, *Specialist Periodical Reports*, Royal Society of Chemistry, Cambridge, UK, 2002, vol. 18, pp. 74–108.
2   K. A. McLauchlan and M. T. Yeung, *Electron Spin Resonance*, eds. N. M. Atherton, M. J. Davies and B. C. Gilbert, *Specialist Periodical Reports*, Royal Society of Chemistry, Cambridge, UK, 1994, vol. 14, pp. 32–62.
3   C. M. R. Clancy, V. F. Tarasov and M. D. E. Forbes, *Electron Paramagnetic Resonance*, eds. B. C. Gilbert, N. M. Atherton and M. J. Davies, *Specialist Periodical Reports*, Royal Society of Chemistry, Cambridge, UK, 1998, vol. 16, pp. 50–78.
4   D. W. Werst and A. D. Trifunac, *Electron Spin Resonance*, eds. M. C. R. Symons, *Specialist Periodical Reports*, Royal Society of Chemistry, Cambridge, UK, 1994, vol. 13A, pp. 161–186.
5   D. Goldfarb, *Electron Spin Resonance*, eds. B. C. Gilbert, N. M. Atherton and M. J. Davies, *Specialist Periodical Reports*, Royal Society of Chemistry, Cambridge, UK, 1996, vol. 15, pp. 182–243.

6   H. Murai, S. Tero-Kubota and S. Yamauchi, *Electron Paramagnetic Resonance*, eds. B. C. Gilbert, M. J. Davies and K. A. McLauchlan, *Specialist Periodical Reports*, Royal Society of Chemistry, Cambridge, UK, 2000, vol. 17, pp. 130–163.

7   S. Weber, *Electron Paramagnetic Resonance*, eds. B. C. Gilbert, M. J. Davies and K. A. McLauchlan, *Specialist Periodical Reports*, Royal Society of Chemistry, Cambridge, UK, 2002, vol. 17, pp. 43–77.

8   J. R. Morton and K. F. Preston, *Electron Spin Resonanance*, eds. B. C. Gilbert, N. M. Atherton and M. J. Davies, *Specialist Periodical Reports*, Royal Society of Chemistry, Cambridge, UK, 1996, vol. 15, pp. 152–168.

9   K. P. Dinse, *Electron Paramagnetic Resonance*, eds. B. C. Gilbert, M. J. Davies and K. A. McLauchlan, *Specialist Periodical Reports*, Royal Society of Chemistry, Cambridge, UK, 2000, vol. 17, pp. 78–108.

10 J. H. Freed and J. B. Pedersen, in *Advances in Magnetic Resonance*, ed. J. S. Waugh, Academic Press, New York, 1976, vol. 8, pp. 1–80.

11 K. M. Salikhov, Y. N. Molin, P. Z. Sagdeev and A. L. Buchachenko, *Spin Polarization and Magnetic Effects in Radical Reactions*, Elsevier, Amsterdam, 1984.

12 U. E. Steiner and T. Ulrich, *Chem. Rev.*, 1989, **89**, 51.

13 H. Murai, *J. Photochem. Photobiol., C: Photochem. Reviews*, 2003, **3**, 183.

14 H. Murai, S. Yamauchi, A. Kawai, K. Obi and N. Hirota, *Appl. Magn. Res.*, 2003, **23**, 249.

15 N. Hirota and S. Yamauchi, *J. Photochem. Photobiol., C: Photochem. Reviews*, 2003, **3**, 109.

16 A. Savitsky and K. Moebius, *Helv. Chim. Acta*, 2006, **89**, 2544.

17 W. Lubitz, F. Lendzian and R. Bittl, *Acc. Chem. Res.*, 2002, **35**, 313.

18 W. Lubitz, *Phys. Chem. Chem. Phys.*, 2002, **4**, 5539.

19 W. Lubitz, *Electron Paramagnetic Resonance*, eds. B. C. Gilbert, M. J. Davies and D. M. Murphy, *Specialist Periodical Reports*, Royal Society of Chemistry, Cambridge, UK, 2002, vol. 19, pp. 174–242.

20 R. Bittl and S. Weber, *Biochim. Biophys. Acta, Bioenergetics*, 2005, **1707**, 117.

21 G. Link, O. G. Poluektov, L. M. Utschig, J. Lalevee, T. Yago, J. U. Weidner, M. C. Thurnauer and G. Kothe, *Magn. Res. Chem.*, 2005, **43**, S103.

22 M. C. Thurnauer, O. G. Poluektov and G. Kothe, *Biol. Magn. Res.*, 2004, **22**, 165.

23 Y. E. Kandrashkin and A. van der Est, *Appl. Magn. Res.*, 2007, **31**, 105.

24 R. Bartucci, D. A. Erilov, R. Guzzi, L. Sportelli, S. A. Dzuba and D. Marsh, *Chem. Phys. of Lipids*, 2006, **141**, 142.

25 P. W. Atkins, K. A. McLauchlan and A. F. Simpson, *Nature*, 1968, **219**, 927.

26 B. Smaller, J. R. Remko and F. C. Avery, *J. Chem. Phys.*, 1968, **48**, 5174.

27 L. Kevan and M. K. Bowman, *Modern Pulsed and Continuous-Wave Electron Spin Resonance*, Wiley-Interscience, New York, 1990.

28 J. Gorcester, G. L. Millhauser and J. H. Freed, in *Advanced EPR: Applications in Biology and Biochemistry*, ed. A. J. Hoff, Elsevier, Amsterdam, 1989, pp. 177–242.

29 J. H. Freed, *Ann. Rev. Phys. Chem.*, 2000, **51**, 655.

30 A. Schweiger and G. Jeschke, *Principles of Pulsed Electron Paramagnetic Resonance*, Oxford, University Press, 2001.

31 T. Kausche, J. Säuberlich, E. Trobitzsch, D. Beckert and K. P. Dinse, *Chem. Phys.*, 1996, **208**, 375.

32 *EPR Newsletter*, The Publication of the International EPR (ESR) Society, 2007, vol. 17, nrs. 6 and 12.

33 For latest commercial available time-resolved EPR technique see: www.bruker-biospin.com.

34 H. van Willigen, in *Molecular and Supramolecular Photochemistry*, eds. V. Ramamurthy and K. Schanze, Marcel Dekker, 2000, vol. 6, pp. 197–247.

35 A. Bussandri and H. van Willigen, *J. Phys. Chem. A*, 2002, **106**, 1524.

36 S. Tero-Kubota, T. Tachikawa, F. Ito, M. Matsui and K. Konishi, *Chem. Phys. Lett.*, 2003, **381**, 340.

37 G. J. Kavarnos and N. J. Turro, *Chem. Rev.*, 1986, **86**, 401.

38 F. Elisei, G. Favaro and H. Görner, *J. Photochem. Photobiol. A: Chem.*, 1991, **59**, 243.

39 A. R. Jones and J. R. Woodward, *Mol. Phys.*, 2006, **104**, 1551.

40 R. Das, *Mol. Phys.*, 2006, **104**, 1581.

41 S. Basu, K. A. McLauchlan and A. J. D. Ritchie, *Chem. Phys. Lett.*, 1984, **105**, 447.

42 M. Jäger, B. C. Yu and J. R. Norris, Jr, *Mol. Phys.*, 2002, **100**, 1323.

43 M. Jäger and J. R. Norris, *J. Phys. Chem. A*, 2002, **106**, 3659.

44 Xinsheng Xu, Hong Xin, Weijun Zhang, Xuehan Ji, Zhifeng Cui and Tongxing Lu, *Spectrosc. Lett.*, 2006, **39**, 13.

45 T. Tachikawa, Y. Kobori, K. Akiyama, A. Katsuki, U. E. Steiner and S. Tero-Kubota, *Chem. Phys. Lett.*, 2002, **360**, 13.

46 T. Tachikawa, Y. Kobori, K. Akiyama, A. Katsuki, Y. Usui, U. E. Steiner and S. Tero-Kubota, *Mol. Phys.*, 2002, **100**, 1413.

47 S. Tero-Kubota, A. Katsuki and Y. Kobori, *J. Photochem. Photobiol. C: Reviews*, 2001, **2**, 17.
48 A. Katsuki, Y. Kobori, S. Tero-Kubota, S. Milikisyants, H. Paul and U. E. Steiner, *Mol. Phys.*, 2001, **99**, 1245.
49 Y. A. Serrebrenikov and B. F. Minaev, *Chem. Phys.*, 1987, **114**, 359.
50 K. Ohara, D. M. Martino and H. van Willigen, *J. Photochem. Photobiol A, Chem.*, 2006, **181**, 325.
51 V. Maurel, J. M. Mouesca, G. Desfonds and Serge Gambarelli, *J. Phys. Chem. A*, 2005, **109**, 148.
52 M. J. Davies and R. T. Dean, *Radical-Mediated Protein Oxidation: From Chemistry to Medicine*, Oxford University Press, Oxford, 1997.
53 C. L. Hawkins and M. J. Davies, *Biochim. Biophys. Acta*, 2001, **1504**, 196.
54 B. Berlett and E. R. Stadtmann, *J. Biol. Chem.*, 1997, **272**, 20313.
55 M. Bonifacic, I. Stefanic, G. L. Hug, D. A. Armstrong and K. D. Asmus, *J. Am. Chem. Soc.*, 1998, **120**, 9930.
56 I. Stefanic, M. Bonifacic, K. D. Asmus and D. A. Armstrong, *J. Phys. Chem. A*, 2001, **105**, 8681.
57 G. L. Hug, M. Bonifacic, K. D. Asmus and D. A. Armstrong, *J. Phys. Chem. B*, 2000, **104**, 6674.
58 P. Tarabek, M. Bonifacic and D. Beckert, *J. Phys. Chem. A*, 2006, **110**, 7293.
59 P. Tarabek, Ph.D. Thesis, University of Leipzig, 2005.
60 P. Tarabek, S. Naumov and D. Beckert, *J. Phys. Chem. A*, 2004, **108**, 929.
61 M. Goez and V. Zubarev, *J. Phys. Chem. A*, 1999, **103**, 9605.
62 H. Yashiro, R. C. White, A. V. Yurkovskaya and M. D. E. Forbes, *J. Phys. Chem. A*, 2005, **109**, 5855.
63 A. Naito, K. Akasaka and H. Hatano, *Mol. Phys.*, 1981, **44**, 427.
64 K. D. Asmus, M. Goebl, K. O. Hiller, S. Mahling and J. Moenig, *J. Chem. Soc., Perkin Trans. 2*, 1985, **5**, 641.
65 G. L. Hug, B. Marciniak and K. Bobrowski, *J. Photochem. Photobiol A: Chem.*, 1996, **95**, 81.
66 G. L. Hug, K. Bobrowski, H. Kozubek and B. Marciniak, *Photochem. Photobiol.*, 2000, **72**, 1.
67 R. C. White and M. D. E. Forbes, *Org. Lett.*, 2006, **8**, 6027.
68 M. D. E. Forbes, N. V. Lebedeva, R. C. White, T. K. Chen, R. MacArthur, P. Caregnato and T. E. Hill, *Mol. Phys.*, 2007, **105**, 2127.
69 Ch. Kolano, G. Bucher, D. Grote, O. Schade and W. Sander, *Photochem. Photobio.*, 2006, **82**, 332.
70 Ch. Kolano, G. Bucher, O. Schade, D. Grote and W. Sander, *J. Org. Chem.*, 2005, **70**, 6609.
71 P. Tarabek, M. Bonifacic and D. Beckert, *J. Phys. Chem. A*, 2004, **108**, 3467.
72 P. Tarabek, M. Bonifacic and D. Beckert, *J. Phys. Chem. A*, 2007, **111**, 4958.
73 V. F. Tarasov, R. C. White and M. D. E. Forbes, *Spectrochim. Acta, Part A*, 2006, **63**, 776.
74 R. C. White, V. F. Tarasov and M. D. E. Forbes, *229th ACS National Meeting*, San Diego, CA, 2005, p. 13.
75 B. L. Seagle, K. A. Rezai, E. M. Gasyna, Y. Kobori, K. A. Rezaei and J. R. Norris, Jr, *J. Amer. Chem. Soc.*, 2005, **127**, 11220.
76 B. L. Seagle, K. A. Rezai, Y. Kobori, E. M. Gasyna, K. A. Rezaei and J. R. Norris, Jr, *Proc. Nat. Acad. Sci., USA*, 2005, **102**, 8978.
77 Y. Kobori and J. R. Norris, Jr, *J. Amer. Chem. Soc.*, 2006, **128**, 4.
78 A. P. Bussandri, C. W. Kiarie and H. van Willigen, *Res. Chem. Intermed.*, 2002, **28**, 697.
79 P. S. Engel, *Chem. Rev.*, 1980, **80**, 99.
80 M. Buback, B. Huckestein, F.-D. Kuchta, G. T. Russel and E. Schmid, *Makromol. Chem. Phys.*, 1994, **195**, 2117.
81 A. N. Savitsky, H. Paul and A. I. Shushin, *J. Phys. Chem. A*, 2000, **104**, 9091.
82 A. N. Savitsky, H. Paul and A. I. Shushin, *Helv. Chim. Acta*, 2006, **89**, 2533.
83 S. Milikisyants, A. Katsuki, U. Steiner and H. Paul, *Mol. Phys.*, 2002, **100**, 1215.
84 S. Nagakura, H. Hayashi and T. Azumi, *Dynamic Spin Chemistry*, Kodansha and Wiley, Tokyo, New York, 1998.
85 T. N. Makarov, A. N. Savitsky, K. Möbius, D. Beckert and H. Paul, *J. Phys. Chem. A*, 2005, **109**, 2254.
86 J. B. Pedersen and J. H. Freed, *J. Chem. Phys.*, 1975, **62**, 1706.
87 M. Yamaji, T. Yoshihara, T. Tachikawa, S. Tero-Kubota, S. Tobita, H. Shizuka and B. Marciniak, *J. Photochem. Photobiol. A: Chem.*, 2004, **162**, 513.
88 M. Yamaji, A. Suzuki, F. Ito, S. Tero-Kubota, S. Tobita and B. Marciniak, *J. Photochem. Photobio. A, Chem.*, 2005, **170**, 253.

89   M. Yamaji, M. Ogasawara, K. Kikuchi, S. Nakajima, S. Tero-Kubota, B. Marciniak and K. Nozaki, *Phys. Chem. Chem. Phys.*, 2007, **9**, 3268.

90   M. Yamaji, S. Inomata, S. Nakajima, K. Akiyama, S. Tobita and B. Marciniak, *J. Phys. Chem. A*, 2005, **109**, 3843.

91   T. Suzuki, K. Maeda, T. Arai, K. Akiyama and S. Tero-Kubota, *Mol. Phys.*, 2003, **101**, 3341.

92   T. Suzuki, Y. Kaneko, K. Maeda, T. Arai, K. Akiyama and S. Tero-Kubota, *Mol. Phys.*, 2002, **100**, 1469.

93   C. Rüchardt, *Angew. Chem. Int. Ed. Engl.*, 1970, **9**, 830.

94   J. M. Tedder, *Angew. Chem. Intl. Ed. Engl.*, 1982, **21**, 401.

95   B. Giese, *Angew. Chem. Int. Ed. Engl.*, 1989, **28**, 969.

96   M. Weber, I. V. Khudyakov and N. J. Turro, *J. Phys. Chem. A*, 2002, **106**, 1938.

97   J. A. Weil, J. R. Bolton and J. E. Werz, *Electron Paramagnetic Resonance. Elementary, Theory and Practical Applications*, John Wiley & Sons, Inc., New York, 1994.

98   I. Gatlik, P. Rzadek, G. Gescheidt, G. Rist, B. Hellrung, J. Wirz, K. Dietliker, G. Hug, M. Kunz and J.-P. Wolf, *J. Amer. Chem. Soc.*, 1999, **121**, 8332.

99   M. Weber and N. J. Turro, *J. Phys. Chem. A*, 2003, **107**, 3326.

100   K. Dietliker, T. Jung, J. Benkhoff, H. Kura, A. Matsumoto, H. Oka, D. Hristova, G. Gescheidt and G. Rist, *Macromol. Symp.*, 2004, **217**, 77.

101   D. Hristova, I. Gatlik, G. Rist, K. Dietliker, J. P. Wolf, J. L. Birbaum, A. Savitsky, K. Moebius and G. Gescheidt, *Macromolecules*, 2005, **38**, 7714.

102   J. P. Fouassier, *Photoinitiation, Photopolymerization and Photocuring, Fundamentals and Applications*, Hanser, Munich, Germany, 1995.

103   M. Kamachi, *J. Polym. Sci. Part A: Polym.Chem.*, 2002, **40**, 269.

104   I. V. Khudyakov, N. Arsu, S. Jockusch and N. J. Turro, *Designed Monomers and Polymers*, 2003, **6**, 91–101.

105   H. Kura, H. Oka, M. Ohwa, T. Matsumura, A. Kimura, Y. Iwasaki, T. Ohno, M. Matsumura and H. Murai, *J. Polym. Sci., Part B: Polymer Physics*, 2005, **43**, 1684.

106   G. Moad, E. Rizzardo and S. H. Thang, *Aust. J. Chem.*, 2005, **58**, 379.

107   M. Buback, M. Egorov, T. Junkers and E. Panchenko, *Macromol. Rapid Comm.*, 2004, **25**, 1004.

108   M. Buback, *Macromol. Symp.*, 2005, **226**, 121.

109   M. Buback, P. Hesse, T. Junkers and P. Vana, *Macromol. Rapid Comm.*, 2006, **27**, 182.

110   P. Vana, *Macromol. Symp.*, 2007, **248**, 71.

111   E. J. Harbron, V. P. McCaffrey, R. Xu and M. D. E. Forbes, *J. Am. Chem. Soc.*, 2000, **122**, 9182.

112   V. P. McCaffrey, E. J. Harbron and M. D. E. Forbes, *J. Phys. Chem. B*, 2005, **109**, 10686.

113   V. P. McCaffrey and M. D. E. Forbes, *Macromolecules*, 2005, **38**, 3334.

114   A. Maliakal, M. Weber, N. J. Turro, M. M. Green, S. Y. Yang, S. Rearsall and M. J. Lee, *Macromolecules*, 2002, **35**, 9151.

115   H. Fischer and J. Bargon, *Acc. Chem. Res.*, 1969, **2**, 110.

116   R. Kaptein and J. L. Oosterhoff, *Chem. Phys. Letters*, 1969, **4**, 195.

117   G. L. Closs, *J. Am. Chem. Soc.*, 1969, **91**, 4552.

118   R. W. Fessenden and R. H. Schuler, *J. Chem. Phys.*, 1963, **39**, 2147.

119   P. Neta, R. W. Fessenden and R. H. Schuler, *J. Phys. Chem.*, 1971, **75**, 1654.

120   F. J. Adrian, *J. Chem. Phys.*, 1971, **54**, 3918.

121   A. B. Doktorov and J. B. Pedersen, *J. Chem. Phys.*, 1998, **108**, 6868.

122   A. B. Doktorov, A. A. Neufeld and J. B. Pedersen, *J. Chem. Phys.*, 1999, **110**, 8869.

123   A. B. Doktorov, A. A. Neufeld and J. B. Pedersen, *J. Chem. Phys.*, 1999, **110**, 8881.

124   A. A. Neufeld, A. B. Doktorov and J. B. Pedersen, *J. Chem. Phys.*, 1999, **115**, 3219.

125   A. A. Neufeld, A. B. Doktorov and J. B. Pedersen, *J. Chem. Phys.*, 1999, **115**, 3230.

126   A. I. Shushin, *J. Chem. Phys.*, 2002, **116**, 9792.

127   A. I. Shushin, *Mol. Phys.*, 2002, **100**, 1303.

128   F. J. Adrian, *J. Phys. Chem. A*, 2003, **107**, 9045.

129   P. R. Levstein and H. van Willigen, *J. Chem. Phys.*, 1991, **95**, 900.

130   K. Ohara, J. N. Hirota, C. A. Steren and H. van Willigen, *Chem. Phys. Lett.*, 1995, **232**, 169.

131   H. Hayashi and Y. Sakaguchi, *J. Photochem. Photobiol., C: Photochem. Reviews*, 2005, **6**, 25.

132   A. N. Savitsky and H. Paul, *Chem. Phys. Lett.*, 2000, **319**, 403.

133   A. Katsuki, Y. Kobori, S. Tero-Kubota, S. Milikisyants, H. Paul and U. Steiner, *Mol. Phys.*, 2002, **100**, 1245.

134   A. Kawai and K. Shibuya, *J. Phys. Chem. A*, 2007, **111**, 4890.

135   Y. Kobori, K. Akiyama and S. Tero-Kubota, *J. Chem. Phys.*, 2000, **113**, 465.

136   N. N. Lukzen, K. L. Ivanov, V. A. Morozov, D. R. Kattnig and G. Grampp, *Chem. Phys.*, 2006, **328**, 75.

137 N. N. Lukzen, K. L. Ivanov, V. A. Morozov, R. Z. Sagdeev, D. Kattnig and G. Grampp, *Dokl. Phys. Chem.*, 2006, **409**, 23.
138 L. Monchick and F. J. Adrian, *J. Chem. Phys.*, 1978, **68**, 4376.
139 J. R. Norris, A. L. Morris, M. C. Thurnauer and J. Tang, *J. Chem. Phys.*, 1990, **92**, 4239.
140 P. L. Hasjim and J. R. Norris, Jr, *J. Phys. Chem. C*, 2007, **111**, 5203.
141 A. L. Buchachenko and V. L. Berdinsky, *Chem. Rev.*, 2002, **102**, 603.
142 K. L. Ivanov, *J. Phys. Chem. A*, 2005, **109**, 5160.
143 T. N. Makarov and H. Paul, *J. Magn. Res.*, 2004, **169**, 335.
144 A. L. Konkin, H.-K. Roth, M. Schroedner, G. A. Nazmutdina, A. V. Aganov, T. Ida and R. R. Garipov, *Chem. Phys.*, 2003, **287**, 377.
145 A. L. Konkin, H.-K. Roth, M. Schroedner, V. G. Shtyrlin, R. R. Garipov, T. Ida, M. Raetzsch, A. V. Aganov and G. A. Nazmutdinova, *Chem. Phys.*, 2006, **324**, 563.
146 V. P. McCaffrey and M. D. E. Forbes, *J. Phys. Chem. A*, 2005, **109**, 4891.
147 T. Ichino and R. W. Fessenden, *J. Phys. Chem. A*, 2003, **107**, 9257.
148 Y. Kobori, S. Sekiguchi, K. Akiyama and S. Tero-Kubota, *J. Phys. Chem. A*, 1999, **103**, 5416.
149 H. Paul and H. Fischer, *Z. Naturforsch.*, 1970, **25a**, 443.
150 A. D. Trifunac, K. W. Johnson, B. E. Clifft and R. H. Lowers, *Chem. Phys. Letters*, 1975, **35**, 566.
151 K. A. McLauchlan, N. J. K. Simpson and P. D. Smith, *Res. Chem. Interm.*, 1991, **16**, 141.
152 B. Bhattacharjee and R. Das, *Mol. Phys.*, 2007, **105**, 1053.
153 T. N. Makarov, E. G. Bagryanskaya and H. Paul, *Appl. Magn. Res.*, 2004, **26**, 197.
154 Y. P. Tsentalovich and M. D. E. Forbes, *Mol. Phys.*, 2002, **100**, 1209.
155 Y. P. Tsentalovich, M. D. E. Forbes, O. B. Morozova, I. A. Plotnikov, V. P. McCaffrey and A. V. Yurkovskaya, *J. Phys. Chem. A*, 2002, **106**, 7121.
156 M. D. E. Forbes, K. E. Dukes, N. I. Avdievich, E. J. Harbron and J. M. DeSimone, *J. Phys. Chem. A*, 2006, **110**, 1767.
157 T. Yago, Y. Kobori, K. Akiyama and S. Tero-Kubota, *J. Phys. Chem. B*, 2002, **106**, 10074.
158 T. Yago, Y. Kobori, K. Akiyama and S. Tero-Kubota, *Chem. Phys. Lett.*, 2003, **369**, 49.
159 T. Yago, Y. Kobori, K. Akiyama and S. Tero-Kubota, *J. Phys. Chem. B*, 2003, **107**, 13255.
160 Y. Kobori, T. Yago and S. Tero-Kubota, *Appl. Magn. Res.*, 2003, **23**, 269.
161 S. Tero-Kubota, K. Zikihara, T. Yago, Y. Kobori and K. Akiyama, *Appl. Magn. Res.*, 2004, **26**, 145.
162 E. E. Chaney and M. D. E. Forbes, *J. Phys. Chem. B*, 2003, **107**, 4464.
163 R. C. White, V. Gorelik, E. G. Bagryanskaya and M. D. E. Forbes, *Langmuir*, 2007, **23**, 4183.
164 K. Akiyama and S. Tero-Kubota, *J. Phys. Chem. B*, 2002, **106**, 2398.
165 J. H. Mu, G. Z. Li, X. H. Tu, T. X. Lu and K. S. Zhao, *Chem. Phys. Lett.*, 2002, **354**, 186.
166 E. G. Bagryanskaya, H. Yashiro, M. Fedin, P. A. Purtov and M. D. E. Forbes, *J. Phys. Chem. A*, 2002, **106**, 2820.
167 E. Bagryanskaya, M. Fedin and M. D. E. Forbes, *J. Phys. Chem. A*, 2005, **109**, 5064.
168 C. Blättler, F. Jent and H. Paul, *Chem. Phys. Lett.*, 1990, **166**, 375.
169 A. Kawai and K. Obi, *Res. Chem. Intermed.*, 1993, **19**, 865.
170 A. I. Shushin, *Chem. Phys. Lett.*, 1999, **313**, 246.
171 A. Kawai and K. Shibuya, *J. Photochem. Photobiol., C: Photochem. Rev.*, 2006, **7**, 89.
172 A. Kawai and K. Shibuya, *J. Phys. Chem. A*, 2002, **106**, 12305.
173 A. Kawai, Y. Watanabe and K. Shibuya, *Chem. Phys. Lett.*, 2003, **372**, 8.
174 A. Kawai, Y. Watanabe and K. Shibuya, *Mol. Phys.*, 2002, **100**, 1225.
175 A. Kawai, *Appl. Magn. Res.*, 2003, **23**, 349.
176 M. Mitsui, Y. Kobori, A. Kawai and K. Obi, *J. Phys. Chem. A*, 2004, **108**, 524.
177 M. Mitsui, K. Takeda, Y. Kobori, A. Kawai and K. Obi, *J. Phys. Chem. A*, 2004, **108**, 1120.
178 C. G. Martinez, S. Jockusch, M. Ruzzi, E. Sartori, A. Moscatelli, N. J. Turro and A. L. Buchachenko, *J. Phys. Chem. A*, 2005, **109**, 10216.
179 A. D. Trifunac and R. G. Lawler, *Magn. Res. Rev.*, 1982, **7**, 147.
180 N. C. Verma and R. W. Fessenden, *J. Chem. Phys.*, 1976, **65**, 2139.
181 D. Beckert and K. Mehler, *Ber. Bunsenges. Phys. Chem.*, 1983, **87**, 587.
182 P. Wisniowski, I. Carmichael, R. W. Fessenden and G. L. Hug, *J. Phys. Chem. A*, 2002, **106**, 4573.
183 M. Bonifacic, D. A. Armstrong, I. Carmichael and K. D. Asmus, *J. Phys. Chem. B*, 2000, **104**, 643.
184 G. L. Hug and R. W. Fessenden, *J. Phys. Chem. A*, 2000, **104**, 7021.
185 V. F. Tarasov, S. D. Chemerisov and A. D. Trifunac, *J. Phys. Chem. B*, 2003, **107**, 1293.

EPR of paramagnetic centres on solid surfaces

Damien M. Murphy*[a] and Mario Chiesa*[b]

1. Introduction

The study of defective surface sites on many oxides has received considerable interest in recent years as these sites are coordinatively unsaturated and quite often exhibit enhanced activity in many catalytic reactions. Despite this importance, the influence of the defect sites on the chemical nature of the oxide surface and their role in the activation of adsorbed substrates is poorly understood. In a number of cases these defects are paramagnetic and can therefore be directly studied by EPR, or indirectly studied using suitable probe molecules. The EPR investigations of these interfacial phenomena are not however confined to the surface defects. Transient radical intermediates, stable inorganic radicals, trapped charge-carrier states and paramagnetic transition metal ions, all play an important part in the heterogeneous catalysis. The aim of this review is to highlight and demonstrate the applications of EPR spectroscopy to this field of research and discuss how EPR is used to characterise all of the aforementioned surface species. As in our previous SPR reviews,[1] we have focussed our attention singularly on surface processes and interfacial states at heterogeneous oxide surfaces. Microporous materials (such as zeolites), soft-solids (such as surfactants and polymers) and bulk states are not covered. The literature in the last four calender years will be covered and the review will be separated into the s-block metal oxides, transition metal oxides and p-block oxides.

2. s-Block metal oxides

Metal oxides of group 2, and MgO in particular, feature large in the surface science and surface chemistry literature. This is primarily due to their simple crystal structure and well defined surface morphology. MgO can be considered a prototype of ionic oxides and an ideal model system to study important aspects related to a number of scientific and technological issues. These range from catalysis to electronic micro-devices and anti-corrosion protection.

A relevant example is provided by the interaction of ns^1 metal atoms with the surface of MgO and other alkaline earth oxides. Due to their paramagnetic nature, alkali metal adatoms are excellent EPR probes, which allow one to unravel the essence of the metal-oxide bonding interaction and the nature of the surface adsorption sites. Through this information it is therefore possible to indirectly examine the abundance of these sites and the morphology of the surface itself. The influence of the matrix on the electronic properties of the metal species (matrix effect) is reflected by the hyperfine coupling constant in the EPR spectra. For example, the EPR spectra of trapped alkali atoms in rare gases and hydrocarbons show departures of a few percent of the metal hyperfine interactions from their gas phase values. A drastically different situation occurs when alkali metal atoms are deposited on the surface of basic oxides such as alkaline-earth oxides. In particular, adsorption of K atoms ($I = 3/2$) onto high surface area MgO produced well resolved EPR spectra characterized by a distinct hyperfine quartet with a separation of about 4 mT.[2] This value represents a consistent reduction (about 50%) of the metal hyperfine coupling constant with respect to the gas phase value. Isotopic substitution with ^{17}O

[a] *School of Chemistry, Cardiff University, Main Building, Park Place, Cardiff, UK, CF10 3AT .
 E-mail: murphydm@cardiff.ac.uk; Fax: 00 44 2920 874030; Tel: 00 44 2920 875850*
[b] *Dipartimento di Chimica IFM and NIS, Università di Torino, Torino, Italy
 E-mail: m.chiesa@unito.it; Fax: +390116707855; Tel: +390116707745*

demonstrated that the interaction occurs through the surface O^{2-} anions and well resolved ^{17}O HYSCORE spectra indicated that the binding site involves three oxygen atoms, two of which are nearly equivalent.[2]

However the small ^{17}O coupling accounts for only a negligible fraction of the unpaired electron spin density which is lacking on the 4s K orbital. This apparent inconsistency has been rationalized within the framework of Pauli repulsion effects induced by the matrix. The interaction of the matrix lone pairs with the ns orbital of the alkali atom destabilizes the orbital containing the valence electron, leading to an "expanded" atom structure reminiscent of a Rydberg state. This implies that the unpaired electron spin density remains largely localized on the K atom, but the hyperfine coupling constant is reduced due to the expansion of the 4s K orbital, an interpretation which was fully supported by accurate theoretical calculations.[2,3]

Similar results have also been obtained by Risse and co-workers[4,5] for Li and Au atoms deposited on MgO thin films, where EPR spectra were obtained under ultra high vacuum (UHV) conditions. Moreover it has also been found that if one adsorbs alkali metals onto different oxides with similar crystal structure, e.g. MgO, CaO, SrO, etc., it is possible to titrate the surface basicity of the oxide in a very accurate way.[6] In fact, the changes in the adsorption properties of the alkali metal adatom provide indirect but detailed information about the tendency of the surface anions to donate charge to an adsorbed species. Furthermore, evidence of full ionisation of alkali metal atoms was found when the MgO surface is decorated by OH^- groups which were capable of inducing spontaneous ionization of the metal atoms.[7]

Hydrogen may be considered as the "first alkali metal" and its behaviour when adsorbed on the same surfaces is just as interesting.[3] Exposure of MgO or CaO surfaces to hydrogen atoms results in the spontaneous ionisation, at temperatures as low as 77 K, of H and the subsequent formation of excess electrons and extra protons on the surface, as schematically represented in eqn (1).

$$Mg_n^{2+}O^{2-} + H^{\bullet} \rightarrow Mg_n^{2+}(e^-)(OH^-) \qquad (1)$$
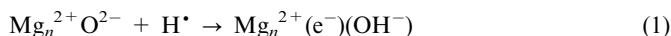
Extensive EPR work has been done in the last few years on this interaction which leads to the stabilization of the fundamental unit of electrical charge on the surface of insulating oxides.[8] Surface ^{17}O substitution has led to the complete mapping of the unpaired electron spin density on both MgO[9,10] and CaO[11] while high field-EPR, together with Q band ENDOR, enabled the full resolution of the g tensor to be obtained.[12]

Just as interesting is the possibility of monitoring separated charged states induced by photon irradiation. UV light has been used by Diwald and co-workers[13] to generate site-selective O^- hole centres at 3-coordinated corner oxygen sites on MgO nanocubes. These highly reactive O^- radicals split H_2 homolytically and, in the course of this reaction, become hydroxylated and produce hydrogen atoms. These hydrogen atoms then undergo the same reactivity described by eqn (1), leading to $(H^+)(e^-)$ centres. The reactivity of these peculiar excess electron centres towards incoming molecules has been explored in detail[8] and recently the full characterization of the surface stabilized CO_2^- radical using ^{17}O and ^{13}C labelled CO_2 has been reported.[14]

Surface trapped hole centres have been generated by X-ray irradiation of a ^{17}O isotope-enriched MgO sample.[15] The complete ^{17}O hyperfine tensor for the O^- anion (A = [1.86, 1.86, −10.48] mT) was experimentally observed and comparison of the measured data with those obtained by embedded cluster density functional theory (DFT) calculations allowed the authors to identify the hole trapping centre with 3-coordinated oxide anions localized at MgO corners. The reactivity of O_2 with surface-trapped holes on MgO (O^- ions) was also recently revisited and specific surface sites (oxygen terminated corners and cation vacancies) were proposed to be active in O_2 adsorption.[16] The surface reactivity of the Li^+ doped MgO nanocrystals

were monitored by EPR and IR spectroscopy using chemisorbed hydrogen, surface trapped electrons and surface complexed O_2 as molecular probes.

Finally, nanoporous $12CaO \cdot 7Al_2O_3$ (mayenite) is a class of porous insulating mixed oxide, which is extremely interesting due to its ability to change its electronic, optical and magnetic properties by excess electrons doping, transforming the solid into a stable electride, *i.e.*, an ionic solid where electrons play the role of the anions. Anionic active oxygen radicals, O^- and O_2^-, are formed efficiently in mayenite cages under high oxygen activity conditions. The configuration and dynamics of O_2^- in cages have been revealed by a combination of continuous-wave (CW) and pulsed EPR.[17,18]

3. Transition metal oxides

3.1 TiO$_2$

Numerous EPR studies have appeared in the review period focussing on the electronic excitation of the TiO_2 semiconductor, on the fate of the separated charged states, on the transfer of trapped charge to adsorbed species and also on the fate of the resulting products. In many cases these various paramagnetic species and products have been detected directly at the surface by EPR, or indirectly when desorbed into the liquid phase using spin-trapping. However, as discussed later, the key areas of exploration in which EPR has played a vital role are in the field of surface sensitization of TiO_2 for solar cell devices, characterisation of various nanoparticulate materials and identification of transient radical intermediates. Thompson and Yates[19] published a general overview on the photochemistry of TiO_2 surfaces. Although the EPR component of the review is not exhaustive, it does offer some elegant examples on the role of EPR in characterising oxygen vacancy defects through the intermediacy of the superoxide radical anion (O_2^-).

A number of papers have appeared concerning the photochemistry of mixed phase (anatase-rutile) titania materials, such as the commonly used form of titania known as Degussa P25. Owing to their importance in photocatalysis, several studies have been carried out on these systems to understand the mechanism of the observed enhanced photoactivities, since the activities are far higher than on the single phase materials. It is now generally accepted that the enhancement is caused by an efficient charge separation, although this mechanism has never been satisfactorily proven. Some authors have ascribed the synergetic effect to the preferential electron transfer (ET) from rutile to anatase,[20] while others have proposed the opposite ET from anatase to rutile.[21] Using *in situ* EPR, Komaguchi *et al.*,[21] followed the photo-response of the Ti^{3+} signal in a partially reduced P25 material using visible light. It is known that the Ti^{3+}_{latt} EPR signal is slightly different in anatase compared to rutile, so even in the mixed phase materials, the relative response of $Ti^{3+}_{anatase}$ *versus* Ti^{3+}_{rutile} can be monitored. In this way, the authors demonstrated that the observed photoresponse in the partially reduced material is caused by the excitation of the trapped electrons and not by the generation of electron hole pairs.[21] These important results indicated the preferential ET from anatase to rutile in TiO_2 (P25) by photoexcitation.

Hurum *et al.*,[22,23] have published some excellent papers on the role of surface defects in recombination pathways of mixed phase TiO_2 (P25). Surface defect sites are known to either inhibit or enhance recombination processes, depending on the nature of the defect itself. Using EPR, the authors revealed how irradiated slurries of P25 at 10 K lead to the formation of electron-hole pairs;[23] the former charged species were found to be trapped at Ti^{4+} sites with different coordination and environments for anatase ($Ti^{3+}_{anatase}$: $g_\parallel = 1.957$, $g_\perp = 1.990$) compared to rutile (Ti^{3+}_{rutile}: $g_\parallel = 1.940$, $g_\perp = 1.975$). In addition, a new site was identified with a g value of 1.979, which was interpreted as arising from an electron trapping site in the distorted interfacial region between the anatase and rutile particles. The important conclusion

from this work[23] was that two distinct classes of electron-trapping sites exist in P25; the anatase surface-trapping sites and the interfacial sites. This latter interfacial electron-trapping site is an important and perhaps unique feature of the rutile/anatase morphology within mixed phase titania materials (P25) and is critical for enhanced photoactivities. The same group[22] have also demonstrated the utility of EPR generally for investigations of interfacial charge transfer, recombination investigations and reaction with organic compounds in titania-based photocatalytic applications.

A number of papers have also appeared on the characterisation of charge separation, defects and photoadsorption of O_2 on TiO_2 nanocrystals.[24–32] The groups of Knözinger and Diwald have published several excellent papers showing how the dynamics of charge separation can be monitored by following the time-resolved responses of the photoexcited O^- species using EPR.[24,25] Whilst some studies have also investigated the dynamics of photogenerated charge carriers in TiO_2 nanoparticles, the reported spectra and photoresponse studies were conducted at very low temperatures (4.2 K).[30,31] The novelty of the Knözinger and Diwald papers is that they have successfully studied these dynamics at elevated temperatures (e.g., 90 K and higher) and therefore these findings are more relevant to the numerous surface radical and dynamic studies of TiO_2 reported in the literature.[24,25] The group have also reported the interesting role of chemical activation of small molecules like H_2 or O_2 at the surface of UV excited nanocrystals.[26]

While numerous studies have explored the nature of the photogenerated charges in nanocrystalline TiO_2, few have considered the effect of size/shape of the nano-objects for the electron-hole separation processes. Using CW and pulsed EPR techniques, Dimitrijevic et al.,[32] confirmed the trapping of the electrons at lattice titanium within the bulk while the holes were trapped at oxygen atoms on the surface. T_1 and T_2 relaxation times were measured using two pulse echo and three pulse inversion recovery techniques, which revealed that the trapped holes were affected by weak dipolar couplings with the surrounding hydrogen nuclei from adsorbed water.[32] The spin relaxation processes of these trapped holes were invariant to the size/shape of the particles and found to depend on the dipolar couplings to surrounding protons. Most importantly the authors[32] demonstrated that distortions to the Ti–O bond, resulting from reconstruction of the surface of nano-particles, caused a variation in the g-tensor values and spin lattice relaxation processes of trapped electrons. In a field largely dominated by CW EPR, this paper shows how pulsed EPR measurements can add further insights into TiO_2 surface chemistry.[32]

In recent years the surface sensitization of TiO_2 has also been widely studied for applications in solar cells. This approach can increase the efficiency of the photo-excitation process and thereby expand the excitation wavelength into the visible through excitation of the sensitizer, followed by ET to the semiconductor (TiO_2). Owing to the paramagnetic nature of the separated charged states and the resulting surface radicals, EPR has been pivotal in these studies. A high quantum efficiency for the conversion of light energy into electricity in dye-sensitized solar cells requires the fast injection of electrons into the conduction band combined with a very slow back transfer of electrons. Charge recombination associated with dye-sensitized TiO_2 systems has been rationalised in terms of the inverted Marcus region, where the recombination rate is slowed because of a highly exergonic reaction. Therefore significant efforts have been devoted to fully understanding the role of the separated charged state as one of the key intermediates in the photosensitization of ET across the semiconductor/solution interface.

In a related study, Akiyama et al.,[33] observed polarized EPR spectra of xanthene dyes adsorbed on colloidal TiO_2 particles after excitation with pulses of visible light using time-resolved EPR spectroscopy (nanosecond timescale). The spectra were interpreted using the polarization mechanism of the spin-correlated radical pair (SCRP) where coherent spin singlet/triplet mixing occurs within the radical pair. An axially symmetric g-tensor ($g_\parallel = 1.958$, $g_\perp = 1.988$), along with exchange (J_{SS}) and

dipolar (D_{SS}) interactions, were used in the simulations of the spectra. The positive sign of the exchange interaction of the radical pair was ascribed to charge recombination in the Marcus inverted region. The relative orientation of the magnetic tensor of the trapped electron and dye radical cation was fixed, thus leading to orientational selectivity in the interfacial ET across the semiconductor-solution interface of the TiO_2 nanoparticle.

Time resolved EPR spectroscopy (seconds timescale) was also used to investigate the visible light sensitization of TiO_2 nanoparticles by surface modification with Mn^{II}-terpyridine complexes.[34] Photoexcitation of the $[Mn^{II}(H_2O)_3$(catechol-terpy)]$^{2+}$/TiO_2 (terpy = 2,2′:6,2″-terpyridine) complex attached to the TiO_2 surface, leads to interfacial ET within 300 fs, accompanied by Mn^{II} to Mn^{III} photooxidation. Using EPR, the half-time for regeneration of the Mn^{II} complex was found to be approximately 23 s (at 6 K). The EPR spectra of the Mn^{II} ion were broad and poorly resolved. Nevertheless the decay and regeneration of the signal intensity under light and dark conditions was clearly evident from the spectra.[34]

The electron transfer process in porphyrin-sensitized TiO_2 was studied using CW EPR by Yu et al.[35] Irradiation of aerated ethanol solution resulted in an EPR signal ascribed to the superoxide anion ($g_1 = 2.0253$, $g_2 = 2.0093$, $g_3 = 2.0031$). The authors state that this is the first EPR signal detected directly at room temperature for this species. However, this statement should really be qualified as the first ever detection of the room temperature superoxide species at a liquid-solid interface. At the gas–solid interface, the superoxide species has been widely studied for the past 40 years using CW EPR. While most of these studies report the spectra at 4–77 K (for improved resolution and sensitivity), the EPR spectra of O_2^- are just as easily observed at 298 K also. They are rarely reported at these temperatures simply because of the motional effects which result in partially averaged g values, but room temperature spectra of surface adsorbed O_2^- radicals are in fact abundant in the literature.

Various organic substrates can also be adsorbed onto TiO_2 nanoparticles in order to increase the lifetimes of the photogenerated separated charge species. In this way electron-accepting biomolecules are typically anchored onto the surface to act as conductive leads for electrons, in conjunction with suitable electron donor molecules achieving stabilization of separated charges. Dimitrijevic et al.,[36] studied such nanoparticles which incorporated pyrroloquinoline quinine (PQQ) as an electron acceptor and dopamine (DA) as electron donor. Using EPR, they successfully demonstrated the enhanced separation of the photogenerated charges, with holes being localised at DA and electrons at PQQ. The EPR spectra were recorded at low temperatures in DMSO solvent and complex patterns arising from $^\bullet CH_3$, trapped electrons (Ti^{3+}), semiquinone radicals (PQQ$^-$) and a weak signal ascribed to the dopamine radical cation (DA$^+$), were all identified in solution. The g value of the semiquinone radical was further resolved at D-band ($g_x = 2.0057$, $g_y = 2.0055$, $g_z = 2.0019$).[36]

This study nicely illustrates the importance of EPR for such studies, since the factors responsible for altering the kinetics of charge transfer (such as temperature or pH) was subsequently followed via the changes to the EPR spectra.[36] The same group[37] also successfully used EPR to study the photoinduced charge transfer between guest molecules and hybrid TiO_2/cyclodextrin nanoparticles, revealing that photo-excitation at 4.6 K leads to localisation of valence band holes at carboxyl groups of surface conjugated cyclodextrin and conduction band electrons at Ti^{4+} centres.

A number of studies have also appeared recently dealing specifically with the characterisation of the defect sites at the surface of polycrystalline TiO_2. Carter et al.,[38] used the characteristic EPR signature of O_2^- as a probe of surface defects on reduced TiO_2 (P25), treated under vacuum at elevated temperatures. Among the heterogeneity of superoxide species identified on the surface, one particular species was assigned to an O_2^- radical adsorbed at a surface vacancy (labelled [Vac$\cdots O_2^-$]: $g_x = 2.005$, $g_y = 2.011$, $g_z = 2.019$), while the remaining anions were attributed to

O_2^- stabilization at coordinatively unsaturated Ti^{4+} cations ($Ti^{4+} \cdots O_2^-$). The former [Vac$\cdots$O$_2^-$] centre exhibited pronounced reactivity under the influence of thermal, photochemical and chemical treatment compared to the remaining surface O_2^- radicals bound at non-vacancy sites. The results also supported the hypothesis that the radicals formed in these mixed phase P25 material, were in fact associated with the anatase component of the oxide.

In another study of surface defects on TiO_2, Suriye et al.,[39] used [Re$_3$(CO)$_{12}$H$_3$] as a probe of the hydroxylated surface. The EPR evidence, supported by IR, revealed that the probe reacted preferentially with the Ti^{3+} sites, becoming deprotonated and forming Ti^{4+} sites with associated OH groups. It was proposed that this step removes most of the oxygen radicals and heals the defect sites. Interestingly, the authors[39] observed Ti^{3+} signals and O_2^- signals in their vacuum reduced sample (without any oxygen exposure), presumably a peculiarity of their hydroxylated material and adopted experimental conditions. As the authors point out,[39] their findings are contrary to the results of Carter et al.[38] However it must be stressed, that the Ti^{3+} and O_2^- signals identified by Carter et al.,[38] were formed on a dehydroxy-lated surface that had first been reduced at 773 K under vacuum, then exposed to excess oxygen at that temperature for one hour (to reoxidise any Ti^{3+} signals and destroy O_2^- species at these high temperatures) before being cooled to room temperature under this oxygen atmosphere. After final removal of the residual oxygen, no paramagnetic signals were found; this process has been widely described in the literature over the years (see for example the classical and early works of Che[40]) so the observation is not unique to the Carter[38] study.

Heterogeneous oxidation of organic pollutants and volatile organic compounds is extensively used for the remediation of waste water and as a means of indoor air purification. As a result several groups have begun to use EPR to probe the nature of the transient radical species involved in these heterogeneous photocatalytic processes.[41–44] Whilst the reactions between surface radicals derived from O_2, H_2O or OH groups and adsorbed substrate have received considerable attention, the participation of organic radicals involving $^{\bullet}OH$, $^{\bullet}OOH$ and $ROO^{\bullet}$ has been largely overlooked. Despite the well known participation of organoperoxy species ($ROO^{\bullet}$) in the oxidation of organic compounds, their involvement in heterogeneous surface mechanisms has scarcely been considered to date.

Using EPR, Carter et al.,[42] demonstrated that a number of different organoperoxy species are indeed involved in the heterogeneous decomposition of ketones (such as acetone, 2-butanone, 4-heptanone, cyclopentanone and cyclohexanone) over dehydrated polycrystalline TiO_2 (P25). These species were generated by charge-transfer events associated with the photo-generated charge carriers in TiO_2. The trapped holes (O^-) were involved in the surface decomposition reactions by hole transfer to the adsorbed ketones (eqn (2)). Subsequent reactivity of the adsorbed cation radical with molecular oxygen leads to the formation of the peroxy species $ROO^{\bullet}$.

$$CH_3COCH_{3(a)} + O^-_{(s)} \rightarrow CH_3COCH_2^{\bullet}{}_{(a)} + OH^-_{(s)} \tag{2}$$

$$CH_3COCH_2^{\bullet}{}_{(a)} + O_{2(a)} \rightarrow CH_3COCH_2OO^{\bullet}{}_{(a)} \tag{3}$$

A similar mechanism was found to operate for other ketones and these generic alkylperoxy radicals of general formula $ROO^{\bullet}$ were characterised by the g values of $g_1 = 2.0345$, $g_2 = 2.009$, $g_3 = 2.003$, $A_{\parallel}(O^{17}O^{\bullet}) = 9.92$ mT, $A_{\parallel}(^{17}OO^{\bullet}) = 5.85$ mT. The ^{17}O data was instrumental in identifying the species as peroxy-based entities, since the ^{17}O hyperfine pattern is distinct for peroxy species possessing inequivalent oxygen spin densities.[42]

By comparison, the reduced Ti^{3+} centres ($g_{\perp} = 1.990$, $g_{\parallel} = 1.957$) were found to be directly and indirectly involved in the oxidative decomposition pathways of adsorbed ketones.[42] The Ti^{3+} involvement occurred either through the generation of stable EPR visible radicals (O_2^-: $g_3 = 2.026$–2.019, $g_2 = 2.008$, $g_3 = 2.003$) under oxygen rich conditions or through the participation of unstable EPR invisible radical

intermediates ($\{CH_3COCH_3^{\cdot-}\}*$) under low oxygen atmospheres.[42] The latter species were found to disproportionate to form methyl ($CH_3^{\cdot}$) and acyl ($CH_3CO^{\cdot}$) radicals, which ultimately react with oxygen forming the corresponding organoperoxy radicals ($CH_3OO^{\cdot}$: $g_3 = 2.034$, $g_2 = 2.007$, $g_1 = 2.003$ and $CH_3CO_3^{\cdot}$: $g_3 = 2.012$, $g_2 = 2.008$, $g_1 = 2.003$). The O_2^- anions were also shown to selectively react with the adsorbed acetone (depending on the temperature) to form an associated paramagnetic [acetone-O_2^-]$_{(a)}$ surface complex, which can also be classified as an organoperoxy type species with g values of $g_3 = 2.035$–2.032, $g_2 = 2.008$, $g_1 = 2.003$. All of these radical intermediates were shown to be thermally unstable above 250 K.[42]

In a separate study of the photocatalytic oxidation of toluene over TiO_2 powders, Coronado and Soria[43] identified a series of oxygenated radicals including O^-, O_2^-, O_3^- as well as Ti^{3+} centres. The proportion of these species was found to depend on the gaseous environment. In contrast, co-adsorption of toluene and oxygen over irradiated TiO_2 resulted in the appearance of a new EPR signal assigned to a benzylperoxy radical (Ph-$CH_2OO^{\cdot}$: $g_3 = 2.035$–2.034, $g_2 = 2.008$, $g_1 = 2.003$). The mechanism of formation is analogous to that described by Carter et al.[42] It therefore appears that these surface organoperoxy radicals may be more abundant in heterogeneous oxidative processes than previously thought. Their thermal instability may partly explain why they have not been widely detected to date and at least these findings emphasise the need to perform the experiments at low temperatures if a complete picture of the decomposition pathways is to emerge.

Murata et al.,[45] published recent results showing how the photoformed O_3^- species on highly dispersed TiO_2 are the active oxidation species for the epoxidation of propene. This work was extended to other light alkenes, such as ethene and butene and the electronic structure of the O_3^- species and the reaction mechanism of the insertion of atomic oxygen into the C=C bond in the olefin was confirmed by EPR. Using $^{17}O_2$ a complex signal arising from superimposed O_2^- and O_3^- species was identified. By computer simulation, the spin Hamiltonian parameters for both radicals were identified as $g_{xx} = 2.0025$, $g_{yy} = 2.0090$, $g_{zz} = 2.025$, $^{17}OA_{xx} = 7.51$ mT, $^{17}OA_{yy} = {}^{17}OA_{zz} = 0$ mT and $g_1 = 2.0080$, $g_2 = 2.003$, $g_3 = 2.0026$, $^{17}OA_1 \approx {}^{17}OA_2 \approx 0$ mT, $^{17}OA_3 = 7.86$ mT, respectively. By deconvolution of the hyperfine tensor, the spin densities on the oxygen nuclei were extracted and the role of the ozonide radical in the epoxidation mechanism clearly proven.

Whilst this current SPR review has focussed on traditional polycrystalline TiO_2 systems, some mention must be finally devoted to the growing importance of titania nanotubes, microporous titanosilicates and layered titanate nanostructures where EPR is being used. Cho et al.,[46] detected a sharp symmetrical EPR signal ($g = 2.003$) assigned to a single electron trapped oxygen vacancy, while a broader asymmetric signal ($g = 1.98$) was attributed to a surface oxygen vacancy related to the Ti^{3+} sites in the reduced nanotube matrix. In the titanosilicate[47] a variety of oxygen centred radicals, including O^-, O_2^- and O_3^- were detected by EPR under continuous illumination conditions, again illustrating the importance of EPR in probing such materials. Riss et al.,[48] also investigated the transfer of photogenerated charges across the gas–solid interface of layered nanostructures for the first time using O_2 as an electron scavenger. While O_2^- species were readily identified ($g_1 = 2.0198$, $g_2 = 2.0093$, $g_3 = 2.0033$) a second unidentified defect with $g = 2.0031$ was also observed.[48] This important study revealed how charge separation can be controlled depending on the morphology of the material.

As in previous years, a large number of studies have been devoted to the characterisation of TiO_2 photoactivity for general oxidation reactions and for understanding the mechanism of photosensitisation, using the spin-trapping technique.[49–57] The numerous short lived radicals formed at the gas-solid interface in heterogeneous oxidative processes can be readily transformed into more stabilised and thus longer-lived ones by spin-trapping, so unsurprisingly this approach continues to be widely exploited. In an excellent EPR study of photoactivity,

Zalomaeva et al.,[49] investigated the mechanism of H_2O_2 based oxidation of alkylphenols over titanium single-site catalysts, such as TS-1. The mechanistic features of this important oxidation catalyst have been described in numerous reviews and two general mechanisms are reported for the selective catalytic oxidation of phenols; a homolytic mechanism (1 electron pathway) and a heterolytic oxygen atom transfer mechanism (2 electron pathway). Both mechanisms were tested by Zalomaeva et al.,[49] via the selective oxidation of 2,3,6-trimethylphenol (TMP) over H_2O_2/TS-1. The formation of phenoxyl and hydroxyl radical intermediates during the oxidation process were identified using 3,5-dibromo-4-nitroso-benzene-sulfonic acid (DBNBS) and 5,5-dimethyl-1-pyrroline-N-oxide (DMPO). The EPR spectra were extremely well resolved and therefore easily assigned to the DMPO-$^{\bullet}$OH and DBNBS-ArO$^{\bullet}$ adducts. By varying the nature of the organic substrate and reaction temperature, the evidence clearly supported a homolytic oxidation mechanism.

A variety of spin traps have been reported recently to evaluate the photoactivity of TiO_2 nanoparticles,[50–52] fluorinated TiO_2,[53] polyoxometalate modified TiO_2[54] and mechanically modified titania,[55,56] including DMPO, 3,3,5,5-tetramethyl-1-pyrroline-N-oxide (TMPO), alpha-(4-pyridyl-1-oxide)-N-tert-butylnitrone (POBN), 4-(N-methylpyridyl)-N-tert-butylnitrone (MePyBN) as well as semi-stable free radicals such as TEMPOL and DPPH. The latter radicals were used to correlate the observed activities to the results from spin trapping. The signals from TEMPOL and DPPH were found to gradually diminish upon irradiation of the TiO_2 and thus can be effectively used as a simple technique for the evaluation of TiO_2 photoactivity,[50] although unlikely to replace the traditional spin trapping approach.

Finally, an interesting multifrequency EPR and ENDOR study (X- and W-band) of the DMPO-O_2^- and PBN-$HO_2^{\bullet}$ adducts formed in the photosensitization of TiO_2 nanoparticles with carotenoids has been reported by Konovalova et al.[57] It was shown that the carotenoids facilitated the generation of the superoxide radical and singlet oxygen in the irradiated suspensions. The dismutation of O_2^- was proposed to generate singlet oxygen through the intermediacy of $HO_2^{\bullet}$. Higher frequencies were employed in an attempt to gain extra resolution of the spin adducts (to separate the g values of different adducts).[57] However, in this case only the PBN-$HO_2^{\bullet}$ species was identified in addition to a broad Ti^{3+} feature not visible at X-band (the latter signal is not surprising considering the TiO_2 powder was illuminated). X-band ENDOR measurements were also performed on the PBN adducts. The spectra were however extremely broad and poorly resolved and without simulation to support the assignment, the authors ascribed the ENDOR signals to two different ^{14}N and ^{1}H patterns; suggesting PBN-O_2^- and PBN-$HO_2^{\bullet}$. Nevertheless the paper[57] offers a good illustration of how advanced EPR methodologies can help resolve spectra in spin-trap EPR experiments.

3.2 ZrO_2

Zirconia-based oxides are widely used as heterogeneous catalysts, particularly in reactions involving dehydration, polymerisation and Fisher-Tropsch synthesis, among others. It has been known for many years[58] that ZrO_2 surfaces possess various surface active sites simultaneously (i.e., acidic and basic), as well as oxidising and reducing sites and several spectroscopic techniques have used probe molecules to investigate these sites. A commonly used EPR surface probe is O_2^- and once again several papers have re-examined the surface properties of modified ZrO_2 by this method in the review period.

Bedilo et al.,[59,60] used in situ EPR to compare the various thermal and light-induced processes responsible for the generation of O_2^- on zirconia and sulphated zirconia surfaces. The same g-tensors were obtained regardless of the generation methods (e.g., UV-illumination, oxygen co-adsorption with hydrocarbons, etc.). It seemed these methods did not disrupt the surface environment of the metal ions

where the superoxide radicals were stabilised. Subsequently the g values (specifically g_z) were used to qualitatively estimate the relative strengths of the Lewis acid sites in various zirconia-based systems.[60] These values were much smaller for sulphated zirconia, indicating stronger Lewis acid sites. The authors[59] also used cluster model DFT calculations to predict the g values for the surface O_2^- species and reported values of $g_z = 2.0327$, $g_y = 2.0093$, $g_x = 2.0017$. This g-tensor was consistent with a T-shaped $Zr^{4+}\cdots O_2^-$ bonding model (side on) and the Zr–O–O angle was found to slightly affect the magnitude of the g values.

Il'ichev et al.,[61,62] also studied the profile of the adsorbed O_2^- anion on ZrO_2. In this case, the anion was formed during $NO + O_2$ adsorption on the Zr^{4+} and O^{2-} Lewis sites. The radical produced well defined g values with $g_1 = 2.033$, $g_2 = 2.008$ and $g_3 = 2.003$, analogous to those reported by Bedilo et al.,[59,60] and typical of a coordinatively unsaturated Zr^{4+} ion at the adsorption site. The authors then investigated how polar molecules, such as ammonia and methanol, interacted with these adsorbed radicals and observed a shift in the g_1 component from 2.033 to 2.042. This was attributed to a decrease in the effective charge of the Zr^{4+} cations in the $Zr^{4+}\cdots O_2^-$ complexes (i.e., a weakening of the electrostatic interaction) due to interaction with NH_3 and CH_3OH. This paper[61] nicely illustrates how subtle perturbations to oxide surfaces can be easily investigated through the well known crystal field sensitive nature of the O_2^- probe.

Zhao et al.,[63] focussed on the EPR properties of the surface Zr^{3+} ion itself (rather than probing the Zr^{4+} ion via the O_2^- probe[59–62]). Well defined axial signals typical of Zr^{3+}_{surf} were identified with $g_\perp = 1.975$ and $g_\parallel = 1.957$. These centres were classified as coordinatively unsaturated Zr sites located at the corner of ZrO_2 microcrystallites. The formation of these reduced centres was then explored under a range of different atmospheres and temperatures. A most curious result was obtained when ZrO_2 was treated under H_2 at elevated temperatures (up to 600 °C). In addition to the earlier observed Zr^{3+} signal, new peaks appeared which were assigned by the authors[63] to O_2^- ($g_1 = 2.031$, $g_2 = 2.009$, $g_3 = 2.000$) and an F-centre ($g = 2.000$). The latter signal was interpreted as an electron trapped in an oxygen vacancy and indeed it was located at the surface since it easily reacted with molecular oxygen forming O_2^-. However, it is not clear why the electron would be stabilised in such a vacancy site, when it could easily form reduced Zr^{3+} ions with the "walls" of the vacancy. Surface localised conduction electrons (as observed in TiO_2) should also be considered as an alternative explanation. Carrasco-Flores and LaVerne[64] also studied the properties of surface species (Zr^{3+} and O_2^-) on irradiated ZrO_2 nanoparticles. Unfortunately, the spectra of the surface species were poorly resolved and no g values were given, so it is difficult to accurately compare their data to the other published work.[59–63]

Owing to its high surface area and cheap readily available form, ZrO_2 is frequently used as a support for highly dispersed and catalytically active metal oxides including vanadium oxides,[65–67] tungsten oxides,[68] gallium oxides[69] and copper oxides.[70–77] Several of the EPR studies in this field however focussed qualitatively on the paramagnetic properties of the supported phase rather than the support (ZrO_2) itself. However, in an excellent paper by Occhiuzzi et al.,[68] well defined spectra of O_2^- radicals were observed arising from Zr^{4+} sites. The EPR evidence revealed two different kinds of surface species, namely small tungsten clusters and polyoxotungstates, in addition to minor amounts of W^{5+}. This study nicely illustrates how EPR can be used to distinguish and characterise the nature of the active species in such supported heterogeneous catalysts.

Finally, a number of studies also examined the nature of paramagnetic defects in sub-surface regions of ZrO_2.[78] Wright et al.,[78] observed axially symmetric EPR spectra corresponding to Zr^{3+} centres. Upon grinding the sample to a fine powder and/or exposing them to γ-radiation, further EPR spectra revealed the presence of additional paramagnetic defects. These defects were attributed to the presence of

oxygen at the near surface region, indicating the possibility of association with oxygen hole-type centres.[78]

3.3 CeO$_2$

Ceria based catalysts are often used for different applications including electro-catalysis over fuel cell electrodes, removal of SO$_x$–NO$_x$ compounds and in three-way catalysts for automobile exhaust emissions. In many of these applications, the ceria component of the catalyst, usually with CeO$_2$ acting as support, are thought to operate mainly as redox states promoting the activity of the primary metal oxide, particularly at interfacial regions. With these possible changes in redox state (Ce$^{4+/3+}$), coupled with a range of possible paramagnetic surface species, EPR spectroscopy has again been widely used to study these systems. A series of excellent papers[79–81] demonstrates this important role played by EPR as described below.

Irradiation of a CeO$_2$ nanoparticle at an appropriate energy ($\lambda < 400$ nm) induces a band gap transition resulting in the formation of electron-hole pairs. Hernández-Alonso et al.,[79] studied the photogenerated charge carrier capabilities of CeO$_2$ samples in both the presence and absence of spin-trapping agents (O$_2$ or DMPO). EPR revealed that these charge carriers can reach the CeO$_2$ surface and can be trapped forming either OH$^\bullet$ radicals (resulting from holes) or, in the presence of oxygen, O$_2^-$ species (resulting from electrons).[79] The EPR parameters for the DMPO-OH$^\bullet$ adduct were reported as $g = 2.0056$, $a_N = 1.5$ mT and $a_H = 1.5$ mT while the O$_2^-$ species were characterised by $g_\parallel = 2.039$, 2.034–2.033 and $g_\perp = 2.011$ for the species adsorbed at isolated vacancy sites and $g_\parallel = 2.044$, $g_\perp = 2.010$ for the species adsorbed on more uncoordinated Ce cations. Oxygen photoadsorption data from EPR analysis allowed assumptions to be made concerning the photocatalytic activity of the nanoparticles in relation to charge separation process efficiency.[79]

The group also studied the formation of oxygen radicals on copper oxide supported ceria.[81] Well defined signals due to (i) Ce$^{4+}\cdots$O$_2^-$ species at CeO$_2$ sites and (ii) Ce$^{4+}\cdots$O$_2^-$ species at copper oxide-ceria interfacial positions were identified with g values of $g_\parallel = 2.036$, $g_\perp = 2.011$ for (i) and $g_z = 2.030$, $g_y = 2.018$, $g_x = 2.013$ for (ii). These g values are entirely consistent with those expected for an O$_2^-$ centre adsorbed at Ce^{4+} sites.[81] However, an additional signal was also observed with reverse g values ($g_\perp = 2.048 > g_\parallel = 1.978$) which are not typical of O$_2^-$. The signal was therefore tentatively assigned to an Ce$^{3+}\cdots$O$^-$ entity.[81] This species is likely to be very unstable, with respect to the Ce$^{4+}\cdots$O^{2-} state, but it was proposed to be present as a metastable species under the adopted (low temperature) conditions.[81] Labelling experiments with ^{17}O will certainly clarify the assignment. The possible presence (and chemistry) of such a species on the ceria surface is most interesting, but it remains unclear why no extensive electron-electron interactions occur in this paramagnetic species.

Il'ichev et al.,[82] studied the formation of O$_2^-$ radical anions upon CO+O$_2$ adsorption on oxidised CeO$_2$ surfaces under different conditions. The subsequent interactions of the radical with NO, NH$_3$ and CO were also studied. The EPR spectra were extremely well resolved and a clear heterogeneity of peaks in the g_{zz} region (of O$_2^-$) could be clearly resolved. Rhombic ($g_1 = 2.029$, $g_2 = 2.016$, $g_3 = 2.011$) and axial ($g_\parallel = 2.037$, $g_\perp = 2.011$) signals were identified and assigned to O$_2^-$ radical anions located in the coordination sphere of Ce^{4+} cations at isolated anionic vacancies. Most unusual however was the observation of a series of peaks at lower field ($g = 2.045$, 2.052).[82] These signals were assigned to the g-tensor of the form $g_1 = 2.052$, $g_2 = 2.009$, $g_3 = 2.006$ and $g_1 = 2.045$, $g_2 = 2.011$, $g_3 = 2.009$ (it is unclear how these g_2/g_3 components were determined) and were attributed to O$_2^-$ radicals adsorbed on cations associated with anionic vacancies possessing increased electron density. It was therefore suggested that the sites were Ce$^{3+}\cdots$O$_2^-$.[82] By analogy to previous work,[81] reduced Ce^{3+} centres may be able to trap paramagnetic centres and produce EPR signals. In this case, it is not clear why the Ce^{3+} centre is not oxidised by

molecular oxygen forming the more stable $Ce^{4+}\cdots O_2^-$ state, or why the initially formed O_2^- species are not trapped at Ce^{4+} sites (as opposed to Ce^{3+} sites).

An attempt to correlate the surface defect sites of ceria with the catalytic activity (for the oxidative dehydrogenation of ethylbenzene in the presence of N_2O) was reported by Murugan and Ramaswamy.[83] They found a good correlation between the concentration of Ce^{4+}–O^-–Ce^{3+} type defects and the reaction rates. The EPR parameters of the latter defect were typical of Ce^{3+} centres ($g_\perp = 1.96$, $g_\parallel = 1.933$). This defect should not be confused with the $Ce^{3+}\cdots O^-$ entity discussed above. However Murugan and Ramaswamy[83] also report that the oxygen ion mobility from the subsurface during the oxidative dehydrogenation occurs, as confirmed by the increase in signal intensity of a surface O^- centre ($g_\perp = 2.035$, $g_\parallel = 2.001$). No EPR spectrum for such a centre was shown (either in the paper or supplementary material), so it is difficult to confirm this assignment and indeed more interestingly, the nature and surface adsorption site for the O^- centre itself.[83]

In the midst of all the recent papers using O_2^- as a surface probe of defect sites on metal oxides, it is easy to forget that other paramagnetic probes can also be used just as successfully. This was demonstrated by Adamski et al.,[84] who investigated the surface composition of $Ce_xZr_{1-x}O_2$ solid solutions using NO and NO_2. The paper provides an elegant demonstration of how IR and EPR combined can be used to probe surface structure. A well defined rhombic signal with $g_x = 1.997$, $g_y = 2.000$, $g_z = 1.908$ and $|^N A_x|g\beta_e = 3.1$ mT, was assigned to a ligand centre radical complex $\{Ce–NO\}^{1*}$. This mononitrosyl complex dominated the EPR spectrum at low ceria loadings, but as the ceria content increased signals assigned to surface dimers $(NO)_2$ were also observed. These dimers were characterised by their easily recognisable fine structure features ($D \approx 22 \pm 1$ mT) originating from dipolar interactions between the unpaired electrons of the two adjacent NO molecules.[84] As a stable 17 electron paramagnetic molecule, NO_2 should produce a detectable EPR signal. However, after adsorption onto the $Ce_xZr_{1-x}O_2$ surface, only an EPR signal with $g_{av} \approx 1.99$ was observed suggesting adsorbate disproportionation or coupling occurs.

Aboukais et al.,[85,86] also performed work on doped transition metal oxides supported on ceria. These were found to possess considerable stabilisation effects on the O_2^- radical ions adsorbed on the ceria lattice. Octahedral voids in and on the lattice with adjacent oxygen vacancies were suspected to be responsible for forming the O_2^- species. Electron transfer was investigated along with oxygen vacancies (both higher for alumina-based samples) and results were derived from the variation in interaction between the active phase and the support (silica alumina). It was found that the superoxide radical formed relatively easily in the lattice giving rise to an understanding of how the lattice reflects considerable oxygen mobility at ambient temperatures. The observed effects were concluded to show importance for catalytic oxidation when relating to the high activity of the prereduced ceria catalysts and low activity of oxidised ones. Further research[87] also employed EPR to study the reducibility of Ce–Al–O and Cu–Ce–Al–O solids, with a focus on investigating the different oxide species generated.

Babu et al.,[88] have used EPR spectroscopy to show how ceria nanoparticles (3–5 nm) can be used as oxygen free radical scavengers at low concentrations. Using DMPO as a spin trap, the variations in DMPO-OH$^\bullet$ adduct concentration as a function of various experimental conditions was monitored by EPR. Lower concentrations were found to yield superior catalytic activity, compared to those at higher concentrations. At higher concentrations a reduction in the effective catalytic surface sites available for radical scavenging was found.

3.4 V_2O_5 Oxides

Vanadia based catalysts have many uses in heterogeneous catalysis, ranging from oxidative transformations and ammoxidation reactions, to selective catalytic reduction of NO_x with NH_3. In all cases, paramagnetic vanadium species are involved, so

EPR is widely used to characterise these systems. The g and A parameters are usually sufficiently well resolved that detailed information on the V^{4+} species can be obtained and interpreted in terms of local environment, micro-structural changes and bonding features of the ion. In the current review period, EPR has been used in this manner to characterise V_2O_5 supported on various metal oxides including TiO_2,[89–91] ZrO_2,[93–95] CeO_2,[96] SiO_2,[97] Al_2O_3,[98] Nb_2O_5[99] or as the bulk vanadium oxide itself.[100–102]

Using a combination of EPR, UV-Vis and laser-Raman spectroscopy Bruckner and Kondratenko[89] investigated the catalytic activity of vanadia supported on TiO_2 for the oxidative dehydrogenation of propane. The simultaneous measurement of all three spectroscopic techniques ("operando") revealed the changes in vanadium oxidation state during the reaction. Two well defined VO^{2+} signals were identified and characterised by the parameters $g_\parallel = 1.939$, $g_\perp = 1.973$, $A_\parallel = 18.0$ mT, $A_\perp = 5.43$ mT and $g_\parallel = 1.925$, $g_\perp = 1.983$, $A_\parallel = 19.9$ mT, $A_\perp = 7.64$ mT, respectively. It was proposed that these two different vanadyl species arose from VO^{2+} bonded to sulfate dopants and bonded directly to TiO_2. The latter species was selectively reduced to a diamagnetic state as the time on stream increased.[89] At elevated temperatures, the TiO_2 support itself was reduced and in the presence of molecular oxygen surface O_2^- radicals were formed in addition to bulk Ti^{3+}. The labelling of the EPR spectrum in ref. 89 is somewhat ambiguous suggesting the O_2^- radical has values of $g_1 = 2.025$, $g_2 = 2.008$, $g_3 = 1.989$ and Ti^{3+} has a g value of 1.944. This is likely a misprint and the correct assignment is $g_\parallel = 1.944$, $g_\perp = 1.989$ for Ti^{3+} and $g_1 = 2.025$, $g_2 = 2.008$, $g_3 = $ unresolved (≈ 2.003) for O_2^-. The same group also used the 'operando' approach to study the reactions of butene with titania supported vanadia.[90]

The uniform dispersion of the vanadia on oxide surfaces is instrumental to achieving optimal catalyst performance and many studies have employed EPR to investigate the preparative conditions on the resulting dispersed VO_x phases.[92–95] Adamski et al.,[92] considered two different preparation methods for VO_x/ZrO_2 catalysts (slurry deposition and wet impregnation) and compared them using EPR. Surface oxovanadium clusters ($g_\parallel \approx 1.952$, $g_\perp \approx 1.979$) were found on both catalysts and their spectroscopic features were largely insensitive to the preparation method. However, magnetically isolated V^{4+} centres were also identified with axial EPR signals that differed markedly for the two catalysts. These V^{4+} centres were characterised by the spin Hamiltonian parameters of $g_\parallel = 1.930$, $g_\perp = 1.979$, $A_\parallel = 18.5$ mT, $A_\perp = 6.1$ mT and $g_\parallel = 1.925$, $g_\perp = 1.977$, $A_\parallel = 17.9$ mT, $A_\perp = 6.4$ mT, respectively for the impregnation and slurry treatments. These signals are consistent with vanadyl ions in square pyramidal or tetragonally distorted octahedral coordination with approximate C_{4v} symmetry. Furthermore, the distortion of the surface vanadyl complexes can be gauged by the factor $B = (g_\parallel - 2.0023)/(g_\parallel - 2.0023)$, which was different in both catalysts. The EPR spectra of the calcined catalysts, revealed a differing trend in the reduction of the isolated V^{4+} ions and this information was discussed in terms of optimal preparation and pre-treatment conditions for these catalysts. From an EPR perspective, this excellent paper reveals the power of EPR to fully interrogate and characterise such heterogeneous catalysts.[92]

De and Kunzru[93] also studied the VO_x/ZrO_2 system, modified with potassium and calcium ions, as a catalyst for oxidative dehydrogenation. They observed weak V^{4+} signals with EPR parameters of $g_\parallel = 1.98$, $g_\perp = 2.03$, $A_\parallel = 17.4$ mT, $A_\perp = 6.6$ mT. This assignment is not completely correct since $g_\perp$ for V^{4+} must be less than 2.0023 (no simulations were given[93]). The authors also reported the presence of octahedral and tetrahedral V^{4+} species, based on changes in temperature dependent behaviour of the EPR spectra, but unfortunately they do not give the precise g values for both species. Nevertheless it is clear from the results that surface vanadia was reduced under oxidative dehydrogenation reaction conditions, the primary aim of this study. In an analogous study, Chary et al.,[94] used wet impregnation to prepare their $VO_x/$

ZrO_2 catalyst, which in this case was used for ammoxidation of toluene to benzonitrile. Once again EPR confirmed the presence of tetrahedrally coordinated V^{4+} ions with parameters of $g_{\parallel} = 1.988\text{–}1.972$, $g_{\perp} = 1.992\text{–}1.989$, $A_{\parallel} = 19.1\text{–}17.7$ mT, $A_{\perp} = 6.5\text{–}7.1$ mT depending on catalyst loading. Unlike the work of Adamski,[92] no further details or analyses of the vanadium spectra were given.[94]

The redox properties of vanadia based ceria catalysts were also studied by combining EPR and TPR (temperature programme reduction).[96] The fresh, as-synthesised sample displayed no signals due to paramagnetic vanadium centres. Instead well resolved rhombic signals with $g < g_e$ were observed and easily attributed to Ce^{3+} ions from the CeO_2 background matrix. Following reduction at 400 °C, at least two separate V^{4+} signals were resolved: $g_{\parallel} = 1.923$, $g_{\perp} = 2.000$, $A_{\parallel} = 17.4$ mT, $A_{\perp} = 7.6$ mT and $g_{\parallel} = 1.890$, $g_{\perp} = 2.000$, $A_{\parallel} = 20.5$ mT, $A_{\perp} = 7.6$ mT.[96] These signals were easily identified as VO^{2+} species possessing octahedral symmetry with axial distortion. Perhaps more interesting was the appearance of a second EPR signal at $g = 3.956$ with eight hyperfine lines of $A = 9.6$ mT. This signal was assigned to the perpendicular component of one of the fine transitions corresponding to the V^{2+} (d^3) spectrum.[96] The theoretical estimation of the EPR parameters for a spin S = 3/2 within the limits of strong axial crystal field ($g\beta B \ll D$) predicts an axial spectrum with $g_{\parallel} \approx 2$ and $g_{\perp} \approx 4$, so the $g_{\parallel}$ region was presumably buried under the intense V^{4+} signals close to g_e. This V^{4+} species has not been observed on other oxides, so it may be a peculiarity of the ceria system, or alternatively it has been missed by other authors, as it is only visible at the low temperatures used by Abi-Aad et al.[96]

For the remaining supports, SiO_2,[97] Al_2O_3,[98] Nb_2O_5,[99] EPR was just one technique used among many others to characterise the nature of the dispersed vanadia species. On SiO_2, only the experimental EPR spectra were presented; no detailed analysis or simulations, to extract the spin Hamiltonian parameters, were given.[97] By comparison, on Al_2O_3[98] the spectra were carefully simulated so that reliable g and A values were obtained. At least two different V^{4+} sites were identified with parameters of $g_{\parallel} = 1.943$, $g_{\perp} = 1.967$, $A_{\parallel} = 17.6$ mT, $A_{\perp} = 5.3$ mT and $g_{\parallel} = 1.938$, $g_{\perp} = 1.971$, $A_{\parallel} = 17.5$ mT, $A_{\perp} = 5.3$ mT. These parameters are in good agreement with those (accurate) values found on TiO_2 and ZrO_2, suggesting the support has limited effect on g and A. However on Nb_2O_5,[99] the spin Hamiltonian parameters appear to be slightly higher. Chary et al.,[99] followed the changes to the V^{4+} signal as a function of vanadia loading on polycrystalline Nb_2O_5. Unsurprisingly, the EPR signal intensity increased up to a loading of 10 wt% and thereafter decreased, presumably due to larger crystallites of V_2O_5. The g and A values for the 4 wt% loading were $g_{\parallel} = 1.970$, $g_{\perp} = 1.987$, $A_{\parallel} = 19.4$ mT, $A_{\perp} = 7.5$ mT (similar values were obtained for the 2, 6 & 10 wt% loadings), noticeably higher than for TiO_2, ZrO_2, Al_2O_3, suggesting Nb_2O_5 may impart some alterations to the V^{4+} environment.

While many studies have utilised "traditional" metal oxides as supports for the active vanadia phase, Narayana et al.,[100] took a different approach and used the non-conventional AlF_3 as a support. This system was found to be a very efficient catalyst for the ammoxidation of 3-picoline to nicotinonitrile.[100] A comprehensive and thorough X-band EPR study was used to characterise the nature of the V^{4+} species. The g and A parameters extracted from the spectra were used to calculate the molecular orbital coefficients α^2 and β^2 defined by the suitable linear combinations of $g_{\parallel}$ and $g_{\perp}$ values (and $A_{\parallel}$, $A_{\perp}$) as follows:

$$\alpha^2 = 7/4[(A_{\parallel} - A_0)/P + 2/3g_{\parallel} - 5/21g_{\perp} - 6/7] \tag{4}$$

$$\beta_2^2 = -7/6\Delta g_{\parallel} + 5/12\Delta g_{\perp} + 7/6[(A_{\parallel} - A_{\perp})/P] \tag{5}$$

As the local structure around the V^{4+} ions changed, due to a change in V–O and V=O bond lengths, the EPR parameters and MO coefficients changed, so the authors were able to monitor precisely the state of the vanadia on the fluoride support. The results confirmed that the VO^{2+} ions are present in a distorted octahedral environment and the high activity for ammoxidation might be due to a

facile redox (V^{4+}/V^{5+}) mechanism. From an EPR perspective, the paper is an excellent illustration of how much information can be obtained from a full analysis of the vanadium EPR spectra and is highly recommended as an overview paper on how this information can be extracted and used.

Finally, Conte et al.,[102] used *in situ* spectroscopic techniques (XRD, Raman, EPR) to elucidate the structural properties of $VOPO_4$ catalysts at catalytically relevant temperatures and conditions (400 °C). A thermally metastable vanadium phosphate phase (ω-$VOPO_4$) was found to undergo a reversible and rapid bulk transition during operating conditions, triggered purely by a surface chemical reaction. This transition (from ω-$VOPO_4$ to δ-$VOPO_4$) was visible in the high temperature EPR spectra, after exposure to a stream of 1.5% butane in air at 400 °C. The transformation occurred by the formation of bulk oxygen vacancies and subsequent lattice oxygen mobility, under the reducing gaseous environment.[102] The metastable phase was only stable at these high temperatures, illustrating the importance of *in situ* spectroscopic techniques for catalyst characterisation and the need to undertake these *in situ* measurements at realistic conditions.

3.5 CrO$_x$ Oxides

Supported chromium oxides are industrially important catalytic materials used in oxidation, polymerisation, dehydrogenation-hydrogenation and $deNO_x$ reactions. In all these reactions the chromium ions undergo redox changes and several techniques, particularly XPS, DRS and EPR, are used to analyse the nature of the chromium active site and oxidation state. Despite the importance of these catalysts, relatively few EPR papers have appeared in the review period on supported CrO_x systems. Most of these have simply used EPR as an analytical technique to monitor the changing oxidation states of the chromium ions during the reactions.[103–107] In many cases, the spectra were broad and poorly resolved, but owing to the characteristic fingerprint of Cr^{3+} versus Cr^{5+}, many authors simply used EPR to monitor the relative changes to these two signal intensities as a function of catalyst reactivity.[107] It should be noted however, that several excellent papers have also appeared on Cr doped or exchanged micro-/meso-porous materials, particularly MCM. Since these microporous materials are not covered in this review, the interested reader is directed to an excellent paper by Lezanska et al.,[108] and references therein for an overview of this subject area.

Liotta et al.,[103] used EPR to monitor the changes in the redox state of the chromium ions in silica and zirconia supported Cr^{6+} oxide for benzyl alcohol oxidation. To gain more understanding on the active sites involved in the catalysis, fresh and aged catalysts were analysed by EPR. The samples were dominated by a broad ($\Delta H_{PP} \sim 50.0$ mT) isotropic signal at $g = 2.0023$, assigned to surface Cr^{3+} ions in α-Cr_2O_3 small particles. The spectrum also showed an axial signal ($g_\parallel = 1.958$, $g_\perp = 1.975$) arising from surface Cr^{5+} chromyl species.[103] The relative abundance of these different Cr species was found to vary depending on the support and based on this data the authors could demonstrate that alcohol oxidation occurred *via* a reduction step incorporating both surface and bulk Cr species.[103]

Although not a direct study of chromium oxides, a very nice EPR study of Cr doped WO_3 was reported by Morazzoni et al.[104] It is widely reported that transition metal doped WO_3 is an excellent material as an NH_3 gas sensing device, whereby the metal ions act as efficient redox centres during the reaction. The air annealed samples displayed a series of broad signals at $g = 3.5$–5.0 attributed to Cr^{3+} centres in strongly distorted octahedral symmetry and at $g = 1.98$ attributed to Cr_2O_3 type clusters.[104] After annealing at higher temperatures well defined axial ($g_\parallel = 1.886$, $g_\perp = 1.967$) and rhombic ($g_1 = 1.949$, $g_2 = 1.912$, $g_3 = 1.823$) signals appeared. These can be easily assigned to isolated surface Cr^{5+} chromyl species. The signal intensities were affected by the presence of NH_3, but the changes were most notable in the sharp Cr^{5+} resonances, as opposed to the broader Cr^{3+} signals. After contact with NO, an

extremely well resolved nitrosyl signal was identified, but it was suggested that this must arise from NO adsorption at W^{6+} sites. The experimental data was instrumental in identifying what oxidation states of chromium were important for NH_3 interactions and more importantly demonstrated the power of *in situ* EPR in monitoring such complex heterogeneous catalytic reactions.[104]

In a similar study of chromium oxides supported on silica, Amano *et al.*,[105] investigated the nature of the active oxygen species responsible for the photocatalytic oxidation of propylene using molecular oxygen. The photocatalytic active site was assumed to be the isolated tetrahedrally coordinated metal oxide sites (*i.e.*, excited $(M^{\delta-}\text{–}O^{\delta+})^*$ states), but it remains unclear what form the active oxygen centres take; either photoexcited lattice oxygen or photoformed O_3^- centres. EPR clearly revealed a change in oxidation state from Cr^{6+} to Cr^{5+} and Cr^{3+} during photocatalytic oxidation.[105] Several types of Cr centres were observed, including Cr^{5+} species (γ-signal; $g_\perp = 1.981$, $g_\parallel = 1.91$) and Cr^{3+} (δ-signal: $g = 4.4$–5.0). The increase of the δ-signal during irradiation and the decrease of the γ-signal clearly indicated the reduction of Cr^{5+} to Cr^{3+}. The results revealed that the type of terminal ligand (hydroxyl or oxo) of the tetrahedrally coordinated CrO_x species on silica decide the nature of the active oxygen species in photocatalytic oxidation.[105]

In a largely quantitative EPR study, Meichtry *et al.*,[106] studied the photocatalysis of Cr^{6+} in the presence of citric acid over TiO_2 particles. Since Cr^{6+} is used in various industrial processes such as leather tanning and paint making, efficient and cheap methods for its removal, are highly desirable; one such method is to photoreduce it to the less toxic Cr^{3+} species and this can be easily done using TiO_2 with suitable organic compounds acting as hole scavengers. Under irradiative conditions, the Cr^{6+} centres were reduced to Cr^{5+} and this rate was significantly enhanced in the presence of citric acid. The EPR spectra revealed that the Cr^{5+} centres were present as Cr^{5+}-citrate species ($CrO(CitH_2)_2^-$). The species was characterised by a $g_{iso} = 1.977$ and with well resolved ^{53}Cr hyperfine satellites ($a_{iso} = 1.87$ mT).

3.6 MoO$_x$ Oxides

Molybdenum oxide and surface supported Mo systems has remained an actively investigated area in the last four years. These oxide based catalysts are used industrially for the partial oxidation of hydrocarbons and alcohols such as methanol. In the latter case of methanol oxidation, the reaction is often used as a probe to test the catalytic performance of new catalyst formulations, since the reaction is very sensitive to the nature of the active site and the acidic properties of the surface. Since the EPR features of Mo^{5+} are easily identified, it is unsurprising that several of these mechanistic investigations of supported MoO_x systems have extensively utilised EPR and methanol as a probe.

In an operando EPR study, Brandhorst *et al.*,[109] studied the oxidation of methanol at evelated temperatures on a Mo/Al_2O_3 catalyst. The EPR spectra were supplemented by IR and Raman spectroscopies, which confirmed the changes in oxidation state of Mo, from Mo^{6+} to Mo^{5+}, during the reaction. After activation under oxygen, only a weak and poorly resolved signal attributed to residual traces of Mo^{5+} were found ($g = 1.926$).[91] However, under reaction conditions (*i.e.*, under a stream of He/CH$_3$OH or O$_2$/CH$_3$OH at 200 °C or 300 °C) a strong signal at $g = 1.938$ could be clearly seen: this was assigned to the Mo^{5+} oxo-molybdenum entities. The intensity of this signal during the reaction was monitored by EPR and quantified with reference to a Mo standard (chosen as an Mo(salen) complex).[109] The relaxation characteristics of the Mo centres in both systems (surface Mo/Al_2O_3 and Mo/Al_2O_3) will be very different, so a direct comparison of the integrals can sometimes be misleading. Nevertheless the trends in the EPR data are very apparent and in excellent agreement with the IR and Raman data.

Sojka and Pietrzyk[110] also investigated the structure sensitivity for selected Mo surface paramagnetic species involved in the oxidative dehydrogenation of methanol over silica grafted molybdenum catalysts. They used DFT to calculate the EPR parameters, which were compared to previously reported literature data. The initial sites for the reaction were the mononuclear Mo^{5+} centres, labelled Mo_{4C}/SiO_2 and identified by $g_\perp = 1.926$, $g_\parallel = 1.755$. After activation, the reactive $\{O^--Mo_{4C}\}/SiO_2$ centres are formed, identified by the parameters $g_\perp = 2.020$, $g_\parallel = 2.005$. These latter sites play a key role in C–H bond activation.[110] Dehydrogenation of methanol involves interaction of CH_3OH with this $\{O^--Mo_{4C}\}/SiO_2$ centre and subsequent formation of the $^\bullet CH_2OH$ surface trapped radical, characterised by $g_1 = 2.0055$, $g_2 = 2.0029$, $g_3 = 2.0021$. These g values were compared using DFT/GIAO calculations employing a spin restricted ZORA method and incorporating a local VWN functional. Excellent agreement was found between the experimental and theoretical values, particularly for the hydroxymethyl radical.[110] As discussed by Neese,[111] in a recent SPR review, DFT calculations have advanced to the stage that they significantly enhance the interpretation of experimental data, but one rarely sees this approach being used in heterogeneous catalytic systems. This excellent paper by Sojka and Pietrzyk[110] is one of the few that clearly illustrates this potential for unravelling surface mechanisms.

A large number of general catalysis papers have also appeared which incorporate EPR, among several other techniques, as an analytical method. Wang et al.,[112] studied the effects of fluorine addition to a titania supported Co–Mo catalyst, used in hydrodesulfurization. Surprisingly there is no evidence of any paramagnetic Co or Mo centres (even residual traces from the preparation methods would be expected) in their spectra. Instead they observed a symmetric signal at $g = 2.0023$, which they assigned to Ti^{3+} from the titania support. As a d^1 transition metal ion, Ti^{3+} should produce a signal with a negative g shift (i.e., $g < g_e$), so it is not clear what is the origin of the $g = 2.002$ signal in the Wang paper,[112] but it is unlikely to be a reduced titanium ion. In a similar study, Liu et al.,[113] studied the effects of chlorine modification on Mo/TiO_2 for oxidative dehydrogenation of propane using EPR. Their EPR spectra showed well resolved Mo^{5+} signals, which changed dramatically in the pre- and post-reduction catalysts, but surprisingly the authors only quoted a single $g_\perp$ value for their spectra (no $g_\parallel$ values or simulations were reported). A broad unresolved feature at $g = 2.011$ was also observed and assigned to surface O_2^-. Again no simulations were provided, so this assignment must be considered very tentative, since the signal lacks any structure or resolution.

Other catalysis studies have appeared on the characterisation of Mo supported on tellurium promoted silica,[114] ceria[115] and potassium promoted alumina.[116] In all cases, EPR was used simply to monitor changes in Mo oxidation state during the reactions under investigation; in particlar methanethiol synthesis,[96] partial oxidation of propene[115] and water–gas shift reaction.[116]

It should be mentioned that many of the EPR investigations involving the characterisation of Mo centres in heterogeneous catalysis are often based on microporous type materials such as alumino-phosphates,[117] faujasites,[118,119] and pentasils.[120,121] Unlike the situation for the supported Mo species on traditional supports such as silica or alumina, the highly dispersed metal ions are usually much better resolved, enabling the more accurate extraction of the spin Hamiltonian parameters. For example, new paramagnetic molybdenum species in a Mo/H-ZSM5 catalyst were identified for the first time as Mo^{3+} and Mo^{5+} in tetrahedral coordination.[119] Exceptionally well resolved EPR signals were obtained, enabling the easy extraction of g and ^{Mo}A tensors. These spin Hamiltonian parameters are discussed in detail and correlated to UV-Vis data. This beautiful study demonstrates the wealth of information available via EPR for isolated and well defined Mo spin systems in microporous materials.[119]

3.7 Iron oxides

Most of the recent papers related to iron oxides (FeO_x) have been concerned with the promoting effects that iron has on the catalytic performance of the catalyst. The catalysts in question are usually oxide based materials, such as ZrO_2,[122,123] TiO_2[124,125] or SiO_2[126] in which the iron is incorporated onto the surface or into sub-surface regions. In some cases the FeO_x activity can be further enhanced by the promoting effects of traces of other oxides (*e.g.*, Rb_2SO_4).[126] In most of these studies EPR was used to directly characterise the nature of the Fe^{3+} ions on the catalyst,[122–124,126] and in one case, for a titania based material, EPR was used to indirectly monitor catalyst performance at the liquid–solid interface using spin trapping.[125]

Wyrwalski *et al.*,[122] investigated the nature of bulk and surface iron in doped zirconia. It is well known that the photocatalytic activity of zirconia can be enhanced significantly by the promoting effects of iron. This enhancement has been linked to the higher activity of the metastable tetragonal phase of ZrO_2 and it appears that this phase can be stabilised by introducing iron into the lattice. The authors[122] therefore used EPR to probe the different structural phases of the catalyst as a function of calcination temperatures, since the EPR features of Fe^{3+} are very sensitive to the surroundings. The EPR spectra revealed two signals at $g = 4.80$ and $g = 4.27$ due to isolated Fe^{3+} ions possessing two different symmetries.[122] These signals were previously shown to arise from iron in monoclinic ($g = 4.80$) and tetragonal ($g = 4.27$) environments. The ratio of the two signals was therefore found to be a direct measure of the two different phases present in the catalyst. As the calcination temperature increased, the $g = 4.27$ peak increased, demonstrating the higher stabilisation of the tetragonal phase, in agreement with XRD results.[122] Zr^{3+} signals were also detected in the spectra, but this is not unexpected owing to the semi-conducting nature of the support and the high (reducing) temperatures.

Carrier *et al.*,[123] also investigated the promoting effects of iron in (tungstated) zirconia catalysts. The addition of transition metal oxides such as iron oxide was found to be beneficial for the catalytic performance in the isomerisation of straight chain alkanes. However, the nature and function of the iron promoters remains controversial, so using EPR (in combination with XANES) the Fe^{3+} environment was explored. Similar to the work of Wyrwalski *et al.*,[122] an isotropic signal at $g = 4.25$ was also detected and assigned to isolated octahedral or tetrahedral Fe^{3+} ions with strong rhombic distortion. In addition, a broad signal at $g = g_e$ was also detected and assigned to aggregated paramagnetic Fe^{3+} ions (effectively iron oxide nanoparticles) present on the zirconia surface.[123] After reduction under H_2, both of the paramagnetic iron signals decreased in intensity and this was accompanied by an increase in the intensity of a W^{5+} signal (W^{5+}: $g_\perp = 1.83$, $g_\parallel = 1.58$). This step was found to be reversible however, clearly proving that the iron centres are incorporated into the surface layers of the zirconia (as opposed to the bulk) and therefore readily available for reactions with surface adsorbates.[123]

The introduction of Fe^{3+} cations into the anatase lattice was found to have improved activity for the UV photocatalytic degradation of aqueous phenol.[124] Well defined Lorentzian lines were easily identified at $g = 4.30$ (narrow) and $g = 2.0$ (6 mT linewidth), but computer simulations revealed the presence of two additional underlying signals with g values close to g_e. These latter two signals had very broad features ($\Delta H_{PP} \sim 30$ mT and 130 mT) and therefore could only be identified by simulations. These signals were collectively assigned to Fe^{3+} centres in substitutional positions within the anatase structure and Fe^{3+} ions in a rhombic environment (attributed to the presence of oxygen vacancies in the anatase lattice). The EPR data, which revealed the nature of the incorporated Fe^{3+} ions was found to depend on the preparation method and was correlated to the catalytic data. This showed that effective Fe^{3+} incorporation was essential for enhanced catalytic performance.

The epoxidation of propylene with nitrous oxide on Rb_2SO_4 modified iron oxide on silica was also investigated by Moens *et al.*[126] In their very thorough and excellent

paper, the authors describe in detail the nature of the EPR signals and carefully considered all possible explanations to account for their g values and temperature dependencies. Three signals were observed; a dominant peak at g_{eff} = 4.39, accompanied by a broad shoulder at g_{eff} = 6.05 and finally a broad peak at g_{eff} = 2.01. As the authors correctly pointed out,[126] precise identification of the Fe^{3+} centre is not really possible based on g_{eff} values only; the correct zero field splitting parameters must be extracted *via* simulation for a confident assignment. Nevertheless extremely valuable qualitative data can still be obtained from the spectra by carefully considering the temperature dependencies of the signals, since the Curie-Weiss law (intensity $\sim 1/T$) can be used as a tool to discriminate between the different possible types of Fe^{3+} centres. In this way, Moens *et al.*,[126] were able to identify and classify the paramagnetic Fe^{3+} ions on the silica based catalyst as Fe^{3+} ions in large clusters (g_{eff} = 2.31; this signal was partially buried under the g = 2.01 signal), Fe^{3+} ions in small Fe_xO_y clusters (g = 2.01) and isolated Fe^{3+} ions in strong rhombic ($g_{eff} \sim 4.3$) and axial ($g_{eff} \geq 6$) distortion. Based on this data, the authors were able to propose a reaction pathway for propylene epoxidation with N_2O over the FeO_x catalyst and in particular explain the role played by the different Fe^{3+} species.

The dispersion of Fe^{3+} ions and FeO_x is of course significantly improved using microporous and mesoporous materials rather than the traditional polycrystalline oxides and the resulting EPR spectra generally show substantially improved resolution. As a result far more information can be obtained from the spectra. Although micro-/meso-porous materials are not covered in this review, some excellent catalysis studies involving Fe doped MCM,[127] MFI[128–131] and a beta zeolite[132] have been reported, providing excellent examples on the role of EPR in the characterisation of such materials.

3.8 Copper oxides

The properties of supported metal oxides are frequently very different compared to the bulk. This is due primarily to the interaction with the support and understanding the nature of this interaction is key to the development and optimisation of supported metal oxide systems in heterogeneous catalytic applications. This is particularly true in the case of copper oxides (CuO_x). Supported CuO_x catalysts are extensively used in a large number of chemical processes and in recent years efforts have moved away from the traditional alumina/silica supports to titania, ceria, zirconia and niobia supported CuO_x catalysts in an attempt to adjust the strength of the interaction between the dispersed phase and the support. These subtle support-oxide interactions are often reflected in the electronic properties of the CuO_x particles, so EPR is an ideal tool to monitor these structural changes. In the review period EPR has been used to monitor these interactions and papers have appeared on CuO_x supported on zirconia,[70–72,133] ceria,[74,81,88,134,135] silica–alumina[136] and activated carbon.[137]

Sagar *et al.*,[70] studied the properties of highly dispersed CuO_x phases on zirconia. At least two different Cu^{2+} signals were identified; the first was a well resolved axial signal, the second was a broad and poorly resolved species. The latter signal was easily attributed to clustered Cu^{2+} ions (the broad profile arising from spin-pairing due to the close proximity of the paramagnetic ions). On the other hand, the former signal was attributed to isolated Cu^{2+} ions in an axially distorted octahedral environment. The g and A values for this species varied systematically depending on the copper loading (*e.g.*, at 1 wt%, $g_{\parallel}$ = 2.37, $g_{\perp}$ = 2.07, $A_{\parallel}$ = 12.8 mT, $A_{\perp}$ = 11.6 mT: at 15 wt%, $g_{\parallel}$ = 2.41, $g_{\perp}$ = 2.08, $A_{\parallel}$ = 10.6 mT, $A_{\perp}$ = 13.6 mT). The values for $A_{\perp}$ are most unusual and based on the experimental spectrum shown in the paper actually wrong (such a large $A_{\perp}$ value is not evident from the spectrum).[70] One can only assume these values were misprinted in the table and should be reported as approximately 1.1–1.3 mT as opposed to 11–13 mT. In any case, the

perpendicular region of the spectrum was so poorly resolved, it is difficult to see how the authors were able to extract their $g_\perp/A_\perp$ spin Hamiltonian parameters so accurately. From a qualitative viewpoint, a systematic trend is certainly visible in the experimental EPR data which supports their main findings. In a related paper by the same group,[71] a similar set of EPR spectra and spin Hamiltonian parameters are reported for CuO_x on zirconia and again with the unusually high $A_\perp$ values of 14.6–15.3 mT. As stated above, these values are approximately an order of magnitude higher than that expected for Cu^{2+} in a distorted octahedral environment, so the reason for this is not clear.

Liu et al.,[72] also studied the dispered CuO_x particles supported on zirconia. Qualitatively their results were similar to those reported earlier,[70,71] with two dominant Cu^{2+} species identified in the EPR spectra. Species 1 was assigned to clustered Cu^{2+} centres, while species 2 was assigned to isolated Cu^{2+} centres. In the latter case, the spin Hamiltonian parameters ($g_\parallel$ = 2.38, $g_\perp$ = 2.04, $A_\parallel$ = 11.0 mT, $A_\perp$ = 3.0–3.5 mT) are entirely consistent with those expected for Cu^{2+} in a distorted octahedral environment. At low copper loadings, highly dispersed copper ion species were detected (species 2 dominated) while paired Cu^{2+} ions became the more abundant species at loadings near the dispersion capacity, as expected. These trends were clearly evident in the EPR data.

A similar approach was also adopted by several groups to characterise the dispersion and structure of copper oxides on ceria.[74,81,88,134,135] The group of Aboukais[88,134] investigated the EPR properties of calcined Cu–Ce–Al oxide systems. As expected in any supported CuO_x system, isolated and clustered Cu^{2+} species usually contribute to the broad EPR spectra and a similar observation was reported by Aboukais.[88,134] The isolated Cu^{2+} ions were characterised by the spin Hamiltonian parameters of $g_\parallel$ = 2.326, $g_\perp$ = 2.054, $A_\parallel$ = 12.8 mT, $A_\perp$ = 3.9 mT, while the clustered species were identified with the parameters g_{iso} = 2.140 and ΔH_{PP} = 40.0 mT. Since the intensity of the EPR signal can be correlated with the dispersion of Cu^{2+} centres, the authors were able to determine the distribution of Cu^{2+} on the support, including the EPR silent spin paired Cu^{2+} centres. At higher calcination temperatures, the profile of the EPR spectra changed dramatically and a new signal appeared which was assigned to Cu^{2+} dimers. This new signal displayed a fine structure corresponding to the $\Delta m_s = \pm 1$ transition of the triplet state, where the two signals with axial symmetry were observed. The spin Hamiltonian parameters for the dimer was $g_\parallel$ = 2.208, $g_\perp$ = 2.036, $A_\parallel$ = 8.6 mT, $A_\perp$ = 1.6 mT. This latter species was only observed for copper interacting with ceria, since the dimers were found to arise from strongly bonded Cu^{2+} centres on the surface O^{2-} anions of the ceria lattice. This is an important paper showing the importance of the support-oxide phase interaction and how it can be interpreted by EPR.

Martinez-Arias et al.,[81,135] investigated the redox behaviour of copper oxide catalysts supported on ceria, for the preferential oxidation of CO in a H_2 rich gas stream. Their results revealed the presence of mainly CuO_x-related species, which were highly dispersed over the nanosized ceria support. The isolated Cu^{2+} centres constituted only a minor part of the copper component and were characterised by the spin Hamiltonian parameters of $g_\parallel$ = 2.233, $g_\perp$ = 2.036, $A_\parallel$ = 16.0 mT, $A_\perp$ = 1.8 mT. It is not clear why the $g_\parallel$ values are so low ($g_\parallel$ = 2.233) compared to other reports for CuO_x on ceria and zirconia ($g_\parallel$ > 2.30). For a Cu^{2+} centre in a distorted octahedral environment, one would expect the $g_\parallel$ values to be higher than 2.233 (usually above 2.30), so presumably this low value reported by Martinez-Arias et al.,[81,135] is somehow related to the type of ceria they used (nanoparticles) and/or the very low levels of Cu^{2+} present. Nevertheless their interesting results showed that reduction of the catalysts at elevated temperatures starts from the interface positions followed by the CuO_x component and eventually extends to the ceria support positions not in contact with CuO_x. Once again, this paper shows how the intimate support—oxide phase interactions has been fully investigated by EPR.[81]

A final comment should be made regarding the EPR characterisation of isolated and highly dispersed copper ions in microporous materials. This field of research has once again been widely studied, particularly in light of the novel advanced microporous materials now available. An excellent review of this area has been reported by Berthomieu and Delahay,[138] highlighting some important EPR contributions in recent years. It is worth specifically mentioning some excellent EPR papers concerned with the characterisation of copper exchanged zeolites for deNO$_x$ catalysis including work by Pietrzyk et al.,[139] Smeets et al.,[140] and Kucherov et al.[141]

3.9 ZnO

Zinc oxide is not widely used as a catalyst or as a support in heterogeneous catalysts. Therefore only a handful of papers have appeared on the interfacial properties of ZnO of relevance to surface science and catalysis. Owing to its semiconducting properties, the formation of electron–hole pairs is quite facile under mild thermal, radiative or reductive treatments. Since the photo-formed oxygen vacancies (which are paramagnetic) are known to play a role in controlling the photoluminencence properties of ZnO, the characterisation of such defects by EPR is very important.

Kakazey and Vlasova[142] studied the surface defects formed on mechanically modified ZnO powders. As surface defects, their importance and relevance to heterogeneous catalysis is clear. A complex EPR spectrum was obtained following mechanical treatment and the numerous signals observed were assigned to specific defects, based on a comparison with known data from previous single crystal work. At least six different types of paramagnetic centres were formed. Among these, species 1 ($g_\perp$ = 2.0130, $g_\parallel$ = 2.0140) was assigned to a V_{Zn}^- defect, species 2 (g_1 = 2.0075, g_2 = 2.060, g_3 = 2.015) was assigned to a $(V_{Zn}^-)_2^-$ defect and species 3 ($g_\perp$ = 1.996, $g_\parallel$ = 1.995) was assigned to a V_O^+ defect. A good correlation was found between the ratio of the various defects formed and the conditions of mechanical treatment. So this work offers some insight into the possibilities of generated ZnO powders with controlled surface defect centres.

Dodd et al.,[143] used EPR and the spin trapping technique to correlate the photocatalytic activity of ZnO to the sizes and shape of the particles. The relationship between particle size and photoactivity is currently of topical interest, since ZnO particles with optimised sizes have been found to promote the destruction of intractable chemical waste in aqueous systems. The photocatalytic activity of these powders was characterised via EPR spectroscopy and measurement of hydroxyl radical concentration was achieved using spin trapping (DMPO). Various particle sizes were studied, ranging from 28–57 nm, but the 33 nm particles were found to have enhanced activity. This optimal size was related to the efficiency of the charge carrier recombination rate and the ability to find the correct balance between surface area and particle size; the higher the surface area, the more states were available for charge recombination.

4. p-Block metal oxides

p-Block metal oxides (Al$_2$O$_3$, SiO$_2$, Ga$_2$O$_3$, SnO$_2$) are widely employed as supports for catalytically active phases as discussed in section 3. In the following section we concentrate on the direct use of EPR to examine the nature of the support itself, which is a necessary prerequisite to understand the reactivity of supported active phases.

Aluminium oxide is widely employed in catalysis as an inert support for active metal species. However, a few papers have been reported, which focus on the properties of the oxide itself. In particular Popple and others have reported elegant CW and pulsed EPR studies aimed at unravelling the effect of non-thermal plasma (NTP) on non-porous and porous alumina model catalysts. A paramagnetic species probably related to an Al–O–O$^\bullet$ aluminium peroxyl group was formed by NTP

processes independently of the oxygen content of the gas atmosphere. The structure of the paramagnetic site was investigated by employing several spectroscopic tools (X- and Q-band EPR, electron spin echo envelope modulation (ESEEM) and EPR measurements after pre-deuteration).[144] An interesting application of EPR to a catalyst model system was proposed by Risse et al.,[145] who also studied the changes of the magnetic properties of ferromagnetic Co particles deposited on a thin alumina film grown on a NiAl(110) substrate as a function of thermal annealing.

A great deal of work involving EPR concerns the characterization of SiO_2 due to its use in semiconducting and opto-electronic devices. One of the most abundant and best characterized defects on SiO_2 is the E′ centre, which consists of a trapped hole at an oxygen vacancy. More than fifty years have elapsed since the first paper on the EPR spectrum of the E′ centre in silica and crystal was published,[146] and research on E′ centres is still an active topic of study. In the ensuing 50 years more than 3000 papers have been published in which the E′ centre is the primary topic or an important part of the papers and more than 15 varieties of E′ centres have been reported.[147] A new variety of the E′ centre was proposed in 2006 by Skuja et al.[148] This centre was characterized by a proton hyperfine splitting of 0.08 mT of the low-field peak in the derivative spectrum. The new E′ centre was assigned to a silicon dangling bond, with the Si atom bonded by two bridging oxygens and an OH^- group. This new centre, which was formed upon laser irradiation of wet silica, is similar to previously reported centres localized on the surface of SiO_2.[149] Density functional theory and theoretical modelling in general, is emerging as a powerful method to complement spectroscopic studies in order to elucidate the local environment of defective centres. The structure and spectroscopic properties of the paramagnetic nonbridging oxygen hole centre and of the E'_γ centre at the hydroxylated silica surfaces was therefore recently modelled.[150] In particular the g tensor, hyperfine coupling constants and the optical transitions between well localized defect states were found to be in excellent agreement with the experimental data for the silica surface. The generation of hydrogen related point defects in silicon layers was also observed following pulsed laser ablation of SiO and SiO_2 targets.[151] Silyl radicals ($\equiv Si^•H$) and silyl hydroperoxide (SiOOH) were detected by means of EPR and FTIR.

Considerable importance in current technological applications is defect control at the Si–SiO_2 interface. The dominant defect in this region is the so called Pb centre, which consists of a silicon dangling bond at the Si–SiO_2 interface. A combination of electron paramagnetic resonance (EPR) and minority carrier lifetime measurements were used to unambiguously demonstrate that the presence of a B diffusion layer at the surface of oxidized Si(111) wafers causes a significant increase in the interface defect density as well as interface recombination, compared to undiffused surfaces.[152]

Interesting studies deal with the toxic potential of mineral dusts, addressing the link between surface properties of micron-sized particle and fibers (silica and asbestos) and the generation of free radicals. A review article addressing these issues has recently appeared in the literature.[153]

Among the reducible metal oxides that are used as catalyst supports, titania, zirconia, ceria and zinc oxides are the most commonly used. Tin oxide is less used as a catalytic material. However it is an extremely important system in gas sensing as its electrical properties are greately influenced by the sourrounding atmosphere. Key to this behaviour is the presence of oxygen deficient centres ($V_0^•$, $V_0^{••}$), which can be reduced at relatively low temperature to the corresponding radical anion. Owing to the importance of these paramagnetic centres, EPR has played a key role in the characterization of this system. While the conductivity of SnO_2 is very sensitive to the sourrounding atmosphere, the selectivity towards a given gas is low and can be improved by metal dopants (Ru, Pt). For example, tin dioxide and ruthenium(platinum)-doped tin dioxide were synthesized in the form of inverted opals, aiming to investigate the interaction of these materials with CO reducing gas.[154] The results of this EPR investigation are interpreted in terms of formation of singly ionized oxygen vacancies

located in the subsurface region following interaction with CO. The so formed centres transfer their electrons to transition metal centres, Ru or Pt, enhancing the SnO_2 surface reactivity towards CO. The reduction of Ru^{4+} and Pt^{4+} was assessed both by EPR and Mossbauer spectroscopy. Resistance measurements showed that the materials are well-suited for use in CO sensor devices because of their reproducible and fast electrical response.

References

1   (a) D. M. Murphy and M. Chiesa, *Specialist Periodical Reports, Electron Spin Resonance*, 2004, **19**, 279; (b) D. M. Murphy and E. Giamello, *Specialist Periodical Reports, Electron Spin Resonance*, 2002, **18**, 183.
2   M. Chiesa, E. Giamello, C. Di Valentin, G. Pacchioni, Z. Sojka and S. Van Doorslaer, *J. Am. Chem. Soc.*, 2005, **127**, 16935.
3   E. Finazzi, C. Di Valentin, G. Pacchioni, M. Chiesa, E. Giamello, H. Gao, J. Lian, T. Risse and H.-J. Freund, *Chem. Eur. J.*, 2008, DOI: 10.1002/chem200702012.
4   J. C. Lian, E. Finazzi, C. Di Valentin, H.-J. Gao, T. Risse, G. Pacchini and H.-J. Freund, *Chem. Phys. Lett.*, 2008, **450**, 308.
5   M. Yulikov, M. Sterrer, M. Heyde, H. P. Rust, T. Risse, H.-J. Freund, G. Pacchioni and A. Scagnelli, *Phys. Rev. Lett.*, 2006, **96**, 146804.
6   M. Chiesa, F. Napoli and E. Giamello, *J. Phys. Chem. C*, 2007, **111**, 5481.
7   F. Napoli, M. Chiesa, E. Giamello, E. Finazzi, C. Di Valentin and G. Pacchioni, *J. Am. Chem. Soc.*, 2007, **129**, 10575.
8   M. Chiesa, M. C. Paganini, E. Giamello, D. M. Murphy, C. Di Valentin and G. Pacchioni, *Acc. Chem. Res.*, 2006, **39**, 861.
9   M. Chiesa, P. Martino, E. Giamello, C. Di Valentin and A. Del Vitto, G. Pacchioni *J. Phys. Chem. B*, 2004, **108**, 11529.
10 M. Chiesa, M. C. Paganini, G. Spoto, E. Giamello, C. Di Valentin, A. Del Vitto and G. Pacchioni, *J. Phys. Chem. B*, 2005, **109**, 7314.
11 M. Chiesa, M. C. Paganini, E. Giamello, C. Di Valentin and G. Pacchioni, *Chem-PhysChem*, 2006, **7**, 728.
12 M. Chiesa, E. Giamello, G. Annino, C. A. Massa and D. M. Murphy, *Chem. Phys. Lett.*, 2007, **438**, 285.
13 M. Sterrer, T. Berger, O. Diwald, E. Knozinger, P. V. Sushko and A. L. Shluger, *J. Chem. Phys.*, 2005, **123**, 064714.
14 M. Chiesa and E. Giamello, *Chem. Eur. J.*, 2007, **13**, 1261.
15 M. Chiesa, E. Giamello, C. Di Valentin and G. Pacchioni, *Chem. Phys. Lett.*, 2005, **403**, 124.
16 M. Sterrer, T. Berger, O. Diwald, E. Knozinger and A. Allouche, *Topics in Catal.*, 2007, **46**, 111.
17 H. Hosono, K. Hayashi and M. Hirano, *J. Mater. Sci.*, 2007, **42**, 1872.
18 M. Ruszak, S. Witkowski and Z. Sojka, *Res. Chem. Intermed.*, 2007, **33**, 689.
19 T. L. Thompson and J. T. Yates, *Topics Catal.*, 2005, **35**, 197.
20 T. Ohno, K. Sarukawa, K. Tokieda and M. Matsumura, *J. Catal.*, 2001, **203**, 82.
21 K. Komaguchi, H. Nakano, A. Araki and Y. Harima, *Chem. Phys. Letts.*, 2006, **428**, 338.
22 D. C. Hurum, A. G. Agrios, S. E. Crist, K. A. Gray, T. Rajh and M. C. Thurnauer, *J. Elec. Spec. Rel. Phenom.*, 2006, **150**, 155.
23 D. C. Hurum, K. A. Gray, T. Rajh and M. C. Thurnauer, *J. Phys. Chem., B*, 2005, **109**, 977.
24 T. Berger, M. Sterrer, O. Diwald, E. Knozinger, D. Panayotov, T. L. Thompson and J. T. Yates, *J. Phys. Chem. B*, 2005, **109**, 6061.
25 T. Berger, M. Sterrer, O. Diwald and E. Knozinger, *ChemPhysChem*, 2005, **6**, 2104.
26 T. Berger, O. Diwald, E. Knozinger, F. Napoli, M. Chiesa and E. Giamello, *Chem. Phys.*, 2007, **339**, 138.
27 T. Berger, O. Diwald, E. Knozinger, M. Sterrer and J. T. Yates, *Phys. Chem. Chem. Phys.*, 2006, **8**, 1822.
28 M. J. Elsert, T. Berger, D. Brandhuber, J. Bernardi, O. Diwald and E. Knozinger, *J. Phys. Chem. B*, 2006, **110**, 7605.
29 J. Soria, J. Sanz, I. Sobrados, J. M. Coronado, F. Fresno and M. D. Hernandez-Alonso, *Catal. Today*, 2007, **129**, 240.
30 S. C. Ke, T. C. Wang, M. S. Wong and N. O. Gopal, *J. Phys. Chem. B*, 2006, **110**, 11628.
31 C. P. Kumar, N. P. Gopal, T. C. Wang, M. S. Wong and S. C. Ke, *J. Phys. Chem. B*, 2006, **110**, 5223.

32 N. M. Dimitrijevic, Z. C. Saponjic, B. M. Rabatic, O. G. Poluektov and T. Rajh, *J. Phys. Chem. C*, 2007, **111**, 14597.

33 K. Akiyama, S. Hashimoto, S. Tojo, T. Ikoma, S. Tero-Kubota and T. Majima, *Angewandte Chemie*, 2005, **44**, 3591.

34 S. G. Abuabara, C. W. Cady, J. B. Baxter, C. A. Schmuttenmaer, R. H. Crabtree, G. W. Brudvig and V. S. Batista, *J. Phys. Chem. C*, 2007, **111**, 11982.

35 J. H. Yu, J. R. Chen, C. Li, X. S. Wang, B. W. Zhang and H. Y. Ding, *J. Phys. Chem. B*, 2004, **108**, 2781.

36 N. M. Dimitrijevic, O. G. Poluektov, Z. C. Saponjic and T. Rajh, *J. Phys. Chem. B*, 2006, **110**, 25392.

37 N. M. Dimitrijevic, T. Rajh, Z. C. Saponjic, L. de la Garza and D. M. Tiede, *J. Phys. Chem. B*, 2004, **108**, 9105.

38 E. Carter, A. F. Carley and D. M. Murphy, *J. Phys. Chem. C*, 2007, **111**, 10630.

39 K. Suriye, R. J. Lobo-Lapldus, G. J. Yeagle, P. Fraserthdam, R. D. Britt and B. C. Gates, *Chem.-Eur. J*, 2008, **14**, 1402.

40 M. Che and A. J. Tench, *Adv. Catal.*, 1983, **32**, 1.

41 M. D. Hernandez-Alonso, J. M. Coronado, J. Soria, J. C. Conesa, V. Loddo, M. Addamo and V. Augugliaro, *Res. Chem. Intermed.*, 2007, **33**, 205.

42 E. Carter, A. F. Carley and D. M. Murphy, *ChemPhysChem*, 2007, **8**, 113.

43 J. M. Coronado and J. Soria, *Catal. Today*, 2007, **123**, 37.

44 T. K. Kim, M. N. Lee, S. H. Lee, Y. C. Park, C. K. Jung and J.-H. Boo, *Thin Solid Films*, 2005, **475**, 171.

45 C. Murata, T. Hattori and H. Yoshida, *J. Catal.*, 2005, **231**, 292.

46 J. M. Cho, W. J. Yun, J. K. Lee, H. S. Lee, W. W. So, S. J. Moon, Y. Jia, H. Kulkarni and Y. Wu, *Appl. Phys. A -Mat. Sci. Engin.*, 2007, **88**, 751.

47 M. Murdoch, R. Yeates and R. Howe, *Micro. Mesopor. Mater.*, 2007, **101**, 184.

48 A. Riss, T. Berger, S. Stankic, J. Bernardi, E. Knozinger and O. Diwald, *Angewandte Chemie*, 2008, **4**, 1496.

49 O. V. Zalomaeva, N. N. Trukhan, I. D. Ivanchikova, A. A. Panchenko, E. Roduner, E. P. Talsi, A. B. Sorokin, V. A. Rogov and O. A. Kholdeeva, *J. Mol. Catal. A —Chem.*, 2007, **277**, 185.

50 V. Brezova, D. Dvoranova and A. Stasko, *Res. Chem. Intermed.*, 2007, **33**, 251.

51 V. Krishna, D. Yanes, W. Imaram, A. Angerhofer, B. Koopman and B. Moudgil, *Appl. Catal. B -Environ.*, 2008, **79**, 376.

52 M. A. Brusa, Y. Di Iorio, M. S. Churio and M. A. Grela, *J. Mol. Catal. A—Chem.*, 2007, **268**, 29.

53 M. Mrowetz and E. Selli, *Phys. Chem. Chem. Phys.*, 2005, **7**, 1100.

54 C. Chen, P. Lei, H. Ji, W. Ma and J. Zhao, *Environ. Sci. Tech.*, 2004, **38**, 329.

55 P. Billik, G. Plesch, V. Brezova, L. Kuchta, M. Valko and M. Mazur, *J. Phys. Chem. Solids*, 2007, **68**, 1112.

56 K. K. Mothilal, J. Johnson Inbaraj, R. Gandhidasan and R. Murugesan, *J. Photochem. Photobiol. A—Chem.*, 2004, **162**, 9.

57 T. A. Konovalova, J. Lawrence and L. D. Kispert, *J. Photochem. Photobiol. A—Chem.*, 2004, **162**, 1.

58 K. Tanabe, *Mat. Chem. Phys.*, 1985, **13**, 347.

59 A. F. Bedilo, M. A. Plotnikov, N. V. Mezentseva, A. M. Volodin, G. M. Zhidomirov, I. M. Rybkin and K. J. Klabunde, *Phys. Chem. Chem. Phys.*, 2005, **7**, 3059.

60 N. V. Mezebtseva, A. F. Bedilo, A. M. Volodin, V. A. Sadykov and V. V. Lunin, *Russ. J. Phys. Chem.*, 2006, **80**, 2006.

61 A. N. Il'ichev, M. D. Shibanova, A. A. Ukharskii, A. M. Kuli-zade and V. N. Korchak, *Kinet. Catal.*, 2005, **46**, 387.

62 A. N. Il'ichev, M. D. Shibanova and V. N. Korchak, *Kinet. Catal.*, 2004, **45**, 114.

63 Q. Zhao, X. P. Wang and T. X. Cai, *Appl. Surf. Sci.*, 2004, **225**, 7.

64 E. A. Carrasco-Flores and J. A. LaVerne, *J. Chem. Phys.*, 2007, **127**, 234703.

65 A. Adamski, P. Zapala, P. Jakubus and Z. Sojka, *J. Alloys & Compds.*, 2007, **442**, 302.

66 M. De and D. Kunzru, *Catal. Letts.*, 2005, **102**, 237.

67 K. V. R. Chary, C. P. Kumar, D. Naresh, T. Bhaskar and Y. Sakata, *J. Mol. Catal. A—Chem.*, 2006, **243**, 149.

68 M. Occhiuzzi, D. Cordischi, D. Gazzoli, M. Valigi and P. C. Heydorn, *Appl. Catal. A—Gener.*, 2004, **269**, 169.

69 M. V. Burova, A. V. Fionov, E. A. Tveritinova, A. N. Kharlanov and V. V. Lunin, *Russ. J. Phys. Chem. A*, 2007, **81**, 164.

70 G. V. Sagar, P. V. R. Rao, C. S. Srikanth and K. V. R. Chary, *J. Phys. Chem., B*, 2006, **110**, 13881.

71 K. V. R. Chary, G. V. Sagar, D. Naresh, K. K. Seela and B. Sridhar, *J. Phys. Chem. B*, 2005, **109**, 9437.

72 Z. Liu, M. D. Amiridis and Y. Chen, *J. Phys. Chem. B*, 2005, **109**, 1251.

73 M. Labaki, J. F. Lamonier, S. Siffert, E. A. Zhilinskaya and A. Aboukais, *Kinet. Catal.*, 2004, **45**, 227.

74 P. Ratnasamy, D. Srinivas, C. V. V. Satyanarayana, P. Manikandan, R. S. S. Kumaran, M. Sachin and V. N. Shetti, *J. Catal.*, 2004, **221**, 455.

75 V. Ramaswamy, M. Bhagwat, D. Srinivas and A. V. Ramaswamy, *Catal. Today*, 2004, **97**, 63.

76 E. G. Kovaleva, L. S. Molochnikov, V. G. Kharchuk, O. V. Kuznetsova, A. B. Shishmakov, M. Y. Yanchenko, L. Y. Buldakova, I. N. Zhdanov, Y. V. Mikushina and L. A. Petrov, *Kinet. Catal.*, 2004, **45**, 752.

77 F. C. Jentoft, A. Hahn, J. Krohnert, G. Lorenz, R. E. Jentoft, T. Ressler, U. Wild, R. Schlogl, C. Hassner and K. Kohler, *J. Catal.*, 2004, **224**, 124.

78 S. Wright and R. C. Barklie, *Mat. Sci. Semicon. Process.*, 2006, **9**, 892.

79 M. D. Hernandez-Alonso, A. B. Hungria, A. Martinez-Arias, M. Fernandez-Garcia, J. M. Coronado, J. C. Conesa and J. Soria, *Appl. Catal. B—Environ.*, 2004, **50**, 167.

80 A. Martinez-Arias, J. C. Conesa and J. Soria, *Res. Chem. Intermed.*, 2007, **33**, 775.

81 A. Martinez-Arias, A. B. Hungria, M. Fernandez-Garcia, J. C. Conesa and G. Munuera, *J. Phys. Chem. B*, 2004, **108**, 17983.

82 A. N. Il'ichev, A. M. Kuli-zade and V. N. Korchak, *Kinet. Catal.*, 2005, **46**, 396.

83 B. Murugan and A. V. Ramaswamy, *J. Am. Chem. Soc.*, 2007, **129**, 3062.

84 A. Adamski, E. Tabor, B. Gil and Z. Soika, *Catal. Today*, 2007, **119**, 114.

85 A. Aboukais, E. A. Zhilinskaya, J. F. Lamonier and I. N. Filimonov, *Colloid Surf. A—Physicochem. Engin. Aspects*, 2005, **260**, 199.

86 R. Flouty, E. Abi-Aad, S. Siffert and A. Aboukais, *Appl. Catal.B—Environ.*, 2003, **46**, 145.

87 S. Babu, A. Velez, K. Wozniak, J. Szydlowska and S. Seal, *Chem. Phys. Lett.*, 2007, **442**, 405.

88 C. Decarne, E. Abi-Aad, B. G. Kostyuk, V. V. Lunin and A. Aboukais, *J. Mater. Sci.*, 2004, **39**, 2349.

89 A. Bruckner and E. Kondratenko, *Catal. Today*, 2006, **113**, 16.

90 U. Bentrup, A. Bruckner, C. Rudinger and H. J. Erberle, *Appl. Catal. A—Gen.*, 2004, **269**, 237.

91 L. Baraket, A. Ghorbel and P. Grange, *Appl. Catal. B—Environ.*, 2007, **72**, 37.

92 A. Adamski, P. Zapala, P. Jakubus and Z. Sojka, *J. Alloys Compds.*, 2007, **442**, 302.

93 M. De and D. Kunzru, *Catal. Letts.*, 2005, **102**, 237.

94 K. V. R. Chary, C. P. Kumar, D. Naresh, T. Bhaskar and Y. Sakata, *J. Mol. Catal. A—Chem.*, 2006, **243**, 149.

95 D. I. Enache, E. Bordes-Richard, A. Ensuque and F. Bozon-Verduraz, *Appl. Catal. A—Gen.*, 2004, **278**, 93.

96 E. Abi-Aad, J. Matta, D. Courcot and A. Aboukais, *J. Mater. Sci.*, 2006, **41**, 1827.

97 Z. Zhao, Y. Yamada, A. Ueda, H. Sakurai and T. Kobayashi, *Catal. Today*, 2004, **93**, 163.

98 N. Steinfeldt, D. Muller and H. Berndt, *Appl. Catal. A—Gen.*, 2004, **272**, 201.

99 K. V. R. Chary, C. P. Kumar, A. Murali, A. Tripathi and A. Clearfield, *J. Mol. Catal. A—Gen.*, 2004, **216**, 139.

100 K. V. Narayana, B. D. Raju, S. K. Masthan, V. V. Rao, P. K. Rao, R. Subrahmanian and A. Martin, *Catal. Comm.*, 2004, **5**, 457.

101 M. Occhiuzzi, D. Cordischi and R. Dragone, *J. Sol. State Chem.*, 2005, **178**, 1551.

102 M. Conte, G. Budroni, J. K. Bartley, S. H. Taylor, A. F. Carley, A. Schmidt, D. M. Murphy, F. Girgsdies, T. Ressler, R. Schlogl and G. J. Hutchings, *Science*, 2006, **313**, 1270.

103 L. E. Liotta, A. M. Venezia, G. Pantaleo, G. Deganello, M. Gruttadauria and R. Noto, *Catal. Today*, 2004, **91**, 231.

104 F. Morazzoni, R. Scotti, L. Origoni, M. D'Arienzo, I. Jimenez, A. Cornet and J. R. Morante, *Catal. Today*, 2007, **126**, 169.

105 F. Amano, T. Yamaguchi and T. Tanaka, *J. Phys. Chem. B*, 2006, **110**, 281.

106 J. M. Meichtry, M. Brusa, G. Mailhot, M. A. Grela and M. I. Litter, *Appl. Catal. B—Environ.*, 2007, **71**, 101.

107 M. Mihaylov, A. Penkova, K. Hadjiivanov and H. Knozinger, *J. Phys. Chem. B*, 2004, **108**, 679.

108 M. Lezanska, G. S. Szymanski, P. Pietrzyk, Z. Sojka and J. A. Lercher, *J. Phys. Chem. C*, 2007, **111**, 1830.

109 M. Brandhorst, S. Cristol, M. Capron, C. Dujardin, H. Vezin, G. Le Bourdon and E. Payen, *Catal. Today*, 2006, **113**, 34.
110 Z. Sojka and P. Pietrzyk, *Spectrochimica Acta Part A*, 2006, **63**, 788.
111 F. Neese, Specialist Periodical Reports, *Electron Spin Resonance*, 2007, **20**, 73.
112 D. Wang, W. Li, M. Zhang and K. Tao, *Appl. Catal. A—Gen.*, 2007, **317**, 105.
113 C. Liu, R. B. Watson and U. S. Ozkan, *Top. Catal.*, 2006, **41**, 63.
114 A. P. Chen, Q. Wang, Y. J. Hao, W. P. Fang and Y. Q. Yang, *Catal. Lett.*, 2007, **118**, 295.
115 R. Flouty, E. Abi-Aad, S. Siffert and A. Aboukais, *Kinet. Catal.*, 2004, **45**, 219.
116 D. Nikolova, R. Edreva-Kardjieva, G. Gouliev, T. Grozeva and P. Tzvetkov, *Appl. Catal. A—Gen.*, 2006, **297**, 135.
117 L. N. Ho, T. Ikegawa, H. Nishiguchi, K. Nagaoka and Y. Takita, *Appl. Surf. Sci.*, 2006, **252**, 6260.
118 M. S. Zina and A. Ghorbel, *Mag. Reson. Chem.*, 2004, **42**, 348.
119 A. S. Rocha, V. L. T. da Silva, A. A. Leitao, M. H. Herbst and A. C. Faro, *Catal. Today*, 2004, **98**, 281.
120 N. T. Vasenin, V. F. Anufrienko, I. Z. Ismagilov, T. V. Larina, E. A. Paukshtis, E. V. Matus, L. T. Tsikoza and M. A. Kerzhentsev, *Top. Catal.*, 2005, **32**, 61.
121 H. M. Liu, W. J. Shen, X. H. Bao and Y. D. Xu, *J. Mol. Catal. A—Chem.*, 2006, **244**, 229.
122 F. Wyrwalski, J. F. Lamonier, S. Siffert, E. A. Zhilinskaya and L. Gengembre, *J. Mater. Sci.*, 2005, **40**, 933.
123 X. Carrier, P. Lukinskas, S. Kuba, L. Stievano, F. E. Wagner and M. Che, *ChemPhysChem*, 2004, **5**, 1191.
124 C. Adan, A. Bahamonde, M. Ferandez-Garcia and A. Martinez-Arias, *Appl. Catal. B—Environ.*, 2007, **72**, 11.
125 P. Billik, G. Plesch, V. Brezova, L. Kuchta, M. Valko and M. Mazur, *J. Phys. Chem. Sol.*, 2007, **68**, 1112.
126 B. Moens, H. De Winne, S. Corthals, H. Poelman, R. De Gryse, V. Meynen, P. Cool, B. F. Sels and P. A. Jacobs, *J. Catal.*, 2007, **247**, 86.
127 V. Umamaheswari, W. Bohlmann, A. Poppl, A. Vinu and M. Hartmann, *Micropor. Mesopor. Mater.*, 2006, **89**, 47.
128 A. M. Volodin, G. M. Zhidomirov, K. A. Dubkov, E. J. M. Hensen and R. A. van Santen, *Catal. Today*, 2005, **110**, 247.
129 M. S. Kumar, M. Schwidder and W. Grunert, *J. Catal.*, 2004, **227**, 384.
130 J. C. Groen, L. Maldonado, E. Berrier, A. Bruckner, J. A. Moulijn and J. Perez-Ramirez, *J. Phys. Chem. B*, 2006, **110**, 20369.
131 M. Devadas, O. Krocher, M. Elsener, A. Wokaun, G. Mitrikas, N. Soger, M. Pfeifer, Y. Demel and L. Mussmann, *Catal. Today*, 2007, **119**, 137.
132 S. Dzwigaj, J. Janas, T. Machej and M. Che, *Catal. Today*, 2007, **119**, 133.
133 D. Courcot, C. Pruvost, E. A. Zhilinskaya and A. Aboukais, *Kinet. Catal.*, 2004, **45**, 580.
134 R. Cousin, E. Abi-Aad, S. Capele, D. Courcot, J. F. Lamonier and A. Aboukais, *J. Mater. Sci.*, 2007, **42**, 6188.
135 A. Martinez-Arias, A. B. Hungria, G. Munuera and D. Gamarra, *Appl. Catal. B—Environ.*, 2006, **65**, 207.
136 A. Gervasini, M. Manzoli, G. Martra, A. Ponti, N. Ravasio, L. Sordelli and F. Zaccheria, *J. Phys. Chem. B*, 2006, **110**, 7851.
137 T. Tsoncheva, S. Vankova and D. Mehandjiev, *J. Mol. Catal. A—Chem.*, 2005, **225**, 245.
138 D. Berthomieu and G. Delahay, *Catal. Rev.—Sci. Engin.*, 2006, **48**, 269.
139 P. Pietrzyk, B. Gil and Z. Sojka, *Catal. Today*, 2007, **126**, 103.
140 P. J. Smeets, M. H. Groothaert, R. M. van Teeffelen, H. Leeman, E. J. M. Hensen and R. A. Schoonheydt, *J. Catal.*, 2007, **245**, 358.
141 A. V. Kucherov, A. N. Shigapov, A. V. Ivanov, T. N. Kucherova and L. M. Kustov, *Catal. Today*, 2005, **110**, 330.
142 M. Kakazey and M. Vlasova, *J. Mol. Catal. A—Chem.*, 2008, **281**, 219.
143 A. C. Dodd, A. J. McKinley, M. Saunders and T. Tsuzuki, *J. Nanopar. Res.*, 2006, **8**, 43.
144 U. Roland, F. Holzer, A. Poppl and F. D. Kopinke, *Appl. Catal. B*, 2005, **58**, 227.
145 T. Hill, T. Risse and H.-J. Freund, *J. Chem. Phys.*, 2005, **122**, 164704.
146 R. A. Weeks, *J. Appl. Phys.*, 1956, 27.
147 R. A. Weeks, R. H. Magruder and A. Stesmans, *J. Non-Cryst. Solids*, 2008, **354**, 208.
148 L. Skuja, K. Kajihara, M. Hirano, A. Saitoh and H. Hosono, *J. Non-Cryst Solids*, 2006, **352**, 2297.
149 V. A. Radtsig, *Chem. Phys. Reports*, 2000, **19**, 17.
150 L. Giordano, P. V. Sushko, G. Pacchioni and A. L. Shluger, *Phys. Rev. B*, 2007, **75**, 024109.
151 V. Drinek, K. Vacek, G. Yuzhakov, Z. Bastl and S. Naumov, *Surf. Sci.*, 2006, **600**, 1462.

152   H. Jin, W. E. Jellett, Z. Chun, K. J. Weber, A. W. Blakers and P. J. Smith, *Appl. Phys. Lett.*, 2008, **92**, 122109.
153   B. Fubini and I. Fenoglio, *Elements*, 2007, **3**, 407.
154   M. Acciarri, R. Barberini, C. Canevali, M. Mattoni, C. M. Mari, F. Morazzoni, L. Nodari, S. Polizzi, R. Ruffo, U. Russo, M. Sala and R. Scotti, *Chem. Mater.*, 2005, **17**, 6167.

EPR of exchange coupled oligomers

Angelika B. Boer, David Collison* and Eric J. L. McInnes*

1. Introduction

This review is an update of our previous SPR reviews on magnetically exchange coupled oligomers,[1] and covers the literature in the calendar years 2006 and 2007. As before we review the publications involving EPR spectroscopy of discrete molecular compounds containing more than one radical centre—polymeric materials are not covered. The discussion is organised into coupled (i) p-block radicals, (ii) d-block radicals, (iii) mixed p/d-block radicals, (iv) mixed d/f-block radicals and (v) biological systems.

2. p-Block

This area is usually dominated by work on nitroxides, given their chemical stability and therefore the relative ease of synthesising polyradicals. However, in the last two years a refreshing number of studies on alternative coupled free-radicals have appeared, including verdazyls,[2,3] arylamines,[4] aminyls,[5] thiazyls,[6] viologens,[7] tri-tyls,[8] hydrazyls and heterodiradical nitroxide-hydrazyls,[9] in addition to several interesting new "twists" on polynitroxides.[10–14] Itoh *et al.* have also published a review of polycarbenes.[15] In this review we do not cover the important area of PELDOR/DEER methods to probe weak (often dipolar) interactions between radicals.
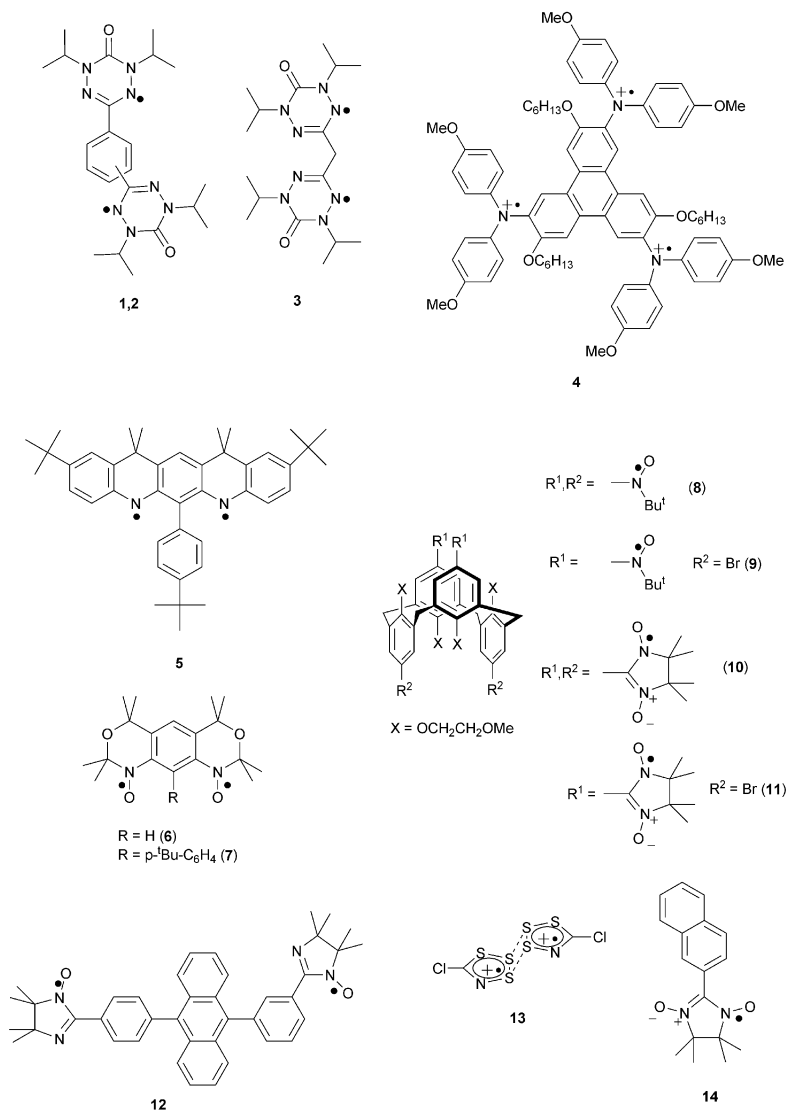
A popular theme has been the exploitation of spin polarisation ideas to control the isotropic exchange interaction (J) between radicals. For example, Hicks and co-workers find J in the *p*- (**1**) and *m*-phenylene (**2**) bridged diverdazyls to be antiferro-[singlet–triplet (S–T) gap 30 cm^{-1}; derived from the EPR intensity as a function of temperature] and ferro-magnetically (T–S gap 20 cm^{-1}) coupled, respectively,[2] as expected from spin polarisation. Both give well-resolved triplet EPR spectra, and a slightly larger zero-field splitting (ZFS) is found for **1** than **2** ($|D| = 0.004$ *cf.* 0.002 cm^{-1}), consistent with a dipolar model. Brook and Yee find a surprisingly much stronger antiferromagnetic coupling (S–T gap 150 cm^{-1}) and larger $|D| = 0.02$ cm^{-1}, in the methylene-bridged **3**.[3] Analogous monoradicals are found to have a significant spin density on the bridgehead C (derived from the CH$_2$ hyperfine) and the authors conclude that there must be a significant through-bond (spin polarisation) contribution to exchange, despite the saturated nature of the linker.

Several groups have attempted to exploit the *meta*-arene "ferromagnetic linker" to prepare organic species with well-isolated high spin ground states. For example, Fukuzaki and Nishide[4] have linked three polyarylamine radical cations via tri-phenylene (**4**) and find a strong (but unquantified) ferromagnetic exchange giving rise to a quartet ground state with $|D| = 0.002$ cm^{-1} from EPR. Similarly, Rajca *et al.*, have reported the first example of a triplet ground state aminyl diradical (**5**),[5] which has a remarkably large T-S gap of >200 K from magnetic susceptibility studies. X-band EPR spectra resolve the triplet fine ($|D| = 9.2 \times 10^{-3}$, $E = 2.1 \times 10^{-3}$ cm^{-1}) and hyperfine ($2x^{14}$N) structure ($|A_z| = 1.0 \times 10^{-3}$ cm^{-1}). Intriguingly, the largest components of **D** and **A** (z) are co-parallel. Given that the nitrogen $2p_\pi$-orbitals are expected to be perpendicular to the molecular plane, this implies that D_z is perpendicular to the inter-radical vector, which is not what would be expected for

School of Chemistry, The University of Manchester, Oxford Road, Manchester, UK, M13 9PL .
E-mail: david.collison@manchester.ac.uk, eric.mcinnes@manchester.ac.uk;
Fax: 0161-275-4616; Tel: 0161-275-4660/4469

a dipolar dominated **D**. This is nicely contrasted with further work from the Rajca group, on the related dinitroxides **6** and **7**.[10] Again, both radicals are strongly ferromagnetically coupled (T–S > 200 K), and well-resolved triplet EPR spectra give $|D| = 1.35 \times 10^{-2}$, $E = 1.75 \times 10^{-3}$ cm^{-1} and $|D| = 1.31 \times 10^{-2}$, $E = 1.00 \times 10^{-3}$ cm^{-1} for **6** and **7**, respectively. In contrast to **5**, hyperfine coupling to two ^{14}N nuclei is observed on the y transitions for **6**. This implies that the inter-radical vector (z) is perpendicular to the nitrogen 2p$_\pi$-orbitals (and to the co-planar N–O vectors). This is also consistent with a large hyperfine to a single ^{1}H observed at this orientation, due to the *ortho,ortho* C–H moiety. The spin Hamiltonian parameters for **7** support a solution structure distorted away from co-planar nitroxides.

1,2   3   4

5

R = H (6)
R = p-^{t}Bu-C$_6$H$_4$ (7)

X = OCH$_2$CH$_2$OMe

$R^1, R^2 =$ (8)

$R^1 =$ $R^2 = Br$ (9)

$R^1, R^2 =$ (10)

$R^1 =$ $R^2 = Br$ (11)

12   13   14

In two papers Rajca and co-workers combine *m*-phenylene and unsaturated (methylene) linkers by exploiting the scaffold provided by the 1,3-alternate calix[4]-arenes in the di- and tetra-nitroxides and nitronyl nitroxides **8–11**.[11,12] In each case, fluid EPR spectra are observed consistent with the full number of nitrogens and $|J| \gg A_N$. On freezing, the diradicals **9** and **11** give well-resolved, axial triplet spectra

with $|D| = 1.39 \times 10^{-2}$ and 4.2×10^{-3} cm^{-1}, respectively. ^{14}N hyperfine is consistent with co-linearity of the (nitronyl)nitroxides, perpendicular to the inter-radical vector. Magnetic susceptibility studies reveal the coupling to be weakly antiferromagnetic (<1 K) and this is concluded to be via a through-space mechanism: the $|D|$ values can be justified by a dipolar model, consistent with the solid state structures and with the smaller $|D|$ observed for **11**. The tetra-radicals are more strongly coupled, and the authors conclude that there must be a significant through-bond component to this. There is no resolution of fine-structure in their frozen-solution EPR measured at *ca.* 140 K. For both the di- and tetra-radicals, the exchange is stronger for the nitroxide than for the nitronylnitroxide species.

Teki *et al.*, report a beautiful study on a dintroxide system with an aromatic linker that can be photoexcited into a low-lying triplet state (**12**).[13] Fluid solution spectra are characteristic of $|J| \approx A_N$ but the exchange is very weak; too weak to determine by susceptibility methods. Time-resolved EPR measurements were performed at 30 K, 0.5 μs after laser excitation at 355 nm, and the spectra can be modelled as a 1:1 superposition of triplet ($|D| = 0.036$ cm^{-1}) and quintet ($|D| = 0.0125$ cm^{-1}) states. Spin polarisation arguments predict a triplet as the lowest lying photoexcited state, since the exchange between the nitroxides and excited anthracene moieties are expected to be antiferro- and ferro-magnetic for the *para-* (J_1) and *meta-* (J_2) links, respectively. The authors calculate the energies and $|D|$ values of the triplet and quintet states as a function of J_2/J_1 based on spin Hamiltonian (1); *i.e.* assuming that the sole contribution to $|D|$ is from the anthracene triplet state.

$$\hat{H} = -2J_1\hat{S}^{\text{nit1}}\hat{S}^T - 2J_2\hat{S}^{\text{nit2}}\hat{S}^T + \sum_i \mu_B Bg_i\hat{S}_i + \hat{S}^T\mathbf{D}^T\hat{S}^T \tag{1}$$

Fitting the experimentally observed $|D|$-values for the quintet and the lower of the two triplets, a ratio of $J_2/J_1 = -0.08$ is concluded, which gives the quintet as a very low-lying excited state above a triplet.

Passmore and co-workers report the first observation of the triplet excited state (and consequently first measure of J) in a thiazyl radical π-dimer.[6] Solid state (**13**)(AsF$_6$)$_2$ is diamagnetic, by magnetic susceptibility methods, as a result of the π-overlap and nascent S···S bonding. Despite this there is a rich EPR spectrum at room temperature which must arise from the excited triplet. Fitting the variable temperature (VT) EPR intensity gives the S–T gap as 1900 cm^{-1}. At room temperature only 0.03% of dimers are in the triplet state, explaining the observed diamagnetism. Single crystal studies show significant non-coincidence of g_z and D_z, consistent with the slipped-coplanar structure. A similar phenomenon was later reported for a diethylviologen cation dimer.[7]

Finally, although not strictly molecular, a beautiful exploitation of host-guest chemistry to induce inter-radical exchange should be mentioned. Fujita and co-workers trap two nitronyl nitroxides, *e.g.*, **14**, inside a diamagnetic {Pd$_6$L$_4$} (L = tris-4-pyridyl-1,3,5-triazine) cage in water, as shown by the observation of the triplet excited state ($J = -0.3$ cm^{-1}) in the EPR spectrum.[14] The same group have encapsulated Cu(II) porphyrins in a trigonal prismatic coordination cage, as demonstrated by characteristic triplet spectra from the trapped cofacial dimer.[16]

3. d-Block

3.1 Dimetallic complexes

Anderlund *et al.* report detailed EPR studies on the redox behaviour of [Mn(II)-Mn(III)L(μ-OAc)$_2$]ClO$_4$ (where L is an asymmetric, dianionic ligand with a bridging phenoxide group).[17,18] Frozen solution EPR spectra at 9.6 GHz and 4 K give a characteristic $S = 1/2$ ground state with 16–20 ^{55}Mn hyperfine lines.[17] Upon electrochemical reduction, EPR spectra typical for Mn(II)$_2$ are obtained. One-electron oxidation gives an EPR-silent species, speculated to be Mn(III)$_2$. Exposure of the

solution to laser flashes in the presence of $[Ru(bpy)_3]^{2+}$ (the excited state of which can be oxidatively quenched to give the oxidising $3+$ cation) and $[Co(NH_3)_5Cl)]^{2+}$ (as sacrificial electron acceptor) gives rise to $S = 1/2$ spectra typical of strongly coupled Mn(III)Mn(IV) pairs, which is speculated to be a (μ-O)(μ-OH) species (replacing the acetates) from the hyperfine pattern. Further irradiation leads to another EPR silent species, proposed to be a strongly coupled Mn(III)Mn(IV)L$^{\bullet}$ complex. In a separate paper, Huang *et al.* simulate the X and Q-band spectra of the Mn(II)Mn(III) species with an effective $S = 1/2$ Hamiltonian, and back-calculate the intrinsic hyperfines for Mn(II) and Mn(III) from projection coefficients in the strong-exchange limit (SEL).[18] This procedure gives a rather anisotropic Mn(II) **A** matrix, which is explained as "transferred anisotropy" from the Mn(III) *via J* and the single-ion *D*, meaning that the SEL expressions are not valid, and the authors then use the analytical expressions given by Sage *et al.*[19] based on a perturbative treatment of the single-ion ZFSs. The same group demonstrates the determination of the sign of excited state ZFS parameters using sufficiently high magnetic fields, in the structurally related $[Mn(II)_2(bpmp)(OAc)_2](ClO_4)$.[20] W-band studies of an unusual oxidation state Mn(I) dimer are reported by Sorace *et al.*[21] Excited state $S = 1$, 2 and 3 transitions are observed in W-band spectra of the antiferromagnetically coupled $[\{HC(CMeAr)_2\}_2Mn]_2$. The authors present evidence (including the derived magnitude of the single ion ZFS) for assignment of the Mn(I) electronic structure as high spin d^5s^1 where the two singly-occupied 4s-orbitals give rise to a weak Mn–Mn bond. Dalal and co-workers study another rare oxidation state dimer, proving the $S = 2$ ground state of $[V(III)_2O(MeCN)_{10}](BF_4)_4$.[22]

Herchel *et al.* demonstrate the use of simultaneous fitting of magnetisation and multiple HF-EPR data to determine the microscopic magnetic parameters in the weakly coupled $[Ni(II)_2(en)_4Cl_2](Cl)_2$,[23] for which a wide range of parameters had previously been given. Data were fit using spin-Hamiltonian (2), based on the single-ion spins, giving the single-ion ZFS as $D_1 (= D_2) = -4.78$ cm^{-1} and the isotropic and anisotropic exchange parameters $J = 9.66$ and $D_{12} = -0.64$ cm^{-1} (*zj* is a molecular-field parameter).

$$\hat{H} = -J(\hat{s}_1\hat{s}_2) + D_1(\hat{s}_{1z}^2 - \tfrac{1}{3}\hat{s}_1^2) + D_2(\hat{s}_{2z}^2 - \tfrac{1}{3}\hat{s}_2^2)$$
$$+ D_{12}(\hat{s}_{1z}\hat{s}_{2z} - \tfrac{1}{3}\hat{s}_1\hat{s}_2) + \mu_B\mathbf{g}\bar{B}_a\hat{s}_a - zj\langle s_a\rangle\hat{s}_a \tag{2}$$

ter Heerdt *et al.* present beautiful single crystal W-band EPR on the antiferromagnetically coupled $[Fe(III)_2(OCH_3)_2(dbm)_4]$ (Hdbm = dibenzoylmethane) and its Fe(III)-doped Ga(III) analogue.[24] Single-ion parameters $g_{iso} = 2.000$, $D = 0.749$ and $E = 0.085$ cm^{-1} are determined from the {GaFe} compound at room temperature. Low temperature single crystal data on {FeFe} (in four planes) show transitions within the $S = 1$, 2 and 3 excited states; modelling these data to Hamiltonian (3) gives single-ion ZFS $D' = 0.794$ and $E' = 0.097$ cm^{-1}, the slight differences compared to the values obtained from the {GaFe} possibly being due to the different temperatures of the experiments.

$$\hat{H} = \mu_B\bar{B}\mathbf{g}\hat{S} + \hat{s}_1\mathbf{D}'\hat{s}_1 + \hat{s}_2\mathbf{D}'s_2 + J_0\hat{s}_1\hat{s}_2 + \hat{s}_1\mathbf{J}\hat{s}_2 \tag{3}$$

The determined anisotropic spin-spin interaction tensor **J** can be parameterised into axial and rhombic terms J_D and $J_E = -0.138$ and 0.093 cm^{-1}, respectively. The dipolar part of **J** can be calculated in a dipolar model and subtracted out, and the anisotropic exchange term is found to be of roughly the same magnitude, but entirely responsible for the rhombic part of **J**. The authors highlight the relevance of the anisotropic exchange in larger clusters.

Trovacene $[(\eta^7\text{-}C_7H_7)V(\eta^5\text{-}C_5H_5)]$ has been studied intensively by Elschenbroich and co-workers to gain insight into spacer-dependent electronic and magnetic communication. Two new series of radical compounds have been reported: $[(TVC)_4Sn]$ (**15**), $[(TVC)_2SnPh_2]$ (**16**) and $[(TVC)_3SnCl_2]^-$ (**17**)[25,26] where the

trovocenyl units {TVC⁻ = [(C₇H₇)V(C₅H₄)]⁻} are linked via Sn(IV), and [(TVC)R₂Si-X-SiR₂(TVC)] with R = Ph, X = O (**18**); R = Me, X = O (**19**) and R = Me, X = CH₂ (**20**).[27] Fluid solution EPR spectra of the tin-linked complexes approach the fast exchange limit, $|J| > A_V$, with 15 (**2**), 29 (**15**) and 22 (**17**) line ⁵¹V hyperfine structures. Simulation gives $|J|$ = 1.4 and 0.5 cm⁻¹ for diradical **16** and the triradical **3**, respectively (in the -$J\hat{s}_i.\hat{s}_j$ formalism). The authors suggest the smaller $|J|$ for **17**, which is an equilateral triangular with respect to TVC⁻, may be a consequence of spin frustration. Modelling the 15 line spectra of **18**, **19** and **20** gives $|J|$ = 0.07(1) cm⁻¹ in each case, a surprising invariance given the significant differences in the bridges.

3.2 Trimetallic complexes

Several groups are involved in ongoing investigations of exchange coupled trigonal trimetallic Cu(II) complexes, reflected in the review by Yoon and Solomon.[28] In the case of equilateral triangles with antiferromagnetic coupling a pair of degenerate S = 1/2 states result—this is spin frustration in its strict definition of an orbitally degenerate ground state. One possible mechanism to break the degeneracy is antisymmetric exchange [$\mathbf{d}(\hat{s}_i \times \hat{s}_j)$] and several authors invoke such effects to explain unusual effective g-values in antiferromagnetically coupled triangular complexes of half-integer spin ions.[29–33] Kajiyoshi et al.[34] and Tsukerblat et al.[35] present detailed studies on K₆[As₆V(IV)₁₅O₄₂(H₂O)]·8H₂O the magnetic properties of which arise solely from a central equilateral {V(IV)₃} triangle at low temperatures. Kajiyoshi et al. study the frequency dependence of resonance fields within the lowest energy doublets, at low frequencies (0.6 and 3 GHz) on a single crystal at 0.5 K.[34] The data can only be modelled by inclusion of a ZFS between the doublets of ca. 30 mK. Tsukerblat et al. report a detailed theoretical analysis of this system[35] and discuss the consequences of the components of the antisymmetric exchange for intra- and inter-multiplet EPR transitions. Belinsky presents a theoretical treatment of the EPR parameters of {Cu(II)₂Cu(III)} triangles, where antisymmetric and double exchange phenomena must be taken into account.[36]

Different groups deal with the problem of the differences in solid state and solution structures and/or magnetic behaviour, and demonstrate the role of EPR in their investigation.[37–39] Mezei et al. observe significant solvent effects on the EPR of the ferromagnetically coupled halide-bridged Cu(II) triangles [Bu₄N]₂[Cu₃(μ₃-X)₂-(μ₄-O₂N-pz)₃X₃] (X = Cl and Br).[37] CH₂Cl₂ glasses at 77 K show S = 3/2 spectra analogous to the solid state. In MeOH two intense S = 1/2 signals appear with different $g_{\parallel}$ (2.40 and 2.45). However, the spectral intensity corresponds only to a third of the total copper concentration and mass spectrometry from MeOH shows only the presence of trimetallic species. The authors argue substitution of μ₃-halide by μ₂-methoxide, giving a strongly coupled (EPR-silent) pair and a magnetically isolated Cu(II). Comba et al. demonstrate the application of molecular mechanics combined with spectrum simulation (MM-EPR) to determine the solution structure of the weakly coupled [Cu₃L(solvent)₆]⁶⁺, where L is a 1,3,5-triazine-bridged tri-macrocyclic ligand.[38] Local spin-Hamiltonian parameters are initially fixed from monometallic analogues and MM calculations used to predict conformations of the multi-metallic system in order to define the distance between the Cu centres and the Euler angles relating them. The parameters are refined by EPR simulation, supported by DFT calculations, allowing discrimination between, for example, possible syn-syn or syn-anti conformations of the molecule in solution. Interesting changes in magnetic properties from solid state to solution have been observed by Reedijk and co-workers on the linear trimetallic [Cu₃(py2O)₂(MeOH)₂](BF₄)₂·0.75MeOH (Hpy2OH = 2-(N,N-bis(2-pyridinylmethyl)-aminomethyl)-6-(hydroxymethyl)-4-methylphenol).[39] Powder X-band EPR at 4.2 K shows an axial S = 1/2 ground state (antiferromagnetic coupling). However, in MeOH the spectrum is dominated by transitions within the S = 3/2 with large ZFS, together with a monometallic

species. Hence, the exchange appears to have flipped to ferromagnetic. Mass spectrometry confirms a consistent structure in solution and solid state, hence the change in J must be due to minor structural differences, for example, coordination of solvent at the central, four-coordinate Cu ion.

3.3 Tetrametallic complexes

EPR of the tetrahedral, mixed-valence tetrametallic cluster [{Mn(II)$_3$Mn(IV)-(μ_4-O)(η^1,μ_2-N$_3$){(ph)(py)CNO}$_4$]·2MeCN has been communicated by Winpenny and co-workers.[40] This is a rare example of a manganese cage with a two electron difference between oxidation states. Magnetic measurements reveal an $S = 6$ ground state, confirmed by well-resolved 34 GHz EPR at 5 K. Simulation within the giant spin approach (GSA) gives $|D| = 0.1$ cm^{-1}. Very unusual spectra are observed by the same group in [Cu(II)$_4$(OH)(Ph$_3$CPO$_3$)$_3$(Ph$_3$CPO$_2$OH)(py)$_4$], which consists of a {Cu$_3$(μ_3-OH)} triangle bound to a remote Cu ion.[41] The spectra have the appearance of half-integer states (with excellent resolution of the Cu hyperfine), which is surprising for this even-electron system. This suggests that the triangle and fourth Cu ion are essentially uncoupled with respect to EPR and the data are modelled as the superposition of $S = 1/2$ states arising from the ground state of the scalene triangle (with multi-Cu hyperfine) and from the isolated Cu(II).

The heterotrimetallic [{^{i}PrtacnCr(CN)$_3$}$_2${Ni(cyclam)}](NO$_3$)$_2$·5H$_2$O (21) and tetra-metallic [{^{i}PrtacnCr(CN)$_3$Ni(Me$_2$bpy)$_2$}$_2$](NO$_3$)$_2$·2CH$_3$CN (22) clusters have been studied by Mallah and co-workers to demonstrate how magnetic anisotropy can be calculated and predicted from the single-ion anisotropy via the angular overlap model (AOM).[42] Both compounds contain ferromagnetically coupled metal ions and are characterized by rich HFEPR spectra (190 and 285 GHz, at 5 and 15 K), which have been successfully simulated within their $S = 4$ (21) and $S = 5$ (22) ground states. In a first step, HFEPR spectra of the monomeric [(^{i}Prtacn)Cr(CN)$_3$], [trans-Ni(cyclam)(NCS)$_2$] and [Ni(bpy)$_2$(NCS)$_2$] were recorded, and the single-ion D and E parameters transferred to the mixed-metal species. The authors show that these values can be reproduced with AOM computations, which also computes the orientation of $\mathbf{D}$ with respect to the metal–ligand geometry. Eqn (4), in the SEL and taking into account the relative orientations, gives good agreement between the calculated cluster ground state $\mathbf{D}$ and the experimental observations. The authors stress that single crystal studies on the clusters are necessary to test the orientation of the $\mathbf{D}$ tensor.

$$\mathbf{D}_{\text{Complex}} = 2d^S_{\text{Cr}}\mathbf{D}_{\text{Cr}} + nd^S_{\text{Ni}}\mathbf{D}_{\text{Ni}} + 2nd^S_{\text{CrNi}}\mathbf{D}_{\text{CrNi}}$$
$$(n = 1 \text{ and } 2 \text{ for } \mathbf{21} \text{ and } \mathbf{22}, \text{ respectively}) \qquad (4)$$

Golze et al. observe crossover of the magnetic ground state of the Ni(II) complex [L$_2$Ni$_4$(N$_3$)(O$_2$C-Ada)$_4$](ClO$_4$) from $S = 0$ to 1 at very high field by HF-EPR and magnetisation.[43] HFEPR up to 739 GHz (using pulsed magnetic fields) only show transitions above 10 K and are assigned to $S = 1$ and 2 excited state transitions. At 1017 GHz, spectra are detected at fields > 25 T and 4.2 K, decreasing with increasing temperature, indicating a magnetic ground state. These data are consistent with a step in magnetisation vs. field data at about 25 T.

3.4 Polymetallic complexes

There are several "routine" uses of EPR to determine the nature of the ground spin state in polymetallic complexes. Boudalis et al.[44] report a $S = 3/2$ ground state from an unusual chain-like {Cu(II)$_5$} complex. At X-band and 4.2 K, spectra are consistent with a relatively large $|D| = 0.4$ cm^{-1} (presumably positive). Several new Fe(III) clusters with EPR active ground states are also reported.[45–47] Jones et al. report two {Fe(III)$_7$} clusters with irregular geometries that give rise to $S = 5/2$ ground states with $D \approx +0.3$ cm^{-1} from X-band EPR.[45] Christou, Hill and co-workers also report $S = \frac{5}{2}$ ground states in

{Fe(III)}$_7$ clusters, [Fe$_7$O$_3$(O$_2$CPh)$_9$(dmem)$_2$] (**23**) and [Fe$_7$O$_3$(O$_2$CBu^t)$_9$(mda)$_3$(H$_2$O)$_3$] (**24**) (dmemH = 2-{[2-dimethylamino)ethyl]methylamino}-ethanol),[46,47] and determine the magnitude and sign of D by single crystal HFEPR. Fitting data for **23** give $D = +0.62$ cm^{-1}, $|E| = \geq 0.067$ cm^{-1} and $g_{xy} = 2.00$, for **24** $D = -0.36$ cm^{-1} and $g = 2.00(1)$. Alongside the above compounds the same group report the related [Fe$_6$O$_2$(OH)$_4$(O$_2$CBu^t)$_8$(dmem)$_2$] complex (**25**) with an $S = 5$ ground state arising from a diamagnetic butterfly core and two parallel oriented Fe(III) ions on the periphery.[47] Variable frequency data at selected orientations of a crystal of (**25**) have a temperature dependence corresponding to a negative D; extrapolations of frequency *vs.* field plots lead to $D = -0.25(1)$ cm^{-1}.

Well resolved 94 GHz EPR have been communicated by Shaw *et al.* on rare examples of high nuclearity vanadium(III) clusters, [N^{n}Bu$_4$]$_2$[V$_8$O$_4$(bta)$_8$(O$_2$CR)$_4$Cl$_6$] (btaH = benzotriazole, R = CMe$_3$ (**26**) and Ph (**27**)) with $S = 4$ ground states.[48] Spectra on powders are consistent with this, but also reveal torquing of the samples in the applied fields, giving pseudo-single orientation spectra. Simulation on this basis gives $g_z = 1.91$ and $D = -0.297$ cm^{-1} for **27** (but no information on E). The authors state that immobilized samples indeed show more complex spectra, but attempts to powder the samples to ensure true powder spectra lead to immediate oxidation.

Hill and co-workers report a breaking of the $\Delta S = 0$ selection rule in EPR experiments on the Mn(II) [3 × 3] grid [Mn$_9$(2POAP-2H)$_6$](ClO$_4$)$_6$ · 3.57MeCN · H$_2$O,[49] due to mixing of ground and excited state total spin multiplets arising from comparable exchange and magneto-anisotropy energies. 50–60 GHz EPR below 20 K on a single crystal orientated with the field parallel to the easy axis of magnetisation shows five transitions within the $S = 5/2$ ground state, and a further much higher field resonance. Extrapolation of frequency *vs* field plots to zero field for the ground state transitions gives the ZFS. However, the high field signal has opposite frequency dependence, extrapolating to *ca.* 230 GHz at zero field, which matches the ground—first excited state gap previously determined by inelastic neutron scattering (INS). The transition is assigned to, and can be modelled as, $|S,M\rangle = |5/2,-5/2\rangle \rightarrow |7/2,-7/2\rangle$. The authors highlight the utility of EPR for direct measurement of exchange splittings in molecular nanomagnets.

3.5 Polymetallic cores encapsulated into polyoxometalates

During the last few years there has been a growing interest in the trapping of paramagnetic transition metal ions with polyoxometalate "ligands".[50–52] For example, Choi *et al.*[50] report the triangular {Cu(II)O$_4$(H$_2$O)}$_3$ containing Na$_9$[Cu$_3$Na$_3$(H$_2$O)$_9$-(α-AsW$_9$O$_{33}$)$_2$] · 26H$_2$O with pseudo-D$_{3h}$ symmetry. The Cu(II) ions are antiferromagnetically coupled, but 0.4 K magnetisation behaviour as a function of field reveals an unusual "half step" between the expected plateaus of *ca.* 1 and 3 μ_B (for total $S = 1/2$ and 3/2 ground states) at *ca.* 4.5 T. 34 GHz single crystal EPR at 8.8 K show "conventional" resonances within the $S = 3/2$ and two $S = 1/2$ states, but also "forbidden" transitions between the two $S = 1/2$ states which are allowed by the antisymmetric exchange interaction. Fitting the angular dependence and magnetisation data to the full exchange spin-Hamiltonian (5), where the $J_{l,l+1}^\alpha$ parameters describe the isotropic and anisotropic exchange interactions and $\mathbf{D}_{l,l+1}$ are the Dzyaloshinskii-Moriya (or antisymmetric exchange) vectors. The latter are found to be *ca.* 12% of $J_{l,l+1}^z$ and induce mixing such that there is complicated anticrossing behaviour between the three lowest states at *ca.* 4.5 T, crudely corresponding to two lowest "$S = 1/2$" and the lowest $S = 3/2$ components, and it is this that leads to the "half-step" magnetisation jump.

$$\hat{H} = \sum_{l=1}^{3} \sum_{\alpha=x,y,z} J_{l,l+1}^\alpha \hat{S}_l \hat{S}_{l+1}$$
$$+ \sum_{l=1}^{3} \vec{\mathbf{D}}_{l,l+1} [\hat{S}_l \times \hat{S}_{l+1}] + \mu_B \sum_{l=1}^{3} \hat{S}_l \mathbf{g}_{ll} \vec{B}_l \tag{5}$$

HF (95–285 GHz) EPR on $KNaCs_{10}[\gamma\text{-}SiW_{10}O_{36}Cu_2(H_2O)(N_3)_2]_2 \cdot 26H_2O$ (**28**) and $[N(C_2H_5)_4]_6[N(C_4H_9)_4]_2H_4[(\gamma\text{-}SiW_{10}O_{36})_2Cu_4(\mu\text{-}1,1,1\text{-}N_3)_2(\mu\text{-}1,1\text{-}N_3)_2] \cdot 12H_2O$ (**29**) have been reported by Mialane *et al.*[51] Ferromagnetic coupling between the Cu(II) ions gives $S = 1$ and 2 ground states for **28** and **29**, respectively. Simulations give $D = -0.55$, $E = 0.065$ cm^{-1} for the triplet state of **28**. One of the exchange interactions in **29** is very small such that the $S = 1$ and 2 states are separated by only 1.6 cm^{-1}, consequently 5–30 K spectra can be simulated as 1:1 superpositions of these states giving $D_1 = -0.96$, $E_1 = 0.08$ and $D_2 = -0.135$, $E_2 = 0.003$ cm^{-1}. The authors note that these are unusually large ZFSs for Cu(II) clusters. In the Section 3.6 we discuss "molecular wheels". One example sandwiched between polyoxotungstate anions has been analysed by Yamase *et al.*[52] In $(n\text{-}BuNH_3)_{12}[(CuCl)_6(AsW_9O_{32})_2] \cdot 6H_2O$ six Cu(II) ions are bridged by terminal oxides from the polytungstates, and are ferromagnetically coupled giving an $S = 3$ ground state. Variable low temperature 190 GHz EPR with the field parallel to the pseudo-6-fold axis of a single crystal confirms this and gives $D = -0.127$ cm^{-1}, which can then be used to model low temperature susceptibility data, which was not possible with an isotropic model.

3.6 Molecular wheels

Cyclic polymetallic complexes have attracted interest in several directions, primarily for the unusual physics that can arise from the apparently simple spin structures. Probably the most intensely studied are cyclic homo- and hetero-metallic chromium(III) clusters, and in the following four publications different aspects of such compounds have been investigated.[53–56] Sharmin *et al.* report the use of HFEPR to explore the low-lying states of the decametallic $[Cr_{10}(OMe)_{20}(O_2CCMe_3)_{10}]$.[53] Magnetic susceptibility data show that the Cr$\cdots$Cr exchange is, on average, ferromagnetic (the molecule has only two-fold symmetry). At frequencies up to *ca.* 200 GHz, multi-line EPR spectra are observed, which can be modelled with $S = 9$ and $D = -0.045$ K. This implies the non-equivalence of the J-values. Above 200 GHz (and *ca.* 10 K) the spectra change dramatically, which the authors explain as due to crossing between the ground state and a first excited, $S = 10$ state at *ca.* 6 T. The magnetic and spectroscopic properties of $[Me_2NH_2]_2[Cr_{10}Cu_2F_{14}(O_2CCMe_3)_{22}]$ have been explored by Winpenny and co-workers,[54] where the anion consists of two {Cr(III)$_5$} horseshoes linked by two Cu(II) ions to form a dodecametallic wheel. The Cr$\cdots$Cr exchange is antiferromagnetic, and Quantum Monte Carlo (QMC) fitting reveals that one of the Cr$\cdots$Cu interactions is antiferro- and the other ferro-magnetic. This gives an $S = 0$ ground state. Low-temperature Q-band spectra are modelled as a sum of $S = 1$ and 2 states and analysing the variable temperature intensities of these two states gives an energy gap between them of 4.0– 6.0 cm^{-1}, in good agreement with that determined by QMC.

Some classes of transition metal cluster (or "molecular nanomagnets"), like the heterometallic rings, have been proposed as components in electron spin based quantum computing. The feasibility of any such application is dependent on the intrinsic spin-lattice (T_1) and phase-coherence (T_2) times, yet according to Ardavan *et al.* direct experimental measurements are rare.[55] To address this problem, the authors use pulsed X-band EPR on the heterometallic rings $(Et_2NH_2)[\{Cr_7MF_8\text{-}(O_2CCMe_3)_{16}\}]$ ["Cr$_7$M"; M = Ni(II) or Mn(II)] to measure T_2 (from the decay of a 2-pulse Hahn-echo sequence) and T_1 (from magnetisation recovery after an inversion pulse). Cr$_7$Ni and Cr$_7$Mn have $S = 1/2$ and 1 ground states, respectively, arising from the mismatch of spins between Cr(III) and M(II). Measurements on natural abundance and perdeuterated materials show that T_2 is dominated by coupling to the ligand protons (and not by the directly bound F). T_2 reaches as long as 3.8 μs at 1.8 K for the deuterated complexes in dilute solution. The authors note that this is orders of magnitude longer than necessary for coherent spin manipulations and hence encouraging for the prospect of construction and manipulation of nontrivial quantum states within individual clusters.

Recently a number of groups have investigated the validity of the strong exchange limit or "giant spin approximation" (GSA) in molecular magnetic systems.[56–59] These assumptions only hold as long as the total spin S is a good quantum number to describe the exchange coupled system and inter-spin state mixing effects are negligible. A more detailed discussion on the limitations of the GSA will be presented in section 3.7 in the context of single-molecule magnets. Piligkos et al. demonstrate an approach to go beyond the GSA model in very large spin systems, using the M = Cd(II) member of the same Cr$_7$M family.[56] Cr$_7$Cd is a good test for such studies because of the unusually well resolved multi-frequency EPR spectra, arising from not just the $S = 3/2$ ground state but also from at least the first two excited states ($S = 1/2$ and $5/2$). The authors use spin-Hamiltonian (6) where the summation runs over all single-ions of the system, R are the Euler rotation matrices, and other symbols have their usual meanings.

$$\hat{H} = \sum_i \mu_B \bar{B} R_i \begin{pmatrix} g_x & 0 & 0 \\ 0 & g_y & 0 \\ 0 & 0 & g_z \end{pmatrix} R_i^T \hat{s}_i + \sum_i \hat{s}_i R_i \begin{pmatrix} -D_i/3 + E_i & 0 & 0 \\ 0 & -D_i/3 - E_i & 0 \\ 0 & 0 & 2D_i/3 \end{pmatrix} R_i^T \hat{s}_i$$
$$+ \sum_{i<j} \hat{s}_i R_{ij} \begin{pmatrix} -2J_{ij} - D_{ij} & 0 & 0 \\ 0 & -2J_{ij} - D_{ij} & 0 \\ 0 & 0 & -2J_{ij} + D_{ij} \end{pmatrix} R_{ij}^T \hat{s}_i \tag{6}$$

The resulting matrix of dimension 16 384 has been numerically diagonalized using the Davidson algorithm,[60] an iterative approach that exploits the sparsity of the Hamiltonian matrix and allows exact computation of the low lying eigenvalues and eigenvectors within realistic computation times. Powder and single crystal data are successfully reproduced with $J_{CrCr} = -5.8$ cm^{-1} and $g_{Cr} = 1.96$ fixed from other methods, leaving just two free parameters: $D_{Cr} = -0.145$ cm^{-1}, and $D_{CrCr} = -0.098$ cm^{-1} [with some assumptions regarding the relative orientations of the various terms in (6)]. The authors emphasise that by using a spin-Hamiltonian that directly relates to the structure of a large exchange coupled system, the quantification of single-ion and exchange anisotropy contributions to magnetic properties of the system has been achieved. In this example, the exchange anisotropy has significant effects on excited state ZFSs.

3.7 Single-molecule magnets (SMMs)

"Electron paramagnetic resonance has played a crucial role in the determination of the properties and in explaining the origin of the peculiar behaviour of molecular nano-magnets, i.e. the slow relaxation of the magnetization at low temperature and the observation of quantum tunnelling of the magnetization."[61] With this sentence Gatteschi et al. open their recent review of EPR on molecular nanomagnets, highlighting the most important aspects in studying SMMs. A second review by McInnes accumulates the "spectroscopy of single-molecule magnets".[62] Ongoing interest in the famous family of Mn$_{12}$ SMMs, which has held the record blocking temperature for two decades, is reflected in new EPR studies, but an increasing number of other SMMs are also reported.

In contrast to the "usual" HF measurements, Rakvin et al. probe the archetypal Mn$_{12}$, [Mn$_{12}$O$_{12}$(OAc)$_{16}$(H$_2$O)$_4$]·2CH$_3$CO$_2$H·4H$_2$O (Mn12Ac), by dual-mode X-band. They observe transitions between states of low $|M|$ in the $S = 10$ ground state, i.e. levels close to the top of the energy barrier to magnetisation reversal.[63] An advantageous technique to establish zero-field parameters is frequency domain magnetic resonance spectroscopy (FDMRS), allowing measurement in actual zero applied field. van Slageren and co-workers have used HFEPR and FDMRS to study the effect of environment on the magnetic anisotropy of [Mn$_{12}$O$_{12}$(O$_2$C'Bu)$_{16}$-(H$_2$O)$_4$].[64] In contrast to other members of the Mn$_{12}$ family, the parameters for solid state ($D = -0.46$, $B_4{}^0 = -1.9 \times 10^{-5}$ cm^{-1}; H $= D\hat{S}_z{}^2 + B_4{}^0\hat{O}_4{}^0$) and frozen

solution ($D = -0.464$, $B_4{}^0 = -2.2 \times 10^{-5}$ cm^{-1}) samples are very similar. By investigating concentration dependence in solution, the authors can discriminate between dissolved and microcrystalline precipitated species in the solution samples. In continuation of their work on the removal of the solvent disorder problem in Mn$_{12}$ crystals, Christou and co-workers report detailed studies on [Mn$_{12}$O$_{12}$(O$_2$CCH$_2$Br)$_{16}$(H$_2$O)$_4$]·4CH$_2$Cl$_2$.[65] The authors show that intrinsic ligand and solvate disorder have no significant local symmetry lowering effects; uniaxial spin-Hamiltonian parameters from single crystal data give $D = -0.468$, $B_4{}^0 = -2.5 \times 10^{-5}$ cm^{-1}. The authors propose that this "truly tetragonal" compound is an attractive alternative to the disordered Mn$_{12}$Ac, although they stress that solvent loss can cause disorder.

The same group has studied a rare case of a ferromagnetically coupled triangular manganese complex [Mn(III)$_3$O(O$_2$CMe)$_3$(mbko)$_3$](ClO$_4$)·3CH$_2$Cl$_2$ (mpkoH = 2-pyridyl ketoneoxime), an SMM that exhibits strong quantum tunnelling of the magnetisation.[66] Single crystal HFEPR confirm an $S = 6$ ground state with $D = -0.3$, $B_4{}^0 = -3 \times 10^{-5}$ and $E \geq 0.015$ cm^{-1}. The supramolecular dimer-of-tetramers [Mn$_4$O$_3$Cl$_4$(O$_2$CEt)$_3$(py)$_3$]$_2$ behaves as a quantum entangled pair of $S = 9/2$ SMMs.[67] Hill and Wilson have extended their theoretical work on simulating the well resolved HFEPR spectra observed between 2 and 18 K.[68] By diagonalising Hamiltonian (7), where each half of the dimer is described in the GSA, the authors reproduce the experimental data with $D = -0.714$ K, $D' = 1.8 \times 10^{-3}$ K, $J = 0.12$ K and $g = 2.00$. Small deviations of the calculated intensity and linewidth from experimental data have been assigned to a possible J-strain.[69]

$$\hat{H}_{\text{Dimer}} = [\hat{H}_1 + \hat{H}_2 + J\hat{S}_{z1}\hat{S}_{z2}] + 1/2J(\hat{S}_1{}^+\hat{S}_2{}^- + \hat{S}_1{}^-\hat{S}_2{}^+)$$
$$\text{with } H_i = D\hat{S}_{zi}{}^2 + D'\hat{S}_{zi}{}^4 + g\mu_{\text{B}}B\hat{S}_{zi} \qquad (7)$$

The mixed-valence SMM [Mn(II)$_3$Mn(III)$_4$(5-NO$_2$-hbide)$_6$]·5C$_2$H$_4$Cl [5-NO$_2$-hbideH$_3$ = N-(2-hydroxy-5-nitrobenzyl)iminodiethanol] has been studied by Koizumi et al.[70] HFEPR (125–190 GHz) gives $D = -0.283$ K in the $S = 19/2$ ground state, and are characteristic of sample torquing in the strong magnetic fields.

Accorsi et al. report a detailed study of the [Fe(III)$_4${RC(CH$_2$O)$_3$}$_2$(dpm)$_6$] family of SMMs (R = Me, CH$_2$Br, Ph, ^{t}Bu; Hdpm = dipivaloylmethane).[71] The centered-triangular topology and antiferromagnetic coupling give $S = 5$ ground states, and the magnetic anisotropy barrier shows a significant dependence on R. Well resolved HF-EPR spectra give the ground state $|D|$ in the order Me > CH$_2$Br > Ph > ^{t}Bu and negative in each case. This correlates with the helical pitch of the {Fe(O$_2$Fe)$_3$} core, i.e. the dihedral angles between the {Fe$_4$} and {Fe$_2$O$_2$} planes. Changing this angle: (i) modifies the single ion ZFS at the central Fe(III) through a trigonal distortion of its coordination sphere, and (ii) changes the orientations of the peripheral single ion $\mathbf{D}$ with respect to the molecular (pseudo)3-fold axis. Remarkably, the 4th-order ZFS parameter $B_4{}^0$ is also found to follow this trend, even changing sign in the series, which has a significant effect on the shape of the anisotropy barrier. This parameter has been noted by several authors to arise from mixing of total S states ("S-mixing"), hence the authors investigate the origin of its variation by diagonalisation of the 6^4-dimension matrix in an exchange spin-Hamiltonian and fitting the lowest 11 eigenvalues (i.e. the $S = 5$ state) to $E(M_S) - E(0) = AM_S{}^2 + BM_S{}^4 + CM_S{}^6$, with the relationships to the "normal" ground state parameters given by $D = A + 875B_4{}^0$ and $B_4{}^0 = B/35$. $B_4{}^0$ is found to be very sensitive to the helical pitch. A further example of the {Fe(III)$_4$} centred triangle topology SMM has been reported by Saalfrank et al. including 17 GHz single crystal data EPR.[72]

The concept of S-mixing as an origin of higher order ZFS terms in a "giant spin" type approximation has led to a re-investigation of some well-known SMMs.

Conventionally, the low temperature magnetic properties of SMMs have been interpreted by attributing a well defined total spin ground state value S in the GSA, for example with a Hamiltonian of the form (8) (or equivalent) for an axially symmetric species. It had been observed that the fourth- and higher-order terms, whose physical origin were unclear, could play a crucial role in the quantum dynamics of high symmetry SMMs.[57,58]

$$\hat{H} = \mu_B B g \hat{S} + D \hat{S}_z^2 + B_0^4 \hat{O}_0^4 + B_6^0 \hat{O}_6^0 + B_4^4 \hat{O}_4^4 + B_6^4 \hat{O}_6^4 \tag{8}$$

Recently a number of groups have attempted to rationalize these high order anisotropy terms within the GSA and to examine its limits.[57–59] Wilson et al. have discussed the problem in [Ni(hmp)(^{t}BuC$_2$H$_4$OH)Cl]$_4$ ("Ni$_4$"; hmpH = 2-hydroxy-methylpyridine).[58,59] This provides an ideal test for investigation of S-mixing effects because of the relatively small size of the spin system (dimension 3^4) and the high S$_4$ symmetry. Previously, EPR and magnetisation data were successfully modelled using the GSA with $S = 4$ including B_4^0 and B_4^4 terms, the latter of which was used to explain the unusually fast zero-field quantum tunnelling of magnetisation. The limitation of the GSA is obvious since the fourth-order terms cannot arise from the $s = 1$ Ni(II) ions. The authors use the exchange Hamiltonian (9) with single-ion parameters (and orientations) derived from the Ni-doped Zn$_4$ compound.

$$\hat{H} = \sum_i \sum_{j>i} J_{ij} \hat{s}_i \cdot \hat{s}_j + \sum_i [D_i \hat{s}_{zi}^2 + E_i(\hat{s}_{xi}^2 - \hat{s}_{yi}^2) + \mu_B \bar{B} g_i \hat{s}_i] \tag{9}$$

They find that a change of J directly modifies the zero-field energies within a given S multiplet, via S-mixing with nearby excited states. For $J \approx D$ these effects are significant, and it is these "effective" fourth order interactions that can be parameterised as B_4^0 and B_4^4 in the GSA. The authors note that the sensitivity of these effects to J give a spectroscopic handle for the determination of this parameter.

Gatteschi and co-workers have shown that similar investigations are possible in larger molecules like the truly axial ($I\bar{4}$) [Mn$_{12}$O$_{12}$(O$_2$CCH$_2^t$Bu)$_{16}$(H$_2$O)$_4$] · 3CH$_3$OH.[57] Beautiful 115 GHz single crystal data at 5 K are presented for the field in the hard plane of magnetisation. The $S = 10$ ground state transitions show remarkable differences in the orientation dependence of their resonance fields. For example, the largest angular dependence is found for $M_S = -10 \rightarrow -9$ while $-9 \rightarrow -8$ is practically insensitive to rotation. To simulate this behaviour within the GSA, it is necessary to include axial terms up to 6th order and, moreover, a sixth order transverse anisotropy ($\hat{O}_6^4$, with B_4^4 and B_6^4 of opposite sign). The exchange Hamiltonian (10) is used to rationalise these terms. The full 10^8 dimension matrix is too large to diagonalise, and a scheme is used where half of the Mn(III) ions are strongly coupled with the Mn(IV) ions to give an (axial) intermediate spin $s_5 = 2$. This, with the remaining four Mn(III) (s_1 to s_4, which are expected to dominate the anisotropy), define the spins in (10) [matrix dimension 3125]. $\mathbf{R}_i$ are rotation matrices.

$$\hat{H} = J\left[\left(\sum_{i=1}^4 \hat{s}_i \hat{s}_5\right) + \hat{s}_1 \hat{s}_4 + \hat{s}_1 \hat{s}_2 + \hat{s}_2 \hat{s}_3 + \hat{s}_3 \hat{s}_4\right]$$
$$+ \sum_{i=1}^4 \hat{s}_i \cdot \mathbf{R}_i \cdot \mathbf{D}_{Mn(III)} \cdot \mathbf{R}_i^T \cdot \hat{s}_i + \hat{s}_5 \cdot \mathbf{D}' \cdot \hat{s}_5 + \mu_B \sum_{i=1}^5 \bar{B} g_i \hat{s}_i \tag{10}$$

The magnetic anisotropy of s_{1-4} are estimated from the AOM and the authors find the easy axis to be 36.4° from the tetragonal axis. The D' value of s_5 is adjusted to reproduce the single crystal data (J is fixed to fit the INS derived $|S,M_S\rangle = |10,\pm10\rangle$ to $|9,\pm9\rangle$ separation). The key contribution to the transverse anisotropy terms are found to be the tilting of the single-ion easy axes with respect to the cluster tetragonal axis. Brechin and co-workers report a further example of the breakdown of the GSA, in the linear trimetallic, $S = 7$ SMM [Mn(II,III,II)$_3$(Hcht)$_2$(bpy)$_4$](ClO$_4$)$_3$.[73] Modelling of W-band EPR within the

GSA requires inclusion of fourth order ZFS terms, and essentially identical spectra can be calculated by diagonalising the full 180×180 matrix when $J \approx D_{Mn(III)}$.

Several papers have appeared on the use of magnetisation methods under microwave irradiation.[74–77] Hendrickson and co-workers report data on single crystals of $[Ni(hmp)(^tBuC_2H_4OH)Cl]_4$ (see above), observing transitions between the ground state $|S,M_S\rangle = |4,\pm4\rangle$ pair, which are split by a transverse applied field.[74] Petukhov et al.[75] and Bal et al.[76,77] investigate magnetisation dynamics in the $S = 10$ ground state $[Fe(III)_8O_2(OH)_{12}(tacn)_6]$ (tacn = 1,4,7-triazacyclononane). Dips in magnetisation vs. applied field at 2 K are observed at resonance frequencies for the $|M_S| = 10 \rightarrow 9$, $9 \rightarrow 8$, $8 \rightarrow 7$ transitions.[75] Petukhov et al. determine the spin temperatures, by reference to measurements in the absence of microwave irradiation, which are higher than the cryostat temperature since the irradiation time is longer than the relaxation times. This effect is lessened with pulsed irradiation, and this also allows probing of the magnetisation dynamics. An immediate fast relaxation after a 10 ms pulse cannot be explained simply by the longitudinal relaxation time T_1, and it must be dominated by longer-lasting effects like the phonon-bottleneck.[75] These authors also warn of sample size effects on relaxation measurements due to spin diffusion.

4.   Mixed p/d- and d/f-block

Wieghardt and co-workers continue their studies of transition metal complexes with coordinated radical ligands.[78–81] In recent work they use the EPR g-values of such species (with, of course, many other methods) to aid assignment of valence electron distribution. For example, an $S = 1/2$ signal is observed for the $[Ni(II)(L1)(L1^\bullet)]^-$ monoanion with g-values 2.313, 2.190 and 2.029.[78] The large g-anisotropy is only consistent with a doublet that arises from strong antiferromagnetic coupling of tetrahedral ($s = 1$) Ni(II) with a single radical ligand $L1^\bullet$, and not with square planar (diamagnetic) Ni(II) with $L1^\bullet$. The $S = 1/2$ $[Co(II)(L2^\bullet)_2]$ has $g = 1.949$, 1.936 and 3.620 with Co hyperfine 50.0, 52.2 and 240×10^{-4} cm^{-1}.[79] The electronic structure is best described as $S = 3/2$ tetrahedral Co(II) strongly coupled to two radical ligands leaving a single unpaired electron on the metal ion, and this predicts, via vector coupling arguments, $g = (5/3)g_{Co} - (2/3)g_L$ and $A = (5/3)A_{Co}$. Two studies of complexes of ligand L3 are reported.[80,81] The redox pair of square-pyramidal complexes $[Fe(III)(L3^\bullet)_2(CN)]^+$ and $[Fe(II)(L3^\bullet)(L3)(CN)]^-$ are both $S = 1/2$ (the intermediate oxidation state is diamagnetic);[80] the former has $g = 2.23$, 2.08, 2.02, the latter has $g = 2.09$, 2.03, 2.03. In the oxidised form, the Fe(III) is intermediate spin 3/2 and coupling to two radical ligands gives $S = 1/2$ with the unpaired electron on the metal ion, consistent with the large g-anisotropy. There are two possible assignments for the reduced form: low spin Fe(II) (diamagnetic) with one $L3^\bullet$, or intermediate spin Fe(II) ($s = 1$) with one $L3^\bullet$. The low g-anisotropy favours the former since the unpaired electron is largely ligand based. The $S = 1/2$ dimetallics $[Fe(III)_2(L3^\bullet)(L3)_3]^-$ and $[Fe(III)_2(L3^\bullet)_3(L3)]^+$ also have low g-anisotropy consistent with strongly coupled intermediate spin Fe(III) ions, leaving the uncompensated spins on the sulfur-based ligands.[81]

L1•   L2•   L3•
                          R = p-C₆H₄-ᵗBu
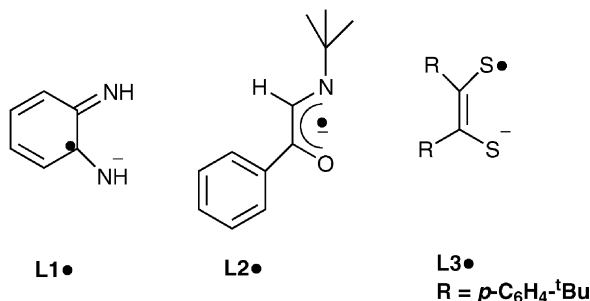
Bagryanskaya and co-workers have prepared a family of $\{Cu(II)(hfac)_2L\}_\infty$ where L is a pyrazole-substituted nitronyl nitroxide.[82–84] The coordination along the chain alternates between Cu axially bound by two pyrazoles and Cu bound axially by two nitronyl nitroxides. Although, these systems are not molecular they are discussed here since the latter groups are essentially magnetically isolated. The nitroxide···Cu···nitroxide "linear" spin system is strongly antiferromagnetically coupled giving rise to two spin doublets and a quartet. The lowest doublet is expected to have $g = 4g_L - g_{Cu}$ from simple vector coupling arguments, and hence this state is observed at $g < 2$ in low temperature EPR spectra [together with the magnetically isolated Cu(II)]. At higher temperatures (> 100 K) this low g feature shifts down-field; the authors ascribe this to a dynamic "spin exchange" process, meaning rapid thermal rearrangement between the three multiplets, due to modulations in J arising from lattice vibrations.[82] A further complication is that some examples undergo significant structural changes at low temperatures, with the Cu···radical distances decreasing by up to 0.3 Å, leading to abrupt increases in J. This is manifested as step-like changes in magnetic susceptibility and the relatively sudden appearance of the ground doublet spectrum in the EPR with decreasing temperature.[84]

Tangoulis and co-workers have published a series of papers addressing the determination of the anisotropic exchange interaction in heterometallic [MLn] dimers, where M is a d transition ion and Ln is a lanthanide ion.[85–87] They treat the Ln ions as effective spin doublets (i.e., this is a low temperature model), with effective g-values determined from analogous systems with diamagnetic M or La where possible. The anisotropic exchange is determined by modelling of parallel and perpendicular mode X-band EPR, with simultaneous fitting of magnetisation and susceptibility data to establish the isotropic part of **J** where possible. For example, for the {CeFe} dimer [Ce(H$_2$O)$_3$(dmf)$_4$(CN)Fe(CN)$_5$],[85] g_{eff} = 1.77, 0.98, 2.82 and g_{eff} = 2.04, 0.72, 2.47 are determined for the Ce(III) and low spin Fe(III) ions, respectively, from measurements on {CeCo} and {LaFe}. Beautiful 4 K spectra are presented for the {CeFe} pair; modelling as coupling of two effective doublets gives axial and rhombic anisotropic exchange parameters $D = 0.06$ and $E = 0.05$ cm^{-1} [defined in terms of the **J** tensor as $D = J_z - (J_x + J_y)/2$ and $E = (J_x - J_y)/2$] while an upper limit of $J [= (J_z + J_x + J_y)/3] < 2.0$ cm^{-1} is determined from low temperature magnetic data.

5. Biological systems

5.1 Methods

Advances in both experimental and theoretical methods in biological EPR spectroscopy are having a huge impact and several timely review articles including polymetallic examples have recently appeared. Van Doorslaer and Vinck[88] have assessed EPR and ENDOR methodologies as applied to structure-function relations in metalloproteins. Techniques such as HYSCORE and ELDOR-detected NMR were included, and monometallic examples dominated. However, the importance of these methods to the study of iron–sulfur clusters and the [NiFe] hydrogenases, including key references, was shown. Very weak, distance dependent, dipole–dipole coupling between electron spins forms the basis for PELDOR (pulsed electron–electron double resonance), and the four-pulse double electron–electron resonance (DEER) experiment is the most commonly used. Jeschke and Polyhach have described methodological aspects,[89] with selected examples, although many possible applications can be envisaged. Schiemann and Prisner have reviewed *Long-range distance determinations in biomacromolecules by EPR spectroscopy*.[90] Techniques included continuous wave EPR (≤ 2 nm), PELDOR, including a consideration of multi-spin clusters, the solid-echo experiment, double quantum coherence EPR, and a discussion of relaxation methods. Distance measurements in the di-iron ribonucleotide reductase, photosystem II, cytochrome *c* oxidase, and [NiFe] hydrogenase

were some of the oligometallic systems that were briefly reviewed. A comparison of EPR methods with NMR and FRET techniques was also presented.

Calvo has reviewed weak exchange interactions between unpaired spins related to long and weak chemical pathways in proteins.[91] Here "weak exchange" is defined for a $J_{ij}\mathbf{S}_i\mathbf{S}_j$ Hamiltonian as 10^{-3} cm^{-1} $< |J_{ij}| < 1$ cm^{-1}. The strong exchange limit of electronic exchange applied in iron–sulfur clusters, both biological and model compounds, produces resultant total spins, S, ranging from 1/2 to 9/2. For half-integer values of $S > 1/2$ broadening effects of resonance lines arise from the phenomenon of D-strain. This strain is normally taken as a signature for a distribution of spatial conformations of the spin-containing sites, by analogy with the widely found g-strain and its assignment to a distribution of g-values. Hagen reports[92] a simple one parameter model to account for D-strain and shows applications to iron–sulfur proteins, as given below:

Table 1

Protein	Spin, S	Rhombicity, $\eta = E/D$	Strain width, $\Delta/\%$	Dummy width, γ/G	Line width, Γ/G	Intensity ratio
Desulfoferredoxin	5/2	0.085	12.0	5	40	1.04
Nitrogenase P-cluster	7/2	0.044	8.0	5	20	0.96
CO dehydrogenase	9/2	0.058	15.0	25	25	0.79

The method was demonstrated with X-band EPR data, and involved estimating the g-value and rhombicity for the spin system and measuring the apparent linewidth of the lowest field feature, Γ. A "dummy" linewidth, γ, fixed to be significantly less than Γ forms a computational device to allow a distribution width, Δ, (expressed as a percentage of D,E) to be calculated iteratively and interactively. Important uses of this method are suggested when performing spin counting, and also where a D-strain simulation might distinguish between an intrinsic and a contaminating resonance line, as shown for examples with a narrow $g = 4.3$ signal. Hinckley and Frey[93] have reported the design of an EPR spectroelectrochemical titrator as applied to the mid-point potential of the [4Fe-4S]$^{2+/1+}$ couple in lysine 2,3-aminomutase, determined at -479 ± 5 mV, where their standard, methyl viologen, was at -460 mV. Experiments were conducted at X-band frequency at 10 K and used 4,4′-dimethyl-1,1′-trimethylene-2,2′-dipyridyl bromide and 1,1′-trimethylene-2,2′-dipyridyl bromide. Noodleman and Han[94] and Neese[95] have reviewed the status of density functional theory (DFT) to the interpretation of EPR data in exchange coupled biological clusters. A broken symmetry (BS) method is discussed for obtaining relative energies of the "spin ladder", and examples of calculation of g-values are given for a [2Fe-2S] Rieske protein and in a mixed valence delocalized di-copper centre.

5.2 Nitrogenases

Peterson and Lowe et al. reported[96] that reduced Fe-protein from nitrogenase from dithionite-free *Azotobacter vinelandii* (Av2) preparations with characteristic g-values at 2.05, 1.94 and 1.86 reduces vanadate to vanadium(IV). Orthovanadate has been used as a transition state mimic, but this work shows that caution needs to be exercised concerning the oxidation state of the Fe-protein; if reduction of vanadium takes place the resultant $\{VO\}^{2+}$ is thought to occupy the divalent metal binding site. Newton and Lowe et al.[97] used stopped-flow and rapid-freeze techniques to investigate different $S = 3/2$ signals from *A. vinelandii* nitrogenase MoFe proteins and suggested that different protonation states led to different conformations. Three mutants (αH195Q, αH195N, αQ191K) each catalytically compromised were chosen

for study, and optical and Mössbauer spectroscopies were used alongside X-band EPR spectroscopy with samples at 10 K. The appearance of a new three-electron-reduced $S = 3/2$ signal was correlated with the ability of the enzyme to bind N_2, noting that the αQ191K variant had previously been shown not to support such binding. No EPR signals assigned to the P-cluster were found.

Hoffman and co-workers reported further on their attempts at identifying the interstitial atom (X) of the iron-molybdenum cofactor (FeMoco).[98] Electron density found inside the 6Fe part of the [MoFe$_7$S$_9$:homocitrate] cofactor of nitrogenase in a high resolution (1.16 Å) X-ray structure provided the starting point for an X-band ESEEM and Q-band ENDOR study in three different environments: (i) native, (ii) extract in N-methylformamide, (iii) in the NifX protein, a chaperone during biosynthesis. ^{13}C and ^{15}N-labelled MoFe protein samples were used. The experimental work was supported by the results of DFT calculations, which used the BS approach in modeling the heterometallic cage. Comparisons of X-band ESEEM spectra with those measured on wild-type (WT) FeMoco were indicative of $X \neq$ N, where *ca.* 2% was the maximum possible population of N, based on considerations of signal:noise ratio and bandwidths. Q-band ENDOR analysis also showed that all responses could be accounted for by coupling to two polypeptide N atoms, α-359^{Arg} and α-356/357^{Gly}. ^{13}C ENDOR also showed a very small upper limit for possible coupling if $X =$ C. The tentative conclusions of this study were that $X \neq$ N/C, unless X were effectively magnetically uncoupled from the $S = 3/2$ spin system, although $X =$ O remains possible.

The same group of workers synthesised labeled (^{13}C, ^{15}N, ^{2}H) methyldiazene (HN = N–CH$_3$) and used it to trap an $S = 1/2$ state of nitrogenase α-195^{Gln}-substituted MoFe protein, which they examined by ENDOR spectroscopy.[99] These data showed the methyldiazene-derived fragment bound through –NH$_x$, and that the internal N atom probably did not bind to FeMoco. The authors used their new data to suggest that the *a*-mechanism is operative in nitrogenase, although not ruling out the *d*-mechanism, noting that their study was performed with a structural variant of the WT. In a further study[100] using *A. vinelandii* strain DJ1373 and expressing the α-20^{Ile} variant of MoFe protein, this group investigated the "H$^+$/H$^-$ intermediate", (A), which appears during turnover in the presence or absence of N_2, and which exhibits an $S = 1/2$ EPR signal. An A → B → C scheme for the relaxation of state A was deduced by step-annealing, which involved rapidly warming a sample initially held below 77 K to 253 K, holding at that temperature for a fixed time, and then quench-cooling for spectroscopic examination. B, with an $S = 3/2$ spectrum, is classified as a new intermediate, which has accumulated two electrons. Both steps in the relaxation show large solvent kinetic isotope effects, and overall the new data were assessed in the context of the Lowe-Thorneley kinetic scheme, which suggested that H_2 was formed in both steps.

A review on nitrogenase has also appeared[101] from the Hoffman/Dean/Seefeldt collaboration considering possible intermediates as N_2 is cleaved, and a revealing set of X-band spectra at *ca.* 4 K for the MoFe protein and freeze-trapped variants was presented, *viz.* wild-type resting, wild-type argon turnover, α-70^{Ala} propargyl alcohol turnover, α-70^{Ile} proton turnover, α-70^{Ala}/α-195^{Gln} hydrazine turnover, α-195^{Gln} methyldiazine turnover, wild-type dinitrogen turnover, with features consistent with $S = 3/2$ and $S = 1/2$ in different proportions. Huang *et al.* studied a putative CrFe protein from mutant UW3 of *A. vinelandii*, for which Na$_2$CrO$_4$ replaced Na$_2$MoO$_4$ in the growing medium.[102] The chromium content was confirmed, and the EPR spectrum of the dithionite-reduced protein was reported to have the same *g*-values (4.3, 3.7, 2.0) as wild-type, but the relative intensities of the resonances were different (recording conditions: 9.38 GHz, 7 K, 5 mW, MA = 10 G); notably the $g = 3.7$ signal being reduced in intensity by *ca.* 1/3.

5.3 Copper

The structure (to 2.30 Å) of hexameric phenoxazinone synthase from *Streptomyces antibioticus* comprises one type 1, one type 2 and one type 3 copper centres and a fifth

copper atom in a novel type 2 site.[103] EPR spectra are reported to show a complex pattern around $g = 2$ said to be characteristic of both type 1 and type 2 centres, and interestingly an overall spin count of 5 (1 spin per copper) was stated. Nitrous oxide reductase from *Achromobacter cycloclastes* contains the bis-thiolate-bridged Cu_A dicopper centre and the μ_4-sulfido-bridged Cu_Z tetracopper cluster. Dooley *et al.* have developed an overexpression system for this enzyme and have identified three redox levels, one of which is EPR-silent and is all Cu(I).[104] The partially oxidised form has Cu_A fully reduced and one Cu in Cu_Z as Cu(II), whereas the fully oxidized form has one Cu(II) in each of Cu_A and Cu_Z. Solomon, Fee and co-workers[105] examined the mixed valence bimetallic Cu_A centre in cytochrome *c* oxidase and nitrous oxide reductase addressing the role of the two proposed electronic ground states, designated σ_u^* and π_u. Consideration of EPR, UV-Vis and MCD spectra and DFT calculations suggest that the σ_u^* state is more efficient at electron transfer and gives g-values consistent with experiment. Prisner *et al.* used X-band and G-band (180 GHz) pulsed EPR spectroscopy to determine relaxation rates in the complex formed between cyctochrome *c* oxidase from *Paracoccus denitrificans* and cytochrome *c*.[106] Transverse relaxation of the Cu_A centre is enhanced on binding cyt *c*, and temperature dependent measurements at X-band and orientation selective measurements at G-band are taken to indicate a broad distribution of structures of the complex with inter-spin distances in the range 2–4 nm.

Yoon and Solomon have reviewed the electronic structures of exchange-coupled trigonal, trimetallic Cu(II) complexes,[28] which are relevant to multi-copper proteins, of which *Rhus vernicifera* tree laccase was used as an example. The importance of antisymmetric and anisotropic exchange interactions was demonstrated, with a spin frustrated ground state shown to be compatible with a low g-value of the native intermediate spectrum of the protein. In the multi-copper oxidase Fet3p the type 2 and type 3 sites form a trimetallic copper cluster, which is the site of four electron O_2 reduction, and the fourth copper atom in a type 1 site mediates electron transfer. Solomon *et al.* used MCD and X- and Q-band EPR spectroscopies to study the effects of specific mutations on the reactivity with O_2.[107] In type 1 deleted mutants, when the type 3 site is diamagnetic, EPR and MCD spectroscopies probe directly the type 2 site of the trimetallic cluster, and the EPR spectra have a monometallic form. In summary, a proton assisted reductive cleavage of the O–O bond at the trimetallic site is suggested.

Chan *et al.* have studied particulate methane monooxygenase, which comprises trimetallic copper clusters (C clusters), proposed as the site of alkane hydroxylation and dioxygen reduction, and electron transfer copper ions (E clusters).[108] The as-isolated enzyme in membranes has an almost featureless, isotropic EPR signal centred on $g \approx 2.1$, assigned to a tri-copper(II) cluster. EPR signal intensity as a function of applied potential was used to support the model of a $(Cu^{II})_3$ cluster being the fully oxidized form after turnover by dioxygen in the absence of alkane.

5.4 Manganese (excluding photosystems)

Manganese homeostasis in *Bacillus subtilis* uses a manganese transport regulator (MntR), which is a member of the diphtheria toxin repressor (DtxR) family of transcription factors. X-ray crystallographic data are available and MntR has a bridged dimetallic active site with the Mn···Mn distance in the range 3.4 to 4.4 Å, distinguishing it from the two monometallic sites found *ca.* 9 Å apart in DtxR. EPR spectra are reported at both room and liquid helium temperatures (14 and 2 K), and spectra were analysed by diagonalisation of a spin Hamiltonian containing isotropic and dipolar exchange and Zeeman and zero-field splitting terms for each centre.[109] Titrations of Mn^{2+} into the protein were followed by EPR, at room temperature and after freezing. Simulation of spectra required: $J = -0.2$ cm^{-1} ($-2JS_1 \cdot S_2$), $S = 5/2$, $I = 5/2$, $A^{Mn} = 250$ MHz, $D = 0.04$ cm^{-1}, $E/D = 0.21$, $r_{Mn-Mn} = 4.4$ Å, $\theta = 45°$. The use of a dipolar interaction alone did not reproduce the experimental

spectrum; this effect was too small on its own. Temperature dependent data also confirmed the very small exchange coupling. The calculated distance between metal ions is consistent with one of the crystallographic reports in the literature. Parallel mode EPR, although of low signal:noise ratio, is consistent with a di-manganese(II) centre.

Krebs, Bollinger and co-workers have identified a manganese/iron ribonucleotide reductase (RR) and possibly a new family of manganese/iron oxygenases.[110,111] X-band freeze-quench EPR spectroscopy of the oxygenated product of the Mn^{II}/Fe^{II} R2 subunit of RR from *Chlamydia trachomatis* showed a well resolved six line pattern around $g = 2$, with splitting of *ca.* 80 G consistent with coupling to ^{55}Mn. Additional splitting is observed when ^{57}Fe is incorporated into the protein. This spectrum develops quickly and decays slowly, and this intermediate is assigned as an $S = 1/2$ ground state from antiferromagnetic coupling between Mn(IV) and high spin Fe(IV), *i.e.* $S_{Mn} = 3/2$ and $S_{Fe} = 2$. Mössbauer spectroscopy was also used, from which the signs of the ^{57}Fe hyperfine parameters were determined, and all of the spin-Hamiltonian parameters are tabulated below:

Table 2

Parameter	Fe(IV) site	Mn(IV) site
g	2.017, 2.030, 2.027	
A/MHz	−55.9, −59.3, −40.5	247, 216, 243
δ/mm s^{-1}	0.17 (6)	
ΔE_{Q}/mm s^{-1}	−0.75	
η	−10	

The similarity of the low temperature X-band EPR spectra from the Mn(III)–Fe(III) cluster of *C. trachomatis*[112] and the N-oxygenase from *Streptomyces thioluteus*,[113] which catalyses the six electron oxidation of *p*-aminobenzoate to *p*-nitrobenzoate, was used to suggest that the latter is a Mn/Fe oxygenase. Estimated spin-Hamiltonian parameters were: *g*-values 2.030, 2.014, 2.015; A^{Mn} values 210, 270, 322 MHz. An $S = 1$ ground state in *C. trachomatis* was reported as arising from coupling Mn(IV) with high spin Fe(III).[114] However, biochemical and spectroscopic evidence was presented to suggest that *p*-aminobenzoate *N*-oxygenase (AurF) is a di-iron enzyme with a mixed valence spectrum characterised by *g*-values at 1.94, 1.79 and 1.70, after expression in *E. coli* and growing on a minimal medium in the presence of a large amount of iron.[115] The as-isolated enzyme, grown on Luria-Bettani medium displayed a six-line Mn spectrum. The identity of this enzyme *in vivo* remains an open question.

5.5 Diiron (including 2Fe2S)

Ribonucleotide reductase (RR) from mouse shows two EPR detectable species, the di-iron cluster, Fe(III)–Fe(IV), designated **X**, and a tyrosyl radical, Y177•, and Bollinger *et al.* used freeze-quench EPR and Mössbauer spectroscopies to investigate a (μ-1,2-peroxo)di-iron(III/III) complex as a precursor to **X**.[116] Sequential X-band EPR spectra with reaction times of 0.037 to 1.0 s comprised the two known spectra in various proportions, and no new EPR active species, and these were used in the construction of a kinetic model. The same group also showed that the slowest step in the formation of the tyrosyl radical in the W103Y variant of RR protein R2 from mouse was the addition of oxygen to the di-iron(II/II) cluster.[117] Again results from the freeze-quench EPR and Mössbauer spectroscopies were used, and a kinetic model constructed. Stubbe, Krebs and co-workers have identified a 2Fe ferredoxin, YfaE, as being used to maintain the diferric–tyrosyl radical in *E. coli* RR.[118] The X-band EPR spectrum, recorded at 77 K has *g*-values 2.036, 1.944 and 1.884, which

are similar to previously reported 2Fe2S ferredoxin from plant sources and also the ferredoxin domain of methane monooxygenase.

The hydroxylase component of toluene/o-xylene monooxygenase has a carboxylate-bridged di-iron active site. The I100W variant, with either ^{56}Fe or ^{57}Fe, and in which the W100 residue blocks access to the active site, was studied by X-band EPR and ENDOR, following reaction of the di-iron(II) enzyme with dioxygen and rapid freeze-quench methods.[119] Mössbauer measurements were performed in parallel. EPR signals with $g = 16$ (di-iron(II) centres) and $g = 2.0$ (di-iron(III/IV)-W$^{\bullet}$ centres) were detected, and the $g = 16$ signal decayed in a biphasic manner (first phase complete by ca. 0.17 s, second phase incomplete at 150 s). The $g = 2.0$ signal rose with a rate constant of 0.77 s^{-1} and decayed at 0.15 s^{-1}, maximizing at ca. 4 s. ENDOR spectra were collected on samples quenched at 4 s, and the di-iron component was only observed at <40 K, whereas the signal from the tyrosyl radical was present up to ca. 77 K. ENDOR signals were assigned to protons of terminal water or hydroxide ($A^H \approx 4$–8 MHz) of the di-iron(III/IV) cluster.

NADH:quinone oxidoreductase (complex 1) contains eight or nine iron–sulfur clusters, and Hirst et al. have proposed that EPR signals N4 and N5 have been misassigned.[120] The previous and revised assignments are below.

Table 3

Cluster	Subunit E. coli	Subunit Bos Taurus	EPR signal (consensus)	EPR signal (revised)
2Fe[E]	NuoE	24 KDa	N1a	N1a
4Fe[F]	NuoF	51 KDa	N3	N3
2Fe[G]	NuoG	75 KDa	N1b	N1b
4Fe[G]C	NuoG	75 KDa	N4	N5
4Fe[G]H	NuoG	75 KDa	N5	—
4Fe[G]*	NuoG	—	N7	N7
4Fe[I]1	NuoI	TYKY	N6a or N6b	N4
4Fe[I]2	NuoI	TYKY	N6a or N6b	N4
4Fe[B]	NuoB	PSST	N2	N2

The NuoG EPR signals produced by dithionite reduction were characterised by spectrum simulation and also by simulation of the saturation properties from power dependence of signal intensity, using the parameters of power for half saturation ($P_{\frac{1}{2}}$) and anharmonicity (b). These results are tabulated in Table 4.

Table 4

Cluster	g_z	g_y	g_x	Signal(s) used	$P_{1/2}$ /μW (T/K)	Anharm-onicity b
2Fe2S (N1b)	2.03	1.939	1.939	2.03	20000 (40) 200 (12) 20 (5)	1
4Fe4S (4Fe[G]*)	2.048	≈1.94	1.916	2.048, 1.916	540 (12) 8 (5)	1
4Fe4S (4Fe[G]C/H)	2.074	≈1.95	1.885	2.074, 1.885	1700 (12) 6 (5)	0.5 0.37

Quinaldine 4-oxidase is a member of the xanthine oxidase family and has two 2Fe2S centres, FeSI and FeSII, which can be distinguished by the g-values from their EPR spectra. Fetzner et al. prepared variants of this enzyme and made a spectroscopic and biochemical study.[121] The EPR parameters of the reduced ferredoxin centres are listed in Table 5.

Table 5

Protein	Relative Fe content	FeSI/FeSII	FeSI			FeSII		
			g_1	g_2	g_3	g_1	g_2	g_3
Recomb.	1	1.13	2.021	1.937	1.937	2.072	1.975	1.877
E736D[a]	0.34	0.754	2.021	1.936	1.916	2.067	1.971	1.874
E736Q[a]	0.50	0.786	2.024	1.937	1.923	2.070	1.976	1.869
C40S[b]	0.41	[1/0]	2.021	1.939	1.923	—	—	—
C45S[b]	ca.0.07	–	2.010	1.935	1.935	2.038	1.910	1.895
C48S[b]	1	0.429	2.021	1.934	1.934	2.028	1.934	1.881
C60S[b]	0.38	1.38	2.018	1.935	1.927	2.072	1.967	1.831
C120S[b]	0.47	2.23	2.006	1.938	1.915	2.071	1.975	1.881
C154S[b]	ca.0.20	4.88	2.009	1.909	1.760	2.066	1.977	1.875

[a] Large subunit. [b] Small subunit.

Overall these data were taken to suggest that Fe1 of both FeSI and FeSII are the sites of reduction, and Fe2 remain as Fe(III). By extension these sites for reduction appear to be conserved in the xanthine oxidase family of enzymes.

Dixon *et al.* showed that the outer mitochondrial membrane protein mitoNEET contains a pH-labile, redox active 2Fe2S cluster, coordinated by one histidine and three cysteine residues.[122] The X-band cwEPR spectrum of the reduced form at 15 K showed a rhombic spectrum, whereas the oxidized form was EPR silent. Argüello *et al.* identified a 2Fe2S cluster in a copper chaperone from *Archaeoglobus fulgidus*.[123] Purified chaperone protein is EPR silent, and at 10 K dithionite-reduced protein has two different sets of EPR signals. In the $g = 2$ region between 7–40 K, $g_1 = (2.06, 1.91, 1.86, g_{av} = 1.94)$ and $g_2 = (2.04, 1.97, 1.90, g_{av} = 1.97)$, and the second type is a "$g = 3$" signal and is axial with $g_\perp = 3.11$ and unresolved $g_{||} = 1.85$, where the value of S is unclear. Nine cysteine to serine mutants were prepared, and C75S, C109S and C119S led to complete disappearance of the $g = 3$ signal, whereas C75S and C109S also collapsed the $g = 2$ signals into a single axial ferredoxin-type signal with $g_{av} < 2$, although C119S left the two signals in this region. C77S altered both types of signal.

The iron–sulfur centres of the NADH:quinine oxidoreductase of *Rhodothermus marinus* were studied by EPR spectroscopy by Pereira *et al.*[124] Temperature and power-dependent EPR spectra and redox titrations showed that a minimum of two 2Fe2S and four 4Fe4S centres were present, with all except one centre having a standard reduction potential in the range -240 ± 20 mV. Assignments of EPR signals are in the table below.

Prisner *et al.* performed 1- and 2-dimensional ESEEM spectroscopy at X-band frequency on the $S = 1/2$ signal of the reduced N1 cluster of NADH:ubiquinone oxidoreductase from *Yarrowia lipolytica*.[125] Measurements were made at 30 K because only signals from the N1 cluster were observable. The hyperfine matrix and quadrupole tensor of a nitrogen nucleus were assigned to a backbone atom of the polypeptide chain, and the isotropic and dipolar couplings from two sets of protons were assigned to the two sets of β-protons of the cysteine ligands in the 2Fe2S ferredoxin.

A 2Fe2S ferredoxin from the halophilic archaeon *Haloferax mediterranei*, when reduced with dithionite, has a rhombic EPR spectrum (2.07, 1.98, 1.91) observed at X-band frequency up to 60 K.[126] This places the cluster spectroscopically into a plant-type category of two iron ferredoxins. Hüttermann and co-workers reported on ^{1}H ENDOR spectra of reduced 2Fe2S proteins from adrenodoxin (ADx) and the Rieske protein from bovine mitochondrial bc1 complex.[127] In Adx (g-values: 2.0241, 1.9347, 1.9331) four large hyperfine couplings were assigned to cysteine β protons located near to the Fe(III) ion. A similar analysis of data from the Rieske protein (2.028, 1.891, 1.757) found two cysteine β protons and one β proton of a histidine residue. Shubin and Dikanov have reviewed g-matrix variations in Rieske-type proteins.[128]

Table 6

Centre	Assignment	g_1	g_2	g_3	g_{av}	E°/mV
2Fe2S	N1a	2.023	1.948	1.935	1.969	−240
2Fe2S	—	2.014	1.936	1.923	1.958	—
2Fe2S	—	2.036	1.938	1.932	1.969	—
2Fe2S	—	2.033	1.937	1.932	1.967	—
4Fe4S	N5	2.020	1.919	1.847	1.929	−240
4Fe4S	N3	2.033	1.918	1.859	1.937	−240
4Fe4S	N2	2.057	1.920	1.907	1.961	< −450
4Fe4S	N4	2.088	1.930	1.884	1.967	−240

Pulsed methods at X- and Q-band frequencies have been applied to samples of ^{57}Fe-enriched [FeFe] hydrogenase from *Desulfovibrio desulfuricans*.[129] Oxidised and CO-inhibited forms showed all six ^{57}Fe hyperfine couplings and the associated 4Fe4S cluster showed four large ^{57}Fe couplings and the 2Fe2S cluster was characterized by two weak couplings (<5 MHz). A comprehensive set of simulation parameters for all of the couplings is presented in ref. 129. Coupling to the "diamagnetic" 4Fe4S cluster is assigned as arising from interactions between the sub-clusters, which is enhanced by the bonding of CO, and is dependent upon the singlet-triplet gap in the cluster and the inter-cluster exchange with the 2Fe2S centre. ^{57}Fe-enriched [FeFe] hydrogenase from *Desulfovibrio desulfuricans* was studied by cw X-band EPR spectroscopy and detailed spectrum simulations to show that hyperfine interaction of the unpaired spin in H_2-reduced enzyme is associated with all six iron atoms of the H-cluster.[130] This cluster comprises a 2Fe component and a cysteine ligand forms a thiolate bridge to a 4Fe4S cluster.

The di-ferrous form of novel forms of the R2 subunit of ribonucleotide reductase from human (hp53R2) and mouse (mp53R2) are EPR inactive, whereas "normal" di-ferrous R2 has a strong EPR signal in ≥ 20% glycerol at X-band frequency with $g_{obs} \approx 12$, in both parallel and perpendicular mode.[131]

5.6 Other iron–sulfur centres

Fontecave *et al.* studied the [Fe-Fe] hydrogenase maturation protein HydF from *Thermotoga maritime* by cw and HYSCORE EPR spectroscopy at X-band frequency.[132] The 4Fe4S cluster of this protein shows the presence of both axial $S = 1/2$ ($g_{||} = 2.045$, $g_\perp = 1.904$) and $S = 3/2$ (resonances at $g_\perp = 5.2$ and $g_{||} = 1.75$) states, with the former showing power saturation and temperature dependence consistent with a $\{Fe_4S_4\}^{1+}$ centre. The HYSCORE spectroscopy provided evidence for one non-cysteinyl ligand on the cluster, which was exchangeable with imidazole.

Reports on the S-adenosylmethionine (SAM) radical enzyme "superfamily" have continued. Working with 4-hydroxyphenylacetate decarboxylases from *Clostridium difficile* and *Clostridium scatologenes*, Selmer *et al.* produced evidence from X-band frequency cwEPR on iron–sulfur centres (at 10 K) and glycyl radicals (at 77 K) and biochemical studies that the 4Fe4S centres are involved in electron transfer to the SAM cluster, but do not take part directly in the reductive cleavage of SAM.[133] Spore photoproduct (SP) lyase, anaerobically purified from *E. coli*, contains a nearly isotropic EPR signal ($g = 2.02$) at X-band frequency and 12 K characteristic of a $\{Fe_3S_4\}^{1+}$ cluster, which is replaced on dithionite reduction by a rhombic signal ($g = 2.03, 1.93, 1.89$) consistent with a $\{Fe_4S_4\}^{1+}$ cluster.[134] Addition of AdoMet did not change this latter signal, but it was reduced in intensity. The Elongator subunit Elp3, studied by Onesti *et al.* was shown to contain a 4Fe4S cluster and to bind S-adenosylmethionine.[135] X-band frequency spectra at 10 K showed a weak axial signal ($g_{||} = 1.96$, $g_\perp = 2.002$) similar to that expected from a $\{Fe_3S_4\}^{1+}$ cluster, but dithionite reduction produced a strong axial signal ($g_{||} = 2.03$,

$g_\perp = 1.93$, $g_{av} = 1.96$) assigned to a $\{Fe_4S_4\}^{1+}$ cluster. This latter assignment was further confirmed by power saturation and temperature dependence studies. Addition of SAM produced a small, reproducible shift and broadening in the spectrum ($g_{||} = 2.020$, $g_\perp = 1.93$) with unchanged integrated spectral intensity.

Golbeck *et al.* have reported on the iron–sulfur clusters in the soil-dwelling phototroph *Heliobacterium modesticaldum*.[136,137] Using low temperature (4.2 K) Mössbauer and EPR (X-band) spectroscopies, the dithionite-reduced cluster formed in the presence of light gives a broad, intense EPR signal at $g \approx 5$ and signals around $g = 2$, which are assigned to $S = 3/2$ and $S = 1/2$ spin states. In further work, the di-cluster ferredoxin containing two 4Fe4S clusters, similar to F_A and F_B in photosystem I was characterised. A method of analysis of the $g \approx 5$ signals arising from $S = 3/2$ iron–sulfur clusters has been outlined by Bertrand *et al.*[138] If two low-field peaks corresponding to Kramers doublets are present in a spectrum, then by studying the temperature dependence of the ratio of the area under the peaks, the spin Hamiltonian parameters can be determined. The theory was derived and applied to the FS0 centres of a nitrate reductase from *E. coli*. It was shown that previous assumptions using an isotropic g matrix ($= 2.0$) could lead to very significant errors, and in this case the three g-values used were: $g_x = 1.935$, $g_y = 2.026$ and $g_z = 1.924$.

Periplasmic selenate reductase from *Thauera selenatis* has EPR signals (X-band frequency, < 40 K) assigned to $\{Fe_3S_4\}^{1+}$ and $\{Fe_4S_4\}^{1+}$ clusters, with further evidence that two $S = 1/2$ 4Fe4S clusters are strongly antiferromagnetically coupled under very low potential (reducing) conditions.[139] In formaldehyde ferredoxin oxidoreductase from *Pyrococcus furiosus* the $\{Fe_4S_4\}^{1+}$ cluster shows $S = 3/2$ and $S = 1/2$ spin states.[140] Hüttermann *et al.* used orientation-selective ^1H ENDOR spectroscopy on HiPIP proteins from *Ectothiorhodospira halophila* (g-values 2.1425, 2.0315 and 2.0296) and *Rhodocyclus tenuis* (2.1140, 2.0392 and 2.0215).[141] Valence-trapping of cubane oxidation states of iron was identified.

Pyruvate ferredoxin oxidoreductase catalyses the anaerobic oxidation of pyruvate with CoA to acetyl-CoA, CO_2, and two electrons are transferred to the 4Fe4S cluster. The thiamine pyrophosphate (TPP) dependence of the enzyme was used by Ragsdale *et al.* to determine which particular iron–sulfur cluster (of three, labeled A–C at increasing distance from TPP) was reduced.[142] Using pulsed ELDOR, the spin echo signal of $\{Fe_4S_4\}^{1+}$ was observed whilst the pumping microwave pulse was in resonance with the hydroxyethylidene(HE)-TPP radical intermediate. The RIDME experiment was used to remove orientational selectivity and the pulsed results indicated that the HE-TPP radical was coupled to cluster B, but it was also suggested that a very fast electron transfer from cluster A must already have taken place. Recombinant acetyl-CoA synthase from *Morella thermoacetica* was studied using low temperature (4.2 K) Mössbauer and EPR (X-band) spectroscopies, with dithionite reduction and incorporation of ^{57}Fe,[143] using nickel activation and also CO binding. The latter causes change in relative intensity of the $S = 3/2$ and $S = 1/2$ spin states.

An iron–sulfur cluster isolated from *Mycobacterium tuberculosis* H37Rv was characterized as 4Fe4S from its X-band EPR spectrum at 145 K with g-values at 4.29, 2.36 and 2.00.[144] Interestingly, freshly purified protein had an optical spectrum consistent with a 2Fe2S cluster, but *in vitro* reconstitution produced the 4Fe4S cluster. The protein functions as a protein disulfide reductase. A new transient EPR signal, from reduction with dithionite (which will not reduce the cluster alone) and 2-C-methyl-D-erythritol-2,4-cyclodiphosphate of a 4Fe4S cluster of the GcpE enzyme from *Thermus thermophilus*, has a rhombic signal at X-band frequency (g-values: 2.000, 2.019, 2.087).[145] The signals saturate below 20 K, but remain observable up to 160 K. The iron–sulfur cluster in the C-terminal domain of the p58 subunit of human DNA primase is of the HiPIP-type, with simulation revealing two slightly different sets of g-values: 2.0870, 2.0405, 2.0126 and 2.0872, 2.0311, 2.0094.[146] The essential iron–sulfur clusters in the ATP-binding cassette protein ABCE1 comprise one ferredoxin-like arrangement of cysteine residues

$(CPX_nCX_2CX_2C)$ and one unique set $(CXPX_2CX_3CX_nCP)$. Only seven of the eight conserved cysteines are essential for viability of the cells. An EPR spectrum characteristic of $\{Fe_3S_4\}^{1+}$ was reported following ferricyanide oxidation (g-values: 2.031, 2.017, 2.002), but attempts at reduction by dithionite or ascorbate were ineffective.[147]

Magnesium chelatase, from the bacteriochlorophyll biosynthetic pathway, from *Rhodobacter capsulatus* has a novel cysteine motif $(^{393}CX_2CX_3CX_{14}C)$, which on dithionite reduction gives a rhombic set of g-values (1.90, 1.93, 2.09) and a signal at $g \approx 2.02$ assigned to a $\{Fe_3S_4\}^{1+}$ cluster.[148] Replacing cysteines with alanine at Cys396 and Cys414 gave a protein that was EPR silent on reduction. *Azotobacter vinelandii* iron protein (Av2) can be reduced with Ti(III) citrate to an $S = 4$ $\{Fe_4S_4\}^0$ state, which has a parallel mode $g = 16.4$ EPR signal at X-band frequency.[149] Subunit B of the heterodisulfide reductase from *Methanothermobacter marbugensis* has an active site 4Fe4S cluster with a cysteine-rich motif $(CX_9CCX_2CX_2C)$ that is the suggested binding site of the cluster,[150] which exhibits a rhombic EPR signal (g-values: 2.015, 1.995, 1.950) following duroquinone oxidation. ^{57}Fe Davies ENDOR and cw EPR spectra of a series of cysteine to serine mutants were also reported. Friedrich *et al.* report EPR spectra from bi-metallic and tetra-metallic iron–sulfur clusters in the NADH:ubiquinone oxidoreductase (complex 1) from *E. coli*, including a spectrum of the non-conserved cluster N7.[151]

Lindahl *et al.* used Mössbauer and EPR spectroscopies to characterize intact mitochondria from respiring *Saccharomyces cerevisiae*.[115] The clusters identified using their average g-values included $\{Fe_2S_2\}^+$ from succinate dehydrogenase, $\{Fe_2S_2\}^+$ of the Rieske protein of cytochrome bc_1, and $\{Fe_3S_4\}^+$ in aconitase (homoaconitase or succinate dehydrogenase), as well as the a_3:Cu_b site of cytochrome c oxidase.

5.7 Coupled haems

The decahaem c-type cytochrome, MtrC, from *Shewanella oneidensis* is associated with the outer cell membrane and shows X-band EPR spectra at 10 K with features spanning g_{obs} values of 5.9 to 1.5.[152] Data were collected as a function of electrochemical potential, which enabled resolution of contributions from spin-coupled and magnetically isolated haems. A detailed EPR study of the isolated b_6f complex of *Chlamydomonas reinhardtii*, during a redox titration and in oriented membranes, was reported by Nitschke *et al.*[153] The inhibitor 2-*n*-nonyl-4-hydroxyquinoline *N*-oxide (NQNO) simplifies the EPR spectrum (X-band, *ca.* 6 K) of the unusual cytochrome c_i component, which has a single thioether link to the protein, no protein-derived axial ligands and possibly a H_2O/OH^- ligand prior to inhibition. A dipolar interaction with the b_H haem is required to interpret splittings in the $S = 5/2$ spectrum. However, strong exchange interactions are required to interpret the spectrum of the uninhibited form. An improved resolution crystal structure of the b_6f complex from *Mastigocladus laminosus* and with inhibitors tridecylstigmatellin (TDS) and with NQNO were used to support the interpretation of the exchange-coupled EPR spectra.[154] Cheesman *et al.* report that cytochrome cd_1 nitrite reductase from *Paracoccus pantotrophus* has haem d_1 EPR silent because of coupling to a radical species that is formed during reaction of the enzyme with nitrite.[155] This reactivity was confirmed with enzyme from *Pseudomonas stutzeri*. 9 and 285 GHz EPR of the haem-containing catalase-peroxidase from *Mycobactrium tuberculosis* encoded by the *katG* gene showed the presence of three protein-based radical species, two from tryptophans and one from tyrosine, using selective deuterium labeling of the amino acids and site-directed mutagenesis.[156] The X-band EPR spectrum of the radical from Trp321 is assigned as being spin-coupled to an oxo-ferryl paramagnet.

5.9 Cobalt

The metallo-β-lactamase CcrA sequentially binds two Co^{2+}, with no evidence for spin-coupling of the metal ions from X-band EPR spectroscopy at 12 K.[157] In BCII

from *Bacillus cereus* loading Co^{2+} with metal:enzyme ratios up to 0.6 in an EPR spectroscopic titration gave two spin active species that were capable of simulation using two different extents of rhombicity, *viz.* $S = 3/2$, $D \approx h\nu$ (50 cm^{-1} was used), $E/D = 0.11$, $g_z = 2.44$ and $g_{x,y} = 2.36$; $S = 3/2$, $D \approx h\nu$ (50 cm^{-1} was used), $E/D = 0.17$, $g_z = 2.65$ and $g_{x,y} = 2.525$, $A^{Co} = 88 \times 10^{-4}$ cm^{-1}.[158] However, above a metal:enzyme ratio of 0.6 the signal intensity did not increase, indicative of spin-coupling of Co^{2+}, and this was accompanied by observation of a derivative-shaped $g_{eff} \approx 10$ in a parallel-mode EPR experiment.

5.10 Photosystems

A 4Fe4S ferredoxin bound to Photosystem I was used to attempt "chemical rescue" of a site-modified ligand to the cluster.[159] PsaC binds two low potential 4Fe4S clusters (F_A and F_B), a subunit of PSI and cysteine was replaced by glycine at position 13 (C13G/C33S), which is a ligand donor site to F_B. Two 4Fe4S clusters are reported to be found in the protein when reconstitution took place in the presence of aryl or alkyl thiolates, including mercaptoethanol. EPR spectra of the thiolate-treated and reduced variant show an almost axial $S = 1/2$ signal assigned to $\{Fe_4S_4\}^{1+}$ with no indication of spin-spin interaction to the second cluster. The low field region of the spectrum showed several signals with effective g-values between 7.52 and 4.29, consistent with $S \geq 3/2$ states. Haddy has reviewed the EPR spectroscopy of the manganese cluster of photosystem II,[160] summarising the EPR signals found and discussing signals from the S_2, S_0, S_1, S_3 and S_2' and S_3' states, along with some radical signals. Heinnickel and Golbeck reviewed heliobacterial photosynthesis, which contain Type 1 reaction centres.[161] The terminal electron acceptors, the F_A and F_B iron–sulfur centres, have characteristic spectra under conditions of illumination or of bisulfite reduction. The intermediate FX centre contains a 4Fe4S cluster with an $S = 3/2$ ground state following dithionite reduction,[136,137] as noted above.

Styring *et al.* have shown that the split EPR signals (X-band, 5 K) of PSII-enriched membranes, induced by illumination, arising from magnetic interaction between the $Y_Z^{\bullet}$ (tyrosyl) radical and the $CaMn_4$ cluster are modified by addition of methanol, which binds to the cluster.[162] It was shown that methanol interacts with the $CaMn_4$ cluster in S_1, S_3 and S_0 states, and it was proposed that an increase in magnetic exchange occurs within the cluster on binding. The same group studied flash-induced changes in the EPR signal intensity of the $Y_D^{\bullet}$ radical spin-coupled to the $CaMn_4$ cluster *ca.* 30 Å away in the Tyr161 residue of the D2 protein of PSII, and suggest that the $Y_D^{\bullet}$ radical could be a probe of kinetic behaviour.[163] EPR spectroscopy at X-band frequency and 5 K has been used to investigate pH-dependent competition between Y_Z and Y_D in PSII under conditions of illumination.[164] Experiments required observation of the appearance of $Y_Z^{\bullet}$, *via* the split S_1 signal, and in the presence of chemically pre-reduced Y_D. Competition took place above pH = 7.2. Wavelength-dependent induction of S_0, S_1 and S_3 states of the water oxidizing centre (WOC) have been reported using PSII-enriched membranes at 5 K with monochromatic laser light between 400 to 900 nm.[165] Interestingly, at 5 K the split-S_3 signal induced by near infra-red light did not decay over a period of 60 minutes, whereas that signal induced by visible light had decayed by 50% after 30 minutes.

Evans, Pace and co-workers also report on methanol-binding to the oxygen-evolving complex (OEC) under conditions of turnover, followed by ESEEM spectroscopy and using D_2O and CD_3OH.[166] From the classes of exchangeable deuterons identified with significant dipolar coupling to the S_2 state (0.65, 0.39($\times$2) MHz) and the S_0 state (0.60, 0.37($\times$2) MHz), it was proposed that there is close binding of one water molecule to a single Mn^{2+} in S_0 and to a Mn^{3+} in S_2. X-band EPR spectroscopy at 77 K, with perpendicular mode to detect Mn^{2+} and parallel mode at 3.7 K to detect Mn^{3+}, was used to follow re-assembly starting from apo-WOC in PSII and detecting photo-oxidised Mn^{3+} bound to the protein.[167]

It was shown that the presence of Ca^{2+} abolishes the pH-dependence of the spin-Hamiltonian parameters and hence is suggested to control the co-ordination environment at the manganese ion. The multi-line signal of the S_2 state in PSII from the cyanobacterium *Thermosynechococcus elongates* has been measured at 94 GHz in frozen solution and in single crystals.[168] Hyperfine structure that is partially resolved in the single crystal spectra has strong angular dependence, and so simulation of the frozen solution spectrum using previously published ^{55}Mn ENDOR data gave principal g-values: 1.997, 1.970 and 1.965, which was noted to give a surprisingly small $g_{av} = 1.977$ when compared to simple manganese complexes in oxidation states III and IV. These g-values were then used in a study by Lubitz, Messinger and co-workers that defined the electronic structure of the $CaMn_4$ cluster of the OEC of PSII in conjunction with new X- and Q-band pulsed EPR and pulsed ^{55}Mn ENDOR measurements.[169] The principal values of the g- and A^{Mn}- matrices for the S_2 and S_0 states are tabulated below.

Table 7

S_2	g	A_1/Mz	A_2/Mz	A_3/Mz	A_4/Mz
x	1.997	310	235	185	170
y	1.970	310	235	185	170
z	1.965	275	275	245	240
iso	1.977	298	248	205	193
Aniso^a	0.032	35	40	60	70
S_0	g	A_1/Mz	A_2/Mz	A_3/Mz	A_4/Mz
x	2.009	320	270	190	170
y	1.855	320	270	190	170
z	1.974	400	200	280	240
iso	1.946	347	247	220	193
Aniso^a	0.154	80	70	90	70

^{a} Difference between the largest and smallest component.

A detailed model for exchange coupling and oxidation states was presented using the published structural and X-ray absorption spectral data.

The role of Ca^{2+} in oxygen evolution was studied by inhibiting PSII membranes with Dy^{3+}, Cu^{2+} or Cd^{2+} monitored by X-band EPR spectroscopy and has shown that the Ca^{2+} cofactor is not specifically required for the transition from the S_1 to the S_2 state.[170] However, the loss of oxygen-evolving activity in the Dy^{3+} and Cd^{2+} inhibited samples show that Ca^{2+} is required to activate water in the O–O bond-forming reaction.

Another single crystal W-band study of the S_2 state of PSII, but from the thermophilic cyanobacterium *Thermosynechococcus vulcanus*, yielded g-values: 1.988, 1.981, 1.965, giving $g_{av} = 1.978$.[171] Un *et al.* used X-band and field-frequency measurements around 190 and 285 GHz to study the split signal from the spin-coupled S_2-$Y_Z^{\bullet}$ state of PSII from a D2-Tyr160Phe mutant from *T. elongates*, which avoids spectral overlap with $Y_D^{\bullet}$.[172] Data were interpreted to show that both ferro- and antiferro-magnetic spin-spin couplings could be detected. Petrouleas' group has studied $Y_Z^{\bullet}$ under various conditions $S_0Y_Z^{\bullet}$, $S_0Y_Z^{\bullet}$(5% MeOH), $S_1Y_Z^{\bullet}$, $S_2Y_Z^{\bullet}$ and $S_0Y_Z^{\bullet}$ (5% MeOH) in the temperature range 11–230 K, using a rapid-scan EPR method at X-band frequency.[173] The overall conclusion was that the tyrosyl radical progressively decouples from the $CaMn_4$ cluster as the relaxation rate at manganese increases with increasing temperature. The rapid scan method was also applied to examine the heterogeneity of the S_2 state of the OEC, by generating states $S_1Y_Z^{\bullet}{}_{vis}$ (from visible light excitation of S_1) and $S_1Y_Z^{\bullet}{}_{NIR}$ (from near infra-red excitation of S_2, wherein the $CaMn_4$ cluster oxidizes Y_Z) and observing their decay by EPR

spectroscopy.[174] Both spectra have a feature at $g = 2.035$ at 11 K, and this is replaced by the S_2 multi-line spectrum on annealing at 200 K. However, the $S_1Y_Z^{\cdot}{}_{vis}$ has an additional faster decaying component 26 G wide, which transforms into a component with $g = 4.1$. Thus, it is stated that the $S_1Y_Z^{\cdot}$ is an intermediate in the transformation of S_1 to S_2, and that heterogeneity already exists in the S_1 state.

5.11 Nickel

Lubitz *et al.* have reviewed the application of advanced magnetic resonance techniques to [NiFe] and [FeFe] hydrogenases, beginning with an overview.[175] Topics for the [NiFe] enzymes include the characteristic EPR spectra of the various redox states, the oxidised (as-isolated) form, the active intermediate state, inhibition of the enzyme by O_2, CO and light sensitivity. The format for the discussion of the [FeFe] hydrogenases follows a similar pattern, and both parts consider electronic structure and the use of DFT calculations. There is a very useful appendix, which includes a section outlining modern methods in EPR spectroscopy. A single crystal ^{1}H ENDOR study at 10 K and X-band frequency alongside analysis by DFT of the oxidized state (a 30:70 mixture of Ni-A and Ni-B, respectively) of [NiFe] hydrogenase from *Desulfovibrio vulgaris* Miyazaki F was reported by Lubitz and co-workers.[176] Two hyperfine interaction matrices with large isotropic coupling were assigned to the β-CH_2 group of the cysteine that bridges between the metal centres, and the hyperfine matrix for the proton of a bridging hydroxide was also identified. The data from the Ni-A state were broader, two large isotropic couplings were identified, but the third was not able to be assigned. The "oxidized ready" (Ni-B) state of the same enzyme was investigated by the HYSCORE method at 5 K and X-band frequency, using both native and ^{15}N-enriched samples.[177] ^{14}N parameters (hyperfine: $+1.32$, $+1.32$, $+2.01$ MHz; quadrupole: $e^2qQ/h = -1.9$ MHz, $\eta = 0.37$) were assigned to N_ϵ of His88 and aided by DFT calculations, the hydrogen bond of this residue with Cys549 was classified as weak, because of the small fraction of spin density delocalized onto the histidine ring.

In the first spectroscopic study of an enzyme from the cyanobacterial uptake hydrogenases, a combined EPR (X-band, VT) and FTIR study has been reported from enzyme isolated from *Acidithiobacillus ferrooxidans*.[178] The results show that the enzyme is similar, but not identical with known [NiFe] hydrogenases, and has a Ni_r*-like signal (g-values: 2.327, 2.185, 2.004), but which was light sensitive at cryogenic temperatures, transforming to the Ni_r-L* state (g-values: 2.483, 2.225, 2.169). Reduction by H_2 gave the Ni_a-C* state (g-values: 2.215, 2.150, 2.008), with illumination below 160 K giving the Ni_a-L* state (g-values: 2.276, 2.116, 2.038). Léger *et al.* engineered the histidine residue of the unusual distal 4Fe4S cluster (his-cys$_3$ ligation) of the [NiFe] hydrogenase from *D. fructosovorans* into a cys or gly residue and found that the cluster assembled, but the rates of electron transfer to and from the cluster were slowed down, even for cys$_4$ coordination.[179] Comparison of the EPR spectra (X-band, $\leq$15 K) of the wild-type, H184C and H184G samples, showed that in the oxidized state mutants and WT were identical, and similar spectra were obtained under potentiometric titrations, although with some broadening for the mutants compared to WT. Long, Albracht and co-workers purified a soluble hydrogenase from *Allochromatium vinosum*, with EPR spectroscopy identifying a Ni-Fe active site and a 4Fe4S cluster, the latter being reduced under H_2 to give g-values of 2.05, 1.90 and 1.88.[180]

Tables 1–7.

References

1 D. Collison and E. J. L. McInnes, *Specialist Periodical Reports Electron Spin Resonance Series*, 2002, **18**, 161; D. Collison and E. J. L. McInnes, *Specialist Periodical Reports Electron Spin Resonance Series*, 2004, **19**, 374; D. Collison and E. J. L. McInnes, *Specialist Periodical Reports Electron Spin Resonance Series*, 2006, **20**, 157.

2   J. B. Gilory, S. D. J. McKinnon, P. Kennepohl, M. S. Zsombor, M. J. Fergusen, L. J. Thomson and R. G. Hicks, *J. Org. Chem.*, 2007, **72**, 8062.

3   D. J. R. Brook and G. T. Yee, *J. Org. Chem.*, 2006, **71**, 4889.

4   E. Fukuzaki and H. Nishide, *Org. Lett.*, 2006, **8**, 1835.

5   A. Rajca, K. Shiraish, M. Pink and S. Rajca, *J. Amer. Chem. Soc.*, 2007, **129**, 7222.

6   T. S. Cameron, A. Decken, R. M. Kowalczyk, E. J. L. McInnes, J. Passmore, J. M. Rawson, K. V. Shuvaev and L. K. Thompson, *Chem. Commun.*, 2006, 2277.

7   C. Femoni, M. C. Iapalucci, G. Longoni, C. Tiozzo, J. Wolowska, S. Zachini and E. Zazzaroni, *Chem. Eur. J.*, 2007, **13**, 6544.

8   M. Castillo, E. Brillas, C. Rillo, M. D. Kuzmin and L. Julia, *Tetrahedron*, 2007, **63**, 708.

9   P. Ionita, F. Tuna, M. Andruh, T. Constantinescu and A. T. Balaban, *Aust. J. Chem.*, 2007, **60**, 173.

10 A. Rajca, M. Takahashi, M. Pink, G. Spagnol and S. Rajca, *J. Amer. Chem. Soc.*, 2007, **129**, 10159.

11 A. Rajca, M. Pink, S. Mukherjee, S. Rajca and K. Das, *Tetrahedron*, 2007, **63**, 10731.

12 A. Rajca, S. Mukherjee, M. Pink and S. Rajca, *J. Amer. Chem. Soc.*, 2006, **128**, 13497.

13 Y. Teki, T. Toichi and S. Nakajima, *Chem. Eur. J.*, 2006, **12**, 2329.

14 K. Nakabayashi, M. Kawano, T. Kato, K. Furukawa, S. Ohkoshi, T. Hozumi and M. Fujita, *Chem. Asian J.*, 2007, **2**, 164.

15 T. Itoh, K. Hirai and H. Tomoika, *Bull. Chem. Soc. Jpn.*, 2007, **80**, 138.

16 K. Ono, M. Yoshizawa, T. Kato, K. Watanabe and M. Fujita, *Angew. Chem. Int. Ed.*, 2007, **46**, 1803.

17 M. F. Anderlund, J. Högblom, W. Shi, P. Huang, L. Eriksson, H. Weihe, S. Styring, B. Åkermark, R. Lomoth and A. Magnuson, *Eur. J. Inorg. Chem.*, 2006, 5033.

18 P. Huang, N. Shaikh, M. F. Anderlund, S. Styring and L. Hammerström, *J. Inorg. Biochem.*, 2006, **100**, 1139.

19 J. T. Sage, Y.-M. Xia, P. G. Debrunner, D. T. Keough, J. de Jersey and B. Zerner, *J. Amer. Chem. Soc.*, 1989, **111**, 7239.

20 P. Huang, M. Anderlund, H. Weihe, A.-L. Barra and L. Sun, *Spectrochim. Acta Part A*, 2006, **63**, 541.

21 L. Sorace, C. Golze, D. Gatteschi, A. Bencini, H. W. Roesky, J. Chai and A. C. Stückli, *Inorg. Chem.*, 2006, **45**, 395.

22 J. A. Cissell, N. Kaur, S. Nellutla, N. S. Dalal and T. P. Vaid, *Inorg. Chem.*, 2007, **46**, 9672.

23 R. Herchel, R. Boca, J. Krzystek, A. Ozarowski, M. Duran and J. van Slageren, *J. Amer. Chem. Soc.*, 2007, **129**, 10306.

24 P. ter Heerdt, M. Stefan, E. Goovaerts, A. Caneschi and A. Cornia, *J. Magn. Reson.*, 2006, **179**, 29.

25 C. Elschenbroich, F. Lu, M. Nowotny, O. Burghaus, C. Pietzonka and K. Harms, *Organometallics*, 2007, **26**, 4025.

26 C. Elschenbroich, F. Lu, O. Burghaus, C. Pietzonka and K. Harms, *Chem. Commun.*, 2007, 3201.

27 C. Elschenbroich, F. Lu, O. Burghaus, K. Harms and M. Nowotny, *Z. Anorg. Allg. Chem.*, 2007, **633**, 2386.

28 J. Yoon and E. I. Solomon, *Coord. Chem. Rev.*, 2007, **251**, 379.

29 T. C. Stamatatos, J. C. Vlahopoulou, Y. Sanakis, C. P. Raptopoulou, V. Psycharis, A. K. Boudalis and S. P. Perlepes, *Inorg. Chem. Commun.*, 2006, **9**, 814.

30 T. Afrati, C. Dendrinou-Samara, C. Raptopoulou, A. Terzis, V. Tangoulis and D. P. Kessissoglou, *Dalton Trans.*, 2007, 5156.

31 A. K. Boudalis, Y. Sanakis, F. Dahan, M. Hendrich and J.-P. Tuchagues, *Inorg. Chem.*, 2006, **45**, 443.

32 Y. Sanakis, A. K. Boudalis and J.-P. Tuchagues, *C. R. Chimie*, 2007, **10**, 116.

33 A. Figuerola, V. Tangoulis, J. Ribas, H. Hartl, I. Brüdgam, M. Maestro and C. Diaz, *Inorg. Chem.*, 2007, **46**, 11017.

34 K. Kajiyoshi, T. Kambe, M. Mino, H. Nojiri, P. Kögerler and M. Luban, *J. Magn. Magn. Mater.*, 2007, **310**, 1203.

35 B. Tsukerblat, A. Tarantul and A. Müller, *J. Chem. Phys.*, 2006, **125**, 054714.

36 M. I. Belinsky, *Inorg. Chem.*, 2006, **45**, 9096.

37 G. Mezei, R. G. Raptis and J. Telser, *Inorg. Chem.*, 2006, **45**, 8841.

38 P. Comba, Y. D. Lampeka, A. I. Prikhod'ko and G. Rajaraman, *Inorg. Chem.*, 2006, **45**, 3632.

39 I. A. Koval, H. Akhideno, S. Tanase, C. Belle, C. Duboc, E. Saint-Aman, P. Gamez, D. M. Tooke, A. L. Spek, J.-L. Pierre and J. Reedijk, *New J. Chem.*, 2007, **31**, 512.

40 C. J. Millos, S. Piligkos, A. R. Bell, R. H. Laye, S. J. Teat, R. Vicente, E. J. L. McInnes, A. Escuer, S. P. Perlepes and R. E. P. Winpenny, *Inorg. Chem. Commun.*, 2006, **9**, 638.

41 V. Baskar, M. Shanmugam, E. C. Sañudo, M. Shanmugam, D. Collison, E. J. L. McInnes, Q. Wei and R. E. P. Winpenny, *Chem. Commun.*, 2007, 37.

42 J.-N. Rebilly, L. Catala, G. Charron, G. Rogez, E. Rivière, R. Guillot, P. Thuéry, A.-L. Barra and T. Mallah, *Dalton Trans.*, 2006, 2818.

43 C. Golze, A. Alfonsov, R. Klingeler, B. Buchner, V. Kataev, C. Mennerich, H.-H. Klauss, M. Goiran, J.-M. Broto, H. Rakoto, S. Demeshko, G. Leibeling and F. Meyer, *Phys. Rev. B*, 2006, **73**, 224403.

44 A. K. Boudalis, C. P. Raptopoulou, V. Psycharis, Y. Sanakis, B. Abarca, R. Ballesteros and M. Chadlaoui, *Dalton Trans.*, 2007, 3582.

45 L. F. Jones, P. Jensen, B. Moubaraki, K. J. Berry, J. F. Boas, J. R. Pilbrow and K. S. Murray, *J. Mater. Chem.*, 2006, **16**, 2690.

46 S. Datta, A. Betancur-Rodriguez, S.-C. Lee, S. Hill, D. Foguet-Albiol, R. Bagai and G. Christou, *Polyhedron*, 2007, **26**, 2243.

47 R. Bagai, S. Datta, A. Betancur-Rodriguez, K. A. Abboud, S. Hill and G. Christou, *Inorg. Chem.*, 2007, **46**, 4535.

48 R. Shaw, F. Tuna, W. Wernsdorfer, A.-L. Barra, D. Collison and E. J. L. McInnes, *Chem. Commun.*, 2007, 5161.

49 S. Datta, O. Waldmann, A. D. Kent, V. A. Milway, L. K. Thompson and S. Hill, *Phys. Rev. B*, 2007, **76**, 052407.

50 K.-Y. Choi, Y.-H. Matsuda, H. Nojiri, U. Kortz, F. Hussain, A.-C. Stowe, C. Ramsey and N. S. Dalal, *Phys. Rev. Lett.*, 2006, **96**, 107202.

51 P. Mialane, C. Duboc, J. Marrot, E. Rivière, A. Dolbecq and F. Sécheresse, *Chem. Eur. J.*, 2006, **12**, 1950.

52 T. Yamase, K. Fukaya, H. Nojiri and Y. Ohshima, *Inorg. Chem.*, 2006, **45**, 7698.

53 S. Sharmin, A. Ardavan, S. J. Blundell, O. Rival, P. Goy, E. J. L. McInnes and D. M. Low, *Phys. Rev. B*, 2006, **73**, 214433.

54 M. Shanmugam, L. P. Engelhardt, F. K. Larsen, M. Luban, E. J. L. McInnes, C. A. Muryn, J. Overgaard, E. Rentschler, G. A. Timco and R. E. P. Winpenny, *Chem. Eur. J.*, 2006, **12**, 8267.

55 A. Ardavan, O. Rival, J. J. L. Morton, S. J. Blundell, A. M. Tyryshkin, G. A. Timco and R. E. P. Winpenny, *Phys. Rev. Lett.*, 2007, **98**, 057201.

56 S. Piligkos, E. Bill, D. Collison, E. J. L. McInnes, G. A. Timco, H. Weihe, R. E. P. Winpenny and F. Neese, *J. Amer. Chem. Soc.*, 2007, **129**, 760.

57 A.-L. Barra, A. Caneschi, A. Cornia, D. Gatteschi, L. Gorini, L. P. Heiniger, R. Sessoli and L. Sorace, *J. Amer. Chem. Soc.*, 2007, **129**, 10754.

58 A. Wilson, E.-C. Yang, D. N. Hendrickson and S. Hill, *Polyhedron*, 2007, **26**, 2065.

59 A. Wilson, J. Lawrence, E.-C. Yang, M. Nakano, D. N. Hendrickson and S. Hill, *Phys. Rev. B*, 2006, **74**, 140403.

60 E. R. Davidson, *J. Comp. Phys.*, 1975, **17**, 87.

61 D. Gatteschi, A.-L. Barra, A. Caneschi, A. Cornia, R. Sessoli and L. Sorace, *Coord. Chem. Rev.*, 2006, **250**, 1514.

62 E. J. L. McInnes, in *'Single-Molecule Magnets and Related Phenomena'*, ed. D. M. P. Mingos, Structure and Bonding, , Springer, Berlin/Heidelberg, 2006, vol. 122, pp. 69–102.

63 B. Rakvin, D. Žilić, N. S. Dalal, A. Harter and Y. Sanakis, *Sol. State Commun.*, 2006, **139**, 51.

64 F. El Hallak, J. van Slageren, J. Gomez-Segura, D. Ruiz-Molina and M. Dressel, *Phys. Rev. B*, 2007, **75**, 104403.

65 N. E. Chakov, S.-C. Lee, A. G. Harter, P. L. Kuhns, A. P. Reyes, S. O. Hill, N. S. Dalal, W. Wernsdorfer, K. A. Abboud and G. Christou, *J. Amer. Chem. Soc.*, 2006, **128**, 6975.

66 T. C. Stamatatos, D. Foguet-Albiol, S.-C. Lee, C. C. Stoumpos, C. P. Raptopoulou, A. Terzis, W. Wernsdorfer, S. O. Hill, S. P. Perlepes and G. Christou, *J. Aerm. Chem. Soc.*, 2007, **129**, 9484.

67 S. Hill, R. S. Edwards, N. Aliaga-Alcalde and G. Christou, *Science*, 2003, **302**, 1015.

68 S. Hill and A. Wilson, *J. Low Temp. Phys.*, 2006, **142**, 271.

69 R. Tiron, W. Wernsdorfer, D. Foguet-Albiol, N. Aliaga-Alcalde and G. Christou, *Phys. Rev. Lett.*, 2003, **91**, 227203.

70 S. Koizumi, M. Nihei, T. Shiga, M. Nakano, H. Nojiri, R. Bircher, O. Waldmann, S. T. Ochsenbein, H. U. Güdel, F. Fernandez-Alonso and H. Oshio, *Chem. Eur. J.*, 2007, **13**, 8445.

71 S. Accorsi, A.-L. Barra, A. Caneschi, G. Chastanet, A. Cornia, A. C. Fabretti, D. Gatteschi, C. Mortalo, E. Olivieri, F. Parenti, P. Rosa, R. Sessoli, L. Sorace, W. Wernsdorfer and L. Zobbi, *J. Amer. Chem. Soc.*, 2006, **128**, 4742.

72 R. W. Saalfrank, A. Scheurer, I. Bernt, F. W. Heinemann, A. V. Postnikov, V. Schünemann, A. X. Trautwein, M. S. Alam, H. Rupp and P. Müller, *Dalton Trans.*, 2006, 2865.

73 A. Prescimone, J. Wolowska, G. Rajaraman, S. Parsons, W. Wernsdorfer, M. Murugesu, G. Christou, S. Piligkos, E. J. L. McInnes and E. K. Brechin, *Dalton Trans.*, 2007, 5282.

74 G. de Loubens, G. D. Chaves-O'Flynn, A. D. Kent, C. Ramsey, E. del Barco, C. Beedle and D. N. Hendrickson, *J. Appl. Phys.*, 2007, **101**, 09E104.

75 K. Petukhov, S. Bahr, W. Wernsdorfer, A.-L. Barra and V. Mosser, *Phys. Rev. B*, 2007, **75**, 064408.

76 M. Bal, J. R. Friedman, E. M. Rumberger, S. Shah, D. N. Hendrickson, N. Avraham, Y. Myasoedov, H. Shtrikman and E. Zeldov, *J. Appl. Phys.*, 2006, **99**, 08D103.

77 M. Bal, J. R. Friedman, M. T. Tuominen, E. M. Rumberger and D. N. Hendrickson, *J. Appl. Phys.*, 2006, **99**, 08D102.

78 K. Chłopek, E. Bothe, F. Neese, T. Weyermüller and K. Wieghardt, *Inorg. Chem.*, 2006, **45**, 6298.

79 C. C. Lu, E. Bill, T. Weyermüller, E. Bothe and K. Wieghardt, *Inorg. Chem.*, 2006, **46**, 7880.

80 A. K. Patra, E. Bill, E. Bothe, K. Chłopek, F. Neese, T. Weyermüller, K. Stobie, M. D. Ward, J. A. McCleverty and K. Wieghardt, *Inorg. Chem.*, 2006, **45**, 7877.

81 A. K. Patra, E. Bill, T. Weyermüller, K. Stobie, Z. Bell, M. D. Ward, J. A. McCleverty and K. Wieghardt, *Inorg. Chem.*, 2006, **45**, 6541.

82 M. V. Fedin, S. L. Veber, I. A. Gromov, V. I. Ovcharenko, R. Z. Sagdeev and E. G. Bagrayanskaya, *J. Phys. Chem. A*, 2007, **111**, 4449.

83 M. V. Fedin, S. L. Veber, I. A. Gromov, V. I. Ovcharenko, R. Z. Sagdeev, A. Schweiger and E. G. Bagrayanskaya, *J. Phys. Chem. A*, 2006, **110**, 2315.

84 M. V. Fedin, S. L. Veber, I. A. Gromov, K. Maryunina, S. Fokin, G. Romanenko, R. Z. Sagdeev, V. I. Ovcharenko and E. G. Bagrayanskaya, *Inorg. Chem.*, 2007, **46**, 11405.

85 A. Figuerola, V. Tangoulis and Y. Sanakis, *Chem. Phys.*, 2007, **334**, 204.

86 V. Tangoulis and A. Figuerola, *Chem. Phys.*, 2007, **340**, 293.

87 V. Tangoulis and J-P. Costes, *Chem. Phys.*, 2007, **334**, 77.

88 S. Van Doorslaer and E. Vinck, *Phys. Chem. Chem. Phys.*, 2007, **9**, 4620.

89 G. Jeschke and Y. Polyhach, *Phys. Chem. Chem. Phys.*, 2007, **9**, 1895.

90 O. Schiemann and T. F. Prisner, *Quart. Rev. Biophys.*, 2007, **40**, 1.

91 R. Calvo, *Appl. Mag. Reson.*, 2007, **31**, 271.

92 W. R. Hagen, *Mol. Phys.*, 2007, **105**, 2031.

93 G. T. Hinckley and P. A. Frey, *Analyt. Biochem.*, 2006, **349**, 103.

94 L. Noodleman and W.-G. Han, *J. Biol. Inorg. Chem.*, 2006, **11**, 674.

95 F. Neese, *J. Biol. Inorg. Chem.*, 2006, **11**, 702.

96 K. Fisher, D. J. Lowe and J. Petersen, *Chem. Commun.*, 2006, 2807.

97 K. Fisher, D. J. Lowe, P. Tavares, A. S. Pereira, B. H. Huynh, D. Edmondson and W. E. Newton, *J. Inorg. Bichem.*, 2007, **101**, 1649.

98 D. Lukoyanov, V. Pelmenschikov, N. Maeser, M. Laryukhin, T.-C. Yang, L. Noodleman, D. R. Dean, D. A. Case, L. C. Seefeldt and B. M. Hoffman, *Inorg. Chem.*, 2007, **46**, 11437.

99 B. M. Barney, D. Lukoyanov, T.-C. Yang, D. R. Dean, B. M. Hoffman and L. C. Seefeldt, *Proc. Nat. Acad. Sci.*, 2006, **103**, 17113.

100 D. Lukoyanov, B. M. Barney, D. R. Dean, L. C. Seefeldt and B. M. Hoffman, *Proc. Nat. Acad. Sci.*, 2007, **104**, 1451.

101 B. M. Barney, H.-I. Lee, P. C. Dos Santos, B. M. Hoffman, D. R. Dean and L. C. Seefeldt, *Dalton Trans.*, 2006, 2277.

102 Z. Zhang, Y. Zhao, C. Zhang, S. Bian, H. Zhou, H. Wang, H. Yin and J. Huang, *Chin. Sci. Bull.*, 2006, **51**, 1729.

103 A. W. Smith, A. Camara-Artigas, M. Wang, J. P. Allen and W. A. Francisco, *Biochemistry*, 2006, **45**, 4378.

104 K. Fujita, J. M. Chan, J. A. Bollinger, M. L. Alvarez and D. M. Dooley, *J. Inorg. Biochem.*, 2007, **101**, 1836.

105 S. I. Gorelsky, X. Xie, Y. Chen, J. A. Fee and E. I. Solomon, *J. Amer. Chem. Soc.*, 2006, **128**, 16452.
106 S. Lyubenova, M. K. Siddiqui, M. J. M. Penning de Vries, B. Ludwig and T. F. Prisner, *J. Phys. Chem. B*, 2007, **111**, 3839.
107 A. J. Augustine, L. Quintanar, C. S. Stoj, D. J. Kosman and E. I. Solomon, *J. Amer. Chem. Soc.*, 2007, **129**, 13118.
108 S. I. Chan, V. C.-C. Wang, J. C.-H. Lai, S. S.-F. Yu, P. P.-Y. Chen, K. H.-C. Chen, C.-L. Chen and M. K. Chan, *Angew. Chemie Int. Ed.*, 2007, **46**, 1992.
109 M. V. Golynskiy, W. A. Gunderson, M. P. Hendrich and S. M. Cohen, *Biochemistry*, 2006, **45**, 15359.
110 W. Jiang, L. M. Hoffart, C. Krebs and J. M. Bollinger, Jr, *Biochemistry*, 2007, **46**, 8709.
111 C. Krebs, M. L. Matthews, W. Jiang and J. M. Bollinger, Jr, *Biochemistry*, 2007, **46**, 10413.
112 W. Jiang, D. Yun, L. Saleh, E. W. Barr, G. Zing, L. M. Hoffart, M.-A. Maslak, C. Krebs and J. M. Bollinger, Jr, *Science*, 2007, **316**, 1188.
113 M. Simurdiak, J. Lee and H. Zhao, *ChemBioChem.*, 2006, **7**, 1169.
114 W. Jiang, J. M. Bollinger, Jr and C. Krebs, *J. Amer. Chem. Soc.*, 2007, **129**, 7504.
115 B. N. Hudder, J. G. Morales, A. Stubna, E. Münck, M. P. Hendrich and P. A. Lindahl, *J. Biol. Inorg. Chem.*, 2007, **12**, 1029.
116 D. Yun, R. Garcia-Serres, B. M. Chicalese, Y. H. An, B. H. Huynh and J. M. Bollinger, Jr, *Biochemistry*, 2007, **46**, 1925.
117 D. Yun, L. Saleh, R. Garcia- Serres, B. M. Chicalese, Y. H. An, B. H. Huynh and J. M. Bollinger, Jr, *Biochemistry*, 2007, **46**, 13067.
118 C.-H. Wu, W. Jiang, C. Krebs and J. Stubbe, *Biochemistry*, 2007, **46**, 11577.
119 L. J. Murray, R. Garcia-Serres, M. S. McCormick, R. Davydov, S. G. Naik, S.-H. Kim, B. M. Hoffman, B. H. Huynh and S. J. Lippard, *Biochemistry*, 2007, **46**, 14795.
120 G. Yakolev, T. Reda and J. Hirst, *Proc. Nat. Acad. Sci.*, 2007, **104**, 12720.
121 R. Kappl, S. Sielker, K. Ranguelova, J. Wegner, K. Parschat, J. Hüttermann and S. Fetzner, *Biochemistry*, 2006, **45**, 14853.
122 S. E. Wiley, M. L. Paddock, E. C. Abresch, L. Gross, P. van der Geer, R. Nechushtai, A. N. Murphy, P. A. Jennings and J. E. Dixon, *J. Biol. Chem.*, 2007, **282**, 23745.
123 M. H. Sazinsky, B. LeMoine, M. Orofino, R. Davydov, K. Z. Bencze, T. L. Stemmler, B. M. Hoffman, J. M. Argüello and A. C. Rosenzweig, *J. Biol. Chem.*, 2007, **282**, 25950.
124 A. S. Fernandes, F. L. Sousa, M. Teixeira and M. M. Pereira, *Biochemistry*, 2006, **45**, 1002.
125 T. Maly, L. Grgic, K. Zwicker, V. Zickermann, U. Brandt and T. F. Prisner, *J. Biol. Inorg. Chem.*, 2006, **11**, 343.
126 R. M. Martinez-Espinosa, D. J. Richardson, J. N. Butt and M. J. Bonete, *FEMS Microbiol. Lett.*, 2007, **277**, 50.
127 R. Kappl, M. Ebelshäuser, F. Hannemann, R. Bernhardt and J. Hüttermann, *Appl. Mag. Reson.*, 2006, **30**, 427.
128 A. A. Shubin and S. A. Dikanov, *Appl. Mag. Reson.*, 2006, **30**, 399.
129 A. Silakov, E. J. Reijerse, S. P. J. Albracht, E. C. Hatchikian and W. Lubitz, *J. Amer. Chem. Soc.*, 2007, **129**, 11447.
130 S. P. J. Albracht, W. Roseboom and E. C. Hatchikian, *J. Biol. Inorg. Chem.*, 2006, **11**, 88.
131 P.-p. Wei, A. B. Tomter, Å. K. Røhr, K. K. Andersson and E. I. Solomon, *Biochemistry*, 2006, **45**, 14043.
132 X. Brazzolotto, J. K. Rubach, J. Gaillard, S. Gambarelli, M. Atta and M. Fontecave, *J. Biol. Chem.*, 2006, **281**, 769.
133 L. Yu, M. Blaser, P. I. Andrei, A. J. Pierik and T. Selmer, *Biochemistry*, 2006, **45**, 958.
134 J. M. Buis, J. Cheek, E. Kalliri and J. M. Broderick, *J. Biol. Chem.*, 2006, **281**, 25994.
135 C. Paraskevopoulou, S. A. Fairhurst, D. J. Lowe, P. Brick and S. Onesti, *Molec. Microbiol.*, 2006, **59**, 795.
136 M. Heinnickel, R. Agalarov, N. Svenson, C. Krebs and J. H. Golbeck, *Biochemistry*, 2006, **45**, 6756.
137 M. Heinnickel, G. Shen and J. H. Golbeck, *Biochemistry*, 2007, **46**, 2530.
138 P. Lanciano, A. Savoyant, S. Grimaldi, A. Magalon, B. Guigliarelli and P. Bertrand, *J. Phys. Chem. B*, 2007, **111**, 13632.
139 E. J. Dridge, C. A. Watts, B. J. N. Jepson, K. Line, J. M. Santini, D. J. Richardson and C. S. Butler, *Biochem. J.*, 2007, **408**, 19.
140 E. Bol, L. E. Bevers, P.-L. Hagedoorn and W. R. Hagen, *J. Biol. Inorg. Chem.*, 2006, **11**, 999.

141 R. Kappl, L. D. Eltis, M. B. Caspersen, H. E. M. Christensen and J. Hüttermann, *Appl. Mag. Reson.*, 2007, **31**, 483.

142 A. Astashkin, J. Seravalli, S. O. Mansoorabadi, G. H. Reed and S. W. Ragsdale, *J. Amer. Chem. Soc.*, 2006, **126**, 3888.

143 M. R. Bramlett, A. Stubna, X. Tan, I. V. Surovtsev, E. Münck and P. A. Lindahl, *Biochemistry*, 2006, **45**, 8674.

144 M. S. Alam, S. K. Garg and P. Agrawal, *Molec. Microbiol.*, 2007, **63**, 1414–1431.

145 D. Adedeji, H. Hernandez, J. Wiesner, U. Köhler, H. Jomaa and E. C. Duin, *FEBS Lett.*, 2007, **581**, 279.

146 B. E. Weiner, H. Huang, B. M. Datillo, M. J. Nilges, E. Fanning and W. J. Chazin, *J. Biol. Chem.*, 2007, **282**, 33444.

147 D. Barthelme, U. Scheele, S. Dinkelaker, A. Janoschka, F. MacMillan, S.-V. Albers, A. J. M. Driessen, M. S. Stagni, E. Bill, W. Mayer-Klaucke, V. Schünemann and R. Tampe, *J. Biol. Chem.*, 2007, **282**, 14598.

148 N. Sirijovski, F. Mamedov, U. Olsson, S. Styring and M. Hansson, *Arch. Microbiol.*, 2007, **188**, 599.

149 T. L. Lowery, P. E. Wilson, B. Zhang, J. Bunker, R. G. Harrison, A. C. Nyborg, D. Thiriot and G. D. Watt, *Proc. Nat. Acad. Sci.*, 2006, **103**, 17131.

150 N. Hamann, G. J. Mander, J. E. Shokes, R. A. Scott, M. Bennati and R. Hedderich, *Biochemistry*, 2007, **46**, 12875.

151 T. Pohl, T. Bauer, K. Dörner, S. Stolpe, P. Sell, G. Zocher and T. Friedrich, *Biochemistry*, 2007, **46**, 6588.

152 R. S. Hartshorne, B. N. Jepson, T. A. Clarke, S. J. Field, J. Fredrickson, J. Zachara, L. Shi, J. N. Butt and D. J. Richardson, *J. Biol. Inorg. Chem.*, 2007, **12**, 1083.

153 F. Baymann, F. Giusti, D. Picot and W. Nitschke, *Proc. Nat. Acad. Sci.*, 2007, **104**, 519.

154 E. Yamashita, H. Zhang and W. A. Cramer, *J. Mol. Biol.*, 2007, **370**, 39.

155 J. H. van Wonderen, C. Knight, V. S. Oganesyan, S. J. George, W. G. Zumft and M. R. Cheesman, *J. Biol. Chem.*, 2007, **282**, 28207.

156 R. Singh, J. Switala, P. C. Loewen and A. Ivancich, *J. Amer. Chem. Soc.*, 2007, **129**, 15954.

157 G. R. Periyannan, A. L. Costello, D. L. Tierney, K.-W. Yang, B. Bennett and M. W. Crowder, *Biochemistry*, 2006, **45**, 1313.

158 L. I. Llarrull, M. F. Tioni, J. Kowalski, B. Bennett and A. J. Vila, *J. Biol. Chem.*, 2007, **282**, 30586.

159 M. L. Antonkine, E. M. Maes, R. S. Czernuszewicz, C. Breitenstein, E. Bill, C. J. Falzone, R. Balasubramanian, C. Lubner, D. A. Bryant and J. H. Golbeck, *Biochim. Biophys. Acta*, 2007, **1767**, 712.

160 A. Haddy, *Photosynth. Res.*, 2007, **92**, 357.

161 M. Heinnickel and J. H. Golbeck, *Photosynth. Res.*, 2007, **92**, 35.

162 J.-H. Su, K. G. V. Havelius, F. Mamedov, F. M. Ho and S. Styring, *Biochemistry*, 2006, **45**, 7617.

163 F. M. Ho, S. F. Morvaridi, F. Mamedov and S. Styring, *Biochim. Biophys. Acta*, 2007, **1767**, 5.

164 K. G. V. Havelius and S. Styring, *Biochemistry*, 2007, **46**, 7865.

165 J.-H. Su, K. G. V. Havelius, F. M. Ho, G. Han, F. Mamedov and S. Styring, *Biochemistry*, 2007, **46**, 10703.

166 K. A. Åhrling, M. C. W. Evans, J. H. A. Nugent, R. J. Ball and R. J. Pace, *Biochemistry*, 2006, **45**, 7069.

167 A. M. Tyryshkin, R. K. Watt, S. V. Baranov, J. Dasgupta, M. P. Hendrich and G. C. Dismukes, *Biochemistry*, 2006, **45**, 12876.

168 C. Teutloff, S. Keßen, J. Kern, A. Zouni and R. Bittl, *FEBS Lett.*, 2006, **580**, 3605.

169 L. V. Kulik, B. Epel, W. Lubitz and J. Messinger, *J. Amer. Chem. Soc.*, 2007, **129**, 13421.

170 C.-I. Lee, K. V. Lakshmi and G. W. Brudvig, *Biochemistry*, 2007, **46**, 3211.

171 H. Matsuoka, K. Furukawa, T. Kato, H. Mino, J.-R. Shen and A. Kawamori, *J. Phys. Chem. B*, 2006, **110**, 13242.

172 S. Un, A. Boussac and M. Suguira, *Biochemistry*, 2007, **46**, 3138.

173 G. Zahariou, N. Ioannidis, G. Sioros and V. Petrouleas, *Biochemistry*, 2007, **46**, 14335.

174 G. Sioros, D. Koulougliotis, G. Karapanagos and V. Petrouleas, *Biochemistry*, 2007, **46**, 210.

175 W. Lubitz, E. Reijerse and M. van Gastel, *Chem. Rev.*, 2007, **107**, 4331.

176 M. van Gastel, M. Stein, M. Brecht, O. Schröder, F. Lendzian, R. Bittl, H. Ogata, Y. Higuchi and W. Lubitz, *J. Biol. Inorg. Chem.*, 2006, **11**, 41.

177 A. G. Agrawal, M. van Gastel, W. Gärtner and W. Lubitz, *J. Phys. Chem. B*, 2006, **110**, 8142.

178 O. Schröder, B. Bleijlevens, T. E. de Jongh, Z. Chen, T. Li, J. Fischer, C. G. Friedrich, K. A. Bagley, S. P. J. Albracht and W. Lubitz, *J. Biol. Inorg. Chem.*, 2007, **12**, 212.

179 S. Dementin, V. Belle, P. Bertrand, B. Guigliarelli, G. Adryanczyk-Perrier, A. L. De Lacey, V. M. Fernandez, M. Rousset and C. Léger, *J. Amer. Chem. Soc.*, 2006, **128**, 5209.

180 M. Long, J. Liu, Z. Chen, B. Bleijlevens, W. Roseboom and S. P. J. Albracht, *J. Biol. Inorg. Chem.*, 2007, **12**, 62.

Continuous wave and pulsed EPR analyses of metalloproteins

Sabine Van Doorslaer*

For many decades, EPR has been used as a tool to study paramagnetic metalloproteins. Recent developments in multi-frequency pulsed EPR and ENDOR have significantly increased the amount of information that, in principle, can be obtained from such an EPR study, but at the same time, modern EPR spectroscopists are facing the difficult task of choosing the optimal techniques to tackle a specific problem. In this chapter, a number of strategies and their possible problems are outlined using different examples of recent multi-frequency EPR/ENDOR studies of metalloproteins and related model systems.

1 Introduction

The way nature uses metal ions to modulate the function of different proteins has intrigued generations of scientists. Since many of the metalloproteins are paramagnetic, electron paramagnetic resonance (EPR) has served as one of the spectroscopic tools used to gain insight into metal-ion coordination in metalloproteins, as is evidenced, for instance, by some of the earlier reviews in this series of specialist periodical reports.[1–3] From the late 1980s onwards, the field of EPR has undergone rapid changes with the introduction of different advanced high-field and/or pulsed EPR techniques.[4–10] These novel techniques allow for more detailed analyses of paramagnetic systems. However, the vast amount of different EPR techniques that are now available is not evident from the current EPR literature on metalloproteins. In fact, not only is the potential of EPR not widely known to biochemists and biophysicists, many of the EPR spectroscopists struggle to keep up with the rapid changes in the field. This boils down to the fact that, in practice, most of the applied EPR studies still mainly involve continuous wave (CW) EPR at the standard X-band microwave frequencies ($\sim$9.5 GHz), leaving many aspects of the EPR techniques unexploited.

This chapter aims at exemplifying the strength of some of the more recent EPR techniques in metalloprotein research, with the emphasis placed on different EPR strategies, their advantages and limitations and the interpretation of the data. It should be noted that this chapter is not meant to present an exhaustive review of the recent EPR literature on metalloproteins, nor does it pretend to give the sole solution to the different presented problems. Examples arising from the author's research group, and those of others, are used to illustrate the potential of different EPR techniques.

In the following sections, some general aspects and some practical guidelines on the use of field-swept EPR methods (section 2) and different EPR techniques to determine nuclear interactions (section 3) are discussed, and illustrated with numerous examples from bioinorganic chemistry. Fig. 1 and 2 show the pulse sequences of the different pulsed EPR experiments that will be mentioned in these sections. An in-depth explanation of these methods falls outside the scope of this review and the advanced pulsed EPR/ENDOR methods will be introduced in the

University of Antwerp, Department of Physics, Universiteitsplein 1, B-2610, Wilrijk-Antwerp, Belgium. E-mail: sabine.vandoorslaer@ua.ac.be; Fax: 0032 3 820 2461; Tel: 0032 3 820 2470
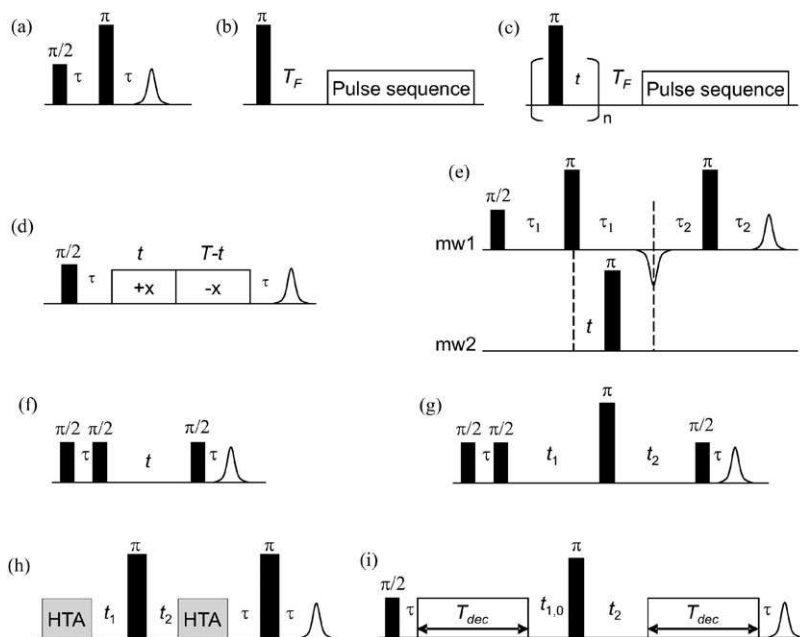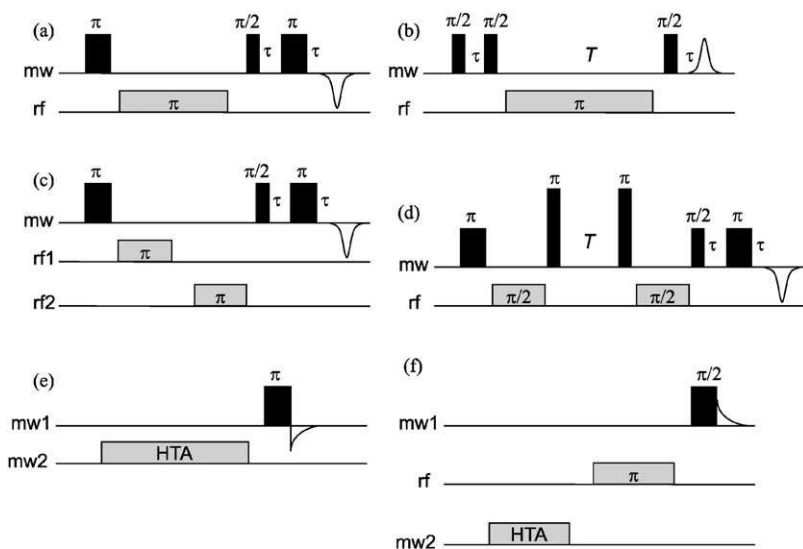
Fig. 1 Microwave pulse sequences of the pulsed EPR experiments mentioned in the text. (a) ESE-detected EPR (τ is kept constant, the magnetic field is varied) or two-pulse ESEEM (variable τ). (b) Simple REFINE filter. (c) Picket-fence REFINE filter. (d) PEANUT scheme (t is varied with fixed T). (e) DEER scheme (t is varied). (f) Three-pulse ESEEM (t is varied). (g) HYSCORE scheme (t_1 and t_2 are varied independently). In a matched HYSCORE experiment, the second and fourth pulse are replaced by HTA pulses. (h) SMART HYSCORE scheme (t_1 and t_2 are varied independently). (i) Hyperfine-decoupled DEFENCE (t_2 and T_{dec} are varied independently, with fixed $t_{1,0}$).

next sections only up to a level necessary to understand the examples. More details on these and other pulsed EPR methods can be found in refs. 4–10. Similarly, the basics of CW EPR and CW ENDOR (electron nuclear double resonance) can be found in many standard books.[11–16] In section 4, some of the pitfalls of pulsed EPR are highlighted. Section 5 discusses the interpretation of the EPR data, including the combination with quantum-chemical computations. In section 6, some general guidelines are outlined for the use of different EPR and ENDOR methods in the study of bioinorganic systems. Finally, sections 7 and 8 illustrate the potential of different multi-frequency CW and pulsed EPR techniques in the analysis of high-spin ferric heme proteins (section 7) and methyl-coenzyme M reductase (section 8).

2 Field-swept EPR methods

Every EPR analysis of a paramagnetic system will start with the recording of a CW-EPR spectrum, usually at the standard X-band microwave frequency. In numerous cases, the X-band CW-EPR analysis provides sufficient information to derive the principle g values and even some of the strong, resolved hyperfine couplings. However, often a single X-band CW EPR spectrum is not sufficient.

This is the case for samples containing several paramagnetic species with over-lapping X-band EPR features. One approach is then to use multi-frequency CW-EPR experiments, as was demonstrated in the S-band (3 GHz), X-band and Q-band (35 GHz) CW-EPR analysis of the polysulfide reductase from *Wolinella succinogenes* which revealed three different Mo^V states of its catalytic molybdenum cofactor.[17] The spectra are crowded with features, since Mo has two naturally abundant isotopes (^{95}Mo and ^{97}Mo (both $I = 5/2$), $\sim 25.5\%$). The authors used the field

Fig. 2 Pulse sequences of the pulsed ENDOR and ELDOR-detected NMR experiments mentioned in the text. mw stands for microwave, rf for radio frequency. (a) Davies ENDOR. In the experiment, the rf frequency is swept. (b) Mims ENDOR. The rf frequency is swept. Time τ can be varied in a second dimension. (c) Triple ENDOR experiment. The rf2 frequency is kept, while rf1 is set to a specific nuclear transition. (d) HYEND experiment. Time T is changed in one dimension, while the frequency of the two rf pulses is simultaneously swept in a second dimension. (e) ELDOR-detected NMR experiment with FID detection. The microwave frequency of the HTA pulse is swept around the fixed mw1 frequency. (f) THYCOS experiment. The mw2 and rf frequency are swept independently.

dependence of the electron Zeeman interaction to identify the individual components. Similarly, the contributions of different Cu^{II} species in oxidized native laccase were unravelled using high-frequency EPR at 115 and 285 GHz.[18]

At an early stage in the development of the EPR technique, it was recognized that the difference in the electron relaxation times of the contributing species offers a possible route to disentangle complex spectra. By performing CW-EPR measurements at various microwave powers, the different saturation behaviour of the individual features can be used to disentangle the spectra. The spectral decomposition may be helped by mathematical tools, such as a maximum-likelihood common-factor analysis.[19] Similarly, differences in spin–spin relaxation (T_2) or spin–lattice relaxation (T_1) have been exploited in pulsed EPR experiments. A much-used tool consists of the detection of ESE (electron spin echo)-detected EPR spectra (Fig. 1a) at different time intervals τ.[4,20] At high values of τ, only the component with the longest phase-memory time, T_m, will contribute to the signal. The phase-memory time is usually largely governed by T_2.[4] In principle, one can also use the fact that the nuclear modulation effect is, in general, different for different paramagnetic species to separate two overlapping EPR spectra.[21] By recording an ESE-detected EPR spectrum at a τ value where the echo intensity of one of the contribution is minimal due to its modulation, the resulting EPR spectrum will be dominated by the contribution of the second species. However, it should be pointed out that this approach is only feasible for single crystals or for EPR spectra with small spectral width, because of the strong field- and orientation-dependence of the nuclear modulations.

Continuing on from an earlier idea of Hoffmann and Schweiger,[22] Thomas Prisner and co-workers introduced an elegant way of separating the EPR spectra of different components based on their difference in T_1 relaxation.[23–25] In these REFINE experiments, an inversion-recovery relaxation filter (either a single π pulse[23]

(Fig. 1b) or a picket-fence sequence[25] (Fig. 1c) followed by a waiting time T_F) is used in combination with different pulse sequences. When the filter in Fig. 1b or c is combined with the two-pulse echo scheme (Fig. 1a), independent variation of T_F and the magnetic field, B_0, followed by an inverse Laplace transformation in the time domain leads to a separation of the components based on their relaxation rate.[25] For two species, the ratio between the two T_1 values can be as small 2, whereas a ratio of 3 to 4 is sufficient for three to five different species. Note that it may sometimes be preferable to detect the EPR signal over a FID (free induction decay) instead of a spin echo in these REFINE EPR experiments in order to avoid strong distortions in the field dimension.[26] Prisner and co-workers have applied the REFINE tool to unravel the EPR spectra of the different iron–sulphur centres in mitochondrial complex I.[24]

Even when only one species is present, X-band CW EPR is not guaranteed to provide sufficient information. In cases of high g strain effects, it may be favourable to move to lower microwave frequencies in order to determine the full $\mathbf{g}$ tensor or get accurate information on the hyperfine couplings. This is true for Cu[II] peptide complexes where the copper and nitrogen hyperfine interactions are better analysed at low microwave frequency as demonstrated for the model peptide complexes mimicking the Cu[II]-binding to the N-terminal portion of prion proteins.[27] On the other hand, X-band microwave frequencies may be too low to reveal small g anisotropies. In these cases, higher microwave frequencies are necessary to separate the different principle values.[8,9] High-frequency EPR also plays an essential role in determining the zero-field parameters of mononuclear metal-ion sites with $S > 1/2$.[8,28] For some high-spin systems, the PEANUT (phase-inverted echo-amplitude detected nutation) experiment (Fig. 1d) may be helpful.[29] This technique allows, for example, the separation of the allowed from the forbidden EPR transitions in Mn[II] complexes.[29]

In multi-centre systems where the different paramagnetic entities are close in space to each other, the CW-EPR spectra will reflect the exchange or dipolar interactions between the different electron spins. Again, multi-frequency CW EPR can facilitate the elucidation of these interactions. In this way, bis(μ-hydroxo)(μ-carboxylato) could be proposed as bridging ligands for the exchange-coupled dimanganese Mn$_2$(II,II) in the putative sulphate thiohydrolase SoxB of *Paracoccus pantotrophus* *via* a detailed temperature-dependent analysis of the EPR signatures at X- and Q-band.[30] Similarly, multi-frequency CW EPR can be used to study the dipolar inter-centre magnetic interactions between several hemes, or between a heme and a radical in cytochromes.[31] Note that the dipolar relaxation of a fast-relaxing paramagnetic centre (*e.g.* a heme Fe[III]) induced on a more slowly relaxing centre (*e.g.* a Cu[II] centre) can be used to measure their distance in the 1–4 nm range by multi-frequency pulsed EPR.[32] Finally, the DEER (double electron electron resonance) technique (Fig. 1e), which has often been successfully employed to determine distances of up to 8 nm between organic radicals, has also been shown to give promising results for multi-centre systems involving transition-metal ions.[33]

3.   Detecting nuclear interactions

In most cases, the hyperfine and nuclear–quadrupole couplings of the surrounding magnetic nuclei are not resolved in a field-swept EPR spectrum. A large variety of techniques exist that allow the determination of these interactions: ESEEM (electron-spin-echo envelope modulation), ENDOR and ELDOR (electron–electron double resonance)-detected NMR.[4] As a rule of thumb, ESEEM-like techniques are ideal for the detection of small nuclear frequencies (<10 MHz), whereas ENDOR-like methods and ELDOR-detected NMR are more appropriate for higher nuclear frequencies. However, there are many cases in which ESEEM and ENDOR perform equally well. In the following section a number of advantages and disadvantages of the most used methods will be discussed.

All ESEEM techniques involve the use of a series of microwave pulses to generate an electron spin echo. In all ESEEM experiments, one or more inter-pulse time intervals are varied and the resulting modulation of the spin-echo intensity is monitored, reflecting the nuclear interactions. Two-pulse ESEEM (Fig. 1a) provides the easiest way to detect nuclear modulations, but due to its dependence on the electron phase-memory time, which is usually short, and its inherent one-dimensionality, it is now used infrequently. In three-pulse ESEEM (Fig. 1f), the line widths are determined by the phase-memory time of the nuclear spins, which is usually of the order of magnitude of the electron T_1. Hence, the lines are sharper and the resolution is better than in two-pulse ESEEM. The three-pulse ESEEM experiment suffers from τ-dependent blind spots, and in general, the three-pulse ESEEM spectra should be summed over different τ values. Although three-pulse ESEEM experiments can still be very useful,[34,35] HYSCORE (hyperfine sublevel correlation) spectroscopy[36] (Fig. 1g) has become the favoured ESEEM technique to determine nuclear frequencies. In HYSCORE, the π pulse transfers the nuclear coherence created by the $\pi/2$-τ-$\pi/2$ preparation sequence from one M_S manifold to the other. Independent variation of the two time intervals, t_1 and t_2, and subsequent Fourier transformation gives rise to cross peaks linking nuclear frequencies of different M_S manifolds. This type of correlation spectroscopy allows for the unravelling of spectral contributions that are overlapping in the corresponding three-pulse ESEEM spectrum.

The majority of the HYSCORE studies published to date are concerned with the analysis of $^1H/^2H$ interactions[37–40] or $^{14}N/^{15}N$ couplings;[40–47] the listed references are exemplary and not exhaustive. In recent years, HYSCORE features stemming from interactions with ^{11}B,[48] ^{13}C,[47,49] ^{19}F,[50] ^{27}Al,[51] ^{29}Si,[52] ^{31}P,[53] ^{39}K,[50] ^{85}Rb,[54] ^7Li,[55,56] ^{33}S,[37,57] ^{17}O[41,58,59] and ^{57}Fe[60] nuclei have been described. From the above list, one may get the false impression that the analysis of HYSCORE spectra is now routine. However, this is not the case. In fact, the majority of studies have focussed on the interpretation of HYSCORE patterns arising from $S = 1/2$, $I = 1/2$ or $S = 1/2$, $I = 1$ systems,[61–64] whereas little information can be found on a more general assessment of $S = 1/2$, $I > 1$ or $S > 1/2$, $I \geq 1/2$ systems[65,66] and the analysis of HYSCORE spectra remains, in many cases, challenging.

Fig. 3A shows the X-band ^{14}N HYSCORE spectrum from a frozen MeOH:H$_2$O (1:1) solution of B$_{12r}$, the paramagnetic Co^{II} form of B$_{12}$ (Fig. 3B). A similar HYSCORE spectrum was obtained for B$_{12r}$ magnetically diluted in hydroxocobalamin (B$_{12b}$).[67] The spectrum looks very unusual with a series of cross peaks parallel to the ν_1 and ν_2 axes. This pattern results from interactions with four corrin nitrogens (marked N_C in Fig. 3B) and with one remote nitrogen of the axially coordinating dimethylbenzimidazole (DBI) base (marked N_R in Fig. 3B). For a disordered $S = 1/2$, $I = 1$ system, the following rule of thumb can be used: the most intense HYSCORE cross peaks, which correlate the two double-quantum (dq, $|\Delta M_I| = 2$) frequencies, will appear in the $(+,+)$ quadrant in cases where the hyperfine coupling, a, is smaller than twice the Larmor frequency, ν_I; where if a is larger than twice the Larmor frequency, the peaks appear in the $(-,+)$ quadrant. These situations are referred to as the weak and strong coupling cases, respectively. In the exact cancellation condition ($|a| \approx |2\nu_I|$), the dq cross peaks are found in both quadrants. In Fig. 3A, the dq cross peaks stemming from the corrin nitrogens (dq$_{\beta,C}$, dq$_{\alpha,C}$) appear in both quadrants, indicating that the exact cancellation condition is fulfilled. In contrast, the dq cross peaks of the remote nitrogen (dq$_{\alpha,R}$, dq$_{\beta,R}$) are found only in the $(+,+)$ quadrant, showing that, at this observer position, the hyperfine value of the remote nitrogen is smaller (in absolute value) than the one of the corrin nitrogens. Furthermore, several cross peaks linking combination frequencies are observed in Fig. 3A. These combination frequencies are sum and difference combinations of nuclear frequencies from different magnetic nuclei. In HYSCORE spectroscopy (and the related three-pulse ESEEM experiment) only combinations between nuclear frequencies from the same M_S manifold can occur. Thus, the occurrence of the cross peak at (6.8, 2.5) MHz (marked 'A' in Fig. 3A)
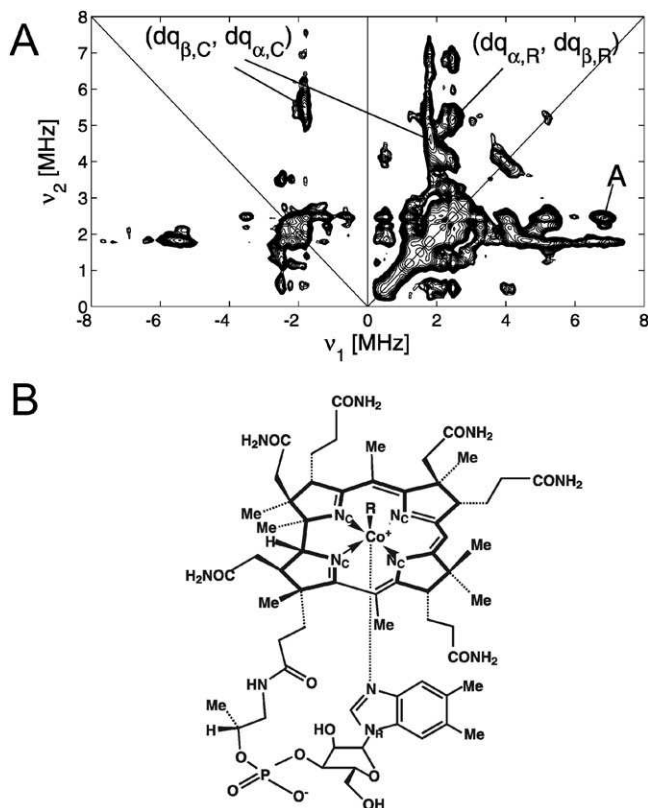
Fig. 3 (A) Experimental X-band HYSCORE spectrum of a frozen MeOH:H_2O solution of B_{12r} (pH 7) taken at 15 K at an observer position corresponding with $g_\parallel$, $M_I = -7/2$ ($B_0 = 382,5$ mT). $t_{\pi/2} = 24$ ns, $t_\pi = 16$ ns, $\tau = 96$ ns. (B) Structure of B_{12r}.

proves that the hyperfine values of the remote and corrin nitrogens have opposite signs, since the largest dq frequency of the remote nitrogen (5 MHz) is combined with the lowest dq frequency of the corrin nitrogens (1.8 MHz). The observation of cross peaks linking combination frequencies can thus reveal essential information about a system, but, at the same time, they complicate the HYSCORE spectrum dramatically, as can be seen in Fig. 3A.

As with the field-swept EPR experiments, a multi-frequency approach may help unravel complicated HYSCORE spectra. A change in the microwave frequency with a correlated alteration of the magnetic field induces a change in the nuclear Zeeman frequency. In the above-mentioned case of B_{12r} magnetically diluted in B_{12b},[67] the ^{14}N hyperfine and nuclear quadrupole principle values could only be determined *via* a combined X- and Q-band HYSCORE analysis.

There are many factors that govern the feasibility of such a multi-frequency HYSCORE approach. First, there is a clear spin-system-dependent factor. Fig. 4 shows the ESE modulation depth, k, as a function of the microwave frequency for four different cases of ^{15}N hyperfine values. For an $S = 1/2$, $I = 1/2$ system, the modulation depth is given by[4]

$$k = \{B\nu_I/(\nu_\alpha\nu_\beta)\}^2 \tag{1}$$

with B the pseudo-secular hyperfine coupling, ν_I the nuclear Zeeman interaction and ν_α and ν_β the basic nuclear frequencies as defined in ref. 4. From Fig. 4, it is clear that the lower microwave frequencies are not very suitable for the detection of the large
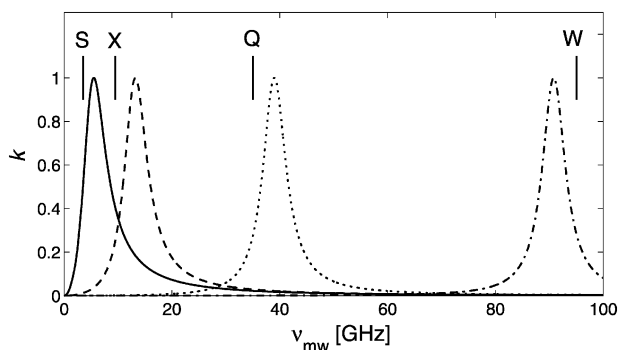
Fig. 4 Illustration of the dependence of the ESE modulation depth k (eqn (1)) on the microwave frequency. k is calculated for an unpaired electron interacting with a ^{15}N nucleus and $g = 2$, whereby the pseudo-secular part of the hyperfine coupling, B, is taken 0.8 MHz for all cases and the secular part, A, is 1.5 MHz (solid line), 4 MHz (dashed line), 12 MHz (dotted line) and 28 MHz (dash–dotted line).

^{15}N hyperfine couplings with ESEEM. Conversely, k is very low or almost zero at W-band frequencies in systems with a small hyperfine coupling. Second, technical factors can play an important role. Whilst HYSCORE experiments are technically easy to perform at S-, X- and Q-band frequencies, high-frequency HYSCORE is hard to realize. Indeed, the HYSCORE scheme (Fig. 1g) requires a strong π pulse able to mix the coherences of the different M_S manifolds. At higher mw frequencies, the energy separation between different M_S manifolds becomes larger, and at the same time it is technically more and more demanding to apply strong microwave pulses. At the moment, W-band HYSCORE using a commercially available Bruker E680 spectrometer is only feasible in special cases of high-electron-spin systems.[41] This is because, due to the dependence of the pulse flip angle on the electron spin, π pulses with smaller pulse lengths can be obtained for $S > 1/2$ systems than needed for the $S = 1/2$ case. HYSCORE experiments at microwave frequencies higher than 95 GHz have not been reported.

Significant ESEEM sensitivity enhancement can be obtained by the use of matched microwave pulses.[68] These pulses are high-turning-angle (HTA) pulses that enhance the efficiency of forbidden transfers, thus increasing the intensity of different nuclear transitions. In matched HYSCORE experiments,[69] the second and third π/2 pulse are replaced by HTA pulses, whereby the efficiency of the forbidden transfers between allowed electron and nuclear coherence are enhanced. It is important to enhance coherence-transfer pathways that lead to allowed electron coherence, since forbidden electron coherence cannot be detected. Note that the chosen matching conditions will determine which interactions are enhanced. For instance, assume an X-band HYSCORE spectrum of an $S = 1/2$ weakly interacting with protons and ^{13}C nuclei. By using HTA pulses with $\nu_1 = 15.625$ MHz (*i.e.* the pulse channel is tuned using π/2 pulses of 16 ns) the ^{1}H spectral contributions can be enhanced ($\nu_H \approx \nu_1$). The optimal length of the HTA pulses is determined using a three-pulse experiment, where both time t and the pulse length of the two last π/2 pulses are varied independently in a 2D experiment. 1D Fourier transform in the normal three-pulse ESEEM dimension allows determination of the optimal HTA pulse length. Conversely, the ^{13}C interactions can be determined using HTA pulses with strength $\nu_1 = 3.9$ MHz (*i.e.* the B_1 field is optimized using π/2 pulses of 64 ns).

Note that the (matched) HYSCORE spectra are still strongly dependent on the time τ between the two first pulses, similar to the three-pulse ESEEM experiment. These τ-dependent blind spots can be avoided by the use of a SMART HYSCORE scheme.[70] (Fig. 1h). Here, the nuclear-coherence generator, π/2-τ-π/2, is replaced by a HTA pulse nuclear-coherence generator, thereby avoiding the τ-dependence. The

second π pulse is needed to refocus the FID and to allow electron-coherence detection over the spin echo. In practice, the frequency-domain spectrum obtained after 2D Fourier transformation of the SMART HYSCORE signal can be very asymmetric with respect to the diagonal, and symmetrising of the spectrum may be necessary to allow a good evaluation of the data.

The four-pulse ESEEM scheme in Fig. 1g can also be used in other ways. In a DEFENCE (deadtime-free ESEEM by nuclear coherence-transfer echoes) experiment, the time t_1 is kept constant and the time t_2 is stepped.[71] The DEFENCE spectrum represents the projection of the HYSCORE spectrum on the ν_2 axis and, unlike the three-pulse ESEEM, the technique allows measurement of nuclear-frequency spectrum without deadtime artifacts and without the need for phase-cycling. In combination-peak (CP) experiments,[72,73] the times t_1 and t_2 are stepped simultaneously. In this way, the combination frequencies can be analysed in detail. This technique has proven to be very important in the determination of the relative orientation of the histidine-imidazole planes in ferric bis-histidine coordinated heme centres.[74,75]

In a DONUT (double nuclear coherence transfer) HYSCORE experiment,[76] the mixing π pulse in the HYSCORE scheme is replaced by a π-τ_2-π mixer. A combination of standard HYSCORE and DONUT-HYSCORE experiments can facilitate the evaluation of spectra of high-nuclear-spin systems[40,76] or help to establish whether two nuclear interactions stem from the same spin system or from two different spin systems with overlapping EPR spectra.[76]

Finally, it should be mentioned that the potential of decoupling ESEEM experiments has been largely left unexploited up till now.[77] Fig. 1i shows an example of a DEFENCE-based decoupling experiment.[78] The decoupling experiment in EPR is based on the well-known decoupling concepts used in NMR for eliminating nuclear spin dipole–dipole and scalar interactions. In EPR, effective hyperfine decoupling of the electron spins and nuclear spins is easily obtained *via* strong microwave irradiation. In practice, the length of one or more strong microwave pulses is varied in a second dimension independently from the usual ESEEM dimension (Fig. 1i: time t and length t_p are varied independently in a 2D experiment). In the frequency-domain spectrum obtained after 2D Fourier transformation, the ESEEM frequencies are linked to frequencies missing all hyperfine information (hyperfine decoupling). In the case of a hyperfine interaction with an $I = 1/2$ nucleus, cross peaks between the Larmor frequency and the nuclear frequencies then allow for a facile identification of the interacting nucleus. In the case of $I > 1$ systems, the decoupled frequency retains both nuclear Zeeman and nuclear–quadrupole information. Although the assignment is now less trivial than in the $I = 1/2$ case, the decoupled dimension can give invaluable information as was demonstrated in the case of the N-confused Cu^{II} tetraphenylporphyrin.[79] In this work, a hyperfine-decoupled DEFENCE experiment allowed determination of the nuclear–quadrupole coupling of the remote nitrogen of the inverted pyrrole ring.

As mentioned above, ENDOR techniques[4,6,16,80,81] allow detection of the higher nuclear frequencies and are, in this way, complementary to the ESEEM techniques. CW ENDOR, introduced by Feher,[82] was for a long time a prominent tool to determine hyperfine and nuclear–quadrupole values, but in the last decade, pulsed ENDOR techniques[6,79] have largely replaced the CW version of the technique. The electron and nuclear relaxation times usually limit CW ENDOR to a small temperature window. However, in pulsed ENDOR, the pulse sequence can be made short enough to avoid relaxation effects. One of the most commonly used pulsed-ENDOR techniques is Davies ENDOR[83] (Fig. 2a). Fig. 5A shows the Davies ENDOR spectra of the Co^{II} corrin complex, Cobester, ligated with ^{14}N-imidazole (top) and ^{15}N-imidazole (bottom). The structure of Cobester is given in Fig. 5B. Overlapping contributions stemming from the interactions with ^{14}N, ^1H and ^{59}Co are observed in the top spectrum. By use of a $^{14}N/^{15}N$ isotope-labelling experiment, the contribution of the ligating imidazole nitrogen can be easily identified (Fig. 5A).
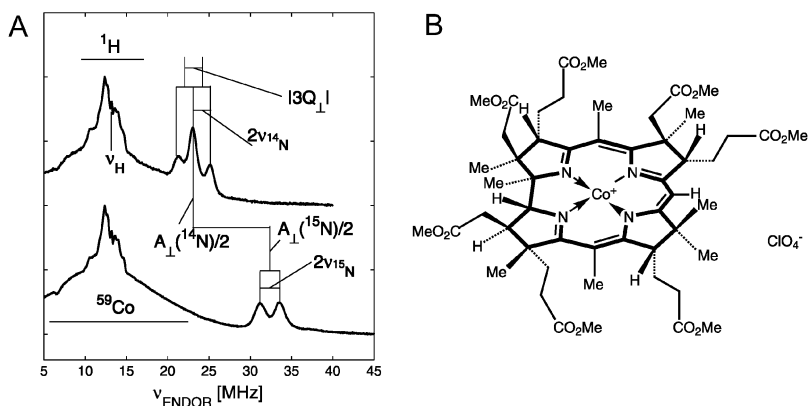
Fig. 5 (A) Experimental X-band Davies ENDOR spectrum of a frozen methanol solution of Cobester ligated with ^{14}N-imidazole (top) or ^{15}N-imidazole (bottom). The spectra were taken at 15 K at an observer position corresponding with $g_\perp$. $t_\pi = 96$ ns, $t_{\pi/2} = 48$ ns, $\tau = 104$ ns, $t_{\pi,rf} = 8.5$ µs. (B) Structure of Cobester.

In the case of overlapping signals, *e.g.* overlapping contributions of weakly coupled protons and strongly coupled nitrogens, the proton contributions can be suppressed in the Davies-ENDOR spectrum by the use of a short inversion π pulse (hyperfine contrast selective ENDOR).[4,10]

Mims ENDOR[84] (Fig. 2b) offers an alternative route to detect the ENDOR spectrum. Mims ENDOR is usually more sensitive than Davies ENDOR, since the detection is done *via* the stimulated echo and not *via* the recovery of an inverted echo. However, Mims ENDOR has two drawbacks: (1) the spectra suffer from τ-dependent blind spots and in general Mims-ENDOR spectra taken at several τ values should be summed; (2) Mims ENDOR is not suited to detect strongly coupled nuclei (*e.g.* the $^{14/15}$N signals in Fig. 5A are not observable in the corresponding Mims-ENDOR experiment).

The electron–nuclear–nuclear triple experiment[85] (Fig. 2c) allows for a determination of the relative sign of the hyperfine coupling. Here, two rf pulses are applied. In a 1D triple experiment, the first rf1 pulse is taken in resonance with one of the nuclear transitions, while the frequency of the second rf2 pulse is swept. Usually, a difference triple spectrum, *i.e.* the difference between the reference ENDOR spectrum and the triple spectrum, is presented. The polarization inversion caused by the first rf1 frequency in one of the M_S manifolds changes the polarization of all nuclear transitions that have a common level with the EPR transition excited by the mw preparation π pulse (direct triple effect). In this way, the nuclear frequencies within one manifold can be identified and the relative signs of the hyperfine values can be determined. If the longitudinal electronic relaxation time is comparable with the duration of the pulse sequence, one can also observe signals due to nuclear transition in another M_S manifold (indirect triple effect). One might think that this would render the assignment of the relative signs of the hyperfine values impossible. However, in the difference triple spectra, peaks stemming from a direct and an indirect triple effect have opposite sign and are thus easily distinguished.

For systems with sufficient long electron phase-memory time, T_m, the 2D version of Mims ENDOR allows for a further unravelling of the EPR spectra.[4] In this experiment, the time τ is varied in a second dimension. Fourier transformation in this dimension leads to a spectrum allowing correlation of the ENDOR frequencies with the hyperfine splitting. This has been nicely shown in the analysis of tropylidene phosphane ligated Rh^0 complexes.[86] In cases where T_m is too short, or for strong hyperfine couplings, the HYEND (hyperfine correlated ENDOR) scheme (Fig. 2d) offers a better alternative.[87] Fig. 6 shows the X-band HYEND spectrum of a frozen
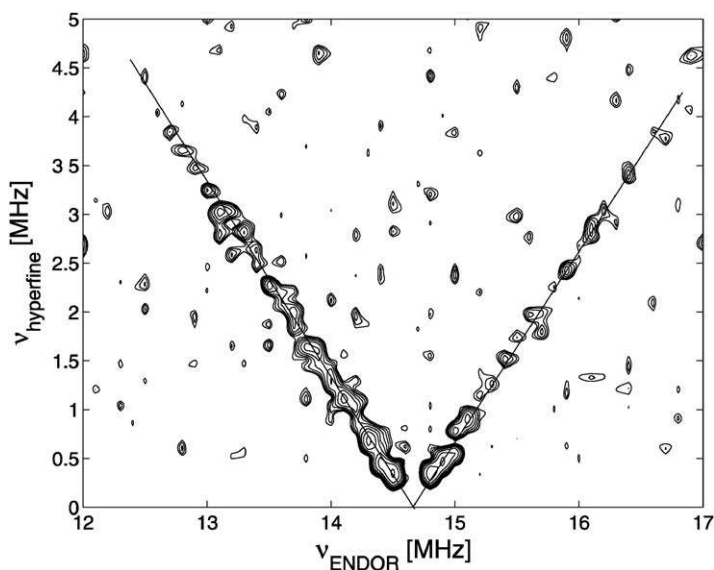
Fig. 6 Experimental X-band HYEND spectrum of a frozen toluene solution of Co^{II} tetra-phenylporphyrin taken at $B_0 = 342.1$ mT. $t_\pi = 96$ ns, $t_{\pi/2} = 48$ ns, $\tau = 104$ ns, $t_{\pi/2,rf} = 4.25$ μs.

toluene solution of oxygenated Co^{II} tetraphenylporphyrin pyridine. In the proton region, two ridges can be seen that cross at the proton Larmor frequency. Each of the nuclear frequencies observed in the ENDOR spectrum is immediately linked to the corresponding hyperfine coupling. HYEND played an essential role in proving the existence of a nickel–methyl species in methyl-coenzyme M reductase[88] as will be explained in section 8. Note, that for systems with $I > 1/2$, HYEND spectra can only be detected for single crystals[87] or for single-crystal-like positions[41] in powders due to insufficient magnetization refocusing in the powder-like case. This explains why for the case depicted in Fig. 6, no HYEND signals stemming from the ^{14}N nuclei could be observed. Furthermore, because of the large number of pulses involved in the experiments and related loss of signal intensity, long accumulation times are required.

Similar to the ESEEM case, a multi-frequency approach facilitates the disentanglement of complex ENDOR spectra. When possible, an ENDOR study at microwave frequencies higher than 9.5 GHz is usually preferable, because the increase in the Larmor frequency induces a gain in the ENDOR resolution.[8] Interesting recent examples of multi-frequency ENDOR studies of bioinorganic systems can be found in refs. 88–95; this list is again only illustrative and not exhaustive.

W-band Davies ENDOR detection of strongly coupled nuclei in disordered systems is notoriously difficult, requiring sometimes thousands of scans. In these cases, ELDOR-detected NMR[96] (Fig. 2e) can provide an elegant alternative as was shown in the analysis of the strong ^{14}N and ^{17}O hyperfine couplings in frozen $^{17}OH_2$ solutions of metmyoglobin (see also section 7).[41] X-band ^{55}Mn ELDOR-detected NMR played an important role in the analysis of the S_2-state of the oxygen evolving complex of photosystem II.[97] In a recent study, D. Goldfarb and co-workers proposed a triple hyperfine sublevel correlation experiment (THYCOS) (Fig. 2f) that combines the ENDOR and ELDOR-NMR experiments in a similar manner to the earlier-mentioned triple experiment.[98] This experiment links forbidden electron-spin transitions ($\Delta M_S = \pm 1$, $\Delta M_I \neq 0$) and allowed nuclear-spin transitions ($\Delta M_I = \pm 1$) and promises to become an important technique at W-band microwave frequencies.

In general, ESEEM, ENDOR and/or ELDOR-detected NMR techniques need to be combined to obtain a full picture of the system under study, as will be evidenced in the two extensive examples in sections 7–8. This principle is also nicely illustrated in the recent EPR/ENDOR study of the active "H-cluster" of ^{57}Fe-enriched [FeFe]-hydrogenase from *Desulfovibrio desulfuricans*.[60] The active site in this hydrogenase consists of a binuclear iron subcluster [2Fe]$_H$ connected *via* a cysteine thiol to a cubane [4Fe–4S]$_H$ cluster; the spin and oxidation states of the iron atoms in this system have been debated extensively in literature. Wolfgang Lubitz and co-workers investigated both the active oxidized form (H$_{ox}$) and the CO-inhibited form (H$_{ox}$–CO). Using Q-band ^{57}Fe HYSCORE, they were able to determine the weak ^{57}Fe hyperfine couplings from the [2Fe]$_H$ subcluster in H$_{ox}$–CO. The four large hyperfine couplings (20–40 MHz) of the [4Fe–4S]$_H$ subcluster could be detected with X- and Q-band Davies ENDOR spectroscopy, whereas triple ENDOR gave insight in the relative sign of the hyperfine couplings. Combined with earlier theoretical findings, these EPR-spectroscopic results allowed the unambiguous assignment of the spin and oxidation states of the iron atoms. In both H$_{ox}$ and H$_{ox}$–CO, the [2Fe]$_H$ subcluster has a [Fe^{I}Fe^{II}] redox configuration with the paramagnetic Fe^I atom attached to the [4Fe–4S]$_H$ subcluster. The latter subcluster is formally diamagnetic, and the observed ^{57}Fe hyperfine couplings stem from an exchange interaction between the two subclusters that is enhanced by binding of the CO ligand.

4. Now you see it, now you don't

Whilst the interpretation of ESEEM and ENDOR spectra can sometimes be very difficult, the situation can get even more frustrating when an expected signal is not observed. Although the lack of a specific signal can in some cases be linked to a chemical or structural characteristic (*e.g.* lack of a hydrogen bond), instrumental and technical reasons may also lie at the heart of the missing signal. Recently, S. Stoll *et al.* revealed, in this respect, one of the hidden pitfalls of ESEEM spectroscopy.[99] In their paper, the authors showed how the contributions of weakly modulating nuclei (*e.g.* weakly coupled protons) can be fully suppressed by the contributions of strongly modulating nuclei (*e.g.* ^{14}N nuclei). It is obvious that this may lead (and probably has led) to serious misinterpretations of experimental data.

In some cases, this problem can be circumvented by appropriate matching of the pulses. As an example, we show in Fig. 7A the standard X-band HYSCORE spectrum of a frozen solution of ferric cyanide-ligated myoglobin taken at the low-field observer position. The HYSCORE spectrum is dominated by the sharp cross peaks stemming from the heme–iron-coordinated histidine nitrogen. At this field, the hyperfine value of this His nitrogen is about twice the ^{14}N Larmor frequency (exact cancellation). This interaction gives rise to very strong modulations, which fully quench the weaker modulations from the strongly coupled heme nitrogens and the weakly coupled protons. By the use of SMART HYSCORE and appropriate matching of the pulses (ν_1 = 15.625 MHz) the latter contributions can be revealed (Fig. 7B). Note also that many cross peaks linking combination frequencies can be resolved in the latter spectrum. Alternatively, a six-pulse ESEEM scheme as recently proposed by B. Kasumaj and S. Stoll can avoid the cross-suppression effects.[100]

In a number of cases, the solution to the cross-suppression effect lies in a change of the microwave frequency. Indeed, by changing the microwave frequency, the relative ratio between the nuclear Zeeman interaction and the hyperfine interaction changes, which directly affects the modulation depth. Weakly or strongly coupled nuclei can be driven into an exact cancellation condition by, respectively, decreasing or increasing the working microwave frequency. In this way, the long-standing problem of the missing hydrogen bond in oxygenated cobaltous myoglobin (CoMbO$_2$) could be solved.[26] The Co^{II} analogues of natural iron-containing globins have been widely used to investigate the interactions of the bound O$_2$ with the surrounding protein
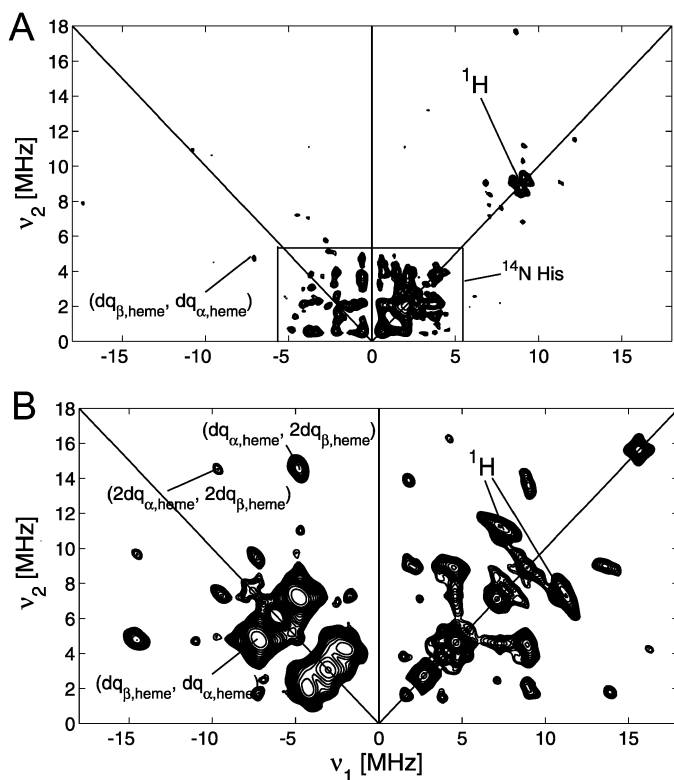
Fig. 7 X-band HYSCORE spectra of a frozen solution of ferric cyanide-ligated myoglobin taken at 4 K with $B_0 = 212.5$ mT. (A) Standard HYSCORE with $t_{\pi/2} = 16$ ns, $t_{\pi} = 16$ ns and $\tau = 176$ ns. (B) SMART HYSCORE with $\nu_1 = 15.625$ MHz, $t_{\text{HTA}} = 32$ ns, $t_{\pi} = 16$ ns, $\tau = 96$ ns.

environment by use of EPR,[101–105] because the natural Fe^{II}–O_2 form is diamagnetic. The use of the cobaltous analogues is supported by different X-ray studies showing a similar geometry for the native oxygenated Mb and $CoMbO_2$.[106] Although a hydrogen bond between the distal histidine and the dioxygen was expected, many attempts to prove the existence of this bond in $CoMbO_2$ and related model systems *via* different X-band pulsed EPR and ENDOR techniques failed. In their CW-ENDOR study of $CoMbO_2$, Hütterman and Stabler identified signals with hyperfine splittings of up to 9 MHz as stemming from the "H-bonded proton" of the distal His.[103] In a recent study,[26] the EPR group at the ETH, Zurich, showed that severe cross-suppression effects prevent a full assessment of the proton hyperfine values with X-band ESEEM or ENDOR techniques. The complete determination of the hyperfine interactions of the proton close to the bound dioxygen can only be assessed using Q-band Davies ENDOR with a short preparation pulse in order to enhance the relative ENDOR intensity of the larger hyperfine splittings. The coupling of the histidine proton stabilizing the O_2 moiety was found to be [−10 −10 19] MHz, showing that Hütterman and Stabler[103] only managed to pick up the inner part of the complete proton spectrum.

5. Interpretation of EPR data

One of the most difficult steps in an EPR analysis is the translation of the EPR data into (bio)physical and (bio)chemical data. This process consists of two steps: (1) the simulation of the different spectra and (2) the interpretation of the derived spin

Hamiltonian values in terms of useful electronic and geometric structural information.

The first step may be facilitated by the use of isotope labelling (*e.g.* ^{2}H$_2$O-exchange experiments) or the use of pulse schemes that allow a separation of different spectral contributions (see sections 3 and 4). However, at a given point, the spectroscopist will have to simulate the spectra at hand. Currently, many computer programs are available that tackle the simulation of CW-EPR spectra,[108–113] but only a limited number of software packages allow simulations of pulsed EPR experiments,[54,112–114] amongst which the matlab-based EasySpin program[112] is probably the most extended and flexible simulation package for both CW and pulsed EPR/ENDOR experiments. It is my belief that the simulation procedure poses, at the moment, one of the most important limitations to many of the pulsed EPR experiments. For instance, in order to reproduce a given HYSCORE spectrum exactly, not only do the magnetic parameters have to be correct, but also the non-ideality of the microwave pulses (including possible imperfections in pulse tuning introduced by the spectroscopist) and the contributions of all magnetic nuclei (see the earlier mentioned cross-suppression effects) should be taken into account. Since this is not feasible for most real cases, HYSCORE simulations are done using a simplified system (*i.e.* individual simulation of the different nuclear contributions) and the evaluation of the accuracy of a given HYSCORE simulation then automatically becomes subjective. Similar considerations can be made for other pulsed EPR and ENDOR experiments. This clearly limits the attainable accuracy for the spin-Hamiltonian parameters. Hence, the generalization of simulation programs and the development of more objective simulation approaches should remain essential targets in the field.

The second step involves the interpretation of the spin Hamiltonian parameters. Although a number of approaches have been used successfully for many decades,[11–15] *e.g.* the point-dipolar approximation[115] to translate hyperfine values into distance information, the ultimate goal is to perform quantum-chemical computations that elucidate the experimental outcomes. In recent years, these quantum-chemical approaches, especially density functional theory (DFT) computations, are being increasingly combined with advanced EPR studies.[116,117] In some cases, the DFT and other methods have been shown to predict the spin Hamiltonian parameters with a fair degree of accuracy,[118,119] although in the majority of the cases, especially for transition-metal complexes, a qualitative agreement (*i.e.* a prediction of trends) is the most that can be achieved[120,121] In fact, given the slow progress in developing DFT functionals since the introduction of hybrid functionals in 1993, it is unclear whether a large improvement in the DFT performance may be expected in the next few years and, it is more likely, that simplified correlated *ab initio* methods will regain importance.[122] Despite the existing limitations, quantum-chemical computations have helped, or even been crucial for, the interpretation of EPR data of paramagnetic metalloproteins and related model compounds.[123–126]

6. Choosing between different experiments

Although sections 2 and 3 give only a brief overview of a number of the available pulsed EPR and ENDOR experiments, they illustrate the difficult task EPR spectroscopists face when trying to decide what experiment will be suitable for a specific problem. It is almost like finding your way through one of Lewis Caroll's labyrinths. Although every specific study will require a different, spin-system-dependent approach, there are still some general starting guidelines that can be followed.

In cases where the material availability does not pose any limitations, it is advisable to start an EPR study with the recording and analysis of the X-band CW-EPR spectrum. This spectrum will immediately determine whether there is need to do further field-swept EPR experiments in order to unravel the electron Zeeman interaction and possible exchange couplings, dipolar couplings or zero-field splittings (see section 2). In those cases where only a small amount of material is

available, one should start with a field-swept EPR analysis at higher microwave frequencies (the lowest permitted by the sample quantity). For W-band frequencies and higher, the spectrometer tuning and recording of the spectra will be considerably less trivial than at lower frequencies and this may hamper the analysis. This is especially the case for newly isolated biomolecules where the spectroscopist has no clear idea about the possible paramagnetic centres and, hence, has no prior information about the optimal detection conditions.

When the scientific question at hand requires the detection of nuclear frequencies, different techniques are available (see section 3). Unless you want to detect a specific interaction with a targeted magnetic nucleus and you know already a lot about the spin system, it is advisable to start the analysis with the more standard pulsed EPR and ENDOR techniques. When starting an ENDOR analysis of metalloproteins, the author usually records and optimizes a ^{1}H Davies and a ^{1}H Mims ENDOR even if the ^{1}H hyperfine interactions are not of direct interest. In the proton-rich biomolecular environment, signals of weakly coupled ^{1}H should be readily detectable. The observation of these signals gives confidence that some of the basic settings for signal detection are fulfilled (temperature, pulse repetition rate, spectrometer performance, sufficient echo intensity, *etc.*). In a second step, one can then focus on the contributions of interest. In many cases, the settings used to detect the ^{1}H interactions may reveal other nuclear interactions of interest (see Fig. 5A) and the settings can then be further optimized (*e.g.* rf-pulse-length optimization *via* observation of the Rabi oscillations, microwave-pulse optimization based on the hyperfine selection criteria[4]). The analysis of weakly coupled low-g_n magnetic nuclei (*e.g.* ^{2}H, ^{13}C, ^{14}N) is better done using high-frequency ENDOR or using ESEEM techniques in the S- to Q-band microwave region (see section 3).

The first step in an ESEEM analysis of biomolecules, consists of checking whether any echo modulation can be detected using a standard two-pulse ESEEM sequence and hard microwave pulses. In most cases, such a modulation can easily be observed, from which one can move on to three-pulse ESEEM and HYSCORE experiments. However, in some cases, no modulation of the two- or three-pulse echo intensity can be observed in this way. If this happens in an S-band or X-band ESEEM experiment, one should try a matched three-pulse ESEEM experiment, where the mw pulse strength is chosen to fit the proton Larmor frequency and the length of the second and third π/2 pulse is varied in a second dimension. Since distant protons (so-called 'matrix' protons) should be observable in a biomolecule, one should be able to find a suitable pulse length to observe proton modulation. This then forms the starting point for further optimization and matching experiments. At Q-band, the proton Larmor frequency is too high to allow detection with ESEEM. In this case, the initial matching can be performed on nitrogen, or other low-g_n nuclei that are expected in the ESEEM spectrum.

From these exploratory experiments onwards, the analysis process is largely spin-system driven and, in many cases, there are several options. Sometimes, a preliminary DFT computation, regardless of its limitations, may help in determining the appropriate technique by predicting the order of magnitude of the expected interaction. For each change of experiment, one should ask oneself why the previous method failed. Usually, this question immediately suggests the type of experiment to perform. For instance, assume you have a disordered $S = 1/2$ system with large g anisotropy (*e.g.* a low-spin Co^{II} system) interacting strongly with a ^{14}N nucleus (hyperfine coupling around 30 MHz) and weakly with ^{1}H nuclei (hyperfine interactions in 1–5 MHz region). In the X-band Davies-ENDOR experiment these contributions are strongly overlapping and you are likely to want to unravel them. The reason these signals overlap is because the proton Larmor frequency at X-band is near to half the hyperfine value of the ^{14}N nucleus. So, the problem will be solved by using a method that is able to separate strongly coupled low-g_n magnetic nuclei, from weakly coupled high-g_n magnetic nuclei. In principle, you have now several options. You can perform Q-band ENDOR, since the proton signals will be shifted

out of the ^{14}N area (increase in nuclear Zeeman interaction). You can use W-band ^{1}H ENDOR combined with a W-band ELDOR-detected NMR experiment to observe the ^{14}N interactions (in principle, W-band ^{14}N ENDOR can be tried, but the success rate is expected to be low). However, in situations where the echo intensity is already low at X-band frequencies, the shift to a higher microwave frequency is not advisable (the large g anisotropy will spread the echo intensity over a broader magnetic-field range which will lead to low or undetectable spin-echo signals). There may also be practical reasons for not moving to higher microwave frequencies (*e.g.* equipment availability). In these cases, one can try to disentangle the X-band Davies ENDOR spectra by changing the strength of the inversion π pulse, possibly in combination with Mims ENDOR and/or ESEEM experiments, which will highlight the ^{1}H contributions.

7.   Example 1. The study of high-spin ferric heme proteins

Heme proteins form an important class of metalloproteins with a variety of functions including gas transport, detoxification, electron transport, protection against reactive oxygen species, *etc.* In many ferric heme proteins the heme iron is in a high-spin (HS) state ($S = 5/2$). Because the microwave quantum energy is at X-band (*ca.* 9.5 GHz) much smaller than the zero-field splitting (5–10 cm^{-1}), the X-band CW-EPR spectrum of such a HS Fe^{III} system arises from the transitions in the lower Kramers doublet and hence the EPR spectrum of the $S = 5/2$ system with $g \approx 2$ resembles that of an effective $S_{\text{eff}} = 1/2$ system with $g_{\perp,\text{eff}} \approx 6$ and $g_{\parallel,\text{eff}} \approx 2$.[127] In order to determine the zero-field splitting from the field-swept EPR experiments, EPR experiments at high microwave frequencies are needed.[28,128] Since the interactions between the electron spin and the surrounding magnetic nuclei are not resolved in the field-swept EPR experiments, ENDOR and pulsed EPR experiments need to be used. The analysis of these HS heme iron systems with these methods is, however, non trivial, which is reflected in the low amount of literature on this topic.[41,129–140]

   In the early 80s, Scholes *et al.* determined the hyperfine and nuclear quadrupole tensors of the iron-coordinating nitrogens in aquometmyoglobin (Fig. 8A) in detail using single-crystal X-band CW-ENDOR. However, the amount of information that can be determined by the standard ENDOR and ESEEM techniques reduces dramatically when single crystals are not available. One of the reasons is related to the fact that the effective hyperfine principal values lying in the heme plane are about three times the real hyperfine values (see similarity with $g_{\perp,\text{eff}} \approx 3g$).[131,138] For the above-mentioned nitrogen interactions, this leads to typical effective hyperfine values of the order of 24 to 30 MHz, which are generally not accessible with the standard ESEEM techniques. Therefore, most ESEEM analyses of disordered high-spin heme systems are limited to the single-crystal-like observer position near $g \approx g_{\parallel,\text{eff}}$ for which the effective hyperfine coupling is quasi equal to the real hyperfine coupling.[134,137,139] Furthermore, there is a large pseudo-nuclear contribution to the nuclear $\boldsymbol{g_n}$ tensors of magnetic nuclei in HS heme systems, given by[131,138]

$$g_{n,x,\text{eff}} = g_n + \frac{2g_x\beta_e A_x}{\beta_n D}, \; g_{n,y,\text{eff}} = g_n + \frac{2g_y\beta_e A_y}{\beta_n D},$$

$$g_{n,z,\text{eff}} = g_n. \tag{2}$$

β_n and β_e the nuclear and Bohr magneton, and A_i and g_i the principal values of the hyperfine and $\boldsymbol{g}$ tensor. This contribution will additionally complicate the spectral analysis, especially for disordered samples and in one-dimensional ENDOR or ESEEM studies.

   In recent work, we compared the performance of different multi-frequency EPR and ENDOR approaches in studies on frozen solutions of high-spin ferric heme proteins.[41,138,141] We showed that different techniques can be used to determine the magnetic parameters of the strongly coupled heme and histidine nitrogens.[41,138]
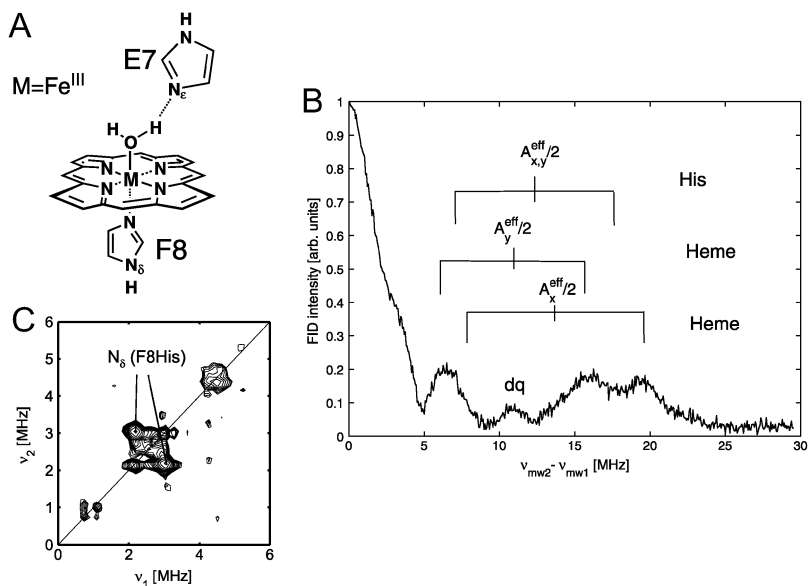
Fig. 8 (A) Schematic representation of the important components in the heme pocket of aquometmyoglobin: the porphyrin ring of the heme, the coordinating imidazole of F8His, the distal water molecule and the imidazole of E7His hydrogen-bonded to the water molecule. (B) W-band ELDOR detected NMR spectrum of the ferric form of the E7Q mutant of human neuroglobin (E7QNGB). The spectrum was taken at the low-field position ($B_0 = 1150$ mT, $g = g_{\perp,\text{eff}}$) at 1.7 K. FID-detection using mw1 π pulse with length 120 ns. $t_{\text{HTA}} = 2$ μs. (C) Part of experimental X-band HYSCORE spectrum of ferric E7QNGB. The spectrum was taken at the $g = g_{\parallel,\text{eff}}$ position at a temperature of 4 K, with $t_{\pi/2} = 16$ ns, $t_\pi = 16$ ns, $\tau = 120$ ns.

Although standard X-band HYSCORE experiments can be used in observer positions near $g \approx g_{\parallel,\text{eff}}$,[137–139] matched and SMART HYSCORE experiments are needed in other observer positions.[41,138] Furthermore, deuterated solvents were found to have an advantageous effect on the detection of the HYSCORE spectra, because of the increase of the phase memory time and the disappearance of proton-related cross suppression effects.

In the single-crystal-like situation, an X-band HYEND experiment can be performed instead of the HYSCORE experiment, to reveal the small inequivalencies between the heme–nitrogen couplings. At the 'powder-like' observer positions, HYEND is not suitable for the detection of $I > 1/2$ systems, as was discussed in section 3.

When only small amounts of protein are available, Q- and W-band HYSCORE and W-band ELDOR-detected NMR experiments can offer an alternative route to determine the spin Hamiltonian parameters of the strongly coupled nitrogens.[41] Note, that W-band HYSCORE at the observer positions $g \approx g_{\perp,\text{eff}}$ can be performed using a commercial E680 Bruker spectrometer, because of the earlier-mentioned dependence of the microwave-pulse flip angle on he electron spin and the low observer field (~ 1.14 T).

W-band ELDOR-detected NMR experiments provide an easy method to screen the interactions with the coordinating nitrogens, but it should be noted that a low temperature is usually required to obtain good spectral resolution (T_m should be maximised). In our case, we performed measurements at 1.7 K (with the use of an immersion cryostat). Fig. 8B shows an ELDOR-detected NMR spectrum of the ferric HE7Q mutant of human neuroglobin. The mutation induces in this heme protein a change from the low to the high spin state.[138] The spectrum shows signals stemming from the directly coordinated heme and F8His ^{14}N nuclei. Only 4 scans

were needed to obtain a good signal-to-noise ratio. The earlier-mentioned pseudo-nuclear contribution to the nuclear Zeeman term is clearly noticeable in this spectrum. Indeed, the in-plane principal hyperfine values of the heme nitrogens vary strongly ($A_x \sim 10$ MHz, $A_y \sim 7$ MHz) whereby the corresponding values of the coordinating F8His nitrogen are quite similar to each other ($A_{x,y} \sim 8$ MHz). Eqn (2) shows that $g_{n,\text{eff}}$ depends strongly on the hyperfine values and this dependence is very pronounced at higher microwave frequencies (field-dependence of nuclear Zeeman interaction). In Fig. 8B, the observed peaks are centred around half the effective hyperfine coupling and separated by twice the effective Larmor frequency. This splitting is highest for the largest hyperfine coupling and in all cases larger than the one corresponding with the tabulated g_n value of ^{14}N. Since all reported D values of heme proteins are positive, the experimentally observed increase of the effective nuclear Zeeman splitting is linked to a positive sign of the corresponding hyperfine value. The signals are broad due to the nuclear quadrupole broadening.

In the past, only partial information about the coupling with the oxygen nucleus of the coordinating water in aquometmyoglobin could be obtained *via* standard ENDOR experiments.[135] In our study of ^{17}OH$_2$-labeled aquometmyoglobin, we showed that X-band Davies ENDOR and HYSCORE experiments allow only for the analysis of the ^{17}O hyperfine interaction in observer positions corresponding to $g_{\text{eff}} < 2.5$. W-band ELDOR-detected NMR was found to offer a facile route to evaluate the in-plane hyperfine values.[41]

X- and Q-band HYSCORE techniques are ideally suited to study the interactions with remote magnetic nuclei.[141] When combined with ^{2}H$_2$O-labelling experiments, X- and Q-band SMART HYSCORE allowed the identification of the hyperfine couplings with two distinct water protons, the mesoprotons of the heme ligand and the protons of the proximal ligand in aquometmyoglobin. The combined X- and Q-band HYSCORE study also revealed the spin-Hamiltonian parameters of two remote nitrogen nuclei identified as the N$_\delta$ of the F8 histidine and the E7His N$_\epsilon$ (Fig. 8A). Fig. 8C shows an X-band HYSCORE spectrum of the HE7Q mutant of neuroglobin. In this case, only the contributions of the F8His N$_\delta$ are observable (E7His is mutated to Gln). Interestingly, our multi-frequency HYSCORE analysis of aquometmyoglobin revealed also the hyperfine interactions with several ^{13}C nuclei of the heme ligand, without the need for isotope labelling.[141]

8.   Example 2. The nickel-containing methyl-coenzyme M reductase

Methyl-coenzyme M reductase (MCR), which contains the nickel-pophyrinoid F$_{430}$, catalyses the formation of methane from methyl-coenzyme M (CH$_3$-CoM) and coenzyme B (HS-CoB) in methanogenic archaea (Fig. 9). The enzyme has two structurally interlinked active sites embedded in an $\alpha_2\beta_2\gamma_2$ subunit structure. Each active site contains one F$_{430}$ prosthetic group. Different forms of the enzyme, and the relationship between these species, have been examined, but the catalytic mechanism is still widely disputed.[142] Since many of these MCR forms, including the enzymatically active ones, are paramagnetic, EPR has played an important role in the analysis of these structures. In fact, because the current X-ray structures of MCR are all for inactive, oxidized Ni^{II} forms, and no crystals of the important paramagnetic forms have been grown up till now, EPR is a major characterization tool for MCR.

Both the X- and Q-band CW-EPR and ENDOR spectra of the active form of MCR, MCR$_{\text{red1a}}$, and the isolated F$_{430}$ complex are very similar.[143,144] They bear all the characteristics of a Ni^I complex (d^9 configuration) with the unpaired electron residing mostly in the d$_{x^2-y^2}$ orbital. The hyperfine couplings of the pyrrole nitrogens are of the order of 25–30 MHz, consistent with the (d$_{x^2-y^2}$)^1 configuration.

One of the proposed mechanisms for the MCR catalysis involves the Ni^I centre acting as a nucleophile, with this attacking the methyl-coenzyme M at the carbon atom of the CH$_3$S group and generating an intermediate CH$_3$–Ni^{III}F$_{430}$$^+$ species.[145,146] In order to examine this postulated mechanism, Hinderberger *et al.*
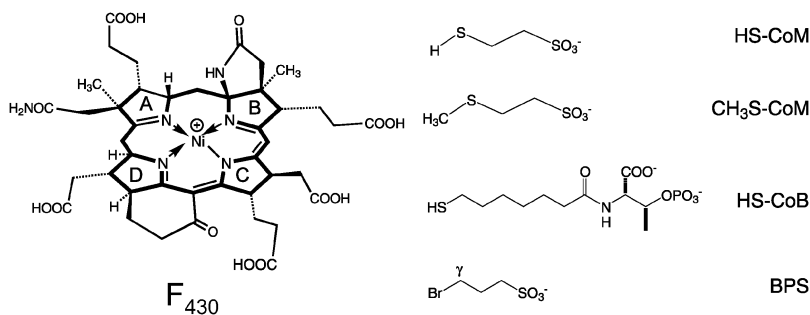
Fig. 9 Structure of F_{430} and of the substrates mentioned in the text: coenzyme M (HS-CoM), methyl-coenzyme M (CH₃S-CoM), coenzyme B (HS-CoB) and 3-bromopropane sulphonate (BPS).

analysed the reaction of MCR with the irreversible inhibitor 3-bromopropane sulphonate (BPS).[49] Using selective ^{13}C-labeling in combination with Q-band Davies ENDOR and HYSCORE, they were able to demonstrate the formation of a bond between the nickel centre of coenzyme F_{430} and the C_γ atom of the propane sulphonate residue *via* the evaluation of the [13]C_γ hyperfine matrix and the hyperfine couplings to the BPS protons. The deduced spin populations on the C_γ and Ni atom are in close agreement with the results of DFT calculation on a $[CH_3–Ni^{III}F^+_{430}]$ model. Similarly, X-band HYEND experiments combined with DFT computations allowed for the identification of a $[CH_3–Ni^{III}F^+_{430}]$ species in MCR incubated with MeBr.[88]

In the presence of coenzyme M (HS-CoM) and coenzyme B, MCR_{red1a} is reversibly converted into a so-called MCR_{red2} state. The CW-EPR spectrum of this form is characterized by an unusual, highly rhombic **g** tensor.[142] [61]Ni-labeling confirmed that the centre that gives rise to this signal is still nickel based.[142] The pyrrole nitrogen hyperfine couplings determined using X- and Q-band ENDOR and HYSCORE, revealed that the pyrrole A of F_{430} is slightly displaced out of the plane of the macrocycle.[148] This results in the smaller nitrogen hyperfine value (~ 14 MHz) of this pyrrole nitrogen when compared to the other three nitrogens (~ 24 MHz). Furthermore, the combination of [33]S labelling and Q-band HYSCORE provided unambiguous evidence for coordination of the sulphur of HS-CoM to the nickel centre.[57] It is this coordination that leads to the strong out-of-plane distortion of the F_{430} ring. Based on the initial X-band CW-EPR data it was thought that only this rhombic form arose from the above reaction. However, a recent W-band CW-EPR study showed that a second red2 form with axial **g** symmetry is formed in the process.[149] This form could not be resolved using X-band microwave frequencies, illustrating the power of high-field EPR. The nature of the latter species still has to be determined.

MCR_{ox1} is an enzymatically inactive form of MCR that can be easily reduced to the active state. The oxidation state of the nickel ion in MCR_{ox1} was for a long time the subject of debate. Using multi-frequency EPR, ENDOR and HYSCORE in combination with ^{2}H, [61]Ni and [33]S labelling, the MCR_{ox1} metal centre has been identified as a Ni[III]-thiolate in resonance with a thiyl radical/high-spin Ni[II] complex.[37] Again, the Q-band [33]S HYSCORE spectra provided critical data on the binding of the HS-CoM thiolate.

9. Conclusion

In this review, a number of the pulsed EPR and ENDOR techniques have been discussed with regard to their suitability and performance at different microwave frequencies. The potential of these techniques in analysing paramagnetic

bioinorganic systems is highlighted using a number of examples from the author's research and that of others. An attempt has been made to outline some general guidelines for pulsed EPR experiments, keeping in mind that each spin system is likely to need a different approach, and that often many routes can lead to the same result.

Acknowledgements

References

1   J. Hüttermann and R. Kappl, *Specialist periodical reports—Electron Paramagnetic Resonance*, eds. B. C. Gilbert, M. J. Davies and K. A. McLauchlan, The Royal Society of Chemistry, 2000, vol. 17, pp. 246–304.
2   J. Hüttermann and R. Kappl, *Specialist periodical reports—Electron Paramagnetic Resonance*, eds. B. C. Gilbert, M. J. Davies and D. M. Murphy, The Royal Society of Chemistry, 2002, vol. 18, pp. 304–346.
3   J. Hüttermann and R. Kappl, *Specialist periodical reports—Electron Paramagnetic Resonance*, eds. B. C. Gilbert, M. J. Davies and D. M. Murphy, The Royal Society of Chemistry, 2004, vol. 19, pp. 116–173.
4   A. Schweiger and G. Jeschke, *Principles of Pulse Electron Paramagnetic Resonance*, University Press Oxford, Oxford, 2001.
5   D. Goldfarb and D. Arieli, *Annu. Rev. Phys. Chem.*, 2004, **33**, 441.
6   D. Goldfarb, *Phys. Chem. Chem. Phys.*, 2006, **8**, 2325.
7   T. Prisner, M. Rohrer and F. MacMillan, *Annu. Rev. Phys. Chem.*, 2001, **52**, 279.
8   K. Möbius, A. Savitsky, A. Schnegg, M. Plato and M. Fuchs, *Phys. Chem. Chem. Phys.*, 2005, **7**, 19.
9   M. Bennati and T. Prisner, *Rep. Prog. Phys.*, 2005, **68**, 411.
10 S. Van Doorslaer and E. Vinck, *Phys. Chem. Chem. Phys.*, 2007, **9**, 4620.
11 A. Abragam and B. Bleaney, *Electron paramagnetic resonance of transition ions*, Clarendon, Oxford, 1970.
12 J. A. Weil, J. R. Bolton and J. E. Wertz, *Electron paramagnetic resonance*, Wiley, New York, 1994.
13 J. R. Pilbrow, *Transition ion electron paramagnetic resonance*, Clarendon, Oxford, 1990.
14 N. M. Atherton, *Principles of electron spin resonance*, Ellis Horwood, New York, 1993.
15 P. Rieger, *Electron Spin Resonance. Analysis and Interpretation*, Royal Society of Chemistry, Cambridge, 2007.
16 H. Kurreck, B. Kirste and W. Lubitz, *Electron Nuclear Double Resonance Spectroscopy of Radicals in Solution*, VCH Publishers, New York, 1988.
17 T. Prisner, S. Lyubenova, Y. Atabay, F. MacMillan, A. Kröger and O. Klimmeck, *J. Biol. Inorg. Chem.*, 2003, **8**, 419.
18 K. K. Andersson and A. L. Barra, *Spectrochim. Acta A*, 2002, **58**, 1101.
19 P. Moens, P. Devolder, R. Hoogewijs, F. Callens and R. Verbeeck, *J. Magn. Reson. A*, 1993, **101**, 1.
20 M. Mehring, H. Seidel, W. Müller and G. Wegner, *Solid State Commun*, 1983, **45**, 1075.
21 M. J. Colaneri and J. Peisach, *J. Magn. Reson. A*, 1993, **102**, 360.
22 E. Hoffmann and A. Schweiger, *Appl. Magn. Reson.*, 1995, **9**, 1.
23 T. Maly and T. Prisner, *J. Magn. Reson.*, 2004, **170**, 88.
24 T. Maly, F. MacMillan, K. Zwicker, N. Kashani-Poor, U. Brandt and T. Prisner, *Biochemistry*, 2004, **43**, 3969.
25 A. Cernescu, T. Maly and T. Prisner, *J. Magn. Reson.*, 2008, **192**, 78.
26 H. Dube, B. Kasumaj, C. Calle, M. Saito, G. Jeschke and F. Diederich, *Angew. Chem. Int. Ed.*, 2008, **47**, 2600.
27 M. Chattopadhyay, E. D. Walter, D. J. Newell, P. J. Jackson, E. Aronoff-Spencer, J. Peisach, G. J. Gerfen, B. Bennett, W. E. Antholine and G. L. Milhauser, *J. Am. Chem. Soc.*, 2005, **127**, 12647.
28 K. K. Andersson, P. P. Schmidt, B. Katterle, K. R. Strand, A. E. Palmer, S.-K. Lee, E. I. Solomon, A. Gräslund and A.-L. Barra, *J. Biol. Inorg. Chem.*, 2003, **8**, 235.
29 S. Stoll, G. Jeschke, M. Willer and A. Schweiger, *J. Magn. Reson.*, 1998, **130**, 86.
30 B. Epel, K.-O. Schäfer, A. Quentmeier, C. Friedrich and W. Lubitz, *J. Biol. Inorg. Chem.*, 2005, **10**, 636.

31 C. More, P. Camensuli, F. Dole, B. Guigliarelli, M. Asso, A. Fournel and P. Bertrand, *J. Biol. Inorg. Chem.*, 1996, **1**, 152.
32 S. Lyubenova, M. K. Siddiqui, M. J. M. P. de Vries, B. Ludwig and T. F. Prisner, *J. Phys. Chem. B*, 2007, **111**, 3839.
33 E. Narr, A. Godt and G. Jeschke, *Angew. Chem. Int. Ed.*, 2002, **41**, 3907.
34 K. Warncke, *Biochemistry*, 2005, **44**, 3184.
35 R. Carmieli, N. Papo, H. Zimmermann, A. Potapov, Y. Shai and D. Goldfarb, *Biophys. J.*, 2006, **90**, 492.
36 P. Höfer, A. Grupp, H. Nebenführ and M. Mehring, *Chem. Phys. Lett.*, 1986, **132**, 279.
37 J. Harmer, C. Finazzo, R. Piskorski, C. Bauer, B. Jaun, E. C. Duin, M. Goenrich, R. K. Thauer, S. Van Doorslaer and A. Schweiger, *J. Am. Chem. Soc.*, 2005, **127**, 17744.
38 M. Brecht, M. van Gastel, T. Buhrke, B. Friedrich and W. Lubitz, *J. Am. Chem. Soc.*, 2003, **125**, 83.
39 S. Nakazawa, A. Ishii, J. Minagawa and T. A. Ono, *Chem. Phys. Lett.*, 2005, **405**, 318.
40 S. Van Doorslaer, R. Bachmann and A. Schweiger, *J. Phys. Chem. A*, 1999, **103**, 5446.
41 M. Fittipaldi, I. García-Rubio, F. Trandafir, I. Gromov, A. Schweiger, A. Bouwen and S. Van Doorslaer, *J. Phys. Chem. B*, 2008, **112**, 3859.
42 B. K. S. Rao, A. M. Tyryshkin, A. G. Roberts, M. K. Bowman and D. M. Kramer, *Biochemistry*, 2000, **39**, 3285.
43 S. Kababya, J. Nelson, C. Calle, F. Neese and D. Goldfarb, *J. Am. Chem. Soc.*, 2006, **128**, 2017.
44 S. Grimaldi, F. MacMillan, T. Ostermann, B. Ludwig, H. Michel and T. Prisner, *Biochemistry*, 2001, **40**, 1037.
45 S. Van Doorslaer, G. Jeschke, B. Epel, D. Goldfarb, R.-A. Eichel, B. Kräutler and A. Schweiger, *J. Am. Chem. Soc.*, 2003, **125**, 5915.
46 M. Fittipaldi, H. J. Wijma, M. P. Verbeet, G. W. Canters, E. J. J. Groenen and M. Huber, *Biochemistry*, 2005, **46**, 15193.
47 S. Van Doorslaer, D. M. Murphy and I. A. Fallis, *Res. Chem. Intermed.*, 2007, **33**, 807.
48 J. Kordas, *J. Non-Crystall. Sol.*, 2003, **331**, 122.
49 D. Hinderberger, R. P. Piskorski, M. Groenrich, R. K. Thauer, A. Schweiger, J. Harmer and B. Jaun, *Angew. Chem. Int. Ed.*, 2006, **45**, 3602.
50 D. Zverev, H. Vrielinck, F. Callens, P. Matthys, S. Van Doorslaer and N. M. Khaidukov, *Phys. Chem. Chem. Phys.*, 2008, **10**, 1789.
51 P. J. Carl, D. E. W. Vaughan and D. Goldfarb, *J. Phys. Chem. B*, 2002, **106**, 5428.
52 M. Chiesa, V. Meynen, S. Van Doorslaer, P. Cool and E. F. Vansant, *J. Am. Chem. Soc.*, 2006, **128**, 8955.
53 S. A. Dikanov, B. D. Liboiron and C. Orvig, *J. Am. Chem. Soc.*, 2002, **124**, 2969.
54 Z. L. Madi, S. Van Doorslaer and A. Schweiger, *J. Magn. Reson.*, 2002, **154**, 181.
55 M. Gutjahr, R. Böttcher and A. Pöppl, *J. Phys. Chem. B*, 2002, **106**, 1345.
56 D. C. Doetschman, D. C. Gilbert and D. W. Dwyer, *Chem. Phys.*, 2000, **256**, 37.
57 C. Finazzo, J. Harmer, C. Bauer, B. Jaun, E. C. Duin, F. Mahlert, M. Goenrich, R. K. Thauer, S. Van Doorslaer and A. Schweiger, *J. Am. Chem. Soc.*, 2003, **125**, 4988.
58 J.-H. Su, W. Lubitz and J. Messinger, *J. Am. Chem. Soc.*, 2008, **130**, 786.
59 M. Chiesa, E. Giamello, C. Di Valentin, G. Pacchioni, Z. Sojka and S. Van Doorslaer, *J. Am. Chem. Soc.*, 2005, **127**, 16935.
60 A. Silakov, E. J. Reijerse, S. P. J. Albracht, E. C. Hatchikian and W. Lubitz, *J. Am. Chem. Soc.*, 2007, **129**, 11447.
61 J. J. Shane, P. Höfer, E. J. Reijerse and E. Deboer, *J. Magn. Reson.*, 1992, **99**, 596.
62 S. A. Dikanov, A. M. Tyryshkin and M. K. Bowman, *J. Magn. Reson.*, 2000, **144**, 228.
63 A. G. Maryasov and M. K. Bowman, *J. Phys. Chem. B*, 2004, **108**, 9412.
64 A. G. Maryasov and M. K. Bowman, *J. Magn. Reson.*, 2006, **179**, 120.
65 M. Gutjahr, R. R. Böttcher and A. Pöppl, *Appl. Magn. Reson.*, 2002, **22**, 401.
66 N. P. Benetis, P. C. Dave and D. Goldfarb, *J. Magn. Reson.*, 2002, **158**, 126.
67 J. Harmer, S. Van Doorslaer, I. Gromov and A. Schweiger, *Chem. Phys. Lett.*, 2002, **358**, 8.
68 G. Jeschke and A. Schweiger, *Mol. Phys.*, 1996, **88**, 355.
69 G. Jeschke, R. Rakhmatullin and A. Schweiger, *J. Magn. Reson.*, 1998, **131**, 261.
70 L. Liesum and A. Schweiger, *J. Chem. Phys.*, 2001, **114**, 9478.
71 A. Ponti and A. Schweiger, *J. Chem. Phys.*, 1995, **102**, 5207.
72 A. Schweiger, *Angew. Chem. Int. Ed. Engl.*, 1991, **30**, 265.
73 S. Van Doorslaer and A. Schweiger, *Chem. Phys. Lett.*, 1997, **281**, 297.
74 E. Vinck, S. Van Doorslaer, S. Dewilde, G. Mitrikas, A. Schweiger and L. Moens, *J. Biol. Inorg. Chem.*, 2006, **11**, 467.
75 A. V. Astashkin, A. M. Raitsimring and F. A. Walker, *Chem. Phys. Lett.*, 1999, **306**, 9.
76 D. Goldfarb, V. Kofman, J. Libman, A. Schanzer, R. Rahmatouline, S. Van Doorslaer and A. Schweiger, *J. Am. Chem. Soc.*, 1998, **120**, 7020.

77 G. Jeschke and A. Schweiger, *J. Chem. Phys.*, 1997, **106**, 9979.
78 G. Mitrikas and A. Schweiger, *J. Magn. Reson.*, 2004, **168**, 88.
79 C. Calle, A. Schweiger and G. Mitrikas, *Inorg. Chem.*, 2007, **46**, 1847.
80 C. Gemperle and A. Schweiger, *Chem. Rev.*, 1991, **91**, 1481.
81 I. A. Gromov and J. Harmer, *Appl. Magn. Reson.*, 2007, **31**, 627.
82 G. Feher, *Phys. Rev.*, 1956, **103**, 834.
83 E. R. Davies, *Phys. Lett.*, 1974, **A47**, 1.
84 W. B. Mims, *Proc. R. Soc.*, 1965, **283**, 452.
85 M. Mehring, P. Höfer and A. Grupp, *Ber. Bunsen-Ges. Phys. Chem.*, 1987, **91**, 1132.
86 S. Deblon, L. Liesum, J. Harmer, H. Schönberg, A. Schweiger and H. Grützmacher, *Chem. Eur. J.*, 2002, **8**, 601.
87 G. Jeschke and A. Schweiger, *Chem. Phys. Lett.*, 1995, **246**, 431.
88 N. Yang, M. Reiher, M. Wang, J. Harmer and E. C. Duin, *J. Am. Chem. Soc.*, 2007, **129**, 11028.
89 K. V. Narasimhulu, R. Carmieli and D. Goldfarb, *J. Am. Chem. Soc.*, 2007, **129**, 5391.
90 L. V. Kulik, B. Epel, W. Lubitz and J. Messinger, *J. Am. Chem. Soc.*, 2007, **129**, 13421.
91 A. M. Raitsimring, A. V. Astashkin, D. Baute, D. Goldfarb, O. G. Poluektov, M. P. Lowe, S. G. Zech and P. Caravan, *Chem. Phys. Chem.*, 2006, **7**, 1590.
92 M. Fittipaldi, G. C. M. Warmerdam, E. C. de Waal, G. W. Canters, D. Cavazzini, G. L. Rossi, M. Huber and E. J. J. Groenen, *Chem. Phys. Chem.*, 2006, **7**, 1286.
93 R. Davydov and B. M Hoffman, *J. Biol. Inorg. Chem.*, 2008, **13**, 357.
94 M. Carepo, D. L. Tierney, C. D. Brondino, T. C. Yang, A. Pamplona, J. Telser, I. Moura, J. J. G. Moura and B. M. Hoffman, *J. Am. Chem. Soc.*, 2002, **124**, 281.
95 S. Weber, C. W. M. Kay, A. Bacher, G. Richter and R. Bittl, *Chem. Phys. Chem.*, 2005, **6**, 291.
96 P. Schosseler, Th. Wacker and A. Schweiger, *Chem. Phys. Lett.*, 1994, **224**, 319.
97 L. Kulik, B. Epel, J. Messinger and W. Lubitz, *Photosynth. Res.*, 2005, **84**, 347.
98 A. Potapov, B. Epel and D. Goldfarb, *J. Chem. Phys.*, 2008, **128**, 052320.
99 S. Stoll, C. Calle, G. Mitrikas and A. Schweiger, *J. Magn. Reson.*, 2005, **177**, 93.
100 B. Kasumaj and S. Stoll, *J. Magn. Reson.*, 2008, **190**, 233.
101 B. M. Hoffman and D. H. Petering, *Proc. Natl. Acad. Sci. USA*, 1970, **67**, 637.
102 H. C. Lee, E. Scheuring, J. Peisach and M. R. Chanc, *J. Am. Chem. Soc.*, 1997, **119**, 12201.
103 J. Hütterman and R. Stabler, in *Electron Magnetic Resonance of Disordered Systems*, ed. N. D. Yordanov, World Scientific, Singapore, 1989, pp. 127–148.
104 F. A. Walker and J. Bowen, *J. Am. Chem. Soc.*, 1985, **107**, 7632.
105 S. Van Doorslaer and A. Schweiger, *J. Phys. Chem. B*, 2000, **104**, 2919.
106 E. A. Brucker, J. S. Olson, G. N. Phillips, Jr, Y. Dou and M. Ikeda-Saito, *J. Biol. Chem.*, 1996, **271**, 25419.
107 S. Van Doorslaer, A. Zingg, A. Schweiger and F. Diederich, *Chem. Phys. Chem.*, 2002, **3**, 659.
108 A. Adamski, T. Spalek and Z. Sojka, *Res. Chem. Intermed.*, 2003, **29**, 793.
109 M. J. Mombourquette and J. A. Weil, *J. Magn. Reson.*, 1992, **99**, 37.
110 G. R. Hanson, K. E. Gates, C. J. Noble, M. Griffin, A. Mitchell and S. Benson, *J. Inorg. Biochem.*, 2004, **98**, 903.
111 C. J. Jacobsen, E. Pedersen, J. Villadsen and H. Weihe, *Inorg. Chem.*, 1993, **32**, 1216.
112 S. Stoll and A. Schweiger, *J. Magn. Reson.*, 2006, **178**, 42.
113 C. P. Keijzers, E. J. Reijerse, P. Stam, M. F. Dumont and M. C. M. Gribnau, *J. Chem. Soc. Faraday Trans. I*, 1987, **83**, 3493.
114 R. Szosenfogel and D. Goldfarb, *Mol. Phys.*, 1998, **95**, 1295.
115 G. C. Hurst, T. A. Henderson and R. W. Kreilick, *J. Am. Chem. Soc.*, 1985, **107**, 7294.
116 *Calculation of NMR and EPR parameters*, eds. M. Kaupp, M. Bühl and V. G. Malkin, Wiley-VCH, Weinheim, 2004.
117 F. Neese and E. I. Solomon, in *Magnetism: molecules to materials IV*, eds. J. S. Miller and M. Drillon, Wiley-VCH, Weinheim, 2003, p. 345.
118 F. Stevens, H. Vrielinck, F. Callens, E. Pauwels and M. Waroquier, *Phys. Rev. B*, 2003, **67**, 104429.
119 G. C. A. M. Vanhaelewyn, E. Pauwels, F. J. Callens, M. Waroquier, E. Sagstuen and P. F. A. E. Matthys, *J. Phys. Chem. A*, 2006, **110**, 2147.
120 F. Neese, *Magn. Reson. Chem.*, 2004, **42**, S187.
121 M. Kaupp, R. Reviakine, O. L. Malkina, A. Arbuznikov, B. Schimmelpfennig and V. G. Malkin, *J. Comput. Chem.*, 2002, **23**, 794.
122 F. Neese, *J. Biol. Inorg. Chem.*, 2006, **11**, 702.
123 J. C. Schoneboom, F. Neese and W. Thiel, *J. Am. Chem. Soc.*, 2005, **127**, 5840.
124 M. van Gastel, C. Fichtner, F. Neese and W. Lubitz, *Biochem. Soc. Trans.*, 2005, **33**, 7.
125 D. Baute, D. Arieli, F. Neese, H. Zimmermann, B. M. Weckhuysen and D. Goldfarb, *J. Am. Chem. Soc.*, 2004, **126**, 11733.

126 M. van Gastel, J. W. A. Coremans, H. Sommerdijk, M. C. van Hemert and E. J. J. Groenen, *J. Am. Chem. Soc.*, 2002, **124**, 2035.

127 M. Ikeda-Saito, H. Hori, L. A. Andersson, R. C. Prince, I. J. Pickering, G. N. George, C. R. Sanders, R. S. Lutz, E. J. McKelvey and R. Mattera, *J. Biol. Chem.*, 1992, **267**, 22843.

128 P. J. M. van Kan, E. van der Horst, E. J. Reijerse, P. J. M. van Bentum and W. R. Hagen, *J. Chem. Soc., Faraday Trans.*, 1998, **94**, 2975.

129 G. Feher, R. A. Isaacson, C. P. Scholes and R. Nagel, *Ann. New. York Acad. Sci.*, 1973, **222**, 86.

130 C. F. Mulk, C. P. Scholes, L. C. Dickinson and A. Lapidot, *J. Am. Chem. Soc.*, 1979, **101**, 1645.

131 C. P. Scholes, A. Lapidot, R. Mascarenhas, T. Inubushi, R. A. Isaacson and G. Feher, *J. Am. Chem. Soc.*, 1982, **104**, 2724.

132 Y.-C. Fann, J.-L. Ong, J. M. Nocek and B. M. Hoffman, *J. Am. Chem. Soc.*, 1995, **117**, 6109.

133 H.-I. Lee, *Bull. Korean Chem. Soc.*, 2002, **23**, 1769.

134 H. Aissaoui, R. Bachmann, A. Schweiger and W. D. Woggon, *Angew. Chemie—Int. Ed.*, 1998, **37**, 2998.

135 A. V. Veselov, J. P. Osborne, R. B. Gennis and C. P. Scholes, *J. Am. Chem. Soc.*, 2000, **122**, 8712.

136 I. García-Rubio, M. Braun, I. Gromov, L. Thony-Meyer and A. Schweiger, *Biophys. J.*, 2007, **92**, 1361.

137 T. Smirnova, R. T. Weber, M. F. Davis and S. Franzen, *J. Am. Chem. Soc.*, 2008, **130**, 2128.

138 F. Trandafir, P. ter Heerdt, M. Fittipaldi, E. Vinck, S. Dewilde, L. Moens and S. Van Doorslaer, *Appl. Magn. Reson.*, 2007, **31**, 553.

139 I. Ioanitescu, S. Van Doorslaer, S. Dewilde, B. Endeward and L. Moens, *Mol. Phys.*, 2007, **105**, 2073.

140 H. Van Camp, C. P. Scholes and C. F. Mulks, *J. Am. Chem. Soc.*, 1977, **99**, 8283.

141 I. García-Rubio, M. Fittipaldi, F. Trandifir and S. Van Doorslaer, *J. Am. Chem. Soc.*, 2008, submitted.

142 F. Mahlert, W. Grabarse, J. Kahnt, R. K. Thauer and E. C. Duin, *J. Biol. Inorg. Chem.*, 2002, **7**, 101; F. Mahlert, C. Bauer, B. Jaun, R. K. Thauer and E. C. Duin, *J. Biol. Inorg. Chem.*, 2002, **7**, 500.

143 J. Telser, Y.-C. Fann, M. W. Renner, J. Fajer, S. Wang, H. Zhang, R. A. Scott and B. M. Hoffman, *J. Am. Chem. Soc.*, 1997, **119**, 733.

144 J. Telser, Y. C. Horng, D. F. Becker, B. M. Hoffman and S. W. Ragsdale, *J. Am. Chem. Soc.*, 2000, **122**, 182.

145 B. Jaun, *Helv. Chim. Acta*, 1990, **73**, 2209.

146 E. C. Duin, L. Signor, R. Piskorski, F. Mahlert, M. D. Clay, M. Groenich, R. K. Thauer and B. Jaun, *J. Biol. Inorg. Chem.*, 2004, **9**, 563.

147 T. Wondimagegn and A. Ghosh, *J. Am. Chem. Soc.*, 2001, **123**, 1543.

148 C. Finazzo, J. Harmer, B. Jaun, E. C. Duin, F. Mahlert, R. K. Thauer, S. Van Doorslaer and A. Schweiger, *J. Biol. Inorg. Chem.*, 2003, **8**, 586.

149 D. I. Kern, M. Groenich, B. Jaun, R. K. Thauer, J. Harmer and D. Hinderberger, *J. Biol. Inorg. Chem.*, 2007, **12**, 1097.

An EPR tool box for exploring the formation and properties of ordered template mesoporous materials

Sharon Ruthstein and Daniella Goldfarb*

The formation of templated mesoporous materials (TMM), where highly ordered mesoporous materials are prepared using surfactant self-assemblies as templates, is an intriguing process. It depends on a delicate interplay between several concomitant basic processes; the self-assembly of the surfactant molecules forming structures that serve as templates, the sol-gel chemistry that generates the inorganic silica network, and the specific interaction at the interface between the organic and forming inorganic phases. In this review we briefly describe the properties of TMM and review some basic principles underlying their formation mechanism. After a short description of the various methods that can be used to investigate the details of such reactions at the molecular level and the mesoscale we focus on the unique contribution of various EPR techniques. This is achieved by introducing nitroxide spin-probes, designed to examine different regions in the forming mesostructure, into the reaction mixture. Continuous wave (CW) EPR measurements, carried out *in situ*, give information on the polarity and microviscosity in the close environment of the spin-probe. These are complemented by electron-spin echo modulation (ESEEM) experiments that follow the water content, presence of additives and interaction with ions and provide an understanding of their effect on the structure of the final material. Finally, double electron-electron resonance (DEER) measurements are used to explore size variation of the micelles during the initial stages of the reaction.

1. Introduction

Porous materials are very useful for many applications, among which are heterogeneous catalysis, energy conversion, adsorption and separations of gases and ion exchange. The discovery that ordered mesoporous materials with a very narrow pore size distribution can be prepared by the hydrolysis and condensation of inorganic precursors in the presence of surfactant assemblies such as micelles, acting as templates, has been a major breakthrough in porous materials synthesis.[1] The first generation of ordered, templated mesoporous materials (TMM) consisted of silica based materials, but later mesoporous materials with other metal oxides, such as titanium, zirconium and vanadium oxides were also synthesized. The formation mechanism of these mesoporous materials is intriguing and depends on a delicate interplay between of several basic processes, the relative rates of which affect the structure and properties of the final structure. These processes are the self-assembly of the organic molecules serving as templates, the sol-gel chemistry that generates the inorganic silica network, and the specific interactions at the interface between the organic and the forming inorganic moieties. These can then further modify the shape

Department of Chemical Physics, Weizmann Institute of Science, Rehovot, Israel, 76100.
E-mail: daniella.goldfarb@weizmann.ac.il; Fax: +972-8-9344123; Tel: +972-8-9342016

of the self-assembled structure of the organic molecules. In this review we present the applications of EPR spectroscopy to explore the properties of templated mesoporous materials, focusing on their formation mechanism at the molecular level *via* the introduction of a variety of spin-probes. The review is organized as follows: in the introductory part, the TMM and the experimental techniques used to characterize them are briefly described. The second part presents models for their formation—along with the common non-EPR methods used in mechanistic studies. The third part describes the EPR tools employed to study the formation mechanism of mesoporous materials. Finally the fourth part discusses insights into formation mechanisms of various mesoporous materials obtained from the EPR studies.

1.1 Templated mesoporous materials

Porous materials are classified according to their pores' size and organization. Microporous materials have pore diameters up to 2 nm whereas in mesoporous materials the diameter is between 2 to 50 nm. Until 1992, mesoporous materials comprised primarily pillared clays and silica gels, where the pores are generally irregularly spaced and broadly distributed in size. In 1992, researchers at Mobil Oil synthesized a new family of organized mesoporous silica, prepared in the presence of organic surfactant and designated as M41S.[1,2] This has opened a whole new field of research in materials science. These materials have a high surface area, a uniform pore size and the pores are easily accessible.[4,5] Most importantly, the pore size can be tuned in the nanometer range by choosing an appropriate surfactant templating system, sometimes with co-solvents or swelling agents.[4,6] In these materials, the ordering stems from the pore organization, while the silica remains amorphous. The organization of nano-channels into ordered nanostructures, the pore size tunability and the large surface area make TMM attractive for a variety of applications such as adsorbent and catalysts[7–10] and they can be further used in nanocasting.[11] Hybrid materials comprising of both organic and inorganic components in the solid matrix have been synthesized as well.[2,12] In this review, we focus on silica based materials.

Silica TMM exhibiting lamellar, 2D hexagonal, 3D hexagonal or cubic organizations, with pore sizes in the range of 1.5–4.0 nm, have been produced with ionic surfactants, such as alkyltrimethylammonium bromide.[1,13,14] Among these are the members of the M41S-family: hexagonal MCM-41, lamellar MCM-50 and cubic MCM-48. The most attention has so far been devoted to MCM-41 because of its straightforward synthesis. In general, the synthesis starts with a dilute aqueous solution of the surfactant; the concentration, however, is above the critical micelle concentration (CMC). Base or acid are then added as catalyst for hydrolysis and condensation of the silica source. Usually TEOS (tetraethoxyorthosilane) or TMOS (tetramethoxyorthosilane), are used but sodium silicate can be employed as well. Above pH = 12 or below pH = 2, the silica hydrolyzes and polymerizes, presumably around the surfactants assemblies, yielding a final ordered mesostructured material. TMM can also be prepared using anionic surfactants as templates, but here a co-directing agent is necessary. Calcination removes the organic template yielding an ordered, mesoporous material. Fig. 1A shows an artistic representation of MCM-41 and MCM-48 after calcination of the surfactant, and Fig. 1B shows TEM (transmission electron microscopy) micrographs of hexagonal and $Ia\bar{3}d$ cubic mesoporous materials.

TMM can also be prepared from non-ionic surfactants, such as polyethylene oxide in neutral media.[16,17] These produce thicker inorganic walls (1.5–4.0 nm) than those prepared with charged surfactants, thus enhancing the TMM hydrothermal stability. In addition, pore diameter tuning is easily attained by varying both type and concentration of the surfactant. The removal of the surfactant by solvent extraction is easy because the H-bonding (instead of electrostatic) interactions between the template and the inorganic framework are easier to dissociate. These materials are, however, not well ordered and are often referred to as worm-like.
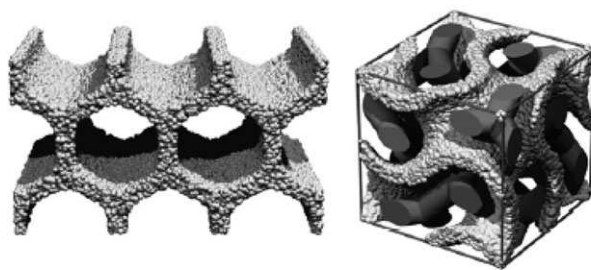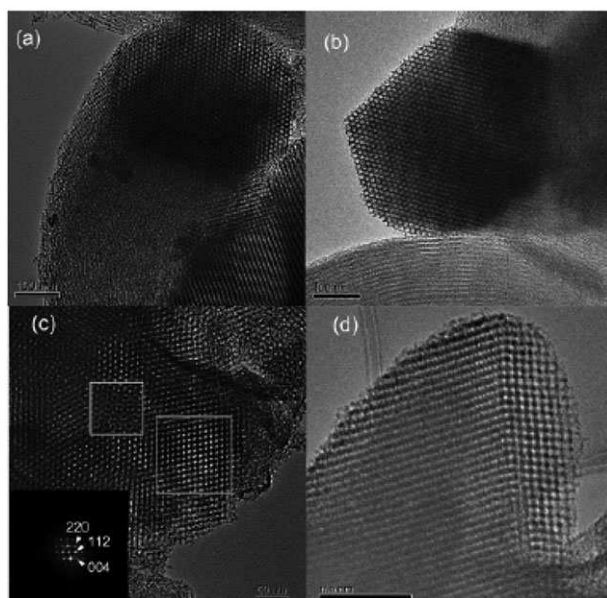
Fig. 1 (A) An artistic representation of MCM-41 and MCM-48 (taken from ref. 2) (B) TEM images of the calcined SBA-materials. (a–b) Hexagonal phase, (c) TEM, and (d) HRTEM of a bi-continuous cubic phase. The area within the large box in (c) is typical of the [110] direction and the corresponding FFT is shown with the assignment of the observe diffractions. The area within the small box of (c) corresponds to an observation along the [111] direction. Reproduced from ref. 3.

A major advance in the field has been the use of amphyphilic non-ionic block copolymers, such as poly(ethylene oxide)-poly(propylene oxide)-poly(ethylene oxide) (Pluronics, $PEO_xPPO_yPEO_x$) as templates.[18] The Pluronics exhibit an atypical temperature dependence; namely at low temperatures the polymer is soluble in water, but the solubility decreases when the temperature is raised, leading to the formation of micelles.[19–21] The micelles comprise a hydrophobic PPO core and a hydrophilic corona of hydrated PEO segments. Block copolymer templates have the advantage that various micellar structures can be tuned by adjusting the solvent composition,

molecular weight or copolymer architecture. Moreover, at low solution concentrations, they enable the organization of structures larger than are possibly obtained with low-molecular weight surfactants.[22] The first promising material that had been synthesized using Pluronic copolymers was the 2D-hexagonal SBA-15, prepared with Pluronic P123 ($PEO_{20}PPO_{70}PEO_{20}$).[23] This material has attracted considerable attention not only because of its structural regularity, thick inorganic walls and excellent thermal and hydrothermal stability, but also because the template is cheap and non-toxic, and the synthesis is simple and reproducible. In addition, one of the interesting properties of SBA-15 is the coexistence of meso- and micropores.[24] The complementary micropores provide connectivities between the ordered mesochannels. The source of the microporosity has been ascribed to PEO chains that are trapped within the silica network during the synthesis, and are removed by calcination, leaving open micropores.[24,25]

Mesoporous materials consisting of interconnected large cage-type pores, (> 5 nm) and organized in a three dimensional network are expected to be superior to hexagonal structures with one-dimensional channels, especially for applications involving selectively tuned diffusion, immobilization of large molecules, or host-guest interactions within nanostructured materials.[26,27] However, mesoporous materials with cubic symmetry, such as SBA-16, are usually more difficult to prepare than the 2D hexagonal counterparts, and often only a narrow range of compositions lead to a cubic phase.[23,26,28] Recent reports indicate that bicontinuous body-cantered cubic mesostructured silica with large pores can be obtained with Pluronics by introduction of additives such as inorganic salts, anionic surfactants with or without a swelling agent like trimethylbenzene (TMB).[29,30] Another synthetic route to high-quality mesoporous $Ia\bar{3}d$ cubic silica prepared with Pluronics is the addition of n-butanol at low acid conditions.[31–33] For more information on mesoporous materials we refer to a number of reviews published recently in a special issue of *Chem. Mater.*[34]

TMM are routinely characterized by Small Angle X-ray (SAX) diffraction, yielding the symmetry of the final material, the d spacings and the lattice parameter. In addition, TEM provides information on the structure, pore/channel configuration and estimates of pore sizes and wall thickness. Adsorption of molecules such as N_2, O_2 and Ar has been widely used to determine the surface area, pore size distribution and the degree of the microporosity.

2. The formation mechanism of TMM

2.1 General principles

The driving force for the interaction between the organic self-assembled aggregates and the inorganic precursors in the case of charged surfactants is electrostatic and several schemes have been suggested.[35] These include direct interaction of the cationic surfactants (S^+) with anionic inorganic species (I^-) to produce ion pairs (S^+I). Similarly anionic templates (S^-) and cationic inorganic species (I^+) will interact through an S^-I^+ ion pair. Two more schemes involve counter ions (X^- or M^+) that act as mediators in interactions of the type $S^+X^-I^+$ (where $X^- = Cl^-$ or Br^-) or $S^-M^+I^-$ (where $M^+ = Na^+$ or K^+). The assembly of mesoporous materials can also be driven by hydrogen bonds relevant for neutral templates such as non-ionic polyethylene oxide (PEO) surfactants ($S°$) and inorganic precursors ($I°$).[16,17] Another suggested mode of interaction is ($S°H^+$)(X^-I^+), as ascribed to TMM formed using block copolymers.[23] Here, TMOS or TEOS are hydrolyzed at low pH (using HCl) to form positively charged $Si(OMe)_{4-n}(OH_2^+)_n$ species and the EO moieties of the block copolymer in strong acid media are associated with hydronium ions. Then, the charged EO units and the cationic silica species are assembled together, *via* Cl^-, by a combination of electrostatic, hydrogen bonding and Van der Waals interactions.

To account for the structure of the different phases formed, the surfactant packing parameter, g, where $g = \upsilon/a_0 l$, has been used to describe the surfactant organization in the self-assembly arrays and to predict the resulting mesostructures. υ is the chain volume of the surfactant, a_0 is the effective hydrophobic/hydrophilic interfacial area, and l is the kinetic surfactant chain length.[36,37] The packing parameter is influenced by the charge matching between the surfactant headgroup and the silica oligomers, and the organic chain packing. The charge-matching is mainly controlled by the pH, co-surfactant concentration and counter-ions. The organic chain packing is influenced by temperature and organic additives. The larger is g, the lower is the aggregate curvature. In the case of charged surfactants, g can be controlled by changing a_0 through charge matching between the surfactant headgroup and the forming charged silica oligomers.[38] For non-ionic surfactants, like Pluronics, a_0 can be controlled by the hydration of the PEO groups, which comprise the corona and serve as an effective head group.[39] Table 1 lists the g-values ranges for various mesophases.[40]

Studies focusing on the formation mechanism of TMM have been summarized in a number of reviews.[41–44] The "liquid-crystal templating" (LCT) mechanism was formulated soon after the discovery of MCM-41 in 1992.[13] It comprises two main pathways, where either (i) a liquid-crystal phase is preformed and the silicate condenses within it, or (ii) the addition of the silicate anions promotes the long range ordering of the surfactant to form the hexagonal arrangement. In dilute systems, where the surfactant concentration is low, such that liquid crystalline phases are not preformed, it is generally accepted that the formation of TMM occurs in two steps. The initial stage involves one of the following processes: (a) preferable adsorption of charged oligomeric silica ions at the micellar interface, driven either by charge matching or hydrogen bonding,[17,45] or (b) the silicate oligomers do not adsorb at the micellar interface, but instead form siliceous prepolymers that bind surfactants molecules in a cooperative manner, and result in the formation of a new silica-surfactant hybrid micellar aggregates.[46] Most of the experimental results are, however, consistent with (a) rather than (b).[47–50] The next step also involves two possibilities: silicate adsorption and polymerization changes the original micellar curvature and shape, mainly lengthening the micelles, followed by condensation of the silicate-covered micelles into an ordered phase. This has been termed the cooperative self-assembly (CSA) mechanism. Another possibility is the formation of disordered collapsed phases that then rearrange into an ordered phase. Alternatively, silicate adsorption may not change the morphology of the micelles, but rather reduce the inter-micellar repulsion and cause aggregation into larger particles and precipitation of a disordered phase, which then may rearrange to form an ordered phase.[51,52] In the next sections we briefly list the methods used for mechanistic investigations and describe several, out of many non-EPR, mechanistic studies that contributed to the above understanding of the formation mechanism.

2.2 Methods for mechanistic studies

The formation of TMM involves three length scales: (i) the molecular one, which includes the interaction between the organic and inorganic precursors and the silica

Table 1 Surfactant packing parameter, g, and its correspondent phase and mesoporous material

g	Phase	Si-mesoprous material
<1/3	Micellar cubic (Pm3n)	SBA-1
1/3–1/2	Hexagonal (P6m)	MCM-41, SBA-15, SBA-3
1/2–2/3	Bicontinuous cubic ($Ia\bar{3}d$)	MCM-48, KIT-6
1	Lamellar	MCM-50

source hydrolysis and polymerization process, (ii) the mesoscopic scale, which corresponds to the development of the micellar structures and the onset of the long-range order, and (iii) the macro-scale, which is related to the shape/morphology of the final product. The molecular level is best probed by spectroscopy such as EPR, NMR, IR, Raman and fluorescence techniques, while SAXS/XRD (small angle X-ray scattering/X-ray diffraction) and cryogenic TEM targets specifically the mesoscale. Scanning electron microscopy (SEM) gives the morphology of the final material. Below, we briefly present the pros and cons of these methods in terms of *in situ* studies.

• Liquid state ^1H NMR can give information on the mobility of the surfactant chains, and can be acquired *in situ*. NMR of quadrupolar nuclei like ^2H and ^{14}N can be used to explore ordering and detect the presence of mesophases and their transformation.[52,53] ^{29}Si NMR can be used to follow hydrolysis and condensation of the silica precursors and the formation of silica networks in solution.[44] However, ^{29}Si NMR has a considerably low time-resolution due to the low-abundance and long relaxation times of the ^{29}Si nucleus, that require long accumulation times. The option of enrichment is always possible but very expensive.

• IR spectroscopy could be a perfect technique for time-resolved *in situ* experiments owing to its fast response time. Unfortunately, the strong adsorption of radiation by water in several regions of far and mid IR requires the use of sensitive attenuated sampling devices, which are not compatible with true *in situ* measurements. Nevertheless, ATR-FTIR (Attenuated Total Reflection-Fourier Transfrom IR) is effective to provide qualitative data regarding the species present during hydrolysis and condensation of silica under water rich conditions.[54]

• Raman spectroscopy can be used to follow the hydrolysis of the inorganic precursors through the signal of the produced ethanol. However, here no fluorescing and limpid solutions are prerequisite.[55]

• Fluorescence spectroscopy can be used to observe ion exchange at the micellar/silica palisade to better understand organic/inorganic interactions. Here the time-scale for signal detection is very fast, but the major drawback of the technique is that solution must be kept transparent at all times.[46,56]

• Continuous wave (CW) EPR is used to obtain information about the silica/micelle interactions. It is a truly time-resolved technique, since measurements can be conducted *in situ*. More sophisticated pulse EPR experiments (see below), however, require low temperatures and the time course is probed *via* freeze-quench at different reaction times, with a resolution of a few seconds. Moreover, EPR techniques require the addition of spin-probes and the information obtained is on the probe, that in-turn reflects the behaviour of its environment.

• Cryogenic-TEM offers an excellent way to observe micelles, their shape evolution as well as their arrangement into macrostructures at different moments of the material synthesis. It is applicable up to the precipitation time where the samples become too thick. Then, TEM of freeze fracture replicas (FFR) can be used.[57] The use of normal TEM is problematic because the specimen preparation requires drying the reaction mixture, which is likely to affect the microstructures.

• Dynamic light scattering (DLS) can also be used to evaluate the sizes of micelles and particles present in solution, but transparent and clear solutions are necessary. In order to keep the solution clear under hydrolysis, large quantities of salt and ions are added to the synthesis mixture. In addition, the shape of the particles is usually assumed to be spherical in the analysis.[58,59]

• SAXS/XRD are excellent techniques to study long-range order, and they can also give information on short range order and shapes of solution structures. Short acquisition times and adaptable experimental setup made it the most frequently applied technique in time-resolved and even temperature-resolved *in situ* experiments.[40] Nevertheless, acquisition times obtained with low energetic X-ray sources are not compatible with time-resolved requirements. Hence, experiments must be

performed in the presence of a high energetic X-ray source, like synchrotron radiation; this makes this type of experiment quite expensive and difficult to access. Nonetheless, films of mesoporous materials can be studied by *in situ* XRD. This method is called grazing incidence XRD (GIXD). It is a powerful method for the study of the in-plane structure of mesoporous films at the air/water interface.[60,61]

2.3 The formation of TMM with ionic templates

So far the most studied TMM has been MCM-41, where the initial condition of the reaction mixture is a dilute micellar solution. Evidence for pathway (ii) of the initial LCT model for MCM-41 was obtained from ^{2}H and ^{29}Si NMR spectroscopy, as well as neutron scattering. This revealed the transformation of a micellar solution of cetyltrimethyl ammonium bromide (CTAB) into a hexagonal lyotropic phase in the presence of silicate anions, as shown in Fig. 2, thus formulating the CSA mechanism.[47] This transformation becomes irreversible through the polycondensation of the silica. *In situ* XRD measurements, using a synchrotron beam, revealed two stages in the formation of MCM-41: the long range order is achieved within 3 min and from then on only silica condensation takes place.[62] The formation of MCM-41 under acidic conditions, at the air-water interface, was examined by grazing incident synchrotron radiation diffraction showing a similar two step mechanism.[60,61] Cryogenic-TEM measurements on a reaction mixture of MCM-41 at a single time point snapshot revealed the formation of elongated micelles and vesicles during the synthesis of MCM-41 in the presence of decanoate.[63] *In situ* IR measurements[54] carried out at high temperatures showed that the ordering of the surfactant molecules increases during the reaction.

The formation of hexagonal SBA-3, prepared with ionic surfactant, such as CTAB in high acidic condition (pH < 2), was explored by DLS.[58] The initial hydrochloric solution of CTAB was found at room temperature to consist of spheroidal micelles, but in the presence of sodium or potassium chloride, worm-like micelles are also present. The addition of TEOS, which is adsorbed and hydrolyzed into siliceous
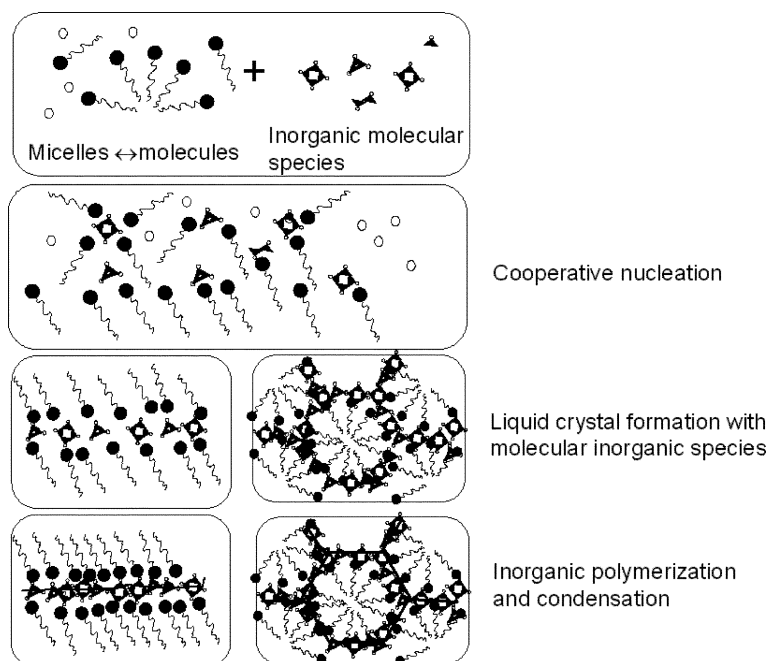

Fig. 2 The Cooperative self-assembly mechanism. Reproduced from ref. 35.

species in the palisade layer of the micelles, favours the formation of the worm-like micelles. The increase of the temperature and of the acid concentration leads to shorter worm-like micelles and at the same time accelerates the polycondensation of the silica. When the inter-micellar repulsion charges vanish, the colloidal system becomes unstable and the micelles aggregate (phase separation). The formation of SBA-3 was also explored by *in situ* Raman, that provides information on the kinetics of the TEOS hydrolysis and by *in situ* XRD.[55]

2.4 The formation of TMM with non-ionic templates

The CSA mechanism has also been proposed for the synthesis of TMM with non-ionic surfactants in neutral media.[59] Here the synthesis was carried out in two steps. TEOS is first hydrolyzed in a micellar solution of $CH_3(CH_2)_{14}(OCH_2CH_2)_{12}OH$ (Tergitol T15S12) at pH = 2 where the polycondensation rate is very low. Then, the addition of fluoride anions (NaF), catalyses the polycondensation and the mesoporous material is formed. The clear solution present during the first step was characterized by liquid state ^{29}Si NMR, SAXS and DLS. The initial diameter of the micelles was found to increase with increasing Si/Surfactant indicating the presence of hybrid micelles. Oligomeric silica species were formed inside the palisade layer between the PEO chains when the Si/Surfactant ratio is less than 4. As the ratio increases above 4, these weakly reticulated oligomers extend out of the palisade layer leading to an increase in size.

Most of the mechanistic studies reported so far have focused on one length scale, and only a few attempts to correlate different length scales using different techniques have been reported. One example is the application of *in situ* ^1H NMR, SAXS and TEM in the formation of SBA-15.[51,52] These lead to a model where the adsorption and polymerization of silica precursors occur within the corona of the micelle, reducing the interaction between micelles, and thereby producing flocs of a number of spheroidal micelles. These flocs then further associate, increasing the particle size and leading to precipitation. Micelle-micelle coalescence then takes place within the flocs to form the cylindrical micelles and hexagonal order. In another study, however, it has been shown through cryo-TEM that the spheroidal micelles transform into thread-like micelles before precipitation.[57]

3. The EPR tool box

3.1 Spin-probes

The use of nitroxide spin-probes to study dynamical and structural properties of a system of interest, first introduced by McConnell in 1965,[64] is by now well established. The basic idea is to label the molecule of interest with a small stable free radical, or introduce a spin-probe, and then from its spectroscopic properties derive information about its close environment, which can be micelles, membranes, proteins, polymers, solid surfaces and many others.[65,66] The most commonly used stable free radicals are nitroxides. The advantages of using spin-probes in the context of TMM are:

• The sensitivity of the nitroxide spectrum to its local environment. Accordingly, in heterogeneous systems, such as encountered in TMM, carefully chosen spin-probes can explore different regions.

• A large range of molecular motion (10^{-5}–10^{-10} sec) can be obtained.

• The absence of interferring signals from the diamagnetic environment.

• High sensitivity that allows adding only a small amount of the spin-probe, thereby not disturbing the reaction pathway. Moreover, spectra can be acquired within a few seconds.

A disadvantage is that the information derived from the spectra is directly related to the spin-probe and not to the native components the system of interest, although the two are closely correlated. Therefore, the location of the spin-label has to be
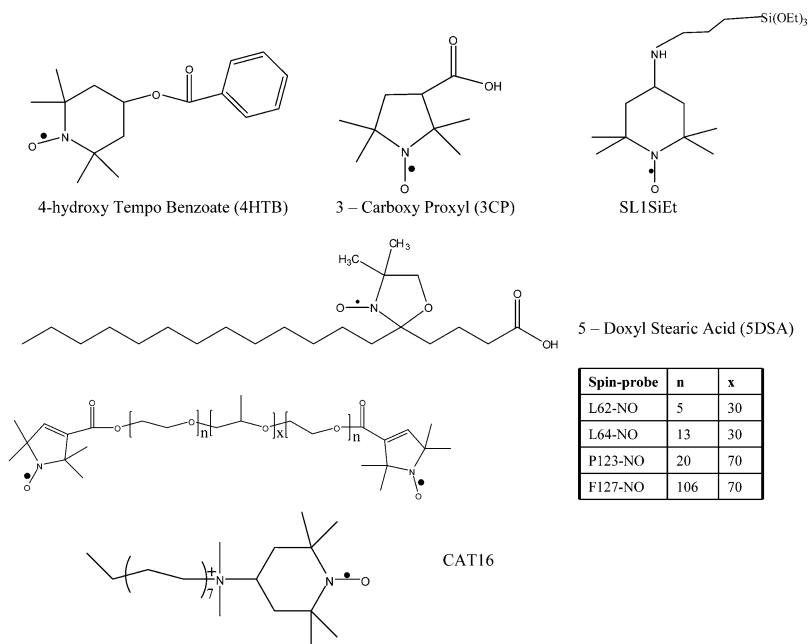
Fig. 3 The structure of various spin-probes used in the study of the formation mechanism of TMM.

Spin-probe	n	x
L62-NO	5	30
L64-NO	13	30
P123-NO	20	70
F127-NO	106	70

determined and it should be verified that it does not have any specific interactions with any of the components of the system. Another drawback is that the spin-probe may assume more than one location and the analysis of the spectrum may require spectral simulation to deconvolute their contributions. A careful choice of the spin-probe may avoid this complication.

Fig. 3 shows several types of spin-probes that are useful in the study of TMM. The charged spin-probes, 5DSA and CAT16, are most useful to probe the behaviour of charged surfactants. While CAT16 probes mainly the polar head region, 5DSA senses the region close to the alkyl chain part. It is also possible to use the CAT probe with different alkyl chain length and nDSA probes with the label at the nth position deeper into the alkyl chain.[67–70] 4HTB is a hydrophobic spin-probe and will therefore probe the hydrophobic core of the micelle. The silane based spin-label SL1SiEt can co-polymerize with the silica source, thereby probing the forming silica. Finally, the spin-labelled Pluronics are most suitable to probe the corona region of Pluronic micelles. Probes with different PEO lengths will be located at different regions within the corona. Those with long PEO's will probe the corona–water interface, whereas shorter ones will sense also the core/corona interface.

3.2 The EPR experiments

3.2.1 CW-EPR. The most simple and standard EPR technique is continuous wave (CW) EPR, used to record the EPR spectrum. It can be applied at different operational frequencies, thereby accessing different dynamic ranges and exhibiting different resolutions. The standard spectrometers operate at X-band, ~ 9.5 GHz. The parameters of interest are the line shape and the line-width that measure the motional characteristics, the ^{14}N hyperfine coupling and the g-values, which depend on the nature of the probe molecule and its environment.[66] Hence, the EPR spectrum can be used to characterize the hydration and the effect of additives in micelles.[71–74]

In the context of the properties of the initial surfactant solution and the formation of TMM, the CW-EPR spectrum gives the following information:

(a) The polarity of the environment of the spin-probe. The ^{14}N isotropic hyperfine coupling, a_{iso}, is proportional to the spin-density on the nitrogen of the nitroxide group. When the solvent polarity is high, the spin-density on the nitrogen is also high, causing a larger a_{iso} value. However, when the polarity of the solvent is low, the hydrogen bonds with the nitroxide are weaker, leading to a smaller spin density on the nitrogen, and thus, smaller a_{iso}[75,76] (see insert in Fig. 4b). Therefore, a_{iso} is a useful measure for the effect of the surrounding environment, such as the formation of micelles. Fig. 4a presents the temperature dependence of the EPR spectrum of L62-NO in a 2.5% wt. P123 aqueous solution, revealing a sharp change in a_{iso} upon the formation of micelles. The spectrum recorded at 25 °C comprises a sharp triplet, characteristic of fast motion, with a_{iso} = 17.3 G, attributed to L62-NO dissolved in water. The 30 °C spectrum exhibits a splitting in the high field hyperfine components, indicating a superposition of two spectra; one with a_{iso} similar to that observed at 25 °C and the other with a_{iso} = 16.3 G, from L62-NO in the micelles. The temperature dependence of a_{iso} is presented in Fig. 4b. Upon further increase in the temperature, a_{iso} exhibits a mild reduction due to the dehydration of the PEO segments with increasing temperature.[25]

(b) The degree of mobility of the spin-probe reflecting the local viscosity. When the movement of the nitroxide spin-label is restricted with a correlation time $\tau_c < 10^{-6}$ sec, it exhibits a powder line-shape, characteristic of a rigid limit spectrum, as shown in the bottom trace of Fig. 4a. It is characterized by a non-averaged $2A_{zz}$ (^{14}N) = 67 G.

The slow tumbling regime corresponds to a range of rotational reorientation times for which the EPR spectrum can no longer be described as a simple superposition of Lorentzian lines, yet the motion is not slow enough as to yield a proper rigid-limit spectrum.[77] For nitroxides at X-band frequencies, this corresponds to range of 10^{-9} sec $\leq \tau_C \leq 10^{-6}$ sec. The analysis of slow-motion spectra is complicated by the fact that the relationship between the spectrum and the rotational correlation times, which are often anisotropic, is indirect. The partial averaging of EPR spectra by molecular motion or spin dynamics can produce complicated line shapes requiring detailed spectral simulation to extract the desired information. The general derivation of the slow tumbling theory has been described by Freed *et al.*[66] The software required for spectral analysis of slow motion spectra is available[65,78] and used in spectral simulations routinely.
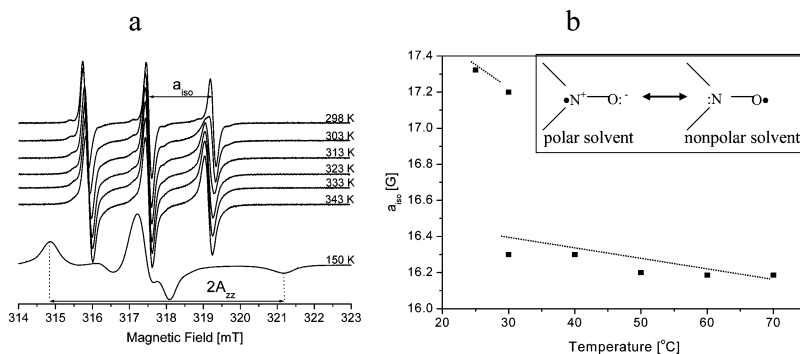
Fig. 4 (a) The CW-EPR spectra of L62-NO in a 2.5% wt. P123 micellar solution at various temperatures (reproduced from ref. 5). (b) The corresponding dependence of a_{iso} on temperature. The insert shows a representation of the change in spin-density on the nitroxide owing to a change in the polarity of the environment.

At the fast tumbling regime the situation is considerably simpler. Here, the spectrum consists of three resolved lines and the isotropic rotational correlation time, τ_c, (in sec) can be calculated according to:[75]

$$\tau_c = (6.51 \times 10^{-10})\Delta H(0)\{h(0)/h(-1)^{\frac{1}{2}} + [h(0)/h(1)]^{\frac{1}{2}} - 2\} \tag{1}$$

where $\Delta H(0)$ is the peak-to-peak line-width (in Gauss) of the $M_I = 0$ component, and $h(-1)$, $h(0)$, and $h(1)$ are the peak-to-peak heights of the $M_I = -1$, 0, and $+1$ lines, respectively.

In the *in situ* CW-EPR measurements, the synthesis is carried out in a very small volume of a quartz flat cell and therefore it is essential to verify that the synthesis can be scaled down and that the final material indeed forms under these conditions. Our experience shows that this is not always the case.

3.2.2 ESEEM. Electron-spin echo envelope modulation (ESEEM) experiments are highly effective for measuring weak superhyperfine interactions of an electron spin with nearby nuclear spins.[79,80] In these experiments, a series of microwave (MW) pulses generates an echo, and the echo decay is followed as a function of one of the time intervals between the pulses. Fig. 5a shows the three-pulse ESEEM sequence. The echo intensity, $V(\tau,T)$, in the three-pulse ESEEM experiment depends on two factors, one determined by the nuclear modulation effect and the other by the echo decay, according to[81]

$$V(\tau,T) = V_{mod}(\tau,T)V_{relax}(\tau,T). \tag{2}$$

$V_{relax}(\tau,T)$ is usually governed by the relaxation times, T_2 and T_1, and spectral and instantaneous diffusion, due to electron spin-spin interactions.[82] It can often be described by an exponential function $V_{relax}(\tau,T) = V_0 e^{(-T/Td)}$, where the τ dependence is ignored as it is a constant in three-pulse ESEEM experiments. $V_{mod}(\tau,T)$ depends on the anisotropic hyperfine interaction between the electron spin and nuclei nearby. The echo intensity for the simplest case of an electron spin $S = 1/2$ interacting with a nucleus with $I = 1/2$ is:

$$V_{mod}(T,\tau) = 0.5[V_\alpha(T,\tau) + V_\beta(T,\tau)] = 0.5\{1 - k/2[1 - \cos(\omega_\beta\tau)] \\ \times[1 - \cos(\omega_\alpha(T + \tau)]\} + 0.5\{1 - k/2[1 - \cos(\omega_\alpha\tau)][1 - \cos(\omega_\beta(T + \tau)]\} \tag{3}$$

where k represent the modulation depth and is given by

$$k = \left(\frac{B\omega_I}{\omega_\alpha\omega_\beta}\right)^2$$
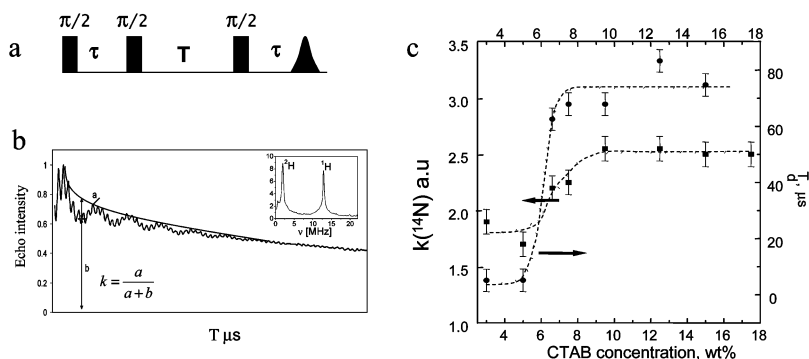
Fig. 5 (a) The three-pulse ESEEM sequence. (b) A three pulse ESEEM trace of L62-NO in D_2O and the definition of $k(^2H)$. The insert is the corresponding FT. (c) Plots of $k(^{14}N)$ (filled squares) and T_d (filled circles) as a function of the [CTAB]. $k(^{14}N)$ was determined from the intensity of the ^{14}N peak in the FT-ESEEM spectrum. Reproduced from ref. 84.

and ω_α and ω_β are the nuclear frequencies, also referred to as ENDOR frequencies:

$$\omega_{\alpha,\beta} = [(\omega_I \mp A)^2 + 0.25B^2]^{0.5} \qquad (4)$$

$\omega_I = g_n\beta_n B_0/\hbar$ is the nucleus Larmor frequency and B_0 is the external magnetic field. For an axially symmetric hyperfine interaction

$$A = a_{iso} + T_\perp (3\cos^2\theta - 1) \text{ and } B = T_\perp (3\cos\theta\sin\theta). \qquad (5)$$

When the distance, r, between the unpaired electron and the nucleus is larger than 2.5 Å and the spin delocalization over the ligand is negligible, $T_\perp$ can be described by the point-dipole approximation according to:

$$T_\perp = \frac{\mu_0}{4\pi\hbar}\frac{g\beta g_n\beta_n}{r^3}. \qquad (6)$$

θ is the angle between the magnetic field direction and the vector connecting the electron-nucleus loci and all the other parameters have their usual meaning. When the hyperfine interaction is very weak $\omega_\alpha \sim \omega_\beta \sim \omega_I$, the modulation frequency is practically the nuclear Larmor frequency. In this case

$$k = \frac{9}{4}\left(\frac{\mu_0}{\pi\hbar}\right)^2\left(\frac{g\beta}{B_0}\right)^2\frac{\sin^2 2\theta}{r^6} \qquad (7)$$

When N nuclei are coupled to the electron spin, $V_{mod}(\tau,T)$ becomes:[83]

$$V_{mod}(\tau, T) = \prod_{i=1}^{N} V^\alpha_{mod,i}(\tau, T) + \prod_{i=1}^{N} V^\beta_{mod,i}(\tau, T) \qquad (8)$$

For a $I > 1/2$ nucleus, such as ^2H, in an orientationally disorder system, such as frozen solutions of a nitroxide spin-probe, k become (after the angular integration):[83]

$$k = \frac{8}{5}I(I+1)\left(\frac{\mu_0}{\pi\hbar}\right)^2\left(\frac{g\beta}{B_0}\right)^2\frac{1}{r^6} \qquad (9)$$

In the derivation of eqn (9) the nuclear quadrupole interaction and the g-anisotropy were neglected. The expressions for $V^{\alpha,\beta}_{mod}(\tau,T)$ is different than that given in eqn (3) but eqn (8) is general and still applicable. Eqns (3), (8) and (9) show that the total modulation depth is a function of the electron-nuclear distance, the number of nuclei, and their nuclear spin.

In the specific application of ESEEM to micellar solutions and reaction mixtures of TMM, the interactions between the spin-probe and nuclei of ions, surfactant molecules or solvent molecules exhibit a distribution of distances and orientations. Therefore, a quantitative analysis of the ESEEM traces to extract these distributions is complicated and time consuming, yet not essential for obtaining qualitative information. The latter can be obtained by considering an average empirical modulation depth parameter, k(X), where X denotes the nucleus involved, as defined in Fig. 5b. Based on eqns (3), (8) and (9) it is clear that a higher value of k(X) indicates a larger density of X in the vicinity of the free radical. As will be shown later, comparison of the k(X) values of spin-probes located at different regions of the system, or comparisons of systems with the same spin-probe and different compositions, or examination of the time dependence of k(X), can provide new insights on the behaviour of the system can be derived under investigation.

Fig. 5b shows the three-pulse ESEEM trace of a L62-NO in D_2O,[84–86] which exhibits ^2H and ^1H modulation. The low frequency modulation corresponds to ^2H, for which $\omega_I/2\pi = 2$ MHz. The corresponding Fourier transform (FT) is shown as well and the peak intensity is proportional to k(X). Kevan and co-workers have extensively applied ESEEM methods to study photoionization and charge separation in micelles and vesicles and the same approach can be applied to TMM.[79,80,87–89]. A

major problem of the application of ESEEM is that it is carried out at low temperatures (< 77 K). This is not a problem for solid samples, but when applied to micellar solutions it raises the question whether the micllear structures are preserved upon rapid freezing. Although it has been shown earlier that it does,[79,80] the following example confirms this and demonstrates the type of information that can be obtained from ESEEM.

ESEEM measurements were carried out on frozen solutions of 5DSA in a series of CTAB solutions, with [CTAB] in the range of 3–17.5 wt% and constant [5DSA]. ^{14}N modulation was observed at 1 MHz, corresponding to the ^{14}N Larmor frequency. This modulation was attributed to hyperfine interaction with the ^{14}N in the polar head of CTAB. The explicit dependence of k(^{14}N), as determined from the intensity of the ^{14}N peak in the FT-ESEEM spectra, and of the T_d values, obtained from the exponential background decay, on [CTAB] are shown in Fig. 5c.[84] We observe that k(^{14}N) and T_d are approximately constant up to 6 wt% CTAB, then they increase and level off at 9.5% CTAB. The transition observed corresponds to the spherical to cylindrical micelles transformation that was detected previously by NMR, microscopy, rheology, and scattering techniques.[90–92] Thus, these ESEEM results confirm the preservation of the micellar structures upon rapid freezing.

Fig. 5c shows that k(^{14}N)$_{spherical}$ < k(^{14}N)$_{cylinder}$. This is consistent with the expected changes in the critical packing parameter where for micelles $g_{spherical}$ < $g_{cylinder}$.[93] The increase in k(^{14}N) was attributed to a decrease in the average distance between neighbouring molecules at the interface due to a decrease in the curvature owing to a decrease in a_o.

The spherical to cylindrical micelles transition also results in an increase of T_d, indicating that the spectral diffusion decreases with increasing [CTAB].[82] Because 5DSA is water insoluble and its concentration is constant in all samples, at low [CTAB] concentrations the number of 5DSA molecules in a single micelle is finite and the local concentration is high and so is the spectral diffusion. As [CTAB] increases, the number of micelles increases too, followed by an increase in their size due to the transition to cylindrical micelles. This causes a redistribution of the 5DSA molecules, increasing their average distance, and reducing the spectral diffusion contribution to the echo decay.

The dependence of k(^{14}N) of 5DSA on the structure of the final products was also investigated. k(^{14}N) of CAT-16 in MCM-41, MCM-50 and MCM-48 showed the following trend: MCM-50 > MCM-48 > MCM-41, consistent with g(lamellar) > g(cubic) > g(hexagonal) in mesophases.[93] This shows that the ESEEM results reflect the aggregation behavior of the surfactant molecules in different mesostructures and solution structures.

ESEEM can be used to determine the location of the spin-probe within the micelle and explore changes in the composition of its local environment. For example changes in water content can be followed by making the TMM in D_2O, rather than in H_2O, the location of additives, such as butanol, can be probed through deuterated butanol[94] and the effects of anions can be explored using $^{15}NO_3^-$ or $H^{31}PO_4^{-2}$.[3]

3.2.3 DEER. Pulse double electron-electron resonance (DEER) is one of the few methods that can measure distances in the range 1.5–8 nm in disordered systems.[95–98] While CW EPR is well suited for the determination of distances between 1–2 nm, larger distances have to be measured by modern pulse techniques that separate the dipole-dipole interaction between the electron spins from all other interactions.[99] The most popular experiments are the three-pulse[97,100] and the four-pulse DEER sequence[95] shown in Fig. 6a. Similar to the ESEEM experiments, the DEER measurements are carried out at low temperatures. Since DEER can be used to determine distribution of spins and their average distance,[97,101] it can also be
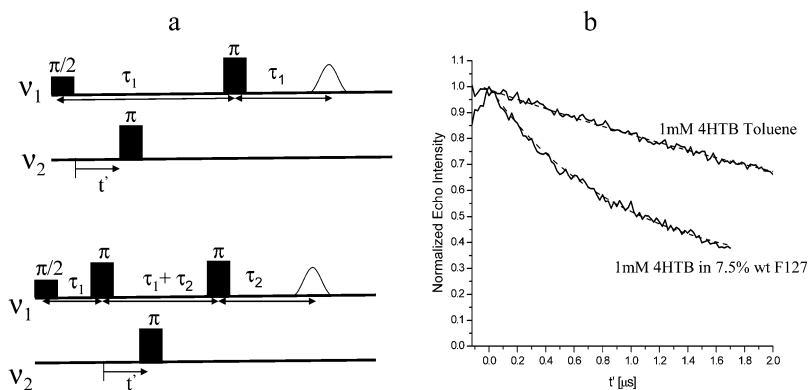
Fig. 6 (a) The three-pulse and four-pulse DEER sequences. (b) The DEER decay of 1 mM 4HTB in toluene and in 7.5% wt. F127. The dashed lines are a first order exponential decay fit for 4HTB in toluene, and a best fit decay for 7.5% wt. F127. Reproduced from ref. 108.

employed to follow the time evolution of the spin distribution during the formation of TMM. This can be further interpreted in terms of changes in micelles size.

In spin echo based DEER experiments, the evolution of the spin echo signal for a single pair (i,k) of spins with a finite dipolar interaction is:[102]

$$V(t) = V_0[1 - \lambda_k(1 - \cos(\omega_{ik}t))] \qquad (10)$$

t is the appropriate variable time interval, which depends on the chosen sequence (see Fig. 6a), and λ_k is the probability to flip one of the two spins by the appropriate pulse and ω_{ik} is:

$$\omega_{ik} = \omega_{dd}^{(ik)}(3\cos^2\theta_{ik} - 1) \qquad (11)$$

The so called dipolar evolution frequency, $\omega_{dd}^{(ik)}$, is:

$$\omega_{dd}^{(ik)} = \frac{\mu_0}{4\pi\hbar}\frac{g_i g_k \mu_B^2}{r_{ik}^3}. \qquad (12)$$

Spin i is the observer spin (A spin) and spin k is the pumped spin (B spin), g_i and g_k are the electron g-values of the two spins and θ_{ik} is the angle between $\vec{B}_0$, and the vector $\vec{r}_{ik}$ connecting the loci of the two spins. Henceforth we assume $g_i = g_k = g$ for all i, k. In a multispin system (many B spins), the echo intensity due to any A spin is given by:

$$V(t) = V_0 \prod_{i \neq k}^{N-1} [1 - \lambda_k(1 - \cos(\omega_{ik}t))] \qquad (13)$$

and the total echo is the sum of the contributions from all A spins. This yields for N interacting spins:

$$V(t) = V_0 \left\langle \prod_{i \neq k}^{N-1} [1 - \lambda_k(1 - \cos(\omega_{ik}t))] \right\rangle \qquad (14)$$

where $<>$ denotes the relevant averaging.

For an isotropic disordered system with a homogeneous distribution of spins, such as a frozen solution, the dipolar time evolution exhibits a mono-exponential decay, which depends on the spin concentration, C, according to:[103,104]

$$V(t) = V_0 \exp(-t/T_{\text{hom}}) \qquad (15)$$

In a system which consists of aggregates, where the average inter aggregate distance is larger than the average distance within the aggregate, the DEER decay is often presented as the following product:[98,101,105–107]

$$V(t) = V_{intra}(t)V_{inter}(t) \qquad (16)$$

where $V_{intra}(t)$ represents the decay due to spins in the same aggregate, and $V_{inter}(t)$ corresponds to the interaction with spins in different aggregates. $V_{inter}(t)$ is usually approximated as a first order exponential decay, where T_{hom} is given by eqn (15), and C, is equal to the total spin concentration in the system.

For spin-probes dissolved in a micellar solution with an average number of spins per micelle given by M_{av}, $V_{intra}(t)$ is:

$$V_{intra}(t) = \sum_{M=1}^{\infty} P(M, M_{av}) \left\langle \prod_{i \neq k}^{M-1} (1 - \lambda_k(1 - \cos \omega_{ik}t)) \right\rangle \qquad (17)$$

Here the averaging is over all possible pair distances, r_{ik}, within the micelle and all possible orientations of r_{ik} with respect to the magnetic field. $P(M,M_{av})$ is the Poisson probability distribution for a given number of spins, M. Eqn (17) can be solved once the distance distribution function of spins is known (or assumed) and then summing over all the spins distances.

The top trace in Fig. 6b shows the four-pulse DEER trace of 1 mM 4HTB in toluene, and the corresponding dotted line represents the best fit to a single exponential decay from which T_{hom} = 5 μs was determined. Fig. 6b also shows the DEER experiment for 1 mM 4HTB in a 7.5% wt. F127 aqueous solution. The decay of the F127 solution is faster than that of the toluene solution due to the confined volume offered by the micelles. Recently, DEER has been used to evaluate the core size of P123 and L64 micelles, employing 4HTB as a probe.[108]

4. EPR investigation of the formation of TMM

4.1 The location of the nitroxide label in micelles

Because the spin-probe senses its close environment, it is essential to determine its location within the initial micellar structure. This can be acheived by a combination of CW-EPR and ESEEM using the parameters: a_{iso}, τ_c and $k(^2H)$ of micelles prepared in D_2O.[23,25] This is demonstrated next on 2.5% wt. P123 micellar solutions with different spin-probes. For the ESEEM measurements, solutions kept at 50 °C (above the CMT) were rapidly quenched by insertion into iso-pentane cooled in liquid nitrogen. Fig. 7a presents $k(^2H)$ and a_{iso} of a 1 mM L62-NO in D_2O compared with 1 mM L62-NO, P123-NO, F127-NO, 3CP, 5DSA and 4HTB in 2.5%wt. P123 in D_2O. The concentration of P123 is the same as that used in the synthesis of SBA-15. The largest $k(^2H)$ and a_{iso} values are observed for L62-NO in D_2O because in this system there are no micelles and the spin-label is surrounded by water molecules. In micelles, $k(^2H)$ depends on the location of the spin-label within the micelles. For instance, $k(^2H)$ of a spin-label that is located in the core of the micelles (PPO region) should be smaller than that of a spin-label situated in the corona of the micelles (PEO region). Indeed, 3CP exhibits the largest $k(^2H)$ within the series because it is hydrophilic and water soluble and therefore it is located at the region of the water/micelle interface; the lowest $k(^2H)$ is exhibited by 4HTB because it is the hydrophobic and located within the core of the micelle. 5DSA is water insoluble and consequently must be dissolved in the micelle, but, due to its polar head group the spin-label should be located in the core-corona interface region. This is indeed observed experimentally, $k(^2H)$ of 5DSA is higher than that of 4HTB and lower than that of 3CP. Finally, the $k(^2H)$ of L62-NO is slightly smaller than that of 5DSA, placing it closer to the core. L62 has shorter PPO and PEO blocks than P123 and therefore the ends of its PEO chains are situated well inside the corona, closer to the
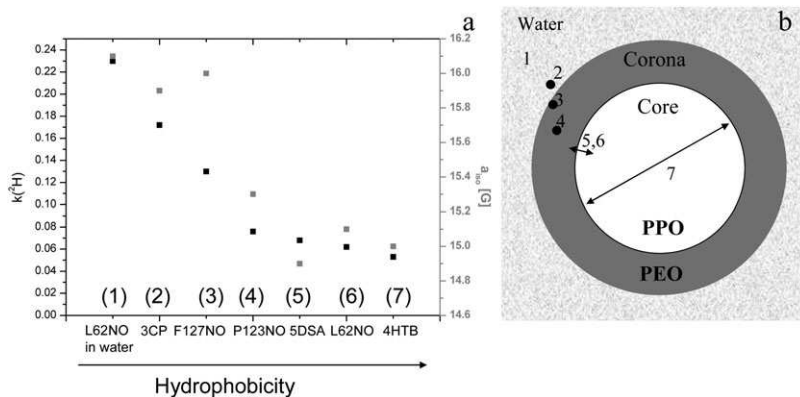
Fig. 7 (a) a_{iso} and $k(^2H)$ values obtained from CW-EPR and ESEEM measurement of various spin-probes in 2.5% wt. P123 in D_2O at 50 °C. (b) A schematic representation of the location of the various spin-probes in P123 micelles.

core. The $k(^2H)$ values of P123-NO and F127-NO are larger than that of L62-NO, owing to their longer PEO blocks, which locate them at the P123 corona. Fig. 7a also depicts the a_{iso} values of all these solutions showing a good correlation between $k(^2H)$ and a_{iso}, considering the differences in the nitroxide rings that has an effect on a_{iso}. Fig. 7b depicts the estimated average location of the different nitroxide spin-labels in the micelle as obtained from the ESEEM experiments.

4.2 EPR studies of MCM-41

The formation of MCM-41 was first investigated by *in situ* CW EPR experiments using CAT16 and 5DSA. The former senses the region of the polar head, whereas the later is located more into the micelle.[67,109,110] The synthesis procedure of MCM-41 includes two parts. The first takes place at room temperature and the hexagonal structure is produced during this stage but the silica condensation is not complete.[13] The second part, carried out under hydrothermal conditions (100 °C), produces a better cross-linked silica. The spectrum of CAT16 in CTAB micelles, prior to the addition of TEOS, is a superposition of two sub-spectra due to spin-probes partitioned between the micelles and in the aqueous environment. An increased resolution of the two spectral components was observed immediately after the addition of TEOS, and after 19 h, the spectrum is characterized by a superposition of a liquid-like spectrum due to CAT16 in the aqueous solution, and a solid-like spectrum attributed to precipitated MCM-41. The temporal evolution of the spectrum shows that while the liquid-like spectrum remains practically invariant throughout the reaction, that of the micellar component gradually broadens until it converts completely to the rigid limit line-shape. The conversion process lasts about 2.5 h, after which the spectrum remained practically invariant. Measurement of the intensity of the $M_I = 0$ component as a function of time generated a phenomenological kinetic profile, showing a fast process up to ~ 12 min, followed by a slower one. This observation is consistent with earlier XRD experiments.[62] The profile generated by the synthesis of the MCM-50 lamellar phase was very different.[67]

5DSA turned out to be a better probe than CAT16 because it is located only within the micelles. Fig. 8a shows the time evolution of its EPR spectrum during the formation of MCM-41 at 25 °C. The major changes in the line shape occur during the first 12 min. Then it undergoes minor changes up to 60 min; thereafter it remains constant and is characteristic of a powder pattern scaled by motional averaging. Simulations of the spectra gave the time evolution of the rotational tumbling rates $R_{||}$ and $R_{\perp}$, when $R_{||}$ is the rotational tumbling rate about the long molecular axis
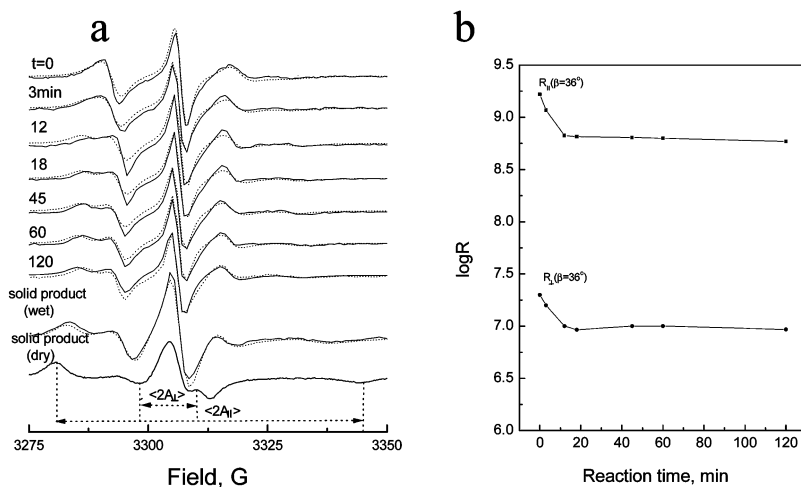
Fig. 8 (a) Experimental EPR spectra of 5DSA in the reaction mixture of MCM-41 recorded as a function of the reaction time (solid traces) at 298 K, and best fit simulated EPR spectra. Zero time ($t = 0$) corresponds to the mixture before adding TEOS. (b) The temporal evolution of $R_\parallel$ and $R_\perp$ as determined by EPR line shape simulations. β is the angle between the principal axis of the ^{14}N hyperfine interaction and the long molecular axis. Reproduced from ref. 109.

and $R_\perp$ is perpendicular to it. The time dependence of $R_{||}$ and $R_\perp$ show a fast initial decrease (up to 12 min) and it remains essentially constant thereafter (Fig. 8b). The simulations also yield an order parameter, the time dependence of which exhibits a monotonic increase with a faster initial growth, levelling off at longer times. The fast process was assigned to the initial stages of the TEOS hydrolysis and condensation, that restricts the motion of the organic template, and the onset of the orientational ordering, occurring simultaneously. The slow process reflects the 'hardening' of the silica wall.

To seek further details on the formation mechanisms of MCM-41, in particular at the early stages of the reaction, when the interaction between silicate anions and the surfactant assemblies play a crucial role, ESEEM measurements were preformed.[84] The temporal evolution of the local environment of the surfactant molecules near the interface, as manifested by the interaction between the spin-probe and nearby CTAB molecules, was followed by $k(^2H)$ of α-d_2-CTAB, again using CAT16 and 5DSA. A fast initial decrease of $k(^2H)$, lasting about 12 min, followed by levelling off, was observed for both spin-probes. This time-course is similar to that of the phenomenological kinetic profile and the rotational diffusion rates obtained from *in situ* CW-EPR experiments. In both cases, the $k(^2H)$ values of the final products are significantly smaller than those observed from initial reaction mixtures. The decrease in $k(^2H)$ indicates a decrease in the density of ^2H nuclei in the vicinity of the nitroxide spin-label. To estimate this change, the ESEEM waveforms of the α-d_2-CTAB/5DSA reaction mixture without TEOS at $t = 0$ and 120 min after the addition of TEOS were simulated. A very simple model was considered where the modulations are assumed to be induced by an effective number of ^2H nuclei, n_{ef}, at an effective distance, r_{ef}, from the unpaired electron. For $t = 0$, $r_{ef} = 4.48$ Å and $n_{ef} = 1$ were obtained, whereas for $t = 120$ min, $r_{ef} = 4.87$ Å and $n_{ef} = 1$. Although the best fit was obtained with $n_{ef} = 1$, additional simulations were carried out with a fixed number of nuclei, in the range of 2–5, the fitted parameter was r_{ef}. These simulations also showed a reasonable agreement with the experimental results, showing a consistent increase in r_{ef} of 0.3–0.4 Å upon increasing t from 0 to 120 min. This reduction in r_{ef} was attributed to displacement of the negatively charged 5DSA away from the interface, towards the organic core, driven by charge repulsion from the negative silicate oligomers.[84]

While k(^{2}H) of α-d$_2$-CTAB decreased during the course of the formation of MCM-41, a reaction mixture with D$_2$O and normal CTAB showed a small increase of k(^{2}H) induced by D$_2$O or OD from the ethanol produced by the TEOS hydrolysis. The increase is rapid during the first 12 min and then it levels off, showing the same kinetics as that obtained from the EPR spectrum and the ESEEM of α-d$_2$-CTAB/5DSA reaction mixture. Interestingly, no ^{2}H modulation was observed in the final products with both 5DSA and CAT16, once the solid product was filtered and dried. The ESEEM results thus indicate that the density of water and OH groups in the vicinity of the spin-probe increases slightly at the early stages of the reaction and the forming silica layer has a high water content. The majority of the water is, however, easily removed just by filtering the solid and drying at RT.

The formation of MCM-41 using sodium silicate as a silica source, instead of TEOS, was also studied with CW-EPR.[68] Under these conditions, the formation process is considerably slower. The probes used were 5DSA, 12DSA and CAT16. The addition of silicate in the first few minutes, decreases the mobility of 5DSA and CAT-16, and the characteristic line-shape at t = 3 min suggested that at this time, the material is already ordered. Owing to the interaction of the spheroidal micelles with silicate, the micelles became "frozen" and "structured" by the silicate layer formed at the micelle/solution interface. However, between 3 min to 3 h, a slight increase in the mobility of 5DSA and 12DSA was observed. This decrease was interpreted in terms of tilting of the hydrocarbon chains caused by a phase transition from spheroidal to thread like micelles (TLMs). After this phase transition, at t > 3 h, the mobility of the spin-probes decreased due to the hardening of the silica layer. Here, the use of a silica source that slows down the reaction, compared to TEOS, revealed a third stage in the formation mechanism of MCM-41.

The spin-probes described so far, 5DSA and CAT16 are surfactant-like, but in order to probe the forming silica layer directly, different spin-probe should be used. One such probe is the siloxane spin-probe, SL1SiEt (shown in Fig. 3), which is expected to co-polymerize with the hydrolyzed TEOS.[111] Here α-d$_2$-CTAB and CTAB with N(CD$_3$)$_3$ (d$_9$-CTAB) were used in the ESEEM experiments. Initially a small amount of hydrolyzed SL1SiEt was added to a CTAB micellar solution without TEOS, and it was shown, through k(^{2}H), that the spin-probe is located close to the surfactant's polar heads. When TEOS was added, under conditions where polymerization occurs, k(^{2}H) decreased showing that SL1SiET is pushed away from the micellar interface region, into a silica network forming around the micelle. This finding, provides experimental evidence for the principle of charge matching at the interface and the cooperative self-assembly mechanism.[47] When following the reaction by *in situ* CW-EPR, it was observed that throughout the formation process, the spectrum of SL1SiEt exhibited three narrow lines showing that it is highly mobile. This indicates that during the room temperature part of the synthesis, the silica layer is highly fluid, yet it reduced the mobility of the surfactant by the ordering it induces. After drying, the spin-probe becomes immobilized. Reintroduction of water to dried MCM-41 formed at room temperature restores the fluidity, indicating a low degree of silica cross-linking. In contrast, the fluidity cannot be restored in MCM-41 after the hydrothermal stage, due to a significantly higher level of silica cross-linking.

4.2.1 Effects of reaction conditions. *In situ* EPR, using 5DSA, was applied to explore the effect of pH and Si/Surfactant ratio on the kinetics of the formation of MCM-41 under basic and acidic condition.[112] The basic pH range suitable for MCM-41 formation is rather narrow, 13.03–13.30. Two mixtures with pH's of 13.10 and 13.3 were compared. The line- shapes evolution in the two cases are generally similar; with time, the spectra exhibit increasing anisotropy, which is characteristic of decreased rotational diffusion rates, R$_⊥$ and R$_{||}$, and increasing order parameter,

S. The difference between the two cases is only in the rate, which is higher for pH = 13.3. The line-shape observed after 3 min of reaction at pH = 13.3 is similar to that recorded after 18 min of the reaction at pH = 13.1.

The reaction was also carried out at pH = 12.96, where the final product is amorphous. The line-shape and its overall time evolution were different from those that do form MCM-41. Although the kinetic profile exhibits two stages characterized by a decrease in the rotational diffusion rates, as observed for MCM-41, the motion of the probe is significantly more restricted. This shows that although the surfactant has been encapsulated by the forming silica, which limits its motional freedom, the structures obtained are not as regular as in the hexagonal structure that enables a uniform higher mobility. Hence, *in situ* EPR measurements not only provide the kinetics profile of the reaction but can also distinguish between reaction conditions leading to amorphous and hexagonal structures. When pH > 13.3, and all the other components are kept the same, the reaction rate becomes unexpectedly slow, and the final product is a lamellar phase. This shows that there is a delicate interplay between the size, charge and structure of the silicate oligomers formed by TEOS hydrolysis and their specific interaction at the interface of the surfactant aggregate.[47] The latter affects the curvature of the aggregate and therefore determines the structure of the final product.

MCM-41 can also form under acidic conditions using HCl. The *in situ* EPR experiments were carried out for reactions with $[Si]/[H^+] = 0.1$, and 0.4, with Si/CTAC = 8.4. In both cases the product is MCM-41. The time evolution of 5DSA EPR spectra shows an increase in anisotropy similar to the basic reaction mixture. However, for $[Si]/[H^+] = 0.4$ the progression was significantly slower. When $[Si]/[H^+] = 0.1$, the reaction progresses with an initial fast stage followed by a slow one, similar to the reaction under basic conditions, although the whole reaction is slower due to slower silica condensation. In contrast, for $[Si]/[H^+] = 0.4$, it was not possible to resolve two rates owing to the slow TEOS hydrolysis.

4.2.2 Effect of additives and surfactant length. The effect of the chain length of the surfactant on the formation of MCM-41, and on the heterogeneity of the pore, was also followed by EPR.[113] The hypothesis was that surfactants with different alkyl chain length produce MCM-41 with different pore diameter, and assuming that the cross section of the pores is hexagonal, this should yield a different ratio between the areas of flat surfaces and zones with a high curvature radius. The CW-EPR spectra of CATn spin-probes with varying alkyl chain length, recorded during the reaction of MCM-41, consisted of three main components. A "free" component, due to radicals in water, a "micellar" component, due to radicals inserted in the micelles and an "interacting" component, which is more immobilized owing to interaction with the forming silica wall. The spectra were analyzed by simulations, extracting the relative contributions of each components. It was observed that the shorter the surfactant chain length is, the later is the appearance of the interacting component. In addition, the extent of the interacting component was found to increase with the surfactant chain length. The amount of the interacting component was correlated with the geometry of pore, assigning it as the component which interacts with the flat surface area. This is an example where a multitude of spin-probe locations complicate the analysis on the one hand but provides new information on the other, derived from their relative populations.

The effect of a swelling agent, tetramethylbenzene, TMB, on the formation of MCM-41 was studied using CAT16.[114] Here, again, two components were distinguished based on their mobility; a fast one and a slow interacting one. It was found that the slow component appears in earlier times of the reaction when TMB is present and it was concluded that TMB accelerated the formation of MCM-41.
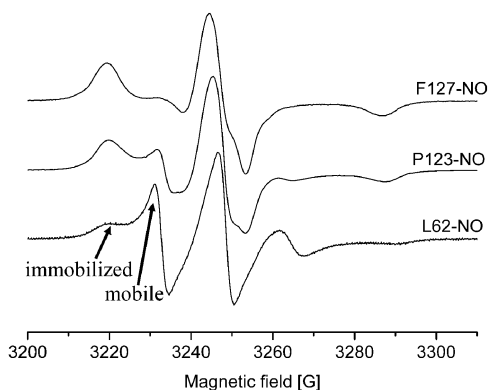
Fig. 9 EPR spectra of L62-NO, P123-NO and F127-NO in as-synthesized SBA-15, dried after the room temperature stage (recorded at room temperature). Reproduced from ref. 50.

4.3 EPR studies of SBA-15

While MCM-41 is usually synthesized under basic conditions, SBA-15 is prepared in a highly acidic solution. It is well known that nitroxide free radicals disproportionate into diamagnetic hydroxyl amines in highly acidic solutions.[115] Therefore, the synthesis had to be modified to an ''EPR friendly'' procedure. This was accomplished by replacing HCl with phosphoric acid, which is a milder acid.[25] This modified procedure gave highly ordered SBA-15, similar to that generated by the original procedure. Similar to MCM-41, the SBA-15 synthesis involves two stages, one at 35–40 °C followed by a hydrothermal stage. The hexagonal structure forms already during the first stage. The spin-probe does undergo some decomposition during the first stage, but a significant amount remains throughout the entire stage.

The formation of SBA-15 was investigated using Pluronic spin-probes. The different locations of these spin-probes in P123 micelles, discussed in 4.1, is well manifested in the spectra of L62-NO, P123-NO and F127-NO in dried SBA-15 obtained after the first reaction stage (see Fig. 9). The spectrum of L62-NO is a superposition of two spectra, attributed to a mobile species in the mesopore region, and an immobilized species, assigned to spin-labels trapped in the micropores.[25,50] Comparison with the spectra of the other two spin-probes shows that the longer the PEO chain is, the higher is the relative amount of the immobilized species, and for F127-NO the mobile species is completely absent. The CW-EPR spectrum of 4HTB in dry, as-synthesized SBA-15 showed the presence of only the mobile species. This observation shows that the silica polymerizes within the corona of P123 and that the origin of the micropores are the trapped chains within the silica, that are removed by calcinations. Hence, EPR can be used to follow the extent and development of the micropores.

Fig. 10a shows the time evolution of the CW-EPR spectrum of L62-NO. In the first 20 min the spectrum is characteristic of a single species; thereafter a splitting in the high field hyperfine component becomes apparent, indicating the appearance of a second species. Analysis of the spectrum showed that the line-shape of one spectral component remains invariant throughout the reaction while the other exhibits a continuous decrease of a_{iso} during the first 100 min and then it levels off (Fig. 10b). P123-NO exhibited the same behaviour. In contrast, the spectra of F127-NO, which has longer PEO blocks than the P123 template, revealed a single component throughout the reaction with an invariant $a_{iso} = 16.0$ G. The latter is similar to the invariant component of the L62-NO spectra. Thus, the invariant component is assigned to a spin-label situated within the forming silica layer in the corona, and the other to a label within the region of the corona–core interface. As the silica network
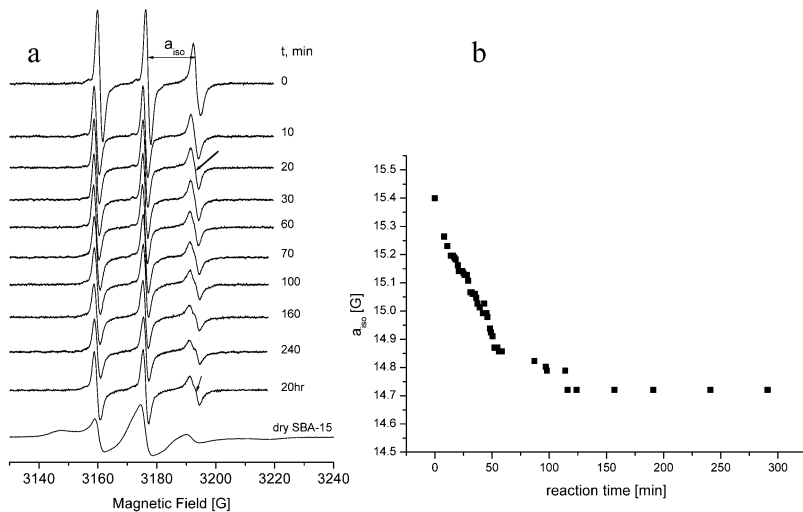
Fig. 10 (a) Time evolution of the EPR spectrum of L62-NO during the formation of SBA-15 at 50 °C and of the dry product recorded at room temperature (Reproduced from ref. 50). The spectral features of the immobilized species are marked by *. (b) The time evolution of a_{iso} of the component in the core/corona interface during the formation of SBA-15.

is formed, the water content in this region is reduced, the hydrophobicity of the environment increases, thus reducing the a_{iso} of spin-labels in this region.

The well resolved triplets observed for all spin-probes throughout the reaction show that the spin-labels are highly mobile (on the EPR time scale) in all regions. After filtering and drying at ambient temperatures the spectrum of L62-NO still shows two species, one fairly mobile while the other exhibits a characteristic rigid limit powder pattern (marked with * in the bottom trace of Fig. 10a). The invariant species turns into an immobilized species, the precursor of the micropores.[24] The spectrum obtained after the hydrothermal stage shows that the relative intensity of the immobile species decrease with temperatures of the hydrothermal stage. This is consistent with the observation that the hydrothermal treatment reduces the extent of the micropores.[116]

While the spectrum of F127-NO is invariant during the reaction, its intensity decreases due to disproportionation of the nitroxide. A plot of the signal intensity *vs.* time identifies two decay rates, a fast one that occurs at $t < 5$ min where a 65% loss is detected, followed by a milder decay; reaching a constant of $\sim 30\%$ after ~ 80 min. This decrease is not due to a pH change, because the pH of the solution was found to be constant throughout the reaction (pH = 1.3). Alternatively, the decomposition rate may reflect the formation of the silica layer. During the first 5 min the spin-label is exposed to the acid attack, but once the TMOS hydrolysis is complete and silicates start to polymerize within the corona region, it becomes "protected" and the disproportionation slows down and eventually stops. Interestingly, in the absence of TMOS, the intensity of the signal of F127-NO in P123 micelles at the same pH decreases during the first 10 min after the addition of the acid by only 10–15%. These results show that the addition of TMOS and its hydrolysis leads to an increase of [H$^+$] in the corona region.

ESEEM measurements were also performed and L62-NO and 4HTB where chosen to probe different environments in the P123 micelles.[50] The reaction mixture was prepared in D$_2$O and the time dependence of k(^{2}H) was examined; $t = 0$ min corresponds to the conditions prior to the addition of TMOS to the acidic micellar solution. First, a remarkable increase (4–7 folds) in k(^{2}H) at $t = 5$ min was observed for both spin-probes. This increase was attributed to the presence of hydrolyzed
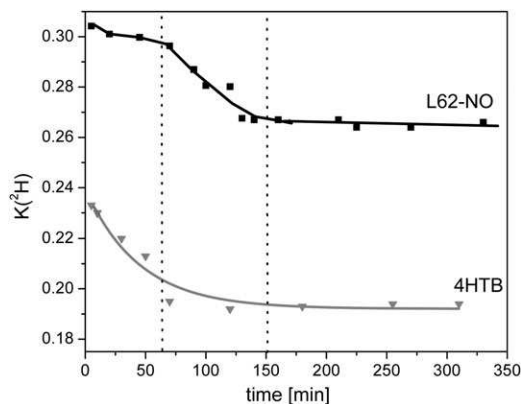
Fig. 11 The time evolution of k(^{2}H) for L62-NO and 4HTB in the SBA-15 reaction mixture. The dashed lines correspond to 60 min and 150 min, and the solid lines were drawn to guide the eye.

TMOS species such as, $Si(OD)_{4-x}(OD_2)_x^{+x}$ and/or smaller oligomers in the micelles. These may also carry significant amounts of D_2O molecules into the corona, and MeOD, which is a hydrolysis product, can also contribute to the k(^{2}H). After this initial considerable increase, k(^{2}H) decreases during the rest of the reaction, as shown in Fig. 11. While for 4HTB the largest decrease occurred up to 60 min; for L62-NO it happened later, between 60–120 min. This shows that the D_2O/OD depletion occurs from the core-corona region towards the corona. This depletion stopped after 120 min, consistent with the kinetic profile observed by the CW-EPR measurements.

The EPR measurements gave information on the time scale of the reaction, it showed that silicate oligomers penetrate into the corona, and that there is a progressive decrease in polarity, associated with reduction in water/OH content that takes place from the core/corona interface outwards. This can also be viewed as a movement of this interface. Such changes are expected to change the micelles curvature and lead to a change in the shape and aggregation of the micelles.
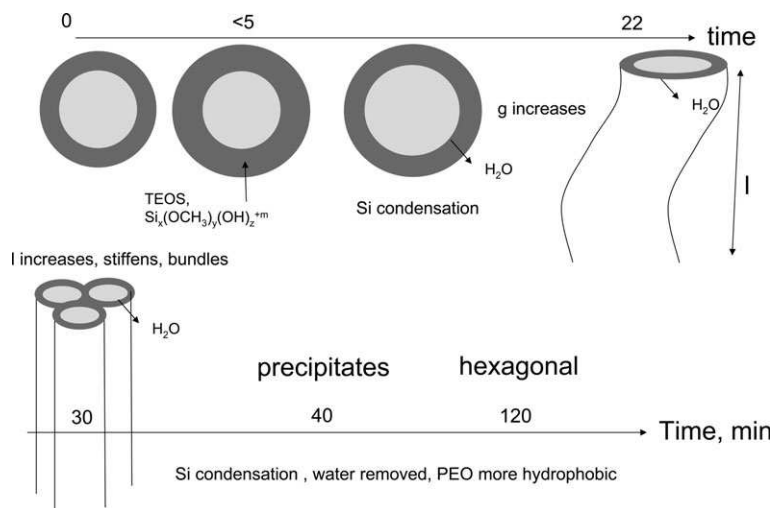
Fig. 12 A schematic model for the formation of SBA-15 (the time scale corresponds to the preparation with phosphoric acid). The light grey represents the core of the micelle, and the darker grey the corona.

Evidence for this, however, cannot be obtained from EPR, but from a method that is sensitive to changes occurring at the mesoscale. This was achieved by cryo-TEM measurements carried out under the same conditions as the EPR experiment. The sampling time was based on the phenomenological kinetic profiles supplied by the EPR measurements.[57] A micrograph taken at t = 22 min showed that a transformation from spheroidal micelles into thread like micelles (TLM) took place. Hence, the silicate adsorption and polymerization that leads to dehydration decreases the effective volume of the PEO segments, owing, for example, to a reduction in the repulsion between neighboring PEO chains and thus increasing the packing parameter, g. The cryo-TEM results further showed that the TLMs continued to grow with time, and become stiffer. Furthermore, aggregates of long threads appeared around 40 min. During all this time, spheroidal micelles coexisting with the various microstructures were also observed in the cryo-TEM micrographs. Interestingly, the EPR results did not show any special feature at 40 min, although this is the time at which a precipitate is observed.

SAXS measurements done on a dried solid after 2 h of reaction, showed a hexagonal order, whereas this hexagonal structure was clearly observed by TEM of freeze-fractured replicas of the reaction mixture after 2 h 50′ min, although some structure was also evident after 2 h. Fig. 12 presents a schematic model that summarizes the formation of SBA-15, based on results from EPR and cryo-TEM studies.

4.4 Studies of cubic mesoporous materials

The formation of the bicontinuous cubic KIT-6 was examined by the same approach applied to SBA-15.[25,50] The synthesis of KIT-6 is in general similar to that of SBA-15, except for the addition of butanol and the lower acidity.[31] Because of the lower acidity it was not necessary to modify the original synthesis procedure to reduce the nitroxide disproportionation. The phenomenological kinetic profile of the reaction was obtained by *in situ* CW EPR measurements of F127-NO. Its spectrum is characteristic of a single, highly mobile species and Fig. 13a shows the time dependence of τ_c, as derived from eqn (1). Because the nitroxide label of F127-NO is located close to the corona–water interface, it is sensitive to the interaction between the micellar interface and the forming silica. Therefore, the variation in τ_c is an indirect measure of the formation of the silica layer. The time dependence of τ_c reveals several stages, distinguished by their slopes: (a) 0–50 min, (b) 50–150 min, (c) 150–350 min and (d) t > 350 min. The largest increase in τ_c occurred between 150–350 min. Turbidity is observed around 120 min and precipitation takes place around 150 min. The CW-EPR spectra of 4HTB, L64-NO and P123-NO show that the spin-probes are partitioned between two environments. 4HTB is in the hydrophobic core of the micelles (majority) and dissolved in single chains in the solution (minority), L64-NO is in the core-corona interface (majority) and as single chains in solution (minority), P123-NO is in two environments within the corona, one closer to the water interface (minority) and the other to the core–corona interface (majority). This assignment was based on the a_{iso} and τ_c values of the individual species.[25,94] Until precipitation, the micellar component of L64-NO exhibited a mild monotonous reduction in a_{iso}, while the spectra of 4HTB and P123-NO remained practically invariant. In contrast, these two probes were highly sensitive to the precipitation. For 4HTB, it was associated with an expulsion of a significant part of the 4HTB molecules from the core to single chains in solution, concomitant with a considerable increase in the hydrophobicity of the core, as manifested by a much smaller a_{iso} value. Interestingly, after these abrupt changes, the spectra restored their characteristics prior to the precipitation. This suggests that some reorganization of the micellar structure took place. After precipitation, as for SBA-15, the spectra were still characteristic of the fast motion regime and a_{iso} of the hydrophobic component
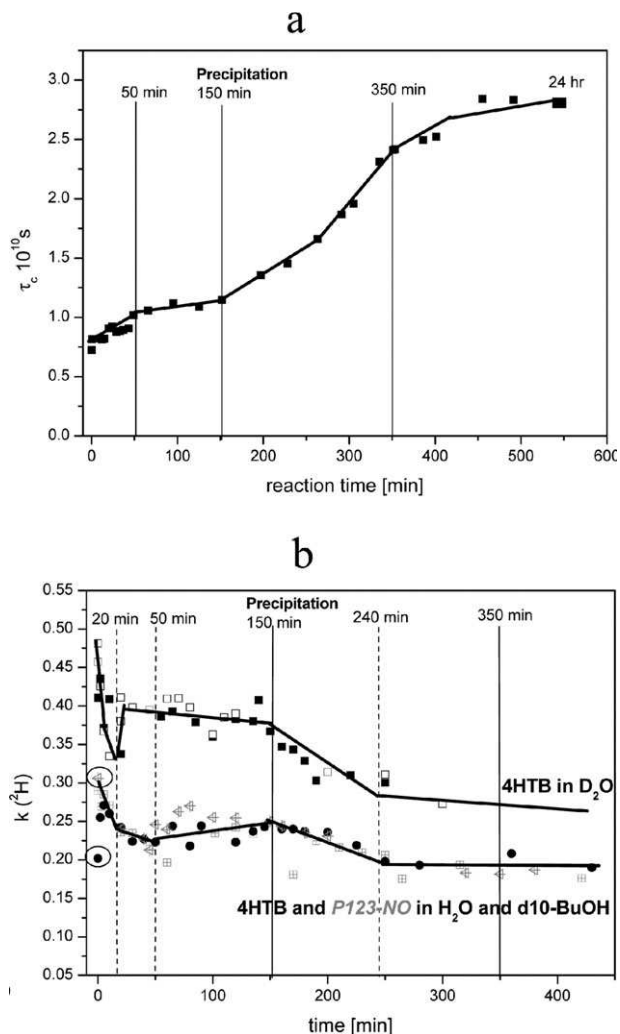
Fig. 13 (a) Time evolution of τ_c of F127-NO during the formation of KIT-6 (40 °C). (b) Time evolution of $k(^2H)$ for: 4HTB in a KIT-6 reaction mixture in D_2O (top trace, solid and hollow squares corresponds to two different experiments), 4HTB (solid circles) and P123-NO (two different experiments, squares and triangles) in a KIT-6 reaction mixture with butanol-d_{10}. The circled data points correspond to $t = -1$ min for 4HTB and P123-NO in a P123 solution with butanol-d_{10} and HCl. Reproduced from ref. 117.

of L64-NO and P123-NO decreased at a faster rate, consistent with the observation from F127-NO.

More information on the reaction prior to precipitation was obtained from ESEEM experiments. Here two types of reaction mixtures were prepared, one in D_2O and the other in H_2O with per-deuterated butanol. The time evolution of $k(^2H)$ for 4HTB and P123-NO in both types of reaction mixtures are shown in Fig. 13b. The addition of BuOH + HCl to P123 micelles in D_2O, increases $k(^2H)$ for 4HTB considerably, from 0.09 to 0.45, showing that the interface between the core and corona is smeared. While a huge effect was observed for $k(^2H)$, a_{iso} has not changed significantly. This reflects the short range interactions affecting a_{iso} compared to the longer range of the electron–nuclear dipolar interaction determining $k(^2H)$.

The time evolution of $k(^2H)$ of 4HTB in the D_2O mixture (Fig. 13b) shows (1) a decrease between $t = 0$–20 min, (2) invariance at 20–150 min, (3) a decrease at 150–240 min, at a lower rate than observed in the first 20 min, and (4) invariance at $t >$ 240 min. The time evolution of $k(^2H)$ in the reaction mixture with butanol-d_{10} is similar for P123-NO and 4HTB, except for $t = 0$ min, where for P123-NO $k(^2H) =$ 0.3 and for 4HTB $k(^2H) = 0.2$. This shows that initially butanol prefers the corona region. However, after the addition of TEOS, at $t = 5$ min, $k(^2H) = 0.27$ for both spin-probes, thus indicating a displacement of butanol molecules from the corona into the core-corona interface. At $t > 5$ min, the time evolution of $k(^2H)$ exhibited four stages as well (Fig. 13b), but with minor difference in early times as compared to $k(^2H)$ of the D_2O solutions. At $t = 5$–20 min both probes experience, a reduction in $k(^2H)$, probably due to depletion of butanol from both regions. Then, up to 150 min, $k(^2H)$ stays fairly constant for both probes, but between 150–240 min, a faster average depletion of butanol molecules from the core and the corona is sensed by both 4HTB and P123-NO. This means that butanol is further displaced into the corona–water interface. From 4 h up to 24 h $k(^2H)$ remained constant.

To summarize, the EPR results provided the timescale of the reaction and showed that although the reduction in polarity and water withdrawal from the micelle takes place after the initial increase as in SBA-15, the silica condensation is much slower due to the lower pH. Interestingly, it increased after precipitation.

As for SBA-15, cryo-TEM and FFR experiments were carried out under the same conditions and the same behaviour was observed, except for the last stage, showing the transformation of spheroidal micelles $\rightarrow$ TLMs $\rightarrow$ bundles of TLMs $\rightarrow$ hexagonal $\rightarrow$ cubic as illustrated in Fig. 14. The observation that the hexagonal phase is a precursor of the $Ia\bar{3}d$ cubic phase raised the question of the role of the butanol in this phase transition. Butanol is known to act as a cosolute in block copolymer–water systems and it co-micellizes with the block copolymer and stabilizes apolar–polar interfaces, determining the micellar interfacial curvature.[118,119] Since butanol is polar, it can interact with both PEO and PPO blocks, with its polar –OH headgroup assumed to be located mostly at the hydrophilic–hydrophobic interface of the micelles.[118,119] In the fourth stage, when the formation of the hexagonal phase takes place, the butanol molecules relocate from the
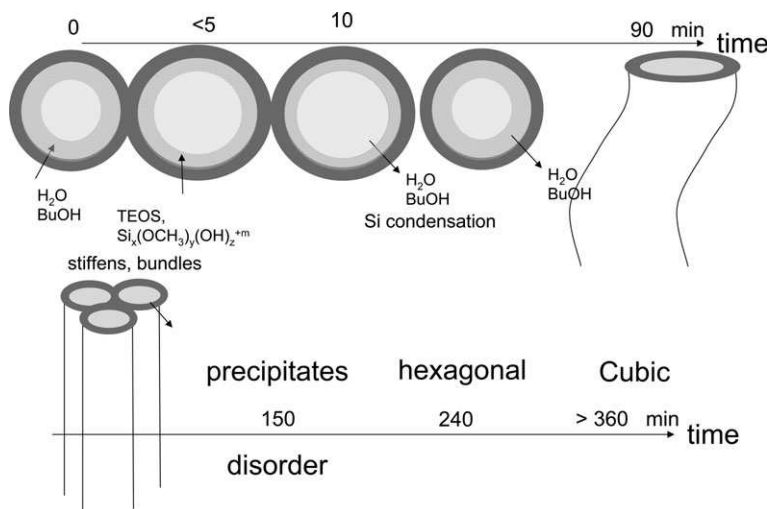
Fig. 14 A schematic model describing the evolution of nanostructures in the formation of KIT-6. The light color represents the core of the micelle, and the darker one, the corona. The intermediate intensity was added to represent the smearing of the interface by the addition of the butanol.

core/corona into a more hydrophilic environment, the corona–water interface. This location of the butanol may be responsible for a pronounced decrease in the interfacial curvature of the rod channels (increase g). The observation of the hexagonal structure in the reaction mixture suggested that it should be possible to obtain the cubic phase by adding butanol to a precipitate of the SBA-15 reaction mixture after the hexagonal mesophase has formed. This has been confirmed experimentally by adding butanol to a reaction mixture of SBA-15 (prepared with HCl) after precipitation and the product was a highly ordered $Ia\bar{3}d$ cubic phase.[94] This is a nice example for mechanistic studies leading to a new synthesis procedure.

Although the reaction mechanism of KIT-6 had been studied in detail, a few questions remained open, one is the sizes of the micelles during the very early stages of the reaction (first 50 min). In this time window, the micelles were not well resolved in the cryo-TEM micrographs and therefore DEER has been applied using 4HTB. The use of 4HTB limits the observation to the volume of the hydrophobic core. Due to S/N limitations the DEER traces could not be acquired with long enough dephasing time, t'; therefore the model used to analyze the data was the simplest possible, where the DEER traces were fitted to an exponential decay according to:

$$V(t') = V_{intra}(t')V_{inter}(t') = \exp\left(-\frac{\lambda t'}{1.0027}(C_{ap}(t))\right).$$ (18)

Here t' corresponds to the DEER experiment evolution time, to distinguish from t that is used for the reaction evolution time. $C_{ap}(t)$, determined from eqn (18), corresponds to an apparent concentration and according to eqn (16) includes contributions of the effective concentration in the micelles, C_{intra}, and the total spin concentration, C_{inter}, where $C_{ap}(t) = C_{intra}(t) + C_{inter}(t)$. C_{intra} is inversely proportional to the total hydrophobic micelles' volume, nV_m, where n is the number of the micelles, and V_m is the individual micelle's hydrophobic volume. Fig. 15 presents the change in C_{intra} during the first 120 min of the reaction, taking into account the amount of 4HTB dissolved in single chain in solution and the reduced concentration due to disproportionation, both obtained from *in situ* EPR experiments.[94] These show that $C_{intra} = 4.5 \pm 0.2$ mM before the addition of butanol + HCl ($t = -5$ min), and decreased to 3.0 ± 0.2 mM upon the addition of butanol + HCl ($t = 0$). Ten min after the addition of TEOS, C_{intra} drops remarkably to 0.25 ± 0.15 mM, but at 10–70 min it increased, reaching $C_{intra} = 2.3 \pm 0.3$ mM. This value is close to the $t = 0$ value. Then, between 70 min to 120 min, C_{intra} is practically invariant.

This shows that during the first ten minutes of the reaction there is a large change in the total micelle volume occupied by 4HTB. The question is, whether it is due to an increase in n (reduction in aggregation number) or in V_m. Simulations of the data
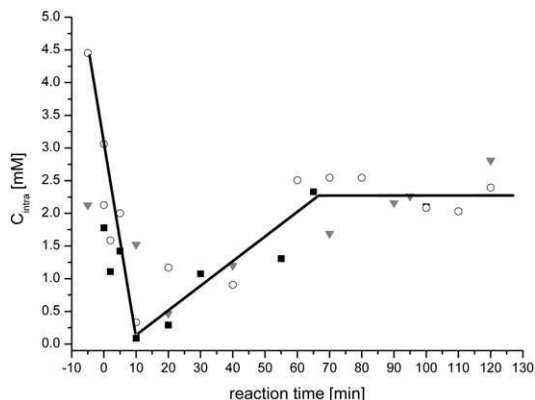

Fig. 15 $C_{intra}(t)$ *vs.* reaction time, obtained from the analysis of the DEER decays according to eqn (18). Reproduced from ref. 117. The different symbols represent different experiments.

using a somewhat more complicated model showed that the prime change is in the volume of the hydrophobic core radius, which almost doubled.[108] This increase was attributed to the penetration of TEOS and partially hydrolyzed products into the micelle core. Then, as hydrolysis and condensation progressed, the products migrate towards the more hydrophilic parts of the micelle and the size of the hydrophobic volume decreases and becomes close to its original size. Fig. 15 summarizes in a schematic model the formation of KIT-6 as derived from the various EPR experiments and the cryo-TEM images.

4.4.1 Effects of additives. While it is clear that anions can be used to tune the reaction conditions and the structure of the TMM[120] due to their effect on the micelles' structure, there is no direct experimental evidence for their specific interaction with the Pluronic and their fate during the synthesis. Such experimental information can be obtained from ESEEM measurements.[3] The focus of the study was the bicontinous cubic phase obtained from a synthesis mixture of SBA-15 by the addition of salt. This was originally demonstrated using NaI[53] and was modified to $NaNO_3$ and replacing HCl with HNO_3.[3]

The penetration of the $NaNO_3$ ions into P123 micelles was followed by ^{23}Na and ^{15}N modulation experienced by P123-NO and L62-NO. ESEEM measurements were carried out on samples with different [$Na^{15}NO_3$], with and without $H^{15}NO_3$, and on micelles prepared in D_2O with non-enriched nitrate compounds to avoid overlap of the ^{15}N and ^2H signals. The dependence of k(^2H), k(^{15}N) and k(^{23}Na) on [$NaNO_3$] is shown in Fig. 16. These show that the ions penetrate the hydrophilic corona, concomitant with penetration of water molecules, reaching saturation at a bulk $NaNO_3$ concentration of 0.2 M. The ^2H peak exhibits a sharp change at [$NaNO_3$] = 0.3 M, which was also clear in the k(^{15}N) and k(^{23}Na) dependence of the spin-probe 3CP on [$NaNO_3$]. This change can be an indication for a phase transition such as spheroidal → thread-like micelles.[3] In acidic micellar solutions, protons replace the Na^+ ions in the corona and for the same total [NO_3^-], the acidity increases the NO_3^- capacity of the corona. However, a general decrease is noted in the nitrate and water content of the corona with an increasing salt concentration in the bulk solution. This effective dehydration of the EO groups, leads to decrease in the curvature of the micellar assembly of the Pluronic, which is responsible for the formation of the bicontinuous cubic phase. Time resolved freeze quench ESEEM measurements, carried out on the reaction mixtures of the hexagonal and cubic phases, presented in Fig. 17, show that in both cases the nitrate concentration within the corona is reduced with time due to depletion of the protons through exchange with TEOS hydrolysis products and their condensation.
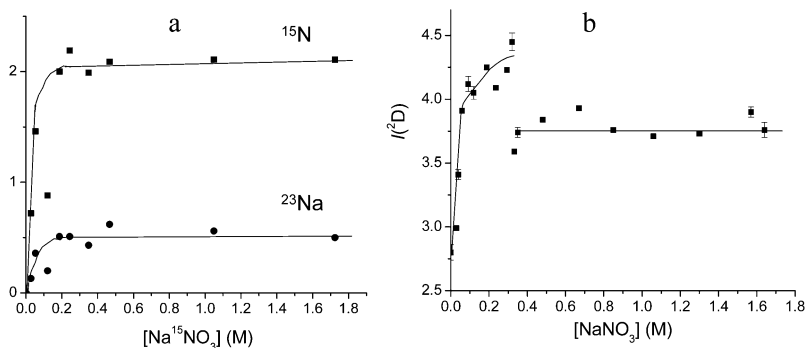
Fig. 16 (a) Plot of the ^{15}N and ^{23}Na peak intensities of the FT-ESEEM spectra of L62-NO in 2.7 %wt P123 as a function [$Na^{15}NO_3$]. (b). The same but for the ^2D peak intensity of the corresponding D_2O solution. Reproduced from ref. 3.
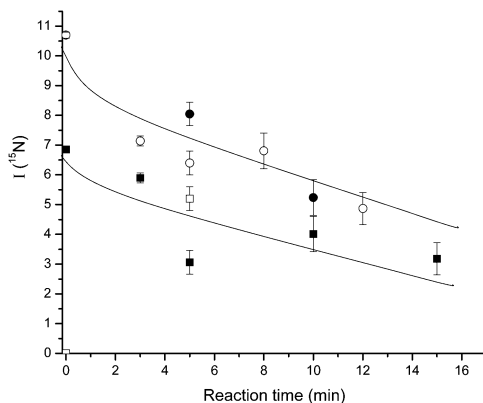
Fig. 17 Plot of I(^{15}N) during the first 15 min of the reaction, both in the cubic precursor reaction mixture with H^{15}NO$_3$ and Na^{15}NO$_3$ (squares) and in the hexagonal precursor mixture with H^{15}NO$_3$ (circles). The full and empty symbols indicate data obtained from reactions performed at different dates.

4.5 Studies of wormlike mesoporous materials

Wormlike TMM synthesized with a neutral template, dodecylamine (DDA), in a ethanol/water mixture and TEOS was investigated by CW-EPR.[69] Because the porosity of the mesoporous material was found to depend on the ethanol/water ratio, two ethanol/water mixtures were examined. The spectra of 5DSA and 7DSA in the water rich micellar solution, prior to TEOS addition, were characterized by an anisotropic motion, which is typical of aggregates with a low curvature interface. In the ethanol rich solution, the anisotropic spectral features of 5DSA and 7DSA were averaged by lateral diffusion and/or micellar tumbling at a rate comparable with the EPR time scale. It was concluded that ethanol leads to a higher area per polar head, higher curvature of the aggregate surface, and a smaller micellar radius.

In the as-synthesized dry mesoporous material, obtained from both mixtures, the spectra of these probes were typical of immobilized species. Even mild drying of the samples, at room temperature, produced progressive immobilization of most spin-probes. The first ones to be immobilized are those whose headgroups are easily attached to silica and whose nitroxide group is relatively close to the headgroup (such as 5DSA, 7DSA and CAT-16). For mesoprous materials synthesized in ethanol rich solution, more drastic changes were observed; there all the spin-probes, including 16DSA, were characterized by an immobilized spectrum in the dry-phase. This shows the importance of strong interactions between the surfactant and the silica, in the presence of ethanol, probably due to solvation of Si–O–CH$_2$–CH$_3$ groups. This shows that water and/or ethanol play an important part in the weak link of the micelles to the silica, especially when the surfactant is neutral.

The pore-size of worm-like alumina prepared by the neutral surfactant pathway, but in organic solvents, can be easily modified by treatment with different solvents. This was shown by measuring nitrogen absorption isotherms of the calcined material. It can also easily be detected by following the changes in the EPR spectrum as a function of the reaction conditions.[121] Here, however, the EPR can only indicate that the structure of the final material had changed due to the different reaction conditions, but can not give details on the mesophase structure.

5. Summary and outlook

Carefully chosen spin-probes and the combination of various EPR techniques, like *in situ* CW-EPR (exploring dynamics and local polarity), ESEEM (following specific interactions between various components through straightforward isotope labelling

schemes), and DEER (that provide spatial distribution), yield a wealth of molecular level information on the formation of templated mesoporous materials. It also provides a phenomenological kinetic profile of the synthesis, based on polarity, local viscosity or water content all of which can be easily obtained. This gives the time scale of the experiment and can then serve as a guide for sampling for other more involved techniques such as cryo-TEM. This integrated EPR approach, is of course, not limited to studies of TMM and can be applied to a variety of systems as shown recently for composite silica/polymer materials.[122] However, to obtain a complete picture of TMM formation, it is essential to combine the local molecular level information provided by EPR with other techniques that can give information on the mesoscales, such as cryo-TEM and/or *in situ* XRD. Finally, the majority of the studies described here mostly made use of surfactant-like spin-probes and the potential of silica-like spin-probes has not been fully realized. These will be probably most useful in studies of organic-inorganic hybrid materials with organic groups within the solid framework.

Below we summarize some of the key observations by EPR.

• At low surfactant concentrations, the formation mechanism of MCM-41, SBA-15 and KIT-6 follows the cooperative self-assembly mechanism[47] and the condensation of the silica precursors at the micelles interface was confirmed.

• Anions are initially present in the corona of the Pluronic micelles used in the synthesis of SBA-15 and the $Ia\bar{3}d$ cubic phase, but as the silicate condensation takes place and the total positive charge is reduced, they are expelled from the corona, into the bulk solvent.

• The organosilane is initially located within the core of the Pluronic micelles.

• For Pluronic based materials the hydrolysis of the organosilane initially increases the water OH content of the micelles, but as the silicate condensation proceeds dehydration takes place. In SBA-15 and KIT-6 the dehydration develops from the core/corona outwards.

• With neutral surfactants, the interaction between the surfactant and the silica layer is weak, thus additives, such as organic solvents and alcohols can influence the curvature of the micelle, g factor, and can results in a different final structure.

• The silica layer in both MCM-41 and in the SBA-type hexagonal and cubic materials is highly fluid also after precipitation (or phase separation). After drying, a rigid silica layer is formed. However, prior to the hydrothermal treatment, the silica is not fully polymerized and its fluidity can be regenerated by the addition of water.

• The microporosity of TMM prepared using Pluronics, originates from silica condensation within the corona.

• In SBA-type materials the interaction between the surfactant and the silica during the reaction is weak, resulting in a CW-EPR spectrum which is isotropic. However, in the MCM-41, due to a stronger interaction, the surfactant mobility is considerably reduced in the polar head region.

• Rapid freezing of micellar solutions preserves the micelles structures.

Acknowledgements

References

1 C. T. Kresge, M. E. Leonowicz, W. J. Roth, J. C. Vartuli and J. S. Beck, *Nature*, 1992, **359**, 710.
2 P. Van der Voort, C. Vercaemst, D. Schaubroeck and F. Verpoort, *Phys. Chem. Chem. Phys.*, 2008, **10**, 347.
3 D. Baute and D. Goldfarb, *J. Phys. Chem. C*, 2007, **111**, 10931.
4 U. Ciesla and F. Schüth, *Microporous Mesoporous Mater.*, 1999, **27**, 131.
5 P. Selvam, S. K. Bhatia and C. G. Sonwane, *Ind. Eng. Chem. Res.*, 2001, **40**, 3237.
6 A. Davidson, *Curr. Opin. Colloid Interface Sci.*, 2002, **7**, 92.
7 A. Corma, *Chem. Rev.*, 1997, **97**, 2373.
8 K. Moller and T. Bein, *Chem. Mater.*, 1998, **10**, 2950.
9 J. F. Diaz and K. J. Balkus, *J. Mol. Catal. B: Enzym.*, 1996, **2**, 115.
10 C. G. Wu and T. Bein, *Science*, 1994, **266**, 1013.
11 A. H. Lu and F. Schüth, *Adv. Mater.*, 2006, **18**, 1793.
12 G. A. A. Ozin and A. C. Arsenault, *Nanochemistry-A chemical approach to nanomaterials*, The Royal Society of Chemistry, 2005.
13 J. S. Beck, J. C. Vartuli, W. J. Roth, M. E. Leonowicz, C. T. Kresge, K. D. Schmitt, C. T. W. Chu, D. H. Olson, E. W. Sheppard, S. B. Mccullen, J. B. Higgins and J. L. Schlenker, *J. Am. Chem. Soc.*, 1992, **114**, 10834.
14 Q. S. Huo, R. Leon, P. M. Petroff and G. D. Stucky, *Science*, 1995, **268**, 1324.
15 D. Y. Zhao and D. Goldfarb, *J. Chem. Soc., Chem. Commun.*, 1995, 875.
16 S. A. Bagshaw, E. Prouzet and T. J. Pinnavaia, *Science*, 1995, **269**, 1242.
17 P. T. Tanev and T. J. Pinnavaia, *Science*, 1995, **267**, 865.
18 D. Y. Zhao, J. L. Feng, Q. S. Huo, N. Melosh, G. H. Fredrickson, B. F. Chmelka and G. D. Stucky, *Science*, 1998, **279**, 548.
19 P. Alexandridis and T. A. Hatton, *Colloids Surf. A*, 1995, **96**, 1.
20 L. Guo, R. H. Colby, M. Y. Lin and G. P. Dado, *J. Rheol.*, 2001, **45**, 1223.
21 G. Wanka, H. Hoffmann and W. Ulbricht, *Macromolecules*, 1994, **27**, 4145.
22 S. Forster, *Colloid Chem. 1*, 2003, **226**, 1.
23 D. Y. Zhao, Q. S. Huo, J. L. Feng, B. F. Chmelka and G. D. Stucky, *J. Am. Chem. Soc.*, 1998, **120**, 6024.
24 R. Ryoo, C. H. Ko, M. Kruk, V. Antochshuk and M. Jaroniec, *J. Phys. Chem. B*, 2000, **104**, 11465.
25 S. Ruthstein, V. Frydman, S. Kababya, M. Landau and D. Goldfarb, *J. Phys. Chem. B*, 2003, **107**, 1739.
26 V. Alfredsson and M. W. Anderson, *Chem. Mater.*, 1996, **8**, 1141.
27 Y. Sakamoto, T. W. Kim, R. Ryoo and O. Terasaki, *Angew. Chem., Int. Ed.*, 2004, **43**, 5231.
28 P. Van Der Voort, P. I. Ravikovitch, K. P. De Jong, A. V. Neimark, A. H. Janssen, M. Benjelloun, E. Van Bavel, P. Cool, B. M. Weckhuysen and E. F. Vansant, *Chem. Commun.*, 2002, 1010.
29 D. H. Chen, Z. Li, C. Z. Yu, Y. F. Shi, Z. D. Zhang, B. Tu and D. Y. Zhao, *Chem. Mater.*, 2005, **17**, 3228.
30 D. H. Chen, Z. Li, Y. Wan, X. J. Tu, Y. F. Shi, Z. X. Chen, W. Shen, C. Z. Yu, B. Tu and D. Y. Zhao, *J. Mater. Chem.*, 2006, **16**, 1511.
31 F. Kleitz, S. H. Choi and R. Ryoo, *Chem. Commun.*, 2003, 2136.
32 F. Kleitz, D. N. Liu, G. M. Anilkumar, I. S. Park, L. A. Solovyov, A. N. Shmakov and R. Ryoo, *J. Phys. Chem. B*, 2003, **107**, 14296.
33 T. W. Kim, F. Kleitz, B. Paul and R. Ryoo, *J. Am. Chem. Soc.*, 2005, **127**, 7601.
34 M. Joroniec and F. Schüth, *Chem. Mater.*, 2008.
35 Q. S. Huo, D. I. Margolese, U. Ciesla, D. G. Demuth, P. Y. Feng, T. E. Gier, P. Sieger, A. Firouzi, B. F. Chmelka, F. Schüth and G. D. Stucky, *Chem. Mater.*, 1994, **6**, 1176.
36 J. N. Israelachvilli, *Intermolecular and surfaces forces*, Academic, 1990.
37 J. N. M. Israelachvilli, D. John and Barry W. Ninham, *J. Chem. Soc., Faraday Trans. 2*, 1976, **72**, 1525.
38 H. P. Lin and C. Y. Mou, *Acc. Chem. Res.*, 2002, **35**, 927.
39 P. Kipkemboi, A. Fogden, V. Alfredsson and K. Flödstrom, *Langmuir*, 2001, **17**, 5398.
40 S. Pevzner and O. Regev, *Microporous Mesoporous Mater.*, 2000, **38**, 413.
41 J. Y. Ying, C. P. Mehnert and M. S. Wong, *Angew. Chem., Int. Ed.*, 1999, **38**, 56.
42 Y. Wan and D. Y. Zhao, *Chem. Rev.*, 2007, **107**, 2821.
43 K. J. Edler, *Aust. J. Chem.*, 2005, **58**, 627.
44 J. D. Epping and B. F. Chmelka, *Curr. Opin. Colloid Interface Sci.*, 2006, **11**, 81.
45 Q. S. Huo, D. I. Margolese, U. Ciesla, P. Y. Feng, T. E. Gier, P. Sieger, R. Leon, P. M. Petroff, F. Schüth and G. D. Stucky, *Nature*, 1994, **368**, 317.
46 J. Frasch, B. Lebeau, M. Soulard, J. Patarin and R. Zana, *Langmuir*, 2000, **16**, 9049.

47   A. Firouzi, D. Kumar, L. M. Bull, T. Besier, P. Sieger, Q. Huo, S. A. Walker, J. A. Zasadzinski, C. Glinka, J. Nicol, D. Margolese, G. D. Stucky and B. F. Chmelka, *Science*, 1995, **267**, 1138.
48   S. M. Holmes, V. L. Zholobenko, A. Thursfield, R. J. Plaisted, C. S. Cundy and J. Dwyer, *J. Chem. Soc., Faraday Trans.*, 1998, **94**, 2025.
49   N. A. Melosh, P. Lipic, F. S. Bates, F. Wudl, G. D. Stucky, G. H. Fredrickson and B. F. Chmelka, *Macromolecules*, 1999, **32**, 4332.
50   S. Ruthstein, V. Frydman and D. Goldfarb, *J. Phys. Chem. B*, 2004, **108**, 9016.
51   K. Flödstrom, C. V. Teixeira, H. Amenitsch, V. Alfredsson and M. Lindén, *Langmuir*, 2004, **20**, 4885.
52   K. Flödstrom, H. Wennerstrom and V. Alfredsson, *Langmuir*, 2004, **20**, 680.
53   K. Flödstrom, H. Wennerstrom, C. V. Teixeira, H. Amenitsch, M. Lindén and V. Alfredsson, *Langmuir*, 2004, **20**, 10311.
54   D. C. V. Calabro, E. W. Valyocsik and F. X. Ryan, *Microporous Mater.*, 1996, **7**, 243.
55   N. T. Baccile, C. V. Teixeira, H. Amenitsch, F. Villain, M. Lindén and F. Babonneau, *Chem. Mater.*, 2008, **20**, 1161.
56   R. Zana, J. Frasch, M. Soulard, B. Lebeau and J. Patarin, *Langmuir*, 1999, **15**, 2603.
57   S. Ruthstein, J. Schmidt, E. Kesselman, Y. Talmon and D. Goldfarb, *J. Am. Chem. Soc.*, 2006, **128**, 3366.
58   M. Mesa, L. Sierra and J. L. Guth, *Microporous Mesoporous Mater.*, 2007, **102**, 70.
59   C. Boissiere, A. Larbot, C. Bourgaux, E. Prouzet and C. A. Bunton, *Chem. Mater.*, 2001, **13**, 3580.
60   A. S. Brown, S. A. Holt, T. Dam, M. Trau and J. W. White, *Langmuir*, 1997, **13**, 6363.
61   S. A. Holt, G. J. Foran and J. W. White, *Langmuir*, 1999, **15**, 2540.
62   M. Lindén, S. Schunk and F. Schüth, *Mesoporous Mol. Sieves 1998*, 1998, **117**, 45.
63   S. Pevzner, O. Regev, A. Lind and M. Lindén, *J. Am. Chem. Soc.*, 2003, **125**, 652.
64   H. M. McConnell, in *Foundations of Modern EPR*, ed. G. E. Eaton, J. and K. M. Salikhov, 1998.
65   D. J. F. Schnider and J. H. Freed, in *Biological Magnetic Resonance Spin Labeling* ed. L. J. R. Berliner and J. Reuben , Plenum, 1989.
66   J. H. Freed, *'In spin labeling (theory and applications)'*, Academic Press, 1976.
67   J. Y. Zhang, Z. Luz and D. Goldfarb, *J. Phys. Chem. B*, 1997, **101**, 7087.
68   A. Galarneau, F. Di Renzo, F. Fajula, L. Mollo, B. Fubini and M. F. Ottaviani, *J. Colloid Interface Sci.*, 1998, **201**, 105.
69   H. Caldararu, A. Caragheorgheopol, F. Savonea, D. J. Macquarrie and B. C. Gilbert, *J. Phys. Chem. B*, 2003, **107**, 6032.
70   A. Caragheorgheopol, H. Caldararu, M. Vasilescu, A. Khan, D. Angelescu, N. Zilkova and J. Cejka, *J. Phys. Chem. B*, 2004, **108**, 7735.
71   B. L. Bales, A. M. Howe, A. R. Pitt, J. A. Roe and P. C. Griffiths, *J. Phys. Chem. B*, 2000, **104**, 264.
72   B. L. Bales, K. Tiguida and R. Zana, *J. Phys. Chem. B*, 2004, **108**, 14948.
73   R. Ranganathan, M. Peric, R. Medina, U. Garcia, B. L. Bales and M. Almgren, *Langmuir*, 2001, **17**, 6765.
74   H. Caldararu, *Spectrochim. Acta, Part A*, 1998, **54**, 2309.
75   J. D. Morrisett, *Spin Labeling, Theory and Applications*, ed. L. J. Berliner, Academic Press, Inc., 1976.
76   G. P. Lozos and B. M. Hoffman, *J. Phys. Chem.*, 1974, **78**, 2110.
77   J. R. W. Bolton, J. A. Weil and J. E. Wertz, *Electron Paramagnetic Resonance*, Wiley, New York, 1994.
78   D. E. Budil, S. Lee, S. Saxena and J. H. Freed, *J. Magn. Reson., Ser. A*, 1996, **120**, 155.
79   Y. S. Kang and L. Kevan, *J. Phys. Chem.*, 1994, **98**, 2478.
80   C. Stenland and L. Kevan, *Langmuir*, 1994, **10**, 1129.
81   L. S. Kevan and R. N. Schwartz, *Time Domain Electron Spin Resonance*, ed. Wiley-Interscience, 1979.
82   M. Romanelli and L. Kevan, *Concepts Magn. Reson.*, 1997, **9**, 403.
83   S. A. T. Dikanov and Yu. D. Tsvetkov, *Electron Spin Echo Envelope Modulation Spectroscopy*, CRC Press, 1992.
84   J. Y. Zhang, P. J. Carl, H. Zimmermann and D. Goldfarb, *J. Phys. Chem. B*, 2002, **106**, 5382.
85   A. Bernheim-Groswasser, E. Wachtel and Y. Talmon, *Langmuir*, 2000, **16**, 4131.
86   M. F. Ottaviani, R. Daddi, M. Brustolon, N. J. Turro and D. A. Tomalia, *Langmuir*, 1999, **15**, 1973.
87   P. Baglioni, A. Bencini, L. Dei, C. M. C. Gambi, P. Lonostro, S. H. Chen, Y. C. Liu, J. Teixeira and L. Kevan, *J. Phys.: Condens. Matter*, 1994, **6**, A369.
88   J. S. Yu, C. W. Lee and L. Kevan, *J. Phys. Chem.*, 1994, **98**, 5736.

89   Y. S. Kang, H. J. D. Mcmanus, K. N. Liang and L. Kevan, *J. Phys. Chem.*, 1994, **98**, 1044.
90   X. Auvray, C. Petipas, R. Anthore, I. Rico and A. Lattes, *J. Phys. Chem.*, 1989, **93**, 7458.
91   T. M. Clausen, P. K. Vinson, J. R. Minter, H. T. Davis, Y. Talmon and W. G. Miller, *J. Phys. Chem.*, 1992, **96**, 474.
92   M. Tornblom, U. Henriksson and M. Ginley, *J. Phys. Chem.*, 1994, **98**, 7041.
93   J. N. M. Israelachvilli, D. John and W. Barry Ninham, *Intermolecular and surfaces forces*, Academic Press, 1985.
94   S. Ruthstein, J. Schmidt, E. Kesselman, R. Popovitz-Biro, L. Omer, V. Frydman, Y. Talmon and D. Goldfarb, *Chem. Mater.*, 2008.
95   M. Pannier, S. Veit, A. Godt, G. Jeschke and H. W. Spiess, *J. Magn. Reson.*, 2000, **142**, 331.
96   M. Pannier, M. Schops, V. Schadler, U. Wiesner, G. Jeschke and H. W. Spiess, *Macromolecules*, 2001, **34**, 5555.
97   A. D. Milov, A. B. Ponomarev and Y. D. Tsvetkov, *Chem. Phys. Lett.*, 1984, **110**, 67.
98   A. D. Milov and Y. D. Tsvetkov, *Appl. Magn. Reson.*, 1997, **12**, 495.
99   A. Schweiger and G. Jeschke, *Principles of Pulse Electron Paramgnetic Resonance*, Oxford University Press, 2001.
100 A. D. Milov, K. M. Salikhov and M. D. Shirov, *Fiz. Tverd. Tela*, 1981, **23**, 975.
101 A. D. Milov, A. G. Maryasov and Y. D. Tsvetkov, *Appl. Magn. Reson.*, 1998, **15**, 107.
102 K. M. Salikhov, S. A. Dzuba and A. M. Raitsimring, *J. Magn. Reson.*, 1981, **42**, 255.
103 A. M. Raitsimring, K. M. Salikhov, B. A. Umanskii and Y. D. Tsvetkov, *Fiz. Tverd. Tela*, 1974, **16**, 756.
104 G. Jeschke, A. Koch, U. Jonas and A. Godt, *J. Magn. Reson.*, 2002, **155**, 72.
105 A. D. Milov, A. G. Maryasov, Y. D. Tsvetkov and J. Raap, *Chem. Phys. Lett.*, 1999, **303**, 135.
106 A. D. Milov, Y. D. Tsvetkov, F. Formaggio, M. Crisma, C. Toniolo and J. Raap, *J. Am. Chem. Soc.*, 2001, **123**, 3784.
107 A. D. Milov, Y. D. Tsvetkov, F. Formaggio, S. Oancea, C. Toniolo and J. Raap, *J. Phys. Chem. B*, 2003, **107**, 13719.
108 S. Ruthstein, A. Potapov, A. M. Raitsimring and D. Goldfarb, *J. Phys. Chem. B*, 2005, **109**, 22843.
109 J. Y. Zhang, Z. Luz, H. Zimmermann and D. Goldfarb, *J. Phys. Chem. B*, 2000, **104**, 279.
110 J. Y. Zhang, H. Zimmermann, Z. Luz and D. Goldfarb, *Mesoporous Mol. Sieves 1998*, 1998, **117**, 535.
111 D. Baute, V. Frydman, H. Zimmermann, S. Kababya and D. Goldfarb, *J. Phys. Chem. B*, 2005, **109**, 7807.
112 J. Zhang and D. Goldfarb, *Microporous Mesoporous Mater.*, 2001, **48**, 143.
113 M. F. Ottaviani, A. Galarneau, D. Desplantier-Giscard, F. Di Renzo and F. Fajula, *Microporous Mesoporous Mater.*, 2001, **44**, 1.
114 M. F. Ottaviani, A. Moscatelli, D. Desplantier-Giscard, F. Di Renzo, P. J. Kooyman, B. Alonso and A. Galarneau, *J. Phys. Chem. B*, 2004, **108**, 12123.
115 E. G. Rozantsev, *Free Nitroxyl Radicals*, Plenum Press, 1970.
116 A. Galarneau, H. Cambon, F. Di Renzo and F. Fajula, *Langmuir*, 2001, **17**, 8328.
117 S. Ruthstein and D. Goldfarb, *J. Phys. Chem. C*, 2008.
118 P. Holmqvist, P. Alexandridis and B. Lindman, *Macromolecules*, 1997, **30**, 6788.
119 P. Holmqvist, P. Alexandridis and B. Lindman, *J. Phys. Chem. B*, 1998, **102**, 1149.
120 K. Flödstrom, V. Alfredsson and N. Kallrot, *J. Am. Chem. Soc.*, 2003, **125**, 4402.
121 A. Caragheorgheopol, H. Caldararu, G. Ionita, F. Savonea, N. Zilkova, A. Zukal and J. Cejka, *Langmuir*, 2005, **21**, 2591.
122 Q. Mao, S. Schleidt, H. Zimmermann and G. Jeschke, *Phys. Chem. Chem. Phys.*, 2008, **10**, 1156.

High-field pulse EPR instrumentation

Graham M. Smith,* Paul A. S. Cruickshank, David R. Bolton and Duncan A. Robertson

1. Introduction

The development of pulsed NMR in high fields in the 1970's opened up vast areas of new science, through accurate molecular structure determination, study of molecular dynamics, MRI and imaging spectroscopy. A huge range of sophisticated pulsed correlation experiments have since been developed, which allow nuclear spins to be accurately and precisely manipulated and allow different magnetic interactions to be differentiated and there has been a continual push to higher and higher magnetic fields for higher sensitivity and spectral resolution. It is only natural to ask the question whether similar techniques might be applied to Electron Paramagnetic Resonance (EPR) studies of electron–electron (or electron–nuclei) interactions where the magnetic moment is approximately 650 times greater and the corresponding magnetic interaction 400 000 times larger. In principle this implies much higher intrinsic sensitivities and the ability to probe magnetic interactions over much larger distances. The fundamental difficulty with this approach to EPR, in comparison to NMR, is that the equivalent resonant frequencies are also 650 times larger and more critically the equivalent relaxation rates are many many orders of magnitude faster. This leads to very broad spectra where it is often difficult to excite a full spectrum with a single pulse. It also leads to Free Induction Decay (FID) signals that usually decay significantly within typical system deadtimes of 50–100 ns. FID detection is thus relatively rare in pulse EPR and spin echo techniques are almost mandatory, often requiring experiments to be performed at cryogenic temperatures to lengthen relaxation times.

Nevertheless, EPR is currently going through the same revolution that pulsed NMR went through over 30 years ago. Cutting edge research, as practised by the worlds leading EPR groups, is now dominated by the use and applications of multi-dimensional pulse techniques, double resonance and multi-frequency EPR (particularly at high fields). Advances in computational techniques and new methodologies such as those related to Site-Directed-Spin Labelling (SDSL) or Dynamic Nuclear Polarisation (DNP) have opened up new opportunities and there is a view that the applications are proving so persuasive that pulse EPR will eventually become a standard technique in every major biochemistry lab.

However, sensitivity is still often a serious issue and many pulse experiments currently require long averaging times. It would also be a tremendous step forward in the development of pulse EPR if FID detection could be made routine and it became possible to excite spectral bandwidths ten times larger than available today. Realistically this requires nanosecond deadtimes combined with very high power nanosecond pulses together with all the functionality and flexibility and fast averaging capabilities of modern commercial spectrometers. This has not been achieved yet and there are very good technical reasons why it is highly unlikely to be achieved at low frequencies. However, enough technical advances have recently been made to show that the twin goals of extra sensitivity and ultra-short deadtime will become available with the future development of high-field pulse EPR instrumentation.

School of Physics and Astronomy, North Haugh, University of St Andrews, St Andrews, UK. E-mail: gms@st-and.ac.uk; Fax: +44 1334 463104; Tel: +44 1334 473691

1.1 Scope of the review

It is the goal of this review to outline the technical challenges, the opportunities and to examine the current approaches currently being undertaken to maximise performance in high-field pulse EPR systems. The review is strongly influenced by our own work in this field, where we have been working to develop a flexible high power 94 GHz pulse system with ultra-low deadtime for the past few years and a system outline is given at the end of the chapter.

We take the usual definition of high field to be at field strengths beyond the operating point of conventional electro-magnets.

2. High-field EPR spectroscopy

There are many spectroscopic reasons for using both cw and pulse EPR in high magnetic fields, and general reviews of high-field EPR have been discussed in previous review chapters in this series by a number of authors including Lebedev,[1] Doubinskii,[2] Smith,[3–5] Riedi[3–6] and Smirnov.[7] A special edition of on High Field EPR in *Applied Magnetic Resonance* was introduced by the Eatons.[8] A recent volume in the *Biological Magnetic Resonance* series was devoted to Very High Frequency ESR/EPR[9] and contains review chapters from virtually all the leading groups on both applications and instrumentation. There have also been a number of specialist reviews on different aspects of HFEPR including: Mobius[10] (photosynthesis), Liang and Freed[11] (theory of dynamics of biomolecules), Freed[12] (Instrumental Techniques), Earle[13,14] (quasi-optical techniques), Hagen[15] (transition metal ion complexes and metalloproteins), Reijerse *et al.*[16] (instrumentation and bio-inorganic systems), van Dam *et al.*[17] (integer spin systems), Gatteschi[18] (molecular magnetic clusters), Murphy *et al.*[19] (catalysis), Katsumata[20] (ferromagnetic and anti-ferromagnetic systems), Martinelli[21] (relaxation), and van Slageren *et al.*[22] (swept frequency techniques). Prisner has reviewed high field pulse EPR[23] and pulse EPR applications in biology[24] including high-field applications, and Goldfarb has reviewed the opportunities in high field ENDOR for biological applications.[25] A large section is devoted to high-field EPR in the well known treatise "Principles of pulse paramagnetic resonance" by Schweiger and Jeschke,[26] which should be required reading for anyone with an interest in pulse EPR.

Usually the main reason to be interested in high-field cw EPR is better g-factor resolution for spectral identification and simplifying complex spectra. The major reason in pulse EPR is the extra orientational selectivity-for both pulse ENDOR and ELDOR. Hyperfine spectroscopy also benefits directly from higher resolution at high fields with better separation of NMR frequencies in ENDOR. Fast dynamic effects are often advantageously studied at high fields, as characteristic changes in g-anisotropy broadened spectra require much faster motional averaging relative to low fields.

High-field (or high frequency) electron magnetic resonance also becomes essential when measuring very high energy interactions associated with zero-field splitting and ferromagnetic and anti-ferromagnetic resonance.

In most cases forbidden transitions become more forbidden at high frequency, which can simplify spectra and reduce the effects of unwanted modulations due to ESEEM, for example in PELDOR measurements. On the other hand, the ESEEM effect can can also be enhanced at high fields for certain nuclei with specific hyperfine couplings *e.g.* strongly coupled nitrogens at W-band.

As a result of increased Boltzmann spin polarisation and smaller cavity volumes the sensitivity can also increase at high magnetic fields. Theoretically, for the same type of cavity, the absolute sensitivity should scale with frequency to the power of seven halves and the concentration sensitivity should scale with the square root of the frequency for both cw EPR (for constant power) and pulse EPR, (for constant cavity bandwidth). Thus huge gains in absolute sensitivity are available in cases

where sample volume is restricted but moderate gains are made in concentration sensitivity.

However, the $f^{1/2}$ scaling is strictly only valid when comparing the same type of cavity and additional gains in concentration sensitivity become possible at high fields for pulse EPR. The key point is that at low frequencies the designs of sample holders are compromised by the need to have a low cavity Q to maximise excitation bandwidth and reduce deadtime. This has led to the development of a number of ingenious solutions where the conversion factor remains high, despite the loss of Q, usually at the cost of reduced sample volume. However, these restrictions start to disappear as one increases frequency and significant further sensitivity gains become possible, either by using standard high Q cavity designs (where bandwidth can still remain high) or by using non-resonant sample holders, which start to become practical at high frequencies due to the increased power density and coupling factors in waveguide. Further gains of between 3 and 10 look practical. At present these gains are not fully realised in most current systems because of limited available source power.

3. History of high-frequency pulse EPR

Modern high frequency pulse EPR spectrometers are sophisticated and complex instruments and there are now only a few groups worldwide that have the technical resources to take on the challenge of attempting to advance the field.

The first high-frequency pulsed EPR system was constructed by the Leiden group[27] at 94 GHz and was soon followed by systems in Moscow[28] (140 GHz) , MIT[23] (140 GHz) and Berlin[29] (94 GHz) and in 1996 Bruker[30] introduced the first commercial pulsed W-band system operating at 90 GHz. In this system their heterodyne design uses a 10 GHz intermediate frequency, and derives its 90 GHz source *via* an upconversion scheme that allows the use of the existing control systems on their flagship X-band spectrometer including their high speed transient averager. This now features sophisticated cw, pulse, ENDOR and ELDOR options. Initially low source power (few mW at the cavity) limited applications but more recently the inclusion of high power solid-state amplifiers have lifted the power levels to beyond 100 mW and have allowed $\pi/2$ pulses of 30 ns duration with a deadtime of 60 ns using cylindrical TE_{110} cavities. This can be compared to performance at X-band, where 6 ns $\pi/2$ pulses and 80 ns deadtime have been achieved with 1 kW of input power.

Another highly successful system is the so-called "Krymov bridge" that has now been installed in several international laboratories.[31,32] This can operate at either 94 GHz or 140 GHz and uses a combination of IMPATT injection-locked amplifiers and IMPATT multipliers to provide a flexible superheterodyne system where both source and local oscillator are derived from a multiplied dielectric resonator source operating at a frequency of around 7 GHz. In this type of scheme, the amplitude and phase modulation is performed at the final output frequency of 94 GHz or 140 GHz where low loss PIN switches are still available.

More recently large increases in efficiency, power output and bandwidth have been achieved with passive multipliers and upconvertors. Power outputs of 400 mW are now available from passive multipliers at 94 GHz, which in turn can act as inputs to high efficiency multiplication chains that can now provide significant power levels at higher frequencies. This has allowed the use of efficient schemes where most of the pulse forming is done at low frequencies before multiplying or upconverting to higher frequencies. As 1 W solid-state amplifiers are now commercially available at 94 GHz (and 6 W solid-state amplifiers have been demonstrated for satellite applications) it appears that this trend of ever increasing power levels from solid-state sources is set to continue. This has also encouraged the design of systems at even higher frequencies.

Above 140 GHz the losses of waveguide components start to become excessive and we move into a frequency regime where it becomes useful to use a mix of waveguide and optical techniques at the front-end of the spectrometer system.

Commonly referred to as quasi-optics, it is possible to make extremely high performance analogs of almost any passive microwave component.

The Frankfurt group has used a combination of optics and waveguide techniques to extend pulse experiments to 180 GHz[33,34] using a fully coherent detection scheme based on based on multiplied sources from 45 GHz, and makes use of second-harmonic mixers and low loss quasi-optical isolators. They achieve 60 ns $\pi/2$ pulses with an input power of only 15 mW using a cylindrical TE_{110} resonator which is only 2 mm long. More recently they have added an additional source for PELDOR measurements and demonstrated that orientational information can be derived.

The Leiden group have further extended the frequency range to 270 GHz[35] and have constructed TE_{110} resonators that are only 1.3 mm in diameter and 1.3 mm long. This remarkable system also features the ability to frequency tune the cavity, change the coupling and incorporates a goniometer and ENDOR facility[36,37]—all with external tuning. It also offers extremely high conversion factors with only 1mW of input power leading to 100 ns $\pi/2$ pulses.

More recently the Milwaukee group have extended loop gap resonator (LGR) technology to 94 GHz and constructed a cavity that features a high conversion efficiency of 9 G/W$^{1/2}$ with a Q of only 90.[38] The group have described initial cw experiments that take advantage of the high cavity bandwidth by using frequency modulation as an alternative to field modulation,[39] and the cavity will also clearly be useful for a range of pulse experiments on aqueous samples.

For the most part all the systems above operate at relatively low powers (1–200 mW), well within the power handling capability of standard mm-wave waveguide components. However recently high power kW amplifiers based on Extended Interaction Klystrons (EIK's) have become commercially available at 94 GHz. These offer power gains in excess of 45 dB and instantaneous bandwidths in excess of 1 GHz.

At these frequencies and power levels it becomes much more challenging to design systems. Power densities in single-mode waveguide increase 100 fold, relative to X-band, and start to approach levels where breakdown can occur in low pressure helium gas environments. There are also few waveguide components and no commercially available switches (for receiver protection) that can handle 1 kW pulses (or more critically 100 W average power) at 94 GHz.

However, the Cornell group have taken advantage of this technology and has clearly demonstrated that using quasi-optical techniques it is possible to construct very high power kW systems operating at 94 GHz.[40] They used a high specification Russian coherent transceiver at 94 GHz, similar in design to the Krymov bridge to provide the 90 mW input to the EIK amplifier. They constructed their own high voltage modulator to rapidly turn off the final pulse. A tunable Fabry-Perot operating in induction mode helps to isolate the source from the detector and quasi-optical isolators help limit reflections from the cavity and detector. They demonstrated 4 ns $\pi/2$ pulses and deadtimes of 50 ns at full kW power levels.

In our own group at St. Andrews we have been trying to develop the technologies to decrease the $\pi/2$ length and deadtime even further, by using non-resonant induction mode schemes and developing spectrometers where reflections are eliminated to an extraordinary degree. Using a similar 94 GHz kW amplifier to the Cornell group we have recently demonstrated 5 ns $\pi/2$ pulses with a non-resonant sample-holder where we can measure signals 80-90 dB down within 2ns of the final pulse. These type of sample holders also look very promising in terms of improved concentration sensitivity for many types of sample. In small volume induction mode TM_{110} cavities we have demonstrated 2 ns $\pi/2$ pulses with longer deadtime. The overall system design is outlined at the end of the chapter.

At even higher frequencies the Santa Barbera group is constructing a kW pulse EPR system at 240 GHz using a free electron laser (FEL) driven by an electrostatic accelerator that can give a stream of high-frequency microsecond pulses that can be tuned from 100 GHz to beyond 1 THz. One problem with these types of sources is

the fact that they are often multi-moded, but it has been shown convincingly that it is possible to injection lock the FEL to provide a single narrow frequency.[41] The group have also demonstrated that it is possible to define pulse widths and pulse spacings (within the microsecond macropulse) using a combination of optical delay lines and multiple free-space photo-activated semiconductor switches (that also act as receiver protection switches).[42] The semiconductor switches operate both in reflection and transmission and use Ti:Sapphire lasers to effect the switching process by optically exciting carriers into the conduction band. It is likely to be challenging to make this system as flexible as lower frequency systems but it does offer a potential route to demonstrating extremely high power pulse EPR at the very highest frequencies.

4. Sensitivity

There are a large numbers of factors that can affect sensitivity of pulse EPR exeriments and many depend on the exact details of the experiment, including the choice of cavity or sample holder, the system deadtime, the measurement bandwidth and the repetition time. We consider each in turn.

4.1 Cavities

For pulse EPR it is sensible to consider the excitation and detection of the spins separately.

4.1.1 Excitation. The average value of B_1^2 in a critically coupled cavity is given by

$$\langle B_1^2 \rangle_c = (2 Q_L P_0 \mu_0 / V_c \omega_0)$$

where Q_L is the loaded Q of the cavity, P_0 is the available power, μ_0 the magnetic permeability, V_c is the cavity volume and ω_0 is the angular frequency. Now using the standard definition for the filling factor

$$\eta_c = (V_s \langle B_1^2 \rangle_s / V_w \langle B_1^2 \rangle_w)$$

where it is implicit in the definition that the $\langle B_1^2 \rangle_s$ term refers only to the B_1 field component in the sample that is perpendicular to the main B_0 field but the $\langle B_1^2 \rangle_c$ and $\langle B_1^2 \rangle_w$ terms refer to all components of the B_1 field in the cavity. Thus a completely filled cavity or waveguide does not necessarily have a filling factor equal to one. The average value of the B_1^2 field across the sample is then given by:

$$\langle B_1^2 \rangle_s = (2 \eta_c Q_L P_0 \mu_0 / V_s \omega_0) = c_c^2 P_0$$

where c_c is the conversion factor of the cavity where by definition we have included the loaded Q_L term. This can be compared with the average transverse B_{1t}^2 field found in transmission of a single-mode in a waveguide of cross-sectional area A_w and impedance Z_w,

$$\langle B_{1t}^2 \rangle_w = (2 \mu_0 P_0 / Z_w A_w)$$

If we consider a shorted section of waveguide then the average B_1 field, over an effective volume $V_w = A_w \lambda_g / 2$ where λ_g is the guide wavelength, will be double this value. We can also define a filling factor η_w in a similar way

$$\eta_w = (V_s \langle B_1^2 \rangle_s / V_w \langle B_1^2 \rangle_w)$$

which after a little manipulation gives the expression for $\langle B_1^2 \rangle_s$ at the sample in terms of the filling factor η_w of the waveguide

$$\langle B_1^2 \rangle_s = (\eta_w 4 \pi P_0 \mu_0 / V_s \omega_0) = c_w^2 P_0$$

where c_w is the conversion factor in the waveguide and V_w is defined as $A_w\lambda_g/2$ with λ_g the guide wavelength.

The above expressions are useful as a guide to designing or comparing different types of cavities and show that it is the conversion factor that is the most important quantity in determining sensitivity. In practice this can be accurately estimated by measuring the effective $\pi/2$ pulse length $t_{\pi/2}$ for a given power input from:

$$c \sim B_{1s}/P_0^{1/2} \sim (\pi/2\gamma t_{\pi/2})/P_0^{1/2} \sim (90 \text{ ns}/t_{\pi/2})/P_0^{1/2}$$

where $B_{1s}^2 = \langle B_1^2 \rangle_s$ and c has units of $G/W^{1/2}$. It should be noted that in this measurement, we are actually finding the maximum of $|\sin(B_1\gamma t)|$ averaged over the sample and so the expression is only exact when the B_{1s} field is homogeneous over the sample. Nevertheless it is a reasonable approximation for most cases of interest. The length of the $\pi/2$ pulse in turn determines the excitation bandwidth and the number of spins excited (for broad lines).

4.1.2 Detection.
The initial thermal magnetic moment m_0 is given by:

$$m_0 = CV_s\tanh(\hbar\omega_0/kT) \sim CV_s(\hbar\omega_0/kT)$$

where C is the number of spins per unit volume, V_s is the sample volume and T_s is the sample temperature. A signal is generated when a component of the magnetic moment m is rotated into the x–y plane and precesses about the z-axis. If the sample is placed in free space then it will initially radiate a circular polarised beam due to coherent spontaneous emission of spins at a power level given by:

$$P_{\text{emit}} = (4\pi\mu_0^2\omega_0^2m^2/3\lambda^2Z_0)$$

where λ is the free space wavelength and Z_0 is the impedance of free space and m is the component of the rotating magnetic moment in the x-y plane. The amount of power emitted by the sample is modified by the surroundings and a small sample placed at the center of a rectangular single-mode waveguide will couple power to the main waveguide mode at a level given by:

$$P_{\text{emit}} = (2\mu_0^2\omega_0^2m^2/A_wZ_w) = (4\pi\mu_0\omega_0m^2/V_w)$$

where m is the rotating magnetic moment, Z_w is the impedance of the guide and A_w is the cross-sectional area of the guide. This power level is only achieved whilst all the spin packets remain substantially in phase with each other, and the signal rapidly becomes undetectable as the spin packets dephase. For inhomogeneously broadened lines it is often possible to refocus the spins within the phase memory time of the system to give a spin echo at comparable power levels.

The above expression can be adapted to give general expressions for the power radiated by a large sample, when placed in a cavity or in a shorted single-mode waveguide. The amount of power emitted by any part of the sample will depend on the coupling to the desired mode in the cavity or waveguide, which in turn can be calculated *via* the definition of the filling factor.

Thus for a critically coupled cavity:

$$P_{\text{emit}} = (\eta_c 2Q_L\omega_0\mu_0/V_S)m^2 = c_c^2\omega_0^2m^2$$

and for a shorted waveguide:

$$P_{\text{emit}} = (2\eta_w\pi\omega_0\mu_0/V_S)m^2 = c_w^2\omega_0^2m^2$$

where it should be remembered that the magnitude of the rotating magnetic component m will depend on the type of pulse experiment, the B_1 inhomogeneity over the sample, relaxation and the excitation bandwidth. If the full spectrum is excited evenly then the maximum power that will be emitted is:

$$P_{\text{max}} = c^2\omega_0^2m_0^2$$

The signal will be proportional to the square root of the power emitted and thus the signal should be proportional to $c.\omega_0.m$. As m is proportional to $\omega_0 V_s$ we can define a figure of merit $F = c.\omega_0^2.V_s$ for either a cavity or for a shorted waveguide, where c can be estimated from pulse experiments and V_s is an effective volume allowing for B_1 inhomogeneity over the sample. For cw measurements the Q is usually chosen to be as high as possible. However, for pulse measurements the Q needs to be chosen to match the desired excitation and detection bandwidth equals $\omega_0/2\pi Q$. It is also desireable to have a low Q to limit the cavity deadtime. Thus at low frequencies there is an emphasis on choosing low Q cavities that maximise the conversion factor and the sample volume. However, at high frequencies these considerations become less important and more optimal cavities can be chosen.

4.1.3 High-frequency cavity design. From the discussion above above it is clear that the important quantities are the conversion factor of the cavity, the bandwidth of the cavity, the available power, the effective sample volume (taking into account B_1 inhomogeneity) and the dielectric loss of the sample. When comparing the same cavity—the conversion factor c is expected to scale roughly with $\omega_0^{3/2}$ (for similar bandwidths) and the sample volume is expected to scale inversely with ω_0^3 and thus the concentration sensitivity and figure of merit F is expected to scale with $\omega_0^{1/2}$. However, for point samples the absolute sensitivity will now scale with $c.\omega_0^2$, leading to an overall frequency dependence that scales with $\omega_0^{7/2}$ (for similar cavities and bandwidths). In practice further gains are possible at high frequencies relative to X-band because more sensitive cavities and sample-holders may be used with high frequencies.

A large variety of different types of cavities have been built for cw high field EPR, including Fabry-Perot resonators,[12,43,44] cylindrical mode TE_{011} resonators,[31,33] loop gap resonators,[38,39] whispering gallery mode resonators[45–47] and non-resonant mode sample-holders.[48]

For high field pulse EPR much of the early development has focussed on the design of Fabry-Perot resonators, largely because of the perception that they are easier to construct and scale to higher frequencies. However, in practice, cavity finesses have rarely approached their theoretical maxima for Fabry-Perots and conversion factors are often significantly worse relative to single-mode cavities. Nevertheless, impressive designs have been described at frequencies as high as 360 GHz[49] and the Fabry-Perot does have a number of unique advantages. Mesh based designs permit the use of induction mode operation,[40,48] which is almost essential for high power and low deadtime applications and Fabry-Perots are well suited to the measurement of aqueous samples, where much larger sample volumes can be used (relative to single-mode cavities. The use of an open structure can also help with the implementation of double resonance techniques.

Cylindrical cavities on the other hand offer excellent conversion factors. Their Q's are too high to be used at low fields but at high fields, the increased bandwidth make them the optimum choice for a large range of pulsed experiments and their use is standard in commercial systems. They should offer both high absolute and con-centration sensitivity and new designs, which incorporate rf coils as part of the cavity, have significantly improved ENDOR performance.[50]

On the other hand, if sufficient source power is available, sample volume can always be traded for conversion factor to increase sensitivity as exemplified by the non-resonant sample holder. In Table 1 we compare a representative variety of high frequency cavities relative to the Bruker MD5 X-band cavity, which offers high concentration sensitivity for PELDOR measurements.

A number of caveats and observations should be made about the above table. Firstly it should be stressed that many of the high frequency cavities listed above were designed with aqueous samples or small single crystals in mind. Real system sensitivity also critically depends on the availability of power, which is often limited

Table 1 Comparison of a selection of high frequency cavities

Sample holder	Frequency (GHz)	3dB Cavity bandwidth (MHz)	Conversion factor c (G/W$^{1/2}$)	Effective volume (micro-litres)	Figure of merit F (relative to MD5)
Dielectric cavity (Bruker MD5)	10	~250	~0.3	160	1
Loop gap (Milwaukee[39])	94	~1000	9	0.5	8
Fabry-Perot (Cornell[40])	94	~300	~0.75	~6	8
Non-resonant (St. Andrews[48])	94	Very broad	~0.6	30^a	33
Cylindrical (Bruker[30])	94	~50	~9.5	1	17
Cylindrical (Frankfurt[34])	180	~100	~13.5	0.14	13
Cylindrical (Leiden[35,36])	270	~130	~28	0.04	17

^{a} In this case the effective volume is approximately half the real volume due to factors related to the inhomogeneity of the sample holder.

at high frequencies. It should also be noted that higher conversion efficiencies are available with the MD5 cavity at higher Q's at the cost of lower cavity bandwidths and increased deadtime. Similarly, bandwidth and conversion factor can be traded with some of the other cavity designs. Many of the conversion factors have been estimated from the published available source power and thus also include system losses. In most cases the quoted effective sample volume assumes that the dielectric losses are not high. Indeed, it should be noted that non-resonant sample holders are never suitable for very lossy samples such as aqueous samples. The high B_1 inhomogeneity associated with these types of sample holders also make them unsuitable for some complex pulse sequences and also reduces the effective sample volume.

Nevertheless, despite these factors, it is striking how the non-resonant sample holder can still offer excellent concentration sensitivity for many samples, in combination with relatively easy sample handling and huge instantaneous excitation and detection bandwidths. This makes these types of sample holders, operating in induction mode, a very attractive option at frequencies above 94 GHz, particularly for applications like PELDOR, where 5ns $\pi/2$ pulses are near optimal and where high bandwidths are useful for orientation studies. The potential gain in sensitivity come from the fact that the increase in sample volume (relative to cavities) more than compensates for the relative loss in conversion factor, and that at this frequency sufficient pulse power is available to provide near optimal pulse lengths for this application. However, with the ongoing development of high frequency Extended Interaction Klystron (EIK) amplifiers and Gyro-amplifiers, it can be anticipated that there will be strong interest in the development of higher frequency systems.

4.2 Sensitivity and deadtime

The deadtime t_D of the system, is the amount of time before a signal can be measured after the final pulse of the sequence due to decay of the high power pulse within the system. The expression $P_{max} = c_c^2 \omega_0^2 m^2$ gives the maximum emitted power, but does not take into account relaxation effects, which can also seriously affect sensitivity mainly through the effects of deadtime t_D.

For any echo-detected pulse sequence the signal will be reduced by a factor $\exp(-2t_D/T_m)$, where T_M is the phase memory time and equal to π/Γ_{hom} where Γ_{hom} is the homogeneous linewidth (FWHM measured in Hz). This can be a serious restriction in dynamics measurements when T_M ($\sim T_2$) can become extremely short.

For FID detection the restrictions are even more severe, as the signal will now be reduced by $\exp(-\pi t_D \Gamma_{inh})$ where Γ_{inh} is the inhomogeneous linewidth (in Hz). For a deadtime of 100 ns this implies that all inhomogeneous linewidth components in the spectra should be less than a Gauss to be able to accurately measure undistorted spectra.

The various contributions to deadtime have been discussed extensively by the Cornell group.[40,51] They can be divided into a number of different catagories, including pulse deadtime, cavity deadtime, system deadtime, source deadtime and detection deadtime. The essential problem is that we would like to be able to detect a sub-nanowatt signal as soon as possible after applying an excitation pulse that could be 13 or 14 orders of magnitude higher in power. Unless great care is taken the excitation pulse will take a finite time to decay away due to reflections within the cavity or spectrometer system. This will provide a large interfering signal which will be coherent with the signal and thus cannot be averaged away. There are also a number of secondary problems associated with the power handling of detectors and the characteristics of high power microwave and millimetre wave amplifiers.

4.2.1 Pulse deadtime.
Deadtime is usually specified from the end of the final pulse to the point where interfering signals are below the single-shot noise floor. However, the length of the final pulse itself limits the maximum signal that can observed from any FID signal (calculated above) and it would be more correct to specify an additional pulse deadtime of at least half the final pulse length.

4.2.2 Cavity deadtime.
At low frequencies the deadtime is normally dominated by the time it takes for the cavity to ring down to thermal noise levels. It should be noted that having a "matched" reflection cavity does not help to reduce this effect, as the cavity is only at "match" when under illumination. Thus at the beginning and end of the pulse there will be an initial large reflection of power from the cavity equal to the input power, which will then decay away with the cavity decay constant $t_R = (Q_L/\omega_0)$.

The cavity deadtime is therefore given by $t_{Dcav} = -(Q_L/\omega_0) \ln[P_{noise}/P_0]$ where P_0 is the input power to the cavity and P_{noise} is the thermal noise level (dependent on the measurement bandwidth), Q_L is the loaded Q and ω_0 is the resonant frequency. For 1 kW input power and typical noise floors and measurement bandwidths $t_{Dcav} \sim 33(Q_L/\omega_0)$. Thus at 10 GHz to achieve a deadtime of 100 ns requires a loaded Q of below ~ 200. At 100 GHz to have a deadtime of 1 ns requires a Q of below 20. It is clearly advantageous to move to higher frequencies.

4.2.3 System deadtime.
The system deadtime is more difficult to quantify and is usually caused by small reflections in the transmission lines from the source to the cavity and the cavity to detector. Power can be reflected by components in the waveguide system such as isolators and circulators that themselves are required to eliminate the much larger reflections from sources and detectors. Discontinuities in waveguide or changes in waveguide cross-section can also lead to small but significant reflections that will all add coherently. Small amounts of mode-conversion in overmoded systems can lead to so called modal resonances where higher order modes are resonantly trapped, usually between sections of single-mode guide, but can back-convert to the main propagating mode, often causing suprisingly large losses in transmission of the main mode. Another more subtle effect is due to the excitation of higher order modes that propagate close to a fast wave or slow wave cut-off, which then travel with much lower group velocity than the main propagating

wave and lead to signals appearing much later than the main pulse. This latter component is currently the dominant source of deadtime in the system built at St Andrews.

All these effects become more important at high frequencies because of the use of overmoded transmission lines to keep losses low, and because propagation distances (relative to the wavelength) are usually large leading to large effective system Q's. Thus system deadtime is often the dominant cause of deadtime at high frequencies.

4.2.4 Source deadtime. Source deadtime is related to how fast and how effectively the source can be switched off from full power, to thermal noise levels, after the final pulse. Typically this is related to the speed and power leakage of switches, and/or the noise output of power amplifiers. At very high frequencies it becomes considerably more challenging to rapidly modulate a fundamental source with very high on-off ratios. It is usually far easier to implement amplitude and phase control at low frequencies and then upconvert or multiply up to the desired frequency and then amplify using a power amplifier, and this has been the design philosophy behind most succesful spectrometers. Multiplication processes are usually highly non-linear and very fast switching speeds can be obtained at low powers. A more serious problem is related to the use of high gain, high power vacuum tube pulse amplifiers, which can produce high levels of ''dark'' noise. At 94 GHz a 1 kW Klystron amplifier will typically produce 1mW of white noise over a 1 GHz bandwidth (with no input power). The amplifier can be switched off, killing the dark noise—but in commercial modulators this typically takes of order 80 ns during which time the detection noise floor is degraded. Cornell has made progress in designing their own modulators to reduce this deadtime to around 20 ns.[40] In St Andrews, we use an alternative method where a fast laser controlled waveguide switch is used to cut-off the dark noise immediately after the final pulse. This has <1 ns switching with >25 dB on/off ratios and will handle 1 kW and can operate at switching speeds approaching 10 kHz. In conjunction with induction mode operation (discussed later) this can take the level of ''dark noise'' to thermal noise levels at the detector.

4.2.5 Detection deadtime. In most pulse ESR systems, the excitation power levels are usually such that they can seriously damage (or saturate) modern low noise solid-state detection systems unless steps are taken to protect the receiver during the main pulse sequence. Recovery times of amplifiers or detection systems can range from nanoseconds to hundreds of nanoseconds depending on components and the severity of saturation. Thus it becomes extremely important to have a large isolation between cavity and detector during the pulse sequence. This usually takes the form of receiver protection based on a fast switch, where the power handling of the switches is crucial. At X-band commercial switches have been developed which can handle 1 kW of power. However, no such high power devices are currently commercially available at 94 GHz or higher frequencies (at least with computer controllable fast switching times). On the other hand, fast semiconductor based switches with 1 nanosecond rise-time are available at lower powers at 94 GHz (50 dB on-off ratio with 2dB insertion loss). The Santa Barbera group is also experimenting with quasi-optical laser driven semiconductor switches operating in reflection.[42] In all cases the use of induction mode operation, to increase isolation between source and detector, eases the experimental requirements considerably.

4.3 Measurement bandwidth

The detected noise power will be proportional to the measurement bandwidth and should be set at a level appropriate for the type of measurement and time response of

the spin system through an appropriate post-detector filter. For a 1 GHz measurement bandwidth the single-shot noise floor will be around the 0.1 nW level.

4.4 Averaging and pulse repetition time

The ability to average in real time at high repetition rates, only limited by the T_1 of the system, is extremely important in pulsed EPR systems. Only in this case can pulsed EPR approach the sensitivity of cw EPR. Real time averagers are now available from Agilent (formerly Acqiris) that offer averaging rates as high as 1 MHz with 1 GHz sampling speeds. Similar specifications are now offered by the Bruker SpecJet sytem. Top end oscilloscopes also continually improve their performance and now offer sampling rates up to 50 GHz with 20 GHz analog bandwidths, albeit with lower averaging speeds. In practice other factors often limit the pulse repetition time at high powers including the pulse generator, high power switches and in some cases software control and detector recovery, and of course, the relaxation of the spin system. When averaging over long periods care should be taken to evaluate the effect of unwanted coherent effects appearing below the noise floor, which can limit the practical number of averages. These can occur, for example, by low level pick-up in the detector or caused by artefacts in the A-to-D convertor.

5. St Andrews system design

In this section we discuss some of the specifics of the St Andrews 94 GHz high field pulse spectrometer, which is designed to offer extremely high power pulses in combination with very low deadtime. Many of the citical components have been designed in-house and offer state-of-the-art performance.

5.1 Current system performance

The spectrometer can be programmed to give arbitrary pulse sequences at kW power levels with sub-nanosecond resolution with phase cycling and ELDOR capabilities integrated. Pulse lengths as short as 800ps can be generated at 250W power levels (or 1.5 ns pulses at 1 kW power levels). Experiments have shown $\pi/2$ pulses as short as 2 ns with a cavity and 5 ns without a cavity. Highest sensitivity has been achieved using the non-resonant sample-holder in both cw and pulse modes for low to medium loss samples. CW concentration sensitivity is comparable with performance obtained from Bruker's commercial W-band system using a high Q cylindrical mode resonator under similar instrumental conditions. However cw sensitivity for non-resonant systems can be considerably higher for systems that saturate because higher power levels can be applied in non-resonant systems. Initial experiments indicate that pulse sensitivity would appear to be in line with the gains predicted in section 4.

Very low deadtime has also been achieved. Source deadtime has been reduced to a few nanoseconds, both cavity and detector deadtime are of the order of 1 ns, and experiments have indicated that deadtime due to reflections within the system optics have almost entirely been eliminated. The current deadtime appears to be dominated by unwanted excitation of higher order modes in the coupling structure above the cavity/sample-holder. This leads to coherent interference signals that are 80–90dB below the final pulse within 2 ns of the end of the final pulse. Thus at low powers (100 mW) almost zero deadtime measurements can be made (albeit with long $\pi/2$ pulses). There is strong evidence that this deadtime is not a fundamental effect and may simply be associated with small imperfections in the coupling structure. If this is true further significant reductions in the level of interfering signals should be possible.

5.2 System overview

The system uses a heterodyne architecture similar to the one used in the "Krymov Bridge" except that high power passive multipliers are used rather than IMPATT multipliers and amplifiers. This allows pulse sequences and phase cycling and frequencies to be defined at low frequencies using a fast word generator with a 2.6 GHz clock. Pulses are generated at power outputs of approximately 100 mW with full 100% amplitude modulation and delivered to the 1 kW power pulse EIK amplifier. A high power waveguide isolator is followed by a laser driven silicon waveguide switch, used to gate out the dark noise following the last pulse. The signal then is transformed to a high quality Gaussian beam with 99.8% beam purity before passing through a series of very high performance quasi-optical isolators that ensure that reflections within the system are negligible. A linearly polarized beam is then transmitted to a wide bore corrugated pipe, which tapers down to a cylindrical waveguide of diameter 3 mm to which non-resonant sample holders or cavities can be attached that operate in induction mode. In induction mode we make use of the fact that the sample will absorb or emit a circularly polarised beam on resonance, which in turn transfers power to the orthogonal linear polarisation state. It is this orthogonal polarisation that is detected, being directed towards the receiver *via* another set of quasi-optical isolators. This has the advantage of providing significant isolation between the source and the detector. The receiver is protected using a fast waveguide switch and operates with a 1.8 GHz IF that is subsequently filtered and passed through an IQ demodulator. Output is monitored *via* a fast scope or a fast averager.

5.3 Induction mode cavities and sample holders

One of the most critical performance parameters for the whole system is the isolation achieved between source and detector and in analogy with NMR systems this is often achieved using induction mode techniques.

The cavity or sample holder is at the field centre of a large superconducting magnet within a flow cryostat. Coupling to the cavity from the optics is *via* a large diameter, thin walled stainless steel, cylindrical corrugated pipe. The depth of the corrugations and the aperture of the pipe are designed to reduce any reflection at the interface of the pipe and optics to negligible levels. To maximise the isolation between the source and detector it is vital that coupling between the orthogonal states is kept to a minimum off-resonance. For the non-resonant sample holder, polarisation isolation has been optimized by placing a miniature roof mirror below the sample that can be rotated and raised *via* miniature piezo-electric motors. This is adjusted to help cancel out any small cross-polar components scattered from the sample or sample-holder. Aligning the pipe accurately relative to the output beam is also very important. In practice cross-polar isolations greater than −50 dB have been routinely obtained using these polarization tuning mechanisms

5.4 Pulse sources and pulse generation

Most of the pulse forming and phase manipulation is done at 7.83 GHz before multiplication to 94 GHz. A low noise 7.83 GHz source is generated by upconverting a low noise DRO or a PMYTO operating at 7.68 GHz, by 150 MHz. The Dielectric Resonator Oscilator (DRO) and Permanent Magnet YIG Tuned Oscillator (PMYTO) are both phase locked to a 10 MHz reference for long term stability. This source is then amplitude modulated using a wideband double balanced mixer that allows pulses as short as 500 ps to be generated at 7.83 GHz with 17 dB on-off ratio. This signal is then multiplied to 94 GHz *via* an active trebler and two passive doublers (from Virginia Diodes). The non-linearity of the multiplication process means full 100% amplitude modulation is achieved in combination with

considerable pulse sharpening. We have generated pulses at 94 GHz as short as 110 ps, at 200 mW power levels, although it is possible to generate any arbitrary pulse sequence with at least 80 ps rise and fall-times[52] (where the measurement was limited by the 12 GHz analog input bandwidth of the fast digital scope used in the measurement).

The desired pulse sequences are generated with a PARBERT word generator operating with a 2.66 GHz clock (from Agilent) that allow arbitrary pulse sequences to be generated with 380 ps resolution. Further control sequences use fast digital delay generators (from Highland Technology).

The spectrometer is also designed to allow the relative phase of the pulses to be manipulated at nanosecond timescales, by switching between different paths with different time delays at 7.83 GHz. This allows phase cycling of pulse sequences, and is used to eliminate offsets, spurious signals and to select particular electronic interactions. After generating the pulses, they are amplified to 1 kW using an Extended Interaction Klystron (EIK) pulse amplifier (from CPI), which has a 1 GHz instantaneous bandwidth. The wideband noise from this amplifier is attenuated by at least 25 dB using a low loss, optically excited waveguide silicon switch capable of handling and switching 1 kW (designed and constructed in-house). A miniature Q-switched laser is used to provide the optical excitation and can provide 1 ns pulses on demand (with 500 ps jitter) at repetition rates up to 50 kHz.

5.5 Phase coherent detection system

The detection architecture is a fully coherent 94 GHz superheterodyne system with a 1.8 GHz intermediate frequency (IF) designed and constructed in-house. The 92.2 GHz local oscillator (LO) is provided by a $12 \times$ multiplication of a 7.68 GHz source. The excitation signal is provided by upconverting the 7.83 GHz by 150 MHz and filtering the LO signal with a tracking high Q YIG filter. This signal can then be amplitude or phase modulated to provide arbitrary pulse sequences before multiplication to 94 GHz. Detection is done *via* a conventional Schottky mixer system and the 1.8 GHz IF frequency is amplified and then mixed in an IQ demodulator with a 1.8 GHz signal derived from the 150 MHz source. This then gives two fully phase coherent quadrature outputs. At present, these signals are observed and averaged *via* a LeCroy 20 Gs/s digital sampling oscilloscope, although integration with a fast averaging card (from Agilent) is currently underway. Pre-amplification at 94 GHz is avoided to improve power handling and maximise dynamic range with only a marginal loss in sensitivity. The receiver is protected with a 94 GHz PIN diode that provides > 50 dB on-off ratios and 2 dB insertion loss that can be switched within 1 ns.

5.6 Spectrometer front end system design

The spectrometer front-end design is largely determined by the need to provide high levels of isolation between source, cavity and detector, extremely low standing wave levels between components and very low loss transmission for both exciting pulses and signal. This is achieved quasi-optically and a schematic of the design and implementation is shown in Fig. 1.

High performance corrugated feedhorns, designed in-house, are used to couple power to fundamental Gaussian modes with > 99.5% efficiency.[53] These beams are then focused through quasi-optical isolators using large off-axis mirrors that are arranged to provide zero gain and frequency independent operation, whilst minimizing beam distortion. The isolators consist of angled high performance Faraday rotators that are placed between angled wire-grid polarisers. The Faraday rotators are temperature tuned to provide optimal performance at 94 GHz. All reflections from polarisers and rotators are terminated with very high performance quasi-optical loads with better than −80 dB return loss. Several isolators are placed in
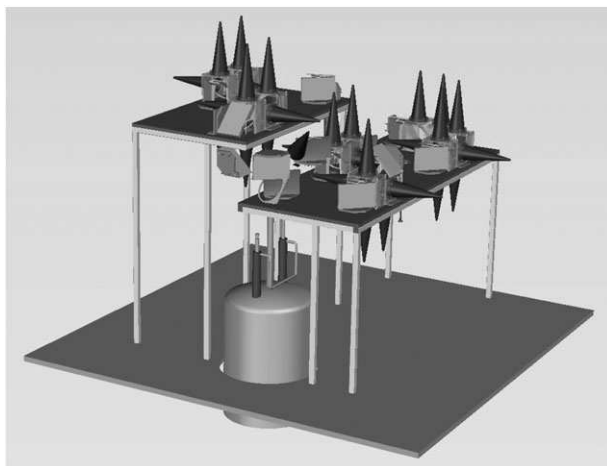
Fig. 1 Schematic figure indicating the overall design and implementation of the front-end of the spectrometer featuring off-axis mirrors, quasi-optical Faraday rotators and high performance loads.

series to provide better than 90 dB isolation between source and cavity and provide better than 70 dB isolation between cavity and detector.[54] The insertion loss of each isolators is ∼0.3 dB.

5.7 Control software

Modern pulse ESR spectrometers are complex and and sophisticated instruments that demand considerable flexibility in the user-interface, whilst incorporating many safety features, and the provision of control software is a major task in itself. The software for the spectrometer is written in C using LabWindows CVJ and offers the user considerable flexibility in setting up pulse sequences.

6.   Discussion

A pulse EPR spectrometer with low deadtimes in conjunction with large excitation bandwidths and high sensitivity opens up a huge range of new experiments based on precise manipulation of electron spins over large bandwidths. These include:

6.1   Fourier transform EPR and FID detection

At present because typical experimental deadtimes are in the 50–100 ns range, effective FID detection is largely restricted to the few cases where inhomogenous linewidths are less than one or two gauss. Similarly echo techniques are generally restricted to cases where the phase memory time is at least comparable to the deadtime. This has proved restrictive especially for studies of motional dynamics using nitroxides where T_2's can be as short as a few nanoseconds. However, a deadtime of a few nanoseconds would transform this situation. It would make FID detection a viable technique for a large range of samples for both 1-D and multi-dimensional experiments similar to those commonly used in NMR and significantly increase the capability of 2-D ESR techniques to study motional dynamics of biomolecules. Many of the potential opportunities have been outlined by Freed in a number of papers and reviews.[11,12,55]

6.2 Hyperfine and electron-dipolar spectroscopies

There are many good spectroscopic reasons to perform ENDOR or PELDOR at high fields, mostly associated with orientation selectivity[34,56] and better resolution. However, for the reasons discussed before, gains in concentration sensitivity scaling with frequency or higher are also expected for many types of spin echo experiments at high fields. This is important for many ENDOR and PELDOR experiments where typical signal to noise often lead to long averaging requirements and place lower limits on the required sample concentration. At the moment this gain in concentration sensitivity with frequency is not usually observed experimentally in modern commercial spectrometer systems simply because of the reduced available power at high frequencies leading to non-optimum excitation bandwidths. However, preliminary high field, high power PELDOR experiments using non-resonant sample-holders, at St Andrews, are currently giving very promising results, consistent with the gains in sensitivity predicted. Similar gains would be expected for many ENDOR methodologies.

6.3 Dynamic nuclear polarisation (DNP)

DNP methodologies have recently been attracting a great deal of attention, due to recent demonstrations of spectacular enhancements in NMR sensitivity. Improvements of over 40 000 have been demonstrated for ^{13}C, in the liquid state, by the Amersham Group (now part of GE).[57] In this method ^{13}C or ^{15}N nuclei are polarized using the trityl radical at very low temperatures (1.5 K) and high fields (3.3 T), before being rapidly dissolved and transferred to a standard NMR spectrometer or MRI instrument at room temperature. This is the basis of Oxford Instruments new Hypersense technology. At present this technique appears largely restricted to small molecule systems, but it is already clear that this approach is likely to have a very significant impact on new MRI methodologies and for a large number of NMR applications.

In solid state DNP, the MIT group have been advancing the field for a large number of years and have recently reviewed the area.[58] They have demonstrated absolute DNP enhancements of several hundred for protons in high magnetic fields, at cryogenic temperatures, in field strengths greater than 5 T, using a number of different approaches, including the use of efficient probe-heads,[50] high power gyrotrons,[59,60] and novel mixtures of radicals and bi-radicals.[61,62] Such demonstrations have encouraged a large number of other groups to enter the field and there are now at least four major commercial companies with active DNP programs (Oxford Instruments, GE, Bruker, JEOL).

DNP methodologies are attractive at high fields and low temperatures because of the very high electron polarisation, that can in principle be transferred to the nuclei. However, all cw polarisation transfer methodologies (Overhauser effect, solid effect, cross effect and thermal mixing) become less efficient at high fields, requiring very high powers or long polarisation times.

In principle, coherent polarisation transfer methods using pulse techniques ought to offer greater efficiency, and a number of methodologies have been suggested and reviewed,[58,63] including rotating frame DNP, the Integrated solid effect and the NOVEL experiment. The latter is based on an electron spin locking sequence, where the electron Rabi frequency is adjusted to equal the NMR frequency, to fulfill the Hartmann-Hahn condition, commonly used to transfer polarization between nuclei in NMR experiments. In theory this methodology ought to be generally applicable to many systems, independent of magnetic field, but requires extremely high B_1 fields for protons (50 G at 3.3 T). This is currently at the absolute limits of what has been experimentally demonstrated on small samples, at 94 GHz. However, this condition is relaxed for nuclei for low γ nuclei, where it is may be possible to use high volume samples consistent with NMR or MAS probeheads.

As yet, these methodologies are largely untested in high magnetic fields, but are likely to be the subject of considerable investigation in the years ahead.

7. Conclusions and outlook

The last few years have seen very significant advances in mm-wave and sub-mm-wave technology and it is becoming clear that considerable increases in performance can be anticipated in the next few years as high power sources and amplifiers are developed. These developments will initially be led by the strong requirements for extra sensitivity and resolution in high field electron dipolar (PELDOR) and hyperfine spectroscopies and the potential for more efficient polarisation transfer routes in High Field Dynamic Nuclear Polarisation. However, perhaps the most tantalising prospect is the development of ultra-low deadtime systems, which would open up a new time-window for EPR and make FID detection a realistic prospect for many of the spin systems currently studied today.

References

1   Y. S. Lebedev, Royal Society of Chemistry, Cambridge, 1994, vol. 14, p. 63.
2   A. A. Doubinskii, eds. B. C. Gilbert, M. J. Davies and D. M. Murphy, Royal Society of Chemistry, Cambridge, 1998, vol. 16, p. 211.
3   G. M. Smith and P. C. Riedi, eds. B. C. Gilbert, M. J. Davies and D. M. Murphy, Royal Society of Chemistry, Cambridge, 2000, vol. 17, p. 164.
4   G. M. Smith and P. C. Riedi, eds. B. C. Gilbert, M. J. Davies and D. M. Murphy, Royal Society of Chemistry, Cambridge, 2002, vol. 18, p. 254.
5   G. M. Smith and P. C. Riedi, eds. B. C. Gilbert, M. J. Davies and D. M. Murphy, Royal Society of Chemistry, Cambridge, 2004, vol. 19, p. 338.
6   P. C. Riedi, eds. B. C. Gilbert, M. J. Davies and D. M. Murphy, Royal Society of Chemistry, Cambridge, 2006, vol. 20, p. 245.
7   A. I. Smirnov, eds. B. C. Gilbert, M. J. Davies and D. M. Murphy, Royal Society of Chemistry, Cambridge, 2002, vol. 18, p. 109.
8   G. R. Eaton and S. S. Eaton, *Applied Magnetic Resonance*, 1999, **16**, 161–166.
9   *Very High Frequency (VHF) ESR/EPR*, Kluwer Acadamic, New York, 2004.
10 K. Mobius, *Chem. Soc. Rev.*, 2000, **29**, 129–139.
11 Z. C. Liang and J. H. Freed, *J. Phys. Chem. B*, 1999, **103**, 6384.
12 J. H. Freed, *Annual Review Phys. Chem.*, 2000, **51**, 655–689.
13 K. A. Earle, D. E. Budil and J. H. Freed, *Advances in Magnetic and Optical Resonance*, 1996, **19**, 253–323.
14 K. A. Earle and J. H. Freed, *Applied Magnetic Resonance*, 1999, **16**, 247–272.
15 W. R. Hagen, *Coord. Chem. Review*, 1999, **192**, 209.
16 E. J. Reijerse, P. J. van dam, A. A. K. Klaasen, W. R. Hagen, P. J. M. van Bentum and G. M. Smith, *Applied Magnetic Resonance*, 1998, **14**, 153.
17 P. J. van Dam, A. A. K. Klaasen, E. J. Reijerse and W. R. Hagen, *Journal of Magnetic Resonance*, 1998, **130**, 140.
18 D. Gatteschi, *J. Phys. Chem.*, 2000, **104**, 9780.
19 D. M. Murphy and C. C. Rowlands, *Current Opinions Solid State Materials Science*, 2001, **5**, 97.
20 K. Katsumata, *J. Phys. Condensed Matter*, 2000, **12**, 589.
21 M. Martinelli, C. A. Massa, L. A. Pardi, V. Bercu and F. F. Popescu, *Physical Review B*, 2003, **67** art.no. 014425.
22 J. van Slageren, S. Vongtragool, B. Gorshunov, A. A. Mukhin, N. Karl, J. Krzystek, J. Tesler, A. Muller, C. Sangregorio, D. Gatteschi and D. Dressel, *Physical Chemistry Chemical Physics*, 2003, **5**, 3837.
23 T. Prisner, *Adv. Magn. Opt.*, 1997, **20**, 245–300.
24 T. Prisner, M. Rohrer and F. MacMillan, *Annual Review Phys. Chem.*, 2001, **52**, 279.
25 D. Goldfarb and D. Arieli, *Annual Review Biophys. Biomol. Struct.*, 2004, **33**, 441–468.
26 A. Schweiger and G. Jeschke, *Principles of pulse electron paramagnetic resonance*, Oxford University Press, New York, 2001.
27 R. T. Weber, J. A. J. M. Disselhorst, L. J. Prevo, J. Schmidt and Wenckebach, *Journal of Magnetic Resonance*, 1988, **81**, 129–144.

28 A. Y. Bresgunov, A. A. Dubinskii, V. Krymov, Y. G. Petrov, O. G. Poluetkov and Y. S. Lebedev, *Applied Magnetic Resonance*, 1991, **2**, 715–728.

29 T. Prisner, M. Rohrer and K. Mobius, *Applied Magnetic Resonance*, 1994, **7**, 167–183.

30 D. Schmalbein, G. G. Maresch, A. Kamlowski and P. Hofer, *Applied Magnetic Resonance*, 1999, **16**, 185–205.

31 I. Gromov, V. Krymov, P. Manikandan, D. Arieli and D. Goldfarb, *Journal of Magnetic Resonance*, 1999, **139**, 8–17.

32 D. A. Schwartz, E. D. Walter, S. J. McIlwain, V. N. Krymov and D. J. Singel, *Applied Magnetic Resonance*, 1999, **16**, 223.

33 M. Rohrer, O. Brugmann, B. Kinzer and T. Prisner, *Applied Magnetic Resonance*, 2001, **21**, 257.

34 M. M. Hertel, V. P. Denysenkov, M. Bennati and T. F. Prisner, *Magn. Reson. Chem.*, 2005, **43 Spec no.**, S248–255.

35 H. Blok, D. J. A. M. Disselhorst, S. B. Orlinskii and J. Schmidt, *Journal of Magnetic Resonance*, 2004, **166**, 92–99.

36 H. Blok, J. A. Disselhorst, H. van der Meer, S. B. Orlinskii and J. Schmidt, *J. Magn. Reson.*, 2005, **173**, 49–53.

37 S. B. Orlinskii, H. Blok, E. J. Groenen, J. Schmidt, P. G. Baranov, C. de Mello Donega and A. Meijerink, *Magn. Reson. Chem.*, 2005, **43 Spec no.**, S140–144.

38 J. W. Sidabras, R. R. Mett, W. Froncisz, T. G. Camenisch, J. R. Anderson and J. S. Hyde, *Rev. Sci. Instrum.*, 2007, **78**, 034701.

39 J. S. Hyde, W. Froncisz, J. W. Sidabras, T. G. Camenisch, J. R. Anderson and R. A. Strangeway, *J. Magn. Reson.*, 2007, **185**, 259–263.

40 W. Hofbauer, K. A. Earle, C. R. Dunnam, J. K. Moscicki and J. H. Freed, *Review of Scientific Instruments*, 2004, **75**, 1194–1208.

41 S. Takahashi, G. Ramiam, M. S. Sherwin, L. C. Brunel and H. van Tol, *Applied Physics Letters*, 2007, **91**, 174102.

42 S. Takahashi, D. G. Allen, J. Seifter, G. Ramiam, M. S. Sherwin, L. C. Brunel and J. van Tol, *Infrared Physics and Technology*, 2008, **51**, 426.

43 J. P. Barnes and J. H. Freed, *Review of Scientific Instruments*, 1998, **69**, 3022–3027.

44 D. E. Budil, K. A. Earle, W. B. Lynch and J. H. Freed, in *Advanced EPR: Applications in Biology and Biochemistry*, ed. A. J. Hoff, Elsevier, Amsterdam, 1989, pp. 307–340.

45 G. Annino, M. Cassettari, I. Longo and M. Martinelli, *Applied Magnetic Resonance*, 1999, **16**, 45.

46 G. Annino, M. Cassettari, M. Fittapaldi, L. Lenci, I. Longo, M. Martinelli, C. A. Massa and L. A. Pardi, *Applied Magnetic Resonance*, 2000, **19**, 495.

47 G. Annino, M. Cassettari, M. Fittapaldi, I. Longo, M. Martinelli, C. A. Massa and L. A. Pardi, *Journal of Magnetic Resonance*, 2000, **143**, 88.

48 G. M. Smith, J. C. G. Lesurf, R. H. Mitchell and P. C. Riedi, *Review of Scientific Instruments*, 1998, **69**, 3924.

49 M. Fuchs, T. Prisner and K. Mobius, *Review of Scientific Instruments*, 1999, **70**, 3681–3683.

50 V. Weis, M. Bennati, M. Rosay, J. A. Bryant and R. G. Griffin, *J. Magn. Reson.*, 1999, **140**, 293–299.

51 P. Borbat, R. Crepeau and J. H. Freed, *Journal of Magnetic Resonance*, 1997, **127**, 155–167.

52 P. Cruickshank, D. Bolton, D. Robertson and G. M. Smith, *Electronics Letters*, 2007, **43**.

53 P. Cruickshank, D. Bolton, D. Robertson, R. Wylde and G. M. Smith, IRMMW, Cardiff, 2007.

54 R. Hunter, D. Robertson, P. Goy and G. M. Smith, *IEEE Microwave Theory and Techniques*, 2007, **55**, 880–898.

55 Z. Liang, R. H. Crepeau and J. H. Freed, *J. Magn. Reson.*, 2005, **177**, 247–260.

56 V. P. Denysenkov, T. Prisner, J. Stubbe and M. Bennati, *Applied Magnetic Resonance*, 2005, **29**, 375–384.

57 J. H. Ardenkjaer-Larsen, B. Fridlund, A. Gram, G. Hansson, L. Hansson, M. H. Lerche, R. Servin, M. Thaning and K. Golman, *Proc. Natl. Acad. Sci. USA*, 2003, **100**, 10158–10163.

58 T. Maly, G. T. Debelouchina, V. S. Bajaj, K. N. Hu, C. G. Joo, M. L. Mak-Jurkauskas, J. R. Sirigiri, P. C. van der Wel, J. Herzfeld, R. J. Temkin and R. G. Griffin, *J. Chem. Phys.*, 2008, **128**, 052211.

59 M. K. Hornstein, V. S. Bajaj, R. G. Griffin and R. J. Temkin, *IEEE Trans. Plasma Sci. IEEE Nucl. Plasma Sci. Soc.*, 2006, **34**, 524–533.

60 V. S. Bajaj, M. K. Hornstein, K. E. Kreischer, J. R. Sirigiri, P. P. Woskov, M. L. Mak-Jurkauskas, J. Herzfeld, R. J. Temkin and R. G. Griffin, *J. Magn. Reson.*, 2007, **189**, 251–279.
61 C. Song, K. N. Hu, C. G. Joo, T. M. Swager and R. G. Griffin, *J. Am. Chem. Soc.*, 2006, **128**, 11385–11390.
62 K. N. Hu, V. S. Bajaj, M. Rosay and R. G. Griffin, *J. Chem. Phys.*, 2007, **126**, 044512.
63 C. T. Farrar, D. A. Hall, G. J. Gerfen, M. Rosay, J. H. Ardenkjaer-Larsen and R. G. Griffin, *J. Magn. Reson.*, 2000, **144**, 134–141.